

**Optical Coherence Tomography for the Assessment of
Coronary Atherosclerosis and Vessel Response after
Stent Implantation**

Nieves Gonzalo

ISBN 978-90-8559-929-6

Front cover illustration: OCT image of a stent restenosis showing neo-intimal growth with a layered tissue structure

Financial support by Lightlab Imaging, Volcano Corporation, Mercé-V Electro-medica, Cardialysis B.V. and Abbott Vascular for the publication of this thesis is gratefully acknowledged.

Printed by Optima Grafische Communicatie, Rotterdam, the Netherlands

© Nieves Gonzalo 2010

Optical Coherence Tomography for the Assessment of Coronary Atherosclerosis and Vessel Response after Stent Implantation

**Optische Coherentie Tomografie voor de beoordeling van coronaire
Arteriosclerose en de Responsie van het Vat na Stent Implantatie**

Thesis

to obtain the degree of Doctor from the
Erasmus University Rotterdam
by command of the
rector magnificus

Prof.dr. H.G. Schmidt

and in accordance with the decision of the Doctorate Board

The public defence shall be held on

Wednesday the 3rd of February 2010 at 13:30 o'clock

by

Nieves Gonzalo
born in Madrid, Spain



DOCTORAL COMMITTEE

Promoter

Prof.dr. P.W.J.C.Serruys

Co-promoter

Dr. E. Regar

Other members:

Prof. dr. W.J. van der Giessen

Prof.dr. P.J. de Feyter

Prof.dr. C. Macaya

Prof.dr. H. Boersma

Prof.dr. C. Di Mario

For my parents

TABLE OF CONTENTS

Introduction	11
Chapter 1. Basic principles of optical coherence tomography	
1.1 Optical coherence tomography.	15
Chapter 2. Safety of optical coherence tomography.	
2.1 A Multi-Center Evaluation of the Safety of Intra-Coronary Optical Coherence Tomography.	57
Chapter 3. Quantitative lumen and stent analysis with optical coherence tomography.	
3.1 Quantitative Ex-vivo and In-vivo Comparison of Lumen Dimensions Measured by Optical Coherence Tomography (OCT) and Intravascular Ultrasound (IVUS) in Human Coronary Arteries.	67
3.2 Reproducibility of quantitative per strut stent analysis with optical coherence tomography.	79
3.3 Full-Automated Quantitative Analysis of Intracoronary Optical Coherence Tomography: Method and Validation.	91
Chapter 4. Coronary plaque characterization with optical coherence tomography.	
4.1 Combined optical coherence tomography and intravascular ultrasound radio frequency data analysis for plaque characterization. Classification accuracy of human coronary plaques in vitro related to image artifacts.	103
4.2 Atherosclerotic tissue characterization in vivo by Optical Coherence Tomography attenuation imaging.	119
4.3 Multi-Modality Intra-Coronary Plaque Characterization: A Pilot Study.	141
Chapter 5. Detection of high-risk coronary plaques with optical coherence tomography.	
5.1 Diagnosis and treatment of Coronary Vulnerable Plaques.	153

5.2	In Vivo Assessment of High-risk Plaques at Bifurcations with Combined Intravascular Ultrasound Virtual Histology and Optical Coherence Tomography.	169
5.3	Assessment of Culprit and Remote Coronary Narrowings Using Optical Coherence Tomography with Long-Term Outcomes.	181
5.4	Witnessed Coronary Plaque Rupture During Cardiac Catheterization.	189

Chapter 6. In vivo assessment of the effect of coronary stent implantation with optical coherence tomography.

6.1	Optical coherence tomography: clinical applications, and the evaluation of drug-eluting stents.	199
6.2	Incomplete Stent Apposition And Delayed Tissue Coverage Are More Frequent In Drug Eluting Stents Implanted During Primary Percutaneous Coronary Intervention For ST Elevation Myocardial Infarction Than In Drug Eluting Stents Implanted For Stable/ Unstable Angina. Insights from Optical Coherence Tomography	217
6.3	Optical Coherence Tomography Patterns of Stent Restenosis	227
6.4	Optical Coherence Tomography Assessment Of The Acute Effects Of Stent Implantation On The Vessel Wall. A Systematic Quantitative Approach.	239
6.5	Relation between plaque type and dissections at the edges after stent implantation: an optical coherence tomography study.	249
6.6	A critical appraisal of the safety concerns tempering the success of drug eluting stents. Novelties in cardiac imaging: Optical Coherence Tomography.	261

Chapter 7. Optical Coherence Tomography for the evaluation of new generation stents. Assessment of biodegradable stents.

7.1	A bioabsorbable everolimus-eluting coronary stent system (ABSORB): 2-year outcomes and results from multiple imaging methods.	271
7.2	Intracoronary optical coherence tomography (OCT) and histology 2, 3 and 4 years after implantation of bioresorbable everolimus-eluting stents in porcine coronary model: An attempt to decipher the human OCT images in the Absorb trial	287

Chapter 8. Optical coherence tomography in secondary revascularisation.

- 8.1 Optical coherence tomography in secondary revascularisation. 307
Stents and grafts assessment.

Chapter 9. New generation optical coherence tomography.

- 9.1 Second Generation Optical Coherence Tomography in 319
Clinical Practice. - High speed data acquisition shows excellent
reproducibility in patients undergoing percutaneous coronary
interventions

Summary and Conclusions	335
Acknowledgements	345
Curriculum Vitae	349
List of Publications	351
Colour Section	355

INTRODUCTION

Coronary angiography is currently the standard modality for the assessment of coronary artery disease. However, this technique is restricted to a two-dimensional representation of the lumen silhouette without providing information about the vessel wall which is the substrate of atherosclerosis. This limitation led to the development of new intracoronary techniques able to image directly the atherosclerotic plaque. The introduction of intravascular ultrasound (IVUS) allowed a much more detailed evaluation of coronary atherosclerosis, but its limited resolution (axial 150–200 μm) precluded the visualization of certain microstructures. Optical Coherence Tomography (OCT) is a light-based imaging modality that can provide *in vivo* high-resolution images of the coronary artery with a level of resolution (axial 10–20 μm) ten times higher than IVUS but with a penetration depth limited to 1.5–2 mm. The technique uses low-coherent near infrared light to create high-resolution cross sectional images of the vessel. OCT, originally described in the early 1990s, was first applied in the field of ophthalmology. The vascular application, initiated in the mid 90s demonstrated the potential of the technique to identify clinically relevant coronary artery morphology with a level of resolution never reached before *in vivo*.

The aims of this thesis were to assess the value of OCT to provide novel *in vivo* information about coronary atherosclerosis and to evaluate the vessel responses after local treatment of atherosclerotic coronary plaques with stents.

The clinical use of OCT was initially limited by the need of removing the blood during image acquisition (due to the multiple light scattering and substantial signal attenuation caused by red blood cells). The technical development and the simplification of the acquisition method achieved in the last years in order to increase the procedure safety and spread the clinical applicability of the technique are discussed in chapters 1 and 2.

Chapter 3 evaluates the accuracy and reproducibility of OCT for the quantitative analysis of several coronary structures.

Regarding atherosclerosis assessment, we have explored the value of the technique for plaque characterization and the possible sources of error in comparison with histology and with other intracoronary imaging techniques (chapter 4). OCT is also one of the most promising tools for the detection of plaques at high risk of rupture due to its ability to provide information about several features related to plaque “vulnerability” such as plaque composition, presence of macrophages and thickness of the fibrous cap covering the necrotic core. The complementary use of

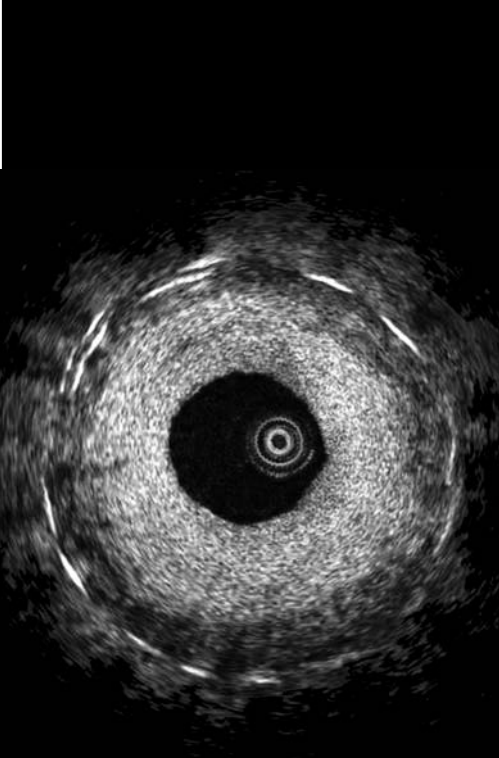
OCT and other imaging techniques (such as IVUS-radiofrequency data analysis) for the detection of high risk plaques is also discussed in this thesis (chapter 5).

Chapter 6 focuses in the use of OCT for the assessment of the acute and long-term effects of stent implantation on the vessel wall. During stenting, OCT allows a detailed evaluation of stent apposition and it is able to detect different types of vessel injury caused by stent implantation. At follow-up, the technique can image the tissue coverage of individual struts even when this consist of tiny layers of tissue as it happens frequently with drug-eluting stents. This unique capability has raised an increasing interest as the absence of struts coverage has been related to stent thrombosis in pathological studies. This thesis shows also the possible influence of the clinical scenario in which the stent is implanted in struts apposition and coverage by tissue at follow up. The new information about stent restenosis provided by OCT is discussed in chapter 6.

We assessed the value of OCT for the evaluation of new generation devices (fully absorbable stents) developed in order to overcome the risks and limitations of conventional metallic stenting (i.e. stent thrombosis) (chapter 7).

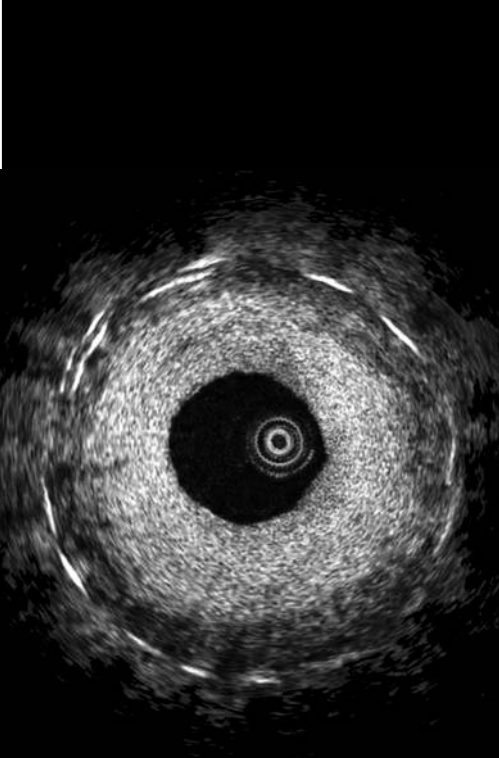
The number of patients with previous procedures (surgical or percutaneous) that are admitted for new catheterization continues to increase worldwide. Chapter 8 aims to illustrate the potential of OCT for the evaluation of these patients. Apart from its ability to assess previously implanted stents and identify causes of stent failure, OCT can also provide new information about coronary venous or arterial grafts.

The final chapter of the thesis is dedicated to the new generation of OCT systems (Fourier Domain, FD-OCT) and their reproducibility for plaque characterization and stent assessment in the clinical practice (chapter 9).



CHAPTER 1

Basic principles of OCT



1.1

Optical coherence tomography

Regar E, Gonzalo N, van Soest G, Serruys PW. In Mukherjee D, Bates E, Roffi M, Moliterno DF editors: Cardiac Catheterization, Coronary and Peripheral Angiography and Interventional Procedures.

Informa Healthcare. In press.

INTRODUCTION

Optical coherence tomography (OCT) is a light based imaging modality showing tremendous potential in the coronary circulation. Compared to traditional intravascular ultrasound (IVUS), OCT has a ten-fold higher image resolution given the use of light rather than sound. This advantage has seen OCT successfully applied to the assessment of atherosclerotic plaque, stent apposition and tissue coverage, introducing a new era in intravascular coronary imaging.

The origins of OCT date back to 1990. David Huang was in his fourth year of an M.D.-Ph.D. program at Massachusetts Institute of Technology (MIT). He had been studying Optical Coherence Domain Reflectometry (OCDR) to perform ranging measurements in the eye. The OCDR project was an offshoot of femtosecond ranging projects that had been ongoing in Professor James Fujimoto's laboratory. The retinal OCDR scans however were very hard to interpret. The thought occurred to Dr. Huang that by adding transverse scanning to OCDR graphs one would create an image that would be much easier for a human to interpret than a set of OCDR waveforms. All that was required was to add a translation stage and a software package to convert a data matrix into an image.

The central problem in making tomographic images using light was to develop a technique that would permit reflections from various depths to be measured and recorded in a fashion analogous to ultrasonic imaging. In the case of sound, electronic circuits are fast enough to separate the echoes from structures that are within the resolution cell of the ultrasonic transducer. In the case of light, an interferometer has to be employed to overcome measurement difficulties caused by the speed of light that is much faster than the speed of sound. By using an interferometer, for the first time it was possible to record reflections from various depths in a biological tissue.

Since 1990, OCT technology has generated over 5000 articles in academic journals. The first manuscript from MIT, published in 1991, describes the basic concept of an OCT imaging system and discusses its possible applications in both retinal and arterial imaging [1]. In 1996 a second manuscript was published, that dealt specifically with the possibility of imaging coronary arteries with an OCT device [2].

It became clear early on that OCT could contribute to the diagnosis of ocular diseases. It was believed that the new technology had the potential to serve as an *in vivo* microscope that could obtain non-excisional biopsy information from locations at which a conventional biopsy was either impossible or impractical to perform. A second research thrust from the MIT group was to push the resolution of the technology to increasingly higher levels using wider bandwidth optical

sources. With sufficiently wide bandwidth sources, one may be able to resolve subcellular structures and measure the ratio of the nuclear volume to the total cell volume in a manner similar to what a pathologist does when diagnosing cancer. In the days since the initial discussions in Professor Fujimoto's office, several members of the MIT OCT team have gone on to start academic OCT research programs throughout the United States.

Compared to an OCT microscope, used in ophthalmology and in most experimental settings, the application of OCT within the human vascular system, particularly within coronary arteries, represents a specific challenge, as a number of principal problems need to be overcome. Therefore, the intracoronary application of OCT has relatively slowly, but steadily increased over the last decade, with a commercially available system for clinical use (Lightlab Imaging Inc, Westford, MA) being currently approved in Europe and Japan. Today, the technology development from "time-domain OCT" to "Fourier-domain OCT" has the potential to dramatically changing the research landscape allowing for a widespread clinical intracoronary application in research and patient care. The chapter will discuss these technical principles of intracoronary OCT, will summarize the preclinical and clinical research, discuss potential clinical applications and explain the practical performance in the catheterization laboratory. Differences in time-domain versus Fourier-domain OCT will be pointed out whenever relevant.

ANATOMIC CONSIDERATIONS

Principally, all epicardial coronary arteries, venous or arterial grafts accessible by a guiding catheter, are eligible for OCT imaging.

Considerations regarding anatomy and patient characteristics arise from the fact (a) that OCT imaging requires a blood-free environment and (b) from OCT catheter design. As the imaging procedure demands temporary blood removal and flush (e.g. lactated ringers or X-ray contrast medium), it should not be performed in patients with severely impaired left ventricular function or those presenting with hemodynamic compromise. Further, OCT should be used with caution in patients with single remaining vessel or those with markedly impaired renal function. Lesions that are ostially or proximally located cannot be adequately imaged using proximal balloon occlusion and thus, a non-occlusive technique may be preferred in these circumstances. Large caliber vessels or very tortuous vessels often preclude complete circumferential imaging as a result of a non-central, non-coaxial position of the OCT imaging probe within the vessel.

These anatomic limitations seem to be significantly attenuated in Fourier-domain OCT, as the pullback speed is much higher and as a result, the duration of ischemia and the amount of potentially nephrotoxic flush is much lower. Increased penetration depth and scanning range allow imaging of the complete circumference of large and tortuous vessels. The design as short monorail catheter enables to negotiate even complex lesions by selecting an appropriate standard guide wire. As there is no proximal balloon occlusion necessary, also ostial lesions, bifurcations and large vessels can be visualized.

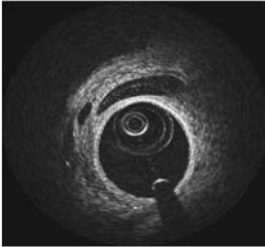
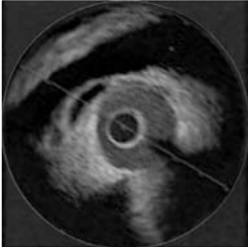
FUNDAMENTALS

The principle is analogous to pulse-echo ultrasound imaging, however light is used rather than sound to create the image. Whereas ultrasound produces images from backscattered sound “echoes,” OCT uses infrared light waves that reflect off the internal microstructure within the biological tissues. The use of light allows for a 10 fold higher image resolution, however this is at the expense of a reduced penetration depth and the need to create a blood-free environment for imaging. In coronary arteries blood (namely red blood cells) represents a non-transparent tissue causing multiple scattering and substantial signal attenuation. As a consequence, blood must be displaced during OCT imaging. This procedure is potentially causing ischemia in the territory of the artery under study. The need for balloon occlusion and intra-coronary flush are at the forefront of emerging developments to simplify the OCT image acquisition process. Automated catheter pullbacks at very high speed are currently under development in OCT systems using optical Fourier-domain imaging. Faster pullback speeds offer the potential to scan an entire stent within a matter of 5-6 seconds.

OCT Principles

OCT utilizes a near infrared light source (approx 1300nm wavelength) in combination with advanced fibre-optics to create a dataset of the coronary artery. Both the bandwidth of the infrared light used and the wave velocity are orders of magnitude higher than in medical ultrasound. The resulting resolution depends primarily on the ratio of these parameters, and is one order of magnitude larger than that of IVUS: the axial resolution of OCT is about 15 μm . The lateral resolution is mainly determined by the imaging optics in the catheter and is approximately 25 μm . The imaging depth of approximately 1.0-1.5mm within the coronary artery wall is limited by the attenuation of light in the tissue [TABLE 1]. Analogous to

Table 1: Comparison OCT and IVUS

	OCT	IVUS
		
Axial Resolution	10-20 μm	100-150 μm
Penetration depth	1.5-2 mm	4-8 mm
Probe size	0.4 mm	1.1 mm
Pullback speed	0.5 mm/s	Up to 40 mm/s
Blood removal needed	Yes	No
Plaque characterization	Yes	Yes
Fibrous cap measurement	Yes	No
Vessel remodelling	No	Yes

ultrasound imaging, the echo time delay of the emitted light is used to generate spatial image information, the intensity of the received (reflected or scattered) light is translated into a (false) colour scale. As the speed of light is much faster than that of sound, an interferometer is required to measure the backscattered light [3]. The interferometer splits the light source into two “arms” – a reference arm and a sample arm, which is directed into the tissue. The light from both arms is recombined at a detector, which registers the so-called interferogram, the sum of reference and sample arm fields. Because of the large source bandwidth, the interferogram is non-zero only if the sample and reference arms are of equal length, within a small window equal to the coherence length of the light source [4, 5].

Time-Domain OCT

In time-domain (TD-) OCT, the length of the reference arm is scanned over a distance of typically a few millimetres, by moving a mirror. The point from which intensity is collected from the sample arm is moved through the tissue accordingly, and the amplitude of the recorded interferogram in a scan corresponds to the reflectivity of the tissue along the direction of the sample beam. By scanning the beam along the tissue, in a rotary fashion for intravascular imaging, an image is built up out of neighbouring lines. Figure 1 shows the currently commercially available TD-OCT system (Lightlab Imaging, Westford, MA, USA)

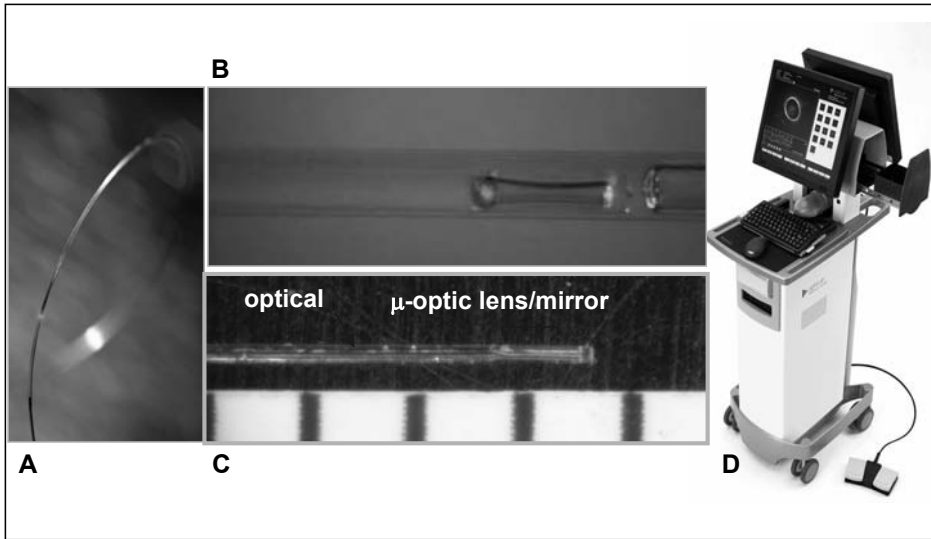


Figure 1 The currently commercially available TD-OCT system (Lightlab Imaging, Westford, MA, USA). A) The OCT imaging wire with an outer diameter of 0.019 inch B) Magnification of the distal catheter tip C) Magnification of the 0.006 inch rotating single-mode fibre-optic core, located within the distal sleeve of the imaging wire D) Imaging console with pullback device allowing for real-time image display and data storage.

Fourier-Domain OCT

A new generation of OCT systems operates in the frequency (rather than time-) domain, also called Fourier domain. The interferogram is detected as a function of wavelength, either by using a broadband source as in the time domain systems, and spectrally resolved detection, or alternatively by incorporating a novel wavelength-swept laser source [6] [7] [TABLE 2]. This latter technique is also called “swept-source OCT”, or optical frequency domain imaging (OFDI), and capitalizes most effectively on the higher sensitivity and signal-to-noise ratio offered by Fourier domain detection. This development has led to faster image acquisition speeds, with greater penetration depth, without loss of vital detail or resolution, and represents a great advancement on current conventional OCT systems. From the signal received in one wavelength sweep, the depth profile can be constructed by the Fourier transform operation that is performed electronically in the data processing unit. All other components of a Fourier-domain system (the interferometer, the catheter, including the imaging optics, display) are comparable in principle to those in a time-domain OCT system.

The scan speed, or line rate, in a time-domain-OCT system are limited by the achievable mechanical scan speed of the reference arm mirror, and by the

Table 2: Characteristics of time domain OCT (TD-OCT) and Fourier domain OCT (FD-OCT). Characteristics of TD-OCT are given for the commercially available Lightlab Imaging (Westford, MA, USA) system, characteristics of FD-OCT are based on non/commercially available prototypes.

	TD-OCT	FD-OCT
	fixed light source and variable reference mirror	light source with variable wavelength and fixed reference mirror
Axial Resolution	10-20 μm	Up to 7 μm
Penetration depth	1.5-2 mm	1.5-2 mm
Optical core	ImageWire	Integrated in catheter
Maximum pullback speed	3 mm/s	Up to 40 mm/s
Scan diameter	7 mm	>10 mm
Blood removal needed	Yes	Yes

sensitivity of the signal detection [8]. The source wavelength in Fourier-domain OCT can be swept at a much higher rate than the position scan of the reference arm mirror in a time-domain OCT system. In addition, Fourier-domain OCT has a higher sensitivity than time-domain OCT at large line rates and scan depths [9-11]. These features can be put to good use in larger scan speeds, of the order of 105 lines per second. In a Fourier domain OCT system, the wavelength range of the sweep determines the resolution of the image, while the imaging depth is inversely related to the instantaneous spectral width of the source.

The increased sensitivity of Fourier-domain OCT also allows for larger imaging depths. The attenuation of light by the tissue is the same for time-domain and for Fourier-domain OCT, but the lower noise of the latter makes it possible to discern weaker signals that would be indistinguishable from the background in time-domain OCT. The depth range from which useful anatomical information can be extracted is extended by a factor of about 3 [12]. Clinically, this advantage enables the assessment of coronary micro-structures well beyond the arterial-lumen border.

Fourier domain OCT systems produce images much faster than standard video-rate, so recorded data has to be replayed for inspection by the operator. Currently, OCT systems scan 200-500 angles per revolution (frame), and 5-10 images per mm in a pullback. If these parameters are maintained with high-speed

systems, 20 mm/s (or higher) pullback speeds are possible at the same sampling density as conventional OCT data. Figure 2 shows different FD-OCT prototypes as used at the Thoraxcenter in 2008. Figure 3 illustrates FD-OCT images as obtained in in-vivo in normal porcine coronary arteries.

The high scan speeds have been employed for real-time volumetric imaging of dynamic phenomena including fast pullbacks for intra-coronary imaging with minimal ischaemia, [12] and retinal scans with minimal motion artefacts. [13] Imaging of dynamic phenomena in time, or rather removing motion artefacts, are the prime applications of high-speed OCT. 3-Dimensional rendering of volumes becomes possible if motion during the scan is limited. The high data rate of novel OCT technologies could also be used to increase sampling density, either in the longitudinal (pullback) or angular direction. A smaller spacing between frames in a pullback would lead to a better sampling of small scale features in the arterial or stent geometry that would be missed at 100 μm inter-frame distance. Denser sampling in the angular direction would facilitate speckle filtering in OCT images. Speckle is a major obstacle for the development of parametric and quantitative imaging techniques. These possibilities are still largely unexplored.

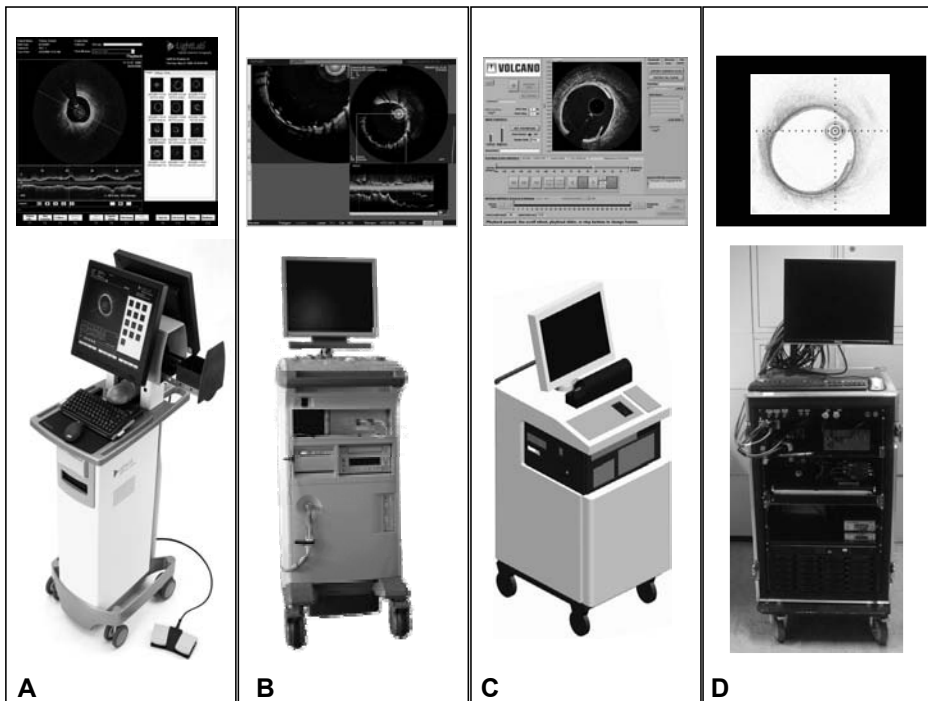


Figure 2 Different FD-OCT prototypes as used at the Thoraxcenter in 2008 A) M4 system, Lightlab Imaging, Westford, MA, USA , B) Terumo OCT C) Volcano OCT D) MGH OFDI system (G. Tearney and B. Bouma, Wellman Center for Photomedicine, MGH, Boston, MA, USA)

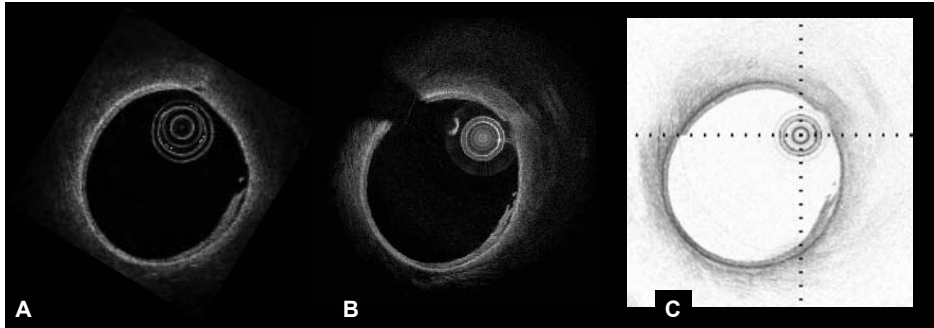


Figure 3 FD-OCT images as obtained in in-vivo in normal porcine coronary artery. The coronary vessel wall shows a three layer appearance and an intimal dissection is visible in 4 o clock position. A) M4 prototype, Lightlab Imaging, Westford, MA, USA , B) Terumo OCT C) MGH OFDI system (G. Tearney and B. Bouma, Wellman Center for Photomedicine, MGH, Boston, MA, USA)

INDICATIONS

To date, there is no established indication for the clinical use of OCT in patient care. However, there are a variety of research applications, where OCT is clearly accepted as the “golden standard”. We summarize the accepted research applications and illustrate the potential clinical implications of OCT findings.

The Role of OCT in Stent Imaging

Coronary artery lesions and results following percutaneous coronary intervention (PCI) are usually assessed angiographically. This luminogram technique provides a unique overview of the coronary tree, information regarding anatomy and topography and can confirm the presence of atherosclerosis with high specificity. The prognostic relevance for subsequent cardiac events, such as myocardial infarction, however, is limited. Furthermore, stent implantation and optimisation undertaken using angiographic guidance alone has been shown to result in more frequent incomplete stent expansion and an increased future risk of target vessel revascularisation when compared to guidance with IVUS.

Assessment of acute stent apposition

For the past two decades, IVUS has been used to assess the acute result following stenting, giving valuable information on stent expansion, strut apposition and signs of vessel trauma including dissections and tissue prolapse. IVUS studies [14, 15] suggested that stent strut malapposition is a relatively uncommon finding, observed in approx 7% of cases, and that strut malapposition does not

increase the risk of subsequent major adverse cardiac events. In contrast, OCT can visualize the complex coronary arterial wall structure after stenting in much greater detail [16]. As a result, OCT studies in the acute post stent setting [17] have demonstrated a relatively high proportion of stent struts, not completely apposed to the vessel wall contact, even after high pressure post-dilatation with this phenomenon being particularly evident in regions of stent overlap. In an evaluation of OCT findings following stent implantation to complex coronary lesions, Tanigawa et al [18] examined a total of 6,402 struts from 23 patients (25 lesions) and found $9.1 \pm 7.4\%$ of all struts in each lesion treated were malapposed. Univariate predictors of malapposition on multilevel logistic regression analysis were the implantation of a sirolimus-eluting stent (likely due to its increased strut thickness and closed cell design) together with the presence of overlapping stents, a longer stent length and a type C lesion. Likely mechanical explanations for stent malapposition include strut thickness, closed cell design or acute stent recoil [19]. While these findings are impressive and helpful for the improvement of future stent designs, today the clinical relevance and potentially long-term sequelae of malapposed struts as detected by OCT are unknown. Figure 4 illustrates OCT

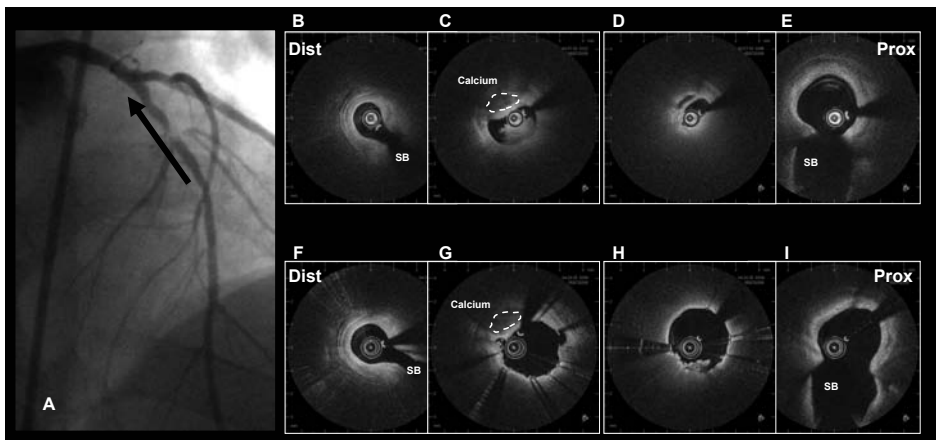


Figure 4 OCT findings before and immediately after stent implantation in a patient presenting with acute myocardial infarction (M4 prototype FD OCT system, Lightlab Imaging, Westford, MA, USA). A) Coronary angiography revealed a subtotal occlusion of the left anterior descending artery. The black arrow indicates the vessel segment imaged by OCT B-E) pre-interventional OCT showing the distal reference (B), the lesion with mural thrombus (C), the minimal lumen area (D) and the proximal reference (E): F-I) postinterventional OCT: corresponding images can be easily identified using anatomical landmark such as side branches (SB) or calcium nodules. Metallic stent struts appear as bright structures with dorsal shadowing. The distal reference (F) and the lesion site that can be easily identified using the small calcium nodule as a landmark (G) the site of the original minimal lumen area shows tissue protrusion in 6 o clock position (H) , the proximal reference (I).

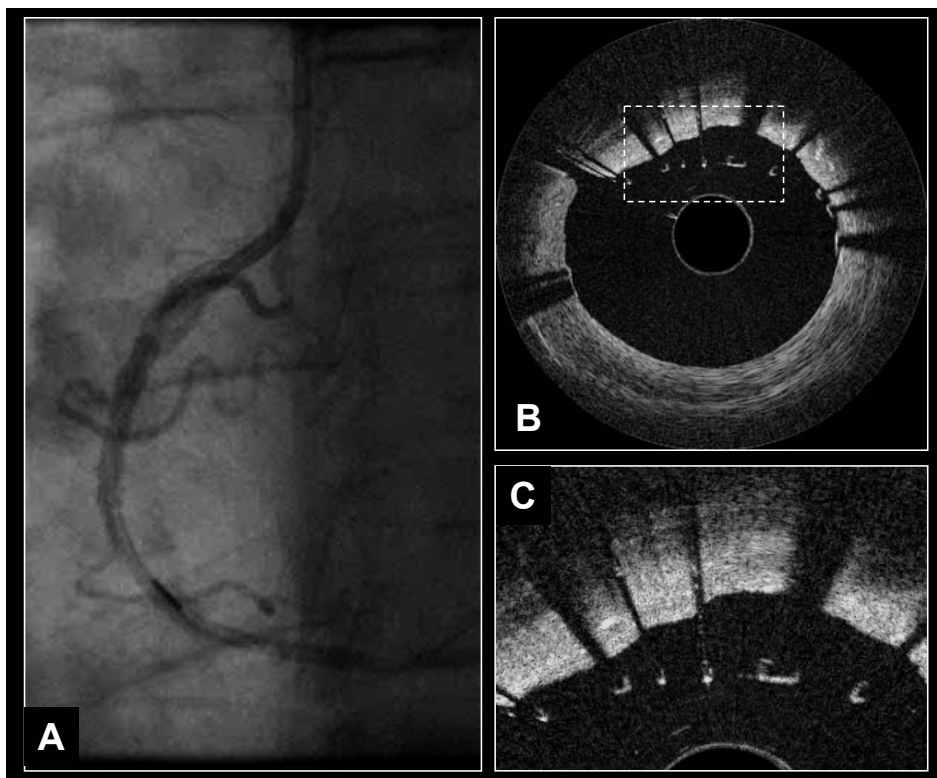


Figure 5 Incomplete stent strut apposition immediately after stenting (Volcano OCT prototype). A) Coronary angiogram of the right coronary artery after stent implantation. B) OCT image of the proximal stent edge showing malapposition of stent struts C) Magnification clearly illustrating that individual stent struts do not have contact to the vessel wall.

findings before and immediately after stent implantation in a patient presenting with acute myocardial infarction, Figure 5 illustrates incomplete stent strut apposition as frequently seen by OCT immediately after stenting.

Assessment of long-term outcome

Visualization and quantification of stent strut tissue coverage

OCT can reliably detect early and very thin layers of tissue coverage on stent struts. Figure 6 illustrates the typical OCT appearance of neointima in bare metal stents and in drug/eluting stents. Several small studies have recently been published highlighting the application of OCT in the detection of stent tissue coverage at follow-up. Importantly, OCT permits the quantification of tissue coverage with high reliability [20]. Matsumoto et al [21] studied 34 patients following sirolimus eluting stent (SES) implantation. The mean neointima thickness was 52.5 microns,

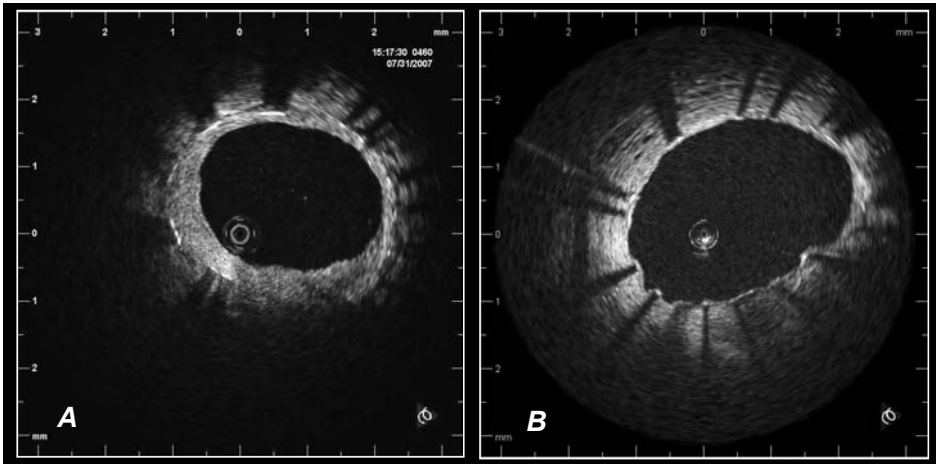


Figure 6 In vivo OCT of human coronaries at 6 months follow up. This figure illustrates the different degree of neointima coverage typically seen in bare metal stents as compared to drug eluting stents. A) bare metal stent B) drug eluting stent (TD OCT system, Lightlab Imaging, Westford, MA, USA).

and the prevalence of struts covered by thin neointima undetectable by IVUS was 64%. The average rate of neointima-covered struts in an individual SES was 89%. Nine SES (16%) showed full coverage by neointima, whereas the remaining stents had partially uncovered struts. Similarly, Takano et al [22] studied 21 patients (4,516 struts) 3 months following SES implantation. Rates of exposed struts and exposed struts with malapposition were 15% and 6%, respectively. These were more frequent in patients with acute coronary syndrome (ACS) than in those with non-ACS (18% vs 13%, $p < 0.001$; 8% vs 5%, $p < 0.005$, respectively). The same group have recently reported 2 year follow-up OCT findings [23] with the thickness of neointimal tissue at 2-years being greater than that at 3-months ($71 \pm 93 \mu\text{m}$ vs. $29 \pm 41 \mu\text{m}$, respectively; $p < 0.001$). Frequency of uncovered struts was found to be lower in the 2-year group compared to the 3-month group (5% vs. 15%, respectively; $p < 0.001$). Conversely, prevalence of patients with uncovered struts did not differ between the 3-month and the 2-year follow-up study (95% vs. 81%, respectively) highlighting that exposed struts continued to persist at long-term follow-up. Chen et al [24] recently used OCT to image SES and bare metal stents (BMS) at different time points following implantation. Of the 10 SES and 13 BMS imaged, the authors identified a significantly higher number of incompletely apposed and uncovered stent struts in patients receiving SES compared to BMS. Figure 7 illustrates OCT finding at long/term follow up after DES implantation.

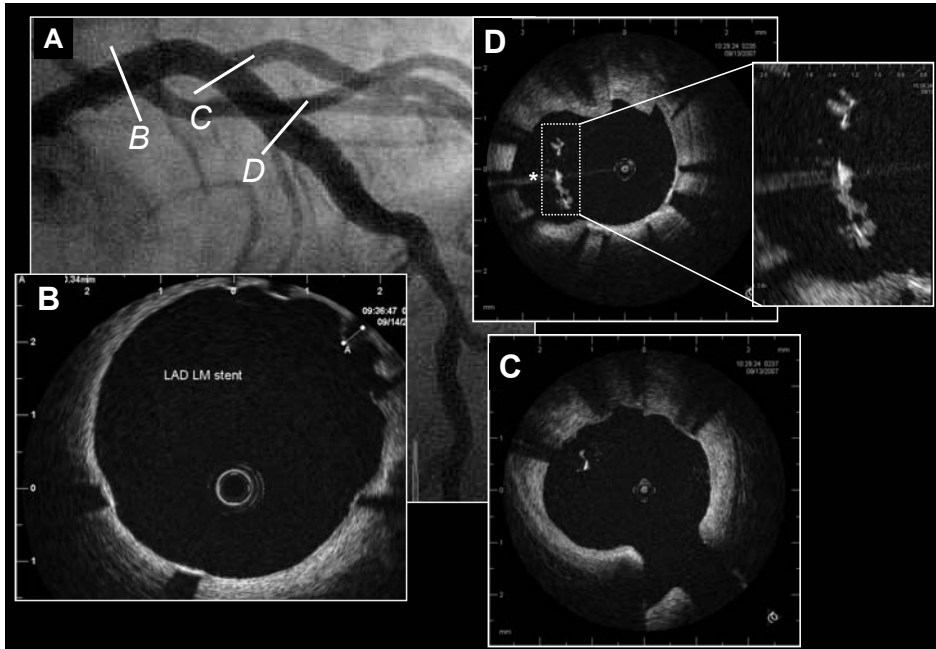


Figure 7 OCT findings at longterm follow up after DES implantation in the LEADERS OCT substudy. A) Coronary angiogram of the left coronary artery. Overlapping stents were implanted in the proximal left anterior descending artery and in the left main stem B) The application of the non-occlusive imaging acquisition technique allowed to image the stent in the left main stem as well as the proximal left anterior descending artery C.,D. C) eccentric stent struts with very thin coverage visible, an individual strut in 11 o clock position is malapposed D) stent struts showing malapposition and tissue coverage with irregular borders, possible indicating thrombus formation. (TD OCT system, Lightlab Imaging, Westford, MA, USA).

Assessment of structural details of tissue coverage

OCT also permits the characterization of neointimal tissue in a qualitative way [25]. This is a great advantage as such information has not been available in-vivo until now. The limited resolution together with artifacts induced by metallic stent struts does not allow the characterisation of such details by IVUS. With OCT, neointimal tissue can show a variety of morphologies ranging from homogenous, bright, uniform tissue to optically heterogeneous tissue or eccentric tissue of various thicknesses. Furthermore, structural details within the tissue can be observed such as intimal neovascularization [26] or a layered appearance [27], typically observed in restenotic regions. Variations in the appearance of strut coverage can be seen within an individual patient, within an individual stent or within stents of different design.

OCT findings, such as dark, signal-poor halos around stent struts may reflect fibrin deposition and incomplete healing, as described in pathologic and animal

experimental series [28]. However, there is paucity of data demonstrating directly the OCT appearance of different components in neointimal tissue as defined by histology. Post-mortem imaging of DES in human coronaries is difficult and might be limited by the fact that the optical tissue properties show variations with temperature and fixation [29]. Long-term animal OCT observations in DES are scarce.

OCT assessment of innovative stent designs and materials

OCT is also becoming an integral tool to assess emerging stent technologies that are increasingly becoming more sophisticated (e.g. bioabsorbable polymers and stents, biodegradable magnesium alloy stents) and thus demanding highly detailed assessments both in the initial animal testing phases but also in the clinical trial setting. Morphologic changes of the absorbable, polylactic acid stent struts and the vessel wall during follow-up have been recently described and show the unique capabilities of this in-vivo imaging modality [30]. The ABSORB trial recently published, showed the feasibility of implantation of the bioabsorbable everolimus-eluting coronary stent (BVS: Abbott Laboratories, IL, USA), composed of a poly-L-lactic acid backbone, coated with a degradable polymer /everolimus matrix. OCT allowed not only a precise characterization of the stent apposition and coverage but also demonstrated structural changes in the bioabsorbable DES over time. At present OCT appears as the best available tool for the assessment of the absorption of the stent struts.

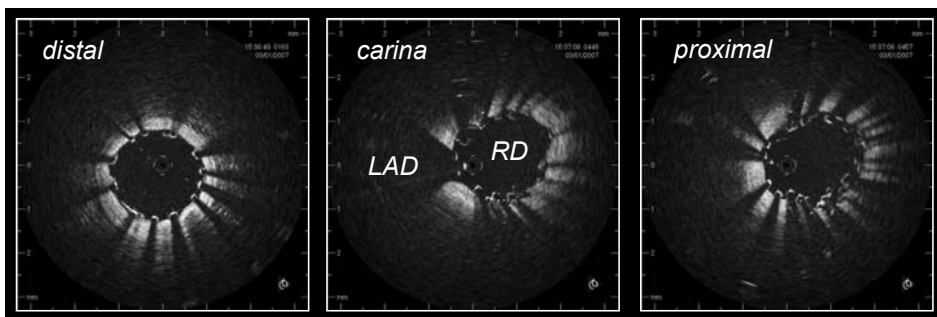


Figure 8 Clinical OCT after bifurcation stenting of the ramus descendens anterior and the ramus diagonalis in crush technique. A) OCT pullback is started distally in the diagonal branch. The stent is well expanded and all struts are apposed against the vessel wall B) OCT at the carina shows the lumen of the ramus descendens anterior in 9 o clock position wide open. Note the double layer of stent struts separating the ostium of the diagonal branch from the ramus descendens anterior. C) proximal stent portion in the ramus descendens anterior. In 12 to 6 o clock position, three layer of struts originating from the proximal, crushed diagonal branch stent and from the stent in the ramus descendens anterior can be observed. (TD OCT system, Lightlab Imaging, Westford, MA, USA).

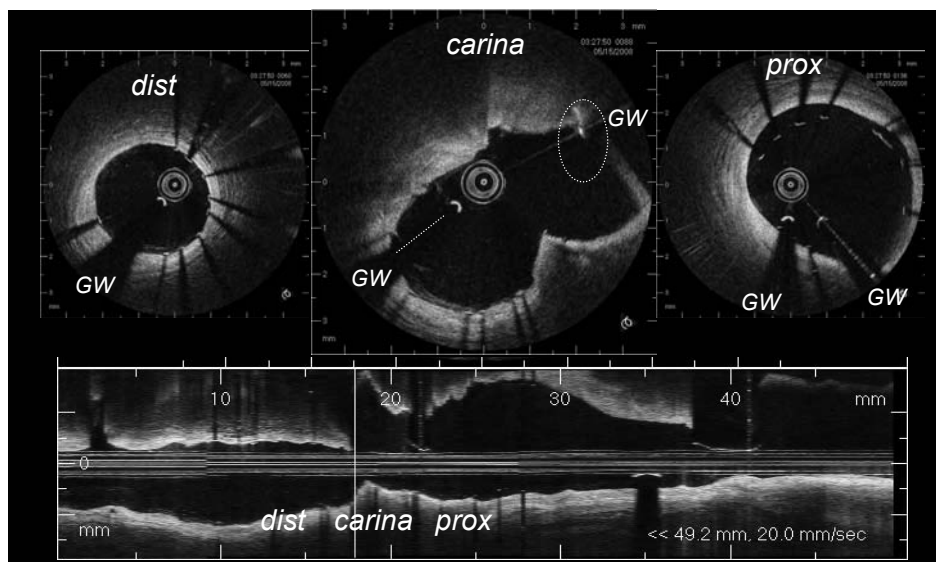


Figure 9 Clinical OCT after bifurcation stenting of the ramus descendens anterior and the ramus diagonalis with a dedicated bifurcation stent (Nile croco stent) A) OCT pullback is started distally in the ramus descendens anterior. The stent is well expanded and all struts are apposed against the vessel wall B) OCT at the carina shows the lumen of the carina wide open, no struts are obstructing the access to the diagonal branch C) proximal stent portion in the ramus descendens anterior. Despite a rather good stent expansion is some strut malapposition visible in 11 to 1 o clock position. GW= guide wire. (M4 prototype FD OCT prototype, Lightlab Imaging, Westford, MA, USA).

Another field of innovation consists in the treatment of bifurcation lesions with a variety of dedicated stents under clinical investigation. Key issues in bifurcation stenting include the ability of a stent to cover different vessel calibers at the proximal lesion site, the carina and the distal lesion site and to provide maximal expansion of the carina on both sides, the main vessel and the side branch. OCT can be a very useful tool to study the stent – vessel wall interaction as well as patency of the carina in this more complex anatomy. Clinical and experimental examples of OCT findings in bifurcation stenting are given in Figures 8–10.

Atherosclerotic plaque assessment

Optical coherence tomography is highly sensitive and specific for the characterization of plaques when compared to histological examination.

Recently, pathophysiology and coronary morphology in patients with acute coronary symptoms (ACS) are getting more and more attention. One reason for this interest is the fact that acute coronary syndromes caused by the rupture of a coronary plaque are common initial and often fatal manifestations of coronary

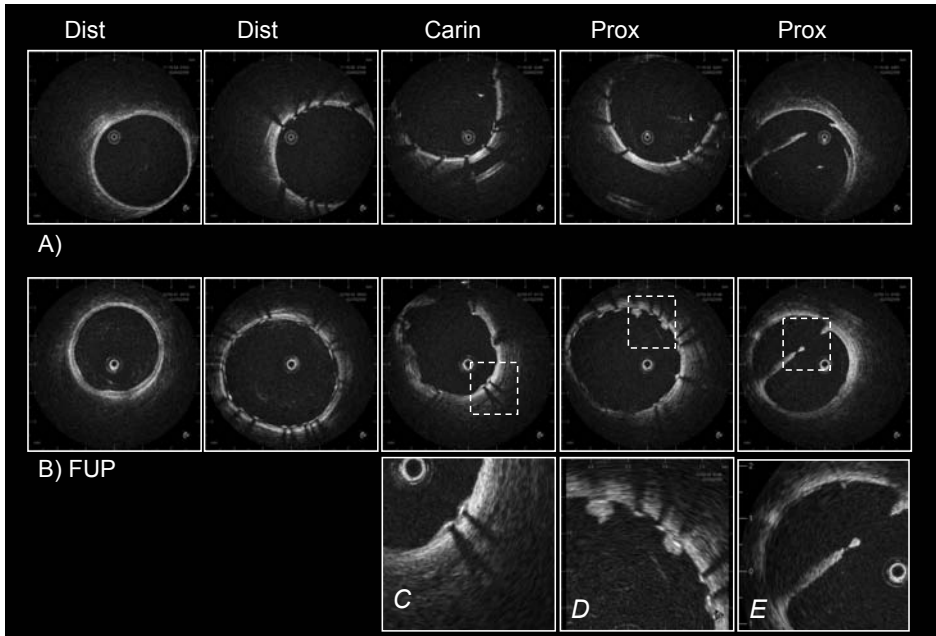


Figure 10 Bifurcation stent implantation in normal pigs. Serial, in vivo OCT A) immediately after stenting and B) at 7 day follow up. Tissue coverage is visible in various degrees from C) very thin coverage to more pronounced, irregular coverage in D) Furthermore, a persistent dissection flap can be observed at the proximal reference segment E) (TD OCT system, Lightlab Imaging, Westford, MA, USA).

atherosclerosis in otherwise healthy subjects. The detection of the lesions with high risk of rupture (the so called “vulnerable plaques”) would be of main importance for the prevention of future ACS. In the last years there has been a growing interest in this field and a lot of different techniques have been developed to evaluate diverse aspects involved in plaque vulnerability. Among them, OCT has emerged as one of the most promising due to its ability to provide unique information about the plaque composition, the thickness of the fibrous cap, the presence of macrophages and tissue collagen composition.

Plaque composition

The propensity of atherosclerotic lesions to destabilize and rupture is highly dependent on their composition. In comparison with histology OCT, has demonstrated to be highly sensitive and specific for characterizing different types of atherosclerotic plaques [TABLE 3, Figure 11]. Yabushita et al [31] performed an in-vitro study of more than 300 human atherosclerotic artery segments. When compared to histological examination, OCT had a sensitivity and specificity of 71-79% and

Table 3. OCT image criteria for plaque type.

Fibrous plaque	Fibrocalcific plaque	Lipid-rich plaque
Homogeneous signal-rich region	Well-delineated, signal-poor region with sharp borders	Signal-poor region with diffuse borders

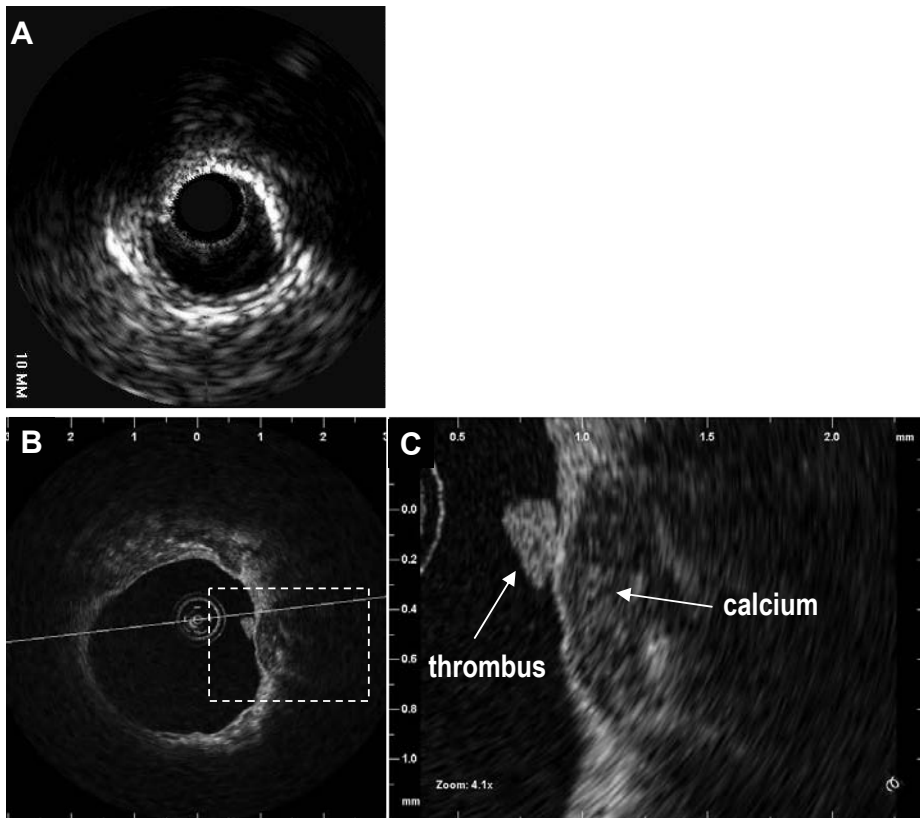
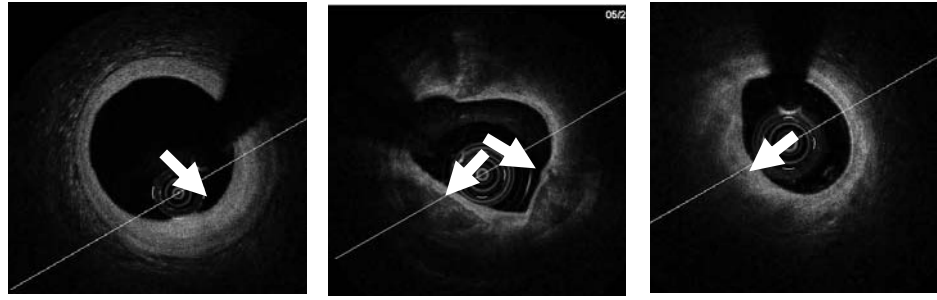


Figure 11 In vivo intravascular imaging of a calcified coronary plaque. A) Intravascular ultrasound shows an eccentric, calcified plaque as echodense structure with typical dorsal shadowing, while 180 degree of vessel wall show normal, three layer appearance B) Intravascular OCT of the same plaque. By OCT, calcium appears signal poor (dark) with sharp, well delineated borders. C) The magnification reveals a small mural thrombus. Note, that the calcium nodule is covered towards the lumen by a thin layer and is not in direct contact to the lumen as seen by IVUS.

97-98% for fibrous plaques, 95-96% and 97% for fibrocalcific plaques, and 90-94.5% and 90-92% for lipid-rich plaques, respectively. Further, the inter-observer and intra-observer reproducibility of OCT measurements were high (κ values of 0.88 and 0.91 respectively). Ex-vivo validations have also shown that OCT is superior to conventional and integrated backscatter IVUS for the characterization of coronary atherosclerotic plaque composition [32-35]. In vivo, OCT is able to identify most of the architectural features identified by IVUS and may be superior for the identification of lipid pools [36]. Several authors have evaluated the OCT appearance of coronary plaques in different groups of patients reporting higher prevalence of lipid-rich plaques in ACS than in patients with stable angina [37] and no differences in the culprit plaque imaged by OCT between diabetics and non-diabetics patients [38] and men or women with ACS[39]. According to histological and IVUS examinations, the percentage of lipid-rich plaque by OCT has been found to be higher in plaques with expansive remodelling [40].

Thickness of the fibrous cap

Autopsy studies of sudden cardiac death victims have shown that the most frequent cause of the coronary occlusion is rupture of a thin-cap fibroatheroma (TCFA) plaque. Such lesions are characterized by a large necrotic core with a thin fibrous cap usually < 65 microns in thickness. While conventional intracoronary imaging techniques such as IVUS-VH do not have enough resolution to evaluate in detail the fibrous cap, OCT has demonstrated in correlation with histological examinations that it is able to provide accurate measurements of the thickness of the fibrous cap[41, 42]. Therefore, it could be useful for the in vivo detection of TCFA. In the study with IVUS, OCT and angioscopy in acute myocardial infarction patients by Kubo et al., the incidence of TCFA was 83% and only OCT was able to estimate the fibrous cap thickness (mean $49 \pm 21 \mu\text{m}$). Two studies have reported that the plaque colour by angioscopy is related to the thickness of the fibrous cap as measured by OCT with yellow plaques often presenting thin caps [43, 44].

Assessment of collagen composition

A fibrous cap is predominantly composed of collagen, synthesized by intimal smooth muscle cells, which together impart mechanical integrity. Mechanisms that weaken the cap and potentially lead to plaque instability include collagen proteolysis and impeded collagen synthesis, resulting in a net reduction in collagen content, thinning and disorganization of collagen fiber orientation.

Polarization-sensitive (PS) imaging enhances OCT by measuring tissue birefringence, a property that is elevated in biological tissues containing proteins with an ordered structure, such as organized collagen [45-47]. PS-OCT imaging can provide both, conventional greyscale OCT as well as PS-OCT images, in one single pullback through the coronary. When light traverses birefringent tissue, light polarized along directions parallel and perpendicular to the fiber orientation of the tissue travels at different velocities, incurring relative phase retardation. The accumulated phase retardation is then displayed with respect to the tissue surface as a greyscale image with black corresponding to 0° and white to 180°. PS-OCT birefringence has been demonstrated to be highly related to total collagen content in atherosclerotic plaques as well as in fibrous plaques in vitro. It has been suggested that the ability of OCT to measure changes in the fibrous cap thickness could be useful to assess the effect of statins in plaque stabilization [48, 49]. Furthermore, recent data suggest that polarization-sensitive OCT could be able to assess the collagen content and smooth muscle cell density in the fibrous cap [50]. This could provide very valuable information about the mechanical stability of the fibrous cap enabling the identification of lesions at high risk of rupture.

Plaque rupture and intracoronary thrombosis

Plaque rupture with subsequent thrombosis is the most frequent cause of ACS. OCT can identify intracoronary thrombus and plaque rupture with high accuracy [51]. Recently, Kubo et al evaluated the ability of OCT for the assessment of the culprit lesion morphology in acute myocardial infarction in comparison with IVUS and angiography. They found an incidence of plaque rupture by OCT of 73%, significantly higher than that detected by both angiography (47%, $p=0.035$) and IVUS (40%, $p=0.009$). Intracoronary thrombus was observed in all cases by OCT and angiography but was identified only in 33% of patients by IVUS [52]. Furthermore, Kume et al. demonstrated that OCT might be able to distinguish between white and red thrombus. Red thrombus appears in OCT as high-backscattering structure with signal-free shadowing while white thrombus does not produce shadowing [53]. OCT could be helpful to identify the culprit lesion in ACS and might provide additional information about the underlying cause that lead to the plaque rupture (Figure 12).

Visualization of macrophage accumulation

Intense infiltration by macrophages of the fibrous cap is another of the features of the vulnerable plaques. An ex-vivo study by Tearney et al., demonstrated that

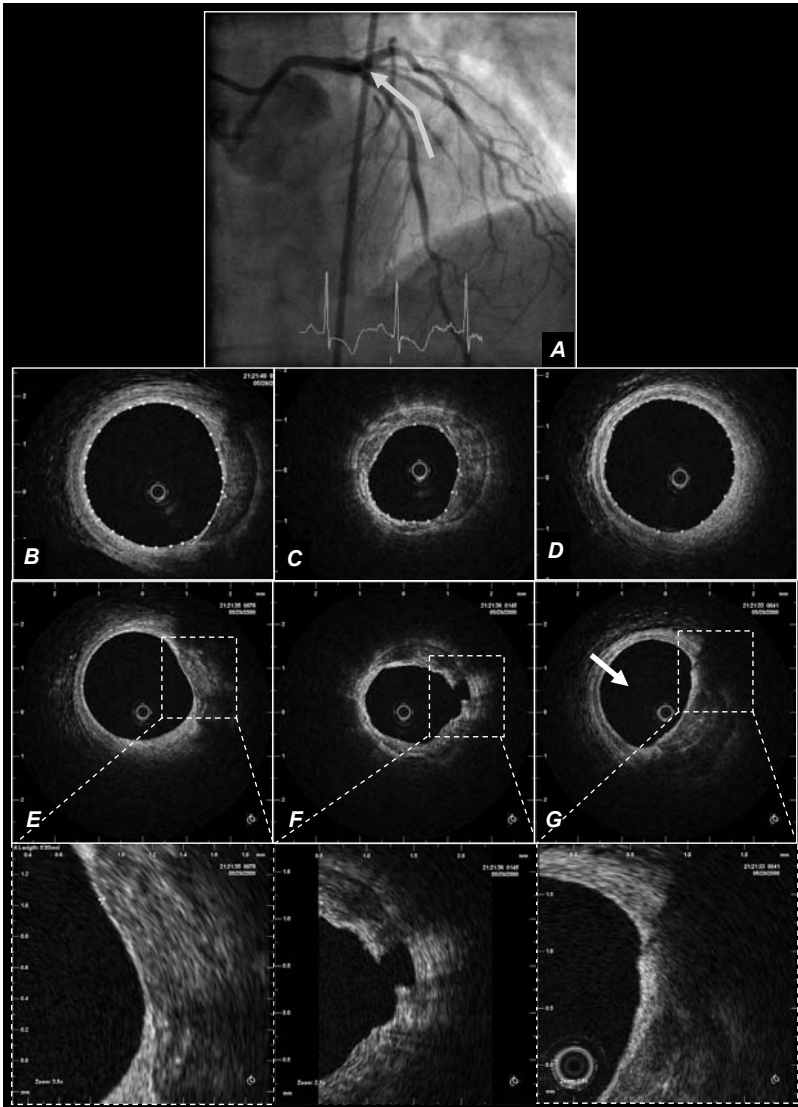


Figure 12 OCT findings in a 74 year old female patient presenting with acute coronary syndrome, Braunwald class IIIIC with positive Trop T ($0.57\mu\text{g/l}$) and CK (181 U/l) at the time of admission to the cathlab. A) Coronary angiography showed a moderate narrowing of the mid left descending anterior artery with TIMI III antegrade flow, the other epicardial arteries were normal. Intracoronary OCT confirmed a moderate lesion with approx 50% area stenosis B) proximal reference lumen area 6.82mm^2 C) minimal lumen area 2.81mm^2 D) distal lumen area 4.49mm^2 . Detailed inspection of the OCT images revealed E) an eccentric plaque that showed a very thin endothelial lining ($<30 \mu\text{m}$) F) a site with plaque rupture/ulceration and G) a fine fissure on the surface of the plaque. Plaque erosion, rupture/ulceration and fissure have been associated with coronary thrombosis in pathology series and could be the possible pathophysiologic substrate for the clinical syndrome observed in our patient, (TD OCT system, Lightlab Imaging, Westford, MA, USA).

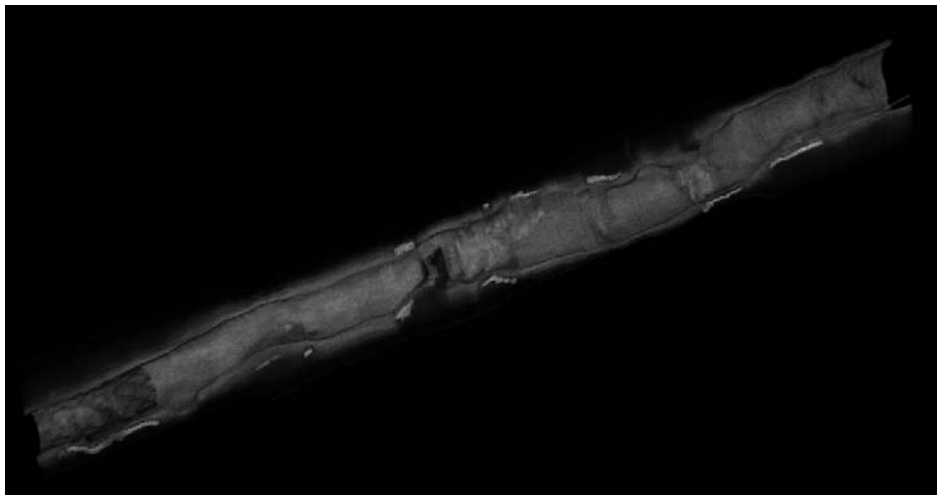


Figure 13 Longitudinal cut view of an in vivo FD OCT pullback through a coronary artery. At the distal end, a coronary stent is visible. Different components of the vessel wall are represented in a color coded way. MGH OFDI system (G. Tearney and B. Bouma, Wellman Center for Photomedicine, MGH, Boston, MA, USA)

OCT could be able to quantify macrophage within the fibrous cap [54]. In vivo, it has been demonstrated that unstable patients present a significantly higher macrophage density detected by OCT in the culprit lesion than stable patients. Furthermore, in the same population, the sites of plaque rupture demonstrated a greater macrophage density than non-ruptured sites [55]. Raffel et al. reported that macrophage density in the fibrous cap detected by OCT correlated with the white blood cell count, and both parameters could be useful to predict the presence of TCFA [56]. Figure 13 illustrates detailed OCT based tissue characterization over a long coronary segment including the distribution of macrophages, calcium and lipid rich tissue.

EQUIPMENT

The equipment for intracoronary OCT generally consists in an OCT imaging catheter, a motorized pullback device and an imaging console, that contains the light source, signal processing units, data storage and display [57]. The imaging catheter is part of the sample arm of the interferometer described above. The optical signal is transmitted by a single-mode fiber, which is fitted with an integrated lens micro-prism assembly to focus the beam and direct it towards the tissue. The focus is approximately 1mm outside the catheter. In order to scan the vessel

lengthwise, the catheter-imaging tip is pulled back while rotating, usually inside a transparent sheath, allowing to collect a three dimensional dataset of the coronary artery. Both rotary and pullback motion are driven proximally by a motor outside the patient. We will describe the currently commercially available equipment for time-domain OCT and the imaging procedure in detail.

Equipment Time-Domain OCT

The mobile M2/M2x OCT System cart (LightLab Imaging Inc., Westford, MA, USA) contains the optical imaging engine and the computer. The mouse, keyboard, two monitors, two storage drawers, and the patient interface unit (PIU) are all mounted on top of the cart [58] (Figure 1).

The ImageWire

The imaging probe (ImageWire™ LightLab Imaging Inc., Westford, MA, USA) has a maximum outer diameter of 0.019” (with a standard 0.014” radiolucent coiled tip) and contains a single-mode fiber optic core within a translucent sheath. The image wire is connected at its proximal end to the imaging console that permitted real-time data processing and two-dimensional representation of the backscattered light in a cross-sectional plane. Since the imaging wire is not torquable, it can be advanced distal to the region of interest using the over-the-wire occlusion balloon (for the occlusive technique, see below) or a simple microcatheter for the non-occlusive technique (see below, e.g. Transit, Cordis Johnson & Johnson, USA or ProGreat, Terumo Japan, with inner lumens >0.020”). Unlike an IVUS transducer, the optical sensor of the ImageWire is invisible under fluoroscopy and therefore one must estimate the correct position, using the distal 15mm radiopaque tip of the ImageWire. When fully advanced, the sensor is located 6-7mm proximal to the radiopaque part and is easily confirmed by direct observation of the red light emitted when the wire is handled out of the body. As there are no direct radiopaque markers for the infrared sensor, it is possible to inadvertently miss imaging an area of interest resulting in incomplete distal lesion edge assessment. Imaging after stent implantation facilitates positioning because it is sufficient to advance the proximal end of the radiopaque wire tip at least 1cm distal to the stent struts to image the entire stented segment. For imaging prior to treatment, it is important to note that the occlusion balloon is too bulky to cross severe stenoses before pre-dilatation and that the imaging wire should be advanced distal to the lesion to ensure that the segment of interest is fully visualised. In such circumstances, the non-occlusive technique is advantageous.

Occlusive imaging technique: Proximal balloon occlusion and flush delivery

The proximal occlusion balloon catheter (Helios, Goodman Co, Japan) is an over-the-wire 4.4Fr catheter (inner diameter 0.025”), compatible with 6Fr guiding catheters (inner lumen diameter ≥ 0.071 ”), which is advanced distal to region of interest using a conventional angioplasty guide wire (0.014”). The guide wire is then replaced by the OCT ImageWire™ (0.019” maximum diameter), and the occlusion balloon catheter is withdrawn proximal to the segment to be assessed leaving the imaging wire in distal position. During imaging acquisition, coronary blood flow is removed by continuous flush of Ringer’s lactate solution via the end-hole of the occlusion balloon catheter at a flow rate of 0.5-0.7ml/sec during simultaneous balloon inflation (0.5-0.7atm). The vessel occlusion time is limited

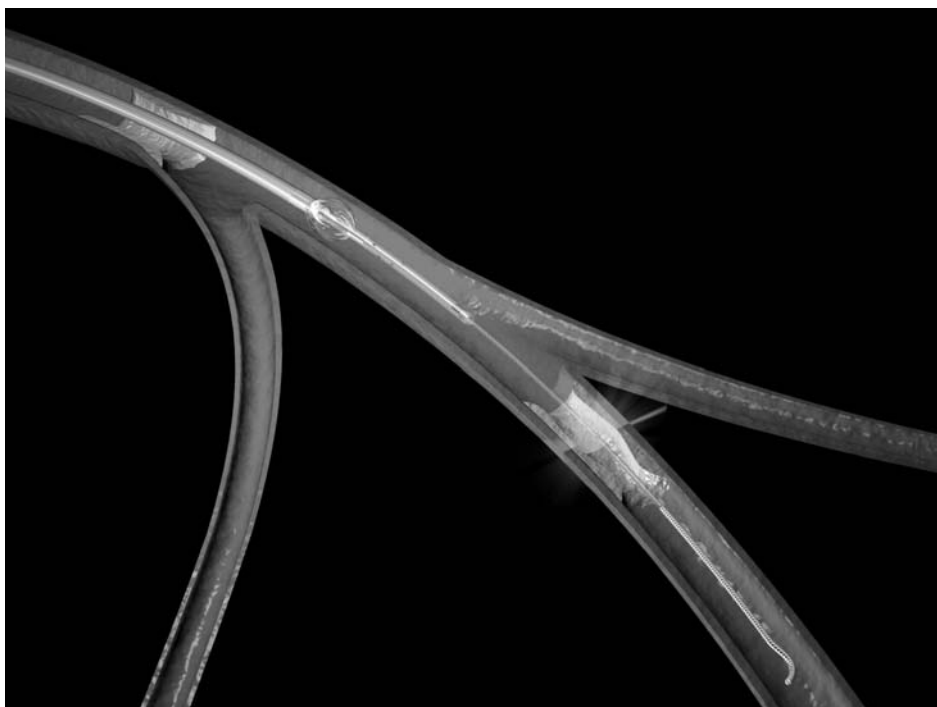


Figure 14 Occlusive image acquisition technique (TD OCT imaging Lightlab Imaging, Westford, MA, USA). The imaging catheter directs the infrared light into the tissue and returns the reflected light back to the optical engine. During imaging, blood flow is limited by a dedicated, over the wire, low pressure (0.4 atm) occlusion balloon catheter (Helios, Goodman, Japan), that is positioned proximally in the artery. The central lumen of the balloon occlusion catheter allows for distal flush deliver during imaging of the target segment with automated pullback. The proximal end of the catheter has a chamber the captures the imaging core and allows it to move along the catheter axis to perform an “automated pullback”. The outside of the imaging catheter is stationary with respect to the vessel wall. The imaging core is rotated and translated inside of the external catheter sheath.

to a maximum of 30sec to avoid haemodynamic instability or arrhythmias. A 1.0 mm/sec pullback permits the assessment of an up to 30mm long coronary segment with a frame rate of 15.4 frames/sec [59] (Figure 14).

Non-occlusive imaging technique

With improvements in the acquisition speeds of OCT data (currently in the vicinity of 3.0mm/sec), blood can be evacuated by continuous flush through the guiding catheter, thus doing away with the cumbersome proximal balloon occlusion and thereby simplifying the acquisition process [60]. Here, the OCT ImageWire is advanced carefully distal to the region of interest. As the fragile wire does not have the properties of a guide wire, it needs to be directed distally using a single lumen micro-catheter (e.g. Transit, Cordis, Johnson & Johnson, ProGreat, Terumo, Japan). With the wire in position, viscous iso-osmolar contrast (Iodixanol 370, Visipaque™, GE Health Care, Ireland) at 37° Celsius is used to clear the artery from blood and connected to the standard Y-piece of the guiding catheter. The contrast is either injected manually through the Y-piece or automatically using an injection pump. During continuous contrast injection, the automated OCT pullback is performed at 3.0mm/sec. The pullback is stopped after visualization of the region of interest or in case of significant signs of ischemia, arrhythmia or patient intolerance. Cross sectional images are acquired at 20 frames/sec.

After completion of the OCT study, the image wire is removed, and intracoronary nitrates are usually administered according to local standards and an angiogram should be taken. The procedure should be terminated if there is any hemodynamic compromise during the infusion and OCT acquisition.

Equipment Fourier-Domain OCT

In the new generation of OCT systems the optical probe is integrated in a short monorail catheter that can be advanced in the coronary artery over any conventional 0.014” guide wire. The catheter profile varies from 2.4Fr to 3.2Fr and is compatible with 6F guiding catheters. The usable length is around 140 cm. The position and number of the radiopaque markers varies for the different systems. During the pullback the optic fiber probe is pulled along the catheter sheath. The dramatically faster pullback speed allows imaging of long coronary segments with 2-3 seconds pullback during injection of flush (x-ray contrast or diluted x-ray contrast) through the guiding catheter without vessel occlusion.

CLINICAL ASPECTS

The interest in the long-term stent strut vessel wall interaction is manifold and includes the assessment of the stability of the acute result, the visualization of complex anatomy that is not accessible by angiography or IVUS and the clearer understanding of reasons for stent failures, when they do occur.

DES failure

Reasons for DES failure are poorly understood. With the reduction of in-stent hyperplasia, other mechanisms of restenosis due to mechanical stent failure have become apparent. Of the two established first generation DES, the sirolimus-eluting stent (Cordis, J&J, Miami, Florida, US) has been particularly linked to cases of stent fracture, likely as a result of its closed cell design compared with other DES employing an open cell system [61]. The higher imaging resolution of OCT compared to IVUS permits a detailed assessment in such cases, as demonstrated recently by Shite et al.

Incomplete strut apposition

Stent strut malapposition remains another important consideration. Postulated causes for stent strut malapposition are various and include incomplete stent expansion, stent recoil or fracture, late outward vessel remodelling or the dissolution of thrombus that was compressed during PCI between the stent strut and the vessel wall. Regardless of the pathophysiologic mechanism, the major concern in stent malapposition remains in the assumption that areas of strut malapposition cause non-laminar and turbulent blood flow characteristics, which in turn can trigger platelet activation and thrombosis. Here, prospective, serial OCT observations immediately and at longer term follow-up after stenting may improve our understanding of these complex mechanisms and shed light on the likely clinical significance of this phenomenon.

Stent strut tissue coverage and thrombosis

Late stent thrombosis is poorly understood. It appears that this condition is multi-factorial with premature discontinuation of dual anti-platelet therapy, stent under-expansion, hypersensitivity and lack of endothelial tissue coverage all being implicated. The results of small observational OCT studies as described above are compatible with evidence from animal and human post-mortem series showing that DES cause impairment in arterial healing, some with suggested incomplete re-endothelialisation and persistence of fibrin(oid) possibly triggering late stent

thrombosis [62, 63]. Pathological data in human suggests that neointimal coverage of stent struts could be used as a surrogate marker of endothelialization due to the good correlation between strut coverage and endothelialization. However, OCT observations need to be interpreted with caution. OCT is limited by its resolution of 15 micron which is lower than the thickness of an individual layer of endothelial cells. Therefore, coverage that is not visible by OCT does not exclude the presence of an endothelial layer. Second, the presence of tissue coverage does not necessarily imply the presence of a functionally intact endothelium. Early experimental stent data showed that endothelial function can vary considerably and show evidence of damage when subjected to the Evan's blue dye exclusion test, even in the presence of a well structured neointimal layer [64].

However, OCT is the only imaging modality to date that offers – within the discussed limits- the possibility to understand tissue coverage and neointima formation in DES over time [65]. Clearly, larger stent trials with OCT at different time periods are needed to obtain a representative assessment of the true time course of endothelial stent coverage of these stents. Recent improvements in OCT technology, with frequency-domain OCT, will allow for a simple imaging procedure and offer the potential for large scale, prospective studies, indispensable to address vexing clinical questions such as the relationship of drug-eluting stent deployment, vascular healing, the true time course of endothelial stent coverage and late stent thrombosis. This may also better guide the optimal duration of dual anti-platelet therapy that currently remains unclear and rather empiric.

DES restenosis

OCT can be very useful in the evaluation of the causes that contribute to restenosis after DES implantation such as incomplete coverage lesion or gaps between stents.

Stent fracture (with subsequent defect of local drug delivery) has also been related to restenosis in DES and could be visualized with OCT [66]. Non-uniform distribution of stent struts can affect the drug concentration within the arterial wall and therefore have an influence in restenosis in DES [67]. This has been confirmed in pre-clinical and IVUS studies. The maximum interstrut angle has been identified in IVUS as predictor of intimal hyperplasia cross-sectional area. OCT allows the assessment of strut distribution in vivo with high accuracy. A study with phantom models showed how the strut distribution of SES and paclitaxel eluting stents (PES) assessed by OCT were significantly different, suggesting that SES maintained a more regular strut distribution despite expansion [68].

OCT safety

The applied energies in intravascular OCT are relatively low (output power in the range of 5.0–8.0 mW) and are not considered to cause functional or structural damage to the tissue. Safety issues thus seem mainly dependent on the need of blood displacement for image acquisition. One recently published study evaluated the safety and feasibility of OCT in 76 patients in the clinical setting using the occlusive technique. Vessel occlusion time was 48.3 ± 13.5 seconds. The most frequent complication was the presence of transient events, such as chest discomfort, brady or tachycardia, and ST-T changes on electrocardiogram, all of which resolved immediately after the procedure. There were no major complications, including myocardial infarction, emergency revascularization, or death. The authors reported that acute procedural complications such as acute vessel occlusion, dissection, thrombus formation, embolism, or vasospasm along the procedure-related artery, were not observed [70]. Comparison of the occlusive versus the non occlusive imaging method in a small patient cohort (n=40) did not show major complications and confirmed superiority of the non-occlusive method in ostial lesion assessment [71]. In our experience, the introduction of the non-occlusive technique in clinical practice has led to an important reduction in the procedural time and in the incidence of chest pain and ECG changes during image acquisition. These side effects are expected to be further reduced by the introduction of Fourier domain OCT. In Fourier domain OCT, high pullback speeds of up to 40mm/s allow data acquisition of a long coronary segment within in few seconds and thus without introducing relevant ischemia.

LIMITATIONS

Generally, the main limitations of intracoronary OCT as compared to the established intravascular ultrasound technology consist firstly in the fact, that light can not penetrate blood. Thus, OCT requires clearing of the artery from blood as additional step during the imaging procedure. Secondly, the high resolution of OCT is at the expense of penetration depth. More specific issues can impede intracoronary OCT quality and interpretation in clinical intracoronary OCT application. The most important practical limitations originating from coronary anatomy and artifacts are summarized below [59].

Vessel tortuosity

Within the human body, peripheral arteries (the vascular access sites) as well as the coronary arteries (imaging target) represent more or less tortuous structures. This requires high flexibility and steerability from the imaging device. This is not trivial given the fact that light transmission requires easily breakable fibre-optics. Another consequence is on the image geometry. In the majority of cases, the imaging device will not be in a co-axial and centred position within the target artery, which may affect penetration depth, brightness and resolution of the imaged structure (Figure 15).

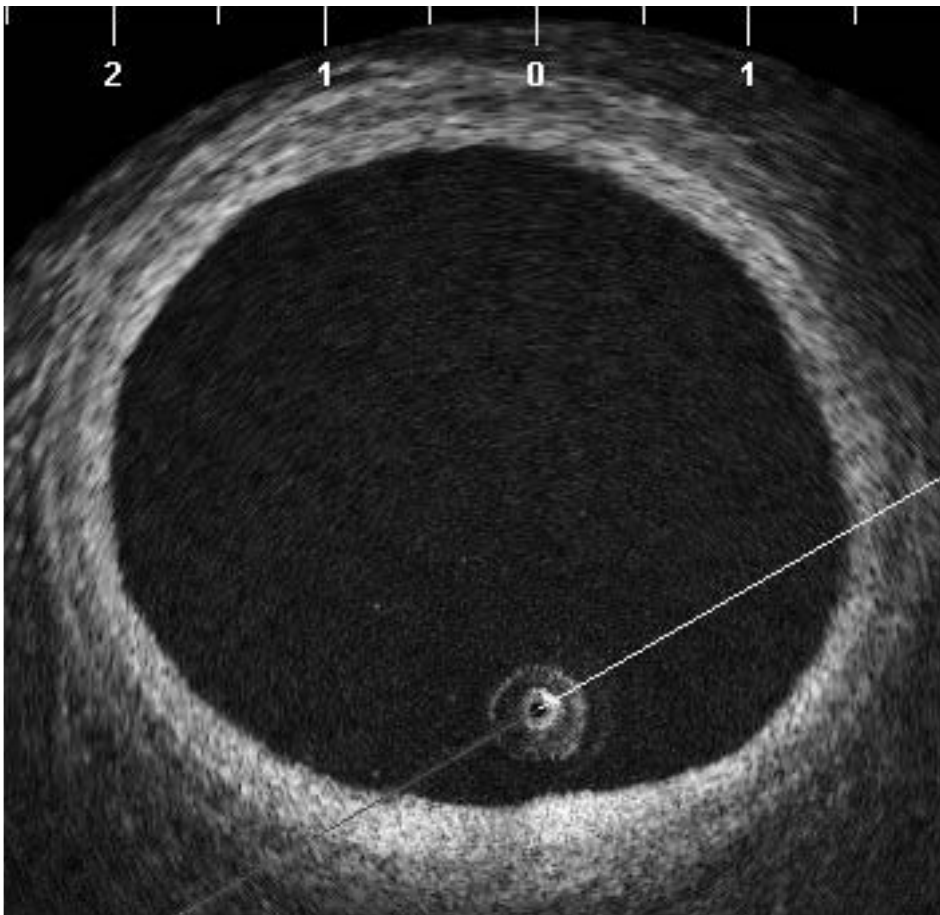


Figure 15 In-vivo intracoronary OCT of an artery with concentric intimal thickening. The imaging catheter is in a non co-axial, non-centred position. In consequence, the vessel wall segment close to the OCT catheter in 6 o'clock position appears brighter and shows a finer structure as the opposite vessel wall segment in 12 o'clock position.

Coronary caliber

Coronary arteries represent relatively small structures for in-vivo imaging; they are however relatively big structures compared to experimental OCT applications that often focus on much smaller sample volumes. Epicardial arteries have a maximal lumen diameter of approx 4-5mm in their proximal portion and taper distally. Typically, arteries with a lumen diameter down to approx. 1.0 mm are considered clinically relevant and accessible to standard imaging equipment, such as coronary angiography and intravascular ultrasound. Ideally, the penetration depth of intravascular OCT should be able to cover the complete calibre range (Figure 16).

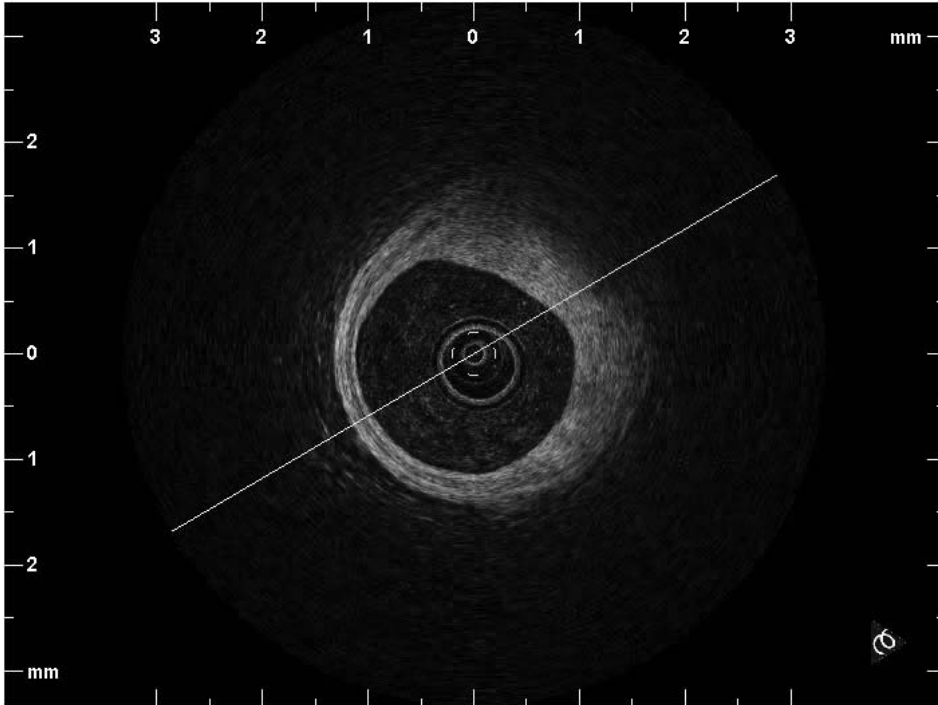


Figure 16 In-vivo intracoronary OCT of an artery with eccentric atherosclerotic plaque. A normal vessel wall sector with typical three-layer appearance is visible in 6 to 9 o'clock position, while the remaining vessel circumference shows thick plaque formation. Despite a centered position of the OCT imaging probe within the lumen, the eccentric plaque can not be completely penetrated and thus, the adventitial layer is not visible from 12 to 5 o'clock position.

Plaque geometry

Atherosclerotic coronary arteries contain a highly variable degree of plaque deposition within the artery wall. Atherosclerotic plaque can form a concentric ring encroaching the lumen, but will be eccentric with a normal vessel wall sector or with relatively big differences in vessel wall thickness in the majority of cases [72]. Intravascular OCT is hampered to penetrate advanced, thick plaque, irrespective of the position of the OCT imaging device within the lumen.

Plaque composition

The limited penetration depth into the vessel wall can reduce the sensitivity of OCT for different plaque components. An in-vitro study comparing OCT to histopathology reported misclassification in 41% of lesions predominantly due to a combination of incomplete penetration depth into the vessel wall and a resulting difficulty to distinguish calcium deposits from lipid pools [73]. Calcium deposits as well as lipidic tissues appear signal-poor by OCT. These two tissue types can be discriminated by the tissue borders, calcium typically shows very sharp, well delineated borders, whereas lipid shows poorly defined borders with diffuse transition to the surrounding tissue.

Motion during heart cycle

Epicardial arteries experience significant three-dimensional motion during heart cycle. This affects (a) the vascular dimensions (with a variability of lumen area of approx 8% between systole and diastole [74]) (b) the OCT device position within the artery (transversal and longitudinal motion) and (c) the image acquisition time (Figure 17).

In coronary stents, typical stent imaging artifacts can be observed (Figure 18)

Shadowing behind stent struts

The light source used for OCT is unable to penetrate metal resulting in dorsal shadowing behind the stent strut. When interpreting OCT images, the thickness of the whole stent strut (including metal and polymer) must be taken into consideration rather than only the visible endo-luminal strut surface. Shadowing also limits the interpretation of structures behind the stent strut and this remains a limitation of OCT, particularly also given its poor tissue penetration (<

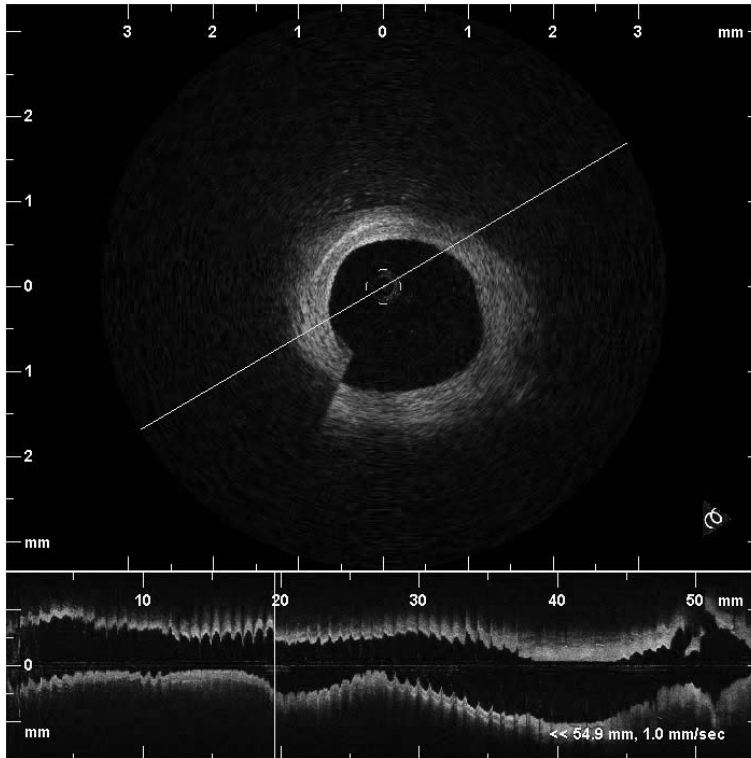


Figure 17 In-vivo intracoronary OCT. A) Illustrates the motion artefact during heart cycle in the cross sectional view, causing a “seamline” B) illustrates the motion artefact caused in the longitudinal view. Note the irregular lumen contour caused by three-dimensional motion of the artery relative to the OCT imaging catheter.

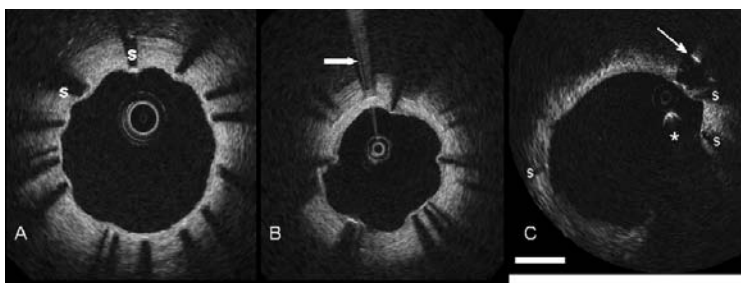


Figure 18 OCT artefacts in stent imaging. A) Circumferential stent struts are shown covered by a thin layer of tissue. Dorsal shadowing is evident behind the stent struts (S) with only the luminal surface of the strut visible with OCT. B) demonstrates circumferential stent struts with shadowing and bright reflections caused by saturation of the detector registering the inferogram (arrow) C) Arrow indicates a double reflection between stent and catheter. This can occur if a stent strut is imaged face-on, and reflects the OCT beam specularly. Shadows of other stent struts are marked by s; stent struts that do not show up as the typical bright dot, but do cast a shadow, are imaged under an oblique angle. * is a guide wire artefact. White bar is 1 mm.

1.5mm). Furthermore, the OCT imaging plane rarely intersects the stent struts perpendicularly thereby resulting in shadows much larger than the actual width of the stent strut.

Bright reflections saturating an entire line (spikes)

If the imaging beam hits a strut perpendicularly, it reflects a very large fraction of the beam back towards the catheter. This strong signal may saturate the detector registering the interferogram, producing a readily recognisable artefact of bright radial streaks centered on struts.

Multiple reflections (stent – catheter – stent)

In a similar geometry, near specular reflection, light may bounce back between catheter and strut more than once. The optical catheter itself reflects part of the received light back into the tissue. Strong reflectors, such as struts, may produce an appreciable signal in the second reflection. The optical path length of light in the secondary reflections doubles that of the primary feature. Hence, a double reflection will show up as an apparent second strut appearing behind the first at twice the distance from the catheter.

SPECIAL ISSUES / CONSIDERATIONS / CONTRADICTIONS

The unique high-resolution OCT imaging modality permits the analysis of coronary structures in great detail. The sharp contrast between the lumen during flushing and the vessel wall allows for a relatively easy image interpretation. It is noteworthy that indeed OCT has a high accuracy when compared to histomorphometry as discussed earlier, but it also has a remarkably high reproducibility in the clinical setting.

The measurement accuracy of intracoronary OCT has been established in post-mortem human coronary arteries and showed good correlation to histomorphometry [75]. However, compared to ex-vivo imaging, quantitative analysis of in-vivo intracoronary imaging is more complicated due to the presence of blood and motion artifacts during cardiac cycle. Furthermore, the OCT dataset acquired during motorized pullback in-vivo is much larger than local imaging of selected cross sections as performed in post mortem studies. A pullback through the region of interest (ROI) is necessary in order to visualize the three-dimensional morphology of the coronary artery. We recently reported on standardized auto-

mated quantification processes for intracoronary OCT pullback data [20]. The inter-observer variability for lumen dimensions as measured by computer-assisted QOCT was extremely low and in a similar range for both, in-vitro as well for in-vivo studies, despite the occurrence of motion induced artefacts during the acquisition in-vivo. Similarly, inter-observer variability in complex vessel anatomy as represented by chronic coronary stents was very low: the absolute and relative difference between lumen area measurements derived from 2 observers was low ($0.02\pm 0.10\text{mm}^2$; $0.3\pm 0.5\%$ respectively) with excellent correlation confirmed by linear regression analysis (R^2 0.99; $p<0.001$). Similarly, in-vivo measurements demonstrated a high correlation with the main source of inter-observer variation occurring as a result of coronary dissection and motion artefact. The absolute and relative difference between measurements were $0.11\pm 0.33\text{mm}^2$ ($1.57\pm 0.05\%$) for lumen area (R^2 0.98; $p<0.001$), $0.17\pm 0.68\text{mm}^2$ ($1.44\pm 0.08\%$) for stent area (R^2 0.94; $p<0.001$) and $0.26\pm 0.72\text{mm}^2$ ($14.08\pm 0.37\%$) for neointima area (R^2 0.78; $p<0.001$).

CONCLUSIONS

OCT has caused intense interest in interventional cardiology. Its application to the assessment of coronary stents has been greeted with strong enthusiasm and is now also being incorporated into large multi-centre randomised stent trials aimed at complementing angiographic and clinical endpoints. Such applications are currently unique to OCT and, despite the recent progress of non-invasive techniques such as 64 multi-slice computed tomography (MSCT), conventional stents still represent a challenge to distinguish lumen and intimal hyperplasia within the stent. Reports showing that reconstruction of MSCT images using specific kernels offer good correlation with angiography are encouraging but unlikely to make this technique a reliable alternative at the present time.

The ability to provide high-resolution imaging in-vivo is the most significant concept circumventing the limitations of other imaging modalities such as IVUS or the need for multiple animal studies. Refinements in acquisition speeds with OFDI will also make the technique less procedurally demanding and thus able to be applied to many more centres, thereby remaining a key tool in the armamentarium of researchers and interventional cardiologists alike.

REFERENCES

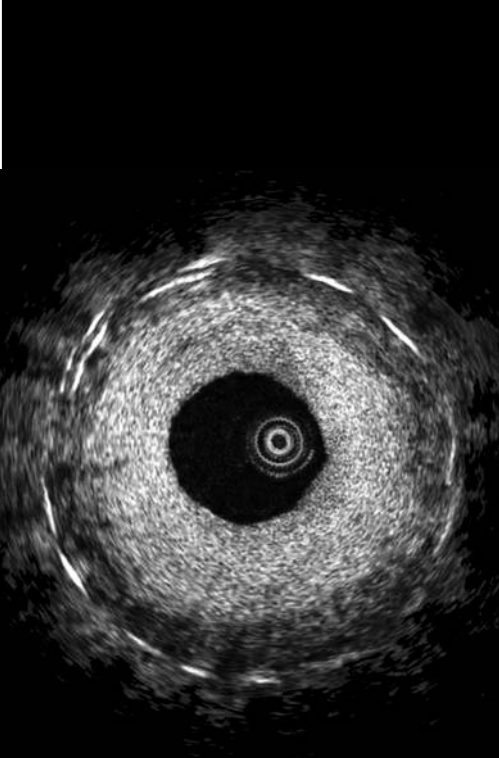
- [1] Huang, D., et al., *Optical coherence tomography*. Science, 1991. **254**(5035): p. 1178-81.
- [2] Brezinski, M.E., et al., *Imaging of coronary artery microstructure (in vitro) with optical coherence tomography*. Am J Cardiol, 1996. **77**(1): p. 92-3.
- [3] Michelson, A. and E. Morley, *On the relative motion of the earth and the luminiferous aether*. Philos. Mag., 1887. **S5**(151): p. 449-463.
- [4] Schmitt, J.M., et al., *Optical-coherence tomography of a dense tissue: statistics of attenuation and backscattering*. Phys Med Biol, 1994. **39**(10): p. 1705-20.
- [5] Schmitt, J.M., *Optical coherence tomography (OCT): a review*. IEEE J. Select. Topics Quantum Electron., 1999. **5**: p. 1205-1215.
- [6] Yun, S., et al., *High-speed optical frequency-domain imaging*. Optics Express, 2003. **11**: p. 2953-2963.
- [7] Chinn, S.R., E.A. Swanson, and J.G. Fujimoto, *Optical coherence tomography using a frequency-tunable optical source*. Optics Letters, 1997. **22**(5): p. 340-342.
- [8] Rollins, A.M., et al., *In vivo video rate optical coherence tomography*. Optics Express, 1998. **3**(6): p. 219-229.
- [9] Leitgeb, R., C.K. Hitzenberger, and A.F. Fercher, *Performance of fourier domain vs. time domain optical coherence tomography*. Optics Express, 2003. **11**(8): p. 889-894.
- [10] Choma, M., et al., *Sensitivity advantage of swept source and Fourier domain optical coherence tomography*. Opt. Express, 2003. **11**(18): p. 2183-2189.
- [11] de Boer, J.F., et al., *Improved signal-to-noise ratio in spectral-domain compared with time-domain optical coherence tomography*. Optics Letters, 2003. **28**(21): p. 2067-2069.
- [12] Yun, S.H., et al., *Comprehensive volumetric optical microscopy in vivo*. Nat Med, 2006. **12**(12): p. 1429-33.
- [13] Lim, H., et al., *High-speed imaging of human retina in vivo with swept-source optical coherence tomography*. Optics Express, 2006. **14**(26): p. 12902-08.
- [14] Hong, M.K., et al., *Late stent malapposition after drug-eluting stent implantation: an intravascular ultrasound analysis with long-term follow-up*. Circulation, 2006. **113**(3): p. 414-9.
- [15] Tanabe, K., et al., *Incomplete stent apposition after implantation of paclitaxel-eluting stents or bare metal stents: insights from the randomized TAXUS II trial*. Circulation, 2005. **111**(7): p. 900-5.
- [16] Bouma, B.E., et al., *Evaluation of intracoronary stenting by intravascular optical coherence tomography*. Heart, 2003. **89**(3): p. 317-320.
- [17] Tanigawa J, et al., *Optical coherence tomography to assess malapposition in overlapping drug-eluting stents*. EuroInterv., 2008. **3**: p. 580-583.
- [18] Tanigawa J, et al., *Stent strut apposition in complex lesions using optical coherence tomography*. Am J Cardiol, 2006. **98**(8): p. Suppl 1: 97M.
- [19] Regar, E., J. Schaar, and P.W. Serruys, *Images in cardiology. Acute recoil in sirolimus eluting stent: real time, in vivo assessment with optical coherence tomography*. Heart, 2006. **92**(1): p. 123.

- [20] Tanimoto, S., et al., *A novel approach for quantitative analysis of intracoronary optical coherence tomography: high inter-observer agreement with computer-assisted contour detection*. Catheter Cardiovasc Interv, 2008. **72**(2): p. 228-35.
- [21] Matsumoto, D., et al., *Neointimal coverage of sirolimus-eluting stents at 6-month follow-up: evaluated by optical coherence tomography*. Eur Heart J, 2007. **28**(8): p. 961-7.
- [22] Takano, M., et al., *Evaluation by optical coherence tomography of neointimal coverage of sirolimus-eluting stent three months after implantation*. Am J Cardiol, 2007. **99**(8): p. 1033-8.
- [23] Takano, M., et al., *Long-term follow-up evaluation after sirolimus-eluting stent implantation by optical coherence tomography: do uncovered struts persist?* J Am Coll Cardiol, 2008. **51**(9): p. 968-9.
- [24] Chen, B.X., et al., *Neointimal Coverage of Bare Metal and Sirolimus-Eluting Stents Evaluated with Optical Coherence Tomography*. Heart, 2007.
- [25] Zimarino, M., et al., *Optical coherence tomography accurately identifies intermediate atherosclerotic lesions--An in vivo evaluation in the rabbit carotid artery*. Atherosclerosis, 2007. **193**(1): p. 94-101.
- [26] Regar, E., et al., *Images in cardiovascular medicine. Optical coherence tomography findings at 5-year follow-up after coronary stent implantation*. Circulation, 2005. **112**(23): p. e345-6.
- [27] Tanimoto S, et al., *Paclitaxel-eluting stent restenosis shows three - layer appearance by optical coherence tomography*. Eurointerv 2006, 2006. **1**(4): p. 484.
- [28] van Beusekom, H.M., et al., *Drug-eluting stents show delayed healing: paclitaxel more pronounced than sirolimus*. Eur Heart J, 2007. **28**(8): p. 974-9.
- [29] Meer, F.J.v.d., et al., *Temperature-dependent optical properties of individual vascular wall components measured by optical coherence tomography*. Journal of Biomedical Optics, 2006. **11**(4): p. 041120.
- [30] Ormiston JA, et al., *First-In-Man Evaluation of a Bioabsorbable-Everolimus Eluting Coronary Stent System (BVS) in the Treatment of Patients with Single de-novo Native Coronary Artery Lesions: The ABSORB Trial*. The Lancet 2, 2008. **371**: p. 899-907.
- [31] Yabushita, H., et al., *Characterization of human atherosclerosis by optical coherence tomography*. Circulation, 2002. **106**(13): p. 1640-5.
- [32] Rieber, J., et al., *Diagnostic accuracy of optical coherence tomography and intravascular ultrasound for the detection and characterization of atherosclerotic plaque composition in ex-vivo coronary specimens: a comparison with histology*. Coron Artery Dis, 2006. **17**(5): p. 425-30.
- [33] Patwari, P., et al., *Assessment of coronary plaque with optical coherence tomography and high-frequency ultrasound*. Am J Cardiol, 2000. **85**(5): p. 641-4.
- [34] Kawasaki, M., et al., *Diagnostic accuracy of optical coherence tomography and integrated backscatter intravascular ultrasound images for tissue characterization of human coronary plaques*. J Am Coll Cardiol, 2006. **48**(1): p. 81-8.
- [35] Kume, T., et al., *Assessment of coronary arterial plaque by optical coherence tomography*. Am J Cardiol, 2006. **97**(8): p. 1172-5.
- [36] Jang, I.K., et al., *Visualization of coronary atherosclerotic plaques in patients using optical coherence tomography: comparison with intravascular ultrasound*. J Am Coll Cardiol, 2002. **39**(4): p. 604-9.

- [37] Jang, I.K., et al., *In vivo characterization of coronary atherosclerotic plaque by use of optical coherence tomography*. *Circulation*, 2005. **111**(12): p. 1551-5.
- [38] Chia, S., et al., *Comparison of coronary plaque characteristics between diabetic and non-diabetic subjects: An in vivo optical coherence tomography study*. *Diabetes Res Clin Pract*, 2008.
- [39] Chia, S., et al., *In-vivo comparison of coronary plaque characteristics using optical coherence tomography in women vs. men with acute coronary syndrome*. *Coron Artery Dis*, 2007. **18**(6): p. 423-7.
- [40] Kume, T., et al., *Relationship between coronary remodeling and plaque characterization in patients without clinical evidence of coronary artery disease*. *Atherosclerosis*, 2008. **197**(2): p. 799-805.
- [41] Kume, T., et al., *Measurement of the thickness of the fibrous cap by optical coherence tomography*. *Am Heart J*, 2006. **152**(4): p. 755 e1-4.
- [42] Cilingiroglu, M., et al., *Detection of vulnerable plaque in a murine model of atherosclerosis with optical coherence tomography*. *Catheter Cardiovasc Interv*, 2006. **67**(6): p. 915-23.
- [43] Takano, M., et al., *In vivo comparison of optical coherence tomography and angiography for the evaluation of coronary plaque characteristics*. *Am J Cardiol*, 2008. **101**(4): p. 471-6.
- [44] Kubo T, I.T., Takarada S, Kuroi A, Ueno S, Yamano T, Tanimoto T, Matsuo Y, Masho T, Kitabata H, Tanaka A, Nakamura N, Mizukoshi M, Tomobuchi Y, Akasaka T, *Implication of Plaque Color Classification for Assessing Plaque Vulnerability*. *J Am Coll Cardiol Intv*, 2008. **1**: p. 74-80.
- [45] Nadkarni, S.K., et al., *Measurement of Collagen and Smooth Muscle Cell Content in Atherosclerotic Plaques Using Polarization-Sensitive Optical Coherence Tomography 10.1016/j.jacc.2006.11.040*. *J Am Coll Cardiol*, 2007. **49**(13): p. 1474-1481.
- [46] Nadkarni, S.K., et al., *Evaluation of collagen in atherosclerotic plaques: the use of two coherent laser-based imaging methods*. *Lasers Med Sci*, 2008.
- [47] Oh, W.Y., et al., *High-speed polarization sensitive optical frequency domain imaging with frequency multiplexing*. *Opt Express*, 2008. **16**(2): p. 1096-103.
- [48] Chia, S., et al., *Association of statin therapy with reduced coronary plaque rupture: an optical coherence tomography study*. *Coron Artery Dis*, 2008. **19**(4): p. 237-42.
- [49] Kubo, T., et al., *Assessment of Culprit Lesion Morphology in Acute Myocardial Infarction: Ability of Optical Coherence Tomography Compared With Intravascular Ultrasound and Coronary Angiography*. *Journal of the American College of Cardiology*, 2007. **50**(10): p. 933-939.
- [50] Nadkarni, S.K., et al., *Measurement of collagen and smooth muscle cell content in atherosclerotic plaques using polarization-sensitive optical coherence tomography*. *J Am Coll Cardiol*, 2007. **49**(13): p. 1474-81.
- [51] Fercher, A.F., K. Mengedocht, and W. Werner, *Eye-length measurement by interferometry with partially coherent light*. *Opt. Lett.*, 1988. **13**: p. 186-188.
- [52] Kubo, T., et al., *Assessment of culprit lesion morphology in acute myocardial infarction: ability of optical coherence tomography compared with intravascular ultrasound and coronary angiography*. *J Am Coll Cardiol*, 2007. **50**(10): p. 933-9.
- [53] Kume, T., et al., *Assessment of coronary arterial thrombus by optical coherence tomography*. *Am J Cardiol*, 2006. **97**(12): p. 1713-7.

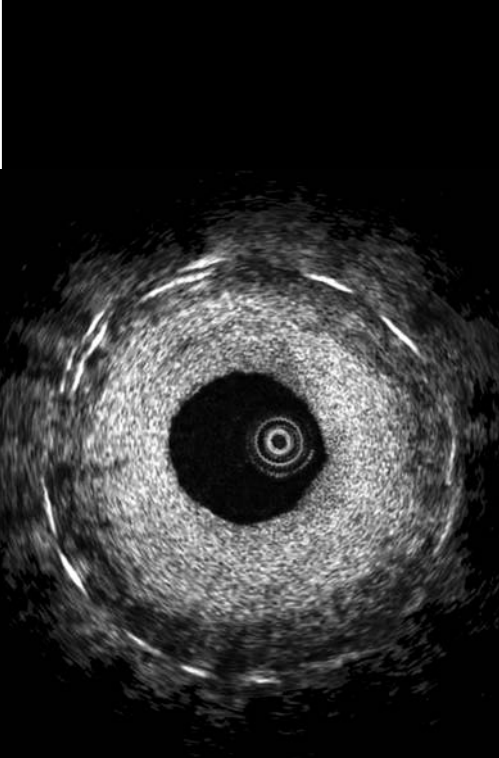
- [54] Tearney, G.J., et al., *Quantification of macrophage content in atherosclerotic plaques by optical coherence tomography*. *Circulation*, 2003. **107**(1): p. 113-9.
- [55] MacNeill, B.D., et al., *Focal and multi-focal plaque macrophage distributions in patients with acute and stable presentations of coronary artery disease*. *J Am Coll Cardiol*, 2004. **44**(5): p. 972-9.
- [56] Raffel, O.C., et al., *Relationship between a systemic inflammatory marker, plaque inflammation, and plaque characteristics determined by intravascular optical coherence tomography*. *Arterioscler Thromb Vasc Biol*, 2007. **27**(8): p. 1820-7.
- [57] Regar, E., et al., *Optical coherence tomography*. *Cardiovasc Radiat Med*, 2003. **4**(4): p. 198-204.
- [58] Regar, E., et al., *Real-time, in-vivo optical coherence tomography of human coronary arteries using a dedicated imaging wire*. *Am J Cardiol*, 2002. **90**(suppl 6A): p. 129H.
- [59] Regar E, van Leeuwen AMGJ, and S. PW, eds. *Optical coherence tomography in cardiovascular research*. . 2007, Informa Healthcare: London.
- [60] Prati, F, et al., *From bench to bedside: a novel technique of acquiring OCT images*. *Circ J*, 2008. **72**(5): p. 839-43.
- [61] Lee, S.H., et al., *Frequency of stent fracture as a cause of coronary restenosis after sirolimus-eluting stent implantation*. *Am J Cardiol*, 2007. **100**(4): p. 627-30.
- [62] Finn, A.V., et al., *Pathological correlates of late drug-eluting stent thrombosis: strut coverage as a marker of endothelialization*. *Circulation*, 2007. **115**(18): p. 2435-41.
- [63] Finn, A.V., et al., *Vascular responses to drug eluting stents: importance of delayed healing*. *Arterioscler Thromb Vasc Biol*, 2007. **27**(7): p. 1500-10.
- [64] van Beusekom, H.M., et al., *Long-term endothelial dysfunction is more pronounced after stenting than after balloon angioplasty in porcine coronary arteries*. *J Am Coll Cardiol*, 1998. **32**(4): p. 1109-17.
- [65] Barlis P, et al., *Novelties in Cardiac Imaging – Optical Coherence Tomography (OCT)*. *Eurointerv* 2006, 2008. **4**(Suppl 4): p. 22-26.
- [66] Shite, J., D. Matsumoto, and M. Yokoyama, *Sirolimus-eluting stent fracture with thrombus, visualization by optical coherence tomography*. *Eur Heart J*, 2006. **27**(12): p. 1389.
- [67] Suzuki, Y., F. Ikeno, and A.C. Yeung, *Drug-eluting stent strut distribution: a comparison between Cypher and Taxus by optical coherence tomography*. *J Invasive Cardiol*, 2006. **18**(3): p. 111-4.
- [68] Hasegawa, T., et al., *Comparison of nonuniform strut distribution between two drug-eluting stent platforms*. *J Invasive Cardiol*, 2007. **19**(6): p. 244-6.
- [69] Buellesfeld, L., et al., *Comparative endoluminal visualization of TAXUS crush-stenting at 9 months follow-up by intravascular ultrasound and optical coherence tomography*. *Z Kardiol*, 2005. **94**(10): p. 690-4.
- [70] Yamaguchi, T., et al., *Safety and feasibility of an intravascular optical coherence tomography image wire system in the clinical setting*. *Am J Cardiol*, 2008. **101**(5): p. 562-7.
- [71] Kataiwa, H., et al., *Safety and usefulness of non-occlusion image acquisition technique for optical coherence tomography*. *Circ J*, 2008. **72**(9): p. 1536-7.
- [72] Freudenberg, H. and P.R. Lichtlen, *[The normal wall segment in coronary stenoses--a postmortal study (author's transl)]*. *Z Kardiol*, 1981. **70**(12): p. 863-9.

- [73] Manfrini, O., et al., *Sources of error and interpretation of plaque morphology by optical coherence tomography*. Am J Cardiol, 2006. **98**(2): p. 156-9.
- [74] Weissman, N.J., I.F. Palacios, and A.E. Weyman, *Dynamic expansion of the coronary arteries: implications for intravascular ultrasound measurements*. Am Heart J, 1995. **130**(1): p. 46-51.
- [75] Kume, T., et al., *Assessment of coronary intima--media thickness by optical coherence tomography: comparison with intravascular ultrasound*. Circ J, 2005. **69**(8): p. 903-7.



CHAPTER 2

Safety of OCT



2.1

A Multi-Center Evaluation of the Safety of Intra-Coronary Optical Coherence Tomography

Barlis P, Gonzalo N, Di Mario C, Prati F, Buellesfeld L, Rieber J, Dalby MC, Ferrante G, Cera M, Grube E, Serruys P.W, Regar E.

Eurointervention 2009;5:90-95

A multicentre evaluation of the safety of intracoronary optical coherence tomography

Peter Barlis¹, MBBS, MPH, FRACP, FESC; Nieves Gonzalo¹, MD; Carlo Di Mario², MD, PhD, FESC; Francesco Prati³, MD, FESC; Lutz Buellesfeld⁴, MD; Johannes Rieber⁵, MD; Miles C. Dalby⁶, MRCP; Giuseppe Ferrante², MD; Maria Cera³, MD; Eberhard Grube⁴, MD, FESC; Patrick W. Serruys¹, MD, PhD, FESC; Evelyn Regar^{1*}, MD, PhD

1. Thoraxcenter, Erasmus Medical Centre, Rotterdam, The Netherlands; 2. Royal Brompton Hospital, London, United Kingdom; 3. San Giovanni Hospital, Rome, Italy; 4. Helios Heart Centre, Siegburg, Germany; 5. Medizinische Klinik Innenstadt, Ludwig-Maximilians University, Munich, Germany; 6. Harefield Hospital, Middlesex, United Kingdom

The authors have no conflict of interest to declare.

KEYWORDS

Imaging, optical coherence tomography, safety, coronary arteries

Abstract

Aims: Optical coherence tomography (OCT) is increasingly being applied to the coronary arteries. However, the risks associated with the imaging procedure are not yet well defined. The purpose of the present multicentre registry was to assess the acute complications associated with the clinical use of intra-coronary OCT in a large number of patients.

Methods and results: Consecutive patients from six centres who had OCT examination were retrospectively included. All adverse events and complications, even if transient, were noted. Risks were categorised into: 1) self-limiting 2) major complications including major adverse cardiac events (MACE) and 3) mechanical device failure. A total of 468 patients underwent OCT examination for evaluation of: plaque (40.0%), percutaneous coronary intervention (28.2%) or follow-up stent tissue coverage (31.8%). OCT was performed using a non-occlusive flush technique in 45.3% with a mean contrast volume of 36.6±9.4ml. Transient chest pain and QRS widening/ST-depression/elevation were observed in 47.6% and 45.5% respectively. Major complications included five (1.1%) cases of ventricular fibrillation due to balloon occlusion and/or deep guide catheter intubation, 3 (0.6%) cases of air embolism and one case of vessel dissection (0.2%). There were no cases of coronary spasm or MACE during or within the 24 hour period following OCT examination.

Conclusions: OCT is a specialised technique with a relatively steep learning curve. Major complications are uncommon and can be minimised with careful procedural planning and having an awareness of the potential contributory risks, especially deep guide catheter intubation during contrast flushing. Upcoming developments will make OCT more practical and less procedurally demanding, also potentially conserving contrast volume considerably.

* Corresponding author: Department of Cardiology, Thoraxcenter, Room Ba 585, Erasmus Medical Center Rotterdam, Dr. Molewaterplein 40, 3015 GD Rotterdam, The Netherlands

E-mail: e.regar@erasmusmc.nl

© Europa Edition. All rights reserved.

Introduction

Optical coherence tomography (OCT) is an intracoronary imaging technique using near infrared light with a much higher spatial resolution than intravascular ultrasound (IVUS). The 15 micron resolution permits detailed characterisation of the vessel wall giving new insights into the *in vivo* characterisation of atherosclerotic plaque and tissue responses following stent implantation. Unlike IVUS however, the technique requires flushing of the coronary artery to allow light transmission with the first generation OCT system also mandating proximal vessel balloon occlusion. Whilst the imaging resolution benefits of OCT are clear, the need for a flush system increases the complexity of the technique, and the risks associated with this have not been evaluated. The purpose of the present multicentre registry was, for the first time, to assess the acute complications associated with the clinical use of intracoronary OCT in a large number of patients.

Methods

Study population and OCT procedure

We conducted a multicentre registry to evaluate the safety of OCT. Data from patients undergoing OCT examination in six centres were reviewed. Consecutive patients who had OCT examination performed before January 31, 2008 were retrospectively included. Weight adjusted heparin was administered as standard prior to OCT imaging. All OCT examinations were carried out using a dedicated optical wire (ImageWire, LightLab Imaging Inc., Westford, MA, USA) connected to either the M2 or M3 OCT console (LightLab Imaging Inc., Westford, MA, USA). All participating centres completed the demographic, clinical and procedural case information using a uniform data sheet that was centrally analysed. The indications to perform OCT were categorised into evaluation of: A), lesion/plaque; B), percutaneous coronary intervention (PCI) (stent apposition); or C), stent tissue coverage at follow-up. The number of vessels imaged, together with the OCT flushing strategy (with or without proximal vessel balloon occlusion, see below) were recorded. OCT exclusion criteria applied by operators/centres included impaired left ventricular ejection fraction (<30%), renal impairment (serum creatinine >1.5 mg/dL), single remaining or tortuous vessel. When the non-occlusive technique was used, the additional contrast load required to permit imaging in a blood-free environment was documented.

Flush strategy

Infra-red light is unable to penetrate blood, thus imaging must be accompanied by transient clearance of the field of view from blood. In clinical intracoronary OCT, two methods have been established: 1), using a proximal occlusion balloon with flushing of crystalloid solution through the end hole of the balloon catheter using a power injector or 2), a non-occlusive approach with contrast flush injection via the guiding catheter.¹

Balloon occlusion method

A low-pressure, short over-the-wire balloon (Helios, Goodman Inc, Nagoya, Japan) with large inner lumen is advanced over a conventional guidewire distal to the region of interest. The

guidewire is then replaced with the dedicated OCT imaging wire and the balloon catheter is positioned in the proximal part of the vessel. Inflation of the balloon is performed using a dedicated deflator to 0.5-0.7 atm during which coronary blood flow is replaced by continuous infusion of Ringer's lactate or physiological saline at a rate of 0.5-1.2 ml/sec using a power injector (e.g. Mark-V ProVis, Medrad, Inc. Indianola, PA, USA).¹⁻³ A motorised pullback of the image wire is then commenced at a rate of 1.0 mm/sec to acquire images.

Non-occlusive technique

As the handling of the OCT image wire is limited by the fact that it contains an optical fibre and is not comparable to a standard guidewire with respect to steerability, pushability and torqueability, its safe passage distal to the region of interest can be facilitated by use of an over-the-wire catheter (e.g., the single lumen Transit, Cordis, Johnson & Johnson, Miami, FL, USA or the double lumen 0.023" TwinPass, Vascular Solutions Inc, Minneapolis, Minnesota, USA). The automated pullback (at 3.0 mm/sec) is then commenced during simultaneous flushing of viscous iso-osmolar contrast (e.g. Iodixanol 320, Visipaque™, GE Health Care, Cork, Ireland) through the guiding catheter. This can be achieved either manually or by use of an automated power injector (e.g. Mark-V ProVis, Medrad, Inc. Indianola, PA, USA).¹⁻³

OCT risks

Any complication judged by the operators to have occurred during or within the immediate 24-hour period following OCT examination was included, even if transient and with no clinical sequelae.

Risks were categorised into:

- 1) Self-limiting events
- 2) Major complications (arrhythmia, embolisation, coronary dissection or spasm) including major adverse cardiac events (defined as MI, emergency revascularisation – including percutaneous or surgical – and death).
- 3) Mechanical device failure

Furthermore, all risks were classified based on their eventual outcome as: A), Immediate correction with no specific action required; B), transient, but requiring specific treatment with resolution before the patient left the catheterisation laboratory; or C), required treatment/surveillance following discharge from the catheterisation laboratory (including lengthening patient's hospitalisation).

Study centres

The six participating centres were located in the Netherlands (one centre), United Kingdom (two centres), Italy (one centre), Germany (two centres). The number of OCT studies contributed by each centre was: Thoraxcenter (Rotterdam, the Netherlands n= 162, 34.6%); Royal Brompton Hospital (London, United Kingdom, n=91 19.4%); St. Giovanni Hospital (Italy, n=85, 18.2%); Helios Heart Centre (Siegburg, Germany, n=64, 13.7%). Medizinische Poliklinik, University of Munich (Munich, Germany, n=36, 7.7%) and Harefield Hospital (Middlesex, United Kingdom, n=30, 6.4%).

Statistical analysis

Descriptive analyses were used. Results are quoted as percentages for categorical data or as mean \pm standard deviation for continuous variables. Continuous and categorical variables were compared with the t-test and the chi-square/Fisher's exact test as appropriate. A p value of <0.05 was considered significant.

Results

Baseline clinical and procedural characteristics

A total number of 468 OCT examinations were recorded between June 2004–November 2007. Table 1 shows the baseline clinical and procedural characteristics. OCT was performed for plaque/lesion evaluation in 187 (40.0%), PCI evaluation in 132 (28.2%) and for the assessment of stent tissue coverage at follow-up in 149 (31.8%) of patients. A total of 510 vessels were imaged (1.1 \pm 0.3/patient). The LAD and RCA were the most frequently imaged vessels. A small proportion of patients had OCT imaging of

Table 1. Baseline clinical and procedural characteristics.

	n=468
Age (yrs)	63.7 \pm 9.1
Males	367 (78.4)
Hypertension	264 (56.4)
Diabetes Mellitus	94 (20.1)
Dyslipidaemia	279 (59.6)
Baseline LVEF (%)	61.5 \pm 11.2
Prior myocardial infarction	138 (29.5)
Prior coronary artery bypass grafting	23 (4.9)
Prior PCI	247 (52.7)
Clinical presentation	
Stable angina	248 (53.0)
Unstable angina	121 (25.9)
ACS/STEMI	99 (21.1)
Indication for OCT	
Plaque/lesion assessment	187 (40.0)
PCI assessment (stent apposition)	132 (28.2)
Follow-up stent tissue coverage	149 (31.8)
Target vessel	n=510
Number of vessels imaged/patient	1.1 \pm 0.3
Left main	6 (1.2)
Left anterior descending	222 (43.5)
Diagonal	14 (2.7)
Right	163 (32.0)
Left circumflex	83 (16.3)
Obtuse marginal	17 (3.3)
Graft	5 (1.0)
OCT System used	
M2	323 (69.0)
M3	145 (31.0)
OCT flushing technique	
Proximal balloon occlusion technique	256 (54.7)
Non-occlusive technique	212 (45.3)
Mean contrast volume (non-occlusive technique, ml)	36.6 \pm 9.4

LVEF-left ventricular ejection fraction; PCI-percutaneous coronary intervention; ACS-acute coronary syndrome; STEMI-ST elevation myocardial infarction; OCT-optical coherence tomography

the left main coronary artery (1.2%) and a bypass graft (1.0%). Of the 468 patients, 256 (54.7%) had images acquired during proximal balloon occlusion while the remaining 212 (45.3%) had OCT using a non-occlusive technique. In these patients, the additional mean contrast load used for flushing during OCT imaging was 36.6 \pm 9.4ml.

Risks of OCT

All observed complications are summarised in Table 2. The eventual outcome of the adverse events and complications encountered is depicted in Table 3.

1) Self-limiting events

As expected, the most frequent observation was transient chest pain during OCT image acquisition (47.6%). In all cases this settled following cessation of imaging and was significantly more frequent in patients imaged using the occlusive compared to non-occlusive technique (69.9% vs. 20.8%, $p<0.001$). In association, transient electrocardiographic changes were also observed with widening of the QRS complex or ST-segment depression in 41.0% and ST-elevation in 4.5%, almost exclusively in those imaged using proximal vessel balloon occlusion. Sinus brady and tachycardia was

Table 2. Risks of OCT.

	All (n=468)	Occlusive technique (n=256)	Non-occlusive technique (n=212)	p-value
Self-limiting events				
Chest pain	223 (47.6)	179 (69.9)	44 (20.8)	<0.001
Widening QRS/ST depression	192 (41.0)	139 (54.3)	53 (25)	<0.001
ST elevation	21 (4.5)	17 (6.6)	4 (1.9)	0.01
Sinus bradycardia	14 (3.0)	11 (4.3)	3 (1.4)	0.07
Sinus tachycardia	10 (2.1)	7 (2.7)	3 (1.4)	0.33
Atrioventricular block	2 (0.4)	2 (0.8)	0	0.19
Major complications				
Arrhythmias				
Atrial fibrillation	0	0	0	–
Ventricular tachycardia	0	0	0	–
Ventricular fibrillation	5 (1.1)	3 (1.2)	2 (0.9)	0.81
Coronary spasm	0	0	0	–
Dissection	1 (0.2)	1 (0.4)	0	0.36
Perforation	0	0	0	–
Thrombus	0	0	0	–
Air embolism	3 (0.6)	2 (0.8)	1 (0.5)	0.68
Mechanical device failure				
Wire tip fracture	1 (0.2)	0	1 (0.5)	0.45
Major adverse cardiac events during the procedure or in the 24 hour period post				
	0	0	0	–

Table 3. Outcome of adverse events/complications.

Immediate resolution	96.7%
Required specific treatment but resolved before leaving the catheterisation laboratory	3.1%
Persisting beyond discharge from catheterisation laboratory (including requiring ongoing clinical surveillance)	0.2%

infrequently observed and settled promptly following cessation of imaging. There were two (0.4%) cases of transient atrioventricular block that spontaneously resolved following deflation of the proximal occlusion balloon and withdrawal of the catheter.

2) Major complications

Ventricular fibrillation

Ventricular fibrillation (VF) occurred in five (1.1%) patients. In all cases, sinus rhythm was promptly restored following cessation of OCT imaging and external defibrillation. Three of the five cases occurred during proximal balloon occlusion. The two cases seen with the non-occlusive technique were in the context of deep guide catheter intubation of the left coronary artery during simultaneous contrast injection.

Air embolism

There were three (0.6%) cases of air embolisation. In one case, this occurred early on in the procedure, when introducing the guiding catheter specifically with the intention to perform OCT. Two other cases occurred during flushing of the crystalloid solution with air inadvertently introduced during connection of the flush lines. All cases responded promptly to air aspiration, treatment with nitrates and in one case, nitroprusside administration.

Coronary dissection

A minor type-A coronary dissection was observed in one (0.4%) patient as a result of the imaging wire. Coronary blood flow was not impaired and further treatment was not indicated.

Coronary spasm

There were no cases of coronary spasm observed during OCT imaging.

MACE

There were no MACE observed during or in the 24 hour period following OCT imaging. In one patient, stenosis was observed at the site of previous balloon occlusion four months following OCT evaluation of the LCx. Due to the presence of multivessel coronary disease with angina, the patient was referred for CABG.

3) Mechanical device failure

Although there was no adverse clinical outcome observed, in one (0.2%) patient having OCT nine months following stent implantation, the imaging wire became entrapped amongst stent struts in the LAD with subsequent fracture at the distal tip. In this case, an over-the-wire catheter was initially used to advance the wire distally however, once positioned, was found to be too proximal and within the stent. Attempts to advance the wire forward resulted in wire entrapment. Four month follow-up was uneventful with control angiography showing patent vessel without flow abnormalities.

Discussion

This is the first registry to demonstrate the acute risks related to OCT imaging in a large number of patients. The high-resolution, together with advantages over other imaging modalities such as IVUS, have made OCT very popular for the detailed assessment of atherosclerotic plaque and coronary stents. As a result, this study provides essential safety information that will see OCT performed in a more informed manner, both for operators and patients alike.

Several groups have reported their clinical experience with OCT over the last few years.²⁻¹¹ Nevertheless, only limited information about acute complications of this procedure is available. Recently,

Yamaguchi et al¹² examined the feasibility of OCT and IVUS imaging in 76 patients. Although transient chest pain and electrocardiographic changes caused by imaging were not considered as part of their study, there were no adverse events reported following both IVUS and OCT, with the latter being performed exclusively using the occlusive method. In contrast, the present study included a large number of consecutive patients undergoing OCT examination, and recorded all potential adverse events, even if transient and benign. We believe this permits a more informed assessment and is therefore representative of the 'real world' application and safety of OCT imaging.

The present study also assessed patients having OCT imaging using the non-occlusive technique that will, because of its simpler procedural requirements, become the mainstay method for OCT image acquisition, eliminating the cumbersome proximal balloon occlusion requirements. Such developments will be realised in the not too distant future, with the introduction into clinical practice of faster image acquisition speeds thanks to optical frequency-domain technologies.¹³ Therefore, the expected rise in OCT use is another reason why comprehensively reporting the safety profile of the technique remains of paramount clinical importance.

The spectrum of adverse events observed in relation to OCT imaging in our study was broad. The majority of events recorded were minor and transient, with chest pain being the most frequent. This is not surprising as, in a significant proportion of patients (54.7%), images were obtained during proximal balloon vessel occlusion. In all cases, the chest pain resolved following cessation of imaging or deflation of the occlusion balloon. The mechanisms purporting to link balloon coronary occlusion and chest pain are complex and include the triggering of several neural responses stimulating coronary mechanoreceptors and vagal/sympathetic cardiac afferent fibres.^{14,15}

Electrocardiographic changes were observed in almost half the patients. Such changes are also frequently observed during angioplasty and stent implantation and are likely reflective of underlying ischaemia. In addition to ST-segment changes, transient prolongation of the QRS interval was seen. Although this study was not designed to measure the QRS interval, prolongation was judged visually during OCT imaging. This remains a highly sensitive marker of ischaemia during percutaneous coronary intervention (PCI), even more so than ST-segment changes and chest pain which is highly subjective.¹⁶ Furthermore, coronary occlusion, particularly of proximal or middle artery segments is directly linked to observations of QRS prolongation.¹⁶ The knowledge that almost half of all patients are likely to experience some level of chest discomfort and/or electrocardiographic changes of ischaemia during OCT imaging should serve to inform patients prior to the procedure and, where indicated, encourage the use of pre-medication, such as short acting analgesics.

The frequency of arrhythmias observed, particularly life-threatening VF that occurred in five (1.1%) of patients, warrants further analysis. Several studies have shown the incidence of VF during coronary angioplasty is about 1.5%,^{17,18} with the rate dropping down to around 0.6% for diagnostic procedures.^{19,20} In addition to ischaemia, other mechanisms have also been identified including reperfusion, electrolyte imbalances, coronary instrumentation, osmolarity and electrolyte composition of contrast agents and intra-coronary thrombus.²¹⁻²⁷

Iodixanol (Visipaque™, GE Health Care, Cork, Ireland) is the contrast agent that is preferentially used for flushing during the non-occlusive method. The advantage lies in its higher viscosity relative to other agents, which permits optimal blood clearance for OCT imaging at the given flush volumes through the guiding catheter. This agent has also been shown to have a lower propensity to cause VF given its lower osmolality, higher viscosity and higher concentration of sodium and calcium chloride molecules compared to other non-ionic media.²⁸⁻³¹

In the two cases in which VF occurred during contrast flush, the operators reported deeply intubating the guide into the left coronary artery in an attempt to optimally deliver the contrast flush. In hindsight, this is thought to potentiate the risk of VF with prior reports showing that the combination of a wedged catheter and contrast flush is a high-risk situation for inducing VF.^{25,32,33} Given that VF also occurred in the patients during the occlusive technique with flush of crystalloid solution and, therefore no contrast, it is obvious that other mechanisms are at play, with ischaemia still a major contributor. Nevertheless, reporting of such events encourages further work in developing alternative, non-contrast based flushing solutions that are bio-compatible while eliminating the potential unwanted effects of contrast agents.

In our experience, the additional contrast volume used for flushing does not translate into adverse nephrotoxic events. However, patients with renal impairment are not subjected to OCT imaging. In such patients, an occlusive technique could be used however acknowledging its inherent limitations such as an inability to visualise ostial or very proximal coronary segments. Refinements in OCT technology with optical frequency domain imaging (OFDI) permit pullback speeds up to 20 mm/sec hence, a single pullback could be accomplished within a matter of a few seconds thereby dramatically reducing the contrast volume needed.¹³

Other complications, such as dissection and air embolisation are not specific to OCT and can be observed at any stage of an invasive procedure. Recently Kim et al³⁴ reported a single case of thrombus formation during elective OCT interrogation of LAD stents at seven months follow-up. Although this is a potential complication with any arterial instrumentation, we did not observe any such cases in our cohort of patients, all treated with weight adjusted heparin prior to OCT assessment. Compared to IVUS, the present study did not identify cases of vessel spasm with dissection seen in one patient and device related failure in one patient. Prior IVUS studies found an incidence of 3% of coronary spasm, in some, also resulting in abrupt vessel occlusion.³⁵ This was irrespective of the size of the IVUS catheter used.³⁵ Technical failure of the IVUS system was observed in 0.4% including guide wire winding or breakage of the catheter.³⁵ Such complications are fortunately uncommon, but are inherent with invasive procedures requiring intracoronary catheter manipulation and instrumentation. The incidence of complications encountered in relation to the OCT procedure is consistent with safety data from coronary angiography. Similarly, angiography requires balloon occlusion during image acquisition although balloon-related vessel injury has not been shown to be a problem six months following angiographic examination.³⁶ The general trend for OCT image acquisition is to eliminate this aspect, thereby simplifying the procedure considerably.

Angioscopic technology has also remained rather stagnant over the years, causing it to be used only by a select few specialised centres worldwide. In contrast, OCT has rapidly evolved from the initial use of angioplasty balloons and catheters to dedicated, low profile materials, all contributing to a safer procedure. Further, OCT permits the accurate quantification of both plaque and tissue strut coverage and is also compatible with 6 Fr guiding catheters.

Limitations

This study was a retrospective analysis, however included a large number of consecutive patients undergoing OCT at different centres. Also, as OCT is a relative 'new comer' to the field of intravascular imaging, cases from the early phase of OCT technology development were included in this study meaning that complication rates were also inclusive of this early experience and might reflect to a certain degree the learning curve of the technique. Nevertheless, to allow an informed assessment about the safety profile, all potential adverse events were included, even if transient and benign.

Conclusions

OCT technology has moved at a rapid pace with greater refinements in materials and technique already contributing to increased clinical uptake. Future developments such as optical frequency domain imaging will see OCT use simplified and therefore become conducive to more centres and operators worldwide. Nevertheless, OCT is a specialised technique with a relatively steep learning curve and therefore, requires adequate proctorship. Major complications are uncommon and can be minimised with careful procedural planning and being aware of the potential contributory risks, especially deep guide catheter intubation during contrast flushing and minimising the duration of image acquisition in preference for more frequent but shorter imaging runs. Developments will also make OCT more practical and less procedurally demanding, also potentially conserving contrast volume considerably. The benefits in relation to a greater understanding of coronary artery disease and responses following stent implantation are enormous, meaning that light-based imaging will continue to develop well beyond the <current, predominantly research based applications. Knowledge of the procedural safety profile is therefore essential to help inform patients and operators.

Acknowledgements

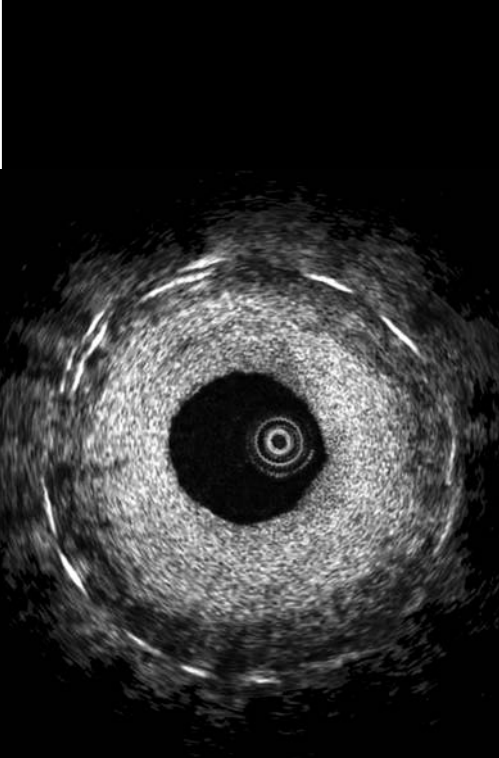
Jurgen Lighthart, Francesca Del Furia, and Philip Moore who provided valuable assistance with data collection. The study was supported in part by Siemens Healthcare.

References

1. Prati F, Cera M, Ramazzotti V, Imola F, Giudice R, Albertucci M, Propri SD, Albertucci M. From bench to bedside. *Circ J* 2008; 72(5):839-843.
2. Prati F, Cera M, Ramazzotti V, Imola F, Giudice R, Albertucci M. Safety and feasibility of a new non-occlusive technique for facilitated intracoronary optical coherence tomography (OCT) acquisition in various clinical and anatomical scenarios. *EuroIntervention* 2007; 3(11):365-370.
3. Tanigawa J, Barlis P, Di Mario C. Intravascular Optical Coherence Tomography: Optimisation of image acquisition and quantitative assessment of stent strut apposition. *EuroIntervention* 2007; 3:128-136.

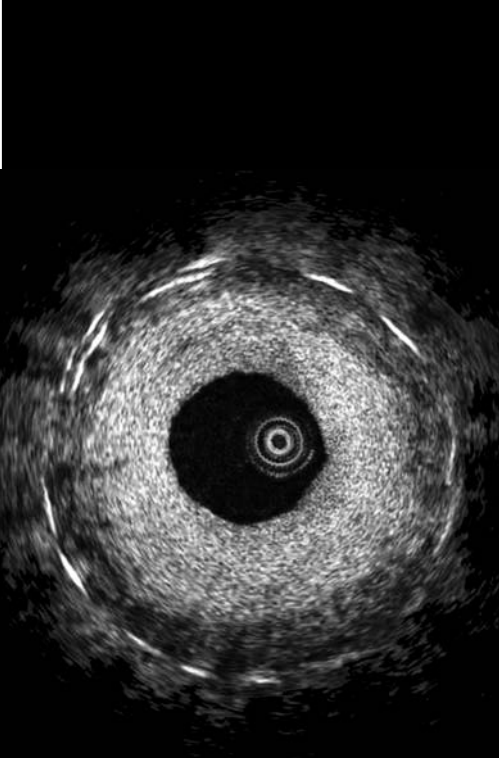
Chapter 2.1

4. Tanigawa J, Barlis P, Kaplan S, Goktekin O, Di Mario C. Stent strut apposition in complex lesions using optical coherence tomography. *Am J Cardiol* 2006; 98(8):Suppl 1: 97M.
5. Tanigawa J, Barlis P, Dimopoulos K, Di Mario C. Optical coherence tomography to assess malapposition in overlapping drug-eluting stents. *EuroIntervention* 2008; 3(13):580-583.
6. Takano M, Yamamoto M, Inami S, Murakami D, Seimiya K, Ohba T, Seino Y, Mizuno K. Long-term follow-up evaluation after sirolimus-eluting stent implantation by optical coherence tomography: do uncovered struts persist? *J Am Coll Cardiol* 2008; 51(9):968-969.
7. Takano M, Inami S, Jang IK, Yamamoto M, Murakami D, Seimiya K, Ohba T, Mizuno K. Evaluation by optical coherence tomography of neointimal coverage of sirolimus-eluting stent three months after implantation. *Am J Cardiol* 2007; 99(8):1033-1038.
8. Matsumoto D, Shite J, Shinke T, Otake H, Tanino Y, Ogasawara D, Sawada T, Paredes OL, Hirata K, Yokoyama M. Neointimal coverage of sirolimus-eluting stents at 6-month follow-up: evaluated by optical coherence tomography. *Eur Heart J* 2007; 28(8):961-967.
9. Chen BX, Ma FY, Wei L, Ruan JH, Xie WL, Zhao XZ, Sun SH, Guo XM, Wang F, Tian T, Chu XW. Neointimal Coverage of Bare Metal and Sirolimus-Eluting Stents Evaluated with Optical Coherence Tomography. *Heart* 2007; hrt.2007.118679.
10. Kubo T, Imanishi T, Takarada S, Kuroi A, Ueno S, Yamano T, Tanimoto T, Matsuo Y, Masho T, Kitabata H, Tsuda K, Tomobuchi Y, Akasaka T. Assessment of culprit lesion morphology in acute myocardial infarction: ability of optical coherence tomography compared with intravascular ultrasound and coronary angiography. *J Am Coll Cardiol* 2007; 50(10):933-939.
11. Tanigawa J, Barlis P, Di Mario C. Heavily calcified coronary lesions preclude strut apposition despite high pressure balloon dilatation and rotational atherectomy: in-vivo demonstration with optical coherence tomography. *Circ J* 2008; 72(1):157-160.
12. Yamaguchi T, Terashima M, Akasaka T, Hayashi T, Mizuno K, Muramatsu T, Nakamura M, Nakamura S, Saito S, Takano M, Takayama T, Yoshikawa J, Suzuki T. Safety and feasibility of an intravascular optical coherence tomography image wire system in the clinical setting. *Am J Cardiol* 2008; 101(5):562-567.
13. Barlis P, Schmitt J. Current and future developments in intracoronary optical coherence tomography imaging. *EuroIntervention* 2009;4:529-534.
14. Malliani A, Pagani M, Lombardi F, Cerutti S. Cardiovascular neural regulation explored in the frequency domain. *Circulation* 1991; 84(2):482-492.
15. Manfrini O, Morgagni G, Pizzi C, Fontana F, Bugiardini R. Changes in autonomic nervous system activity: spontaneous versus balloon-induced myocardial ischaemia. *Eur Heart J* 2004; 25(17):1502-1508.
16. Cantor AA, Goldfarb B, Ilija R. QRS prolongation: a sensitive marker of ischemia during percutaneous transluminal coronary angioplasty. *Catheter Cardiovasc Interv* 2000; 50(2):177-183.
17. Bredlau CE, Roubin GS, Leimgruber PP, Douglas JS, Jr., King SB, 3rd, Gruentzig AR. In-hospital morbidity and mortality in patients undergoing elective coronary angioplasty. *Circulation* 1985; 72(5):1044-1052.
18. Dorros G, Cowley MJ, Simpson J, Bentivoglio LG, Block PC, Bourassa M, Detre K, Gosselin AJ, Gruntzig AR, Kelsey SF, Kent KM, Mock MB, Mullin SM, Myler RK, Passamani ER, Stertzer SH, Williams DO. Percutaneous transluminal coronary angioplasty: report of complications from the National Heart, Lung, and Blood Institute PTCA Registry. *Circulation* 1983; 67(4):723-730.
19. Davis K, Kennedy JW, Kemp HG, Jr., Judkins MP, Gosselin AJ, Killip T. Complications of coronary arteriography from the Collaborative Study of Coronary Artery Surgery (CASS). *Circulation* 1979; 59(6):1105-1112.
20. Nishimura RA, Holmes DR, Jr., McFarland TM, Smith HC, Bove AA. Ventricular arrhythmias during coronary angiography in patients with angina pectoris or chest pain syndromes. *Am J Cardiol* 1984; 53(11):1496-1499.
21. Goldstein JA, Butterfield MC, Ohnishi Y, Shelton TJ, Corr PB. Arrhythmogenic influence of intracoronary thrombosis during acute myocardial ischemia. *Circulation* 1994; 90(1):139-147.
22. Gorenek B. Tachyarrhythmias in percutaneous coronary interventions. *J Electrocardiol* 2006; 39(4):412 e411-415.
23. Huang JL, Ting CT, Chen YT, Chen SA. Mechanisms of ventricular fibrillation during coronary angioplasty: increased incidence for the small orifice caliber of the right coronary artery. *Int J Cardiol* 2002; 82(3):221-228.
24. Missri J, Jeresaty RM. Ventricular fibrillation during coronary angiography: reduced incidence with nonionic contrast media. *Cathet Cardiovasc Diagn* 1990; 19(1):4-7.
25. Pedersen HK, Jacobsen EA, Mortensen E, Refsum H. Contrast-medium-induced ventricular fibrillation: arrhythmogenic mechanisms and the role of antiarrhythmic drugs in dogs. *Acad Radiol* 1995; 2(12):1082-1088.
26. Quigley PJ, Maurer BJ. Ventricular fibrillation during coronary angiography: association with potassium-containing glyceryl trinitrate. *Am J Cardiol* 1985; 56(1):191.
27. Rudolf J, Phillips L. High-osmolality and low-osmolality contrast agents. *N Engl J Med* 1992; 327(3):203-204.
28. Baath L, Almen T. Reducing the risk of ventricular fibrillation by adding sodium to ionic and non-ionic contrast media with low iodine concentration. Coronary perfusion of the isolated rabbit heart with meglumine diatrizoate or iopentol at 140 mg I/ml and 0-154 mmol Na+/l. *Acta Radiol* 1989; 30(2):207-212.
29. Hayakawa K, Yamashita K. Low-osmolality contrast media-induced ventricular fibrillation. *Invest Radiol* 1989; 24(4):298-301.
30. Morris TW, Ventura J. Incidence of fibrillation with dilute contrast media for intra-arterial coronary digital subtraction angiography. *Invest Radiol* 1986; 21(5):416-418.
31. Chai CM, Karlsson JO, Almen T. Incidence of ventricular fibrillation during left coronary arteriography in pigs: comparison of a solution of the nonionic dimer iodixanol with solutions of five different nonionic monomers. *Acta Radiol* 2008; 49(2):150-156.
32. Pedersen HK. Electrolyte addition to nonionic contrast media. Cardiac effects during experimental coronary arteriography. *Acta Radiol Suppl* 1996; 405:1-31.
33. Pedersen HK, Jacobsen EA, Refsum H. Contrast media-induced ventricular fibrillation: an experimental study of the effects of dimeric contrast media during wedged catheter injection in dogs. *Acad Radiol* 1994; 1(2):136-144.
34. Kim JS, Choi EY, Choi D, Jang Y. Images in cardiovascular medicine. Catastrophic thrombus formation during optical coherence tomography. *Circulation* 2008; 118(6):e101-102.
35. Hausmann D, Erbel R, Alibelli-Chemarin MJ, Boksich W, Caracciolo E, Cohn JM, Culp SC, Daniel WG, De Scheerder I, DiMario C, et al. The safety of intracoronary ultrasound. A multicenter survey of 2207 examinations. *Circulation* 1995; 91(3):623-630.
36. Hamon M, Lablanche JM, Bateurs C, McFadden EP, Quandalle P, Bertrand ME. Effect of balloon inflation in angiographically normal coronary segments during coronary angiography: a quantitative angiographic study. *Cathet Cardiovasc Diagn* 1994; 31(2):116-121.



CHAPTER 3

Quantitative lumen and stent analysis with OCT



3.1

Quantitative Ex-vivo and In-vivo Comparison of Lumen Dimensions Measured by Optical Coherence Tomography (OCT) and Intravascular Ultrasound (IVUS) in Human Coronary Arteries

Gonzalo N, Serruys PW, Garcia-Garcia HM, van Soest G, Okamura T, Ligthart J, Knaapen M, Verheye S, Bruining N, Regar E.

Rev Esp Cardiol. 2009 Jun;62(6):615-24

Quantitative Ex Vivo and In Vivo Comparison of Lumen Dimensions Measured by Optical Coherence Tomography and Intravascular Ultrasound in Human Coronary Arteries

Nieves Gonzalo,^a Patrick W. Serruys,^a Héctor M. García-García,^a Gijs van Soest,^a Takayuki Okamura,^a Jurgen Ligthart,^a Michiel Knaapen,^c Stefan Verheye,^b Nico Bruining,^a and Evelyn Regar^a

^aDepartment of Cardiology, Thoraxcenter, Erasmus MC, Rotterdam, The Netherlands

^bAntwerp Cardiovascular Institute Middelheim Hospital, Antwerp, Belgium

^cHistogenex, Antwerp, Belgium

Introduction and objectives. The relationship between the lumen dimensions obtained in human coronary arteries using intravascular ultrasound (IVUS) and those obtained using optical coherence tomography (OCT) is not well understood. The objectives were to compare the lumen measurement obtained *ex vivo* in human coronary arteries using IVUS, OCT, and histomorphometry, and *in vivo* in patients using IVUS and OCT with and without balloon occlusion.

Methods. *Ex vivo* study: the lumen areas of matched anatomical sections of human coronary arteries were measured using IVUS, OCT, and histology. *In vivo* study: the lumen areas in matched sections were measured using IVUS and OCT with and without occlusion.

Results. *Ex vivo*: in the 8 specimens studied, the lumen area obtained using OCT and IVUS was larger than that obtained using histomorphometry: mean difference 0.8 (1) mm² (28%) for OCT and 1.3 (1.1) mm² (40%) for IVUS. *In vivo*: in the 5 vessels analyzed, the lumen area obtained using IVUS was larger than that obtained using OCT: mean difference 1.67 (0.54) mm² (33.7%) for IVUS relative to OCT with occlusion and 1.11 (0.53) mm² (21.5%) relative to OCT without occlusion. The lumen area obtained using OCT without occlusion was larger than that obtained using OCT with occlusion: mean difference 0.61 (0.23) mm² (13%).

Conclusions. In fixed human coronary arteries, both IVUS and OCT overestimated the lumen area compared with histomorphometry. *In vivo* the lumen dimensions obtained using IVUS were larger than those obtained using OCT, with or without occlusion. Moreover, the OCT image acquisition technique (ie, with or without occlusion) also had an impact on lumen measurement.

Key words: *Optical coherence tomography. Intravascular ultrasound. Lumen dimensions. Ex vivo. In vivo. Intracoronary imaging.*

SEE EDITORIAL ON PAGES 599-602

Correspondence: Dr E. Regar, Thoraxcenter, Bd 585, 's-Gravendijkwal 230, 3015-CE Rotterdam, The Netherlands
E-mail: e.regar@erasmusmc.nl

Received January 13, 2009.

Accepted for publication February 19, 2009.

Comparación cuantitativa *ex vivo* e *in vivo* de las dimensiones del lumen medidas por tomografía de coherencia óptica y ecográfica intravascular en arterias humanas

Introducción y objetivos. La relación entre las dimensiones del lumen medidas por ecografía intravascular (IVUS) y tomografía de coherencia óptica (OCT) en arterias coronarias humanas no es bien conocida. Los objetivos son comparar las dimensiones del lumen en IVUS, OCT e histología en arterias coronarias humanas *ex vivo*, y comparar *in vivo* las dimensiones del lumen obtenidas en pacientes con IVUS, OCT con occlusión y OCT sin occlusión.

Métodos. Estudio *ex vivo*: el área luminal se midió en secciones anatómicas correspondientes en IVUS, OCT e histología en arterias coronarias humanas. Estudio *in vivo*: el área luminal se midió en regiones correspondientes en IVUS y OCT con y sin occlusión.

Resultados. *Ex vivo*: en las 8 muestras estudiadas, el área del lumen fue más grande en IVUS y OCT que en histología —diferencia media, 0,8 ± 1 mm² (28%) para OCT y 1,3 ± 1,1 mm² (40%) para IVUS—. *In vivo*: en los cinco vasos analizados las dimensiones del lumen fueron más grandes en IVUS que en OCT —diferencia área media del lumen, 1,67 ± 0,54 mm² (33,7%) para IVUS y OCT con occlusión y 1,11 ± 0,53 mm² (21,5%) para IVUS y OCT sin occlusión—. Las dimensiones del lumen fueron más grandes en OCT sin occlusión que en OCT con occlusión —diferencia media, 0,61 ± 0,23 mm² (13%).

Conclusiones. En arterias coronarias humanas fijadas, IVUS y OCT sobrestimaron el área del lumen en comparación con la histología. *In vivo*, las dimensiones del lumen fueron más grandes en IVUS que en OCT con o sin occlusión. La técnica de adquisición de OCT (con o sin occlusión) influye en las dimensiones del lumen.

Palabras clave: *Tomografía de coherencia óptica. IVUS. Dimensiones del lumen. Ex vivo. In vivo. Imagen intracoronaria.*

ABBREVIATIONS

IVUS: intravascular ultrasound
LAD: left anterior descending coronary artery
LCX: left circumflex artery
MLA: minimum lumen area
OCT: optical coherence tomography

INTRODUCTION

Optical coherence tomography (OCT) is a new intracoronary imaging modality that provides *in vivo* high-resolution images of the coronary artery.¹ The OCT imaging technique is, in general, similar to that of intravascular ultrasound (IVUS), but whereas IVUS works by applying radiofrequency radiation, OCT uses light radiation. In both techniques the imaging probe is automatically pulled back through the coronary segment of interest. In contrast to IVUS, in OCT acquisition the coronary vessel needs to be cleared of blood. This is necessary since red blood cells are non-transparent causing multiple light scattering and substantial signal attenuation. This was achieved in the first commercially available OCT system by proximal occlusion of the vessel with a dedicated low-pressure balloon and simultaneous distal flush delivery (occlusive technique) during OCT probe pullback.² However, the recent increase in pullback speed (from 1 mm/s to 3 mm/s) enabled OCT pullback while displacing blood by continuous flush (x-ray contrast medium) delivery through the guide catheter without the need for vessel occlusion (non-occlusive technique).³ The impact of these 2 different acquisition techniques on lumen dimension when measured by OCT has not yet been reported.

The present study had 2 aims: to compare lumen size when measured by IVUS, OCT and histology in human coronary arteries *ex vivo*; to compare, *in vivo*, intracoronary lumen size when measured in patients by OCT with balloon occlusion, OCT without balloon occlusion, and IVUS.

METHODS

Ex Vivo Human Coronary Arteries

Specimens

Ten left anterior descending coronary artery (LAD) segments were excised within 24 h post-mortem, 1 cm proximal to the bifurcation with the left circumflex artery (LCX) and fixed in 4%

formaldehyde. Standard 6 F coronary sheaths (Arrow, Reading, PA, USA) were introduced and fixed at the distal and proximal ends of the arteries.

Intracoronary Imaging

For intracoronary imaging, the specimens were immersed in a saline bath at room temperature and perfused with saline at physiologic pressure. IVUS data were acquired using the Atlantis™ 40 MHz catheter with an automated motorized pullback device at a constant speed of 0.5 mm/s. OCT data were acquired using a commercially available system for intracoronary imaging and a 0.019" ImageWire™ (LightLab Imaging, Westford, MA, USA) with automated pullback at 1 mm/s. Lumen measurements in both IVUS and OCT were performed with the same dedicated coronary vessel analysis software (CURAD, Wijk bij Duurstede, Netherlands).⁴⁻⁶

Histology Preparation and Analysis

Following the intracoronary imaging procedures, the specimens were sectioned for histological analysis. The distal side of the bifurcation of the LAD to the LCX was used as the starting point for the first histology section. From this point to the distal and proximal side, histology sections were taken at 5-mm intervals to the end of the specimen.⁷

Matching Procedure

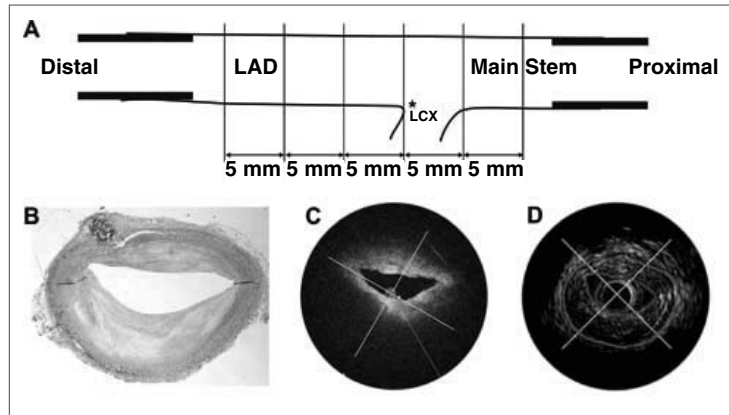
The OCT and IVUS pullbacks were matched by vessel analysis software (CURAD), which can synchronize image data acquired with different modalities onto a single computer screen. The proximal and distal sheaths were used as longitudinal landmarks. After histology tissue processing, the sections (eg, microscopic images) were used to identify the corresponding location in the OCT image data set based on the similar visual appearance of the lumen morphology. Following this identification process, the visualization software synchronized the OCT and the IVUS image data sets and identified the corresponding IVUS image⁸ (Figure 1). To avoid the Dotter effect, only cross-sections where the IVUS catheter was moving freely in the lumen were selected.

In Vivo Human Coronary Arteries

Study Population

Patients who were undergoing OCT examination of 1 coronary artery were included in the study. The medical ethics committee of the Erasmus MC

Figure 1. Matching of IVUS, OCT, and histology ex vivo. The distal side of the bifurcation of the LAD to the LCX (*) was used as the starting point for the first histology section. From this point to the distal and proximal side, histology sections were taken at 5-mm intervals to the end of the specimen (A). The histology sections (B) were used to identify the corresponding location in the OCT image data set (C) based on the similar visual appearance of the lumen morphology. Following this identification, the visualization software synchronized the OCT and IVUS image data sets and identified the corresponding IVUS image (D).



approved the study and all patients gave written informed consent.

IVUS Acquisition and Analysis

IVUS was acquired after intracoronary nitroglycerine administration using the Eagle Eye 20 MHz catheter (Volcano, Rancho Cordova, USA) with automatic continuous pullback at 0.5 mm/s. Before analysis, the IVUS data were retrospectively processed with an image-based gating system (Intelligate).⁹ The lumen was measured with the dedicated quantitative analysis software (CURAD).^{4,5}

OCT Acquisition and Analysis

Optical coherence tomography acquisition was performed using the same system as described for the ex vivo study. Firstly, pullback was performed with proximal balloon occlusion and distal flush delivery, after which pullback was performed in the same segment without occlusion.

Occlusive technique: the occlusion balloon (Helios, Goodman, Japan) was advanced distal to the region of interest over a conventional angioplasty guidewire (0.014"). The conventional guidewire was then replaced by the OCT ImageWire and the occlusion balloon catheter was positioned proximal to the segment of interest. Pullback of the ImageWire was performed during inflation of the proximal occlusion balloon catheter at low pressure (0.4 atm) with simultaneous distal flush delivery (lactated Ringer's solution at 37°C; flow rate 0.8 mL/s). Images were acquired during pullback at 1 mm/s.

Non-occlusive technique: the ImageWire was placed in the artery using a double lumen catheter (Twin Pass catheter, Vascular Solutions). Pullback was performed during continuous injection of contrast medium (3 mL/s, Iodixanol 370, Visipaque, GE Health Care, Cork, Ireland) through the guide catheter with an injection pump. In this case, the automated pullback rate was 3 mm/s.

The lumen measurements were performed with proprietary software for offline analysis (LightLab Imaging, Westford, MA, USA). For all OCT studies, the settings for the refraction index were adjusted to the flush solution used (saline, Ringer's lactate, and x-ray contrast, respectively).

Matching of OCT and IVUS Pullbacks

The region of interest was matched in the 3 pullbacks (occlusive OCT, non-occlusive OCT, and IVUS) using landmarks such as side branches (Figure 2). Differences in pullback speed were adjusted to appropriately compare the 2 OCT pullbacks per frame.

Statistical Analysis

Statistical analysis was performed using SPSS 12.0.1 for Windows (SPSS, Chicago, IL, USA). Continuous variables are expressed as mean (standard deviation) and categorical variables are expressed as percentages. The absolute and relative differences between measurements obtained with the different techniques were calculated. The relative difference was defined as the absolute difference divided by the average. Data are also expressed in

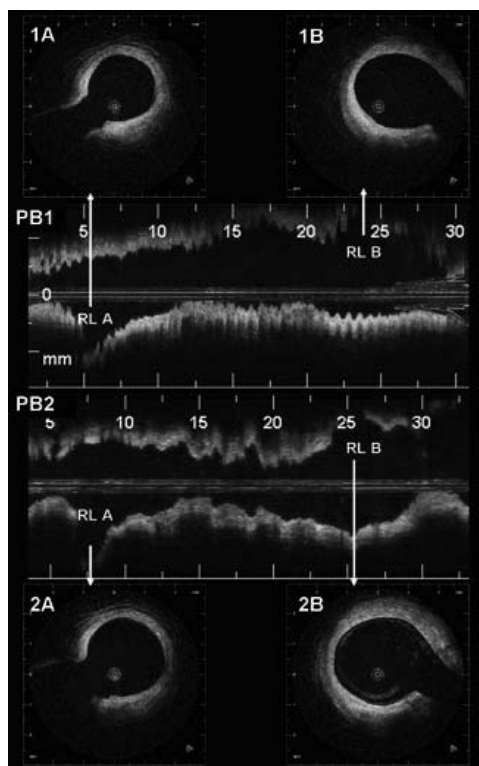


Figure 2. Selection of the region of interest in OCT pullbacks acquired with and without occlusion. PB1 and PB2 show the longitudinal view of the pullbacks acquired with and without occlusion, respectively. The white arrows indicate the side branches (SBA and SBB) used for matching of the region of interest. 1A and 2A show corresponding cross-sections of SBA with and without occlusion. 1B and 2B show corresponding cross-sections of the SBB with and without occlusion.

Bland-Altman plots showing the absolute difference between corresponding lumen measurements for both techniques (y-axis) versus the average of both techniques (x-axis). The limits of agreement were calculated as the mean difference (+2SD).

RESULTS

Ex Vivo Human Coronary Arteries

Intravascular ultrasound and OCT were successfully performed in 8 out of 10 specimens. Intracoronary imaging was not possible in 2 cases due to the lumen being totally occluded. A good match between OCT, IVUS, and histology images

was obtained in 35 frames. Overall, the mean lumen, plaque and vessel area when measured by histomorphometry were 2.5 (1.7) mm², 3.7 (1.9) mm², and 7.6 (3.2) mm², respectively. The mean percentage of stenosis was 59% (18%).

Bland-Altman and regression analyses were performed on the lumen area measurements between the 3 imaging modalities (Figure 3). The average relative differences of the lumen measurements were 28% between OCT and histology, 40% between IVUS and histology, and 11% between IVUS and OCT.

In Vivo Human Coronary Arteries

Clinical and Procedural Characteristics

Five patients (5 vessels) were included in the study. The average age was 61.2 (8.9) years and 4/5 were male. Three out of 5 had hypertension, 1 of 5 had diabetes, 4 of 5 had hyperlipidemia, and none were smokers. The imaged vessel was the LAD in 1 case and the LCX in the other 4 cases. Only 1 patient presented chest pain and ST depression during acquisition with balloon occlusion, which disappeared immediately after balloon deflation.

Comparison Lumen Measurements With OCT and IVUS

Overall, the mean lumen, plaque, and vessel area measured by IVUS were 6.3 (1.0) mm², 6.9 (1.4) mm², and 13.3 (1.7) mm², and mean cross-sectional area stenosis was 52% (6%).

Comparison IVUS and OCT With Occlusion

The mean relative difference for the mean lumen area was 33.7%, and the mean absolute difference for the mean lumen area was 1.67 (0.54) mm², with limits of agreement of 0.62-2.73 mm² (Table 1). The mean relative difference for the minimum lumen area (MLA) between IVUS and OCT with occlusion was 55.5%, and the mean absolute difference was 1.90 (0.37) mm², with limits of agreement of 1.17-2.63 mm².

Comparison IVUS and OCT Without Occlusion

The average relative difference for the mean lumen area was 21.5%, and the absolute difference was 1.11 (0.53) mm², with limits of agreement of 0.05-2.14 mm² (Table 2). The average relative difference for MLA was 29%, and the average absolute difference was 1.10 (0.37) mm², with limits of agreement 0.37-1.83 mm².

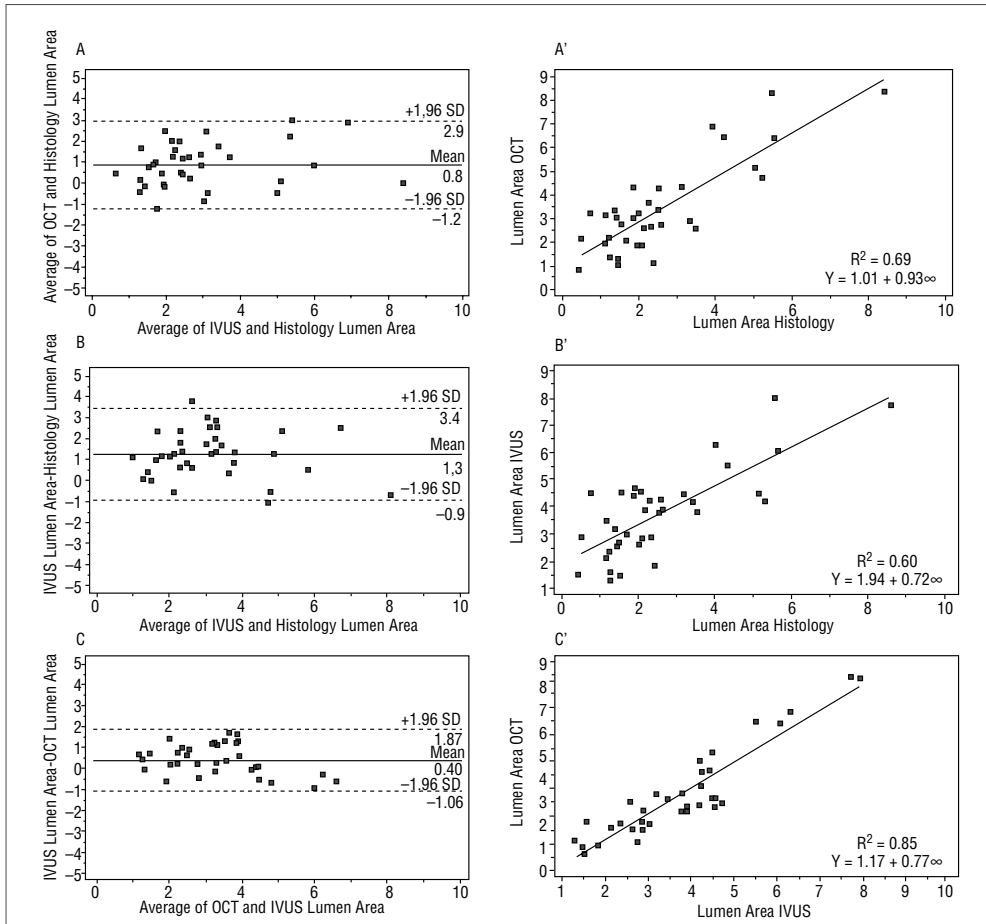


Figure 3. Lumen measurements in ex vivo coronary arteries. Bland-Altman plots showing the differences in lumen measurements between OCT and histology (A), IVUS and histology (B), and OCT and IVUS (C). Correlation for lumen measurements between OCT and histology (A'), IVUS and histology (B'), and OCT and IVUS (C').

TABLE 1. Differences in the Mean and Minimum Lumen Area (MLA) Between IVUS and OCT Pullbacks Acquired With the Occlusive technique

Vessel	Mean Lumen Area IVUS, mm ²	Mean Lumen Area OCT Occlusion, mm ²	Absolute Difference, mm ²	Difference %	MLA IVUS, mm ²	MLA OCT Occlusion, mm ²	Absolute Difference, mm ²	% Difference
1	5.57 (0.93)	3.40 (0.89)	2.17	48.50	4.04	1.89	2.15	72.51
2	6.76 (0.73)	5.53 (0.75)	1.23	20.02	5.33	3.74	1.59	35.06
3	7.81 (0.74)	6.58 (0.95)	1.23	17.09	6.35	4.91	1.44	25.58
4	5.21 (0.53)	2.87 (0.55)	2.34	57.77	4.10	1.78	2.32	78.91
5	6.19 (2.32)	4.81 (2.29)	1.38	25.06	4.06	2.05	2.01	65.79

Values are expressed as mean (SD).

TABLE 2. Differences in the Mean and Minimum Lumen Area (MLA) Between IVUS and OCT Pullbacks Acquired With the Non-occlusive Technique

Vessel	Mean Lumen Area IVUS, mm ²	Mean Lumen Area OCT Non-occlusion, mm ²	Absolute Difference, mm ²	% Difference	MLA IVUS, mm ²	MLA OCT Non-occlusion, mm ²	Absolute Difference, mm ²	% Difference
1	5.57 (0.93)	3.83 (0.72)	1.74	37.04	4.04	2.76	1.28	37.65
2	6.76 (0.73)	5.90 (0.63)	0.86	13.59	5.33	4.16	1.17	24.66
3	7.81 (0.74)	7.39 (1.01)	0.42	5.52	6.35	5.86	0.49	8.03
4	5.21 (0.53)	3.68 (0.55)	1.53	34.47	4.10	2.61	1.49	44.41
5	6.19 (2.32)	5.24 (2.08)	0.95	16.70	4.06	2.99	1.07	30.35

Values are expressed as mean (SD).

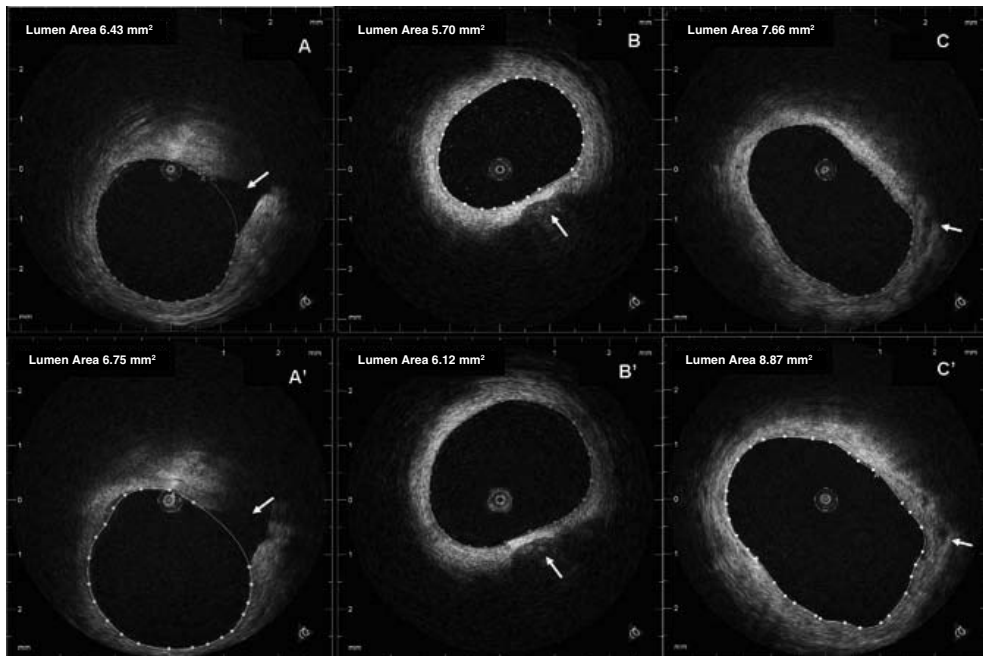


Figure 4. Example of differences in lumen measurements between OCT with and without occlusion. The figure shows corresponding images acquired with occlusion (A, B, and C) and without occlusion (A', B', and C'). The white arrows indicate the landmarks used for matching of the pullbacks (side branches in A and C and calcium spot in B). In all the examples, the lumen dimensions are smaller in the pullback acquired with occlusion.

Comparison of the Lumen Measurements by OCT With and Without Occlusion

For the comparison of lumen dimensions when measured by OCT, 373 matched frames obtained with and without occlusion were analyzed (Figure 4). The mean length of the region analyzed was 11.34 (3.87) mm with occlusion and 11.23 (3.86) mm without occlusion

($P=.96$). Bland-Altman and regression analyses were also performed for these measurements (Figure 5).

The mean absolute and relative differences for mean lumen area were 0.61 (0.23) mm² (13%) (limits of agreement, 0.15-1.07 mm²). The mean absolute and relative differences for MLA were 0.80 (0.21) mm² (28%) (limits of agreement, 0.37-1.23 mm²) (Tables 3 and 4).

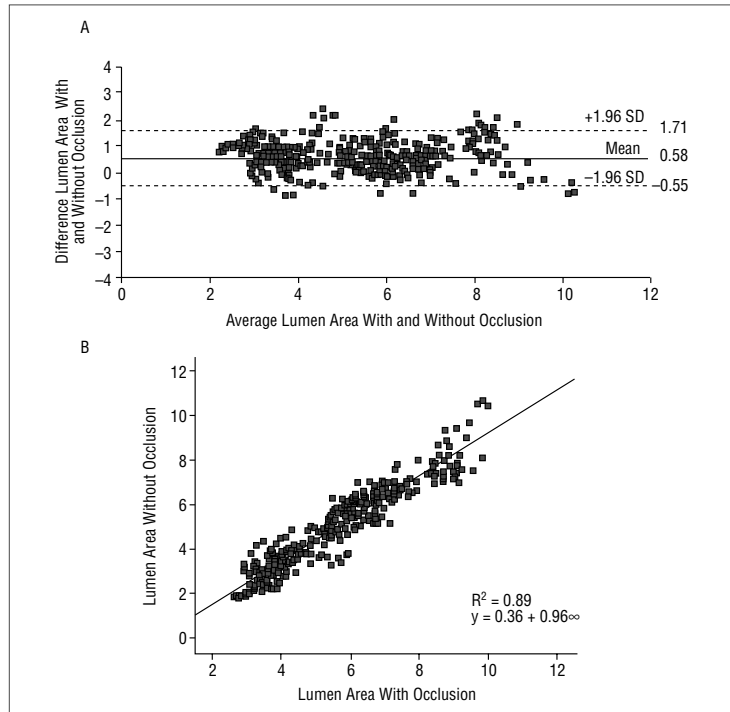


Figure 5. Comparison of lumen measurements with optical coherence tomography (OCT) with and without occlusion. Bland-Altman plot showing the differences between lumen measurements in OCT pullbacks acquired with the occlusive and non-occlusive technique (A). Correlation between the lumen measurements in the OCT pullbacks acquired with and without occlusion (B).

TABLE 3. Differences in the Mean Lumen Area Between OCT Pullbacks Acquired With the Occlusive and Non-Occlusive Technique

Vessel	Mean Lumen Area Occlusive, mm ²	Mean Lumen Area Non-occlusive, mm ²	Absolute Difference, mm ²	% Difference
1	3.40 (0.89)	3.83 (0.72)	0.43	12.00
2	5.73 (0.89)	6.20 (0.95)	0.47	7.87
3	6.58 (0.95)	7.39 (1.01)	0.81	11.58
4	3.10 (0.78)	4.02 (0.91)	0.92	25.90
5	4.81 (2.29)	5.24 (2.08)	0.42	8.45
Average	4.72 (1.49)	5.34 (1.49)	0.61 (0.23)	13.16

Values are expressed as mean (SD).

TABLE 4. Differences in the Minimum Lumen Area (MLA) Between OCT Pullbacks Acquired With the Occlusive Non-occlusive Technique

Vessel	MLA occlusive, mm ²	MLA Non-Occlusive, mm ²	Absolute Difference, mm ²	% Difference
1	1.89	2.76	0.87	37.42
2	3.74	4.16	0.42	10.63
3	4.91	5.86	0.95	17.64
4	1.78	2.61	0.83	37.81
5	2.05	2.99	0.94	37.30
Average	2.87 (1.39)	3.67 (1.36)	0.80 (0.21)	28.16

Values are expressed as mean (SD).

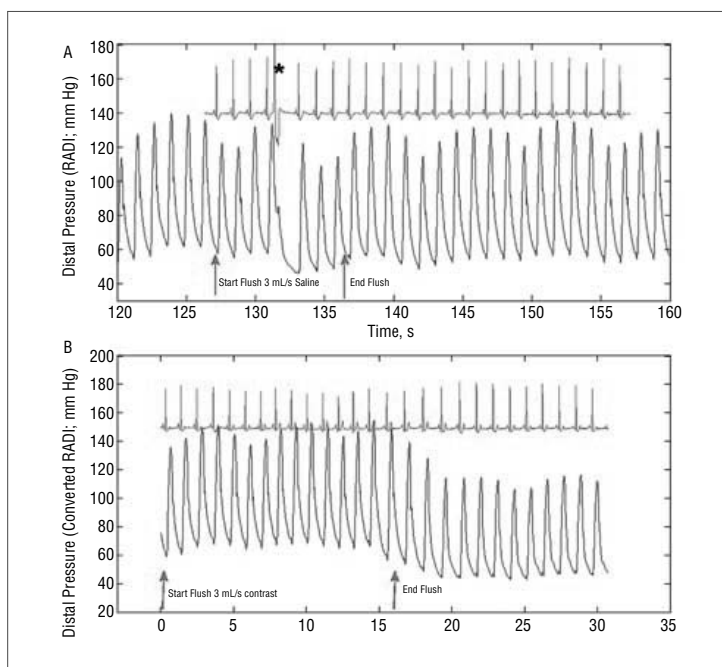


Figure 6. Intracoronary pressure recorded during saline or contrast injection. The figure shows the ECG (red) and intracoronary pressure (blue) records obtained in a left anterior descending coronary artery during injection of saline or contrast medium (Iodixanol 370). The distal intracoronary pressure was registered using the RADI pressure wire. The saline injection at 3 mL/s did not significantly modify intracoronary pressure (A). However, an increase in intracoronary pressure can be observed during contrast injection at 3 mL/s, (B). *Ventricular extrasystole.

The mean lumen volumes were 55 (29.5) and 60.4 (30.4) mL³ with and without occlusion, respectively, with a relative difference of 11.7%. The mean absolute difference was 5.4 (2.7) mL³ and the limits of agreement were 0.0-10.7 mm³.

DISCUSSION

Optical coherence tomography is emerging as one of the most promising intracoronary imaging modalities due to its capacity to provide very high-resolution images of the coronary vessel wall. It enables the very detailed assessment of atherosclerotic plaque and the interaction between implanted coronary stents and the vessel wall.^{10,11} In recent years, there has been continuous technical development that has led to changes in the OCT acquisition technique (changing from the need to occlude the vessel to a non-occlusive procedure) which have simplified the use of the technology and reduced patient discomfort.^{12,13} However, even though the non-occlusive technique is currently gradually replacing the occlusive technique in many centers, it remains “off-label.” Furthermore, many of the recently published OCT data were obtained by using the occlusive technique.¹⁴⁻²⁰ The impact of the acquisition technique in relation to quantitative

lumen measurements obtained by OCT and compared to quantitative IVUS has not yet been reported. The present study showed the following: *a)* in fixed human coronary arteries, both OCT and IVUS overestimated the lumen area compared to histology; *b)* lumen dimensions when measured by IVUS are larger than those when measured by OCT with or without occlusion in vivo; and *c)* the OCT acquisition technique (occlusive or non-occlusive) has an impact on lumen dimension measurements.

Differences in Lumen Measurements Between IVUS, OCT, and Histology

In the present study, the lumen areas when measured by IVUS and OCT were larger than those measured by histology in fixed human coronary arteries. The mean differences with histomorphometry were 0.8 mm² (28%) for OCT and 1.3 mm² (40%) for IVUS. These results are in line with a previous study in stented porcine coronary arteries that showed that lumen area was largest when measured by IVUS, followed by OCT, and was smallest when measured by histology.²¹ However, it should be borne in mind that the ex vivo processing of the specimen for histology analysis may have had an influence on lumen size. It is well established that

tissue shrinkage occurs in different phases when preparing specimens for histology.²²

Regarding the comparison of IVUS and OCT, our *in vivo* data are in agreement with the *ex vivo* findings. In our study, the lumen dimensions measured by IVUS in living patients were always higher than those measured by OCT with or without balloon occlusion. There are several studies in the literature comparing lumen dimensions measured by IVUS and OCT with occlusion that show contrasting results. Kawase et al, performed IVUS and OCT with occlusion *in vivo* in 6 coronary arteries in pigs and reported no differences in lumen areas and volumes between IVUS and OCT with occlusion.²³ However, another study in pigs with a larger sample size reported an absolute difference of 0.49 mm² between mean lumen area by IVUS and OCT acquired with the occlusive technique in stented segments.²¹ Yamaguchi et al evaluated *in vivo* differences in humans and found that the MLA was significantly smaller when measured by OCT with occlusion than when measured with IVUS (mean difference, 0.4 mm²). The greater differences found in our data could be explained by the fact that we did not include coronary segments treated with bare-metal stents. Bare-metal stents are probably less affected by variations in intracoronary pressure caused by proximal vessel occlusion as they have considerable radial strength.

To our knowledge, no published studies have reported differences in measurements between IVUS and OCT acquired with the non-occlusive technique. In the present study, the lumen dimensions were even larger by IVUS, but the differences, as expected, were smaller than with occlusion.

The greater overestimation of lumen dimensions when measured by IVUS compared to OCT could be related to the difficulty in differentiating the lumen border by IVUS due to blood speckle or presence of artefacts.²⁴ OCT shows the lumen-intima interface as a sharply defined border, clearly visible in most cases.²⁵ IVUS also overestimates the lumen area compared to quantitative angiography measurements (both by videodensitometry and edge detection).²⁶⁻²⁸ In our study, the differences between lumen measurements by IVUS and OCT were higher *in vivo* than *ex vivo*. This could be related to the frame selection for *in vivo* analysis. The IVUS pullback obtained *in vivo* was processed with a gating system that selects end-diastolic frames (the moment in the cardiac cycle when the vessel is biggest), whereas OCT pullback is not gated and therefore the frames could correspond to any moment in the cardiac cycle. Previous IVUS studies have suggested a variation in lumen area during the cardiac cycle in the range of 8%.²⁹

The differences found between lumen size when measured by IVUS and OCT may have clinical

implications if OCT is going to be used to define lesion severity. An MLA <4 mm² has been associated with myocardial ischemia and has been considered a criterion for coronary lesion revascularization. In the present study, whereas all the patients had an MLA >4 mm² when measured by IVUS, 4 out of 5 patients had an MLA <4 mm² when measured by OCT with occlusion. All the patients were asymptomatic and were not treated. This reinforces the idea that IVUS criteria cannot be directly translated to OCT and emphasizes the need for new specific cut-off points to define lesion severity by OCT.

Impact of OCT Acquisition Technique on Lumen Measurements

The present report consistently shows that the mean and minimum lumen areas were smaller when OCT was performed with balloon occlusion than acquisitions without occlusion. These differences could be related to the decrease of intracoronary pressure due to the vessel occlusion that is not completely compensated by continuous flush injection. Furthermore, the injection of contrast medium during the non-occlusive procedure increases intracoronary pressure (Figure 6). These phenomena are likely to be more accentuated in healthy arteries and in coronary segments not treated with bare-metal stents (as in this study). The relative differences were higher in smaller vessels, suggesting that they may have a greater tendency to collapse after occlusion.

Limitations

Even though a complex matching process was used, the difference in slice thickness between IVUS, OCT, and histology cross-sections may have influenced the results of the *ex vivo* study. The main limitations of the *in vivo* study are the small sample size and the limited type of coronary segments that could be analyzed. More data are needed to evaluate the quantitative differences between OCT pullbacks acquired with different techniques and IVUS in human coronary arteries treated with bare-metal stents. Further studies with a larger sample size and using different types of coronary segments are warranted before definite conclusions can be drawn.

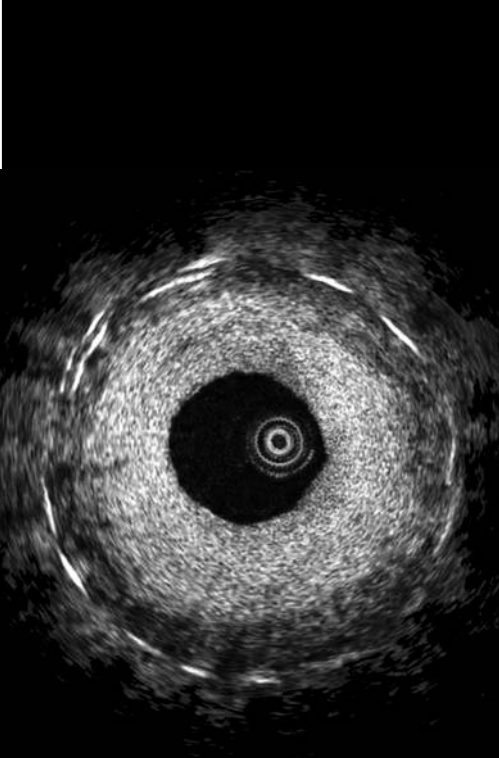
CONCLUSION

In fixed human coronary arteries, both OCT and IVUS overestimated lumen areas compared to histomorphometry. Lumen dimensions measured by IVUS are larger than those measured by OCT with or without occlusion *in vivo*. The OCT acquisition

technique (occlusive or non-occlusive) has an impact on quantitative lumen dimension measurements.

REFERENCES

1. Regar E, Gonzalo N, van Soest G, Serruys PW. Optical coherence tomography. In: Mukherjee D, Bates E, Roffi M, Moliterno DF, editor. *Cardiac Catheterization, Coronary and Peripheral Angiography and Interventional Procedures*. Informa Healthcare, 2009 [In press].
2. Yamaguchi T, Terashima M, Akasaka T, Hayashi T, Mizuno K, Muramatsu T, et al. Safety and feasibility of an intravascular optical coherence tomography image wire system in the clinical setting. *Am J Cardiol*. 2008;101:562-7.
3. Prati F, Cera M, Ramazzotti V, Imola F, Giudice R, Albertucci M. Safety and feasibility of a new non-occlusive technique for facilitated intracoronary optical coherence tomography (OCT) acquisition in various clinical and anatomical scenarios. *Eurointervention*. 2007;3:365-70.
4. Serruys PW, Degertekin M, Tanabe K, Russell ME, Guagliumi G, Webb J, et al. Vascular responses at proximal and distal edges of paclitaxel-eluting stents: serial intravascular ultrasound analysis from the TAXUS II trial. *Circulation*. 2004;109:627-33.
5. Tanabe K, Serruys PW, Degertekin M, Grube E, Guagliumi G, Urbaszek W, et al. Incomplete stent apposition after implantation of paclitaxel-eluting stents or bare metal stents: insights from the randomized TAXUS II trial. *Circulation*. 2005;111:900-5.
6. Tanimoto S, Rodriguez-Granillo G, Barlis P, de Winter S, Bruining N, Hamers R, et al. A Novel Approach for Quantitative Analysis of Intracoronary Optical Coherence Tomography. High inter-observer agreement with computer-assisted contour detection. *Catheter Cardiovasc Interv*. 2008;72:228-35.
7. Gundersen HJ, Jensen EB. The efficiency of systematic sampling in stereology and its prediction. *J Microsc*. 1987;147:229-63.
8. Bruining N, Verheye S, Knaapen M, Somers P, Roelandt JR, Regar E, et al. Three-dimensional and quantitative analysis of atherosclerotic plaque composition by automated differential echogenicity. *Catheter Cardiovasc Interv*. 2007;70:968-78.
9. de Winter SA, Hamers R, Degertekin M, Tanabe K, Lemos PA, Serruys PW, et al. Retrospective image-based gating of intracoronary ultrasound images for improved quantitative analysis: the intelligent method. *Catheter Cardiovasc Interv*. 2004;61:84-94.
10. Gonzalo N, Serruys PW, Regar E. Optical coherence tomography: clinical applications and the evaluation of DES. *Minerva Cardioangiol*. 2008;56:511-25.
11. Xie Y, Takano M, Murakami D, Yamamoto M, Okamatsu K, Inami S, et al. Comparison of neointimal coverage by optical coherence tomography of a sirolimus-eluting stent versus a bare-metal stent three months after implantation. *Am J Cardiol*. 2008;102:27-31.
12. Gonzalo N, Ligthart J, Regar E. Percutaneous cardiac interventions beyond stenting. Tips and tricks for new technology. In: Sabate M, editor. *Informa Healthcare*. 2009 [In press].
13. Prati F, Cera M, Ramazzotti V, Imola F, Giudice R, Giudice M, et al. From bench to bedside. *Circ J*. 2008;72:839-43.
14. Takano M, Inami S, Jang IK, Yamamoto M, Murakami D, Seimiya K, et al. Evaluation by optical coherence tomography of neointimal coverage of sirolimus-eluting stent three months after implantation. *Am J Cardiol*. 2007;99:1033-8.
15. Takano M, Yamamoto M, Inami S, Murakami D, Seimiya K, Ohba T, et al. Long-term follow-up evaluation after sirolimus-eluting stent implantation by optical coherence tomography: do uncovered struts persist? *J Am Coll Cardiol*. 2008;51:968-9.
16. Kubo T, Imanishi T, Takarada S, Kuroi A, Ueno S, Yamano T, et al. Assessment of culprit lesion morphology in acute myocardial infarction: ability of optical coherence tomography compared with intravascular ultrasound and coronary angiography. *J Am Coll Cardiol*. 2007;50:933-9.
17. Kume T, Akasaka T, Kawamoto T, Okura H, Watanabe N, Toyota E, et al. Measurement of the thickness of the fibrous cap by optical coherence tomography. *Am Heart J*. 2006;152:755 e1-4.
18. Barlis P, Serruys PW, Gonzalo N, van der Giessen W, Jaegere PJ, Regar E. Assessment of Culprit and Remote Coronary Narrowings Using Optical Coherence Tomography with Long-Term Outcomes. *Am J Cardiol*. 2008;102:391-5.
19. Gonzalo N, Serruys PW, Barlis P, Ligthart J, Garcia-Garcia HM, Regar E. Multi-Modality Intra-Coronary Plaque Characterization: A Pilot Study. *Int J Cardiol*. Sep 5, 2008 [Epub ahead of print].
20. Gonzalo N, Garcia-Garcia HM, Regar E, Barlis P, Wentzel J, Onuma Y, et al. In Vivo Assessment of High-risk Coronary Plaques at Bifurcations with Combined Intravascular Ultrasound Virtual Histology and Optical Coherence Tomography. *J Am Coll Cardiol Img*. 2009 [In press].
21. Suzuki Y, Ikeno F, Koizumi T, Tio F, Yeung AC, Yock PG, et al. In Vivo Comparison Between Optical Coherence Tomography and Intravascular Ultrasound for Detecting Small Degrees of In-Stent Neointima after Stent Implantation. *J Am Coll Cardiol Interv*. 2008;1:168-73.
22. Choy JS, Mathieu-Costello O, Kassab GS. The effect of fixation and histological preparation on coronary artery dimensions. *Ann Biomed Eng*. 2005;33:1027-33.
23. Kawase Y, Hoshino K, Yoneyama R, McGregor J, Hajjar RJ, Jang IK, et al. In vivo volumetric analysis of coronary stent using optical coherence tomography with a novel balloon occlusion-flushing catheter: a comparison with intravascular ultrasound. *Ultrasound Med Biol*. 2005;31:1343-9.
24. Mintz GS, Nissen SE, Anderson WD, Bailey SR, Erbel R, Fitzgerald PJ, et al. American College of Cardiology Clinical Expert Consensus Document on Standards for Acquisition, Measurement and Reporting of Intravascular Ultrasound Studies (IVUS). A report of the American College of Cardiology Task Force on Clinical Expert Consensus Documents. *J Am Coll Cardiol*. 2001;37:1478-92.
25. Kume T, Akasaka T, Kawamoto T, Watanabe N, Toyota E, Neishi Y, et al. Assessment of coronary intima-media thickness by optical coherence tomography: comparison with intravascular ultrasound. *Circ J*. 2005;69:903-7.
26. von Birgelen C, Kutryk MJ, Gil R, Ozaki Y, Di Mario C, Roelandt JR, et al. Quantification of the minimal luminal cross-sectional area after coronary stenting by two- and three-dimensional intravascular ultrasound versus edge detection and videodensitometry. *Am J Cardiol*. 1996;78:520-5.
27. Tsuchida K, Serruys PW, Bruining N, Dudek D, Drzewiecki J, Banning AP, et al. Two-year serial coronary angiographic and intravascular ultrasound analysis of in-stent angiographic late lumen loss and ultrasonic neointimal volume from the TAXUS II trial. *Am J Cardiol*. 2007;99:607-15.
28. Reiber JH, Serruys PW, Kooijman CJ, Wijns W, Slager CJ, Gerbrands JJ, et al. Assessment of short-, medium-, and long-term variations in arterial dimensions from computer-assisted quantitation of coronary cineangiograms. *Circulation*. 1985;71:280-8.
29. Ge J, Erbel R, Gerber T, Gorge G, Koch L, Haude M, et al. Intravascular ultrasound imaging of angiographically normal coronary arteries: a prospective study in vivo. *Br Heart J*. 1994;71:572-8.



3.2

Reproducibility of quantitative per strut stent analysis with OCT

Gonzalo N, Garcia-Garcia HM, Serruys P.W,
Commissaris KH, Bezerra H, Gobbens P, Costa MA,
Regar E.

EuroIntervention. 2009 Jun;5(2):224-32

Reproducibility of quantitative optical coherence tomography for stent analysis

Nieves Gonzalo¹, MD; Hector M. Garcia-Garcia¹, MD, MSc; Patrick W. Serruys¹, MD, PhD; Koen H. Commissaris², MSc; Hiram Bezerra³, MD, PhD; Pierre Gobbens², MSc; Marco Costa³, MD, PhD; Evelyn Regar^{1*}, MD, PhD

1. Thoraxcenter, Erasmus MC, Rotterdam, The Netherlands; 2. Cardialysis BV, Rotterdam, The Netherlands; 3. Cardialysis-Cleveland Core Laboratory and University Hospitals, Case Medical Center, Cleveland, OH, USA

K. Commissaris and P. Gobbens are employees of Cardialysis, the remaining authors have no conflict of interest to declare.

KEYWORDS

Optical coherence tomography, stent analysis, reproducibility

Abstract

Aims: To assess the inter- and intra- observer reproducibility for strut count, strut apposition and strut tissue coverage measurements with optical coherence tomography (OCT).

Methods and results: Ten drug-eluting stents (244 frames, 1712 struts) imaged with OCT nine months after implantation were analysed by two independent analysts. One of the analysts repeated the analysis of five stents (120 frames, 795 struts) one week later. Offline analysis was performed with the proprietary LightLab Imaging software. The number of struts was counted and lumen and stent area contours were traced. Tissue coverage thickness was measured at 360 degrees of vessel circumference and in front of every individual strut. The number of malapposed struts was determined. There was good agreement for strut number count (Kendall's Tau-b 0.90 for inter- and 0.94 for intra- observer variability). The relative difference for lumen area, stent area and tissue coverage measurements was around 1%. There was complete inter- and intra- observer agreement for malapposed struts classification (4 out of 1708 struts, Kappa=1).

Conclusions: In a Corelab setting, the inter- and intra- observer reproducibility for strut count, strut apposition and strut tissue coverage measurements with OCT is excellent. This emphasises the value of OCT as a tool for the clinical long-term assessment of stents.

* Corresponding author: Thoraxcenter, Bd 585, 's-Gravendijkwal 230, 3015-CE Rotterdam, The Netherlands

E-mail: e.regar@erasmusmc.nl

Abbreviations and acronyms

OCT:	optical coherence tomography
DES:	drug-eluting stent
ROI:	region of interest

Introduction

Optical Coherence Tomography (OCT) is a light-based imaging modality that can provide *in vivo* high-resolution images of the coronary artery¹. This technique offers the possibility of identifying coronary stents and individual stent struts². Further, it is able to provide detailed information about struts apposition and tissue coverage. This is of special interest in drug-eluting stents (DES) in which the neointimal proliferation is inhibited to such an extent that it might not be visualised with conventional intravascular ultrasound (IVUS)³. Animal studies demonstrated good correlation between intracoronary OCT and pathology for neointimal thickness measurements^{4,5}. However, no criteria have been established for the quantitative analysis of stents on a per strut level with OCT. The objective of the present study was to assess the inter- and intra-observer reproducibility for strut count, strut apposition and strut tissue coverage measurements with OCT.

Methods

Study population

Ten stents (244 frames, 1712 struts) were analysed in eight asymptomatic patients undergoing an intracoronary OCT study nine months after sirolimus (Cypher Select, Cordis, Johnson & Johnson, Miami, FL, USA; 40%) or biolimus-eluting (Biomatrix III, Biosensors, Morges, Switzerland; 60%) stent implantation. The target vessel was the LAD in 50%, the LCX in 20% and the RCA in the 30% of the cases.

OCT acquisition

The OCT acquisition was performed using a commercially available system for intracoronary imaging (LightLab Imaging Inc, Westford, MA, USA). The ImageWire (LightLab Imaging Inc, Westford, MA, USA) consists of an optical fibre core (125 µm) covered by a protective sheath with a maximum outer diameter of 0.019". It was positioned distal to the region of interest using a double lumen catheter (Twin Pass catheter, Vascular Solutions Inc, Minneapolis, MN, USA) that had been previously placed in the artery over a conventional guidewire. The automated pullback was performed at 3 mm/s while the blood was removed by the continuous injection of iso-osmolar contrast (Iodixanol 370, Visipaque™, GE Health Care, Ireland) at 3 ml/s through the guiding catheter. The data was stored on CD for offline analysis.

OCT quantitative analysis

The analysis was performed with the proprietary LightLab software for off-line analysis (LightLab Imaging, Westford, MA, USA). The data was imported in the workstation using the LightLab database format.

Z-OFFSET CORRECTION

The Z-Offset was adjusted in the catheterisation laboratory before image acquisition while holding the ImageWire between two fingers. The Z-Offset is set properly when the ImageWire sheath is aligned with the yellow fiducials in the OCT image. During image acquisition, the optical fibres can stretch, especially at the beginning of the pullback. This may produce changes in the size of the Z-Offset along the pullback that can affect the accuracy of the measurements. Therefore, the Z-Offset was checked and modified if necessary in all the pullbacks before performing any measurement. To correct the Z-offset in saved pullbacks, a frame in which the ImageWire sheath was in direct contact with the vessel wall was selected. In this frame the Z-Offset was corrected aligning the ImageWire sheath and the vessel wall with the yellow fiducials. This value of the Z-Offset was applied at the beginning of the pullback. If needed, the Z-Offset was recalibrated again along the pullback. The corrected Z-Offset was the same for both analysts.

DEFINITION OF THE REGION OF INTEREST AND FRAME SELECTION

The region of interest (ROI) comprised the stented region and the reference segments. The ROI was systematically analysed in 1 mm longitudinal intervals throughout the pullback. The stented region was defined as the region comprised between the first and the last frame with circumferentially visible struts. The reference segments were defined as the 5 mm proximal and distal to the stent. Frames were excluded when more than 45° of the lumen border was not visible and when they presented severe artefacts such as incomplete blood clearance or non-uniform rotation distortion. When a frame was not analysable an alternative frame located within the two proximal or distal frames was selected for analysis. No overlapping stent segments were included in the analysis.

LUMEN ANALYSIS

The lumen contour was obtained with an automated detection algorithm available in the LightLab proprietary software and additional manual corrections were performed if necessary.

STENT ANALYSIS

Strut definitions

stent struts can show different appearances in OCT. In the present study structures were considered struts according to the following definitions.

- Highly reflective surfaces (metal) with cast dorsal, radial shadows.
- Highly reflective surfaces without dorsal shadowing.
- Sector shaped shadows with sharp defined borders radial to the lumen.

Stent area

The stent contour was traced using a multiple point detection function. A support point for the contour was set in the middle of the endoluminal border of each stent strut. A semi-automated contour was then applied linking the points.

STRUTS COVERAGE DEFINITIONS AND MEASUREMENTS

The tissue coverage area was calculated as stent area minus lumen area. Assessment of tissue coverage thickness was performed using a new function of the software which provides 360 degrees measurements, at 1 degree incremental, around the circumference of a given cross sectional image, developed in collaboration by Cardialysis-Cleveland, Cardialysis-Rotterdam and Lightlab (Figure 1).

This also permits the measurement of the tissue located in front of every strut that was defined as strut coverage. The mean, maximum and minimum tissue coverage per strut were calculated.

MALAPPOSITION DEFINITIONS AND MEASUREMENTS

Malapposition was defined as separation of at least one stent strut from the vessel wall. To evaluate apposition by OCT, especially with DES, some considerations must be taken into account. Most DES are constituted by a metal body covered by a polymer. Since OCT can show only the endoluminal surface of the strut due to limited penetration through the metal, strut and polymer thickness must be considered in assessing apposition for each type of stent design. For the present study, a strut was considered malapposed if the distance from its endoluminal surface to the vessel wall was higher than the sum of the metal and polymer thickness (Figure 2).

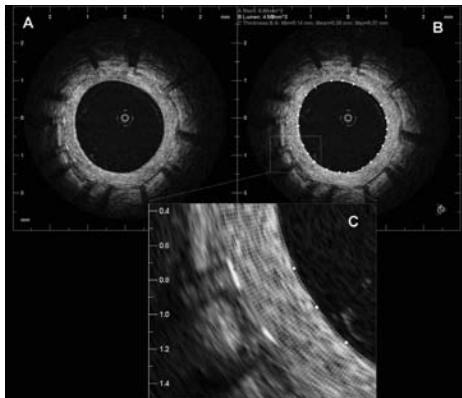


Figure 1. Tissue coverage measurement. **A.** Sirolimus eluting stent 9 months after stent implantation. **B.** The figure shows the lumen contour (white) and the stent contour (green). The tissue coverage area was calculated as stent area minus lumen area. The tissue coverage thickness was measured in 360 points (represented by the white chords). **C.** Magnification of 2 struts showing all the measurements (white chords) of the tissue coverage in front of every strut. For every strut the minimum, maximum and mean strut coverage was calculated.

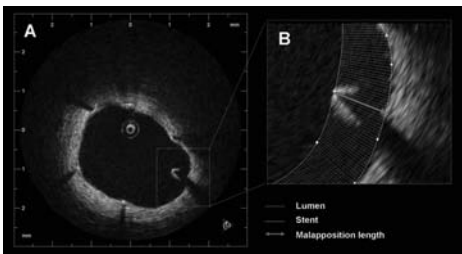


Figure 2. Malapposition. **A.** Example of a malapposed strut in a sirolimus eluting stent at 9 months follow up. **B.** Magnification of the malapposed strut. The yellow line represents the lumen contour and the white line corresponds to the stent contour. The distance from the endoluminal surface of the strut to the vessel wall (red arrow) was 440 μm (higher than the sum of the metal and polymer thickness for this type of stent).

The reproducibility for the struts count and the malapposition and tissue coverage thickness measurements were tested independently.

STRUT COUNT REPRODUCIBILITY

In order to assess the inter-observer variability for the struts count, two experienced observers analysed independently 100 cross sections and counted the number of struts in each one. To test the intra-observer variability one of the two observers repeated the analysis of 50 randomly selected cross sections one week later.

STRUT APPPOSITION AND TISSUE COVERAGE REPRODUCIBILITY

Two experienced observers analysed independently 10 stents in order to assess the inter-observer variability for the struts apposition and tissue coverage measurements. One of the observers repeated the analysis in five of the cases one week later to evaluate the intra-observer variability.

Statistical analysis

The agreement of the number of struts counted in the same frame was estimated by calculating the Kendall's Tau-b rank correlation coefficient with its 95% confidence interval.

The inter and intra-observer reproducibility for lumen, stent and tissue coverage measurements were tested at three levels: per stent, per frame and per strut.

On a per stent level the mean and minimum lumen and stent area and the mean lumen and stent diameters were compared. The mean tissue coverage area and the mean, minimum and maximum tissue coverage thickness and strut coverage were also compared. The lumen, stent and tissue coverage volume were calculated by the Trapezoidal rule. In the proximal and distal reference, the mean luminal area, diameter and volume were compared.

On a per frame level, the luminal and stent areas and diameters were compared as well as the tissue coverage area and the mean, minimum and maximum tissue coverage thickness and strut coverage. In the frames corresponding to the proximal and distal edge, the mean luminal area and diameter were compared.

On a per strut level, the mean, minimum and maximum tissue coverage in front of every strut were compared.

The reproducibility was calculated by estimating the residual standard deviation in an ANOVA model. The true value is expected to be within 1.96 times the calculated reproducibility of the single measurement for 95% of the observations. In addition the agreement between both observations has been expressed in Bland-Altman plots. The Bland-Altman plot depicts the differences of each pair of observations versus their mean values with reference lines for the mean difference of all paired observations and its 95% confidence limits, the so-called limits of agreement.

The Kappa coefficient for the agreement between observers for struts classification as incompletely apposed was tested for being not equal to zero.

Results

A total of 244 frames and 1,712 struts were evaluated for the inter-observer reproducibility and 120 frames, 795 struts were evaluated for the intra-observer variability. The mean stent length and diameter of the analysed stents were 17.8 mm and 2.8 mm² respectively.

Strut count reproducibility

INTEROBSERVER VARIABILITY

There was complete agreement in the number of struts between the two observers in 55% of the cross sections, difference of one strut in 31%, difference of two struts in 9% and difference of more than two struts in only 5% of the cross sections. The correlation between both observers was high, i.e. Kendall's Tau-b was 0.90 (95% confidence interval 0.85 – 0.94).

INTRA-OBSERVER VARIABILITY

There was complete agreement in the number of struts in 72% of the cross sections, difference of one strut in 24% and difference of two struts in 4% of the cross sections. The correlation between both observations was very high, i.e. Kendall's Tau-b was 0.94 (95% confidence interval 0.91 – 0.97).

Lumen, stent and tissue coverage measurements reproducibility

STENT LEVEL

The results for the inter and intra-observer reproducibility at the stent level are summarised in Tables 1 and 2 respectively.

FRAME LEVEL

The results for the inter- and intra- observer reproducibility at the frame level are summarised in Tables 3 and 4 respectively. Figures 3 and 4 show the results for the lumen, stent and tissue

coverage area and mean neointimal thickness for inter- and intra-observer reproducibility respectively.

STRUT LEVEL

Tables 5 and 6 show the inter (A) and intra-observer (B) reproducibility for the measurements at the strut level. Figure 5 shows the variability for the mean strut coverage.

Malapposition classification reproducibility

The observers had complete agreement for the classification of malapposed struts (four out of 1,712 struts malapposed, Kappa coefficient 1). The intra-observer analysis show the same result (four out of 795 struts malapposed, Kappa coefficient 1).

Discussion

Due to its high resolution, OCT can be a very valuable tool for the evaluation of the acute and long-term impact of stent implantation. OCT offers the possibility to assess stent apposition in great detail and allows the visualisation and measurement of the tissue covering the struts, even if this consists of tiny layers as it is frequently observed in DES³. As the use of OCT is increasing rapidly, standardisation of the methodology to measure and report stent apposition and tissue coverage is needed, as well as data about the reproducibility of these measurements. Our results show that the methodology described in the present study allows analysis of stents by experienced analysts in a highly reproducible way.

Table 1. Inter-observer reproducibility at stent level.**

		Observer 1	Observer 2	Difference			Limits of agreement*	
				Absolute	Relative (Obs1/Obs2)	Reproducibility**	Lower	Upper
Stent	Mean stent area (mm ²)	5.44±1.6	5.47±1.5	-0.02±0.2	1.0	0.1043	-0.32	0.28
	Mean luminal area (mm ²)	4.71±1.5	4.70±1.5	0.00±0.0	1.0	0.0173	-0.05	0.05
	Mean tissue coverage area (mm ²)	0.60±0.5	0.63±0.5	-0.03±0.1	0.9	0.0780	-0.25	0.20
	Min stent area (mm ²)	3.89±1.2	3.84±1.1	0.05±0.2	1.0	0.1549	-0.39	0.49
	Min luminal area (mm ²)	3.24±1.1	3.26±1.1	-0.01±0.0	1.0	0.0158	-0.05	0.02
	Mean tissue coverage thickness (mm)	0.08±0.1	0.08±0.1	0.00±0.0	0.9	0.0100	-0.03	0.02
	Min tissue coverage thickness (mm)	0.00±0.0	0.00±0.0	0.00±0.0	0.0	0.0000	0.00	0.00
	Max tissue coverage thickness (mm)	0.33±0.1	0.33±0.1	0.01±0.0	1.1	0.0179	-0.04	0.06
	Mean strut coverage (mm)	0.08±0.1	0.09±0.1	-0.01±0.0	0.9	0.0066	-0.02	0.01
	Min strut coverage (mm)	0.00±0.0	0.00±0.0	0.00±0.0	0.0	0.0067	-0.02	0.02
	Max strut coverage (mm)	0.31±0.1	0.32±0.1	0.00±0.0	1.0	0.0158	-0.05	0.04
	Mean stent diameter (mm)	2.60±0.4	2.61±0.4	-0.01±0.0	1.0	0.0253	-0.08	0.07
	Mean luminal diameter (mm)	2.41±0.4	2.41±0.4	0.00±0.0	1.0	0.0038	-0.01	0.01
	Stent volume (mm ³)	101.58±48.2	102.15±48.3	-0.58±2.7	1.0	1.8894	-5.97	4.81
Luminal volume (mm ³)	91.76±48.0	91.67±47.9	0.09±0.5	1.0	0.3347	-0.87	1.05	
Tissue coverage volume (mm ³)	13.49±11.6	14.13±10.3	-0.65±2.5	0.9	1.7454	-5.57	4.27	
In-stent obstruction volume (%)	13.73±10.3	14.46±9.0	-0.73±2.2	0.9	1.5341	-4.95	3.49	
Distal reference	Mean luminal area (mm ²)	4.13±1.5	4.14±1.4	0.00±0.0	1.0	0.0085	-0.03	0.02
	Mean luminal diameter (mm)	2.20±0.3	2.20±0.3	0.00±0.0	1.0	0.0067	-0.02	0.02
	Luminal volume (mm ³)	18.39±11.1	18.40±11.1	-0.02±0.1	1.0	0.0492	-0.16	0.12
Proximal reference	Mean luminal area (mm ²)	5.33±2.4	5.27±2.3	0.06±0.1	1.0	0.1051	-0.23	0.35
	Mean luminal diameter (mm)	2.55±0.6	2.54±0.6	0.01±0.0	1.0	0.0198	-0.04	0.07
	Luminal volume (mm ³)	23.05±8.6	22.87±8.5	0.17±0.4	1.0	0.3030	-0.67	1.01

N: 10 stents; Min: minimum; Max: maximum; Obs1: observer 1; Obs2: observer 2; * Bland-Altman limits of agreement defined as mean±1.96 SD of absolute difference; ** Reproducibility defined as residual standard deviation.

Reproducibility of quantitative stent analysis with OCT

Table 2. Intra-observer reproducibility at stent level.**

		Observation 1	Observation 2	Difference			Limits of agreement*	
				Absolute	Relative (Obs1/Obs2)	Reproducibility**	Lower	Upper
Stent	Mean stent area (mm ²)	5.95±1.7	5.90±1.6	0.05±0.1	1.0	0.0621	-0.11	0.21
	Mean luminal area (mm ²)	4.97±1.6	4.98±1.6	-0.01±0.0	1.0	0.0186	-0.06	0.05
	Mean tissue coverage area (mm ²)	0.80±0.7	0.76±0.8	0.04±0.1	1.1	0.0518	-0.09	0.17
	Min stent area (mm ²)	4.01±1.0	3.88±0.9	0.13±0.2	1.0	0.1487	-0.24	0.49
	Min luminal area (mm ²)	3.14±0.6	3.14±0.6	0.00±0.0	1.0	0.0077	-0.02	0.02
	Mean tissue coverage thickness (mm)	0.10±0.1	0.09±0.1	0.00±0.0	1.1	0.0060	-0.01	0.02
	Min tissue coverage thickness (mm)	0.00±0.0	0.00±0.0	0.00±0.0		0.0000	0.00	0.00
	Max tissue coverage thickness (mm)	0.37±0.1	0.35±0.2	0.02±0.0	1.1	0.0161	-0.02	0.05
	Mean strut coverage (mm)	0.11±0.1	0.11±0.1	0.00±0.0	1.1	0.0029	-0.01	0.01
	Min strut coverage (mm)	0.00±0.0	0.00±0.0	0.00±0.0		0.0000	0.00	0.00
	Max strut coverage (mm)	0.35±0.2	0.34±0.2	0.01±0.0	1.1	0.0122	-0.01	0.04
	Mean stent diameter (mm)	2.72±0.4	2.71±0.4	0.01±0.0	1.0	0.0138	-0.02	0.05
	Mean luminal diameter (mm)	2.48±0.4	2.48±0.4	0.00±0.0	1.0	0.0043	-0.01	0.01
	Stent volume (mm ³)	112.26±58.0	111.37±57.3	0.89±1.5	1.0	1.1265	-2.00	3.78
	Luminal volume (mm ³)	98.63±58.2	98.74±58.3	-0.11±0.5	1.0	0.3502	-1.17	0.94
Tissue coverage volume (mm ³)	18.05±15.2	17.03±16.0	1.02±1.6	1.1	1.2617	-2.18	4.23	
In-stent obstruction volume (%)	16.81±13.8	16.07±13.9	0.74±1.1	1.1	0.8790	-1.44	2.93	
Distal reference	Mean luminal area (mm ²)	3.93±1.4	3.93±1.4	0.00±0.0	1.0	0.0039	-0.01	0.01
	Mean luminal diameter (mm)	2.19±0.3	2.19±0.3	0.00±0.0	1.0	0.0023	-0.01	0.01
	Luminal volume (mm ³)	17.14±8.6	17.14±8.6	-0.01±0.0	1.0	0.0239	-0.08	0.07
Proximal reference	Mean luminal area (mm ²)	5.86±4.9	5.79±4.8	0.07±0.1	1.0	0.0628	-0.07	0.21
	Mean luminal diameter (mm)	2.60±1.2	2.58±1.2	0.02±0.0	1.0	0.0121	-0.01	0.04
	Luminal volume (mm ³)	18.61±14.4	18.38±14.2	0.23±0.3	1.0	0.2035	-0.27	0.72

N: 5 stents; Min: minimum; Max: maximum; Obs1: observation 1; Obs2: observation 2; * Bland-Altman limits of agreement defined as mean±1.96 SD of absolute difference; ** Reproducibility defined as residual standard deviation.

Table 3. Inter-observer reproducibility at frame level.**

		Observer 1	Observer2	Difference			Limits of agreement*	
				Absolute	Relative (Obs1/Obs2)	Reproducibility**	Lower	Upper
Stent	Stent area (mm ²)	5.67 ± 1.7	5.71 ± 1.7	-0.03 ± 0.2	1.0	0.1694	-0.50	0.44
	Luminal area (mm ²)	4.95 ± 1.7	4.95 ± 1.7	0.00 ± 0.1	1.0	0.0380	-0.10	0.11
	Tissue coverage area (mm ²)	0.56 ± 0.7	0.59 ± 0.6	-0.03 ± 0.2	0.9	0.1400	-0.41	0.36
	Mean tissue coverage thickness (mm)	0.07 ± 0.1	0.07 ± 0.1	0.00 ± 0.0	0.9	0.0177	-0.05	0.05
	Min tissue coverage thickness (mm)	0.02 ± 0.0	0.02 ± 0.0	0.00 ± 0.0	0.4	0.0132	-0.04	0.03
	Max tissue coverage thickness (mm)	0.15 ± 0.1	0.15 ± 0.1	0.00 ± 0.0	1.0	0.0207	-0.06	0.06
	Mean strut coverage (mm)	0.08 ± 0.1	0.08 ± 0.1	-0.01 ± 0.0	0.9	0.0099	-0.03	0.02
	Min strut coverage (mm)	0.03 ± 0.1	0.04 ± 0.1	-0.01 ± 0.0	0.6	0.0125	-0.04	0.03
	Max strut coverage (mm)	0.14 ± 0.1	0.14 ± 0.1	0.00 ± 0.0	1.0	0.0141	-0.04	0.04
	Stent diameter (mm)	2.66 ± 0.4	2.66 ± 0.4	-0.01 ± 0.1	1.0	0.0409	-0.12	0.10
	Luminal diameter (mm)	2.47 ± 0.4	2.47 ± 0.4	0.00 ± 0.0	1.0	0.0090	-0.02	0.03
Distal reference	Luminal area (mm ²)	4.34 ± 1.6	4.35 ± 1.6	-0.01 ± 0.0	1.0	0.0148	-0.05	0.03
	Luminal diameter (mm)	2.28 ± 0.4	2.28 ± 0.4	0.00 ± 0.0	1.0	0.0077	-0.02	0.02
Proximal reference	Luminal area (mm ²)	5.25 ± 2.1	5.20 ± 2.0	0.05 ± 0.1	1.0	0.0944	-0.21	0.30
	Luminal diameter (mm)	2.54 ± 0.5	2.53 ± 0.5	0.01 ± 0.0	1.0	0.0180	-0.04	0.06

N=244 frames; Min: minimum; Max: maximum; Obs1: observer 1; Obs2: observer 2; * Bland-Altman limits of agreement defined as mean±1.96 SD of absolute difference; ** Reproducibility defined as residual standard deviation.

Table 4. Intra-observer reproducibility at frame level.

		Observation 1	Observation 2	Difference		Limits of agreement*		
				Absolute	Relative (Obs1/Obs2)	Lower	Upper	
Stent	Stent area (mm ²)	6.28±1.7	6.23±1.7	0.05±0.2	1.0	0.1224	-0.27	0.38
	Luminal area (mm ²)	5.33±1.8	5.34±1.8	-0.01±0.1	1.0	0.0596	-0.17	0.16
	Tissue coverage area (mm ²)	0.75±0.9	0.70±0.9	0.05±0.1	1.6	0.1021	-0.22	0.32
	Mean tissue coverage thickness (mm)	0.09±0.1	0.08±0.1	0.00±0.0	1.2	0.0117	-0.03	0.04
	Min tissue coverage thickness (mm)	0.03±0.1	0.03±0.1	0.00±0.0	1.1	0.0197	-0.06	0.05
	Max tissue coverage thickness (mm)	0.17±0.2	0.17±0.2	0.00±0.0	1.1	0.0168	-0.04	0.05
	Mean strut coverage (mm)	0.10±0.1	0.10±0.1	0.00±0.0	1.1	0.0083	-0.02	0.02
	Min strut coverage (mm)	0.05±0.1	0.05±0.1	0.00±0.0	1.1	0.0181	-0.05	0.05
	Max strut coverage (mm)	0.17±0.2	0.16±0.2	0.00±0.0	1.1	0.0125	-0.03	0.04
	Stent diameter (mm)	2.80±0.4	2.79±0.4	0.01±0.0	1.0	0.0272	-0.06	0.08
Distal reference	Luminal diameter (mm)	2.57±0.4	2.57±0.4	0.00±0.0	1.0	0.0131	-0.04	0.04
	Luminal area (mm ²)	3.98±1.6	3.98±1.6	0.00±0.0	1.0	0.0109	-0.03	0.03
Proximal reference	Luminal diameter (mm)	2.20±0.4	2.20±0.4	0.00±0.0	1.0	0.0041	-0.01	0.01
	Luminal area (mm ²)	5.86±3.8	5.79±3.7	0.07±0.1	1.0	0.0826	-0.12	0.27
	Luminal diameter (mm)	2.60±0.9	2.58±0.9	0.02±0.0	1.0	0.0164	-0.02	0.05

N=120 frames; Min: minimum; Max: maximum; Obs1: observation 1; Obs2: observation 2; * Bland-Altman limits of agreement defined as mean±1.96 SD of absolute difference; ** Reproducibility defined as residual standard deviation.

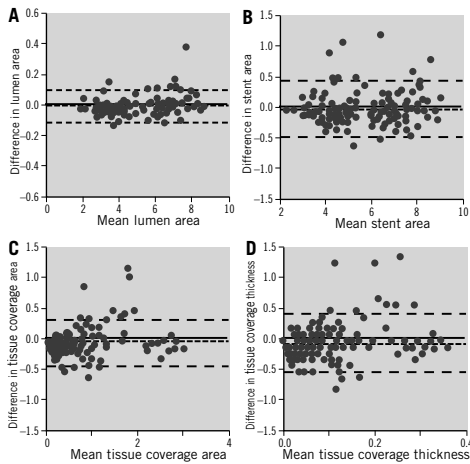


Figure 3. Inter-observer reproducibility. Bland-Altman plots for the inter-observer variability for mean lumen (A), stent (B) and tissue coverage area (C) and mean tissue coverage thickness (D).

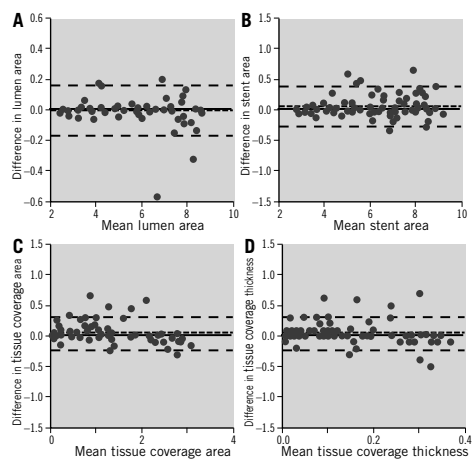


Figure 4. Intra-observer reproducibility. Bland-Altman plots for intra-observer variability for mean lumen (A), stent (B) and tissue coverage area (C) and mean tissue coverage thickness (D).

Stent struts can have different appearances by OCT. The most common appearance is a highly reflective surface with cast dorsal, radial shadow. However, very often only the shadow is observed (probably when the borders of the stent cells are imaged). In our study, shadows were considered struts only when they were sector shaped with sharp defined borders radial to the lumen and the presence of metal (high reflective surface) could be confirmed in the two contiguous distal or proximal frames. The reproducibility of struts

count has not been previously reported. Our data suggests that the inter- and intra- observer variability for strut count is low when applying strict strut definitions. For the intra-observer variability, only in 4% of the cases the difference between the two observations was more than one single strut, while for the inter-observer in only 5% of the cases the difference was higher than two struts. High accuracy and precision for diameters measurement *in vitro* using proprietary software from LightLab has been reported⁶.

Table 5. Inter-observer reproducibility at strut level.

	Observer 1	Observer 2	Difference		Reproducibility**	Limits of agreement*	
			Absolute	Relative (Obs1/Obs2)		Lower	Upper
Min coverage strut (mm)	0.09±0.1	0.10±0.1	-0.01±0.0	0.9	0.0179	-0.05	0.04
Mean coverage strut (mm)	0.10±0.1	0.11±0.1	-0.01±0.0	0.9	0.0174	-0.05	0.04
Max coverage strut (mm)	0.11±0.1	0.11±0.1	-0.01±0.0	0.9	0.0175	-0.05	0.04

N=1712 struts; Min: minimum; Max: maximum; Obs1: observer 1; Obs2: observer 2; * Bland-Altman limits of agreement defined as mean±1.96 SD of absolute difference; ** Reproducibility defined as residual standard deviation.

Table 6. Intra-observer reproducibility at strut level.

	Observation 1	Observation 2	Difference		Reproducibility**	Limits of agreement*	
			Absolute	Relative (Obs1/Obs2)		Lower	Upper
Min coverage strut (mm)	0.13±0.1	0.13±0.1	0.00±0.0	1.1	0.0161	-0.04	0.05
Mean coverage strut (mm)	0.14±0.1	0.13±0.1	0.00±0.0	1.1	0.0153	-0.04	0.04
Max coverage strut (mm)	0.14±0.1	0.14±0.1	0.00±0.0	1.0	0.0154	-0.04	0.04

N=795 struts; Min: minimum; Max: maximum; Obs1: observation 1; Obs2: observation 2; * Bland-Altman limits of agreement defined as mean±1.96 SD of absolute difference; ** Reproducibility defined as residual standard deviation.

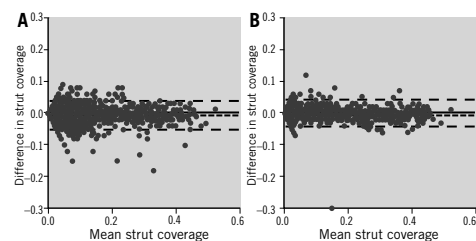


Figure 5. Strut coverage measurement reproducibility. Bland-Altman plots for the inter (A) and intra-observer (B) reproducibility for mean strut coverage measurements.

Tanimoto et al showed a low inter-observer variability for lumen and stent area measurements with OCT using dedicated computer-assisted contour analysis⁷. However, no specific study to assess the reproducibility of strut apposition and strut tissue coverage measurements by OCT has been reported.

Recently several OCT studies evaluating the struts apposition and tissue coverage in DES in humans at different time intervals using proprietary off-line software provided by LightLab Imaging have been published⁹⁻¹¹.

In most of these studies, the operator manually traced the stent and lumen area, to derive the tissue coverage area. Stent struts apposition and tissue coverage are usually individually measured at 1-mm intervals. However, the way of reporting the tissue coverage varies between studies. Some authors report just tissue coverage thickness without detailed methodology^{6,12}. Other studies report the minimum, maximum or average tissue coverage but the selection method, the number of measurements and calculations method was not specified^{9,10}. The methodology used in the present study provides 360 data points for tissue coverage thickness for each cross section. Further the mean, the minimum and the maximum

tissue coverage is reported for each individual strut. The mean tissue coverage per strut is derived from all the measurements at equidistal intervals along the strut.

Prati et al reported high inter- and intra- observer reproducibility for neointima thickness measurements with OCT in carotid rabbit model (r^2 0.88 and 0.90 respectively)⁴. Another study in humans comparing tissue coverage between SES and BMS reported $6\pm 8\ \mu\text{m}$ and $8\pm 8\ \mu\text{m}$ intra- and inter- observer variability for the measurement of tissue coverage⁸. However, the authors did not specify if the measurements correspond to mean, minimum or maximum tissue coverage, how many measurements were performed per strut or in which part of the strut measurements were taken. In the present study we observed absolute differences around $10\ \mu\text{m}$ for the maximum and minimum strut coverage in repeated measurements. Those differences are in the limit of resolution of the technique. The absolute differences for tissue coverage area were $0.04\pm 0.1\ \text{mm}^2$ and $0.03\pm 0.1\ \text{mm}^2$ for the intra- and inter- observer variability respectively. Similar results were found when comparing stent and lumen area. A very good reproducibility for lumen measurement was expected as the automatic contour detection was used and not modified by the analyst in the majority of cases. The differences found in the present study are smaller than the ones reported previously by Xie et al for area measurements with OCT ($0.3\pm 0.5\ \text{mm}^2$ and $0.2\pm 0.4\ \text{mm}^2$ for the intra- and inter- observer variability respectively). There are no reports on the reproducibility of lumen, stent and tissue coverage volumes derived from OCT. We found absolute differences around $1\ \text{mm}^3$ for the intra and $0.65\ \text{mm}^3$ for the interobserver variability for tissue coverage volume. Similar values (0.89 and $0.58\ \text{mm}^3$ for the intra and interobserver respectively) were obtained for the stent volume. As expected, the lumen volume variability was even lower (around $0.10\ \text{mm}^3$) as it was derived from automatic contour detection.

The higher resolution of OCT makes this technique superior to IVUS for the detection and measurement of tissue covering the stent struts.

An IVUS study reported 62% of inter-observer agreement for the presence of neointimal tissue with discrepancy between observers in very thin neointimal layers and when the neointimal area was $<2 \text{ mm}^2$ ¹³. In the present study evaluating DES, a very good agreement was found between observers for the measurement of tissue coverage, even when the mean tissue coverage area was less than 1 mm^2 . An increased variability in the classification of individual struts was observed when the tissue coverage was below $50 \mu\text{m}$. This may be related to the image resolution, but also to software limitations. Automatic algorithms for detecting stent coverage from OCT datasets are under development¹⁴. This could help eliminating the remaining small observer-related variability found in our study.

Kubo et al reported a good intra- and inter- observer agreement ($\text{Kappa}=0.90$ and 0.75 respectively) for malapposed struts classification in sirolimus eluting stents¹⁵. Those results are in line with our study in which the agreement between observers for malapposed struts was excellent ($\text{kappa}=1$), even when applying customised cut-off points for each stent. However, our results are limited by the small number of malapposed struts found in our population.

Clinical implications

The evaluation of strut apposition is essential in the evaluation of new stents designs as IVUS data have suggested a possible relation between apposition and the risk of stent thrombosis in DES^{16,17}. However, interpretation of malapposition as assessed by OCT requires caution. Due to the high image resolution, malapposition of stent struts is a relatively common finding by OCT⁸, but its clinical implications remain poorly understood. Incomplete endothelial struts coverage has been identified in pathology as the most powerful histological predictor of stent thrombosis^{18,19}. Pathological data in humans suggest that neointimal coverage of stent struts could be used as a surrogate marker of endothelialisation due to the good correlation between strut coverage and endothelialisation. Animal data suggest good correlation between mean neointimal thickness measured by histology and OCT⁴. The present study confirms that the tissue covering the strut can be measured with high reproducibility. However, the clinical relevance of uncovered struts as detected by OCT is not clear as some studies have reported presence of uncovered struts at follow-up not associated to clinical events¹⁵. Further investigation and studies with longer follow-up are needed in this field.

Although OCT has proved to be a highly informative imaging technique in assessing stents, standardisation of the analysis of such images is not yet in place. In addition, OCT is a rapidly evolving imaging technology and there is lack of large stent trials with long-term clinical follow-up linking OCT findings and clinical events. Thereby this methodology of analysis is prone to changes in the future in order to adjust to the new clinical needs.

Conclusions

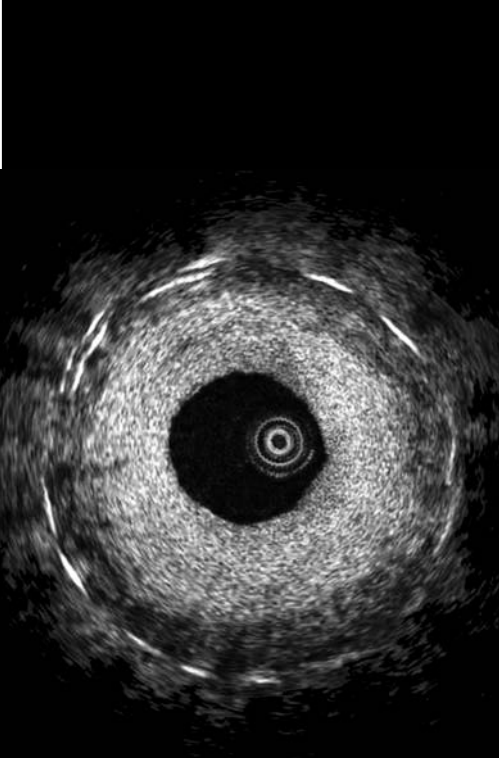
In a Corelab setting, the inter- and intra- observer reproducibility for strut count, strut apposition and strut tissue coverage measurements with OCT is excellent. This finding emphasises the value of OCT as a tool for the clinical long-term assessment of stents.

References

1. Regar E, van Leeuwen A, Serruys PW. 2007. Optical coherence tomography in cardiovascular research. *London: Informa Healthcare*. 338 p.
2. Gonzalo N, Serruys PW, Regar E. Optical coherence tomography: clinical applications and the evaluation of DES. *Minerva Cardioangiol*. 2008;56:511-25.
3. Aoki J, Colombo A, Dudek D, Banning AP, Drzewiecki J, Zmudka K, Schiele F, Russell ME, Koglin J, Serruys PW. Persistent remodeling and neointimal suppression 2 years after polymer-based, paclitaxel-eluting stent implantation: insights from serial intravascular ultrasound analysis in the TAXUS II study. *Circulation*. 2005;112:3876-83.
4. Prati F, Zimarino M, Stabile E, Pizzicannella G, Fouad T, Rabozzi R, Filippini A, Pizzicannella J, Cera M, De Caterina R. Does optical coherence tomography identify arterial healing after stenting? An in vivo comparison with histology, in a rabbit carotid model. *Heart*. 2008;94:217-21.
5. Suzuki Y, Ikeno F, Koizumi T, To F, Yeung AC, Yock PG, Fitzgerald PJ, Fearon WF. In Vivo Comparison Between Optical Coherence Tomography and Intravascular Ultrasound for Detecting Small Degrees of In-Stent Neointima after Stent Implantation. *J Am Coll Cardiol Interv*. 2008;1:168-73.
6. Tsuchida K, vd Giessen W, Patterson M, Tanimoto S, Garcia-Garcia H, Regar E, Ligthart J, Maugeness AM, Maatrijk G, Wentzel JJ, Serruys P.W. In-vivo validation of a novel three-dimensional quantitative coronary angiography system (CardioOp-B™). Comparison with a conventional two-dimensional system (CASS II™) and with special reference to optical coherence tomography. *Eurointervention* 2007;3:100-108.
7. Tanimoto S, Rodriguez-Granillo G, Barlis P, de Winter S, Bruining N, Hamers R, Knappen M, Verheye S, Serruys PW, Regar E. A novel approach for quantitative analysis of intracoronary optical coherence tomography: high inter-observer agreement with computer-assisted contour detection. *Catheter Cardiovasc Interv*. 2008;72:228-35.
8. Xie Y, Takano M, Murakami D, Yamamoto M, Okamoto K, Inami S, Seimiya K, Ohba T, Seino Y, Mizuno K. Comparison of neointimal coverage by optical coherence tomography of a sirolimus-eluting stent versus a bare-metal stent three months after implantation. *Am J Cardiol*. 2008;102:27-31.
9. Chen BX, Ma FY, Luo W, Ruan JH, Xie WL, Zhao XZ, Sun SH, Guo XM, Wang F, Tian T and others. Neointimal coverage of bare-metal and sirolimus-eluting stents evaluated with optical coherence tomography. *Heart*. 2008;94:566-70.
10. Matsumoto D, Shite J, Shinke T, Otake H, Tanino Y, Ogasawara D, Sawada T, Paredes OL, Hirata K, Yokoyama M. Neointimal coverage of sirolimus-eluting stents at 6-month follow-up: evaluated by optical coherence tomography. *Eur Heart J*. 2007;28:961-7.
11. Takano M, Yamamoto M, Inami S, Murakami D, Seimiya K, Ohba T, Seino Y, Mizuno K. Long-term follow-up evaluation after sirolimus-eluting stent implantation by optical coherence tomography: do uncovered struts persist? *J Am Coll Cardiol*. 2008;51:968-9.
12. Yao ZH, Matsubara T, Inada T, Suzuki Y, Suzuki T. Neointimal coverage of sirolimus-eluting stents 6 months and 12 months after implantation: evaluation by optical coherence tomography. *Chin Med J (Engl)*. 2008;121:503-7.
13. Regar E, Werner F, Siebert U, Rieber J, Theisen K, Mudra H, Klauss V. Reproducibility of neointima quantification with motorized intravascular ultrasound pullback in stented coronary arteries. *Am Heart J*. 2000;139:632-7.

Reproducibility of quantitative stent analysis with OCT

14. Bonnema GT, Cardinal KO, Williams SK, Barton JK. An automatic algorithm for detecting stent endothelialization from volumetric optical coherence tomography datasets. *Phys Med Biol.* 2008;53:3083-98.
15. Kubo T IT, Kitabata H, Kuroi A, Ueno S, Yamano T, Tanimoto T, Matsuo Y, Masho T, Takarada S, Tanaka A, Nakamura N, Mizukoshi M, Tomobuchi Y, Akasaka T. Comparison of vascular response after sirolimus eluting stent implantation between patients with unstable and stable angina pectoris. *J Am Coll Cardiol Img.* 2008;1:475-84.
16. Alfonso F, Suarez A, Perez-Vizcayno MJ, Moreno R, Escaned J, Banelos C, Jimenez P, Bernardo E, Angiolillo DJ, Hernandez R, Macaya C. Intravascular ultrasound findings during episodes of drug-eluting stent thrombosis. *J Am Coll Cardiol.* 2007;50:2095-2097.
17. Cook S, Wenaweser P, Togni M, Billinger M, Morger C, Seiler C, Vogel R, Hess O, Meier B, Windecker S. Incomplete stent apposition and very late stent thrombosis after drug-eluting stent implantation. *Circulation.* 2007;115:2426-34.
18. Finn AV, Joner M, Nakazawa G, Kolodgie F, Newell J, John MC, Gold HK, Virmani R. Pathological correlates of late drug-eluting stent thrombosis: strut coverage as a marker of endothelialization. *Circulation.* 2007;115:2435-41.
19. Joner M, Finn AV, Farb A, Mont EK, Kolodgie FD, Ladich E, Kutys R, Skorija K, Gold HK, Virmani R. Pathology of drug-eluting stents in humans: delayed healing and late thrombotic risk. *J Am Coll Cardiol.* 2006;48:193-202.



3.3

Full-Automated Quantitative Analysis of Intracoronary OCT: Method and Validation.

Sihan K, Botha C, Post F, de Winter S, Gonzalo N, Regar E, Serruys P.W, Hamers R, Bruining N.

Catheter Cardiovasc Interv. 2009 May 7. [Epub ahead of print]

Basic Science

Fully Automatic Three-Dimensional Quantitative Analysis of Intracoronary Optical Coherence Tomography: Method and Validation

Kenji Sihan,^{1,2} BSc, Charl Botha,² PhD, Frits Post,² PhD, Sebastiaan de Winter,² BSc, Nieves Gonzalo,¹ MD, Evelyn Regar,¹ MD, PhD, Patrick J.W.C. Serruys,¹ MD, PhD, Ronald Hamers,¹ PhD, and Nico Bruining,^{1*} PhD

Objectives and background: Quantitative analysis of intracoronary optical coherence tomography (OCT) image data (QOCT) is currently performed by a time-consuming manual contour tracing process in individual OCT images acquired during a pullback procedure (frame-based method). To get an efficient quantitative analysis process, we developed a fully automatic three-dimensional (3D) lumen contour detection method and evaluated the results against those derived by expert human observers. **Methods:** The method was developed using Matlab (The Mathworks, Natick, MA). It incorporates a graphical user interface for contour display and, in the selected cases where this might be necessary, editing. OCT image data of 20 randomly selected patients, acquired with a commercially available system (Lightlab imaging, Westford, MA), were pulled from our OCT database for validation. **Results:** A total of 4,137 OCT images were analyzed. There was no statistically significant difference in mean lumen areas between the two methods (5.03 ± 2.16 vs. 5.02 ± 2.21 mm²; $P = 0.6$, human vs. automated). Regression analysis showed a good correlation with an r value of 0.99. The method requires an average 2–5 sec calculation time per OCT image. In 3% of the detected contours an observer correction was necessary. **Conclusion:** Fully automatic lumen contour detection in OCT images is feasible with only a select few contours showing an artifact (3%) that can be easily corrected. This QOCT method may be a valuable tool for future coronary imaging studies incorporating OCT. © 2009 Wiley-Liss, Inc.

Key words: angiography; coronary; diagnostic cardiac catheterization; quantitative vascular angiography

INTRODUCTION

Optical coherence tomography (OCT) has been rapidly accepted as an additional invasive coronary imaging tool [1]. It allows highly detailed imaging of the coronary lumen and vessel wall morphology at resolutions of 10 times higher than what current intracoronary ultrasound (ICUS) can offer. The details shown within OCT images are close to histopathology, allowing accurate evaluation of by example apposition of stent struts and—in longitudinal studies—tissue-coverage of drug-eluting stents (DES) [2]. This advantage has resulted in an increasing use of OCT in studies evaluating new therapeutic treatments, in addition to ICUS, the current de facto reference method for intravascular imaging [3,4].

To apply an imaging method in studies, accurate quantitative analysis tools are required, as has been

proven by quantitative angiography (QCA) [5] and quantitative ICUS (QCU) [6,7]. Recently, results of

¹Thoraxcenter, Delft, The Netherlands

²Department of Cardiology, Erasmus MC, Rotterdam, The Netherlands and TU-Delft, Delft, The Netherlands

Conflict of interest: Dr. Hamers is an employee of CURAD BV, Wijk Bij Duurstede, The Netherlands.

*Correspondence to: Nico Bruining, PhD, Erasmus MC, P.O. Box 1738, 3000 DR Rotterdam, The Netherlands. E-mail: n.Bruining@erasmusmc.nl

Received 25 March 2009; Revision accepted 23 April 2009

DOI 10.1002/ccd.22125

Published online 11 June 2009 in Wiley InterScience (www.interscience.wiley.com)

computer-assisted quantitative OCT (QOCT) have been reported showing good results for coronary lumen measurements [8]. However, because an OCT examination contains hundreds of individual images, such analysis can, despite the use of computer-assisted tools, be a tedious and time-consuming process [8]. However, because the lumen-intima interface is so clearly visualized in OCT, far better than in ICUS, a fully automatic lumen contour detection approach could be feasible.

This article reports on a novel in-house developed fully automatic three-dimensional (3D) OCT lumen contour detection approach and its validation using expert human observer computer-assisted analysis as a reference.

MATERIALS AND METHODS

OCT Imaging System

OCT imaging was performed with a commercially available system (Lightlab imaging, Westford, MA). This system uses a 1,310-nm broadband light-source generated by a super luminescent diode with an output power in the range of 8.0 mW. The average tissue penetration depth is approximately 1.5 mm with an axial and lateral resolution of 15 and 25 μm , respectively. The imaging probe has the size of a guide-wire with a maximum outer diameter of 0.019 inch (ImagewireTM, LightLab Imaging). The wire contains a single-mode fiber optic core within a translucent sheath. The imaging-wire is connected to an imaging console, similar as ICUS, which performs the real-time image data processing, visualization, and image storage. Systematic imaging of a coronary segment is also analogue to ICUS by an automatic continuous speed pullback (between 1 and 3 mm/sec) of the imaging wire [6]. OCT images are generated at a rate of 10–20/sec (cf. ICUS 30 frames/sec). The accuracy of OCT for dimensional measurements—determined using a phantom—has been recently reported to be excellent (mean difference in measured length of -0.03 mm with 0.02 mm precision) [8].

Patients and OCT Image Acquisition

For validation of the automated method, we made a random selection of 20 OCT cases from our database of patients participating in different studies. In all cases a standard femoral approach with 7F guiding catheters was used. Before imaging, all patients received weight-adjusted heparin intravenously to maintain an activated clotting time of >300 sec as well as intravenous analgesics. To be able to see the coronary vessel wall, the coronary artery must be cleared of blood by replacing it with lactated Ringer's solution. This procedure is performed by occlusion of the artery with a dedicated occlusion catheter (Helios, Goodman, Japan) including a short balloon (6.0 mm length) that can be inflated by

a low pressure (0.3 atm). The Ringer's is infused distally from the balloon at a rate of 0.5 ml/sec at a temperature of 37°C). Sufficient occlusion of the coronary is checked by contrast injection via the guiding catheter and the balloon pressure is increased (at 0.5 atm increments) when necessary. The images were digitally stored in the AVI file format on DVD's and were translated later into the DICOM medical imaging standard by in-house developed software.

Automated Quantitative OCT Method

The automated OCT lumen contour detection method was developed in the Matlab environment (The Mathworks, Natick, MA). The method has five stages:

Preprocessing. Each individual OCT frame is preprocessed to remove speckle noise and gaps and to adapt the contrast for proper image normalization. Preprocessing consists of the application of a Gaussian filter and using different relative thresholds (Fig. 1B). The relative thresholds are applied on the pixel values to remove extreme values and to improve image normalization.

Edge detection. A Canny [9] filter is applied to detect edges in the OCT image. The final lumen contour is the result of appropriately selected edges, which are positioned on the lumen-intima border only. Straightforward application of the standard Canny filter to the OCT images leads to many false and/or missed contours. Therefore, we iteratively apply the Canny filter to match the constraints necessary for OCT images (percentage of image pixels classified as true edges). This percentage is based on a test-set where it is set in such a way that the lumen contour is detected while detecting as little noise as possible. Within this procedure, the threshold of the Canny filter is optimized using a binary search algorithm.

Lumen edge selection. The result of the Canny edge detection stage includes some edges that do not belong to the lumen-intima interface, for example radially behind bright areas (Fig. 1C). These false edges are mostly due to noise caused by the catheter and by speckle noise which was not removed by the preprocessing step without significantly impairing image details. The majority of these false edges are identified by two constraints:

1. The angle between the gradient orthogonal to the line segment and the line connecting it to the catheter center should be smaller than a certain threshold.
2. The length of the edge should be longer than a certain threshold (Fig. 1).

Lumen edge linking. The final lumen contour is the optimal combination of the resulting true edges. This is

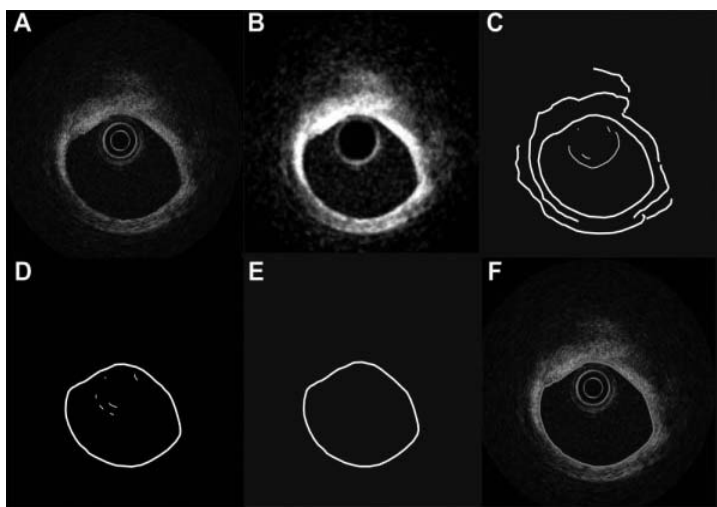


Fig. 1. This figure shows the results of the different processing steps. (A) An original OCT image is presented. (B) The image after the application of a Gaussian filter. (C) The detected edges as a result of the iteratively applied Canny filter. (D) The remaining edges after application of the angle con-

straint. Short edges are removed after application of a length threshold (E). The postprocessed and smoothed final contour is presented in (F). [Color figure can be viewed in the online issue, which is available at www.interscience.wiley.com.]

performed using a quality score determined by the resultant lumen area, length (relative to the area), and gaps in the contour (relative to the length). For all possible combinations of edge selections, the quality score is calculated and the combination with the highest score results in the final lumen contour.

Postprocessing. Postprocessing is applied to overcome possible errors introduced by the pre-processing and those inherent to the nature of OCT imaging itself (such as large side-branches, gaps caused by guide-wire artifacts, etc.). The postprocessing is divided into several subprocesses:

Contour correction and smoothing. The iterative application of the Canny filter does not select the edges with local maximum gradient. In a postprocessing step, the maximum gradient search is automatically performed within a 5 pixel radius from the initially found contour. Subsequently, the contour is smoothed, weighing neighbor coordinates with the gradient magnitude in a normal distribution.

Side-branch gaps and out-of-range borders. The resulting luminal contours may still have gaps, which are mostly caused by side-branches and/or guide-wire artifacts. Furthermore, often in OCT images the lumen border is out of range, in large vessels, or is not pronounced enough to produce an edge (Fig. 2). To close

these gaps and omissions, a mathematical circular correction model is applied (Fig. 2).

Replacement of falsely detected contours (3D analysis). In the case of large side-branches, heavy noise or large parts of missing visible lumen data within the OCT images (Fig. 3), it is still possible that the automated contour detection does not result in the desired contour. For each consecutive image, the enclosed area of the lumen contour is calculated. Frames showing a relatively large deviation in areas compared to their neighbors are labeled as incorrect. A search and substitute algorithm replaces these contours by the closest available correct contour in the longitudinal direction.

Final approval and correction. It is very difficult, or even impossible, to develop a 100% accurate fully automatic detection method in medical image processing. The large differences found in coronary morphology will always result in unexpected images that could not have been foreseen during development. Therefore, the results must be validated by an expert. To facilitate this, a user interface was developed, similar to that used for QCU [10].

Validation

For validation of the automated method, the quantitative results were compared against those derived by application of a computer-assisted lumen detection

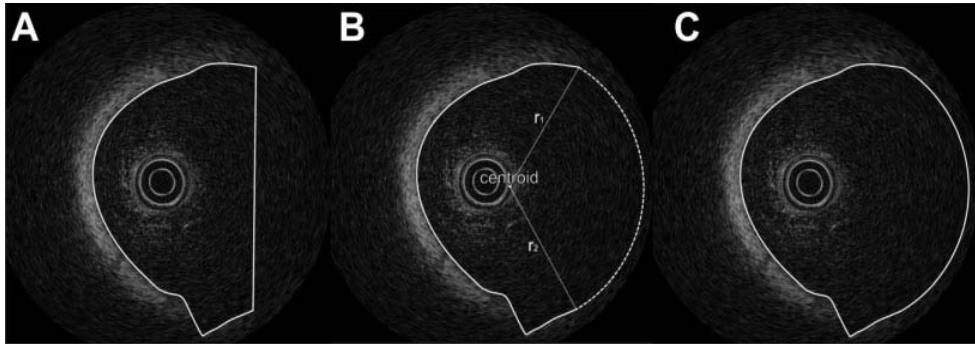


Fig. 2. To close the remaining gaps, the straight line at the right-hand side (A), a circular arc interpolation is performed automatically using the center of gravity of the contour as the center of the circle (B). For the radius, linear interpolation is used from r_1 to r_2 . The repaired contour is presented in (C).

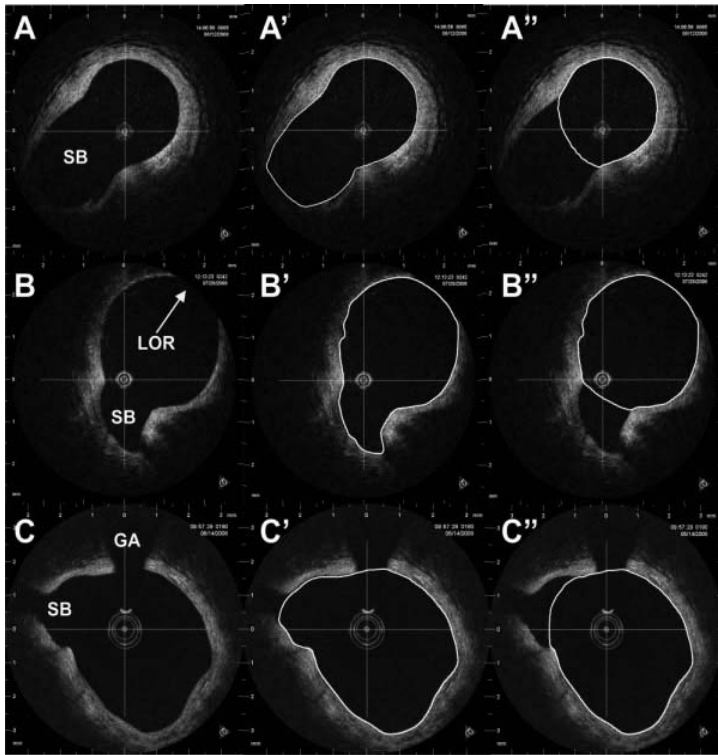


Fig. 3. This figure presents a few different lumen morphologies which are difficult to detect correctly fully-automated. (A) A large side-branch can be appreciated (indicated by SB). (A') The detected automated contour, which has been corrected by the human observer (A''). (B) In addition to a side-branch also a case were part of the lumen is out of range for the OCT catheter. The automated contour detection applied the automated

circular correction (B') and the human observer corrected for the large side-branch artifact (B''). Finally, in (C) a guide-wire artifact is presented (C, GA). This relatively small gap is automatically repaired by the correction algorithms (C'). Again, also in this example the observer corrected for the large side-branch (C''). [Color figure can be viewed in the online issue, which is available at www.interscience.wiley.com.]

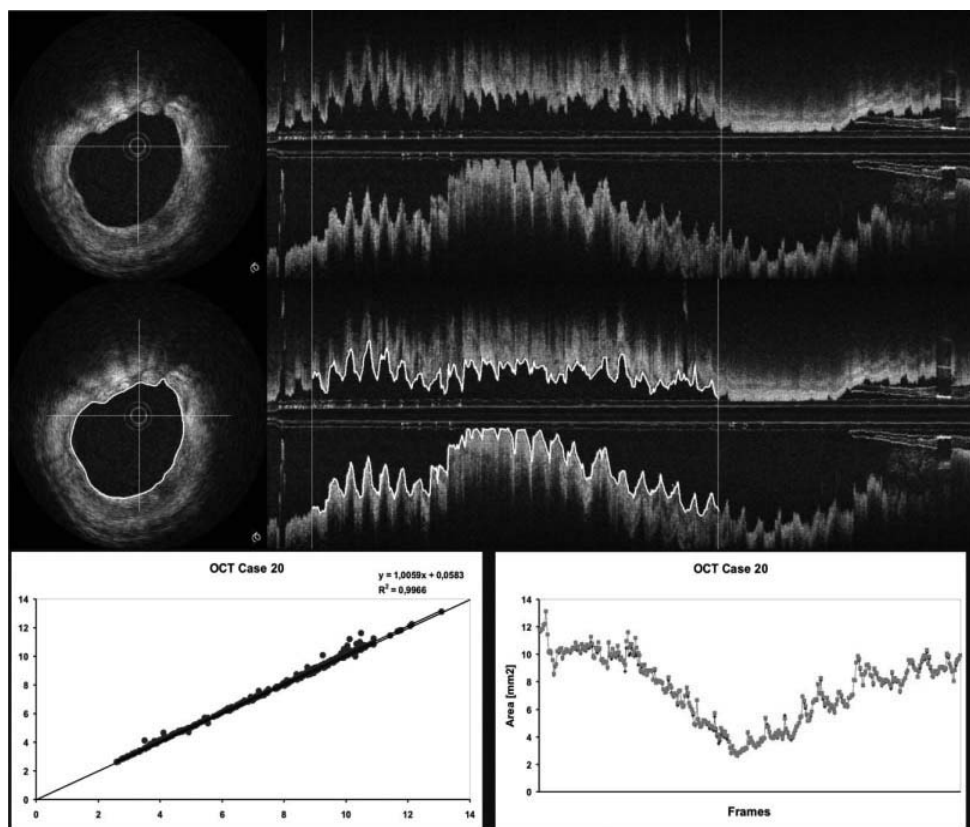


Fig. 4. A typical analysis example is presented. In (A) an individual cross-sectional image is shown and in (A') the longitudinal reconstruction of the pullback examination. In (B and B'), the same images are presented with the automated contour detected result superimposed. It can be appreciated that the cross-sectional OCT images present a lot of details of the

lumen-intima morphology. (C) The regression analyses of the area measurements of all frames with the manual results on the x-axis and the automated results on the y-axis. Finally in (D), all the area measurements are presented of both methods. [Color figure can be viewed in the online issue, which is available at www.interscience.wiley.com.]

method (CURAD vessel analysis, CURAD BV, Wijk bij Duurstede, The Netherlands) [8]. The expert (N.G.) was blinded for the automated results.

Statistical Analysis

Quantitative data are presented as mean \pm standard deviation (SD). Comparison between the methods was performed by the two-tailed paired Student's *t*-test. A *P* value < 0.05 was considered statistically significant. In addition, regression analysis and the method as proposed by Bland and Altman [11] was performed.

RESULTS

In the 20 OCT cases a total of 4,167 frames were analyzed (208 ± 92 frames on average per patient). In each case, the OCT images were analyzed consecutively, without intervals (Fig. 4). Although the human analysis time was not measured, it is well known that this is usually a lengthy process. The automated method required on average approximately 2–5 sec of calculation time per frame. In 125 OCT frames (3%), the automatic results had to be corrected.

The computer-assisted manual analysis showed a mean lumen area of $5.0 \pm 2.2 \text{ mm}^2$ versus $5.1 \pm$

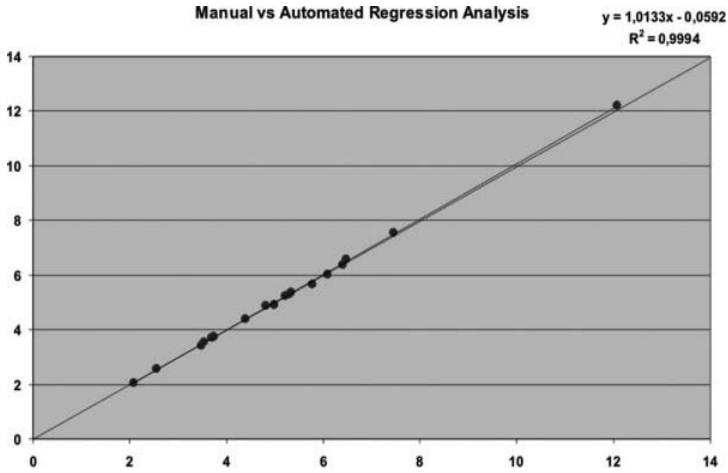


Fig. 5. The linear regression analysis for the 20 OCT cases analysed computer-assisted (e.g., manual) versus fully automatic. [Color figure can be viewed in the online issue, which is available at www.interscience.wiley.com.]

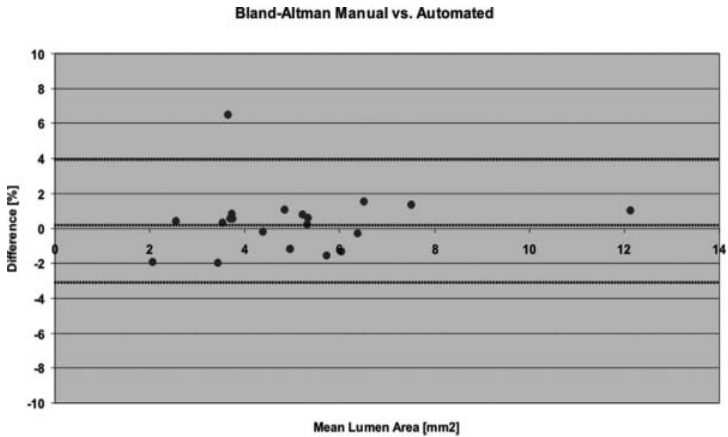


Fig. 6. The relative differences according to the method as proposed by Bland and Altman [11]. [Color figure can be viewed in the online issue, which is available at www.interscience.wiley.com.]

2.2 mm² for the fully automatic method, with no statistical significant difference ($P = 0.26$). The relative difference was $0.4\% \pm 1.8\%$. Regression analysis yielded $r = 0.999$ (Fig. 5).

Bland and Altman analysis revealed a single outlier (Fig. 6). All other cases were within an interval of $\pm 2\%$. Inspection of the outlier showed a deviated contour detection by the expert observer, which resulted in a relative difference of 6%. If this outlier is disre-

garded, the results are 5.1 ± 2.2 mm² (expert) versus 5.1 ± 2.2 mm² (automated), $P = 0.52$; relative difference $0.02\% \pm 1.1\%$.

DISCUSSION

This study shows that fully automatic 3D lumen contour detection for quantitative OCT analysis is

feasible. The quantitative results are similar to those derived manually by an expert.

To evaluate new interventional therapies, quantitative imaging tools are mandatory, such as QCA [5] and QCU [6,10]. Although a computer-assisted method for QOCT has been presented showing excellent results [8], the advantages of fully automatic contour detection are obvious. It does not consume the valuable time of an expert neither does it suffer from possible interobserver- and intraobserver-related deviations. Furthermore, as the outlier case in this report shows, contours which are not precisely positioned on the lumen border can result in a relatively large deviation (in this case 6%). The human expert will most likely be more motivated to analyze all images in a pullback (and not a limited subset of images selected at by example 1 mm intervals, e.g. every 15th frame) if the majority of the contours are already correctly detected and the human effort required is purely for inspection and a limited number of corrections (Fig. 3).

OCT is a relatively new coronary imaging technique, but it has gained considerable enthusiasm in a very short period. It can reveal much more information of the region around the lumen border than is achievable with the current available ICUS technology. However, on the down-side, the penetration depth into the coronary vessel wall and present plaques is still limited (1–2 mm). Therefore, at this moment an automated outer vessel contour detector cannot be developed. Furthermore, because OCT cannot be used to perform coronary plaque measurements, the advantages and disadvantages of OCT in several different clinical scenarios have been described recently [8].

At present, several different commercial OCT systems are available. For this study the system of Lightlab was used [12,13]. This system has an integrated quantitative analysis tool that is limited to single frames. Furthermore, to our knowledge the method has not been published. This single frame approach requires a time consuming and operator dependent manual frame selection at 1 mm intervals. It has been reported that depending on the length of the analyzed region it can take up 2–4 hr to complete an analysis [8].

Independent third party quantitative software tools are, to our knowledge, not yet reported, except for one study presented by Tanimoto et al. [8]. In this article, a computer-assisted dedicated OCT analysis tool was reported, showing good inter and intraobserver quantitative results ($1.57\% \pm 0.05\%$ for lumen areas). However, only well-visualized OCT images were included. Images suffering from motion-induced artifacts, dissections, and side-branches—hampering analysis—were excluded (9%). In this study, all available imaging data (real world data) was analyzed and no exclusions were made. To our

knowledge, to date, no other reports have been published concerning fully automatic QOCT methods.

Limitations

Unfortunately, because of the nature of OCT, the penetration depth is currently too low to be able to visualize the coronary vessel wall in diseased segments and therefore only the coronary lumen could be quantified in this study. Developments of newer OCT methods, such as OFDI, and application of other light sources, could possibly enhance the penetration depth making it hopefully possible to visualize advanced coronary plaques in the near future.

The number of cases included in this study is limited, a larger number of cases must reveal if the excellent score of fully automatic detection in 97% of the images can be maintained for larger populations. However, we evaluated almost 4,200 individual OCT images of very different lumen morphology, because of the high spatial resolution.

Future Developments

This full-automated approach to quantify the coronary lumen by OCT is the first step towards further developments of highly anticipated additional quantification tools. On the requirements list are currently: detection of stent struts, protrusion of plaque contents through stent struts, in-stent thrombi, fibrous caps (detection and thickness measurements), and plaque composition. If these requirements could be detected automatically remains topic for further research and developments. However, measurements of in-stent intima hyperplasia, lumen-eccentricity and -remodeling (if base-line and follow-up OCT measurements are available) are already possible using the automated approach (for lumen) in combination by computer-assisted tools (for stent contouring) [8].

The described method has been developed in a generic mathematical research environment on a normal desktop personal computer running Microsoft Windows. The processing time of 2–5 sec could most likely be reduced in the near future if the software were to be ported to a dedicated QOCT environment.

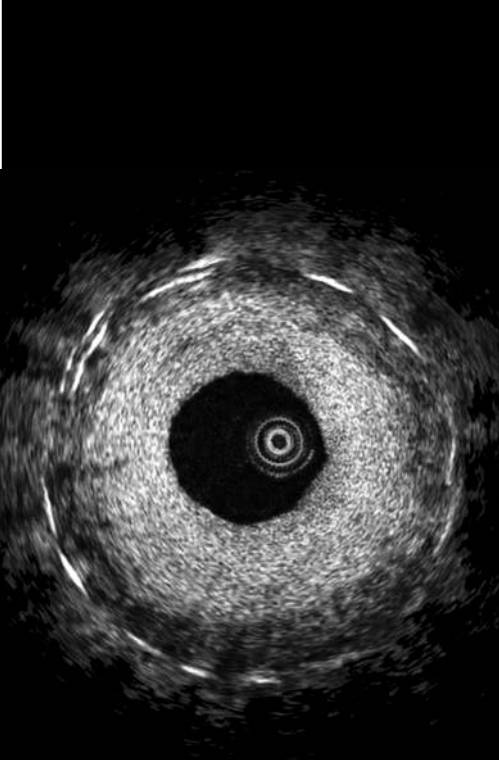
Many of the OCT images suffer from motion artifacts, which are caused by the low temporal resolution of current OCT systems as compared to the relatively rapid motion of the heart. The heart motion also causes the saw-tooth shaped appearance of the coronary vessel wall in the longitudinal reconstructions (Fig. 4). These motion-related artifacts could probably be overcome by the application of optical frequency domain imaging (OFDI) to coronary vessel imaging. However, these systems are still in the research phase and not commercially available yet.

CONCLUSION

This study shows that fully automatic lumen contour detection in OCT images is feasible with only a few contours showing an artifact (3%) that can be easily corrected. This QOCT method may be a valuable tool for future coronary imaging studies incorporating OCT.

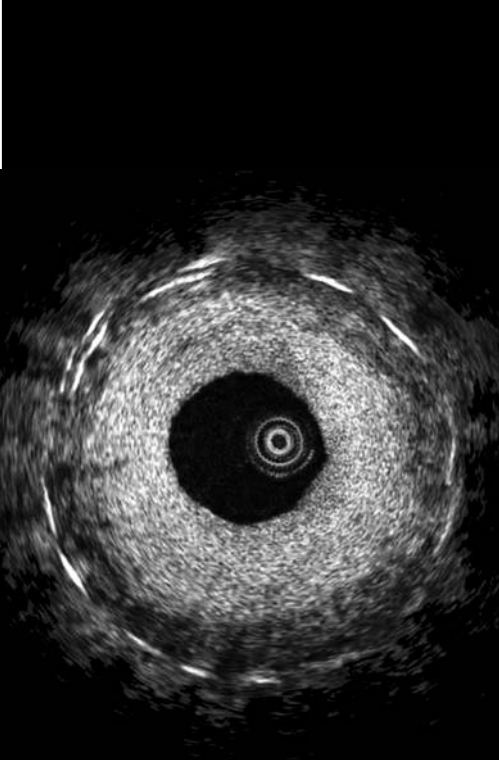
REFERENCES

1. Regar E, Schaar JA, Mont E, Virmani R, Serruys PW. Optical coherence tomography. *Cardiovasc Radiat Med* 2003;4:198–204.
2. Prati F, Zimarino M, Stabile E, Pizzicannella G, Fouad T, Rabozzi R, Filippini A, Pizzicannella J, Cera M, De Caterina R. Does optical coherence tomography identify arterial healing after stenting? An in vivo comparison with histology, in a rabbit carotid model. *Heart* 2008;94:217–221.
3. Guagliumi G, Sirbu V. Optical coherence tomography: High resolution intravascular imaging to evaluate vascular healing after coronary stenting. *Catheter Cardiovasc Interv* 2008;72:237–247.
4. Ormiston JA, Serruys PW, Regar E, Dudek D, Thuesen L, Webster MW, Onuma Y, Garcia-Garcia HM, McGreevy R, Veldhof S. A bioabsorbable everolimus-eluting coronary stent system for patients with single de-novo coronary artery lesions (ABSORB): A prospective open-label trial. *Lancet* 2008;371:899–907.
5. Haase J, Escaned J, van Swijndregt EM, Ozaki Y, Gronenschild E, Slager CJ, Serruys PW. Experimental validation of geometric and densitometric coronary measurements on the new generation Cardiovascular Angiography Analysis System (CAAS II). *Cathet Cardiovasc Diagn* 1993;30:104–114.
6. Mintz GS, Nissen SE, Anderson WD, Bailey SR, Erbel R, et al. Document on Standards for Acquisition, Measurement and Reporting of Intravascular Ultrasound Studies (IVUS). A report of the American College of Cardiology Task Force on Clinical Expert Consensus Documents. *J Am Coll Cardiol* 2001;37:1478–1492.
7. von Birgelen C, Mintz GS, Nicosia A, Foley DP, van der Giesen WJ, Bruining N, Airriian SG, Roelandt JRTC, de Feyter PJ, Serruys PW. Electrocardiogram-gated intravascular ultrasound image acquisition after coronary stent deployment facilitates on-line three-dimensional reconstruction and automated lumen quantification. *J Am Coll Cardiol* 1997;30:436–443.
8. Tanimoto S, Rodriguez-Granillo G, Barlis P, de Winter S, Bruining N, Hamers R, Knappen M, Verheye S, Serruys PW, Regar E. A novel approach for quantitative analysis of intracoronary optical coherence tomography: High inter-observer agreement with computer-assisted contour detection. *Catheter Cardiovasc Interv* 2008;72:228–235.
9. Canny J. A computational approach to edge detection. *IEEE Trans Pattern Anal Mach Intel* 1986;8:679–714.
10. Hamers R, Bruining N, Knook M, Sabate M, Roelandt JRTC. A novel approach to quantitative analysis of intravascular ultrasound images. *Comput Cardiol* 2001:589–592.
11. Bland JM, Altman DG. Statistical methods for assessing agreement between two methods of clinical measurement. *Lancet* 1986;1:307–310.
12. Matsumoto D, Shite J, Shinke T, Otake H, Tanino Y, Ogasawara D, Sawada T, Paredes OL, Hirata K, Yokoyama M. Neointimal coverage of sirolimus-eluting stents at 6-month follow-up: Evaluated by optical coherence tomography. *Eur Heart J* 2007;28:961–967.
13. Takano M, Inami S, Jang IK, Yamamoto M, Murakami D, Seimiya K, Ohba T, Mizuno K. Evaluation by optical coherence tomography of neointimal coverage of sirolimus-eluting stent three months after implantation. *Am J Cardiol* 2007;99:1033–1038.



CHAPTER 4

Atherosclerotic coronary plaque characterization with OCT



4.1

Combined OCT and intravascular ultrasound radio frequency data analysis for plaque characterization. Classification accuracy of human coronary plaques in vitro related to image artifacts

Goderie T, van Soest G, Garcia-Garcia HM, Gonzalo N, Koljenovic S, van Leenders A, Mastik F, Regar E, Oosterhuis JW, Serruys PW, van der Steen AFW.

Submitted.

ABSTRACT

Objectives: The purpose of this study was to characterize coronary plaque types, with special interest in misclassification in both optical coherence tomography (OCT) and in intravascular ultrasound (IVUS) radiofrequency (RF) data analysis, and to investigate the possibility of error reduction by combining both techniques.

Background: Intracoronary imaging methods have greatly enhanced our understanding of the atherosclerotic disease process and have revolutionized the diagnostic capabilities for the detection of high-risk atherosclerotic plaques. IVUS RF data analysis and OCT are two techniques focusing on plaque morphology and composition.

Methods: Regions of interest were selected and imaged with OCT in 50 cross-sections and IVUS in 36 cross-sections, from 14 human coronary arteries, sectioned post-mortem from 14 hearts of patients dying of non-cardiovascular causes. Plaques were classified based on IVUS RF data analysis (VH-IVUSTM), OCT and the combination of those. Histology was the benchmark.

Results: OCT was able to correctly classified 32 out of 50 cross-sections; VH-IVUS correctly classified 26 out of 36 cross-sections. VH-IVUS and OCT combined were able to correctly classify 28 out of 36 cross-sections. Systematic misclassifications in OCT were intimal thickening (IT) classified as fibroatheroma (FA) in 7 cross-sections and IT classified as thin-cap fibro-atheroma (TCFA) in 3 cross-sections. Misclassifications in VH-IVUS were mainly IT as FA in 3 cross-sections and IT as calcified fibro-atheroma in 3 cross-sections.

Conclusions: Typical image artifacts, both new ones and previously identified, were found to affect the interpretation of OCT data, misclassifying intimal thickening as fibro-atheroma or thin cap fibro-atheroma. Adding VH-IVUS to OCT reduced the error rate.

BACKGROUND

Pathology studies have demonstrated that most of acute coronary syndromes originate from vulnerable plaques.¹⁻⁵ These plaques have a mechanically weak cap, consisting of a thin fibrotic layer that is infiltrated by macrophages, overlying a lipid-rich necrotic core.^{2, 6-9} The current challenge is to specifically identify *in vivo* plaques that exhibit these characteristics and thus are likely to cause acute coronary syndrome¹⁰. Clinical diagnosis may benefit from complementary information gathered by different imaging technologies, as they may be sensitive to specific aspects of the anatomy.^{6, 11-16}

Grayscale Intravascular Ultrasound (IVUS) has since long been a standard diagnostic tool in cath labs worldwide, and intravascular Optical Coherence Tomography (OCT) looks set to rapidly become one as well.^{14, 17-20} Radio frequency (RF) data analysis adds plaque composition information to grayscale IVUS, which may help to distinguish high-risk lipid-rich necrotic plaques from other types of plaques.²¹⁻²³ IVUS RF data analysis (commercially available as VH-IVUS™; Volcano, Rancho Cordova, CA) aims to provide quantitative information on plaque composition classifying plaque as fibrotic, fibro-fatty, necrotic core or dense calcium, based on spectral analysis of the RF signal.¹² Although criteria have been formulated for VH-IVUS to detect TCFA, as a standalone technique it is not able to recognize this type of lesion because of its limited resolution (> 250 μm).^{16, 24-26} In this article, we will refer to IVUS RF data analysis as VH-IVUS, since we used that technology specifically.

Optical coherence tomography (OCT) generates real time tomographic images from backscattered infrared light with a high resolution (10-15 μm axial).^{14, 27} Its resolution allows direct imaging of a thin fibrotic cap, in principle. Main disadvantages are the limited depth of penetration (approximately 1.5 mm) and the need to flush blood from the imaged artery.¹⁴ This latter issue is relieved by the advent of high-speed intracoronary imaging systems that allow full imaging of a coronary artery with only short flush.¹⁷

The relatively small penetration depth of OCT limits the reliability of differentiation of heterogeneous plaques.²⁸ Misinterpretations of calcified tissue as lipid in OCT have been reported, leading to misclassified OCT-derived TCFA.¹⁶

The cause of misclassification of a lesion may be an interpretation error by the image reader, or image artifacts inherent to the technique. As confounders are likely to be specific to a certain technique, studies using the combined strengths of multiple modalities, for instance OCT and VH-IVUS, could lead to a better classification of plaques than interpretation of the techniques' imagery separately.

The aim of this study was to compare the ability of OCT and VH-IVUS to classify plaque and to assess the performance of a combination of the two modalities to identify different plaque types. While a few *in-vivo* studies have been published,^{16, 29} in this work we present the first comparison between VH-IVUS and OCT, using histology as a benchmark.

METHODS

Study population

Between June 2007 and January 2008, 14 coronary arteries have been collected from 14 human hearts acquired during autopsy (57% men, 12 left anterior descending arteries, 2 right coronary arteries, mean age 64) at the Department of Pathology of the Erasmus MC. All patients died of non-coronary causes. Permission to use autopsy material for scientific study was obtained from the relatives. This study was approved by the local institutional review board.

Tissue preparation and data acquisition

Atherosclerotic human coronary artery segments were excised from the heart and imaged within 36 hours postmortem. During the excision all side branches were closed with sutures. The arteries were mounted between 2 sheaths in a water tank filled with physiological saline. A water column system, also containing physiological saline solution, was connected to the proximal sheath, to pressure-load the vessel. The vessels were pressurized to 100 mmHg to close up remaining leakages.

The vessels were imaged with OCT (M2-CV and ImageWire 2 catheters; Lightlab Imaging, Westford, MA) and IVUS (In-vision Gold; Eagle-Eye™ 20 MHz catheters; Volcano, Rancho Cordova, CA). Regions of interest (ROIs) were selected based on the presence of plaque and plaque size. ROIs were marked with a needle.¹² After imaging the needle was replaced by a suture.

ROIs were first imaged with the IVUS-system, followed by OCT. The vessels were pressurized to 100 mmHg for imaging. For IVUS, the vessels were kept at room temperature 20 ± 2 °C; OCT was performed at 37°C.^{30, 31}

After imaging, the artery sections were pressure fixed at 100 mmHg in formaldehyde for 24h at room temperature, and subsequently stored in formaldehyde at 4°C for further processing. Vessels were partially decalcified for 24 hours in formic acid.³² After fixation and decalcification, sutures marking the imaged cross-sections were replaced by ink dots. The tissue was embedded in paraffin and

serially sectioned for histological staining. Each imaged cross-section was stained with Hematoxylin-Eosin (H&E), Picrosirius red, Elastic van Gieson (EvG) and immunohistochemical stain CD68.

Data classification

Plaques were characterized in the images acquired with the two modalities, as well as in histology. As histological tissue slices are much thinner (5 μm) than the thickness sampled by OCT (25 μm) or IVUS (~200 μm)^{33, 34} there is an unavoidable sampling error. Imaged cross-sections that were obviously mismatched with histology, based on anatomical features, were removed from the data set before analysis.

VH-IVUS

VH-IVUS constructs tissue maps that classify plaque into four major components (fibrous – green, fibrofatty – light green, NC – red, and dense calcium – white).³⁵ Data were acquired, and B-mode images were reconstructed from the RF data by customized software (pcVH 2.2, Volcano Corporation), which allows a semiautomatic detection of the lumen and the media-adventitia borders and provides the compositional parameters. VH cross-sections were quantitatively measured and were classified as one of the categories described in table 1 by an experienced analyst that was blind for pathological and OCT findings.³⁶⁻³⁸

Table 1 Criteria for plaque characterization

Lesion type	Brief description in VH ³⁶⁻³⁸	Brief description in OCT ^{14, 36, 37, 39}
Intimal thickening	Plaque with <10% of NC and <10% of calcified tissue	Homogeneous signal-rich region
Fibro-atheroma	plaque with >10% of confluent NC	Heterogeneous signal poor regions poorly delineated
Fibrocalcific plaque	>10% of confluent DC with <10% of confluent NC	Homogeneous sharply delineated signal poor regions
Calcified FA	FA containing >10% of confluent DC	Areas of heterogeneous signal poor regions mixed with sharply defined signal poor regions
TCFA	>10% Confluent NC in contact with the lumen	FA with a cap <65 μm measured at the thinnest point
CaTCFA	TCFA containing >10% of confluent DC	Same as CaFA but the NC is covered by a cap <65 μm

NC = necrotic core, DC = dense calcium, FA = fibro-atheroma, CaFA = calcified fibro-atheroma, TCFA = thin-cap fibro-atheroma, CaTCFA = calcified TCFA.

OCT

Classification of OCT was based on characteristics as mentioned in table 1 by an experienced OCT reader.^{14, 36, 37, 39} Because of the limited depth of imaging and the

limited penetration in OCT, tissue types could not be expressed as percentages of the intima like in VH-IVUS, but had to be based on the visible part of the OCT image. In cross-sections with no visible cap, defined by a transition of signal from homogeneous signal rich to otherwise, the cross-section was classified as intimal thickening. In presence of a cap the dominant tissue type behind the cap was used to assess lesion type.

Combined OCT and VH

After independent analysis of each technique, side-by-side visual assessment of VH-IVUS and OCT cross-sections allowed us to evaluate the plaque types in a combined fashion. The criteria in Table 1 were applied for both techniques. If the classifications diverged between VH-IVUS and OCT, signal rich regions in OCT overruled VH-IVUS tissue characterization. In signal poor regions in OCT, VH-IVUS overruled OCT. This choice was made because a loss of OCT signal can occur due to artifacts, whereas artifacts are unlikely to cause a gain in image intensity.

Histology

Histological cross-sections were characterized by two observers blinded for the VH-IVUS and OCT results. Characterization was done by making a map of all the cross-sections, with color coding for different types of tissue, separating fibrotic tissue, lipid pool, necrotic core and dense calcium. In case of disagreement between the two pathologists, pathologist 1 and pathologist 2 re-evaluated the slides and reached a consensus diagnosis. Classification of cross-sections was done using the modified American Heart Association (AHA) classification.³⁷

RESULTS

OCT imaging, with positively matched histology, succeeded in 50 cross-sections of 14 vessels. Of these, 36 cross-sections of 9 vessels also had VH-IVUS data. Table 2 lists the results of the comparison between histology and OCT, VH and the combination of VH and OCT for 36 cross-sections. Table 3 lists the results of the comparison between histology and OCT for 50 cross-sections. Figure 1 shows misclassifications and directions of misclassifications. Only repetitive misclassifications are included.

Table 2 Classification and misclassification by OCT, VH-IVUS and OCT/VH-IVUS combined, using histology as a benchmark, in 36 cross-sections.

	OCT+	OCT-	VH+	VH-	OCT/VH+	OCT/VH-	Histology
IT+	19	10	25	4	26	3	29
IT-	2	5	6	1	5	2	7
FC+	1	0	0	1	0	1	1
FC-	1	34	1	34	1	34	35
FA+	1	1	0	2	0	2	2
FA-	5	29	3	31	1	33	35
CaFA+	3	1	1	3	2	2	4
CaFA-	1	31	0	32	0	32	32
TCFA+	0	0	0	0	0	0	0
TCFA-	3	33	0	36	1	35	36
CaTCFA+	0	0	0	0	0	0	0
CaTCFA-	0	36	0	36	0	36	36

IT = intimal thickening, FC = fibrocalcific, FA = fibro-atheroma, CaFA = calcified fibroatheroma, TCFA = thin-cap fibro-atheroma, CaTCFA = calcified thin-cap fibro-atheroma, OCT = optical coherence tomography, VH = VH-IVUS.

Table 3 Classification and misclassification by OCT in 50 cross-sections.

	OCT+	OCT-	Histology
IT+	21	12	33
IT-	2	15	17
FC+	2	2	4
FC-	3	43	46
FA+	3	3	6
FA-	7	37	44
CaFA+	6	1	7
CaFA-	2	41	43
TCFA+	0	0	0
TCFA-	3	47	50
CaTCFA+	0	0	0
CaTCFA-	1	49	50

IT = intimal thickening, FC = fibrocalcific, FA = fibro-atheroma, CaFA = calcified fibroatheroma, TCFA = thin-cap fibro-atheroma, CaTCFA = calcified thin-cap fibro-atheroma, OCT = optical coherence tomography.

DISCUSSION

The results in Tables 2 and 3 demonstrate that the classifications by both OCT and VH-IVUS agree with histology in most cases. Figure 2 illustrates a representative example, where both OCT and VH detect a calcified fibro-atheroma, which is in accordance with the histological classification.

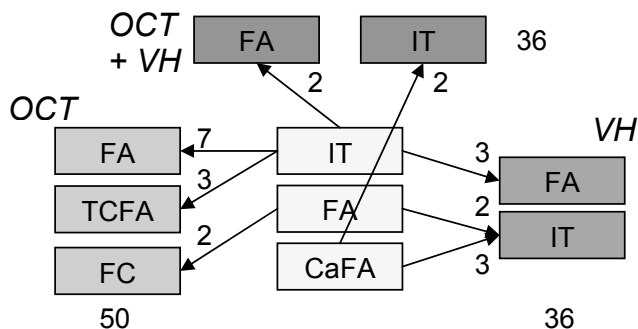


Figure 1. Chart of misclassifications. Only misclassifications occurring ≥ 2 are included in the figure. Misclassifications are derived from 36 cross-sections in VH-IVUS and OCT and VH-IVUS combined, misclassifications in OCT are derived from 50 cross-sections. Yellow = histology, green = VH-IVUS, orange = OCT, OCT/VH-IVUS = red. IT = intimal thickening, FC = fibrocalcific, FA = fibro-atheroma, CaFA = calcified fibroatheroma, TCFA = thin-cap fibro-atheroma. For example: of the lesions that were identified as IT in histology, 7 were classified as FA in OCT, 3 as FA in VH-IVUS, and 2 as FA in OCT and VH-IVUS combined.

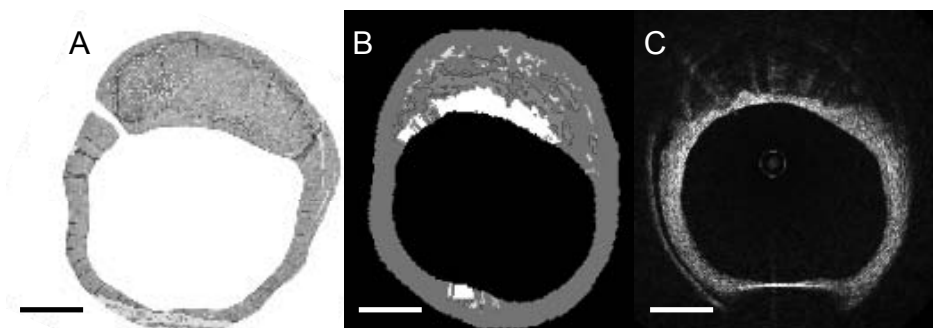


Figure 2. (A) Histology of a calcified fibroatheroma. (B) Corresponding VH-IVUS classified as calcified fibroatheroma. (C) Corresponding OCT classified as calcified fibroatheroma. The needle used to mark the site can be seen in the bright feature at 6 o'clock in OCT, as well as in the appearance of dense calcium in that location in VH-IVUS.

Manfrini et al. were the first to apply the American Heart Association criteria to lesion classification with OCT.²⁸ Classification was done in four groups using the AHA criteria of 1995.³⁶ In this study we used a modified version of the AHA criteria, including the extra categories, calcified fibro-atheroma, TCFA and calcified TCFA.³⁷ The study of Manfrini showed a sensitivity of 45% for FA, 68% for calcified lesions and 86% for fibrotic lesions. Similar results in our study were seen in the detection of FA (3/6 correctly classified). Our study used three categories for calcified plaque FC, CaFA, and CaTCFA, having the following results; 2/4, 6/7 and 0/0 classified correctly, respectively. Subclassification of calcified plaque did

not affect the results, compared to the Manfrini study. Fibrotic plaque, categorised in our study as intimal thickening, showed slightly different results compared to the Manfrini study (21/33 correctly classified).

The sample size in our study was sufficient to detect repetitive misclassifications and provide an explanation of those misclassifications based on the image data. These systematic misinterpretations of the data also suggest future possibilities how combining intravascular imaging techniques could help reduce errors in classification. The limited size of our study did not permit reliable calculation of sensitivities and specificities, however.

Recent studies in OCT showed difficulties detecting TCFA in OCT and in characterizing plaques with OCT.^{16, 28} Misclassifications were reported as a result of limited penetration depth, problems in distinguishing lipid pool from calcifications and vice versa, or heterogeneity of necrotic cores, consisting of necrotic debris and calcifications.^{14-16, 28, 29}

In our data we have encountered the same confounders. In addition, we observed the following features, compromising the classification of lesions based on OCT. Dense infiltration of macrophages in the intima or the outer layers of a fibrotic plaque led to high scattering of OCT signal, causing the underlying collagen/glycoprotein matrix to appear as a (thin-cap) FA. Figure 3 shows an example. In such sections, signal-poor regions were seen, with poorly delineated borders, which is the exact definition of lipid pool.^{14, 39} The possibility of detecting macrophages with OCT has been reported earlier, but their potential to confound lesion classification was not noted at that time.^{40, 41} In four cross-sections, scattering caused by dense macrophage infiltration led to misclassification in which two times an IT in pathology was called a FA in OCT and in two times an IT in pathology was called a TCFA in OCT.

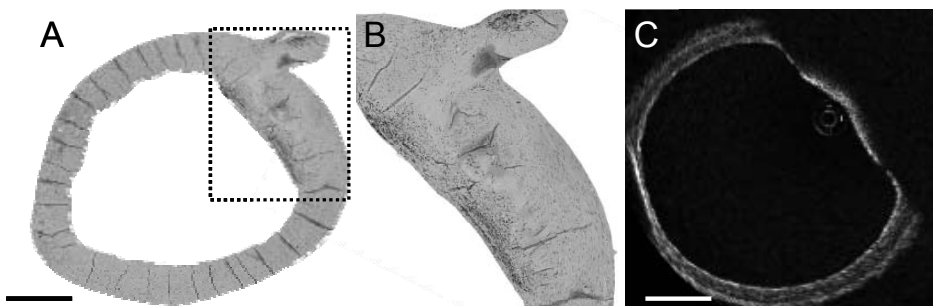


Figure 3 (A) CD68 stained cross-section. The intima consisting of a collagen/glycoprotein matrix is densely infiltrated by macrophages. (B) Magnification of selected region in A. (C) Corresponding OCT image. The region infiltrated by macrophages appears as a thin-cap fibro-atheroma. The bar indicates 1 mm.

Catheter position may also interfere with image features and definition. The published image classification schemes are based on features that are routinely observed with a catheter that is well centered in the lumen. Light from an eccentric catheter, or one that is even touching the vessel wall, may be incident on the tissue under a glancing angle. The light path through tissue to a certain radial depth in the vessel wall is longer in such an imaging geometry than in one where the imaging beam strikes the interface perpendicularly. The limited penetration depth or large attenuation occurring over a limited radial distance, leads to fibrotic areas misinterpreted as FA or TCFA. This situation is illustrated in Figure 4.

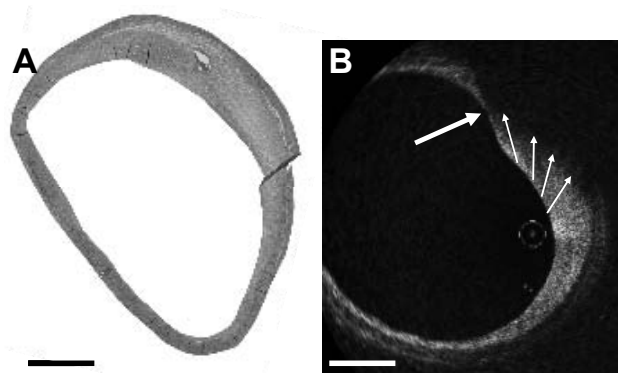


Figure 4. (A) Hematoxylin-eosin stained cross-section. (B) Intimal thickening is misinterpreted as thin-cap fibro-atheroma (TCFA) in optical coherence tomography (OCT). The large arrow points at the spot interpreted as a thin-cap. The four small arrows indicate the OCT beams and are all of the same length. The loss of signal due to tissue penetration is similar for each arrow. Because of eccentric catheter position this cross-section, classified as intimal thickening in histology, appears as a thin-cap fibro-atheroma (TCFA) in OCT. The bar indicates 1 mm.

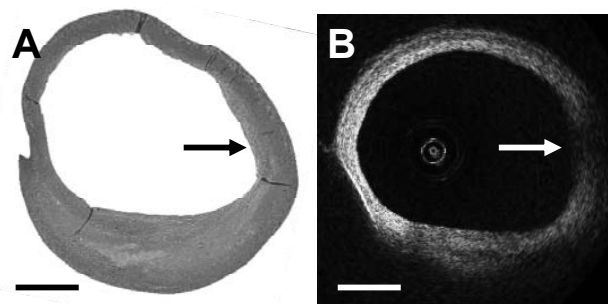


Figure 5. (A) H&E stained cross-section with (B) the corresponding optical coherence tomography (OCT). The arrow indicates a collagenous region in histology mistaken for a lipid region in OCT. Reduced optical efficiency of the catheter in this image section creates a dark sector, making mild intimal thickening appear as a fibro-atheroma. The bar indicates 1 mm.

Finally, we observed that the efficiency of the optical catheter to emit or receive the imaging light beam may vary with rotation scan angle in some catheter specimens. This leads to darker sectors in the image, and these regions can appear as signal poor regions like FAs, see Figure 5. A possible cause for this observation is optical impurities sticking to the outside of the catheter. These can be picked up on insertion of the catheter, for example. While the in vitro setting, in absence of flow, may aggravate this problem compared to clinical use, it is difficult to ascertain intra-procedurally that the image quality is constant across the rotation.

In VH-IVUS incorrect drawing of lumen and media borders may have led to misclassification in 3 cross-sections. Incorrect drawing of borders was seen in two typical situations: lumen borders at sites where the catheter was against the lumen wall, and media borders at sites where the adventitia was invisible due to acoustic shadowing. Drawing borders with knowledge of histology retrospectively corrected the misclassifications in 2 out of 3 cross-sections.

Cross-sections were imaged in a static situation, not performing a pullback. In this situation a plaque can not be seen in the context of its surrounding which complicates identification of correct borders. Also, excised specimens do not always have sufficient adventitia to help differentiate the media border from its surroundings.

Qualification of plaques in VH-IVUS is straight-forward and the lesion type could often easily be assessed by the bare eye. Plaques with confluent NC or Ca around 10% might fall in one or the other classification group, and hence may be sensitive to misclassification.

In VH-IVUS, classification is an automatic process, giving less inter-observer variability, but also giving no explanation of errors in VH-IVUS compared to histology. Misclassification that could not be explained was seen in five cross-sections. In three cross-sections it involved classification as FA while there was in histology little NC (2x) or no NC (1x) at all. In two cross-sections it involved histological FA classified as IT in VH-IVUS.

Overall, VH-IVUS classified plaque correctly 26 out of 36 cross-sections. Detection of IT (25/29 correctly identified) corresponds to the sensitivity as reported by Dietrich et al (89%).³⁸ However, detection of FA (sensitivity = 54,1% by Dietrich et al) did not correspond to our data (0/2 correctly identified).³⁸ Our sample size is too small to draw definitive conclusions out of these numbers however our results are in line with previous findings of Granada who reported lower sensitivities and specificities.^{12, 35, 42, 43} Misclassification in VH-IVUS alone typically also led to misclassification in OCT and VH-IVUS combined. VH-IVUS could positively influence OCT in cases where OCT misclassified plaques as FA, that were IT according to histology. The artifacts mentioned above led to a high

false-positive number of FAs in OCT. FA or TCFA in OCT, which was classified as IT in VH-IVUS, meant in 6 out of 7 times it was indeed an IT in histology. In three out of six it involved plaques classified as TCFAs by OCT.

A recent study describes the low incidence of histology-derived TCFA and FA (1.5% and 10.5% of advanced lesions, respectively).⁴⁴ Our data show a relatively high false-positive rate for TCFA or FA: IT in histology was classified in OCT as TCFA or FA in 10 cross-sections.³⁷ Given the incidence of FA and especially of TCFA, the positive predictive value of OCT, an important parameter in rare incidence, could be small for these clinically significant plaque types. Since the group of non-TCFAs appears to be 98.5% in advanced lesions, the finding of a TCFA in OCT must be regarded with caution, and corroborated with other evidence if possible. An *in vivo* study by Sawada et al. combined VH-IVUS and OCT for detection of TCFA. Only lesions classified as TCFA both in OCT and in VH-IVUS were considered real TCFAs.¹⁶ This definition is indeed a sensible one, as the resolution of VH-IVUS is insufficient per se to identify thin caps, and OCT is seen to suffer from many false positives.

In conclusion, adding VH-IVUS to OCT could help reduce misclassification by OCT of FAs and TCFAs. *In vitro* studies with larger sample sizes are needed to assess the full potential of the added value of OCT and VH-IVUS combined. Criteria for classifying VH-IVUS combined with OCT have not been optimally validated and could possibly be improved using larger datasets.

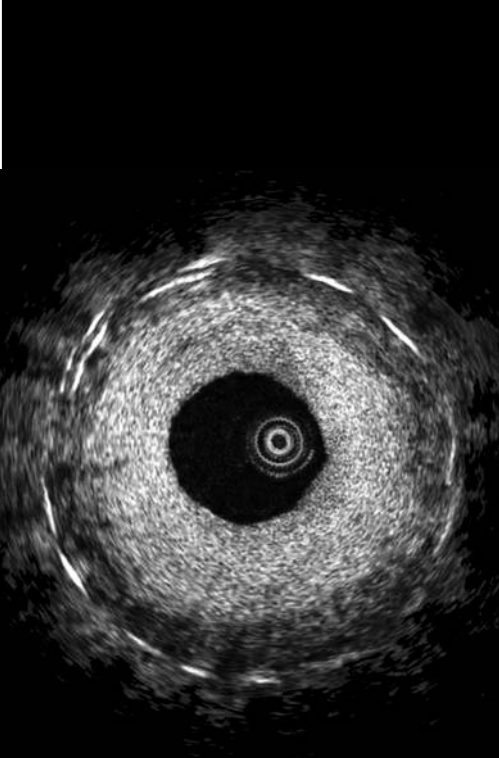
REFERENCES

1. F. D. Kolodgie, R. Virmani, A. P. Burke, A. Farb, D. K. Weber, R. Kutys, A. V. Finn, and H. K. Gold, *Pathologic assessment of the vulnerable human coronary plaque*. Heart, 2004. **90**(12): p. 1385-1391.
2. J. A. Schaar, J. E. Muller, E. Falk, R. Virmani, V. Fuster, P. W. Serruys, A. Colombo, C. Stefanadis, S. Ward Casscells, P. R. Moreno, A. Maseri, and A. F. van der Steen, *Terminology for high-risk and vulnerable coronary artery plaques. Report of a meeting on the vulnerable plaque, June 17 and 18, 2003, Santorini, Greece*. Eur Heart J, 2004. **25**(12): p. 1077-82.
3. J. F. Granada, G. L. Kaluza, A. E. Raizner, and P. R. Moreno, *Vulnerable plaque paradigm: Prediction of future clinical events based on a morphological definition*. Catheterization And Cardiovascular Interventions, 2004. **62**(3): p. 364-374.
4. J. E. Muller, G. S. Abela, R. W. Nesto, and G. H. Tofler, *Triggers, acute risk factors and vulnerable plaques: the lexicon of a new frontier*. J Am Coll Cardiol, 1994. **23**(3): p. 809-13.
5. M. J. Davies and A. C. Thomas, *Plaque Fissuring - the Cause of Acute Myocardial-Infarction, Sudden Ischemic Death, and Crescendo Angina*. British Heart Journal, 1985. **53**(4): p. 363-373.
6. J. A. Schaar, C. L. de Korte, F. Mastik, C. Strijder, G. Pasterkamp, E. Boersma, P. W. Serruys, and A. F. W. van der Steen, *Characterizing vulnerable plaque features with intravascular elastography*. Circulation, 2003. **108**(21): p. 2636-2641.
7. R. Virmani, A. P. Burke, A. Farb, and F. D. Kolodgie, *Pathology of the vulnerable plaque*. Journal of the American College Of Cardiology, 2006. **47**(8): p. C13-C18.
8. E. Falk, P. K. Shah, and V. Fuster, *Coronary plaque disruption*. Circulation, 1995. **92**(3): p. 657-71.
9. P. D. Richardson, M. J. Davies, and G. V. Born, *Influence of plaque configuration and stress distribution on fissuring of coronary atherosclerotic plaques*. Lancet, 1989. **2**(8669): p. 941-4.
10. S. Waxman, F. Ishibashi, and J. E. Muller, *Detection and treatment of vulnerable plaques and vulnerable patients - Novel approaches to prevention of coronary events*. Circulation, 2006. **114**(22): p. 2390-2411.
11. R. A. Baldewsing, M. G. Danilouchkine, F. Mastik, J. A. Schaar, P. W. Serruys, and A. F. W. van der Steen, *An Inverse Method for Imaging the Local Elasticity of Atherosclerotic Coronary Plaques*. Information Technology in Biomedicine, IEEE Transactions on, 2008. **12**(3): p. 277-289.
12. A. Nair, B. D. Kuban, E. M. Tuzcu, P. Schoenhagen, S. E. Nissen, and D. G. Vince, *Coronary plaque classification with intravascular ultrasound radiofrequency data analysis*. Circulation, 2002. **106**(17): p. 2200-2206.
13. M. Naghavi, P. Libby, E. Falk, S. W. Casscells, S. Litovsky, J. Rumberger, J. J. Badimon, C. Stefanadis, P. Moreno, G. Pasterkamp, Z. Fayad, P. H. Stone, S. Waxman, P. Raggi, M. Madjid, A. Zarrabi, A. Burke, C. Yuan, P. J. Fitzgerald, D. S. Siscovick, C. L. de Korte, M. Aikawa, K. E. J. Airaksinen, G. Assmann, C. R. Becker, J. H. Chesebro, A. Farb, Z. S. Galis, C. Jackson, I. K. Jang, W. Koenig, R. A. Lodder, K. March, J. Demirovic, M. Navab, S. G. Priori, M. D. Rekhter, R. Bahr, S. M. Grundy, R. Mehran, A. Colombo, E. Boerwinkle, C. Ballantyne, W. Insull, R. S.

- Schwartz, R. Vogel, P. W. Serruys, G. K. Hansson, D. P. Faxon, S. Kaul, H. Drexler, P. Greenland, J. E. Muller, R. Virmani, P. M. Ridker, D. P. Zipes, P. K. Shah, and J. T. Willerson, *From vulnerable plaque to vulnerable patient - A call for new definitions and risk assessment strategies: Part I*. *Circulation*, 2003. **108**(14): p. 1664-1672.
14. I. K. Jang, B. E. Bouma, D. H. Kang, S. J. Park, S. W. Park, K. B. Seung, K. B. Choi, M. Shishkov, K. Schlendorf, E. Pomerantsev, S. L. Houser, H. T. Aretz, and G. J. Tearney, *Visualization of coronary atherosclerotic plaques in patients using optical coherence tomography: Comparison with intravascular ultrasound*. *Journal Of The American College Of Cardiology*, 2002. **39**(4): p. 604-609.
 15. M. Kawasaki, B. E. Bouma, J. Bressner, S. L. Houser, S. K. Nadkarni, B. D. MacNeill, I. K. Jang, H. Fujiwara, and G. J. Tearney, *Diagnostic accuracy of optical coherence tomography and integrated backscatter intravascular ultrasound images for tissue characterization of human coronary plaques*. *Journal Of The American College Of Cardiology*, 2006. **48**(1): p. 81-88.
 16. T. Sawada, J. Shite, H. M. Garcia-Garcia, T. Shinke, S. Watanabe, H. Otake, D. Matsumoto, Y. Tanino, D. Ogasawara, H. Kawamori, H. Kato, N. Miyoshi, M. Yokoyama, P. W. Serruys, and K. Hirata, *Feasibility of combined use of intravascular ultrasound radiofrequency data analysis and optical coherence tomography for detecting thin-cap fibroatheroma*. *Eur Heart J*, 2008. **29**(9): p. 1136-46.
 17. S. H. Yun, G. J. Tearney, B. J. Vakoc, M. Shishkov, W. Y. Oh, A. E. Desjardins, M. J. Suter, R. C. Chan, J. A. Evans, I. K. Jang, N. S. Nishioka, J. F. de Boer, and B. E. Bouma, *Comprehensive volumetric optical microscopy in vivo*. *Nat Med*, 2006. **12**(12): p. 1429-33.
 18. S. E. Nissen and P. Yock, *Intravascular ultrasound: novel pathophysiological insights and current clinical applications*. *Circulation*, 2001. **103**(4): p. 604-16.
 19. T. Kubo, T. Imanishi, S. Takarada, A. Kuroi, S. Ueno, T. Yamano, T. Tanimoto, Y. Matsuo, T. Masho, H. Kitabata, K. Tsuda, Y. Tomobuchi, and T. Akasaka, *Assessment of culprit lesion morphology in acute myocardial infarction - Ability of optical coherence tomography compared with intravascular ultrasound and coronary angiography*. *Journal Of The American College Of Cardiology*, 2007. **50**(10): p. 933-939.
 20. P. W. Serruys, H. M. Garcia-Garcia, and E. Regar, *From Postmortem Characterization to the In Vivo Detection of Thin-Capped Fibroatheromas: The Missing Link Toward Percutaneous Treatment: What If Diogenes Would Have Found What He Was Looking For?* *Journal of the American College of Cardiology*, 2007. **50**(10): p. 950-952.
 21. M. P. Moore, T. Spencer, D. M. Salter, P. P. Kearney, T. R. Shaw, I. R. Starkey, P. J. Fitzgerald, R. Erbel, A. Lange, N. W. McDicken, G. R. Sutherland, and K. A. Fox, *Characterisation of coronary atherosclerotic morphology by spectral analysis of radiofrequency signal: in vitro intravascular ultrasound study with histological and radiological validation*. *Heart*, 1998. **79**(5): p. 459-67.
 22. N. Komiyama, G. J. Berry, M. L. Kolz, A. Oshima, J. A. Metz, P. Preuss, A. F. Brisken, M. P. Moore, P. G. Yock, and P. J. Fitzgerald, *Tissue characterization of atherosclerotic plaques by intravascular ultrasound radiofrequency signal analysis: an in vitro study of human coronary arteries*. *Am Heart J*, 2000. **140**(4): p. 565-74.
 23. A. Murashige, T. Hiro, T. Fujii, K. Imoto, T. Murata, Y. Fukumoto, and M. Matsuzaki, *Detection of lipid-laden atherosclerotic plaque by wavelet analysis of radiofrequency*

- intravascular ultrasound signals: in vitro validation and preliminary in vivo application.* J Am Coll Cardiol, 2005. **45**(12): p. 1954-60.
24. A. Nair, D. Calvetti, and D. G. Vince, *Regularized autoregressive analysis of intravascular ultrasound backscatter: improvement in spatial accuracy of tissue maps.* IEEE Trans Ultrason Ferroelectr Freq Control, 2004. **51**(4): p. 420-31.
 25. G. A. Rodriguez-Granillo, H. M. Garcia-Garcia, E. P. Mc Fadden, M. Valgimigli, J. Aoki, P. de Feyter, and P. W. Serruys, *In vivo intravascular ultrasound-derived thin-cap fibroatheroma detection using ultrasound radiofrequency data analysis.* Journal Of The American College Of Cardiology, 2005. **46**(11): p. 2038-2042.
 26. H. M. Garcia-Garcia, D. Goedhart, J. C. H. Schuurbiers, N. Kukreja, S. Tanimoto, J. Daemen, M. A. M. Morel, M. Bressers, G. A. van Es, J. J. Wentzel, F. Gijzen, A. F. W. van der Steen, and P. W. Serruys, *Virtual histology and remodelling index allow in vivo identification of allegedly high-risk coronary plaques in patients with acute coronary syndromes: a three vessel intravascular ultrasound radiofrequency data analysis.* EuroIntervention, 2006. **2**(3): p. 338-344.
 27. D. Huang, E. A. Swanson, C. P. Lin, J. S. Schuman, W. G. Stinson, W. Chang, M. R. Hee, T. Flotte, K. Gregory, C. A. Puliafito, and et al., *Optical coherence tomography.* Science, 1991. **254**(5035): p. 1178-81.
 28. O. Manfrini, E. Mont, O. Leone, E. Arbustini, V. Eusebi, R. Virmani, and R. Bugiardini, *Sources of Error and Interpretation of Plaque Morphology by Optical Coherence Tomography.* The American Journal of Cardiology, 2006. **98**(2): p. 156.
 29. N. Gonzalo, P. W. Serruys, P. Barlis, J. Ligthart, H. M. Garcia-Garcia, and E. Regar, *Multi-modality intra-coronary plaque characterization: A pilot study.* Int J Cardiol, 2008.
 30. J. A. Schaar, C. L. de Korte, F. Mastik, and A. F. van der Steen, *Effect of temperature increase and freezing on intravascular elastography.* Ultrasonics, 2002. **40**(1-8): p. 879-81.
 31. F. J. van der Meer, D. J. Faber, I. Cilesiz, M. J. van Gemert, and T. G. van Leeuwen, *Temperature-dependent optical properties of individual vascular wall components measured by optical coherence tomography.* J Biomed Opt, 2006. **11**(4): p. 041120.
 32. G. J. Friedrich, N. Y. Moes, V. A. Muhlberger, C. Gabl, G. Mikuz, D. Hausmann, P. J. Fitzgerald, and P. G. Yock, *Detection of intralumenal calcium by intracoronary ultrasound depends on the histologic pattern.* Am Heart J, 1994. **128**(3): p. 435-41.
 33. N. Bruining, S. Verheye, M. Knaapen, P. Somers, J. Roelandt, E. Regar, I. Heller, S. de Winter, J. Ligthart, G. Van Langenhove, P. J. de Feijter, P. W. Serruys, and R. Hamers, *Three-dimensional and quantitative analysis of atherosclerotic plaque composition by automated differential echogenicity.* Catheterization and Cardiovascular Interventions, 2007. **70**(7): p. 968-978.
 34. J. Rieber, O. Meissner, G. Babaryka, S. Reim, M. Oswald, A. Koenig, T. M. Schiele, M. Shapiro, K. Theisen, M. F. Reiser, V. Klauss, and U. Hoffmann, *Diagnostic accuracy of optical coherence tomography and intravascular ultrasound for the detection and characterization of atherosclerotic plaque composition in ex-vivo coronary specimens: a comparison with histology.* Coronary Artery Disease, 2006. **17**(5): p. 425-430.
 35. A. Nair, M. P. Margolis, B. D. Kuban, and D. G. Vince, *Automated coronary plaque characterization with intravascular ultrasound backscatter: ex vivo validation.* EuroIntervention, 2007. **3**(9): p. 113-120.

36. H. C. Stary, A. B. Chandler, R. E. Dinsmore, V. Fuster, S. Glagov, W. Insull, Jr., M. E. Rosenfeld, C. J. Schwartz, W. D. Wagner, and R. W. Wissler, *A definition of advanced types of atherosclerotic lesions and a histological classification of atherosclerosis. A report from the Committee on Vascular Lesions of the Council on Arteriosclerosis, American Heart Association*. *Circulation*, 1995. **92**(5): p. 1355-74.
37. R. Virmani, F. D. Kolodgie, A. P. Burke, A. Farb, and S. M. Schwartz, *Lessons from sudden coronary death - A comprehensive morphological classification scheme for atherosclerotic lesions*. *Arteriosclerosis Thrombosis And Vascular Biology*, 2000. **20**(5): p. 1262-1275.
38. E. B. Diethrich, M. P. Margolis, D. B. Reid, A. Burke, V. Ramaiah, J. A. Rodriguez-Lopez, G. Wheatley, D. Olsen, and R. Virmani, *Virtual histology intravascular ultrasound assessment of carotid artery disease: the Carotid Artery Plaque Virtual Histology Evaluation (CAPITAL) study*. *J Endovasc Ther*, 2007. **14**(5): p. 676-86.
39. H. Yabushita, B. E. Bouma, S. L. Houser, T. Aretz, I. K. Jang, K. H. Schlendorf, C. R. Kauffman, M. Shishkov, D. H. Kang, E. F. Halpern, and G. J. Tearney, *Characterization of human atherosclerosis by optical coherence tomography*. *Circulation*, 2002. **106**(13): p. 1640-1645.
40. G. J. Tearney, H. Yabushita, S. L. Houser, H. T. Aretz, I. K. Jang, K. H. Schlendorf, C. R. Kauffman, M. Shishkov, E. F. Halpern, and B. E. Bouma, *Quantification of macrophage content in atherosclerotic plaques by optical coherence tomography*. *Circulation*, 2003. **107**(1): p. 113-119.
41. B. D. MacNeill, I. K. Jang, B. E. Bouma, N. Iftimia, M. Takano, H. Yabushita, M. Shishkov, C. R. Kauffman, S. L. Houser, H. T. Aretz, D. DeJoseph, E. F. Halpern, and G. J. Tearney, *Focal and multi-focal plaque macrophage distributions in patients with acute and stable presentations of coronary artery disease*. *J Am Coll Cardiol*, 2004. **44**(5): p. 972-9.
42. K. Nasu, E. Tsuchikane, O. Katoh, D. G. Vince, R. Virmani, J. F. Surmely, A. Murata, Y. Takeda, T. Ito, M. Ehara, T. Matsubara, M. Terashima, and T. Suzuki, *Accuracy of in vivo coronary plaque morphology assessment: a validation study of in vivo virtual histology compared with in vitro histopathology*. *J Am Coll Cardiol*, 2006. **47**(12): p. 2405-12.
43. J. F. Granada, D. Wallace-Bradley, H. K. Win, C. L. Alviar, A. Builes, E. I. Lev, R. Barrios, D. G. Schulz, A. E. Raizner, and G. L. Kaluza, *In vivo plaque characterization using intravascular ultrasound-virtual histology in a porcine model of complex coronary lesions*. *Arterioscler Thromb Vasc Biol*, 2007. **27**(2): p. 387-93.
44. P. K. Cheruvu, A. V. Finn, C. Gardner, J. Caplan, J. Goldstein, G. W. Stone, R. Virmani, and J. E. Muller, *Frequency and distribution of thin-cap fibroatheroma and ruptured plaques in human coronary arteries: A Pathologic study*. *Journal Of The American College Of Cardiology*, 2007. **50**(10): p. 940-949.



4.2

Atherosclerotic tissue characterization in vivo by Optical Coherence Tomography attenuation imaging.

van Soest G, Goderie T, Regar E, Koljenovic S,
van Lenders GLJH, Gonzalo N, van Noorden S,
Okamura T, Bouma BE, Tearney GJ, Oosterhuis W,
Serruys PW, van der Steen AFW

J Biomed Opt. In press

Quantitative Optical Coherence Tomography for In-Situ Atherosclerotic Plaque Characterization

Gijs van Soest,^{1,*} Thadé Goderie,¹ Evelyn Regar,¹ Senada Koljenovic,²
G. L. J. H. van Leenders,² Nieves Gonzalo,¹ Sander van Noorden,¹
Takayuki Okamura,¹ Brett E. Bouma,^{3,4,5} Guillermo J. Tearney,^{3,5,6} J.
Wolter Oosterhuis,² Patrick W. Serruys,¹ and Anton F. W. van der Steen^{1,7}

¹*Thorax Center, Erasmus MC, Rotterdam, The Netherlands*

²*Josephine Nefkens Institute, Erasmus MC, Rotterdam, The Netherlands*

³*Wellman Center for Photomedicine, Massachusetts General Hospital, Boston, MA*

⁴*Department of Dermatology, Harvard Medical School, Boston, MA*

⁵*Harvard-MIT Division of Health Sciences and Technology, Cambridge, MA*

⁶*Department of Pathology, Harvard Medical School, Boston, MA*

⁷*Interuniversity Cardiology Institute of the Netherlands, Utrecht, The Netherlands*

(Dated: April 9, 2009)

Abstract

Optical Coherence Tomography (OCT) is rapidly becoming the method of choice for assessing arterial wall pathology in vivo. Atherosclerotic plaques can be diagnosed with high accuracy, including measurement of the thickness of fibrous caps, permitting an assessment of the risk of rupture. While the OCT image presents morphological information in highly resolved detail, it relies on interpretation of the images by trained readers for the identification of vessel wall components and tissue type. We present a framework to enable systematic and automatic classification of atherosclerotic plaque constituents, based on the optical attenuation coefficient μ_t of the tissue. OCT images of 65 coronary artery segments in vitro, obtained from 14 vessels harvested at autopsy, were analyzed and correlated with histology. Vessel wall components can be distinguished based on their optical properties: necrotic core and macrophage infiltration exhibit strong attenuation, $\mu_t \geq 10 \text{ mm}^{-1}$, while calcific and fibrous tissue have a lower $\mu_t \approx 2\text{--}5 \text{ mm}^{-1}$. The algorithm is successfully applied to OCT patient data, demonstrating that the analysis can be used in a clinical setting and assist diagnostics of vessel wall pathology.

*Corresponding author; email: g.vansoest@erasmusmc.nl

I. INTRODUCTION

It is generally accepted that the majority of acute coronary events is precipitated by the rupture of a vulnerable atherosclerotic plaque in the coronary system, and subsequent thrombogenesis [1–3]. The thin-cap fibroatheroma is currently hypothesized to be the most likely class of arterial wall pathology to constitute a vulnerable plaque [4, 5]. The key to plaque vulnerability is still elusive [6], even though recent technological advances in intravascular imaging technology have enabled the collection a wealth of data on unstable atherosclerosis in all its stages of development [7], both in clinical and in *ex vivo* settings. It appears very likely that combined information on physiological, anatomical, chemical, and mechanical parameters [8–10] is needed for a reliable assessment of the proneness of a specific lesion to rupture. Some of these parameters may be accessible through intravascular imaging methods [11–19]. In addition, plaque type and morphology prior to intervention influence the long-term procedure outcome significantly [20]. Among the parameters that influence plaque vulnerability are, the thickness of the fibrous cap overlying the necrotic core, inflammation, intraplaque haemorrhage, and composition [9, 21]. Data on plaque composition and stability, complementing the image, may inform the decision, if and how to treat a particular section of coronary artery.

The advent of optical coherence tomography (OCT) for cardiovascular applications has boosted the resolving power of intravascular imaging to a level where imaging the thin cap of a vulnerable plaque is possible [22]. Insight into the physiology of a plaque is complementary to the structural information offered by the OCT grayscale image.

In intravascular ultrasound (IVUS) imaging, parametric imaging techniques have been developed that quantify properties of the underlying tissue in the image. Examples of this approach are IVUS elastography, characterizing local elasticity [11, 12, 23, 24], and spectral analysis methods for tissue identification [25–27]. In intravascular OCT, published research into parametric imaging methods has been very limited to date. One obvious cause for this is the high quality of OCT data, making visual interpretation easier than in IVUS.

Recent publications have highlighted the possibility of tissue identification in OCT imagery. Yabushita *et al.* [28] published a qualitative image classification scheme, which has become the *de facto* standard, distinguishing fibrous, calcified and lipid-rich tissues. A comparison with later work by Kume *et al.* [29] reveals, however, that the interpretation of OCT images based on qualitative criteria can be ambiguous in some cases. In this study, we attempt to resolve some of

the ambiguity associated with qualitative OCT tissue classification, by developing a parametric imaging technique that images the optical extinction coefficient (sum of scattering and absorption: $\mu_t = \mu_s + \mu_a$) in atherosclerotic plaques *in situ*.

A few studies were published over the past years [30–32] that targeted the optical attenuation coefficient for arterial tissue identification with OCT. All these studies used benchtop, scanning-stage-based OCT setups, and hence required longitudinal dissection of the arteries. We used an intracoronary, catheter-based OCT system, allowing us to image the optical attenuation *in situ* and even *in vivo*. Xu *et al.* [33] published a study in which both the backscatter coefficient μ_b and the extinction coefficient μ_t were measured on intact human coronaries *ex vivo*, using a microscope type OCT setup. The latter study can be interpreted as a quantitative basis for the qualitative scheme of Yabushita *et al.* [28].

The expectation value of the detected OCT signal intensity $\langle I_d(r) \rangle$ can be modeled using a single scattering model, that incorporates the axial point spread function due to the coupling of the emitted and backscattered intensity to the Gaussian mode profile of a single mode fiber (SMF) [34].

$$\langle I_d(r) \rangle = I_0 T(r) \exp(-\mu_t r); \quad T(r) = \left[\left(\frac{r - z_0}{z_R} \right)^2 + 1 \right]^{-\frac{1}{2}} \quad (1)$$

In this equation, the intensity is modeled by a Lambert-Beer exponential decay curve, multiplied by the coupling factor. The expectation value operator $\langle \cdot \rangle$ denotes the ensemble average over many realizations of the speckle generated by the beam in the tissue. $T(r)$ is the longitudinal point spread function (PSF) for an SMF-based OCT system, governed by the position of the beam waist z_0 and the Rayleigh length z_R . We are interested in the attenuation coefficient μ_t , appearing in the exponent of this relation. The scale factor I_0 is the locally available intensity multiplied by the backscattering coefficient μ_b , $I_0 = \mu_b(r)I'(r)$. The backscatter efficiency is a tissue property that can be measured independently in homogeneous media [33]. This local intensity is equal to the source intensity incident upon the vessel wall, I_{in} , diminished by the attenuation along the path from the lumen border to the imaged depth, $I'(r) = I_{in} \int_0^r \exp(-\mu_t r') dr'$. As the OCT image traces provide only one intensity measurement of for every depth, it is not possible, in practice, to extract two depth-dependent parameters, $\mu_b(r)$ and $\mu_t(r)$, from the analysis.

Equation (1) describes the OCT signal in a homogeneous medium. The vessel wall, and biological tissue in general, are heterogeneous structures. An OCT A-line $I_d(r)$ usually samples more than one tissue type. Hence, the signal intensity has to be fitted in windows, of a length that is

unknown a priori [31]. Here, variations in $\mu_b(r)$ may confound the analysis of $\mu_t(r)$. In addition, the presence of speckle means that the contrast-to-noise ratio (CNR) in the image is inherently low [35, 36], and several frames will have to be averaged in order to reduce speckle. Averaging is complicated by artifacts due to cardiac motion, and by non-uniform catheter rotation, which can usually be corrected [37, 38].

In this paper, we present a method for intracoronary imaging of the optical extinction coefficient μ_t . The principle is demonstrated in human coronary arteries *ex vivo*. The optical attenuation maps are compared with histopathology, in order to identify the correspondence between tissue type and extinction coefficient. After validation, we recorded suitable intracoronary OCT movies in patients and applied the algorithm to the data. Analysis was successful and the resulting optical attenuation maps both corroborated and complemented the qualitative interpretations of plaque type.

II. MATERIALS AND METHODS

A. Specimens

We examined 14 human coronary arteries, acquired during autopsy at the Department of Pathology of the Erasmus MC, from 14 human hearts (57% men, 12 left anterior descending arteries, 2 right coronary arteries, mean age 64). Inclusion criteria were age > 40 years and non-cardiac death. Permission to use autopsy material for scientific study was obtained from the relatives; this study was approved by the Ethics Committee of the Erasmus MC.

The length of the artery segments varied between 5 and 9 cm. In these vessels, 65 sites were identified (up to 5 per segment) for imaging and further histologic processing. All vessels except one were observed to be atherosclerotic based on gross pathology. During excision of the arteries, side branches were closed with sutures. OCT imaging was performed within 24h post mortem.

B. Imaging protocol *in vitro*

OCT imaging was performed with a M2CV time-domain OCT system, and ImageWire 200 catheters (Lightlab Imaging Inc., Westford, MA). A vessel cross-section is imaged by an infrared light beam, central wavelength 1310 nm, that is swept along the vessel wall by the rotating fiber inside the catheter sheath. The OCT system had an axial resolution of 14 μm , and a tangential resolution of 25 μm in the focus. The imaging depth was 3.3 mm. Each frame consisted of

312 lines \times 752 pixels, corresponding to 4.5 μm per pixel. Imaging was performed at a rate of 10 frames per second (fps).

The artery under investigation was excised from the heart and placed in a water bath filled with saline solution at 37°C [32]. Both ends were mounted on plastic sheaths, and the vessel was pressurized to 100 mmHg using a water column system filled with saline. The vessel was inspected longitudinally by moving the imaging catheter along the lumen. During imaging, these sites were marked with a needle, visible in the OCT images. After removal from the water tank, the needle was replaced by a color coded suture. At sites of interest, a stationary movie of 40–50 frames was recorded and stored in polar coordinates in stacked TIFF format.

C. Histopathology

After imaging, the artery sections were pressure fixed at 100 mmHg in formaldehyde for 24h at room temperature, and subsequently stored in formaldehyde at 4°C for further processing. Vessels were partially decalcified for 24 hours in formic acid [39]. After fixation and decalcification, sutures marking the imaged cross-sections were replaced by ink dots. The tissue was embedded in paraffin and serially sectioned for histological staining. Each imaged cross-section was stained with Hematoxylin-Eosin (H&E), Picrosirius red, Elastic van Gieson (EvG) and immunohistochemical stain CD68.

Histological cross-sections were characterized by two observers blinded for the OCT results. Characterization was done by making a map of all the cross-sections, called cartoon histology, with color coding for different types of tissue. We distinguished fibrous tissue and smooth muscle cells (SMC), lipid pool, necrotic core in early or advanced stage, haemorrhage, and dense calcium. In case of disagreement, the two pathologists re-evaluated the slides and reached a consensus diagnosis. A summary of the used color coding is displayed in Table I.

D. Imaging protocol *in vivo*

Quantitative analysis of intracoronary OCT imagery is complicated by motion and other artifacts, resulting from catheter eccentricity or blood remnants in the lumen. The influence of cardiac motion can be mitigated by increasing the imaging speed. The diastolic filling phase, where coronary motion is minimal, lasts about 0.2 s, measured from the end of the T-wave in the ECG to the

beginning of atrial systole, marked by the start of the P-wave. At a frame rate of 100 fps, each heart cycle will have 15–20 frames in which the effects of cardiac motion are limited, and allow averaging of those frames.

In vivo imaging was performed in the catheterization laboratory of the Thorax Center of the Erasmus MC (Rotterdam, The Netherlands) using an optical frequency domain imaging (OFDI) system [40, 41], built at the Wellman Center for Photomedicine (Boston, MA). This swept-source system has a center wavelength of 1310 nm and an axial resolution of 10 μm . It images the coronary at a frame rate of 105 fps, using 512 lines per frame. The ranging depth in tissue is about 4.7 mm.

Patients undergoing percutaneous coronary intervention (PCI) were enrolled in this study, having given informed consent. In the OFDI pullback and X-ray angiography, lesions of interest are identified for optical extinction imaging. The catheter imaging tip is then positioned at such a site, and a stationary (i.e. no pullback) movie is recorded. The blood is cleared from the artery by flushing with 100% Iodixanol 370 (VisipaqueTM, GE Healthcare, Cork, Ireland) at 37°C using an injection pump (Mark-V Pro Vis, Medrad Inc., Indianola, PA). Recording was started as soon as clearing was achieved, and stopped after about 5 heart cycles; flushing was also stopped at this time. ECG is recorded synchronously with the OCT acquisition at a sampling rate equal to the A-line frequency (54 kHz). In the acquired data, we select the frames corresponding to the cardiac phase between the T- and P-waves for further analysis. The imaged plaques are classified [28] by two experienced OCT readers for comparison with the assessment based on optical attenuation.

E. Catheter characterization

Individual catheters of the type used in this study may have non-identical focal length z_0 and Rayleigh length z_R . It is necessary to characterize the catheters before attempting to analyze the received OCT signal. Catheter beam parameters were determined by recording the OCT signal in a series of Intralipid (Fresenius Kabi, 's-Hertogenbosch, The Netherlands) dilutions (base solution 20% w/w; diluted 1:4 to 1:128) in water. Every recording consisted of about 15000 A-lines. These are averaged to reduce speckle. An r -dependent (catheter-independent) intensity offset I_{offset} was determined by recording and averaging the OCT signal in water, with negligible attenuation and backscattering. This offset was subtracted from the averaged OCT traces.

To reduce the dynamic range of the fitted signal and reduce sensitivity to noise, we linearized

Eq. (1) by logarithmic compression:

$$\log [I_d(r) - I_{\text{offset}}(r)] + \log [T(r; z_0, z_R)] = \log (I_0) - \mu_t r. \quad (2)$$

The second term in Eq. (2), representing the catheter-specific PSF, is calculated using several combinations of z_0 and z_R , and added to the offset-corrected intensity profile. The range of values included in the fit is limited to the area where noise and catheter artefacts are negligible. The root mean square (rms) difference between measured data and the fitted line, is calculated for a matrix of (z_0, z_R) combinations, with $0.7 \leq z_0 \leq 1.7$ mm, and $0.2 \leq z_R \leq 1.2$ mm, both with 0.01 mm increments. All catheters yielded a unique, paraboloid minimum. The values of z_0 and z_R at the minimum of the cost function represent the best estimate of the beam parameters.

F. Data analysis

All data analysis was performed in MATLAB R2007b (The Mathworks, Natick, MA). Frames from the OCT movies were aligned using our nonlinear rotation correction algorithm [37, 38], and then averaged for speckle reduction. This mean OCT image is used as the basis for analysis of the optical attenuation coefficients. If there is evidence of remaining motion artifacts (e.g. blurring in the averaged frame) in the corrected sequence, the data is discarded.

The intensity traces are linearized in the manner of Eq. (2), using the beam parameters specific for the catheter that was used for imaging the vessel. Starting at the lumen boundary, the log-compressed data is least-squares fitted with a linear model

$$\tilde{I}(r) = \log (I_0) - \mu_t r, \quad (3)$$

in a window of variable length L . With a linear optimization, there is a unique optimum for each set of data, and results are independent of the initial guess needed for an iterative nonlinear model. Speed is another advantage.

A schematic representing the data flow in the fitting procedure is shown in Fig. 1. Using an adaptive threshold criterion, the lumen boundary is determined in the mean image. A linear least-squares fit is performed in a window of minimum length $L_{\text{min}} = 200 \mu\text{m}$, corresponding to $w = 44$ pixels. Results with $\mu_t < 0$ are discarded. The cost function is defined as the root of mean square (rms) difference between the averaged measured OCT trace $\langle I_d \rangle$ and the model \tilde{I} , divided by the window length: $\delta = \sqrt{[\langle I_d \rangle - \tilde{I}]^2} / L$. This normalization biases the cost function to larger windows and so reduces the sensitivity to changes in intensity that occur at inhomogeneities.

Now the window is iteratively extended with $s = 0.1w$ pixels at a time until a decrease in fit quality is detected. The optimum values (for smallest δ) are stored. This method automatically searches for the longest homogeneous region to fit: the window is extended until an inhomogeneity is encountered that degrades the result. Once the window has been extended to its maximum length the window is moved forward. This procedure is repeated until the window reaches the end of the A-line. All parameters in the fitting procedure have been optimized in a simulation study [42].

This fitting procedure results in an estimate for $\mu_t(r)$ for every A-line. The extinction coefficients are color coded and plotted in the regular grayscale OCT image as an overlay or side-by-side. The *in vitro* data are then compared with the tissue type maps based on histology to identify a correspondence between tissue type and μ_t . As histological tissue slices are much thinner ($5\ \mu\text{m}$) than the accuracy of the needle marker ($\approx 0.5\text{mm}$) there is an unavoidable sampling error [43–45]. Imaged cross-sections that were obviously mismatched with histology, based on anatomical features, were removed from the data set before analysis.

III. RESULTS

A. *In vitro* imaging

We analyzed OCT data of 39 lesions. Other sites had too much catheter motion, preventing the averaging of the data, or the match between the OCT data and histology was inaccurate. Results for different lesion types are shown in Figs. 2, 3, and 4. Figure 2 displays data for a lesion containing a large calcification and an advanced necrotic core. Low attenuation is found in areas with fibrous tissue and calcification. The necrotic core exhibits higher attenuation. It stands out much more clearly in the attenuation image than in the grayscale OCT. The adventitia also has a high attenuation, but can be distinguished from pathological features by its morphology and location: the high attenuation occurs outside the media and is circumferential. A concentric fibrous lesion shows up as a homogenous, circumferential, low attenuation region in Fig. 3. Again, the attenuation coefficient rises in the adventitial region.

A more complex plaque type is analyzed in Fig. 4. The OCT image is very heterogeneous, and this is reflected by the morphology in the histology. The cartoon histology shows intraplaque haemorrhage and necrotic core, embedded in a mostly fibrous matrix. The green and orange boxes highlight areas with high attenuation coefficient. The green box contains some necrotic core,

which is in accordance with the example in Fig. 2. The orange box, however, is only fibrous tissue and SMC. The CD68 stain reveals strong topical macrophage infiltration in both these areas. Macrophages, being strong optical scatterers, attenuate the OCT beam. An example intimal xanthoma is shown in Fig. 5. Macrophages in a lesion that is mostly fibrous otherwise cause strong attenuation.

The limited size of our data set does not permit a definitive formulation of a quantitative classification scheme for automatic identification of necrotic core and macrophages, or plaque type in general. We can, however, formulate tentative criteria based on the appearance of certain pathologies in our *in vitro* optical attenuation data. The characteristics we observed are summarized in Table II.

B. *In vivo* imaging

Stationary OCT movies with ECG registration were obtained from 6 plaques in 3 patients. Of these, 5 plaques had OFDI data with small enough catheter motion that the residual shifts could be corrected and frames could be averaged in at least one heart cycle. Of these plaques, 3 were classified as fibroatheroma, and 2 were fibrous lesions. Figure 6 presents an example of the optical attenuation of an atherosclerotic lesion *in vivo*. We show data from three consecutive heart cycles, demonstrating the reproducibility of the algorithm.

The characteristics noted in Table II were also observed *in vivo*; plaque identification by application of these criteria agreed with the interpretation by two OCT readers for 4 out of 5 cases; interpretation of the fifth one was complicated by the presence of the guidewire shadow. A conspicuous difference with the *in vitro* data is that the optical attenuation coefficients in areas classified as necrotic core were found to be lower by $2\text{--}3\text{ mm}^{-1}$ in the patient data.

IV. DISCUSSION

A. Results of this study

In this study, we have compared the optical attenuation coefficient, measured by OCT, with the composition of atherosclerotic lesions, based on histology. High optical attenuation— $\mu_t \gtrsim 10\text{ mm}^{-1}$ —is associated with two important markers of atherosclerotic plaque vulnerability: necrotic core and macrophage infiltration. Other common plaque tissue types, fibrous and calcific,

were found to have a low attenuation coefficient— $\mu_t \approx 2\text{--}4 \text{ mm}^{-1}$. The *in vitro* measurements were done on intact excised human coronary arteries, with a commercially available, clinically approved OCT system and catheters.

We have demonstrated that the analysis can be performed, with similar results, to patient data. Application in interventional procedures is easy, quick, and does not cause any patient discomfort. It requires the recording of a stationary movie of about 5 heart cycles at a spot of interest, and about 25 ml of extra flush medium for clearing. Automated, real-time attenuation analysis should be possible. The only steps that presently require user attention are the selection of end-diastolic frames for processing, and a check if the lumen contour detection did not produce any errors. Data processing is computationally light: analysis of cross-section takes about 1 s in Matlab without any optimizations.

This study is the first to report in-situ tissue typing of atherosclerotic lesions in intact human coronary arteries by means of the optical attenuation coefficient. It is also the first to demonstrate the *in vivo* feasibility of such an approach, and to assess the diagnostic potential of this parameter for plaque type in a clinical setting.

The analyzed attenuation coefficients in necrotic tissue are lower *in vivo* than *in vitro* by about $2\text{--}3 \text{ mm}^{-1}$. Given the variation in necrotic core optical properties, and the small number of *in vivo* cases in this study, there is a significant uncertainty in this estimate, but we do see a systematic difference, that is also apparent in Fig. 6. Slight changes in the tissue optical properties after death or after excision may be the cause of this observation.

B. Comparison with literature

Our results are in general agreement with those presented by Xu *et al.* [33]. Using a bench-top OCT system, they measured low μ_t for fibrous and calcific tissue, and high μ_t for necrotic core. Macrophage infiltration was not identified in this study. The scale is also comparable, taking uncertainty margins into account and reading the “lipid” category of Ref. 33 as our category “necrotic”: necrotic core has $\mu_t > 10 \text{ mm}^{-1}$. Xu *et al.* report a value of the fibrous and calcific, $\mu_t \approx 6 \text{ mm}^{-1}$, that is slightly larger than the one we find ($\mu_t \approx 2\text{--}5 \text{ mm}^{-1}$). This may be a result of the fixation procedure applied in Ref. 33.

Other literature reports both higher [30] and lower [31] values for necrotic core attenuation. Our data do confirm the observation [33] that lipid-rich tissue attenuates more strongly than other

atherosclerotic tissue types, or healthy vascular tissue.

C. Image artifacts and study limitations

We were not able to determine the backscatter coefficient μ_b from our data, because of the heterogeneities encountered in every A-line, and the lack of an intensity calibration (I_{in} on page 3) that is constant for all lines and frames. We have put in a large effort to reduce the sensitivity of the fitting algorithm to sudden steps in intensity, that result from a drop in μ_b at a sharp interface between different tissues. Evidence of artifacts, resulting from changes in μ_b being interpreted as large μ_t , is still present in the data, however. An example may be seen in Fig. 2, where fibrous and calcified tissue are adjacent. Both fibrous and calcified tissue have a low μ_t , but the transition from high to low μ_b produces a spot of high fitted μ_t near 3 o'clock. This illustrates that the attenuation display should always be interpreted in conjunction with the grayscale OCT image.

The model we used for analysis is a single-scattering model, assuming straight light paths to and from the scattering site where backreflection occurs, and not incorporating interfaces between different tissues. In reality, there is evidence of multiple scattering, especially where the tissue is close to the catheter. Multiple scattering leads to a higher signal than predicted by the model, given a set of optical parameters, and hence an artificially high attenuation as the multiple scattering weakens farther away from the catheter. Likewise, interface reflections at the boundary between different tissues—with differing refractive indices [32]—may produce a strong signal locally, which cannot be accounted for by Eq. (1). More sophisticated optical modeling [46] could reduce these artifacts, but will substantially complicate the analysis and increase dependence on parameter guesses.

Two aspects of the comparison with histology merit discussion. The first is image registration: the histologic processing inevitably deforms the tissue. This complicates automated correlation between tissue type and optical attenuation. For this reason we had to resort to visual inspection. Second, density variations are apparent in the histology slides, particularly in fibrous tissue. Certain areas seem to be more tightly packed than others. While this may be an artifact due to histologic processing in some cases, these regions can often be identified in the OCT images. They will undoubtedly reflect in the attenuation coefficient. Our standard—tissue type, color coded in the cartoon histology—does not represent these density variations. This is a source of μ_t variation that our analysis cannot account for.

V. CONCLUSIONS

We have developed a framework for imaging of the optical attenuation coefficient μ_t in human coronary arteries using intravascular OCT. *In vitro* studies demonstrate that μ_t is a suitable parameter to distinguish between different tissue types in atherosclerotic lesions. Two markers of plaque vulnerability, the presence of necrotic core and macrophage infiltration, can be identified as areas of high attenuation ($\mu_t \gtrsim 10 \text{ mm}^{-1}$). Fibrous and calcified tissue have $\mu_t \approx 2\text{--}5 \text{ mm}^{-1}$. The analysis was successfully applied to OCT images acquired in patients. Optical-attenuation based plaque classification, using the criteria developed with the *in vitro* analysis, corroborated the plaque classification based on the grayscale OCT.

-
- [1] E. Falk, P. K. Shah, and V. Fuster. Coronary plaque disruption. *Circulation*, 92(3):657–671, 1995.
 - [2] R. Virmani, F. D. Kolodgie, A. P. Burke, A. Farb, and S. M. Schwartz. Lessons from sudden coronary death — A comprehensive morphological classification scheme for atherosclerotic lesions. *Arterioscler. Thromb. Vasc. Biol.*, 20(5):1262–1275, 2000.
 - [3] E. Falk. Plaque rupture with severe pre-existing stenosis precipitating coronary thrombosis. characteristics of coronary atherosclerotic plaques underlying fatal occlusive thrombi. *Br. Heart J.*, 50(2):127–134, 1983.
 - [4] F. D. Kolodgie, A. P. Burke, A. Farb, H. K. Gold, J. Y. Yuan, J. Narula, A. V. Finn, and R. Virmani. The thin-cap fibroatheroma: A type of vulnerable plaque — The major precursor lesion to acute coronary syndromes. *Curr. Opin. Cardiol.*, 16(5):285–292, 2001.
 - [5] J. A. Schaar, J. E. Muller, E. Falk, R. Virmani, V. Fuster, P. W. Serruys, A. Colombo, C. Stefanadis, W. S. Casscells, P. R. Moreno, A. Maseri, and A. F. W. van der Steen. Terminology for high-risk and vulnerable coronary artery plaques. *Eur. Heart J.*, 25(12):1077–1082, 2004.
 - [6] P. W. Serruys, H. M. Garcia-Garcia, and E. Regar. From postmortem characterization to the in vivo detection of thin-capped fibroatheromas: The missing link toward percutaneous treatment: What if Diogenes would have found what he was looking for? *J. Am. Coll. Cardiol.*, 50(10):950–952, 2007.
 - [7] S. Waxman, F. Ishibashi, and J. E. Muller. Detection and treatment of vulnerable plaques and vulnerable patients — Novel approaches to prevention of coronary events. *Circulation*, 114(22):2390–2411, 2006.

- [8] P. D. Richardson, M. J. Davies, and G. V. Born. Influence of plaque configuration and stress distribution on fissuring of coronary atherosclerotic plaques. *Lancet*, 334(8669):941–944, 1989.
- [9] R. Virmani, F. D. Kolodgie, A. P. Burke, A. V. Finn, H. K. Gold, T. N. Tulenko, S. P. Wrenn, and J. Narula. Atherosclerotic plaque progression and vulnerability to rupture — Angiogenesis as a source of intraplaque hemorrhage. *Arterioscler. Thromb. Vasc. Biol.*, 25(10):2054–2061, 2005.
- [10] E. Falk. Pathogenesis of atherosclerosis. *J. Am. Coll. Cardiol.*, 47(8):C7–C12, 2006.
- [11] J. A. Schaar, C. L. de Korte, F. Mastik, C. Strijder, G. Pasterkamp, E. Boersma, P. W. Serruys, and A. F. W. van der Steen. Characterizing vulnerable plaque features with intravascular elastography. *Circulation*, 108(21):2636–2641, 2003.
- [12] C. L. de Korte, M. J. Sierevogel, F. Mastik, C. Strijder, J. A. Schaar, E. Velema, G. Pasterkamp, P. W. Serruys, and A. F. W. van der Steen. Identification of atherosclerotic plaque components with intravascular ultrasound elastography in vivo: A yucatan pig study. *Circulation*, 105(14):1627–1630, 2002.
- [13] D. E. Goertz, M. E. Frijlink, D. Tempel, V. Bhagwandas, A. Gisolf, R. Krams, N. de Jong, and A. F. W. van der Steen. Subharmonic contrast intravascular ultrasound for vasa vasorum imaging. *Ultrasound Med. Biol.*, 33(12):1859–1872, 2007.
- [14] D. E. Goertz, M. E. Frijlink, D. Tempel, L. C. A. van Damme, R. Krams, J. A. Schaar, F. J. ten Cate, P. W. Serruys, N. de Jong, and A. F. W. van der Steen. Contrast harmonic intravascular ultrasound — A feasibility study for vasa vasorum imaging. *Invest. Radiol.*, 41(8):631–638, 2006.
- [15] P. R. Moreno, R. A. Lodder, K. R. Purushothaman, W. E. Charash, W. N. O’Connor, and J. E. Muller. Detection of lipid pool, thin fibrous cap, and inflammatory cells in human aortic atherosclerotic plaques by near-infrared spectroscopy. *Circulation*, 105(8):923–927, 2002.
- [16] B. D. MacNeill, I. K. Jang, B. E. Bouma, N. Iftimia, M. Takano, H. Yabushita, M. Shishkov, C. R. Kaufman, S. L. Houser, H. T. Aretz, D. DeJoseph, E. F. Halpern, and G. J. Tearney. Focal and multifocal plaque distributions in patients with macrophage acute and stable presentations of coronary artery disease. *J. Am. Coll. Cardiol.*, 44(5):972–979, 2004.
- [17] M. Takano, I. K. Jang, S. Inami, M. Yamamoto, D. Murakami, K. Okamatsu, K. Seimiya, T. Ohba, and K. Mizuno. In vivo comparison of optical coherence tomography and angiography for the evaluation of coronary plaque characteristics. *Am. J. Cardiol.*, 101(4):471–476, 2008.
- [18] O. C. Raffel, F. M. Merchant, G. J. Tearney, S. Chia, D. D. Gauthier, E. Pomerantsev, K. Mizuno, B. E. Bouma, and I.-K. Jang. In vivo association between positive coronary artery remodelling and

- coronary plaque characteristics assessed by intravascular optical coherence tomography. *Eur. Heart J.*, 29(14):1721–1728, 2008.
- [19] P. Barlis, P. W. Serruys, N. Gonzalo, W. J. van der Giessen, P. J. de Jaegere, and E. Regar. Assessment of culprit and remote coronary narrowings using optical coherence tomography with long-term outcomes. *Am. J. Cardiol.*, 102(4):391–395, 2008.
- [20] T. Kubo, T. Imanishi, H. Kitabata, A. Kuroi, S. Ueno, T. Yamano, T. Tanimoto, Y. Matsuo, T. Masho, S. Takarada, A. Tanaka, N. Nakamura, M. Mizukoshi, Y. Tomobuchi, and T. Akasaka. Comparison of vascular response after sirolimus-eluting stent implantation between patients with unstable and stable angina pectoris: A serial optical coherence tomography study. *J. Am. Coll. Cardiol. Img.*, 1(4):475–484, 2008.
- [21] R. Virmani, A. P. Burke, A. Farb, and F. D. Kolodgie. Pathology of the vulnerable plaque. *J. Am. Coll. Cardiol.*, 47(8):C13–C18, 2006.
- [22] T. Kubo, T. Imanishi, S. Takarada, A. Kuroi, S. Ueno, T. Yamano, T. Tanimoto, Y. Matsuo, T. Masho, H. Kitabata, K. Tsuda, Y. Tomobuchi, and T. Akasaka. Assessment of culprit lesion morphology in acute myocardial infarction — Ability of optical coherence tomography compared with intravascular ultrasound and coronary angiography. *J. Am. Coll. Cardiol.*, 50(10):933–939, 2007.
- [23] B. M. Shapo, J. R. Crowe, A. R. Skovoroda, M. J. Eberle, N. A. Cohn, and M. O’Donnell. Displacement and strain imaging of coronary arteries with intraluminal ultrasound. *IEEE Trans. Ultrason. Ferroel. Freq. Contr.*, 43(2):234–246, 1996.
- [24] E. I. Cespedes, C. L. de Korte, and A. F. W. van der Steen. Intraluminal ultrasonic palpation: Assessment of local and cross-sectional tissue stiffness. *Ultrasound Med. Biol.*, 26(3):385–396, 2000.
- [25] A. Nair, B. D. Kuban, N. Obuchowski, and D. G. Vince. Assessing spectral algorithms to predict atherosclerotic plaque composition with normalized and raw intravascular ultrasound data. *Ultrasound Med. Biol.*, 27(10):1319–1331, 2001.
- [26] A. Nair, B. D. Kuban, E. M. Tuzcu, P. Schoenhagen, S. E. Nissen, and D. G. Vince. Coronary plaque classification with intravascular ultrasound radiofrequency data analysis. *Circulation*, 106(17):2200–2206, 2002.
- [27] A. Katouzian, S. Sathyanarayana, B. Baseri, E. E. Konofagou, and S. G. Carlier. Challenges in atherosclerotic plaque characterization with intravascular ultrasound (ivus): From data collection to classification. *IEEE Trans. Inf. Technol. Biomed.*, 12(3):315–327, 2008.
- [28] H. Yabushita, B. E. Bourna, S. L. Houser, T. Aretz, I. K. Jang, K. H. Schlendorf, C. R. Kauffman,

- M. Shishkov, D. H. Kang, E. F. Halpern, and G. J. Tearney. Characterization of human atherosclerosis by optical coherence tomography. *Circulation*, 106(13):1640–1645, 2002.
- [29] T. Kume, T. Akasaka, T. Kawamoto, N. Watanabe, E. Toyota, Y. Neishi, R. Sukmawan, Y. Sadahira, and K. Yoshida. Assessment of coronary arterial plaque by optical coherence tomography. *Am. J. Cardiol.*, 97(8):1172–5, 2006.
- [30] D. Levitz, L. Thrane, M. Frosz, P. Andersen, C. Andersen, J. Valanciunaite, J. Swartling, S. Andersson-Engels, and P. Hansen. Determination of optical scattering properties of highly-scattering media in optical coherence tomography images. *Opt. Express*, 12(2):249–259, 2004.
- [31] F. J. van der Meer, D. J. Faber, D. M. Baraznji Sassoon, M. C. Aalders, G. Pasterkamp, and T. G. van Leeuwen. Localized measurement of optical attenuation coefficients of atherosclerotic plaque constituents by quantitative optical coherence tomography. *IEEE Trans. Med. Imaging*, 24(10):1369–76, 2005.
- [32] F. J. van der Meer, D. J. Faber, I. Cilesiz, M. J. C. van Gemert, and T. G. van Leeuwen. Temperature-dependent optical properties of individual vascular wall components measured by optical coherence tomography. *J. Biomed. Opt.*, 11(4):041120, 2006.
- [33] C. Xu, J. M. Schmitt, S. G. Carlier, and R. Virmani. Characterization of atherosclerosis plaques by measuring both backscattering and attenuation coefficients in optical coherence tomography. *J. Biomed. Opt.*, 13(3):034003, 2008.
- [34] T. G. van Leeuwen, D. J. Faber, and M. C. Aalders. Measurement of the axial point spread function in scattering media using single-mode fiber-based optical coherence tomography. *IEEE J. Sel. Top. Quant. Electr.*, 9(2):227–233, 2003.
- [35] J. M. Schmitt, S. H. Xiang, and K. M. Yung. Speckle in optical coherence tomography. *J. Biomed. Opt.*, 4(1):95–105, 1999.
- [36] J. Rogowska and M. E. Brezinski. Evaluation of the adaptive speckle suppression filter for coronary optical coherence tomography imaging. *IEEE Trans. Med. Imaging*, 19(12):1261–6, 2000.
- [37] G. van Soest, J. G. Bosch, and A. F. W. van der Steen. Azimuthal registration of image sequences affected by nonuniform rotation distortion. *IEEE Trans. Inf. Technol. Biomed.*, 12(3):348–355, 2008.
- [38] G. van Soest, J. G. Bosch, and A. F. W. van der Steen. Alignment of intravascular optical coherence tomography movies affected by non-uniform rotation distortion. In *Coherence Domain Optical Methods and Optical Coherence Tomography in Biomedicine XII*, volume 6847, pages 684721–8, San Jose, CA, USA, 2008. SPIE.

- [39] G. J. Friedrich, N. Y. Moes, V. A. Muhlberger, C. Gabl, G. Mikuz, D. Hausmann, P. J. Fitzgerald, and P. G. Yock. Detection of intralésional calcium by intracoronary ultrasound depends on the histologic pattern. *Am. Heart J.*, 128(3):435–441, 1994.
- [40] S. H. Yun, G. J. Tearney, B. J. Vakoc, M. Shishkov, W. Y. Oh, A. E. Desjardins, M. J. Suter, R. C. Chan, J. A. Evans, I.-K. Jang, N. S. Nishioka, J. F. de Boer, and B. E. Bouma. Comprehensive volumetric optical microscopy in vivo. *Nat. Med.*, 12(12):1429, 2007.
- [41] G. J. Tearney, S. Waxman, M. Shishkov, B. J. Vakoc, M. J. Suter, M. I. Freilich, A. E. Desjardins, W.-Y. Oh, L. A. Bartlett, M. Rosenberg, and B. E. Bouma. Three-dimensional coronary artery microscopy by intracoronary optical frequency domain imaging. *J. Am. Coll. Cardiol. Img.*, 1(6):752–761, 2008.
- [42] G. van Soest, T. P. M. Goderie, S. van Noorden, and A. F. W. van der Steen. Algorithm optimization for quantitative analysis of intravascular optical coherence tomography data. In *Photonic Therapeutics and Diagnostics V*, volume 7161, pages 71612C–8, San Jose, CA, USA, 2009. SPIE.
- [43] J. Rieber, O. Meissner, G. Babaryka, S. Reim, M. Oswald, A. Koenig, T. M. Schiele, M. Shapiro, K. Theisen, M. F. Reiser, V. Klaus, and U. Hoffmann. Diagnostic accuracy of optical coherence tomography and intravascular ultrasound for the detection and characterization of atherosclerotic plaque composition in ex-vivo coronary specimens: A comparison with histology. *Coron. Artery Dis.*, 17(5):425–430, 2006.
- [44] O. A. Meissner, J. Rieber, G. Babaryka, M. Oswald, S. Reim, U. Siebert, T. Redel, M. Reiser, and U. Mueller-Lisse. Intravascular optical coherence tomography: Comparison with histopathology in atherosclerotic peripheral artery specimens. *J. Vasc. Interv. Radiol.*, 17(2):343–9, 2006.
- [45] N. Bruining, S. Verheye, M. Knaapen, P. Somers, J. Roelandt, E. Regar, I. Heller, S. de Winter, J. Ligthart, G. Van Langenhove, P. J. de Feijter, P. W. Serruys, and R. Hamers. Three-dimensional and quantitative analysis of atherosclerotic plaque composition by automated differential echogenicity. *Catheter. Cardiovasc. Interv.*, 70(7):968–978, 2007.
- [46] L. Thrane, M. H. Frosz, T. M. Jørgensen, A. Tycho, H. T. Yura, and P. E. Andersen. Extraction of optical scattering parameters and attenuation compensation in optical coherence tomography images of multilayered tissue structures. *Opt. Lett.*, 29(14):1641–1643, 2004.

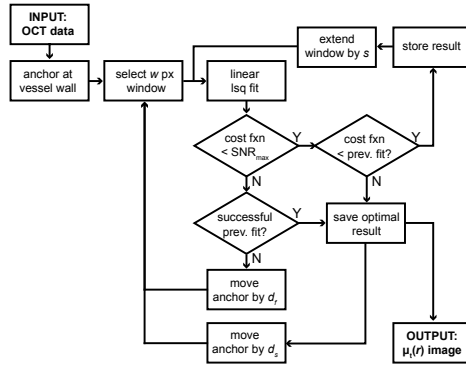


FIG. 1: Flow diagram of the fitting process. Several intermediate steps enable the algorithm to handle discontinuities and noise. Full description in the text.

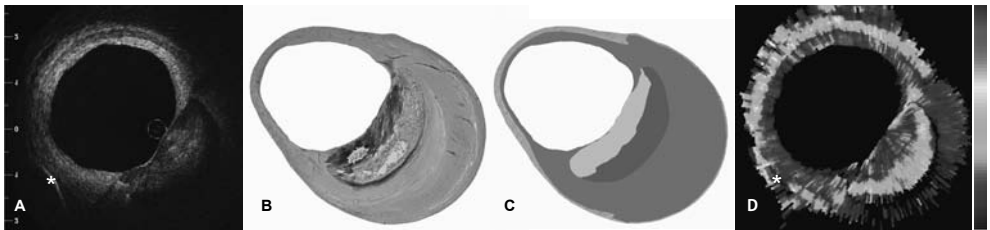


FIG. 2: A: OCT image of a coronary atherosclerotic lesion *ex vivo*. * indicates the needle used for marking the imaged site. B: Corresponding histology, H&E stain. C: Cartoon histology, overlaid on the original histology slide. It indicates an advanced necrotic core (red) behind a calcification (gray), and a slight fibrotic (green) circumferential intimal thickening. D: OCT-derived attenuation coefficient μ_t , plotted on a continuous color scale from 0 mm^{-1} to 15 mm^{-1} . The area corresponding to the necrotic core exhibits a higher attenuation coefficient ($8\text{--}10 \text{ mm}^{-1}$) than the calcification next to it or the surrounding fibrous tissue ($2\text{--}3 \text{ mm}^{-1}$).

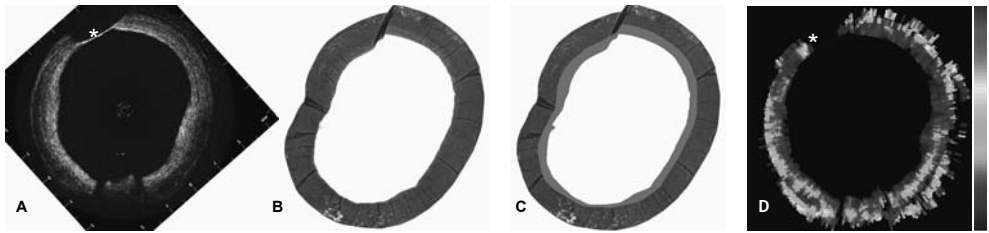


FIG. 3: A: OCT image of a circumferential homogeneous intimal thickening case. B: Corresponding histology, EvG stain. C: Cartoon histology, confirming a fibrous thickened intima. D: The attenuation coefficient μ_t is uniform and low, $2\text{--}4\text{ mm}^{-1}$, in the area corresponding to the fibrous lesion. The color scale runs from $0\text{--}15\text{ mm}^{-1}$.

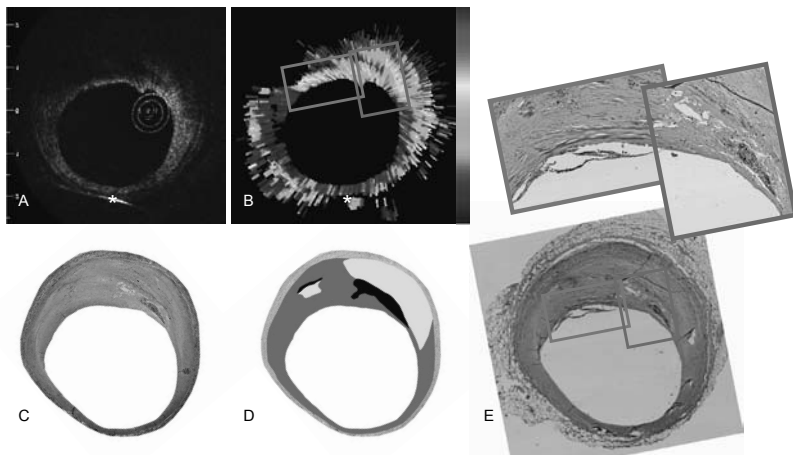


FIG. 4: A complex lesion containing necrotic core, haemorrhage, and macrophages. A: OCT image. B: Attenuation coefficient; scale from $0\text{--}15\text{ mm}^{-1}$. C: Histology, H&E stain. D: Cartoon, indicating an early stage necrotic lesion, with a thin fibrous cap, and intraplaque haemorrhage. E: CD68 stain, showing macrophage infiltration. The green and orange boxes are magnified above, and correspond to the indicated areas in B. Both areas show high attenuation coefficient ($10\text{--}12\text{ mm}^{-1}$), coinciding with the presence of necrotic core (green box) and macrophages (green and orange boxes).

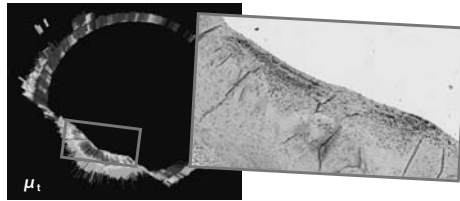


FIG. 5: An intimal xanthoma case. High attenuation (color scale 0–15 mm^{-1} as before) in a fibrous lesion occurs due to macrophage infiltration, as evidenced by the CD68 stain in the inset.

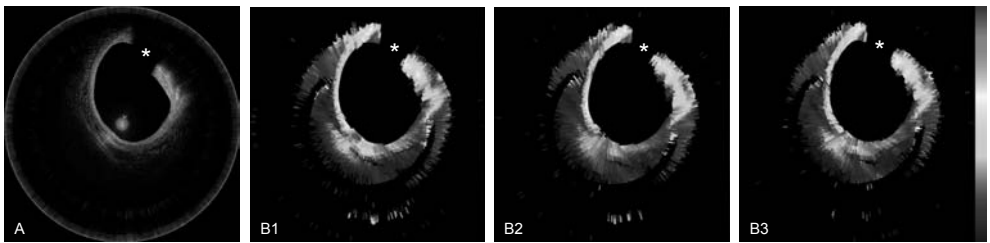


FIG. 6: Optical attenuation imaging *in vivo*. A: OFDI image of a coronary fibroatheroma (12–3 o'clock); marks the guidewire shadow. B1–3: Optical attenuation coefficient of three consecutive heart cycles, B1 corresponding to the data shown in A. The color scale runs from 0–12 mm^{-1} .

TABLE I: Color coding used for tissue type in the cartoon histology.


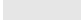



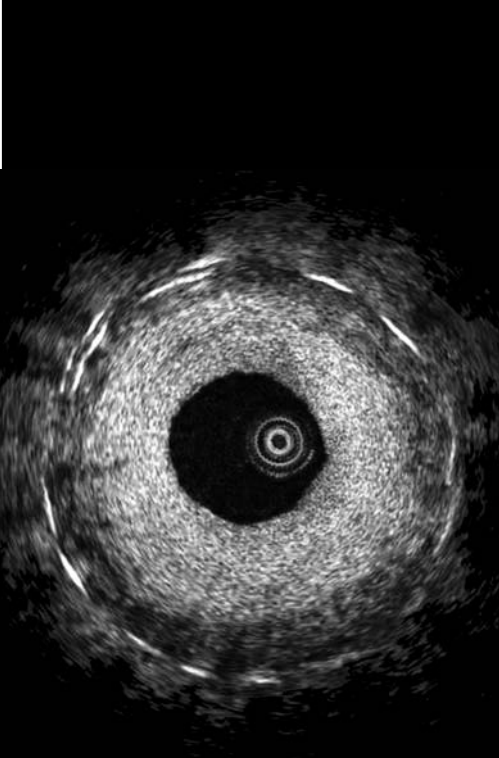
	Fibrous and smooth muscle cells
	Early necrotic core
	Advanced necrotic core
	Calcification
	Haemorrhage

TABLE II: Appearance of vessel wall condition in the attenuation image.

<i>Condition</i>	<i>Appearance</i>	<i>Typical μ_t</i>
Healthy vessel wall	Thin ($< 300 \mu\text{m}$) circumferential layer of low attenuation, adjacent to the lumen;	$2\text{--}5 \text{ mm}^{-1}$
	enveloped by a circumferential high-attenuation layer	$> 12 \text{ mm}^{-1}$
Intimal thickening	Circumferential layer of low attenuation adjacent to the lumen; thickness $\geq 500 \mu\text{m}$	$2\text{--}5 \text{ mm}^{-1}$
Necrotic core	Area of high attenuation	$\approx 10 \text{ mm}^{-1}$
Macrophage infiltration	Layer of high attenuation, usually missing data behind it	$> 12 \text{ mm}^{-1}$



4.3

Multi-Modality Intra-Coronary Plaque Characterization: A Pilot Study.

Gonzalo N, Serruys PW, Barlis P, Ligthart J, Garcia-Garcia HM, Regar E.

International Journal of Cardiology. Sep 5. [Epub ahead of print]

Multi-modality intra-coronary plaque characterization: A pilot study[☆]

Nieves Gonzalo, Patrick W. Serruys, Peter Barlis, Jurgen Ligthart,
Hector M. Garcia-Garcia, Evelyn Regar*

Thoraxcenter, Erasmus MC, Rotterdam, The Netherlands

Received 7 February 2008; received in revised form 4 June 2008; accepted 8 August 2008
Available online 6 September 2008

Abstract

Background: The risk of rupture and subsequent thrombosis of the atherosclerotic coronary plaques is related to the presence of necrotic core with high lipid content.

We conducted an exploratory pilot trial to compare the capability for lipid tissue detection using four intra-coronary diagnostic techniques: greyscale intravascular ultrasound (GS IVUS), IVUS radiofrequency data (IVUS RFD) analysis, optical coherence tomography (OCT) and intravascular magnetic resonance spectroscopy (IVMR).

Methods: Twenty-four matched target plaques were analyzed with the 4 techniques in non-culprit lesions in five patients with stable angina. Following IVUS pullback, OCT and IVMR was performed. Plaque composition was assessed using established criteria of each technology.

Results: Atherosclerotic plaques classified as soft by GS IVUS were mainly composed by fibro-fatty (80%) or necrotic core (20%) by IVUS RFD. These soft plaques were classified as "lipid-rich" by OCT in the majority of cases (80%). IVMR confirmed the presence of lipid with a lipid fraction index ranging between 36 and 79 in these soft plaques. Besides this good agreement for soft plaques, GS IVUS, IVUS RFD and OCT had 100% agreement in the identification of calcified plaques.

Conclusion: The present study explored multi-modality imaging of atherosclerotic plaque *in-vivo*. Assessing specifically lipid-rich plaques, there was generally good agreement for plaque components identified as soft by traditional GS IVUS with RFD and OCT whereas IVMR showed a varying amount of lipid in these regions. Nevertheless there continues to remain inherent variation, namely as a result of the different imaging resolutions and the lack of common nomenclature and classification.

© 2008 Elsevier Ireland Ltd. All rights reserved.

Keywords: Intra-coronary imaging; Atherosclerotic plaque characterization; IVUS RFD analysis; Optical coherence tomography; Intravascular magnetic resonance spectroscopy

Abbreviations: ACS, acute coronary syndromes; TCFA, thin cap fibroatheroma; IVUS, intravascular ultrasound; GS, greyscale; RFD, radio-frequency data; NC, necrotic core; OCT, optical coherence tomography; IVMR, intravascular magnetic resonance spectroscopy; LFI, lipid fraction index; PCI, percutaneous coronary intervention; QCA, quantitative coronary angiography; FOV, field of view.

[☆] All authors have approved the final manuscript, which has not been published and is not under consideration elsewhere. We declare that there is no conflict of interest for any author. Dr Gonzalo has received a Research Grant from the Spanish Society of Cardiology.

* Corresponding author. Thoraxcenter, Bd 585, 's-Gravendijkwal 230, 3015 CE Rotterdam, The Netherlands. Tel.: +31 10 70 35729; fax: +31 10 70 32357.

E-mail address: e.regar@erasmusmc.nl (E. Regar).

1. Introduction

Acute coronary syndromes (ACS) are common initial manifestations of coronary atherosclerosis. The propensity of atherosclerotic lesions to destabilize is highly dependent on their composition, with autopsy studies of sudden cardiac death victims showing that the most frequent cause of the coronary occlusion is rupture of a thin cap fibroatheroma (TCFA) plaque [1]. Such lesions are characterized by a large necrotic core (tissue with lipid-rich necrotic areas containing remnants of foam cells, lymphocytes, cholesterol clefts and microcalcification) with a thin, fibrous cap, usually <65 μm

in thickness [2]. Since the necrotic core is a tissue with high lipid content, discrimination of lipid-rich tissue may have an important impact on the detection of lesions prone to rupture.

Greyscale (GS) intravascular ultrasound (IVUS) is the most often evaluated diagnostic technique for the evaluation of extent and distribution of coronary atherosclerotic plaque [3], however, its specificity and sensitivity for tissue identification are limited [4,5]. Spectral analysis of IVUS radiofrequency data (RFD) is a tool developed in the last few years for more reliable analysis of plaque composition [6]. Optical coherence tomography (OCT) is a high-resolution imaging modality that uses reflected near-infrared light to visualize vascular microstructures and it has been successfully applied for the characterization of coronary atherosclerotic plaques *in-vivo* [7]. Intravascular magnetic resonance spectroscopy (IVMR) is a new technique developed to identify specifically the lipid component of plaques based on the self-diffusion of water molecules that is translated into a lipid fraction index (LFI) [8].

These four imaging modalities have in common the ability to give a detailed assessment of the composition of atherosclerotic plaques but do differ in the means of achieving this. Currently, it is unclear to what extent these techniques, with different physical properties and varying resolution, are able to give comparable results. We conducted this exploratory pilot trial to compare the capability for lipid tissue detection using these four intra-coronary diagnostic modalities (GS IVUS, IVUS RFD analysis, OCT and IVMR) while comparing these findings to each other and to GS IVUS, the most widely used and standardized method for plaque characterization.

2. Methods

2.1. Study population

Patients with stable angina undergoing percutaneous coronary intervention (PCI) were included in this pilot study. Following treatment of the culprit vessel, an IVUS pullback was performed in a non-culprit vessel containing a non-flow limiting stenosis (defined as less than 50% diameter stenosis by online quantitative coronary angiography, QCA). Following the IVUS pullback, OCT and IVMR acquisitions were performed. Heavily calcified and tortuous vessels and those with a minimal lumen diameter <2 mm were excluded. Patients with depressed left ventricular function, coronary chronic total occlusions and impaired renal function were also excluded. The study protocol was approved by the Ethics Committee of our Institution and all patients gave written informed consent.

2.2. Coronary angiography

All angiograms were evaluated after intra-coronary administration of nitrates using commercially available software

for QCA [Cardiovascular Angiography Analysis System II (CAAS II), Pie Medical, Maastricht, The Netherlands].

2.3. IVUS and RFD acquisition and analysis

IVUS was performed using the Eagle Eye 20 MHz catheter (Volcano Corporation, Rancho Cordova, USA) with an automatic continuous pullback at a rate of 0.5 mm/s. The 20 MHz catheter was used because it allows GS and RFD acquisition during the same pullback [6]. GS IVUS plaque analysis was performed by visual assessment and consensus of two experienced observers. Plaque type was classified according to the Consensus Document of the American College of Cardiology [9] as: normal vessel wall, soft plaque (echogenicity lower than the adventitia), fibrous plaque (intermediate echogenicity), and calcified plaque (echogenicity higher than the adventitia with acoustic shadowing).

The RFD analysis was performed offline with pcVH software (Volcano Corporation Rancho Cordova, USA) that permits semi-automated contour detection and provides the compositional structure of the vessel. The IVUS RFD analysis remains observer independent, using spectral analysis to classify the four different components of the atherosclerotic plaque and gives a colour-coded map distinguishing between fibrous tissue (green), fibro-lipid tissue (light green), necrotic core (red) and dense calcium (white).

2.4. OCT acquisition and analysis

The OCT acquisition was performed using a commercially available system for intra-coronary imaging (LightLab Imaging, Westford, Massachusetts, US). It operates at a wavelength of 1310 nm and has an axial resolution of 10 μ m and a lateral resolution of 20 μ m. We used a 0.019" ImageWire (LightLab Imaging, Westford, Massachusetts) in combination with a proximal, low pressure (0.4 atm) occlusion balloon (Helios, Goodman Inc, Japan) with simultaneous distal flush delivery (lactated ringers at 37 °C; flow rate 0.5 ml/s). Images were acquired during a pullback rate of 1.0 mm/s.

Plaque components were assessed by two experienced observers and classified according to previously published data as: normal vessel wall, fibrous plaque (homogeneous, signal-rich regions), lipid-rich plaque (signal-poor regions with diffuse borders) and fibro-calcific plaque (well-delineated, signal-poor regions with sharp borders) [7].

2.5. IVMR acquisition and analysis

The IVMR system consisted of a self-contained 5.2 F over-the-wire IVMR catheter, without external magnets or coils, a patient interface unit and a console. A pullback through the region of interest was performed using a dedicated device allowing controlling stepwise rotation (120°) and withdrawal (1.6 mm) of the catheter. To eliminate motion artefacts, and to improve image resolution, the IVMR catheter was stabilized against the arterial wall by inflation of a partially occlusive,

low-pressure balloon (1 atm). The time required for each acquisition was 51 s. The magnetic fields generated by the probe located at the tip of the catheter, created a sector shaped (60°), field of view (FOV) looking sideways into the artery wall. Acquired data was displayed as colour-code sectors of the LFI for the FOV. Blue indicated no lipid; grey corresponded to intermediate lipid content and yellow indicated high lipid content.

The characteristics of the four intra-coronary diagnostic techniques used in this study are summarized in Table 1.

2.6. Matching of the different diagnostic pullbacks to the target plaque

Due to the different resolution and pullback speed of the systems used (0.5 mm/s for IVUS and IVUS RFD, 1 mm/s for OCT) a very strict matching process was needed. Documentation of all catheter positions was made using angiographic landmarks. The localization of the IVUS, OCT and IVMR probes in the vessel were filmed using bi-plane angiography both pre and post-acquisition. Biplane angiography served to determine the target segment and for orientation of the catheter position in a longitudinal (IVUS, OCT, IVMR) and cross-sectional (IVMR) plane. The longitudinal orientation of the probes was determined by angiographically visible side branches (Fig. 1). The cross-sectional orientation of the probe was determined by the presence of side branches visible in the longitudinal and cross-sectional views of IVUS [10] and OCT and the specifically designed, radiopaque rotation markers for IVMR. Acquisitions, in which rotation of the probe could not be clearly confirmed by the marker, were excluded from the analysis.

Matched samples from all 4 diagnostic modalities were analyzed in 1.6 mm longitudinal intervals (corresponding to the withdrawal of the IVMR catheter in each rotation). The target plaques were defined as 60° sectors of the vessel

wall in accordance to the acquired IVMR datasets (Fig. 2A and B).

2.7. Statistical analysis

Data are expressed as mean±standard deviation for continuous variables and as percentages for categorical variables. The different terminologies and number of categories in the classifications used for the different techniques did not allow the use of statistical test to compare concordance.

3. Results

3.1. Patient and procedural characteristics

Twenty-four matched target plaques were collected from five patients. The intra-coronary diagnostic devices were successfully advanced to the area of interest in all the patients. There were no cases of coronary spasm, dissection, acute closure or perforation. During OCT and IVMR pullbacks transient signs of ischemia with ST segment changes were documented. Following the procedure, all patients remained symptom-free with no detected elevation in the creatinine kinase-MB or Troponin-T enzymes.

GS IVUS, IVUS VH and OCT imaging were successfully performed in all target lesions. IVMR pullbacks contained 6 acquisition cycles in 3 patients and 4 in the remaining 2 patients due to chest pain or transient ECG changes that completely resolved immediately after balloon deflation. 2 IVMR acquisitions were excluded, as complete, 120-degree rotation could not be judged definitively.

3.2. Target plaque characteristics

The interrogated artery was the proximal LAD in 80% of the cases, and the proximal RCA in 20%. The reference vessel diameter, minimal lumen diameter and percent diameter stenosis by QCA were 3.2 ± 0.2 mm, 2.2 ± 0.4 mm and $34\pm 11\%$, respectively. By IVUS, the vessel area was 14.3 ± 4.9 mm², the mean luminal area was 8.3 ± 3.2 mm² and the mean plaque burden was $41\pm 22\%$ in the imaged vessel.

3.3. Characteristics of the target plaques by the different techniques

We analyzed 24 matched target plaques using the four techniques.

3.3.1. Plaque morphology by GS IVUS

GS IVUS identified normal vessel wall, soft plaque, fibrous plaque and calcific plaque in 62.5%, 20.8%, 8.3% and 8.3% of cases respectively.

3.3.2. Plaque composition by IVUS RF analysis

Using IVUS RF, the analyzed target plaque was defined as normal vessel wall in 62.5% of the cases. The remainder

Table 1
Characteristics of the different intra-coronary imaging techniques used.

	GS IVUS	IVUS RFD	OCT	IVMR
Axial resolution (μm)	100–150	100–150	10–20	200
Probe size (mm)	1.1	1.1	0.4	1.8
Penetration depth	4–8 mm	4–8 mm	1.5–2 mm	200 μm
Vessel occlusion	No	No	Yes ^a	Yes
Morphological information	Yes	Yes	Yes	No
Lipid identification	+	+++	++	+++
Thin cap detection	+	+	+++	–
Remodelling	+++	+++	+	–
Inflammation	–	–	+	–

GS IVUS: greyscale intravascular ultrasound, IVUS RFD: IVUS radio-frequency data, OCT: optical coherence tomography IVMR: intravascular magnetic resonance spectroscopy.

^a In the moment of the study balloon occlusion was required for OCT acquisition. At present with the increase in the pullback speed in the new OCT systems the pullback can be performed during injection of contrast without the need for balloon occlusion.

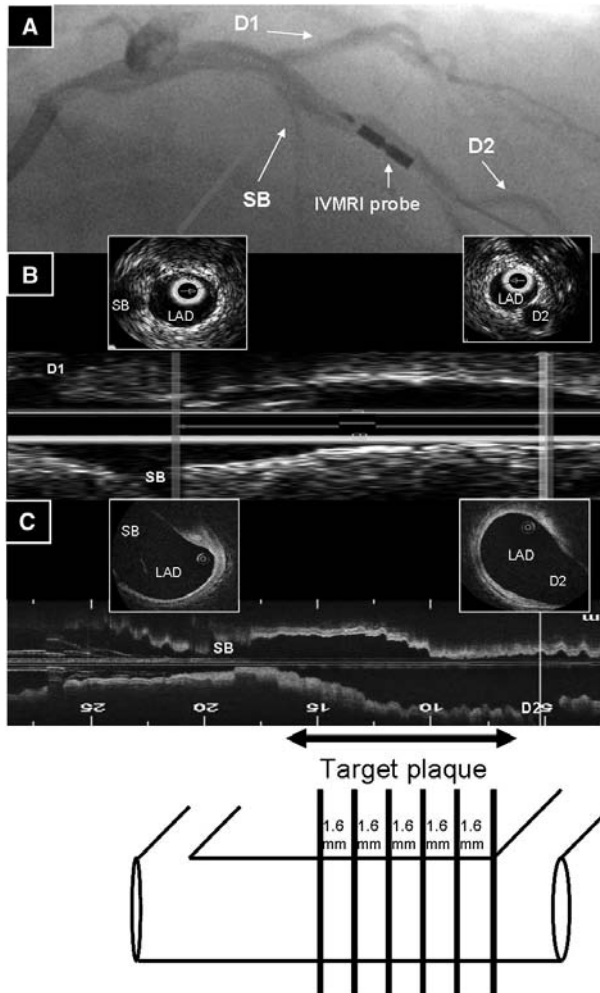


Fig. 1. Matching of the OCT and IVUS pullbacks. The position of the IVUS, optical coherence tomography (OCT) and intravascular magnetic resonance spectroscopy (IVMR) probe along the vessel was filmed before and after each acquisition (A). The “matching” of the region of interest in the IVUS (B) and OCT (C) pullback was based on the presence of anatomical landmarks (e.g. side branches visible in the longitudinal and cross-sectional views). To determine the longitudinal position of the IVMR probe in the vessel, a side branch was used as a marker. From the landmark to the proximal part of the vessel one frame every 1.6 mm was selected. D1: first diagonal, D2: second diagonal, SB: septal branch, LAD: left anterior descending coronary artery. CS: cross section.

were necrotic core (4.2%), fibro-fatty (16.7%) and fibrous (8.3%), dense calcium was the main component in 8.3% of the cases.

3.3.3. Plaque morphology by OCT

The evaluated target plaque was considered normal by OCT in 54.2% of the cases, lipid-rich plaque in 20.8%, fibrous

plaque in 16.7% of the cases, and fibro-calcific plaque in 8.3% of the cases.

3.3.4. Plaque composition by IVMR

The result of the IVMR was yellow (high LFI) in 16.7%, grey (intermediate LFI) in 25% and blue (indicating low LFI) in 45.8% of the analyzed target plaques. In 12.5% the result

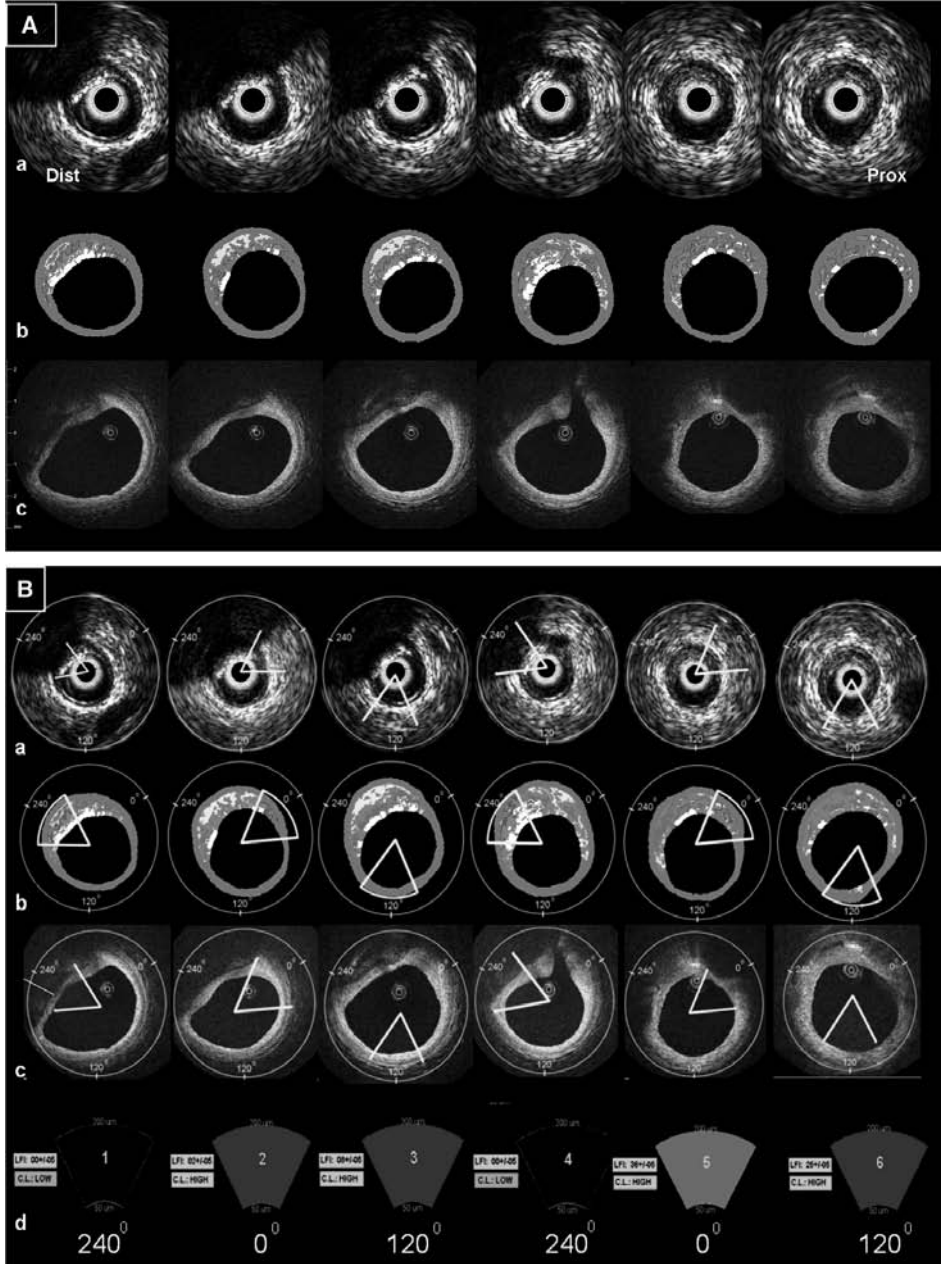


Table 2
Results of the interrogated 24 matched target plaques with the four techniques.

		IVUS GS				Total
		Normal	Soft	Fibrous	Calcified	
IVUS RFD	Normal	15	0	0	0	15
	NC	0	1	0	0	1
	Fibro-fatty	0	4	0	0	4
	Fibrous	0	0	2	0	2
	DC	0	0	0	2	2
	Total	15	5	2	2	24
OCT	Normal	12	1	0	0	13
	Lipid-rich	0	4	1	0	5
	Fibrous	3	0	1	0	4
	Fibro-calcific	0	0	0	2	2
	Total	15	5	2	2	24
IVMR	Blue	10	0	1	0	11
	Grey	3	3	0	0	6
	Yellow	1	2	1	0	4
	Black	1	0	0	2	3
	Total	15	5	2	2	24

DC: dense calcium; IVMR: intravascular magnetic resonance spectroscopy; IVUS: intravascular ultrasound; NC: necrotic core; OCT: optical coherence tomography; RFD: radiofrequency data.

was black, which indicates signal void. The minimum LFI was 0 and the maximum was 80, with a mean of 30 ± 48 . The mean LFI was 73 ± 3.9 in the yellow regions, 42 ± 1.5 in the grey regions and 17.2 ± 2.8 in the blue regions.

3.4. Comparison of GS IVUS findings with other techniques

3.4.1. Comparison GS IVUS and IVUS RFD analysis

When the vessel was defined as normal by GS IVUS, it was normal by IVUS RF analysis in 100% (15/15) of the segments (Table 2). When the plaque was defined as soft by GS IVUS, it was predominantly composed of fibro-fatty tissue by RF analysis in 80% (4/5) of the cases and necrotic core in 20% (1/5) of cases. The fibrous plaques by GS IVUS where also (2/2) fibrous in the RFD analysis. When the plaque was calcified by GS IVUS, it was composed predominantly of dense calcium in all the RFD analysis (2/2) matched plaques.

3.4.2. Comparison IVUS GS and OCT findings

When the vessel was normal by GS IVUS, it was normal by OCT in 80% (12/15) of the cases, but in 20% (3/15) of the matched sectors considered normal by GS IVUS examination, it was possible to identify fibrous plaques with OCT. When the plaque was defined as soft by GS IVUS it was mainly "lipid-rich" by OCT (80% of the cases 4/5). The

fibrous plaques by GS were fibrous by OCT in 50% of the cases (1/2) and normal vessel wall in another 50% (1/2). As with RFD analysis, all the calcified plaques by GS IVUS were also fibro-calcific plaques by OCT (2/2).

3.4.3. Comparison IVUS GS and IVMR findings

When the analyzed segment was normal by GS IVUS, it was blue by IVMR in 66% of cases (10/15). The normal vessel wall was identified as grey by IVMR in 20% (3/15) and as yellow in 6% (1/15). In 6% (1/15) of the normal vessel wall sectors the result of the IVMR was black. When the target plaque was described as soft by GS IVUS assessment, it was grey by IVMR in 60% (3/5) of the cases and yellow in 40% (2/5) of the cases. Of the two target plaques identified as fibrous by GS IVUS, one was classified as blue by the IVMR and the other as yellow. The calcified target plaques by GS IVUS were classified in 100% (2/2) of the cases as black (signal void) in the IVMR. The mean LFI was 52 ± 17 in the soft plaques, 46 ± 36 in the fibrous and 25 ± 21 in the normal vessel wall.

4. Discussion

A body of various clinical, post-mortem and experimental observations suggest that the composition of atherosclerotic plaque is an important determinant for subsequent clinical outcome. This knowledge triggered the development of a variety of new technological approaches for the analysis of plaque structure and chemical composition. It is however challenging to estimate the accuracy of a given diagnostic method *in vivo* due to the fact that no 'gold standard' method is available. A pragmatic way to get an indication for the plausibility of the information acquired in the clinical setting can be the cross correlation of different techniques. In the present study, the ability of four different intra-coronary diagnostic modalities to detect the lipid components of atherosclerotic plaque was tested. The atherosclerotic plaques classified as soft by GS IVUS were mainly composed by fibro-fatty or necrotic core in the RFD analysis. These soft plaques were classified as "lipid-rich" by OCT in most of the cases while IVMR always classified as intermediate or high lipid content the plaques identified as soft by GS IVUS. The 3 techniques of GS IVUS, IVUS RFD and OCT had a 100% agreement in the identification of calcified plaques. All these plaques were displayed as signal void by IVMR.

The detection of plaque components by IVUS is based on visual assessment of GS images and is highly influenced by the observer's experience and interpretation. It has been reported that soft (hypo-echoic) plaques usually have a high lipid content [11,12], but histological correlations have shown that GS IVUS, has low sensitivity (46%) for lipid detection [5,13]. In the present study, when compared with

Fig. 2. Analysis of the target matched plaques. A) Matching of the cross sections in a) greyscale IVUS b) IVUS radiofrequency data analysis and c) optical coherence tomography pullbacks. B) Analysis screen. After matching corresponding cross sections based on their longitudinal orientation, the region of interest is defined according to the orientation of the intravascular magnetic resonance probe towards the vessel wall. The figure illustrates the results of the six target matched plaques (60° sector) analyzed in one patient with the four techniques. Prox: proximal Dist: distal.

the findings of the IVUS RFD, all plaques classified as soft by GS IVUS were composed of fibro-fatty or necrotic tissue. The spectral analysis of IVUS RFD has been validated with histopathology *ex-vivo* [14] and *in vivo* [15], demonstrating high predictive accuracy. This technique has the advantage of being observer independent and importantly, permits the identification of necrotic core. However, histological comparisons have shown some misclassification due to overlap between tissues in the RFD spectrum [14]. GS IVUS and IVUS RFD analysis allow the detection of positive vessel remodeling, another feature associated with plaque rupture and high risk plaques [16,17]. Furthermore, vessel remodeling is related to plaque composition, as it has been demonstrated that lesions with positive remodelling have a significantly larger lipid core than lesions with negative remodeling [18].

The use of OCT and GS IVUS showed good correlation for the detection of soft and lipid-rich plaques respectively. For lipid-rich plaques, in comparison with histology, OCT has shown better sensitivity and specificity (95% and 98% respectively) than GS and integrated backscatter IVUS [19]. Despite its high resolution, one drawback of current OCT systems is the limited penetration depth (1.5–2.0 mm) that does not allow the detection of lipid pools or calcium behind thick fibrous caps. Further, the tissue characterization by OCT is observer dependent. An incorrect classification between calcium and lipid deposits by OCT has been described in comparisons with histology [20] and this may explain this phenomenon in a study by Jang et al. where there was no difference in lipid-rich plaques defined by OCT criteria in ACS and stable angina patients [21]. In the present study, we found concordance between the techniques for calcified and “lipid-rich” plaques with all plaques identified as fibro-calcific by OCT also found to be calcified by GS IVUS and RFD analysis and were displayed as black (“signal void”) by the IVMR system. Inflammation with macrophages infiltration is one of the characteristics of high risk plaques. Among all the techniques used in this study, OCT is the only one that may potentially give insights into the inflammatory state of the plaque as it has been reported that it could be able to identify macrophages [22].

IVMR is a technique specifically developed to identify the lipid composition of plaque. It has demonstrated a strong correlation with histology in lipid-rich tissue detection in both the aorta and coronary arteries of patients suspected of dying of cardiovascular causes [23]. In the present study, plaques classified as soft by GS IVUS were identified as regions with intermediate to high LFI by IVMR. However there were 4 plaques that had intermediate or high lipid content by IVMR but were classified as normal vessel wall by GS IVUS and one fibrous plaque by IVUS showed high LFI in the IVMR analysis. This may reflect higher sensitivity of IVMR for lipid detection compared to IVUS. One of the main advantages of IVMR is that it is observer independent and that it allows the quantification of the lipid component. A previous *ex vivo* study suggested that IVMR could identify TCFA [23,24]. However this application is not possible at present in the

in vivo scenario where the scan area is restricted to 60° sectors of the vessel wall. The small sample volume, the lack of structural information and the complex definition of the location of the probe in the arterial wall are the main limitations of the IVMR system at this point in time.

Presently, a number of imaging modalities are vying to accomplish plaque characterization and detection. Our study demonstrates the feasibility of assessing different physical aspects of atherosclerotic plaques *in-vivo* by multi-modality imaging. However, such an approach is complicated by a rather cumbersome matching process originating from varying sample volumes, resolutions and accuracies and, secondly, different terminologies, thresholds and cut-off values for the different technologies. Obviously, the “gold standard” for lipid detection is histopathology, but the reported classifications are qualitative and difficult to apply homogeneously to the findings of all these *in-vivo* techniques. This may be aided by defining histological plaque composition based on quantitative and uniformly applied criteria [25]. Currently, findings gained from different diagnostic modalities cannot be considered equivalent. This should be considered when interpreting and designing clinical trials involving plaque detection and characterization.

5. Limitations

The main limitations of the present study are: 1) the small sample size 2) lack of histological correlation 3) the localization of the sector scanned by IVMR was difficult to precisely assess due to the simplified spatial representation associated with the technique; however specifically designed rotation markers, meticulous inspection and exclusion of doubtful rotations were used to optimize data analysis. The multi-modality plaque characterization described in this study is at present limited by the need of advancing different relatively bulky imaging devices inside the coronary artery some of them requiring vessel occlusion. The development of integrated systems that could acquire different information with only one catheter would be basic for the applicability of this strategy.

6. Conclusions

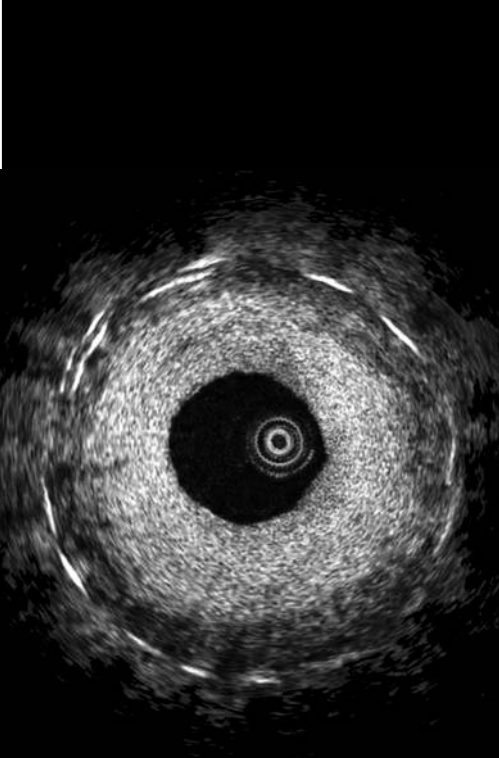
The present study explored multi-modality imaging of atherosclerotic plaque *in-vivo*. Assessing specifically lipid-rich plaques, there was generally good agreement for plaque components identified as soft by traditional GS IVUS with RFD and OCT whereas IVMR showed a varying amount of lipid in these regions. Nevertheless there continues to remain inherent variation, namely as a result of the different imaging resolutions and the lack of common nomenclature and classification.

Acknowledgement

The authors of this manuscript have certified that they comply with the Principles of Ethical Publishing in the International Journal of Cardiology [26].

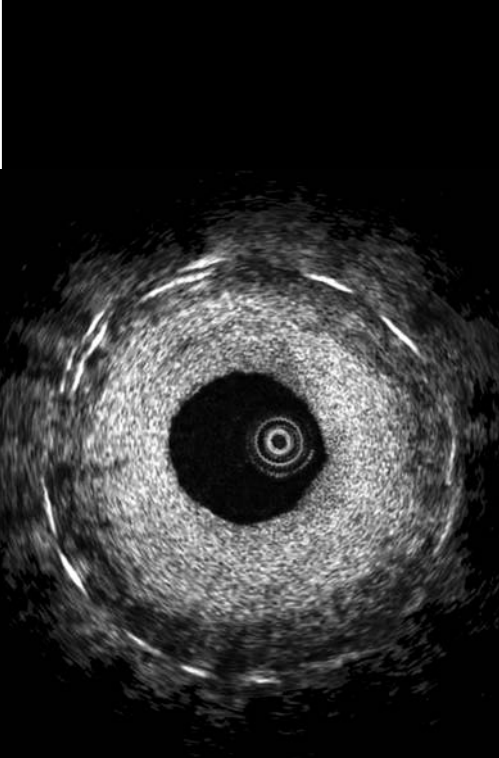
References

- [1] Virmani R, Kolodgie FD, Burke AP, et al. Lessons from sudden coronary death: a comprehensive morphological classification scheme for atherosclerotic lesions. *Arterioscler Thromb Vasc Biol* May 2000;20(5):1262–75.
- [2] Virmani R, Burke AP, Farb A, et al. Pathology of the vulnerable plaque. *J Am Coll Cardiol* Apr 18 2006;47(8 Suppl):C13–18.
- [3] Rasheed Q, Dhawale P, Anderson J, Hodgson JM. Intracoronary ultrasound-defined plaque composition: computer-aided plaque characterization and correlation with histologic samples obtained during directional coronary atherectomy. *Am Heart J* 1995;129:631–7.
- [4] Di Mario C, The S, Madretsma S, van Suylen RJ, Wilson RA, Bom N, et al. Detection and characterization of vascular lesions by intravascular ultrasound: an in vitro study correlated with histology. *J Am Soc Echocardiogr* 1992;5:135–46.
- [5] Peters RJ, Kok WE, Havenith MG, et al. Histopathologic validation of intracoronary ultrasound imaging. *J Am Soc Echocardiogr* May–Jun 1994;7(3 Pt 1):230–41.
- [6] Rodriguez-Granillo GA, Garcia-Garcia HM, Mc Fadden EP, et al. *In vivo* intravascular ultrasound-derived thin-cap fibroatheroma detection using ultrasound radiofrequency data analysis. *J Am Coll Cardiol* Dec 6 2005;46(11):2038–42.
- [7] Yabushita H, Bouma BE, Houser SL, et al. Characterization of human atherosclerosis by optical coherence tomography. *Circulation* Sep 24 2002;106(13):1640–5.
- [8] Regar E, Hennen B, Grube E, Halon D, Wilensky RL, Virmani R, et al. First-In-Man application of a miniature self-contained intracoronary magnetic resonance probe. A multi-centre safety and feasibility trial. *Eurointervention* 2006;2:77–83.
- [9] Mintz GS, Nissen SE, Anderson WD, Bailey SR, Erbel R, Fitzgerald PJ, et al. American College of Cardiology Clinical Expert Consensus Document on Standards for Acquisition, Measurement and Reporting of Intravascular Ultrasound Studies (IVUS). A report of the American College of Cardiology Task Force on Clinical Expert Consensus Documents. *J Am Coll Cardiol* Apr 2001;37(5):1478–92.
- [10] Fitzgerald PJ, Yock C, Yock PG. Orientation of intracoronary ultrasonography: looking beyond the artery. *J Am Soc Echocardiogr* Jan 1998;11(1):13–9.
- [11] DeMaria AN, Narula J, Mahmud E, et al. Imaging vulnerable plaque by ultrasound. *J Am Coll Cardiol* Apr 18 2006;47(8 Suppl):C32–39.
- [12] Gronholdt ML. Ultrasound and lipoproteins as predictors of lipid-rich, rupture-prone plaques in the carotid artery. *Arterioscler Thromb Vasc Biol* Jan 1999;19(1):2–13.
- [13] Hiro T, Leung CY, De Guzman S, et al. Are soft echoes really soft? Intravascular ultrasound assessment of mechanical properties in human atherosclerotic tissue. *Am Heart J* Jan 1997;133(1):1–7.
- [14] Nair A, Margolis P, Kuban B, Vince DG. Automated coronary plaque characterization with intravascular ultrasound backscatter: *ex vivo* validation. *Eurointervention* 2007;3:113–30.
- [15] Nasu K, Tsuchikane E, Katoh O, Vince DG, Virmani R, Surmely JF, et al. Accuracy of *in vivo* coronary plaque morphology assessment: a validation study of *in vivo* virtual histology compared with *in vitro* histopathology. *J Am Coll Cardiol* 2006;47:2405–12.
- [16] Varnava AM, Mills PG, Davies MJ. Relationship between coronary artery remodeling and plaque vulnerability. *Circulation* Feb 26 2002;105(8):939–43.
- [17] Maehara A, Mintz GS, Bui AB, et al. Morphologic and angiographic features of coronary plaque rupture detected by intravascular ultrasound. *J Am Coll Cardiol* Sep 4 2002;40(5):904–10.
- [18] Rodriguez-Granillo GA, Serruys PW, Garcia-Garcia HM, et al. Coronary artery remodelling is related to plaque composition. *Heart* Mar 2006;92(3):388–91.
- [19] Kawasaki M, Bouma BE, Bressner J, et al. Diagnostic accuracy of optical coherence tomography and integrated backscatter intravascular ultrasound images for tissue characterization of human coronary plaques. *J Am Coll Cardiol* Jul 4 2006;48(1):81–8.
- [20] Manfrini O, Mont E, Leone O, et al. Sources of error and interpretation of plaque morphology by optical coherence tomography. *Am J Cardiol* Jul 15 2006;98(2):156–9.
- [21] Jang IK, Bouma BE, Kang DH, et al. Visualization of coronary atherosclerotic plaques in patients using optical coherence tomography: comparison with intravascular ultrasound. *J Am Coll Cardiol* Feb 20 2002;39(4):604–9.
- [22] Tearney GJ, Yabushita H, Houser SL, et al. Quantification of macrophage content in atherosclerotic plaques by optical coherence tomography. *Circulation* Jan 7 2003;107(1):113–9.
- [23] Schneiderman J, Wilensky RL, Weiss A, et al. Diagnosis of thin-cap fibroatheromas by a self-contained intravascular magnetic resonance imaging probe in *ex vivo* human aortas and *in situ* coronary arteries. *J Am Coll Cardiol* Jun 21 2005;45(12):1961–9.
- [24] Wilensky RL, Song HK, Ferrari VA. Role of magnetic resonance and intravascular magnetic resonance in the detection of vulnerable plaques. *J Am Coll Cardiol* Apr 18 2006;47(8 Suppl):C48–56.
- [25] Bruining N, Verheye S, Knaapen M, et al. Three-dimensional and quantitative analysis of atherosclerotic plaque composition by automated differential echogenicity. *Catheter Cardiovasc Interv* Dec 1 2007;70(7):968–78.
- [26] Coats AJ. Ethical authorship and publishing. *Int J Cardiol* 2009;131:149–50.



CHAPTER 5

**Detection of high-risk coronary
plaques with OCT**



5.1

Diagnosis and treatment of Coronary Vulnerable Plaques.

Garcia-Garcia HM, Gonzalo N, Granada JF, Regar E, Serruys PW

Expert Rev Cardiovasc Ther. Feb 2008; 6(2):209-222.

Diagnosis and treatment of coronary vulnerable plaques

Expert Rev. Cardiovasc. Ther. 6 (1), 209–222 (2008)

Héctor M
García-García,
Nieves Gonzalo,
Juan F Granada,
Evelyn Regar and
Patrick W Serruys[†]

[†]Author for correspondence
Thoraxcenter, Ba-583,
Erasmus MC, Dr.
Molewaterplein 40, 3015 GD
Rotterdam, The Netherlands
Tel.: +31 104 635 260
Fax: +31 104 369 154
p.w.j.c.serruys@
erasmusmc.nl

Thin-capped fibroatheroma is the morphology that most resembles plaque rupture. Detection of these vulnerable plaques *in vivo* is essential to being able to study their natural history and evaluate potential treatment modalities and, therefore, may ultimately have an important impact on the prevention of acute myocardial infarction and death. Currently, conventional grayscale intravascular ultrasound, virtual histology and palpography data are being collected with the same catheter during the same pullback. A combination of this catheter with either thermography capability or additional imaging, such as optical coherence tomography or spectroscopy, would be an exciting development. Intravascular magnetic resonance imaging also holds much promise. To date, none of the techniques described above have been sufficiently validated and, most importantly, their predictive value for adverse cardiac events remains elusive. Very rigorous and well-designed studies are compelling for defining the role of each diagnostic modality. Until we are able to detect *in vivo* vulnerable plaques accurately, no specific treatment is warranted.

KEYWORDS: acute coronary syndrome • atherosclerosis • plaque rupture • thin-capped fibroatheroma

Unheralded acute coronary syndromes (ACS) are common initial manifestations of coronary atherosclerosis and are frequently caused by plaque ruptures [1]. Histopathological studies have identified several plaque morphologies associated with ACS and sudden cardiac death, such as calcified nodule, plaque erosion and thin-capped fibroatheroma (TCFA). The plaques that are at increased risk of thrombosis and rapid progression of lumen encroachment are referred to as high-risk or vulnerable lesions [2]. However, the natural history of these lesions remains unknown and the limited knowledge about their eventual prognosis is provided by retrospective histopathological studies [3]. Detection of these vulnerable plaques *in vivo* is essential to study their natural history and to evaluate potential treatment modalities and, therefore, may ultimately have an important impact on the prevention of acute myocardial infarction (AMI) and death. Coronary angiography offers valuable information on the long-term behavior of the complex lesions. Goldstein *et al.* reported that patients with ST-segment elevation myocardial infarction (STEMI) and multiple complex lesions during the year after STEMI had an increased incidence of recurrent ACS compared with patients with single complex lesions (19.0 vs 2.6%; $p < 0.001$, respectively) and repeated angioplasty, particularly of

noninfarct-related lesions (32.0 vs 12.4%; $p < 0.001$) [4]. However, angiography is limited to fully evaluate the vessel wall. Therefore, there are currently several diagnostic invasive imaging techniques aiming at specifically evaluating indicators of plaque vulnerability [5]. These techniques can provide information on the vessel, lumen and wall size, tissue composition, and the status of inflammation. This article aims to review the current histopathological definitions, state-of-the-art of invasive imaging techniques and treatment of coronary vulnerable plaques, with focus on TCFAs.

Histopathological vulnerable plaque definitions

The 'classical', most described phenotype of a vulnerable plaque is a TCFA [6], which has a large necrotic core with an overlying thin cap infiltrated by macrophages. Smooth muscle cells in the cap are absent or few. The thickness of the fibrous cap near the rupture site measures $23 \pm 19 \mu\text{m}$, with 95% of the caps measuring less than $65 \mu\text{m}$ [1,7]. Rupture of a TCFA with exposure of the thrombogenic necrotic core to circulating platelets could be responsible for 60% of all ACS [1]. Macrophage infiltration of the thin cap with release of matrix metalloproteinases and local inflammation can cause extracellular matrix degradation

and subsequent plaque rupture [8,9]. Excessive mechanical strain, particularly at the junction of the TCFA and the normal vessel wall is another factor contributing to rupture [10,11].

Chevuru *et al.* reported new pathological evidence on TCFA characterization [12]. The prevalence of TCFA and ruptured TCFA is low (0.46 ± 0.95 and 0.38 ± 0.70 per heart, respectively), focal and located in the proximal segments of the coronaries. In earlier studies, up to three TCFA were found per heart [13]. Necrotic core size was relatively small for both, TCFA (1.6 ± 1.8 mm²; length: 2.7 ± 2.0 mm) and ruptured plaques (2.2 ± 1.9 mm²; length: 1.9 ± 3.6 mm). In previous studies, the size of necrotic core in TCFA was 1.7 ± 1.1 mm² with a length of 8 mm (range: 2–17 mm), and in ruptured plaques 3.8 ± 5.5 mm², with a length of 9 mm (range: 2.5–22 mm) [14].

The second recognized phenotype of vulnerable plaque, accounting for approximately 40% of coronary thromboses in pathology series, is plaque erosion in lesions consisting of either pathological intimal thickening or thick-capped fibroatheroma [15]. These lesions typically have a high smooth muscle cell content, are rich in proteoglycans and are more common in young women and smokers, but are not associated with other conventional risk factors, such as hypercholesterolemia [1,16].

Third, there are calcified nodules, which may protrude into the vessel lumen and comprise up to 5% of lesions in pathological series. These lesions are characterized by an absence of endothelium and inflammatory cells [1]. In addition, intraplaque hemorrhage secondary to leakage from the vasa vasorum may also play a role [17].

Imaging of vulnerable plaques

Coronary angiography

Although coronary angiography represents the standard modality for visualization of the coronary artery disease, there is a clear discrepancy between the appearance of the opacified vascular lumen and the actual extent of atherosclerosis (FIGURE 1). Additionally, the percentage diameter stenosis of a lesion does not provide reliable information concerning the risk for myocardial infarction and death [18,19]. Large randomized lipid-lowering trials using both angiographic and clinical assessment have shown minimal or no improvement of angiographic lumen diameter but a much more impressive reduction in clinical endpoints, including myocardial infarction [20]. In fact, the 'luminogram' is unable to provide information on the composition of the artery wall and is therefore unable to distinguish between stable and high-risk, vulnerable plaques.

Angioscopy

Intracoronary angioscopy (CAS) is a well-established technique that allows direct visualization of the plaque surface and intraluminal structures. It enables assessment of the plaque color (white, red or yellow), and can illuminate plaque complications, such as rupture, intimal tears and thrombosis with a higher sensitivity than angiography [21–24]. Angioscopically, normal artery segments appear as glistening white, whereas atherosclerotic plaques can be categorized based on their angioscopic color as yellow or white. Platelet-rich thrombus at the site of plaque rupture is characterized as white granular material and fibrin/erythrocyte-rich thrombus as an irregular, red structure protruding into the lumen. Yellow plaques are associated with ACS and thrombosis [25,26]. They have also been correlated with other features of vulnerability, such as positive remodeling and increased distensibility [27].

The major limitation of angioscopy is that it requires a blood-free field during image acquisition, which can be obtained either by complete vessel occlusion or by continuous saline flushing in front of the angioscope. Specifically, nowadays, CAS (Vecmova®, Clinical Supply Co., Gifu, Japan) can be made while blood is cleared away from view by the injection of 5–10 ml saline. Furthermore, only a limited part of the coronary tree can be investigated (i.e., vessels > 2 mm in diameter) and assessment of stenotic lesions may prove difficult. Finally, angioscopy only images the luminal surface and, although changes in the vessel wall are reflected on the surface, this might not be sufficiently sensitive to detect subtle alterations in plaque composition or plaque burden in the presence of positive remodeling [28].

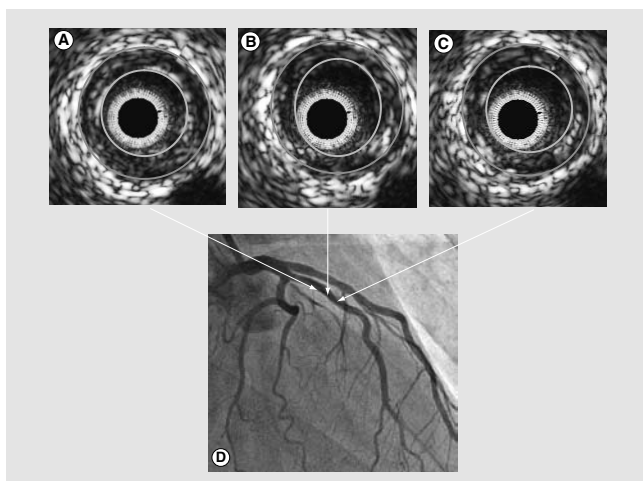


Figure 1. (A, B & C) show three consecutive intravascular ultrasound images of the proximal left anterior descending (D), which is disease-free angiographically. Note that the intravascular ultrasound images show a plaque burden of 50%.

Kubo *et al.* reported the ability of optical coherence tomography (OCT) for assessment of the culprit lesion morphology in AMI in comparison with intravascular ultrasound (IVUS) and CAS [24]. The incidence of plaque rupture observed by OCT was 73%, 47% by CAS ($p = 0.035$) and 40% by IVUS, ($p = 0.009$). Furthermore, OCT (23%) was superior to CAS (3%; $p = 0.022$) and IVUS (0%; $p = 0.005$) in the detection of fibrous cap erosion. The intracoronary thrombus was observed in all cases by OCT and CAS, but it was identified in 33% by IVUS (vs OCT; $p < 0.001$).

Intravascular ultrasound

Currently, the gold standard for intracoronary imaging is IVUS. Positive vessel remodeling can readily be evaluated with IVUS [29–31]. In addition to the lumen and vessel borders, IVUS examination can provide real-time, high-resolution images of the plaque (FIGURE 2). Visual assessment of plaque echogenicity provides semiquantitative tissue characterization [32]. Calcification can be identified with a sensitivity and specificity of approximately 90%, as bright echo signals with acoustic shadowing [33]. Lipid deposits, visualized as echolucent zones, can be detected with high sensitivity (78–95%), but low specificity (30%) [34,35]. Moreover, the axial resolution of IVUS is in the range of 100–150 μm , whereas the fibrous cap of a TCFA is thinner than

65 μm and, therefore, cannot be visualized by IVUS. Despite these limitations, large eccentric plaques containing an echolucent zone by IVUS were associated with the development of ACS in a prospective study [36]. Microbubble contrast-enhanced IVUS can measure activity and inflammation within atherosclerotic plaques by imaging vasa vasorum density, which is increasingly considered as a strong marker for plaque vulnerability [37]. A few limitations of IVUS can be improved by analyzing the backscattered ultrasound signal using more sophisticated techniques for tissue characterization [38].

Intravascular ultrasound radiofrequency analysis: virtual histology

IVUS gray-scale imaging is formed by the envelope (amplitude) of the radiofrequency signal, discarding a considerable amount of information lying beneath and between the peaks of the signal. The frequency and power of the signal commonly differ between tissues, regardless of similarities in the amplitude. IVUS-virtual histology (IVUS-VH, Volcano Corp., Rancho Cordoba, USA) involves spectral analysis of the data and evaluates different spectral parameters (e.g., Y-intercept, minimum power, maximum power, mid-band power, frequency at minimum power, frequency at maximum power, slope) to construct

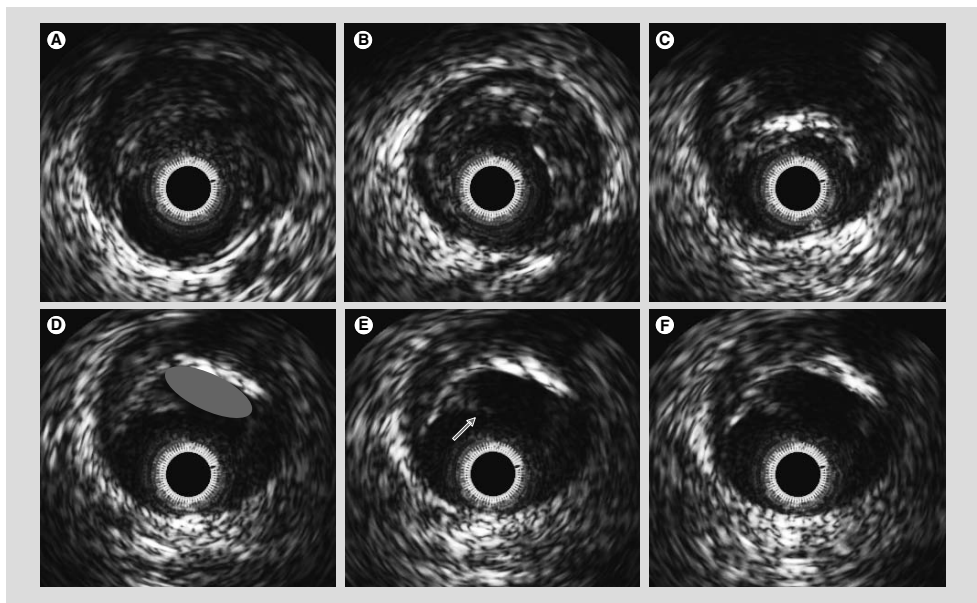


Figure 2. IVUS plaque types. These IVUS images, taken from distal to proximal in the same vessel (A–F), represent different IVUS gray scale plaque types. (A) shows a soft plaque, large plaque burden and positive remodeling. On the contrary, (B) shows a fibrotic plaque (similar echogenicity to adventitia). (C) Depicts a superficial calcified plaque (see shadowing). (D–F), a plaque rupture is illustrated; a large empty cavity (red oval, [D]) with the remnant of fibrous cap is overhanging the lumen (arrow, [E]).

tissue maps that classify plaque into four major components (fibrous, fibrolipidic, necrotic core and calcium). Different plaque components are assigned different color codes: calcified (white), fibrous (green), fibrolipidic (greenish–yellow) and necrotic core (red) [39]. Although this classification was initially evaluated *in vitro*, more recently IVUS-VH pre- and post-procedure has also been correlated with pathological specimens obtained by atherectomy with good correlation for all four tissue types [40]. As assessed by IVUS-VH, the sensitivity and specificity for fibrous tissue was 86 and 90.5%, fibrofatty 79.3 and 100%, necrotic core 67.3 and 92.9%, and dense calcium 50 and 98.9%, respectively.

IVUS-VH data are currently acquired using a commercially available 64-element phased-array catheter (Eagle Eye™ 20 MHz catheter, Volcano Corporation, Rancho Cordova, USA). Using an automated pullback device, the transducer is withdrawn at a continuous speed of 0.5 mm/s up to the ostium. IVUS-VH acquisition is ECG-gated at the R-wave peaks using a dedicated console.

IVUS B-mode images are reconstructed by customized software and contour detection is performed using cross-sectional views with semi-automatic contour detection software to provide quantitative geometrical and compositional measurements. Due to the unreliability of manual calibration, the radiofrequency data is normalized using a technique known as ‘blind deconvolution’, an iterative algorithm that deconvolves the catheter transfer function from the backscatter, thus accounting for catheter-to-catheter variability [41–43].

It has been our observation that in the near field an excessive amount of necrotic core was present. The developers have accounted for this and a proper correction was introduced in the current version of classification tree.

Our group recently evaluated the incidence of IVUS-derived TCFA (IDTCFA) using IVUS-VH [44]. Two independent IVUS analysts defined IDTCFA as a lesion fulfilling the following criteria in at least three consecutive cross-sectional areas (CSAs): necrotic core of 10% or more without evident overlying fibrous tissue, and lumen obstruction greater than or equal to 40%. In this study, 62% of patients had at least one IDTCFA in the interrogated vessels. ACS patients had a significantly higher incidence of IDTCFA than stable patients (3.0 [interquartile range: 0.0–5.0] IDTCFA/coronary vs 1.0 [interquartile range: 0.0–2.8] IDTCFA/coronary; $p = 0.018$) Finally, a clear clustering pattern was seen along the coronaries, with 66.7% of all IDTCFAs located in the first 20 mm, whereas further along the vessels the incidence was significantly lower (33.3%; $p = 0.008$). This distribution of IDTCFAs is consistent with previous *ex vivo* and clinical studies, with a clear clustering pattern from the ostium demonstrating a nonuniform distribution of vulnerable plaques along the coronary tree [45]. Patients presenting with ACS had a significantly higher prevalence of IDTCFA even in nonculprit vessels, supporting the concept of a multifocal process [46]. Of note, the lesion percent area stenosis and the mean necrotic

core areas of the IDTCFAs detected by IVUS-VH were also similar to previously reported histopathological data (55.9 vs 59.6% and 19 vs 23%, respectively) [14].

It is worth mentioning that, although the most accepted threshold to define a cap as ‘thin’ has previously been set at less than 65 μm , this was based on postmortem studies that looked at ruptured plaques [7]. Extrapolation of such criteria to *in vivo* studies requires caution. It is well established that tissue shrinkage occurs during tissue fixation [47]. Shrinkage (particularly of collagen tissue, the main component of fibrous caps) of up to 60, 15 and 80% can occur during critical-point-drying, free-drying and air-drying, respectively [48]. Furthermore, postmortem contraction of arteries is an additional confounding factor [49,50]. Since the axial resolution of IVUS-VH is 246 μm , we assumed that the absence of visible fibrous tissue overlying a necrotic core suggested a cap thickness of below 246 μm and used the absence of such tissue to define a thin fibrous cap [51].

We have recently developed software to quantify the amount of necrotic core in contact with the lumen, enabling refinement of our analysis. Our current definition of an IVUS-derived TCFA (IDTCFA) is a lesion fulfilling the following criteria in at least three consecutive CSAs:

- Plaque burden greater than or equal to 40%;
- Confluent necrotic core of 10% or more in direct contact with the lumen (i.e., no visible overlying tissue) in the investigated CSA;
- All consecutive CSAs having the same morphologic characteristics are considered as part of the same IDTCFA lesion [53].

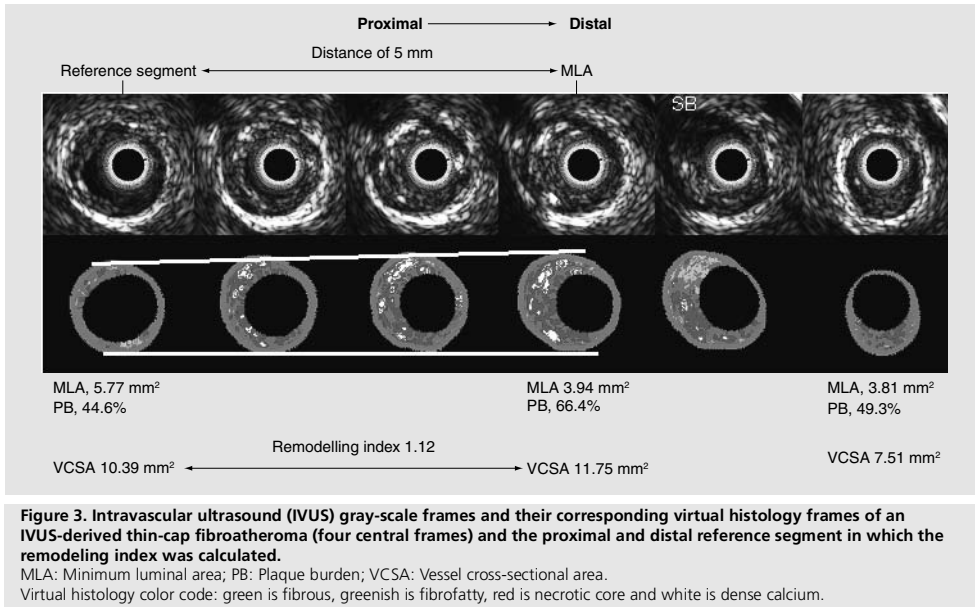
In a recent study, using this refined definition of TCFA as assessed by IVUS-VH, in patients with ACS underwent IVUS of all three epicardial coronaries, on average, there were two IDTCFA per patient with half of them showing outward remodeling [52] (FIGURE 3).

The potential value of IVUS-VH in the prediction of adverse coronary events is currently under evaluation in two international multicenter prospective studies (the PROSPECT study and the Integrated Biomarker and Imaging Study [IBIS] II trial).

Intravascular ultrasound radiofrequency analysis: palpography

This technique allows the assessment of local mechanical tissue properties. For a defined pressure difference, soft tissue (e.g., lipid-rich) components will deform more than hard tissue components (e.g., fibrous, calcified) [53,54]. Radiofrequency data obtained at different pressure levels are compared to determine the local tissue deformation.

Each palpogram represents the strain information for a certain cross section over the full cardiac cycle. The longitudinal resolution of the acquisitions depends on heart rate and pullback speed. With a heart rate of 60 bpm and a pullback speed of 1.0 mm/s, the longitudinal resolution is 1.0 mm. Palpograms are acquired using a 20-MHz phased array IVUS catheter (Eagle Eye). Digital radiofrequency data are acquired using a custom-designed workstation.



The local strain is calculated from the gated radiofrequency traces using cross-correlation analysis and displayed, color-coded, from blue (for 0% strain) to red to yellow (for 2% strain) [55]. Plaque strain values are assigned a Rotterdam classification (ROC) score ranging from I–IV (ROC I = 0 to <0.6%; ROC II = 0.6 to <0.9%; ROC III = 0.9 to <1.2%; ROC IV > 1.2%) (FIGURE 4) [56]. A region is defined as a high-strain spot when it has a ROC III–IV that spans an arc of at least 12° at the surface of a plaque (identified on the IVUS recording) adjacent to low-strain regions (<0.5%). Our group has demonstrated that palpography has a high sensitivity (88%) and specificity (89%) to detect vulnerable plaques *in vitro* [53]. Postmortem coronary arteries were investigated with intravascular elastography and subsequently processed for histology. There was a positive correlation between the presence of high strain and the amount of macrophages ($p < 0.006$) and an inverse relation between the amount of smooth muscle cells and strain ($p < 0.0001$). Vulnerable plaques identified by palpography had a thinner cap than nonvulnerable plaques ($p < 0.0001$). In a subsequent study, 55 patients with stable angina, unstable angina or AMI were analyzed. Among patients with stable angina, the prevalence of deformable plaques per vessel was significantly fewer (0.6 ± 0.6) than in unstable angina patients (1.6 ± 0.7 ; $p = 0.0019$) or AMI patients (2.0 ± 0.7 ; $p < 0.0001$). In IBIS I study, on palpography, both the absolute number of high-strain spots (grade 3/4) in the ROI ($p = 0.009$) and their density per centimeter ($p = 0.012$) decreased

significantly between baseline and follow-up. This decrease in the overall population was largely driven by changes in the subgroup of patients with STEMI; this group had both the highest number of high-strain spots at baseline and the most marked relative decrease during follow-up, compared with patients with other clinical presentations. At 6-month follow-up, the density of high-strain spots ($1.2 \pm 1.4/\text{cm}$) was comparable among clinical subgroups [57].

Optical coherence tomography

Optical coherence tomography (OCT) is an optical analogue of ultrasound; however, it uses light instead of sound to create an image [58,59]. For OCT imaging, low coherence, near infrared (NIR) light with a wavelength around 1300 nm is used since it minimizes the energy absorption in the light beam caused by protein, water, hemoglobin and lipids. The light waves are reflected by the internal microstructures within biological tissues as a result of their differing optical indices.

This technique provides a resolution of 10–20 μm *in vivo*; this level of detail is well beyond the level of resolution of IVUS (100–150 μm) [60,61]. OCT has been demonstrated to be highly sensitive and specific for characterizing atherosclerotic plaques *in vitro* when compared with histological analysis [62–64] with a sensitivity and specificity of 71–79% and 97–98% for fibrous plaques, 95–96% and 97% for fibrocalcific plaques, and 90–94% and 90–92% for lipid-rich plaques, respectively. In addition, the interobserver and intraobserver reliabilities of

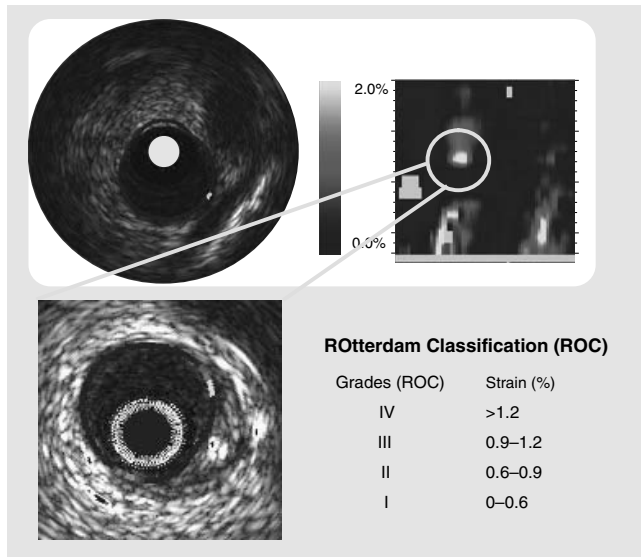


Figure 4. IVUS palpography. The local strain is calculated from the gated radiofrequency traces using cross-correlation analysis and displayed, color-coded, from blue (for 0% strain) to red to yellow (for 2% strain). Plaque strain values are assigned a Rotterdam Classification (ROC) score ranging from 1 to 4 (ROC I= 0 to <0.6%; ROC II= 0.6 to <0.9%; ROC III= 0.9 to <1.2%; ROC IV >1.2%).

OCT assessment were high (κ values of 0.88 and 0.91, respectively) [64]. *In vitro* comparison of OCT with IVUS demonstrated superior delineation by OCT of structural details such as thin caps, lipid pools or tissue proliferation [65]. An *in vitro* comparison of OCT, integrated backscatter IVUS (similar methodology to IVUS-VH) and conventional IVUS found that OCT had the best potential for tissue characterization of coronary plaques, with higher sensitivity and specificity compared with the other imaging modalities [66]. However, a recent study comparing OCT with histopathology reported a lower sensitivity for plaque components. Misclassification occurred in 41% of lesions, predominantly due to a combination of incomplete penetration depth into the vessel wall and the inability to distinguish calcium deposits from lipid pools [67].

In a pilot clinical study, our group performed *in vivo* OCT analysis of the coronary arterial wall in patients who were undergoing percutaneous coronary interventions. Imaging was possible in all patients and the entire vessel circumference was visualized at all times. A wide spectrum of different plaque morphologies was observed. OCT allowed for differentiation of the normal artery wall and inhomogeneous, mixed plaques, as well as TCFA with inhomogeneous, low-reflecting necrotic cores, covered by highly reflecting thin fibrous caps [61].

As a result of its high axial resolution, there is no doubt that OCT is the *in vivo* gold standard for identifying and measuring the thickness of the fibrous cap (FIGURE 5); an *in vivo* study found a significant difference in minimal cap thickness between AMI and stable angina patients, with median (interquartile range) values of 47.0 μm (25.3–184.30) and 102.6 μm (22.0–291.1), respectively ($p = 0.02$) [68]. On top of its reliability as a tool to measure the thickness of the cap *in vivo*, recent postmortem and *in vivo* studies have shown that OCT is capable of evaluating the macrophage content of infiltrated fibrous caps [69,70].

Kubo *et al.* evaluated the ability of intracoronary OCT to assess culprit lesions during primary PCI in patients with AMI. The thickness of the remnants of the fibrous cap after symptomatic rupture measured *in vivo* was 49 \pm 21 μm [24].

The main limitation of OCT is the shallow penetration depth (2 mm) into the tissue, which hampers imaging of the entire vessel wall in large vessels and light absorbance by blood that currently needs to be overcome by saline infusion and balloon occlusion, thereby precluding interrogation of long and proximal

segments of the coronary tree, which may limit the clinical applications of this technique.

Thermography

Atherosclerosis is accompanied by inflammation, and vulnerable plaques have been associated with increased macrophage activity, metabolism and inflammation [71]. Activated macrophages produce thermal energy, which might be detected on the surface of these atherosclerotic lesions using specially designed catheters equipped with thermistor sensors at the distal tip [72]. A rise in temperature can be found in atherosclerotic plaques compared with disease-free coronary segments. Temperature differences between an atherosclerotic plaque and normal vessel wall increase progressively from patients with stable angina to patients with AMI with a maximum temperature difference to the background temperature of 1.5 \pm 0.7°C [73]. In a prospective study, the same investigators reported an association between temperature heterogeneity and the incidence of adverse events at follow-up in patients with coronary artery disease undergoing a successful percutaneous intervention [74]. In addition, treatment with statins seems to affect the thermographic results: in nonculprit lesions the temperature difference was lower in the group treated with statins compared with the untreated group (0.06 \pm 0.05°C vs 0.11 \pm 0.10°C; $p = 0.05$) [75].

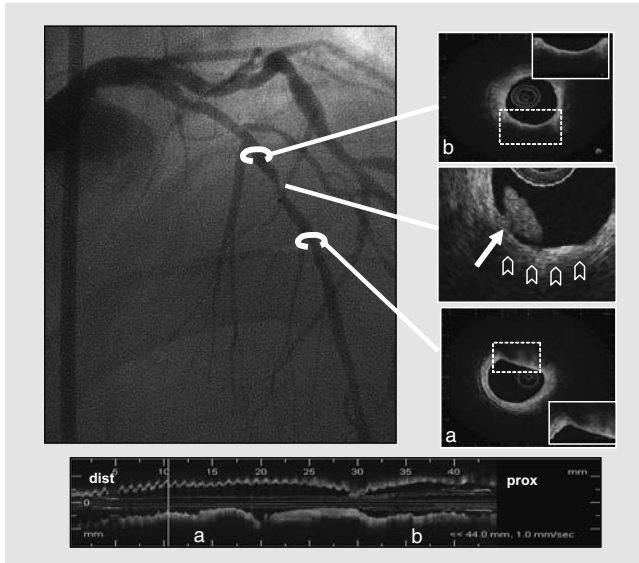


Figure 5. OCT and standard coronary angiography correlation. Angiography shows a complex lesion in the mid left anterior descending. The optical coherence tomography image shows a ruptured plaque with thrombus at that site (white arrow). Proximally and distally to the culprit lesion, thin-capped fibroatheroma lesions are present (**B**) and (**A**) respectively).

However, there are several different aspects that deserve further investigation. The prevalence and distribution of inflammatory cells in stable and unstable atherosclerotic plaque is unclear, and the predictive value of 'warm' lesions remains elusive. Furthermore, the impact of different coronary flow conditions on plaque temperature ('cooling effect') is still not completely understood [76,77]. Simulations have revealed that the correct interpretation of intravascular thermographic measurements requires data on the flow and on the morphologic characteristics of the atherosclerotic plaque [78].

There are a few limitations to the routine use of thermography in the catheterization laboratory:

- Most of the catheters used still comprise over-the-wire systems;
- Accurate temperature assessment requires direct contact of the thermistors with the vessel wall, with the associated potential risk of endothelial damage;
- Since the temperature within the vessel changes rapidly with fluid application, any intracoronary injection of contrast dye, flush or medication has to be avoided before and during measurements [79].

Intravascular magnetic resonance

Magnetic resonance (MR) is a nonionizing diagnostic tool exploiting the spins of the nuclear protons in a strong magnetic

field. For intravascular diagnosis, two different approaches have been introduced.

The first, conventional approach visualizes the anatomical structure by using a coil placed in a catheter or wire in combination with an external magnet (MR imaging [MRI]). While this approach has been (10 years ago) [80] principally shown to be able to provide detailed information on structure and composition of the arterial wall and plaque, the procedure has yet to be performed in a MR magnet, not in a cardiac catheterization laboratory. The accuracy for MRI differentiation of plaque components has been validated *in vitro* and feasibility demonstrated *in vivo* [81]. The 0.030-inch intravascular (IV)-MRI coil had a sensitivity and specificity of 73 and 85%, respectively, for lipid, 83 and 81%, respectively, for fibrous tissue and 100 and 97%, respectively, for calcification. Subsequently, the same system was applied in human iliac arteries *in vivo* using a 1.5-T magnet with a resolution of 312 μm . Complete vessel wall analysis was possible in all 25 patients and required 20 min for an arterial segment of 20 mm length. Compared to IVUS, mean lumen diameters were similar, but the outer wall area was overestimated by IVMRI (mean $116.4 \pm 4.7 \text{ mm}^2$ vs $86.6 \pm 5.8 \text{ mm}^2$; $p = 0.0001$). However, interobserver agreements for IVMRI were much higher (κ : 0.68–0.79) than for IVUS (κ : 0.21).

The other, novel approach analyses the chemical composition by placing both, the coils and miniaturized magnets on the tip of a catheter, without the need of external magnets (MR spectroscopy) and can be performed in the cardiac catheterization laboratory [82].

MR spectroscopy can identify fibrous and lipid-rich tissue by measuring differential water diffusion in a field of view. Acquired data are displayed as color-code sectors based on the lipid fraction index for each zone of the field of view. Blue indicates no lipid, gray corresponds to intermediate lipid content and yellow indicates high lipid content (FIGURE 6). Clinical feasibility of catheter-based, self-contained IV MR spectroscopy has been demonstrated recently in patients scheduled for coronary catheterization [83].

Preclinical trials employing this technology demonstrated its capability to differentiate plaque composition of human aortas, coronary and carotid arteries *in vitro*. IVMR spectroscopy could accurately detect different components (fibrous cap, smooth muscle cells, organizing thrombus, fresh thrombus, edema, lipid and calcium) with sensitivities and specificities ranging from 84 to 100%. Agreement with histology for

grading the extent of intraplaque lipid accumulation was 74% for grading of intimal thickness 80%. Further analysis revealed high correlation to histological analysis of a wide spectrum of plaque types in 15 of 16 (94%) aortic lesions and 16 of 18 (89%) coronary lesions (sensitivity: 100%; specificity: 89%), including one plaque rupture, three TCFAs, seven thick cap fibrous atheromas, four fibrocalcific plaques, two intimal xanthomas and one adaptive intimal thickening [84].

Current limitations include the limited field of view, the size of the catheter, the need for direct vessel wall contact and the time required for acquisition. In the past, the use of an autoperfusion balloon during data acquisition has been proposed to limit ischemia [85].

Clearly, IVMR diagnostics remain an exciting area still under development. Catheter-based systems will further increase the user friendliness, their sample volume and allow for scanning of longer arterial segments. Upcoming developments include the improvement MR plaque differentiation by the use of contrast agents, such as paramagnetic gadolinium-based contrast or superparamagnetic contrast agents (iron oxide nanoparticles), that can accumulate in macrophages [86,87]. There are still a few unanswered questions, including the effect of the thermal energy generated on small arteries and on coronary artery stents, although conventional MRI appears safe in this setting [88]. In addition, the presence of a permanent pacemaker is a contra-indication for any MRI imaging due to reports of arrhythmias and death.

Raman & near-infrared spectroscopy

A number of spectroscopic intravascular imaging techniques have been developed recently and are still under investigation [89]. Spectroscopy can provide qualitative and quantitative information about chemical plaque composition. The Raman effect is created when incident laser light (typically 750–850 nm wavelength) excites molecules in a tissue sample, which scatter light at a different wavelength. This change in wavelength, called the Raman effect is dependent on the chemical components of the tissue sample [90,91] and can therefore provide quantitative information about molecular composition [92–94]. Raman spectroscopy has shown acceptable correlation compared with histology ($r = 0.68$ for cholesterol and $r = 0.71$ calcification) and with IVUS *in vitro* [94,95].

Alternatively, NIR molecular vibrational transitions can be measured in the NIR region (750–2500 nm) and laser spectroscopy using wavelengths of 360–510 nm has been evaluated *in vitro* [95,96].

In near-infrared spectroscopy, it is observed how different substances absorb and scatter NIR light to different degrees at various wavelengths. An NIR spectrometer emits light into a sample and measures the proportion of light that is returned over a wide range of optical wavelengths. The return signal is then plotted as a graph of absorbance (y-axis) at different wavelengths (x-axis) called a spectrum.

In aortic and coronary artery autopsy, specimens have confirmed the ability of the technique to identify lipid-rich TCFAs through blood [97]. A catheter-based system has been developed to address the challenges of access to the coronary artery, blood, motion and the need to scan, which must be overcome for use in patients. Initial clinical experience in six patients with stable angina demonstrates that high-quality NIR spectra can be safely obtained [89]. Additional studies are planned to validate the ability of the technique to identify lipid-rich coronary artery plaques and ultimately link chemical characterization with subsequent occurrence of an ACS (FIGURE 7) [98,99].

Treatment

Treatment of asymptomatic, nonobstructive coronary lesions may be a desirable pursuit, but the pre-emptive strike may be a risky, time-consuming and expensive proposition. Assumptions include:

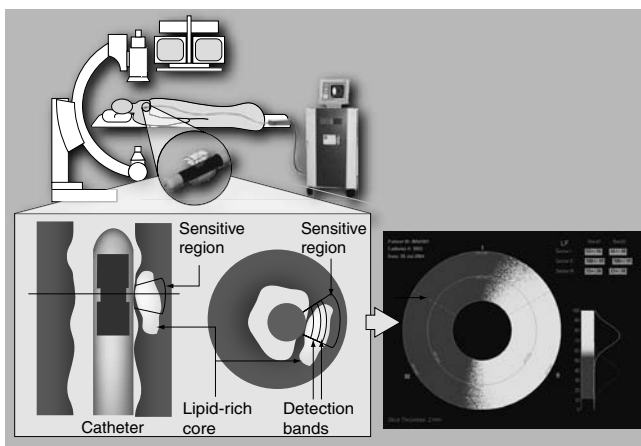


Figure 6. Intravascular magnetic resonance. The magnetic fields generated by the probe located at the tip of the catheter, create a FOV with a sector shape, looking sideways into the artery wall. The FOV has a lateral resolution of 60°, a longitudinal length of 2 mm and a depth of 200 μm . It makes the analysis for the area comprised between 50 and 200 μm from the lumen.

Acquired data is displayed as color-code sectors based of the lipid fraction index for each zone of the FOV. Blue indicates no lipid, gray correspond to intermediate lipid content and yellow indicates high lipid content.

FOV: Field of view.

- Accepting that the specific pathology can be defined in living subjects
- Presuming that this particular pathology is responsible for future clinical events
- The ‘fingerprint’ of this pathology can be reliably detected
- These findings are predictive of future adverse clinical events [3]

Based on these assumptions, initial risk stratification of asymptomatic patients drawn from the general population will be required, probably using an early screening method able to detect nonobstructive suspicious lesions. Then, patients will have to be further stratified based on noninvasive/invasive imaging (‘regional stratification tool’). Once a suspect lesion is identified, focal treatment will be based on a prediction model to prove both safety and efficacy, assuming the endovascular detection modality was correct. Among symptomatic patients (non-obstructive, non-culprit lesion in the setting of an ACS), a regional stratification strategy may be sufficient to justify therapy in the future. The main question still remains as if the therapy should focus on the entire segment containing the lesion or the ‘focal’ area in which the TCFA is identified.

Segmental therapy

Treating all three major coronary arteries or their proximal parts requires a technology capable of delivering the therapeutic effect across long segments without the need for multiple interventions or guidance to a particular lesion. Current stenting technology is simply not up to the task to consider so-called ‘full-metal-jacket’ stenting of an entire vessel [100]. Until further improvements in vascular prosthesis are made, the industry is seeking methods for passivating at-risk vessels through therapeutic applications of drugs and energy. The merge between targeted nanoparticles and local drug delivery are of special interest as potential therapeutic alternatives capable of treating large vascular territories [101].

Sonotherapy directs energy in the form of ultrasonic vibrations to the lesion and vessel wall and has been shown to decrease cell proliferation and smooth muscle cell migration *in vitro*, but very little clinical experience exists. Cryotherapy involves the therapeutic application of heat removal or hyperthermia in a segment to induce a passivation effect on the intima to halt disease progression [102,103]. Photodynamic therapy utilizes pharmaceutical compounds, which are activated locally to reduce damage outside of the treatment zone [104]. A more selective approach to photo-angioplasty is a cell targeting technique known as selective photothermolysis, which targets particular cells (e.g., macrophages) for apoptosis using nanomarkers, limiting damage to nearby structures. The other directed energy techniques are still in early stage research and there are not available data on their safety and efficacy.

Focal therapy

Myocardial infarctions are typically the result of focal complex or vulnerable lesions, and it is quite reasonable that many interventionists have suggested treating high-risk plaques with the same tools currently employed for these symptomatic lesions (bare metal stents or drug-eluting stents). Balloon-expandable metallic scaffoldings provide substantial radial forces for dilating hard, obstructive plaques leading to the unavoidable and uncontrollable disruption of the vascular structures intended to treat. Restenosis after treating a lesion with a bare metal stent has been curbed by slow-release antiproliferative drug coatings applied directly to the stent. Unfortunately, recent clinical evidence points to increased risk of late thrombosis as a result of the drug and its effect on endothelial cell functioning and vascular healing, especially in the setting of ACS [105]. Based on these risks, these devices, in their current form, do not appear to be a proper approach to pre-emptive treatment of vulnerable or at-risk plaques.

It is clear that current practices and available technologies in focal treatment are primarily focused on improving luminal diameter in occlusive plaques and are not well suited for treatment of vulnerable plaques. More focus is needed on achieving the main objectives of focal therapy: mechanical stabilization, promotion of vascular healing and reduction of inflammation. If mechanical stabilization is the objective, the proposed device must find a point of equilibrium its intrinsic expansive force radial force and its capability to induce excessive vascular injury. Computational finite element and fluid structure interaction models are critical in the development of these devices. Recently, it has been shown that geometrical changes in the shape of the lumen may affect unfavorably or favorably the distribution of local stress, either leading to plaque rupture or reinforcing of the thin fibrous cap [106,107]. Preliminary data using self-expandable nitinol-based devices designed with the objective of inducing reinforcement of the cap and necrotic core compression but not cap rupture have been published [108,109]. Conceptually, these devices must reinforce the fibrous cap, reshape the necrotic core and mechanically stabilize the lesion at risk of disruption. Another important aspect of device development is the possibility of *in situ*

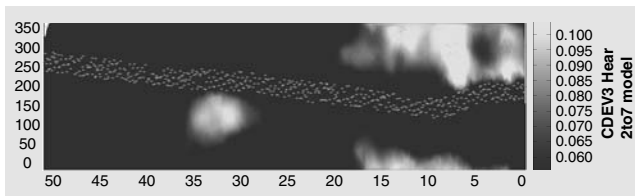


Figure 7. Near infra-red spectroscopy. Demonstration of spectral findings in the left anterior descending coronary artery of an autopsy specimen (unpublished data, on file InfraReDx, Inc., Burlington, Massachusetts). The panel shows the results of the scan, with distance along the lumen on the x-axis and arc of rotation on the y-axis. As indicated by the yellow signal, the scan successfully detected lipid necrotic core rich areas. Image courtesy of James E Muller.

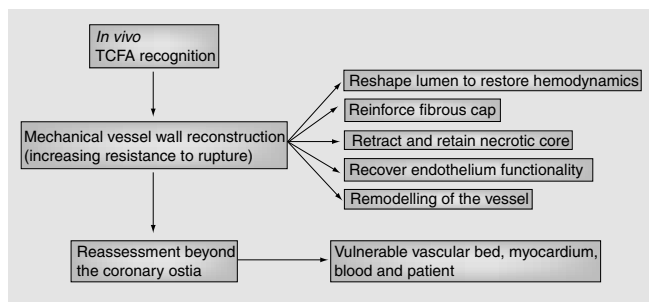


Figure 8. Treatment of coronary vulnerable plaques.

promoting tissue regeneration. Specifically, the regeneration of the endothelium and recovery of its functionality by means of passive or active endothelial cell attraction is also under development [110]. Ideally, drug elution specifically targeting the inflammatory components of the plaque must be required to mitigate inflammation with the use of these devices. Although still early for human application, several technologies specifically designed to passivate vulnerable plaques are under validation phases in animal models. Their potential as therapeutic alternatives will probably depend on the development of accurate risk stratification strategies and the validation of device safety in the appropriate clinical setting.

Conclusion

Several invasive imaging techniques are currently under development to detect vulnerable coronary plaques in human coronary arteries *in vivo*. To date, none of the techniques described previously have been sufficiently validated and, most importantly, their predictive value for adverse cardiac events remains elusive. Intravascular palpography and virtual histology, based on conventional IVUS catheters, appear to be very promising and their predictive role is presently under investigation in a large international trial.

Very rigorous and well-designed studies are compelling for defining the role of each imaging modality. Noninvasive techniques and the assessment of humoral and genetic factors comprise complementary and important tools in this direction.

At present, the main purpose of all these evolving techniques is to improve our understanding of atherosclerotic disease and to define its natural history. Ultimately, the aims are to identify patients at high risk for future cardiovascular events and to evaluate the benefit from either local or systemic therapeutic interventions.

Expert commentary & five-year view

Unheralded ACS are common initial manifestations of coronary atherosclerosis and are frequently caused by plaque rup-

tures. TCFA is the morphology that most resembles plaque rupture. However, the natural history of these high-risk or vulnerable lesions remains unknown and the limited knowledge about their eventual prognosis is provided by retrospective histopathological studies. Detection of these vulnerable plaques *in vivo* is essential to study their natural history and to evaluate potential treatment modalities and, therefore, may ultimately have an important impact on the prevention of AMI and death. Several invasive imaging techniques are currently under development to detect vul-

nerable coronary plaques in human coronary arteries *in vivo*. The optimal device for imaging vulnerable plaque would combine several techniques, overcoming the deficiencies of each and providing information on different aspects of vulnerability. Currently, conventional grayscale IVUS, IVUS-VH and palpography are imaged with the same catheter during the same pullback. A combination of this catheter with either thermography capability or alternative imaging such as OCT or spectroscopy would be an exciting development. IVMRI also holds much promise. To date, none of the techniques described previously have been sufficiently validated and, most importantly, their predictive value for adverse cardiac events remains elusive. Very rigorous and well-designed studies are compelling for defining the role of each imaging modality. Noninvasive techniques and the assessment of biohumoral and genetic factors comprise complementary and important tools in this direction.

Financial & competing interests disclosure

The authors have no relevant affiliations or financial involvement with any organization or entity with a financial interest in or financial conflict with the subject matter or materials discussed in the manuscript. This includes employment, consultancies, honoraria, stock ownership or options, expert testimony, grants or patents received or pending, or royalties.

No writing assistance was utilized in the production of this manuscript.

Key issues

- The natural history of the so-called vulnerable plaque is unknown.
- There is not a single imaging technique able to fully characterize vulnerable plaques.
- Combination of some of these techniques may improve accuracy on vulnerable plaque detection.
- Ongoing studies using these techniques would provide better understanding of this intricate process.

References

Papers of special note have been highlighted as:

- of interest
- of considerable interest

- 1 Virmani R, Kolodgie FD, Burke AP, Farb A, Schwartz SM. Lessons from sudden coronary death: a comprehensive morphological classification scheme for atherosclerotic lesions. *Arterioscler. Thromb. Vasc. Biol.* 20, 1262–1275 (2000).
- 2 Schaar JA, Muller JE, Falk E *et al.* Terminology for high-risk and vulnerable coronary artery plaques. Report of a meeting on the vulnerable plaque, June 17th to 18th 2003, Santorini, Greece. *Eur. Heart J.* 25, 1077–1082 (2004).
- 3 Serruys PW, Garcia-Garcia HM, Regar E. From postmortem characterization to the *in vivo* detection of thin-capped fibroatheromas: the missing link toward percutaneous treatment: what if Diogenes would have found what he was looking for? *J. Am. Coll. Cardiol.* 50, 950–952 (2007).
- 4 Goldstein JA, Demetriou D, Grines CL, Pica M, Shoukfeh M, O'Neill WW. Multiple complex coronary plaques in patients with acute myocardial infarction. *N. Engl. J. Med.* 343, 915–922 (2000).
- 5 Waxman S, Ishibashi F, Muller JE. Detection and treatment of vulnerable plaques and vulnerable patients: novel approaches to prevention of coronary events. *Circulation* 114, 2390–2411 (2006).
- 6 Kolodgie FD, Burke AP, Farb A *et al.* The thin-cap fibroatheroma: a type of vulnerable plaque: the major precursor lesion to acute coronary syndromes. *Curr. Opin. Cardiol.* 16, 285–292 (2001).
- 7 Burke AP, Farb A, Malcom GT, Liang YH, Smialek J, Virmani R. Coronary risk factors and plaque morphology in men with coronary disease who died suddenly. *N. Engl. J. Med.* 336, 1276–1282 (1997).
- 8 Moreno PR, Falk E, Palacios IF, Newell JB, Fuster V, Fallon JT. Macrophage infiltration in acute coronary syndromes. Implications for plaque rupture. *Circulation* 90, 775–778 (1994).
- 9 Ross R. Atherosclerosis – an inflammatory disease. *N. Engl. J. Med.* 340, 115–126 (1999).
- 10 Loree HM, Kamm RD, Stringfellow RG, Lee RT. Effects of fibrous cap thickness on peak circumferential stress in model atherosclerotic vessels. *Circ. Res.* 71, 850–858 (1992).
- 11 Richardson PD, Davies MJ, Born GV. Influence of plaque configuration and stress distribution on fissuring of coronary atherosclerotic plaques. *Lancet* 2, 941–944 (1989).
- 12 Cheruvu PK, Finn AV, Gardner C *et al.* Frequency and distribution of thin-cap fibroatheroma and ruptured plaques in human coronary arteries: a pathologic study. *J. Am. Coll. Cardiol.* 50, 940–949 (2007).
- 13 Kolodgie FD, Virmani R, Burke AP *et al.* Pathologic assessment of the vulnerable human coronary plaque. *Heart* 90, 1385–1391 (2004).
- 14 Virmani R, Burke AP, Kolodgie FD, Farb A. Vulnerable plaque: the pathology of unstable coronary lesions. *J. Interv. Cardiol.* 15, 439–446 (2002).
- 15 Farb A, Burke AP, Tang AL *et al.* Coronary plaque erosion without rupture into a lipid core: a frequent cause of coronary thrombosis in sudden coronary death. *Circulation* 93, 1354–1363 (1996).
- 16 Arbustini E, Dal Bello B, Morbini P *et al.* Plaque erosion is a major substrate for coronary thrombosis in acute myocardial infarction. *Heart* 82, 269–272 (1999).
- 17 Kolodgie FD, Gold HK, Burke AP *et al.* Intraplaque hemorrhage and progression of coronary atheroma. *N. Engl. J. Med.* 349, 2316–2325 (2003).
- 18 Ambrose JA, Tannenbaum MA, Alexopoulos D *et al.* Angiographic progression of coronary artery disease and the development of myocardial infarction. *J. Am. Coll. Cardiol.* 12, 56–62 (1988).
- 19 Little WC, Constantinescu M, Applegate RJ *et al.* Can coronary angiography predict the site of a subsequent myocardial infarction in patients with mild-to-moderate coronary artery disease? *Circulation* 78, 1157–1166 (1988).
- 20 Topol EJ, Nissen SE. Our preoccupation with coronary luminology. The dissociation between clinical and angiographic findings in ischemic heart disease. *Circulation* 92, 2333–2342 (1995).
- 21 Mizuno K, Saromura K, Miyamoto A *et al.* Angioscopic evaluation of coronary-artery thrombi in acute coronary syndromes. *N. Engl. J. Med.* 326, 287–291 (1992).
- 22 Sherman CT, Litvack F, Grundfest W *et al.* Coronary angiography in patients with unstable angina pectoris. *N. Engl. J. Med.* 315, 913–919 (1986).
- 23 de Feyter PJ, Ozaki Y, Baptista J *et al.* Ischemia-related lesion characteristics in patients with stable or unstable angina: a study with intracoronary angiography and ultrasound. *Circulation* 92, 1408–1413 (1995).
- 24 Kubo T, Imanishi T, Takarada S *et al.* Assessment of culprit lesion morphology in acute myocardial infarction: ability of optical coherence tomography compared with intravascular ultrasound and coronary angiography. *J. Am. Coll. Cardiol.* 50, 933–939 (2007).
- 25 Thieme T, Wernecke KD, Meyer R *et al.* Angioscopic evaluation of atherosclerotic plaques: validation by histomorphologic analysis and association with stable and unstable coronary syndromes. *J. Am. Coll. Cardiol.* 28, 1–6 (1996).
- 26 Ueda Y, Ohtani T, Shimizu M, Hirayama A, Kodama K. Assessment of plaque vulnerability by angioscopic classification of plaque color. *Am. Heart J.* 148, 333–335 (2004).
- 27 Takano M, Mizuno K, Okamatsu K, Yokoyama S, Ohba T, Sakai S. Mechanical and structural characteristics of vulnerable plaques: analysis by coronary angiography and intravascular ultrasound. *J. Am. Coll. Cardiol.* 38, 99–104 (2001).
- 28 Smits PC, Pasterkamp G, de Jaegere PP, de Feyter PJ, Borst C. Angioscopic complex lesions are predominantly compensatory enlarged: an angiography and intracoronary ultrasound study. *Cardiovasc. Res.* 41, 458–464 (1999).
- 29 Nakamura M, Nishikawa H, Mukai S *et al.* Impact of coronary artery remodeling on clinical presentation of coronary artery disease: an intravascular ultrasound study. *J. Am. Coll. Cardiol.* 37, 63–69 (2001).
- 30 Maehara A, Mintz GS, Bui AB *et al.* Morphologic and angiographic features of coronary plaque rupture detected by intravascular ultrasound. *J. Am. Coll. Cardiol.* 40, 904–910 (2002).
- 31 Kotani J, Mintz GS, Castagna MT *et al.* Intravascular ultrasound analysis of infarct-related and non-infarct-related arteries in patients who presented with an acute myocardial infarction. *Circulation* 107, 2889–2893 (2003).
- 32 Aoki J, Abizaid AC, Serruys PW *et al.* Evaluation of four-year coronary artery response after sirolimus-eluting stent implantation using serial quantitative intravascular ultrasound and computer-

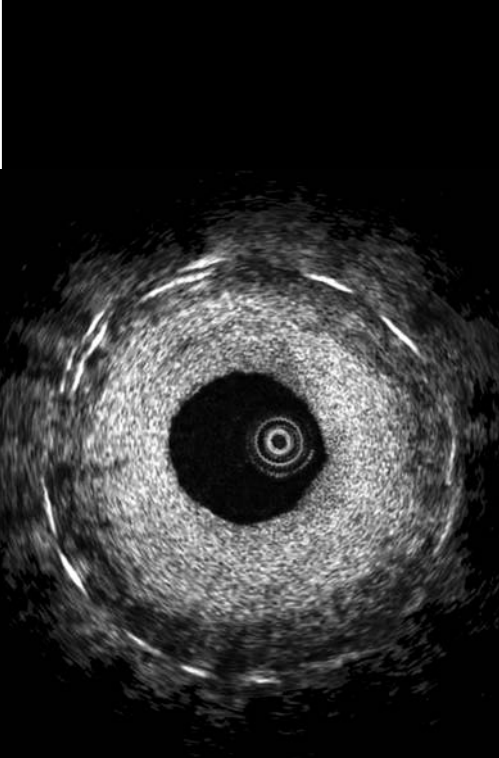
- assisted grayscale value analysis for plaque composition in event-free patients. *J. Am. Coll. Cardiol.* 46, 1670–1676 (2005).
- 33 Di Mario C, The SH, Madretsa S *et al.* Detection and characterization of vascular lesions by intravascular ultrasound: an *in vitro* study correlated with histology. *J. Am. Soc. Echocardiogr.* 5, 135–146 (1992).
- 34 Potkin BN, Bartorelli AL, Gessert JM *et al.* Coronary artery imaging with intravascular high-frequency ultrasound. *Circulation* 81, 1575–1585 (1990).
- 35 Rasheed Q, Dhawale PJ, Anderson J, Hodgson JM. Intracoronary ultrasound-defined plaque composition: computer-aided plaque characterization and correlation with histologic samples obtained during directional coronary atherectomy. *Am. Heart J.* 129, 631–637 (1995).
- 36 Yamagishi M, Terashima M, Awano K *et al.* Morphology of vulnerable coronary plaque: insights from follow-up of patients examined by intravascular ultrasound before an acute coronary syndrome. *J. Am. Coll. Cardiol.* 35, 106–111 (2000).
- 37 Carlier S, Kakadiaris IA, Dib N *et al.* Vasa vasorum imaging: a new window to the clinical detection of vulnerable atherosclerotic plaques. *Curr. Atheroscler. Rep.* 7, 164–169 (2005).
- 38 Jeremias A, Kolz ML, Ikonen TS *et al.* Feasibility of *in vivo* intravascular ultrasound tissue characterization in the detection of early vascular transplant rejection. *Circulation* 100, 2127–2130 (1999).
- 39 Nair A, Kuban BD, Tuzcu EM, Schoenhagen P, Nissen SE, Vince DG. Coronary plaque classification with intravascular ultrasound radiofrequency data analysis. *Circulation* 106, 2200–2206 (2002).
- 40 Nasu K, Tsuchikane E, Katoh O *et al.* Accuracy of *in vivo* coronary plaque morphology assessment: a validation study of *in vivo* virtual histology compared with *in vitro* histopathology. *J. Am. Coll. Cardiol.* 47, 2405–2412 (2006).
- 41 Rodriguez-Granillo GA, Aoki J, Ong AT *et al.* Methodological considerations and approach to cross-technique comparisons using *in vivo* coronary plaque characterization based on intravascular ultrasound radiofrequency data analysis: insights from the Integrated Biomarker and Imaging Study (IBIS). *Int. J. Cardiovasc. Intervent.* 7, 52–58 (2005).
- 42 Kaaresen K. Deconvolution of sparse spike trains by iterated window maximization. *IEEE Trans. Signal Process* 45, 1173–1183 (1997).
- 43 Kaaresen K, Bolvikken E. Blind deconvolution of ultrasonic traces accounting for pulse variance. *IEEE Trans. Ultrason. Ferroelectr. Freq. Control* 46, 564–573 (1999).
- 44 Rodriguez-Granillo GA, Garcia-Garcia HM, Mc Fadden EP *et al.* *In vivo* intravascular ultrasound-derived thin-cap fibroatheroma detection using ultrasound radiofrequency data analysis. *J. Am. Coll. Cardiol.* 46, 2038–2042 (2005).
- 45 Wang JC, Normand SL, Mauri L, Kuntz RE. Coronary artery spatial distribution of acute myocardial infarction occlusions. *Circulation* 110, 278–284 (2004).
- 46 Rioufol G, Finet G, Ginon I *et al.* Multiple atherosclerotic plaque rupture in acute coronary syndrome: a three-vessel intravascular ultrasound study. *Circulation* 106, 804–808 (2002).
- 47 Lowder ML, Li S, Carnell PH, Vito RP. Correction of distortion of histologic sections of arteries. *J. Biomech.* 40(2), 445–450 (2007).
- 48 Boyde A, Jones SJ, Tamarin A. Dimensional changes during specimen preparation for scanning electron microscopy. *Scan. Electron Microsc.* 1, 507–518 (1977).
- 49 Fishbein MC, Siegel RJ. How big are coronary atherosclerotic plaques that rupture? *Circulation* 94, 2662–2666 (1996).
- 50 Siegel RJ, Swan K, Edwalds G, Fishbein MC. Limitations of postmortem assessment of human coronary artery size and luminal narrowing: differential effects of tissue fixation and processing on vessels with different degrees of atherosclerosis. *J. Am. Coll. Cardiol.* 5, 342–346 (1985).
- 51 Nair A, Calverti D, DG V. Regularized autoregressive analysis of intravascular ultrasound data: improvement in spatial accuracy of plaque tissue maps. *IEEE Trans. Ultrason. Ferroelectr. Freq. Control* 51, 420–431 (2004).
- 52 Garcia-Garcia HM, Goehardt D, Schuurbiens JC *et al.* Virtual histology and remodeling index allow *in vivo* identification of allegedly high risk coronary plaques in patients with acute coronary syndromes: a three vessel intravascular ultrasound radiofrequency data analysis. *Eurointervention* 2, 338–344 (2006).
- 53 Schaar JA, de Korte CL, Mastik F *et al.* Characterizing vulnerable plaque features with intravascular elastography. *Circulation* 108, 2636–2641 (2003).
- 54 Schaar JA, Regar E, Mastik F *et al.* Incidence of high-strain patterns in human coronary arteries: assessment with three-dimensional intravascular palpography and correlation with clinical presentation. *Circulation* 109, 2716–2719 (2004).
- 55 de Korte CL, Carlier SG, Mastik F *et al.* Morphological and mechanical information of coronary arteries obtained with intravascular elastography; feasibility study *in vivo*. *Eur. Heart J.* 23, 405–413 (2002).
- 56 van Mieghem CAG, Bruining N, Schaar JA *et al.* Rationale and methods of the integrated biomarker and imaging study (IBIS): combining invasive and non-invasive imaging with biomarkers to detect subclinical atherosclerosis and assess coronary lesion biology. *Int. J. Cardiovasc. Imaging* 21, 425–441 (2005).
- 57 Van Mieghem CA, McFadden EP, de Feyter PJ *et al.* Noninvasive detection of subclinical coronary atherosclerosis coupled with assessment of changes in plaque characteristics using novel invasive imaging modalities: the Integrated Biomarker and Imaging Study (IBIS). *J. Am. Coll. Cardiol.* 47, 1134–1142 (2006).
- 58 Regar E vLA, Serruys PW. *Optical Coherence Tomography in Cardiovascular Research*. Informa Healthcare, London, UK (2007).
- 59 Huang D, Swanson EA, Lin CP *et al.* Optical coherence tomography. *Science* 254, 1178–1181 (1991).
- 60 Brezinski ME, Tearney GJ, Bouma BE *et al.* Imaging of coronary artery microstructure (*in vitro*) with optical coherence tomography. *Am. J. Cardiol.* 77, 92–93 (1996).
- 61 Regar E, Schaar JA, Mont E, Virmani R, Serruys PW. Optical coherence tomography. *Cardiovasc. Radiat. Med.* 4, 198–204 (2003).
- 62 Jang IK, Bouma BE, Kang DH *et al.* Visualization of coronary atherosclerotic plaques in patients using optical coherence tomography: comparison with intravascular ultrasound. *J. Am. Coll. Cardiol.* 39, 604–609 (2002).
- 63 Patwari P, Weissman NJ, Boppart SA *et al.* Assessment of coronary plaque with optical coherence tomography and high-frequency ultrasound. *Am. J. Cardiol.* 85, 641–644 (2000).

- 64 Yabushita H, Bouma BE, Houser SL *et al*. Characterization of Human Atherosclerosis by Optical Coherence Tomography. *Circulation* 106, 1640–1645 (2002).
- 65 Brezinski ME, Tearney GJ, Weissman NJ *et al*. Assessing atherosclerotic plaque morphology: comparison of optical coherence tomography and high frequency intravascular ultrasound. *Heart* 77, 397–403 (1997).
- 66 Kawasaki M, Bouma BE, Bressner J *et al*. Diagnostic accuracy of optical coherence tomography and integrated backscatter intravascular ultrasound images for tissue characterization of human coronary plaques. *J. Am. Coll. Cardiol.* 48, 81–88 (2006).
- 67 Manfrini O, Mont E, Leone O *et al*. Sources of error and interpretation of plaque morphology by optical coherence tomography. *Am. J. Cardiol.* 98, 156–159 (2006).
- 68 Jang IK, Tearney GJ, MacNeill B *et al*. *In vivo* characterization of coronary atherosclerotic plaque by use of optical coherence tomography. *Circulation* 111, 1551–1555 (2005).
- 69 Tearney GJ, Yabushita H, Houser SL *et al*. Quantification of macrophage content in atherosclerotic plaques by optical coherence tomography. *Circulation* 107, 113–119 (2003).
- 70 MacNeill BD, Jang IK, Bouma BE *et al*. Focal and multi-focal plaque macrophage distributions in patients with acute and stable presentations of coronary artery disease. *J. Am. Coll. Cardiol.* 44, 972–979 (2004).
- 71 Fuster V. Human lesion studies. *Ann. NY Acad. Sci.* 811, 207–224, discussion 224–225 (1997).
- 72 Casscells W, Hathorn B, David M *et al*. Thermal detection of cellular infiltrates in living atherosclerotic plaques: possible implications for plaque rupture and thrombosis. *Lancet* 347, 1447–1451 (1996).
- 73 Stefanadis C, Diamantopoulos L, Vlachopoulos C *et al*. Thermal heterogeneity within human atherosclerotic coronary arteries detected *in vivo*: a new method of detection by application of a special thermography catheter. *Circulation* 99, 1965–1971 (1999).
- 74 Stefanadis C, Toutouzas K, Tsiamis E *et al*. Increased local temperature in human coronary atherosclerotic plaques: an independent predictor of clinical outcome in patients undergoing a percutaneous coronary intervention. *J. Am. Coll. Cardiol.* 37, 1277–1283 (2001).
- 75 Toutouzas K, Drakopoulou M, Mitropoulos J *et al*. Elevated plaque temperature in non-culprit *de novo* atheromatous lesions of patients with acute coronary syndromes. *J. Am. Coll. Cardiol.* 47, 301–306 (2006).
- 76 Stefanadis C, Toutouzas K, Tsiamis E *et al*. Thermal heterogeneity in stable human coronary atherosclerotic plaques is underestimated *in vivo*: the 'cooling effect' of blood flow. *J. Am. Coll. Cardiol.* 41, 403–408 (2003).
- 77 Diamantopoulos L, Liu X, De Scheerder I *et al*. The effect of reduced blood-flow on the coronary wall temperature: are significant lesions suitable for intravascular thermography? 10.1016/S0195-668X(03)00440-00448. *Eur. Heart J.* 24, 1788–1795 (2003).
- 78 ten Have AG, Gijzen FJ, Wentzel JJ, Slager CJ, van der Steen AF. Temperature distribution in atherosclerotic coronary arteries: influence of plaque geometry and flow (a numerical study). *Phys. Med. Biol.* 49, 4447–4462 (2004).
- 79 Verheye S, De Meyer GRY, Krams R *et al*. Intravascular thermography: Immediate functional and morphological vascular findings. *Eur. Heart J.* 25, 158–165 (2004).
- 80 Correia LC, Atalar E, Kelemen MD *et al*. Intravascular magnetic resonance imaging of aortic atherosclerotic plaque composition. *Arterioscler. Thromb. Vasc. Biol.* 17, 3626–3632 (1997).
- 81 Larose E, Yeghiazarians Y, Libby P *et al*. Characterization of human atherosclerotic plaques by intravascular magnetic resonance imaging. *Circulation* 112, 2324–2331 (2005).
- 82 Blank A, Alexandrowicz G, Muchnik L *et al*. Miniature self-contained intravascular magnetic resonance (IVMI) probe for clinical applications. *Magn. Reson. Med.* 54, 105–112 (2005).
- 83 Regar E HB, Grube E, Halon D, Wilensky RL, Virmani R, Schneiderman J, Sax S, Friedmann H, Serruys PW, Wijns W. First-in-man application of a miniature self-contained intracoronary magnetic resonance probe. A multi-centre safety and feasibility trial. *Eurointervention* 2, 77–83 (2006).
- 84 Schneiderman J, Wilensky RL, Weiss A *et al*. Diagnosis of thin-cap fibroatheromas by a self-contained intravascular magnetic resonance imaging probe in *ex vivo* human aortas and *In situ* coronary arteries. *J. Am. Coll. Cardiol.* 45, 1961–1969 (2005).
- 85 Quick HH, Ladd ME, Hilfiker PR, Paul GG, Ha SW, Debatin JF. Autoperfused balloon catheter for intravascular MR imaging. *J. Magn. Reson. Imaging* 9, 428–434 (1999).
- 86 Barkhausen J, Ebert W, Heyer C, Debatin JF, Weinmann HJ. Detection of atherosclerotic plaque with Gadofluorine-enhanced magnetic resonance imaging. *Circulation* 108, 605–609 (2003).
- 87 Kooi ME, Cappendijk VC, Cleutjens KB *et al*. Accumulation of ultrasmall superparamagnetic particles of iron oxide in human atherosclerotic plaques can be detected by *In Vivo* magnetic resonance imaging. *Circulation* 107, 2453–2458 (2003).
- 88 Porto I, Selvanayagam J, Ashar V, Neubauer S, Banning AP. Safety of magnetic resonance imaging one to three days after bare metal and drug-eluting stent implantation. *Am. J. Cardiol.* 96, 366–368 (2005).
- 89 Moreno PR, Muller JE. Identification of high-risk atherosclerotic plaques: a survey of spectroscopic methods. *Curr. Opin. Cardiol.* 17, 638–647 (2002).
- 90 Brennan JF 3rd, Romer TJ, Lees RS, Tercyak AM, Kramer JR Jr, Feld MS. Determination of human coronary artery composition by Raman spectroscopy. *Circulation* 96, 99–105 (1997).
- 91 Baraga JJ, Feld MS, Rava RP. *In situ* optical histochemistry of human artery using near infrared fourier transform raman spectroscopy. *Proc. Natl Acad. Sci. USA* 89, 3473–3477 (1992).
- 92 Romer TJ, Brennan JF, Fitzmaurice M *et al*. Histopathology of human coronary atherosclerosis by quantifying its chemical composition with raman spectroscopy. *Circulation* 97, 878–885 (1998).
- 93 Romer TJ, Brennan JF, Puppels GJ *et al*. Intravascular ultrasound combined with raman spectroscopy to localize and quantify cholesterol and calcium salts in atherosclerotic coronary arteries. *Arterioscler. Thromb. Vasc. Biol.* 20, 478–483 (2000).
- 94 van de Poll SWE, Kastelijn K, Schut TCB *et al*. On-line detection of cholesterol and calcification by catheter based Raman spectroscopy in human atherosclerotic plaque *ex vivo*. *Heart* 89, 1078–1082 (2003).
- 95 Wang J, Geng YJ, Guo B *et al*. Near-infrared spectroscopic characterization of human advanced atherosclerotic plaques. *J. Am. Coll. Cardiol.* 39, 1305–1313 (2002).

- 96 Marcu L, Fishbein MC, Maarek JM, Grundfest WS. Discrimination of human coronary artery atherosclerotic lipid-rich lesions by time-resolved laser-induced fluorescence spectroscopy. *Arterioscler. Thromb. Vasc. Biol.* 21, 1244–1250 (2001).
- 97 Moreno PR, Lodder RA, Purushothaman KR, Charash WE, O'Connor WN, Muller JE. Detection of lipid pool, thin fibrous cap, and inflammatory cells in human aortic atherosclerotic plaques by near-infrared spectroscopy. *Circulation* 105, 923–927 (2002).
- 98 Caplan JD, Waxman S, Nesto RW, Muller JE. Near-infrared spectroscopy for the detection of vulnerable coronary artery plaques. *J. Am. Coll. Cardiol.* 47, C92–C96 (2006).
- 99 Waxman S, Ishibashi F, Caplan JD. Rationale and use of near-infrared spectroscopy for detection of lipid-rich and vulnerable plaques. *J. Nucl. Cardiol.* 14, 719–728 (2007).
- 100 Aoki J, Ong AT, Rodriguez Granillo GA *et al.* 'Full metal jacket' (stented length > =64 mm) using drug-eluting stents for de novo coronary artery lesions. *Am. Heart J.* 150, 994–999 (2005).
- 101 Wickline SA, Neubauer AM, Winter PM, Caruthers SD, Lanza GM. Molecular imaging and therapy of atherosclerosis with targeted nanoparticles. *J. Magn. Reson. Imaging* 25, 667–680 (2007).
- 102 Serruys PW, Hoye A, Grollier G, Colombo A, Symons J, Mudra H. A European multi-center trial investigating the anti-restenotic effect of intravascular sonotherapy after stenting of de novo lesions (EUROSPAH: European Sonotherapy Prevention of Arterial Hyperplasia). *Int. J. Cardiovasc. Intervent.* 6, 53–60 (2004).
- 103 Kandzari DE, Chu A, Brodie BR *et al.* Feasibility of endovascular cooling as an adjunct to primary percutaneous coronary intervention (results of the LOWTEMP pilot study). *Am. J. Cardiol.* 93, 636–639 (2004).
- 104 Chou TM, Woodburn KW, Cheong WF *et al.* Photodynamic therapy: applications in atherosclerotic vascular disease with motexafin lutetium. *Catheter Cardiovasc Interv* 57, 387–394 (2002).
- 105 Finn AV, Nakazawa G, Joner M *et al.* Vascular responses to drug eluting stents: importance of delayed healing. *Arterioscler. Thromb. Vasc. Biol.* 27, 1500–1510 (2007).
- 106 Slager CJ, Wentzel JJ, Gijssen FJ *et al.* The role of shear stress in the generation of rupture-prone vulnerable plaques. *Nat. Clin. Pract. Cardiovasc. Med.* 2, 401–407 (2005).
- 107 Slager CJ, Wentzel JJ, Gijssen FJ *et al.* The role of shear stress in the destabilization of vulnerable plaques and related therapeutic implications. *Nat. Clin. Pract. Cardiovasc. Med.* 2, 456–464 (2005).
- 108 Moreno PR, Kilpatrick D, Purushothaman KR, Coleman L, O'Connor WN. Stenting vulnerable plaques improves fibrous cap thickness and reduces lipid content: understanding alternatives for plaque stabilization. *TCT*(2002).
- 109 Kaluza G, Alviar CL, Tellez A, Kolodgie F, Virmani R, Granada JE. First *in-vivo* experience with a novel low-pressure self-expanding intraarterial shield: a one-month study comparing to balloon expandable stents in porcine coronary arteries. *TCT*(2007).
- 110 Aoki J, Serruys PW, van Beusekom H *et al.* Endothelial progenitor cell capture by stents coated with antibody against CD34: the HEALING-FIM (Healthy Endothelial Accelerated Lining Inhibits Neointimal Growth-First In Man) Registry. *J. Am. Coll. Cardiol.* 45, 1574–1579 (2005).

Affiliations

- Héctor M García-García MD, MSc
Thoraxcenter, Erasmus MC, Rotterdam, The Netherlands
Tel.: +31 104 632 917
Fax: +31 104 633 292
h.garciagarcia@erasmusmc.nl
- Nieves Gonzalo MD
Thoraxcenter, Erasmus MC, Rotterdam, The Netherlands
Tel.: +31 104 632 917
Fax: +31 104 633 292
m.gonzalolopez@erasmusmc.nl
- Evelyn Regar MD, PhD
Thoraxcenter, Erasmus MC, Rotterdam, The Netherlands
Tel.: +31 107 035 729
Fax: +31 107 032 357
e.regar@erasmusmc.nl
- Juan F Granada
Skirball Center for Cardiovascular Translational Research, The Cardiovascular Research Foundation, New York, NY, USA
jgranada@crf.org
- PW Serruys, MD, PhD
Professor, Thoraxcenter, Ba-583, Erasmus MC, Dr. Molewaterplein 40, 3015 GD Rotterdam, The Netherlands
Tel.: +31 104 635 260
Fax: +31 104 369 154
p.w.j.c.serruys@erasmusmc.nl



5.2

In Vivo Assessment of High-risk Plaques at Bifurcations with Combined Intravascular Ultrasound Virtual Histology and Optical Coherence Tomography.

Gonzalo N, Garcia-Garcia HM, Regar E, Barlis P, Wentzel J, Onuma Y, Lighthart J, Serruys P.W.

J. Am. Coll. Cardiol. Img. 2009;473-482

In Vivo Assessment of High-Risk Coronary Plaques at Bifurcations With Combined Intravascular Ultrasound and Optical Coherence Tomography

Nieves Gonzalo, MD, Hector M. Garcia-Garcia, MD, MSc, Evelyn Regar, MD, PhD, Peter Barlis, MBBS, MPH, Jolanda Wentzel, PhD, Yoshinobu Onuma, MD, Jurgen Ligthart, BSc, Patrick W. Serruys, MD, PhD

Rotterdam, the Netherlands

OBJECTIVES This study sought to evaluate the in vivo frequency and distribution of high-risk plaques (i.e., necrotic core rich) at bifurcations using a combined plaque assessment with intravascular ultrasound–virtual histology (IVUS-VH) and optical coherence tomography (OCT).

BACKGROUND Pathological examinations have shown that atherosclerotic plaque rich in necrotic core is prone to develop at bifurcations. High-risk plaque detection could be improved by the combined use of a technique able to detect necrotic core (IVUS-VH) and a high-resolution technique that allows the measurement of the fibrous cap thickness (OCT).

METHODS From 30 patients imaged with IVUS-VH and OCT, 103 bifurcations were selected. The main branch was analyzed at the proximal rim of the ostium of the side branch, at the in-bifurcation segment and at the distal rim of the ostium of the side branch. Plaques with more than 10% confluent necrotic core by IVUS-VH were selected and classified as fibroatheroma (FA) or thin-cap fibroatheroma (TCFA) depending on the thickness of the fibrous cap by OCT (>65 or ≤ 65 μm for FA and TCFA, respectively).

RESULTS Twenty-seven FA (26.2%) and 18 TCFA (17.4%) were found out of the 103 lesions studied. Overall the percentage of necrotic core decreases from proximal to distal rim (16.8% vs. 13.5% respectively, $p = 0.01$), whereas the cap thickness showed an inverse tendency (130 ± 105 μm vs. 151 ± 68 μm for proximal and distal rim, respectively, $p = 0.05$). The thin caps were more often located in the proximal rim (15 of 34, 44.1%), followed by the in-bifurcation segment (14 of 34, 41.2%), and were less frequent in the distal rim (5 of 34, 14.7%).

CONCLUSIONS The proximal rim of the ostium of the side branch has been identified as a region more likely to contain thin fibrous cap and a greater proportion of necrotic core. (J Am Coll Cardiol Img 2009;2:473–82) © 2009 by the American College of Cardiology Foundation

From the Thoraxcenter, Erasmus Medical Center, Rotterdam, the Netherlands.

Manuscript received September 30, 2008; revised manuscript received November 10, 2008, accepted November 16, 2008.

High-risk atherosclerotic plaques (i.e., rich in necrotic core) are prone to develop at bifurcations because of the specific shear stress conditions present in these regions (1,2). Stented bifurcations lesions represent a complex lesion subset at high risk of restenosis and thrombosis (3,4). These phenomena may reflect certain procedural aspects such as incomplete stent apposition, underexpansion, or gap regions (5,6), but may also be asso-

See page 483

ciated with specific compositional and morphological plaque features in these regions. Thin-cap fibroatheroma (TCFA) has been described as the plaque with an increased risk of rupture (7). Such lesions are characterized by a large necrotic core with a thin fibrous cap, usually $<65 \mu\text{m}$ in thickness (8). Recently, it has been reported that TCFA detection could be improved by the combined use of intravascular ultrasound-virtual histology (IVUS-VH) and optical coherence tomography (OCT) (9).

IVUS-VH uses spectral analysis of IVUS radiofrequency data to identify 4 tissue types in the atherosclerotic plaque, among them necrotic core (10). Optical coherence tomography is a high-resolution imaging modality that uses reflected near-infrared light, allowing a very precise visualization and measurement of vascular microstructures such as the fibrous cap (11). To our knowledge, in vivo characterization of necrotic core rich plaques at bifurcation regions has not been explored. The objective of the present study was therefore to evaluate in vivo the frequency and distribution of high-risk plaques at bifurcation lesions using a combined plaque assessment with IVUS-VH and OCT.

METHODS

Study population. All of the patients admitted to our hospital between January 2005 and March 2008 in whom IVUS-VH and OCT were performed in the same vessel were investigated for bifurcations adequately visualized by both imaging techniques. The indication for the IVUS-VH and OCT was the assessment of intermediate, nonflow-limiting lesions by angiography or post stent implantation assessment. Only regions located more than 5 mm

beyond the stent were included. All patients gave written informed consent.

IVUS-VH acquisition. The IVUS was performed using the Eagle Eye 20 MHz catheter (Volcano Corp., Rancho Cordova, California) with an automatic continuous pullback at a rate of 0.5 mm/s. Grayscale images and radiofrequency data required for VH analysis were acquired during the same pullback. The VH processing was performed offline with pcVH 2.1 software (Volcano Corp.) that permits semiautomated contour detection and provides the compositional structure of the vessel. The IVUS-VH uses spectral analysis to classify the 4 different components of the atherosclerotic plaque and gives a color-coded map distinguishing between fibrous tissue (green), fibrofatty tissue (light green), necrotic core (red), and dense calcium (white).

OCT acquisition. The OCT acquisition was performed using a commercially available system for intracoronary imaging and a 0.019-inch ImageWire (LightLab Imaging, Westford, Massachusetts). Red blood cells represent a nontransparent tissue causing multiple light scattering and substantial signal attenuation. Therefore, for adequate OCT image acquisition blood must be temporarily removed from the vessel. In 77% of the cases this was achieved with the occlusion technique in which a proximal, low-pressure (0.4 atm) occlusion balloon (Helios, Goodman Inc., Nagoya, Japan) is inflated with simultaneous distal flush delivery (lactated Ringer solution; flow rate 0.8 ml/s) to remove blood from the vessel lumen. Images were acquired during a pullback rate of 1.0 mm/s. The possibility to increase the pullback speed up to 3 mm/s in the new OCT system permitted 23% of the cases to be acquired exclusively using a nonocclusive technique in which the blood was removed by the continuous injection of contrast (Iodixanol 370, Visipaque, GE Health Care, Cork, Ireland) through the guiding catheter. The nonocclusive technique reduces the procedural time and the incidence of chest pain and electrocardiographic changes during image acquisition without affecting the image quality (12).

Bifurcation selection and analysis. Simultaneous visual assessment of IVUS-VH and OCT pullbacks, in 2 contiguous screens, allowed the selection of all bifurcations that could be identified with both techniques (13). To ensure proper matching between 2 imaging modalities that have different lateral resolutions ($20 \mu\text{m}$ for OCT and $300 \mu\text{m}$ for IVUS) and depth penetration, a strict selection of the frames was followed. Only the main branch was analyzed. The lesion analysis included: 1) proximal

ABBREVIATIONS AND ACRONYMS

ACS = acute coronary syndrome
AIT = adaptive intimal thickening
CaFA = calcified fibroatheroma
CaTCFA = calcified thin-cap fibroatheroma
FA = fibroatheroma
IVUS-VH = intravascular ultrasound-virtual histology
LAD = left anterior descending artery
LCX = left circumflex artery
MMP = matrix metalloproteinase
NC = necrotic core
OCT = optical coherence tomography
PIT = pathological intimal thickening
RCA = right coronary artery
TCFA = thin-cap fibroatheroma

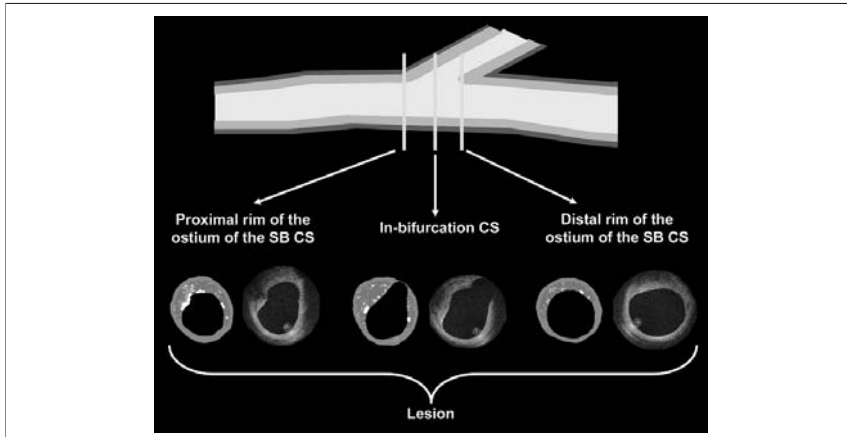


Figure 1. Bifurcation Selection and Analysis

Bifurcations that could be identified in both intravascular ultrasound-virtual histology (IVUS-VH) and optical coherence tomography (OCT) pullbacks were included. A strict selection of the analyzed cross-sections (CS) was followed to ensure correct matching between the 2 techniques. Plaques were analyzed only in the main branch. The lesion analysis included: 1) proximal rim of the ostium of the side branch (SB) CS (first frame proximal to the take-off of the SB); 2) in-bifurcation CS (frame with the larger ostial diameter of the SB); and 3) distal rim of the ostium of the SB CS (first frame distal to the take off of the SB).

rim of the ostium of the side branch cross-section (first frame proximal to the take-off of the side branch); 2) in-bifurcation cross-section (frame with the larger ostial diameter of the side branch); and 3) distal rim of the ostium of the side branch cross-section (first frame distal to the take off of the side branch) (Fig. 1). In each bifurcation the plaque location in relation to the flow divider was analyzed (Fig. 2).

Plaque type classification. Two experienced observers jointly analyzed the IVUS-VH data and the OCT measurements in the selected frames to characterize the plaque type according to the following hierarchical classification (7,14,15) (Figs. 3 to 5):

1. Adaptive intimal thickening (AIT): intimal thickening of $<600 \mu\text{m}$ for $<20\%$ of the circumference.

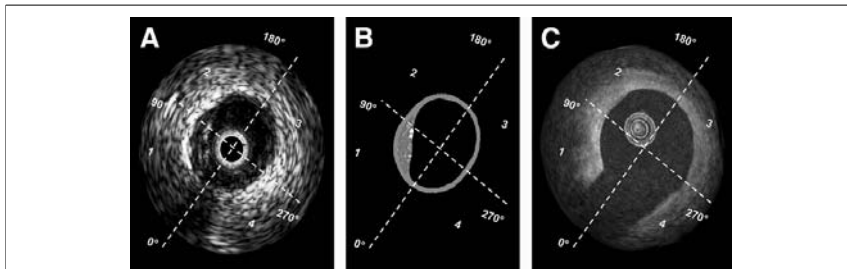
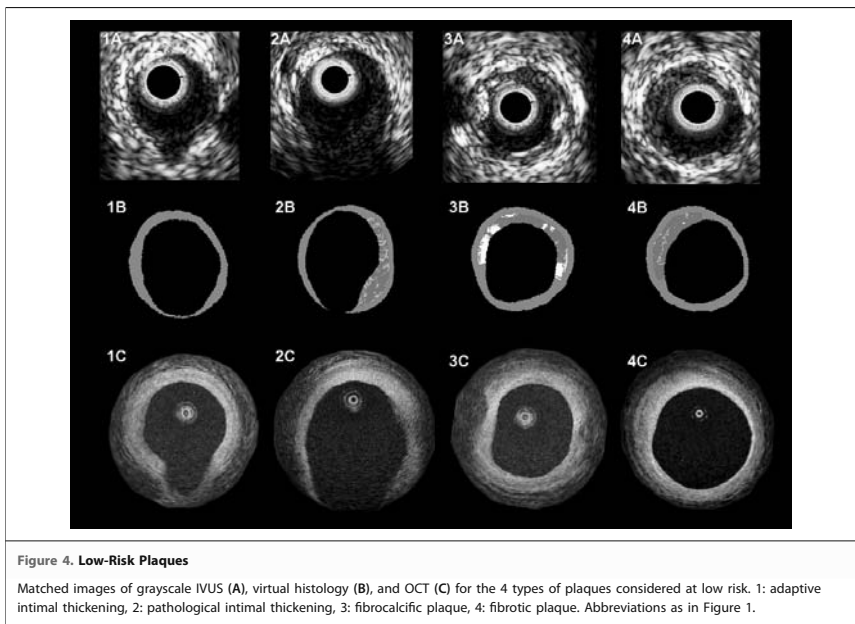
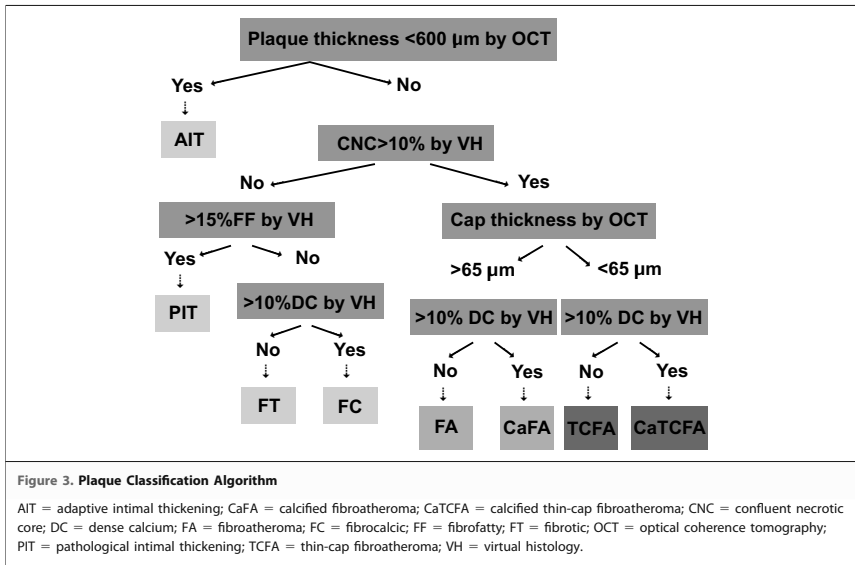
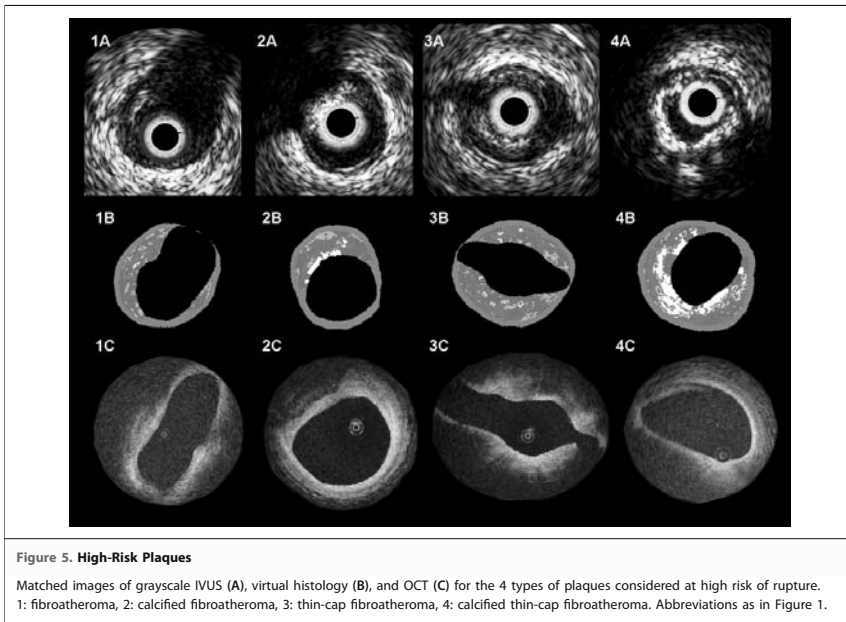


Figure 2. Location of the Plaque in Relation to the Flow Divider

To describe the plaque location in relation to the flow divider, the vessel cross-section was divided in 4 quadrants according to the position of the side branch. Quadrants 1 and 4 correspond to the ostium of the side branch, whereas quadrants 2 and 3 correspond to the part of the vessel wall located in front of the ostium of the side branch. (A) Grayscale IVUS. (B) Virtual histology. (C) OCT. Abbreviations as in Figure 1.





2. Pathological intimal thickening (PIT): intimal thickening $\geq 600 \mu\text{m}$ for more than 20% of the circumference with more than 15% of fibrofatty tissue, and no confluent necrotic core or dense calcium.
3. Fibrotic plaque: plaque constituted predominantly by fibrous tissue without confluent necrotic core (NC) or dense calcium.
4. Fibrocalcific plaque: more than 10% of confluent dense calcium without confluent NC.
5. Fibroatheroma (FA): plaque characterized by the presence of more than 10% confluent NC covered by a fibrous cap thicker than $65 \mu\text{m}$.
6. Calcified fibroatheroma (CaFA): fibroatheroma that contains more than 10% of confluent dense calcium.
7. IVUS/OCT-derived thin-capped fibroatheroma (TCFA): defined as the presence of more than 10% confluent NC at the lumen covered by a thin fibrous cap ($< 65 \mu\text{m}$).
8. IVUS/OCT-derived calcified thin-capped fibroatheroma (CaTCFA): TCFA that contains more than 10% of confluent dense-calcium.

FAs and TCFA are considered high-risk plaques in American Heart Association and Virmani classifications (7,16). The necrotic core was considered

confluent when it was forming a major pool. This definition was used to avoid misclassification as high-risk plaques of lesions with isolated islets or individual pixels of necrotic core, which can be artifacts. The presence of confluent NC $> 10\%$ at the lumen was measured using dedicated in house developed software (MATLAB MathWorks, Natick, Massachusetts) (9). A validation with pathology of a similar algorithm was reported in the CAPITAL (Carotid Artery Plaque Virtual Histology Evaluation) study (14). The diagnostic accuracy of IVUS-VH compared with histology in different carotid plaque types was 99.4% for TCFA, 96.1% for CaTCFA, 85.9% in FA, 85.5% for fibrocalcific, 83.4% in PIT, and 72.4% for CaFA. To overcome the limitations of IVUS-VH in the fibrous cap evaluation, the classification used in our study combines the information about plaque composition provided by IVUS-VH and the measurements of fibrous cap as assessed by OCT (9). The thinnest part of the fibrous cap was measured by OCT in all the plaques that contain more than 10% of confluent NC to distinguish between FA and TCFA. The fibrous cap measurement by OCT was guided by the IVUS-VH to avoid misclassification between lipid pools and calcium. The cap was measured in the area where the NC was closer to the lumen. The repro-

ducibility of fibrous cap measurements has previously been reported (12). If different morphologies were present along the lesion, the highest degree plaque was established as the definite plaque type.

Statistical analysis. Statistical analyses were performed using SPSS 12.0.1 for Windows (SPSS Inc., Chicago, Illinois). Continuous variables are expressed as mean \pm SD. Categorical variables are expressed as percentages. The bifurcation (lesion) was the unit of analysis without corrections for correlated observations in the same subjects. To compare continuous variables between lesions, *t* test or analysis of variance was used. To compare continuous variables between different segments of the bifurcation, paired samples *t* test or Wilcoxon signed ranks test for 2 dependent samples was used. Comparison among groups for categorical variables was made with the chi-square method.

RESULTS

Clinical and procedural characteristics. One hundred and three bifurcations were selected in 32 pullbacks performed in 30 patients. The mean age was 60 ± 7 years, and 73% were male. Regarding cardiac risk factors, 48.3%, 6.9%, and 72.4% had hypertension, diabetes mellitus, and hyperlipidemia, respectively, and 27.6% were smokers. Seven percent had prior myocardial infarction, and 43.3% had undergone a prior percutaneous coronary intervention. The clinical presentation was stable angina in 86.7%, unstable angina in 10%, and acute myocardial infarction in 3.3%. The investigated vessel was the left anterior descending artery (LAD) in 34%, left circumflex artery (LCX) in 33% and right coronary artery (RCA) in 33% of the cases. The type of bifurcations studied were LAD/diagonal, LAD/septal branch, LCX/marginal, and RCA/right ventricular branch in 21.4%, 12.6%, 33%, and 33% of the cases, respectively. The indication for IVUS-VH and OCT was assessment of intermediate, non-flow limiting lesions by angiography in 40% of the cases and post-stent implantation assessment in the remaining 60% of cases. All studied lesions were considered nonsignificant by angiographic criteria and had a lumen area >4 mm² by IVUS. Overall the mean vessel and lumen area and plaque burden were 13.9 ± 3.7 mm², 7.7 ± 2.2 mm², and $43.2 \pm 13\%$, respectively. Table 1 shows the number of quadrants containing plaque and the location of the thickest part of the plaque in relation to the side branch.

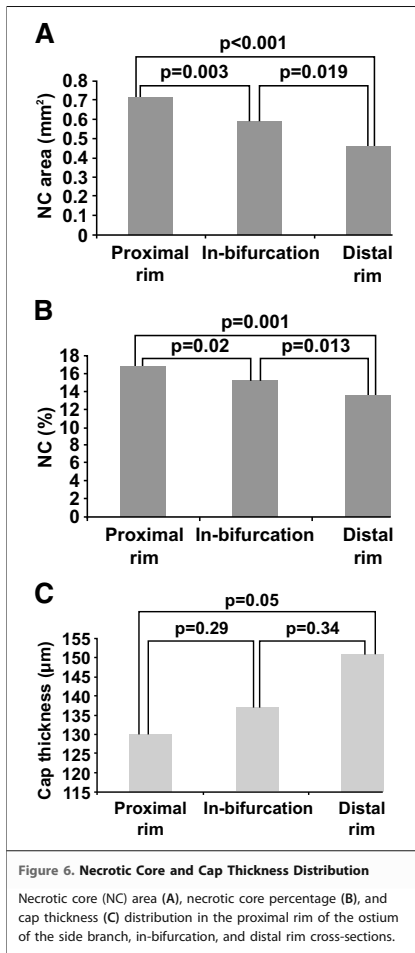
Table 1. Number of Quadrants Containing Plaque and Location of the Thickest Part of the Plaque in Relation to the Flow Divider

Number of quadrants containing plaque	
1	25/103 (24.3%)
2	33/103 (32.0%)
3	29/103 (28.2%)
4	16/103 (15.5%)
Location of the thickest part of the plaque	
Quadrant 1	28/103 (27.2%)
Quadrant 2	18/103 (17.5%)
Quadrant 3	26/103 (25.2%)
Quadrant 4	31/103 (30.1%)

Frequency of plaque type. The plaque type was analyzed in 103 lesions and 293 cross-sections. Eight distal and 8 proximal rims could not be analyzed because of artifacts. Overall, the frequency of each plaque type per lesion was: AIT 20 (19.4%), PIT 16 (15.5%), fibrocalcific 15 (14.6%), fibrotic 7 (6.8%), FA 8 (7.8%), CaFA 19 (18.4%), TCFA 10 (9.7%), and CaTCFA 8 (7.8%). In the analyzed cross-sections the distribution was as follows: AIT 76 (25.9%), PIT 53 (18.1%), fibrocalcific 42 (14.3%), fibrotic 28 (9.6%), FA 18 (6.1%), CaFA 42 (14.3%), TCFA 21 (7.2%), and CaTCFA 13 (4.4%).

NC and cap thickness distribution. The NC and cap thickness distribution in the proximal rim, in-bifurcation, and distal rim cross-sections are shown in Figure 6. Overall, the mean NC area and mean percentage of NC decreased from proximal to distal, whereas the mean cap thickness showed an inverse tendency.

High-risk plaque distribution and compositional and geometrical analysis. The distribution of the different plaque types in relation to the location is shown in Table 2. Figure 7 shows the number of cross-sections with high-risk plaque morphology in the proximal rim, in-bifurcation, and distal rim. The thin caps were more often located in the proximal rim (15 of 34, 44.1%), followed by the in-bifurcation (14 of 34, 41.2%), and were less frequent in the distal rim (5 of 34, 14.7%). The location of the thin cap in the 18 lesions classified as TCFAs was as follows: In 4 cases the thinning of the cap extended from the proximal rim into the distal rim, in 7 cases the thin cap was located in the proximal rim and in the in-bifurcation; in 3 TCFAs the thinning of the cap was located only in the in-bifurcation and, in 3 cases only in the proximal rim; there was 1 TCFA that presented the thin cap at both rims whereas the cap at the



in-bifurcation frame was thicker. There were no cases in which the thin cap was located only in the distal rim. The mean cap thickness in proximal rim,

in-bifurcation, and distal rim in TCFA is shown in Figure 8.

The vessel area and the plaque burden was significantly greater in the subgroup of lesions considered high risk (FA, CaFA, TCFA, and CaTCFA) than in the rest of lesions ($16.5 \pm 3 \text{ mm}^2$ vs. $14.1 \pm 3 \text{ mm}^2$, $p = 0.002$ and $55 \pm 9\%$ vs. $42 \pm 12\%$, $p < 0.001$ for vessel area and plaque burden, respectively), whereas the lumen area was not significantly different ($6.8 \pm 2 \text{ mm}^2$ vs. $7.1 \pm 2 \text{ mm}^2$, $p = 0.39$). Table 3 shows the plaque burden, NC percentage, and cap thickness in FA, CaFA, TCFA, and CaTCFA.

Plaque type in relation to the clinical presentation. As exploratory analysis, patients with acute coronary syndromes (ACS) had a significant higher proportion of lesions with high-risk morphology plaques than stable patients (17 of 23 [73.9%] vs. 28 of 80 [35%], $p = 0.002$). Specifically the number of lesions with TCFA morphology was 6 of 23 (26.1%) vs. 12 of 80 (15%), $p = 0.2$, for ACS and stable patients respectively, and the number of lesions with FA morphology was 11 of 23 (47.8%) vs. 16 of 80 (20%), $p = 0.01$, for ACS and stable patients respectively.

DISCUSSION

To our knowledge this is the first in-vivo study evaluating the frequency and distribution of high-risk plaques at bifurcations in coronary arteries using a combined plaque assessment with IVUS-VH and OCT. The main finding is that the thinning of the fibrous cap occurs more often in the proximal rim of the ostium of the side branch. The NC shows also a differential distribution along the bifurcation being higher at the proximal rim.

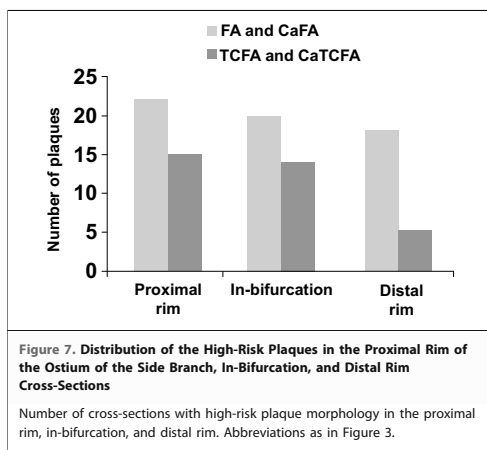
Multi-modality plaque assessment. The detection of plaques at potentially high risk of rupture could prevent future occurrence of ACS. At present, multiple techniques are available that evaluate different aspects of the atherosclerotic plaque, such as its structure, composition, or mechanical properties (17). The combined information pro-

Table 2. Distribution of the Different Plaque Types in the Proximal Rim of the Ostium of the Side Branch, In-Bifurcation, and Distal Rim Cross Sections

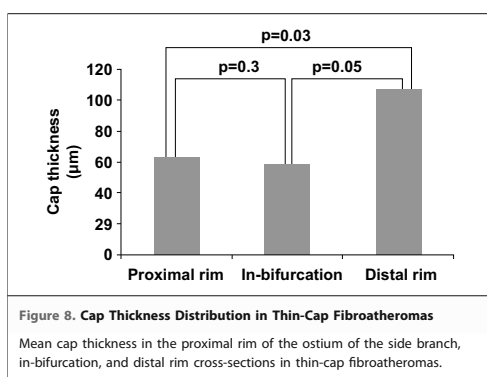
	AIT	PIT	FC	FT	FA	CaFA	TCFA	CaTCFA	Total
Proximal rim	21 (22.1%)	19 (20%)	13 (13.7%)	5 (5.3%)	8 (8.4%)	14 (14.7%)	10 (10.5%)	5 (5.3%)	95
In-bifurcation	24 (23.3%)	18 (17.5%)	15 (14.6%)	12 (11.7%)	5 (4.9%)	15 (14.6%)	8 (7.8%)	6 (5.8%)	103
Distal rim	31 (32.6%)	16 (16.8%)	14 (14.7%)	11 (11.6%)	5 (5.3%)	13 (13.7%)	3 (3.2%)	2 (2.1%)	95

N = 293 cross-sections.

AIT = adaptative intimal thickening; CaFA = calcified fibroatheroma; CaTCFA = calcified thin-cap fibroatheroma; FA = fibroatheroma; FC = fibrocalcic; FT = fibrotic; PIT = pathological intimal thickening; TCFA = thin-cap fibroatheroma.



vided by the different methods is essential for better identification of high-risk coronary lesions. In this study, a combined approach with IVUS-VH and OCT was used. The IVUS-VH allows the detection and quantification of NC, one of the main components of high-risk plaques. However, the limited axial resolution of IVUS (approximately 200 μm) does not permit an accurate evaluation of the fibrous cap. On the contrary, OCT has a very high resolution (10 to 20 μm), allowing a very precise measurement of the fibrous cap. Sawada et al. (9) recently reported that the combined use of IVUS-VH and OCT improved the accuracy for TCFA detection. They studied 126 plaques in 56 patients with angina. Of the 61 plaques diagnosed as TCFA by IVUS-VH criteria, only 28 had a thin fibrous cap, as measured by OCT. In addition, 8



OCT-derived TCFA did not have NC in the VH analysis, mainly because of the misinterpretation in the OCT analysis caused by dense calcium. This source of error in plaque characterization by OCT has previously been described and indicates the difficulty in identifying TCFA using only OCT (18). To avoid this misclassification in our study, the measurement of the fibrous cap in OCT was guided by IVUS-VH. At the present stage neither modality independently is sufficient for detecting the highest risk plaques; the combined approach seems to be mandatory for the accurate diagnosis of TCFA *in vivo*.

High-risk plaque frequency, distribution, composition, and geometrical analysis. The *in vivo* frequency of TCFA at bifurcations is not known. In our study, in which a highly selected population was included, 18 of 103 bifurcations presented TCFA (17%). Considering that the number of bifurcations in the complete coronary tree is approximately 15 (19), the frequency of TCFA per heart would be approximately 2.5. This is in agreement with reported pathological data (1). The bifurcation left main/LAD has been studied with IVUS-VH showing that the plaque burden and the amount of necrotic core are higher in the LAD than in the left main artery. However, plaque morphology in the different segments of other bifurcations has not been previously evaluated *in vivo*. The present study, which extended the assessment of bifurcation lesions beyond the left main artery, showed that the amount of necrotic core is higher at the proximal rim of the ostium of the side branch with a thin fibrous cap more often identified in the proximal rim. The fibrous cap thickness is determined by the balance between matrix synthesis by the smooth muscle cells and matrix degradation by metalloproteinases (MMP) produced by macrophages (20). It has been shown that the distribution of inflammatory cells in atherosclerotic plaques relates to the direction of the flow with higher concentration of macrophages and MMP activity in the upstream or proximal part (21). One of the mechanisms that have been proposed for the differential distribution of the high-risk plaques along the artery is the influence of endothelial shear stress. Bifurcations are geometrically irregular regions in which disturbed laminar flow occurs, generating abnormal endothelial shear stress patterns that may play a role in plaque destabilization. Previous studies showed that atherosclerosis develops preferentially at low shear stress locations such as the outer wall of bifurcations (2). However, in our data the thickest part of the plaque did not show a preferential location for this region.

Table 3. PB and NC Percent and Cap Thickness in FA, CaFA, TCFA, and CaTCFA

	FA (n = 8)	CaFA (n = 19)	TCFA (n = 10)	CaTCFA (n = 8)	p Value
PB (%)	51.7 ± 11	53.7 ± 10	54.2 ± 6	61.8 ± 5	0.13
NC (%)	20.1 ± 5.3	27.1 ± 6	33.0 ± 8	31.7 ± 8	0.002
Cap thickness (µm)	165 ± 59	174 ± 88	49 ± 15	51 ± 13	<0.001

NC = necrotic core; PB = plaque burden; other abbreviations as in Table 2.

Different pathological and IVUS studies have confirmed that plaque rupture occurs usually at sites of significant plaque accumulation associated with positive remodeling (2,22). This is in agreement with our data showing that the vessel area and the plaque burden were higher in high-risk plaques compared with stable lesions. In line with pathological series, TCFA in our study were located in areas with nonsignificant lumen compromise, with a mean luminal area of $6.8 \pm 2 \text{ mm}^2$ (8). Similarly, NC in TCFA in this population is concordant with previously published pathological findings (8).

High-risk plaques in relation to clinical presentation.

Although the comparison between ACS and stable patients in this study was exploratory, patients with unstable clinical presentation showed a high-risk profile of plaque types at bifurcations with a higher proportion of TCFA and FA. This is in agreement with previous data regarding TCFA detection with IVUS-VH showing that ACS patients present a significantly higher prevalence of IVUS-derived TCFA than stable patients (10).

Study limitations. Currently VH-derived necrotic core rich plaques can only be considered as allegedly high-risk lesions because it has not been shown

whether they are associated with a higher incidence of clinical events at follow-up. In the present study, OCT and VH were restricted to 1 or 2 vessels; therefore, and unlike pathological studies, this does not allow us to draw conclusions on the incidence of TCFA in bifurcations within the complete coronary tree. No comparison with nonbifurcation lesions was performed. Still the detailed plaque assessment combining 2 imaging modalities has given the first insight into the distribution of these allegedly high-risk lesions at bifurcations.

CONCLUSIONS

This study has given unique, in vivo data on the localization of plaque occurring at bifurcation lesions. Further, the proximal rim of the ostium of the side branch has been identified as a region more likely to contain thin fibrous cap and a greater proportion of necrotic core.

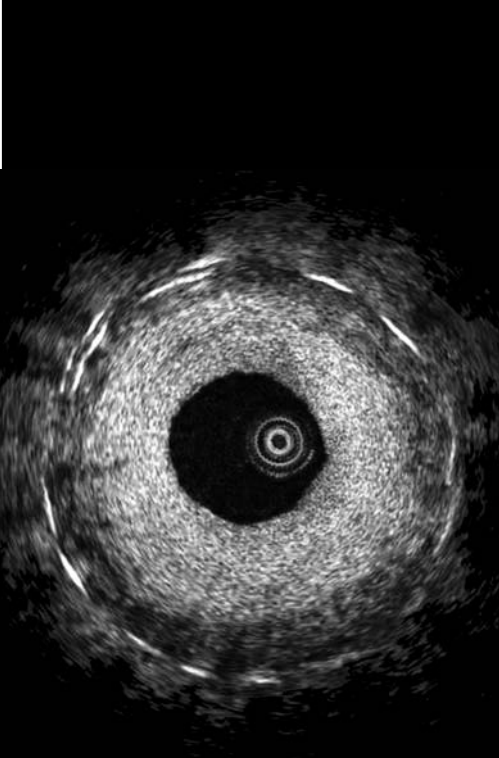
Reprint requests and correspondence: Prof. Patrick W. Serruys, Thoraxcenter, Ba583a, Gravenijckwal 230, 3015 CE Rotterdam, the Netherlands. E-mail: p.w.f.c.serruys@erasmusmc.nl.

REFERENCES

- Virmani R, Burke A, Farb A, Kolodgie FD, Finn AV, Gold HK. Pathology of the vulnerable plaque. In: Waksman R, Serruys PW, Schaar J, editors. *The Vulnerable Plaque*. London, UK: Informa Healthcare, 2007: 13–27.
- Slager CJ, Wentzel JJ, Gijzen FJ, et al. The role of shear stress in the generation of rupture-prone vulnerable plaques. *Nat Clin Pract Cardiovasc Med* 2005;2:401–7.
- Al Suwaidi J, Berger PB, Rihal CS, et al. Immediate and long-term outcome of intracoronary stent implantation for true bifurcation lesions. *J Am Coll Cardiol* 2000;35:929–36.
- Iakovou I, Schmidt T, Bonizzi E, et al. Incidence, predictors, and outcome of thrombosis after successful implantation of drug-eluting stents. *JAMA* 2005;293:2126–30.
- Costa RA, Mintz GS, Carlier SG, et al. Bifurcation coronary lesions treated with the “crush” technique: an intravascular ultrasound analysis. *J Am Coll Cardiol* 2005;46:599–605.
- Alfonso F, Suarez A, Perez-Vizcaino MJ, et al. Intravascular ultrasound findings during episodes of drug-eluting stent thrombosis. *J Am Coll Cardiol* 2007;50:2095–7.
- Virmani R, Kolodgie FD, Burke AP, Farb A, Schwartz SM. Lessons from sudden coronary death: a comprehensive morphological classification scheme for atherosclerotic lesions. *Arterioscler Thromb Vasc Biol* 2000;20:1262–75.
- Virmani R, Burke AP, Farb A, Kolodgie FD. Pathology of the vulnerable plaque. *J Am Coll Cardiol* 2006;47:C13–8.
- Sawada T, Shite J, Garcia-Garcia HM, et al. Feasibility of combined use of intravascular ultrasound radiofrequency data analysis and optical coherence tomography for detecting thin-cap fibroatheroma. *Eur Heart J* 2008;29:1136–46.
- Rodriguez-Granillo GA, Garcia-Garcia HM, Mc Fadden EP, et al. In vivo intravascular ultrasound-derived thin-cap fibroatheroma detection using ultrasound radiofrequency data analysis. *J Am Coll Cardiol* 2005;46:2038–42.
- Kume T, Akasaka T, Kawamoto T, et al. Measurement of the thickness of the fibrous cap by optical coherence tomography. *Am Heart J* 2006;152: 7551–4.
- Prati F, Cera M, Ramazzotti V, et al. From bench to bedside: a novel technique of acquiring OCT images. *Circ J* 2008;72:839–43.

13. Bruining N, Verheye S, Knaepen M, et al. Three-dimensional and quantitative analysis of atherosclerotic plaque composition by automated differential echogenicity. *Catheter Cardiovasc Interv* 2007;70:968–78.
14. Diethrich EB, Margolis P, Reid DB, et al. Virtual histology intravascular ultrasound assessment of carotid artery disease: The Carotid Artery Plaque Virtual Histology Evaluation (CAPITAL) study. *J Endovasc Ther* 2007;14:676–86.
15. Garcia-Garcia HM, Gonzalo N, Barlis P, Serruys PW. Novel intravascular imaging technologies. In: Nicholls S, Worthley S, editors. *Imaging in Clinical Management*. Sudbury, MA: Jones and Bartlett, 2009.
16. Stary HC, Chandler AB, Dinsmore RE, et al. A definition of advanced types of atherosclerotic lesions and a histological classification of atherosclerosis. *Arterioscler Thromb Vasc Biol* 1995;15:1512–31.
17. Garcia-Garcia HM, Gonzalo N, Granada JF, Regar E, Serruys PW. Diagnosis and treatment of coronary vulnerable plaques. *Expert Rev Cardiovasc Ther* 2008;6:209–22.
18. Manfrini O, Mont E, Leone O, et al. Sources of error and interpretation of plaque morphology by optical coherence tomography. *Am J Cardiol* 2006;98:156–9.
19. Scanlon PJ, Faxon DP, Audet AM, et al. ACC/AHA guidelines for coronary angiography. A report of the American College of Cardiology/American Heart Association Task Force on practice guidelines (Committee on Coronary Angiography). *J Am Coll Cardiol* 1999;33:1756–824.
20. Shah PK, Falk E, Badimon JJ, et al. Human monocyte-derived macrophages induce collagen breakdown in fibrous caps of atherosclerotic plaques. Potential role of matrix-degrading metalloproteinases and implications for plaque rupture. *Circulation* 1995;92:1565–9.
21. Dirksen MT, van der Wal AC, van den Berg FM, van der Loos CM, Becker AE. Distribution of inflammatory cells in atherosclerotic plaques relates to the direction of flow. *Circulation* 1998;98:2000–3.
22. Cunningham KS, Gotlieb AI. The role of shear stress in the pathogenesis of atherosclerosis. *Lab Invest* 2005;85:9–23.

Key Words: high-risk coronary plaques ■ optical coherence tomography ■ IVUS virtual histology ■ bifurcation.



5.3

Assessment of Culprit and Remote Coronary Narrowings Using Optical Coherence Tomography with Long-Term Outcomes.

Barlis P, Serruys P.W, Gonzalo N, Van der Giessen W, Jaegere P.J, Regar E.

Am J Cardiol. 2008 Aug 15;102(4):391-5.

Assessment of Culprit and Remote Coronary Narrowings Using Optical Coherence Tomography With Long-Term Outcomes

Peter Barlis, MBBS, MPH, Patrick W. Serruys, MD, PhD, Nieves Gonzalo, MD, Willem J. van der Giessen, MD, PhD, Peter J. de Jaegere, MD, PhD, and Evelyn Regar, MD, PhD*

Much currently known information about vulnerable plaque stems from postmortem studies that identified several characteristics making them prone to rupture, including the presence of a thin fibrous cap and a large lipid core. This study used optical coherence tomography (OCT) to assess culprit and remote coronary narrowings and investigate whether intracoronary OCT in living patients was able to visualize morphologic features associated with vulnerable plaque in postmortem studies. Twenty-three patients successfully underwent OCT before percutaneous coronary intervention. The culprit lesion and mild to moderate coronary narrowings remote from the target stenosis were investigated. Using OCT, the culprit lesion was found to be fibrous in 39.1%, fibrocalcific in 34.4%, and lipid rich in 26.1% of cases. Two patients met criteria for thin-cap fibroatheroma (TCFA; defined as the presence of a signal-rich fibrous cap covering a signal-poor lipid/necrotic core with cap thickness <0.2 mm). Most plaques at remote segments were proximal to the culprit lesion (73.9%) and predominantly fibrous and lipid rich. OCT identified 7 TCFA lesions in 6 patients with a mean cap thickness of 0.19 ± 0.05 mm, extending for $103^\circ \pm 49^\circ$ of the total vessel circumference. At 24 months of clinical follow-up, the only event occurred in a patient with in-stent restenosis who underwent repeated percutaneous revascularization. There were no clinically apparent plaque rupture-related events in the 6 patients found to have remote TCFA. This study showed that OCT can be safely applied to image beyond the culprit lesion and can detect in vivo morphologic features associated with plaque vulnerability using retrospective pathologic examination. In conclusion, detection of TCFA, particularly in stable patients, is desirable and may principally allow for early intervention and prevention of adverse events. © 2008 Elsevier Inc. All rights reserved. (Am J Cardiol 2008;102:391–395)

Acute coronary syndromes (ACSs), including myocardial infarction (MI), are leading causes of death in industrialized countries, often caused by rupture of vulnerable plaque (VP). Detection of VP in the early phase of coronary artery disease therefore is essential to limit morbidity and mortality while helping target specific therapeutic interventions. Using retrospective postmortem studies, several characteristics of plaques that are prone to rupture were identified, including the presence of a thin fibrous cap (<65 μm thick), large lipid core, and activated macrophages near the cap. However, the limitation of such studies was their inability to provide crucial detail regarding the natural history and progression of VP and therefore the prognosis. Several imaging modalities have been used to assess and identify VP, including coronary angiography, intravascular ultrasound, and magnetic resonance imaging.^{1–3} Recently, there has been significant interest in the field of VP detection using optical coherence tomography (OCT)^{1,4–13} because it permits high-resolution (10 to 20 μm) imaging, principally suited to detect and quantify the thickness of a thin cap fibroatheroma

(TCFA) and estimate macrophage distribution.^{9,14,15} In this study, we investigated whether intracoronary OCT in living patients was able to visualize morphologic features associated with VP in postmortem studies.

Methods

From February to August 2004, this single-center observational pilot study examined patients with coronary artery disease. Twenty-three patients scheduled for coronary stent implantation underwent OCT before angioplasty. The culprit lesion and mild to moderate coronary lesions remote from the target stenosis were investigated. Patients were selected based on the presence of stable or unstable angina pectoris with objective evidence of ischemia. Clinical exclusion criteria were poor renal function (serum creatinine >1.5 mg/dl), left ventricular ejection fraction $<30\%$, and hemodynamic instability. Angiographic exclusion criteria were lumen diameter proximal to the lesion <2.5 or >4.0 mm using visual estimate, ostial lesion, and chronic total occlusion. All patients were pretreated with aspirin and clopidogrel (600-mg loading dose) and both were continued for 1 year. Heparin was used to maintain an activated clotting time >250 seconds. All patients provided written informed consent before the procedure. Clinical follow-up was performed using regular outpatient visit and telephone interview up to 2 years.

Thoraxcenter, Erasmus Medical Center, Rotterdam, The Netherlands. Manuscript received February 10, 2008; revised manuscript received and accepted March 24, 2008.

*Corresponding author: Tel: +31-10-703-5729; fax: +31-10-703-2357.

E-mail address: e.regar@erasmusmc.nl (E. Regar).

The OCT system used in this study (LightLab Imaging Inc., Westford, Massachusetts) has been described previously.^{1,16} Briefly, an OCT balloon catheter (Helios; Goodman, Nagoya, Japan) was advanced distal to the lesion over a conventional coronary guidewire, which was then replaced with the OCT imaging wire (ImageWire, LightLab Imaging Inc., Westford, Massachusetts). The OCT catheter was then withdrawn proximally, and the lesion and segments distal and proximal to the lesion were visualized using an automated pullback system at 1.0 mm/s. During image acquisition, coronary blood flow was replaced by continuous infusion of Ringer's lactate at 0.8 ml/s using a power injector (Mark V ProVis; Medrad Inc., Indianola, Pennsylvania). The highly compliant occlusion balloon remained inflated proximal to the lesion at 0.5 or 0.7 atm for a maximum of 30 seconds. Cross-sectional images were acquired at 15.6 frames/s.

Analysis of contiguous cross sections was performed at 1-mm intervals. In each selected cross section, plaque characterization was according to the established OCT criteria of (1) fibrous, (2) fibrocalcific, and (3) lipid rich.¹⁷ Capped fibroatheroma was defined as the presence of a signal-rich fibrous cap covering a signal-poor lipid/necrotic core with a cap thickness <0.2mm and extending for >1 quadrant of the vessel circumference. The plaque had to be visualized in ≥ 5 consecutive frames.

After OCT examination, coronary interventions were performed according to standard practice with stent implantation. Stent optimization was accomplished using conventional angiographic guidance aiming at a residual diameter stenosis <20% using on-line quantitative coronary angiography. Statistical analyses were performed using SPSS, version 12.0.1 (SPSS Inc., Chicago, Illinois) for Windows (Microsoft Corp., Redmond, Washington). Data were expressed as mean \pm SD for continuous variables or median and interquartile range, if appropriate, and as percentages for categorical variables. To evaluate interobserver agreement for plaque characterization, a subset of plaques was classified by a second observer and the κ statistic was calculated. To assess the reproducibility of cap thickness, a set of fibrous caps was also measured by a second independent observer, and the absolute mean difference between 2 observers' measurements and its SD were calculated.

Results

Baseline clinical and lesion characteristics are listed in Table 1. There was 1 case of transient atrioventricular block during OCT pullback in a 72-year-old man with single-vessel disease. The rest of his clinical course was uneventful, and he was discharged as planned the next day.

OCT analysis of the coronary artery wall was possible in all patients. Mean OCT pullback length was 28.8 ± 12.2 mm. Quantitative measurements at the culprit site showed a mean minimal lumen area and mean minimal lumen diameter of 2.38 ± 0.93 mm² and 1.45 ± 0.33 mm, respectively. A wide spectrum of plaque morphologic characteristics was seen both at the culprit lesion and in remote segments.

Culprit-lesion OCT characteristics were also listed in Table 1. Agreement between observers for determining plaque type was good ($\kappa = 0.85$). Two patients met criteria

Table 1
Baseline clinical and lesion characteristics

Variable	n = 23
Age (yrs)	61 \pm 11
Men	18 (78%)
Diabetes mellitus	2 (9%)
Hypertension	13 (57%)
Dyslipidemia*	11 (48%)
Current smoker	5 (22%)
Previous myocardial infarction	6 (26%)
No. of coronary arteries narrowed >50%	
1	14 (61%)
2	5 (22%)
3	4 (17%)
Clinical presentation	
Silent myocardial ischemia	1 (4%)
Stable angina pectoris	18 (78%)
Unstable angina pectoris	4 (17%)
Target vessel	
Left anterior descending artery	14 (61%)
Left circumflex artery	3 (13%)
Right coronary artery	6 (26%)
Culprit lesion morphologic characteristics assessed using OCT	n = 23 lesions
Fibrous	9 (39%)
Fibrocalcific	8 (35%)
Lipid-rich	6 (26%)

* Total cholesterol ≥ 5.0 mmol/L or treatment with a lipid-lowering drug.

for TCFA. A 58-year-old woman with type 1 diabetes mellitus and hypertension presented with non-ST elevation MI. Coronary angiography showed single-vessel disease in the left anterior descending artery. OCT showed a tight lesion with a minimal lumen area of 0.68 mm², irregular lumen contours, signs of plaque fissure/rupture, and mural thrombus. The other patient was a 62-year-old man with a history of MI presenting with angina (Canadian Cardiovascular Society [CCS] III). Angiographically, 3-vessel disease was present with a culprit lesion in the left anterior descending artery. OCT visualized a nonruptured TCFA with a cap thickness of 180 μ m and circumferential extent of 100° with a minimal lumen area of 3.42 mm². Both patients underwent uneventful coronary stent implantation.

Most plaques (73.9%) at remote segments were found to be proximal to the culprit lesion. Fibrous and lipid-rich plaques were more common, whereas 1 patient had a fibrocalcific plaque distal to the culprit lesion in the right coronary artery (Figure 1). OCT identified 7 TCFA lesions in 6 patients. One patient presented with stable angina, 3 presented with unstable angina, and 2 patients had a recent history of ACS. These latter patients had undergone primary percutaneous coronary intervention for acute MI caused by thrombotic occlusion in another vessel 2 weeks before and were rescheduled for elective percutaneous coronary intervention to a residual lesion in a non-infarct-related artery. Mean cap thickness was 0.19 ± 0.05 mm, extending for $103^\circ \pm 49^\circ$ of the total vessel circumference. Three of these TCFA lesions showed an irregular inner lumen contour with evidence of mural thrombi in 2 lesions (Figure 2). The reproducibility of fibrous cap measurements showed an absolute mean difference between 2 observers of 0.010 \pm

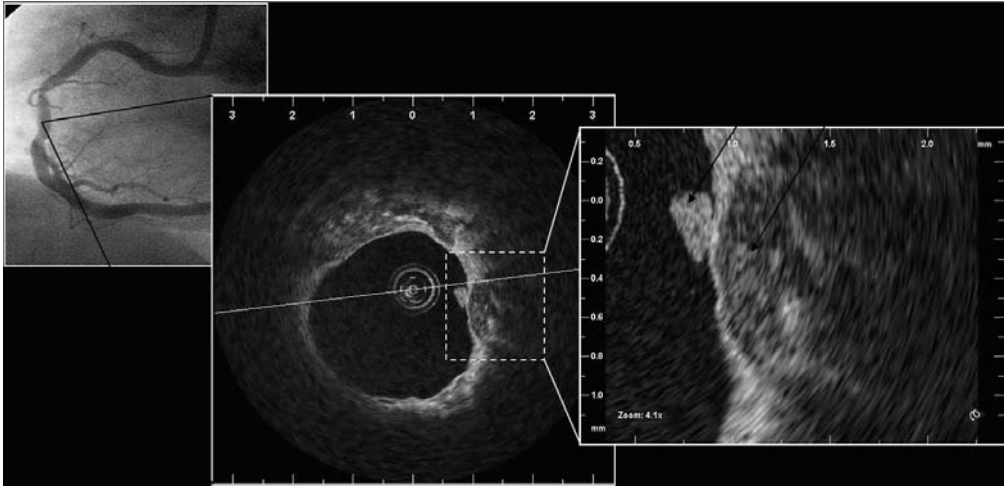


Figure 1. Angiography shows a calcific midvessel lesion. An additional calcific plaque with sharp and well-delineated margins was also observed using OCT remote and distal to the culprit lesion with attached mural thrombus.



Figure 2. TCFA assessed using OCT overlying a large lipid-rich plaque (2 to 5 o'clock position). The bright highly reflective fibrous cap measured 30 to 80 μm .

0.016 mm, with limits of agreement (i.e., 1.96 SD of mean difference) of 0.043 to -0.023 .

Two-year clinical follow-up was available for all patients. There were no deaths or MIs. There was 1 case of target-lesion revascularization caused by in-stent restenosis in a 65-year-old man 8 months after the index procedure. The patient was successfully treated with repeated percutaneous coronary intervention. There were no adverse events in patients with TCFA at remote segments during 24 months of follow-up, with most patients classified as CCS 1 angina pectoris. All patients were on treatment with statins.

Discussion

The main findings of this study were that (1) OCT could be safely used in vivo to show the heterogeneity of coronary plaques at culprit and remote sites, (2) intravascular OCT could detect in vivo morphologic features associated with plaque vulnerability using retrospective pathologic examination, and (3) the lack of long-term clinical events in our patients with TCFA gave unique antemortem insight into such lesions, although the sample size was small.

The recent introduction of OCT has proved to be an innovative contribution to the in vivo detection of VP and TCFA. Its unique image resolution in the range of 10 to 15 μm is in the magnitude of 10 times higher than that of intravascular ultrasound and permitted superior visualization of plaque morphologic characteristics.¹⁸ Although OCT has an inherent lack of tissue penetration (<2 mm), it is ideally served to examine the arterial lumen and lumen-vessel interface. Yabushita et al¹⁷ performed an in vitro study of >300 human atherosclerotic artery segments. Compared with histologic examination, OCT had sensitivity and specificity of 71% to 79% and 97% to 98% for fibrous plaques, 95% to 96% and 97% for fibrocalcific plaques, and 90% to 94.5% and 90% to 92% for lipid-rich plaques, respectively. In addition, inter- and intraobserver variabilities of OCT measurements were high ($\kappa = 0.88$ and 0.91, respectively).

The use of OCT to assess culprit lesions in vivo has shown favorable results. In 57 patients, Jang et al⁸ found lipid-rich plaques in 90%, 75%, and 59% of patients presenting with recent acute MI, ACS, and stable angina, respectively. Frequencies of TCFA (defined as lipid-rich plaque with cap thickness <65 μm) were 72%, 50%, and 20% in patients with acute MI, ACS, and stable patients, respectively ($p = 0.012$). Our study showing TCFA pre-

dominantly in patients with a recent history of ACS seems to be in line with these observations.

Of note, the study by Jang et al⁸ did not use a motorized pullback for OCT image acquisition. The investigators positioned the OCT wire at the level of the tightest stenosis, judged angiographically. This had several limitations, particularly the inability to detect continuous cross sections of the coronary artery. Our study used an automated pullback at 1.0 mm/s with a relatively long pullback of the coronary artery permitting visualization of additional plaques, both proximal and distal to the culprit lesion. We judged the severity of the culprit lesion using OCT rather than angiography, which was associated with its inherent limitations, namely, its low resolution and inability to accurately discriminate between plaques.

Recently, Kubo et al⁴ used OCT with intravascular ultrasound and angiography to assess culprit plaque characteristics in 30 patients presenting with acute MI. The imaging devices were consecutively used after the initial mechanical thrombectomy. The incidence of plaque rupture using OCT was 73%, significantly higher than that detected using both angiography (47%; $p = 0.035$) and intravascular ultrasound (40%; $p = 0.009$). The incidence of TCFA was 83% in this patient population, and only OCT was able to estimate fibrous cap thickness (mean $49 \pm 21 \mu\text{m}$). In addition, intracoronary thrombus was observed in all patients using OCT and angiography, but was identified in only 33% of patients using intravascular ultrasound ($p < 0.001$). The different patient populations evaluated likely explained the lower frequency of thrombi in our study compared with that of Kubo et al.⁴ We did not recruit patients with acute MI because of the relatively prolonged OCT imaging required to visualize both culprit and remote segments. Moreover, compared with the study by Kubo et al,⁴ our study extended OCT imaging beyond the culprit lesion, thereby giving a more representative indication about the presence of TCFA in nonculprit segments.

The presence of TCFA in regions remote to the culprit lesion in 26% of patients in our study was an interesting observation not shown previously using OCT. One possible explanation related to the widely accepted understanding that atherosclerosis is a systemic disease with focal manifestations. In a study using multislice computed tomography, Kunimasa et al¹⁹ assessed 21 patients with ACS and 53 patients with non-ACS. The presence of computed tomographic low-density plaques (defined as computed tomographic density < 68 Hounsfield units) was more frequent in the ACS group than the non-ACS group (81% vs 43%; $p = 0.03$). In addition, computed tomographic density of the nonculprit lesion was significantly lower in patients with ACS than those with non-ACS. Although the presence of > 1 unstable plaque was a relatively common occurrence in patients with ACS and acute MI,^{19,20} this did not provide a comprehensive explanation of our findings, particularly given that patients with acute MI were excluded and most patients had presented with stable angina pectoris.

Localization of TCFA in proximal coronary segments was not previously reported using in vivo OCT. Such a finding had been confirmed in postmortem studies with a low incidence of TCFA in patients who died of sudden cardiac death (1.3 ± 1.4 TCFA/heart), of which most were

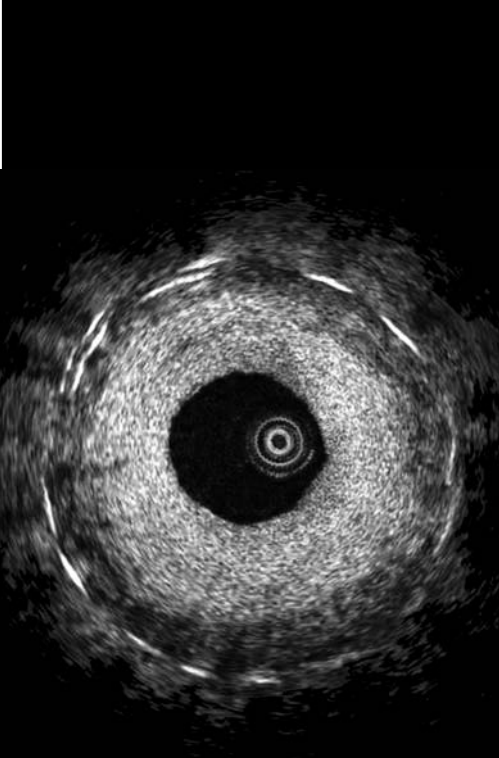
clustered in the proximal segment of the artery, particularly the left anterior descending artery.^{21,22} It is believed that focal areas of low shear stress in proximal segments contributed to this phenomenon, resulting in migration of lipids and monocytes into the vessel wall, accelerating the atherosclerotic process.^{23–25}

The incidence of TCFA was dependent on the OCT criteria applied to make the diagnosis. We used conservative criteria requiring a relatively extensive lipid/necrotic core occupying > 1 quadrant of the vessel circumference. This approach was chosen to exclude the chance for confusion with calcification, a potential limitation described in a pathology series.²⁶ We applied a relatively high cut-off value of $< 200 \mu\text{m}$ for cap thickness, possibly overestimating the incidence of true TCFA. However, it was difficult to translate a cut-off value defined using pathologic criteria into the clinical setting. Although the most accepted threshold to define a cap as “thin” had been set as $< 65 \mu\text{m}$, this was based on postmortem studies.²⁷ Extrapolation to in vivo studies required caution. It was well established that anisotropic tissue shrinkage occurs during tissue fixation.²⁸ Shrinkage (particularly of collagen tissue, the main component of fibrous cap) of up to 60%, 15%, and 80% can occur during critical-point drying, free drying, and air drying, respectively.²⁹ Furthermore, postmortem contraction of arteries was an additional confounding factor.³⁰ It was therefore likely that the threshold used to define a thin cap in vivo should be $> 65 \mu\text{m}$. Finally, a number of important ex vivo studies used a higher ($> 200 \mu\text{m}$) threshold.^{31–33} One of these studies identified a mean cap thickness of 260 and 360 μm for VP and nonvulnerable plaque, respectively.³³

The present study was not randomized and included a relatively small sample size. In addition, OCT was restricted to a relatively short coronary artery segment, and therefore, unlike pathologic studies, does not allow us to draw conclusions about the incidence of TCFA within the complete coronary tree. Also, the study did not involve routine angiographic and OCT follow-up. Still, its prospective design and use of a sensitive imaging device gave the first insight into the potential time course of such lesions. Obviously, larger studies, possible using multimodal imaging that allows the assessment of macrophage accumulation and collagen composition, will help make the pathogenesis and natural history of such VP clearer, with a tremendous potential to reduce the burden of cardiovascular disease.

1. Regar E, Schaar JA, Mont E, Virmani R, Serruys PW. Optical coherence tomography. *Cardiovasc Radiat Med* 2003;4:198–204.
2. Garcia-Garcia HM, Goehardt D, Serruys PW. Relation of plaque size to necrotic core in the three major coronary arteries in patients with acute coronary syndrome as determined by intravascular ultrasonic imaging radiofrequency. *Am J Cardiol* 2007;99:790–792.
3. Garcia-Garcia HM, Gonzalo N, Granada JF, Regar E, Serruys PW. Diagnosis and treatment of coronary vulnerable plaques. *Expert Rev Cardiovasc Ther* 2008;6:209–222.
4. Kubo T, Imanishi T, Takarada S, Kuroi A, Ueno S, Yamano T, Tanimoto T, Matsuo Y, Masho T, Kitabata H, et al. Assessment of culprit lesion morphology in acute myocardial infarction: ability of optical coherence tomography compared with intravascular ultrasound and coronary angiography. *J Am Coll Cardiol* 2007;50:933–939.
5. Chia S, Christopher Raffel O, Takano M, Tearney GJ, Bouma BE, Jang IK. In-vivo comparison of coronary plaque characteristics using optical coherence tomography in women vs. men with acute coronary syndrome. *Coron Artery Dis* 2007;18:423–427.

6. Tearney GJ, Jang IK, Bouma BE. Optical coherence tomography for imaging the vulnerable plaque. *J Biomed Opt* 2006;11:021002.
7. Giattina SD, Courtney BK, Herz PR, Harman M, Shortkroff S, Stamper DL, Liu B, Fujimoto JG, Brezinski ME. Assessment of coronary plaque collagen with polarization sensitive optical coherence tomography (PS-OCT). *Int J Cardiol* 2006;107:400–409.
8. Jang IK, Tearney GJ, MacNeill B, Takano M, Moselewski F, Ifitima N, Shishkov M, Houser S, Aretz HT, Halpern EF, Bouma BE. In vivo characterization of coronary atherosclerotic plaque by use of optical coherence tomography. *Circulation* 2005;111:1551–1555.
9. Tearney GJ, Yabushita H, Houser SL, Aretz HT, Jang IK, Schlenndorf KH, Kauffman CR, Shishkov M, Halpern EF, Bouma BE. Quantification of macrophage content in atherosclerotic plaques by optical coherence tomography. *Circulation* 2003;107:113–119.
10. Jang IK, Bouma BE, Kang DH, Park SJ, Park SW, Seung KB, Choi KB, Shishkov M, Schlenndorf K, Pomerantsev E, et al. Visualization of coronary atherosclerotic plaques in patients using optical coherence tomography: comparison with intravascular ultrasound. *J Am Coll Cardiol* 2002;39:604–609.
11. Tsuchida K, van der Giessen WJ, Patterson M, Tanimoto S, Garcia-Garcia H, Regar E, Ligthart J, Maugeness AM, Maatrijk G, Wentzel JJ, Serruys PW. In-vivo validation of a novel three-dimensional quantitative coronary angiography system (CardioOp-B TM): comparison with a conventional two-dimensional system (CASS II TM) and with special reference to optical coherence tomography. *EuroIntervention* 2007;3:100–108.
12. Barlis P, Serruys PW, DeVries A, Regar E. Optical coherence tomography assessment of vulnerable plaque rupture: predilection for the plaque 'shoulder'. *Eur Heart J* 2008;doi:10.1093/eurheartj/ehn1085.
13. Tanimoto S, Rodriguez-Granillo G, Barlis P, de Winter S, Bruining N, Hamers R, Knappen M, Verheye S, Serruys PW, Regar E. A novel approach for quantitative analysis of intracoronary optical coherence tomography: high inter-observer agreement with computer-assisted contour detection. *Catheter Cardiovasc Interv* 2008;doi: 10.1002/ccd.21482.
14. MacNeill BD, Jang IK, Bouma BE, Ifitima N, Takano M, Yabushita H, Shishkov M, Kauffman CR, Houser SL, Aretz HT, et al. Focal and multi-focal plaque macrophage distributions in patients with acute and stable presentations of coronary artery disease. *J Am Coll Cardiol* 2004;44:972–979.
15. Raffel OC, Tearney GJ, Gauthier DD, Halpern EF, Bouma BE, Jang IK. Relationship between a systemic inflammatory marker, plaque inflammation, and plaque characteristics determined by intravascular optical coherence tomography. *Arterioscler Thromb Vasc Biol* 2007;27:1820–1827.
16. Tanigawa J, Barlis P, Di Mario C. Intravascular optical coherence tomography: optimisation of image acquisition and quantitative assessment of stent strut apposition. *EuroIntervention* 2007;3:128–136.
17. Yabushita H, Bouma BE, Houser SL, Aretz HT, Jang IK, Schlenndorf KH, Kauffman CR, Shishkov M, Kang DH, Halpern EF, Tearney GJ. Characterization of human atherosclerosis by optical coherence tomography. *Circulation* 2002;106:1640–1645.
18. Jang IK, Bouma BE, Kang DH, Park SJ, Park SW, Seung KB, Choi KB, Shishkov M, Schlenndorf K, Pomerantsev E, et al. Visualization of coronary atherosclerotic plaques in patients using optical coherence tomography: comparison with intravascular ultrasound. *J Am Coll Cardiol* 2002;39:604–609.
19. Kunimasa T, Sato Y, Sugi K, Moroi M. Evaluation by multislice computed tomography of atherosclerotic coronary artery plaques in non-culprit, remote coronary arteries of patients with acute coronary syndrome. *Circ J* 2005;69:1346–1351.
20. Goldstein JA, Demetriou D, Grines CL, Pica M, Shoukfeh M, O'Neill WW. Multiple complex coronary plaques in patients with acute myocardial infarction. *N Engl J Med* 2000;343:915–922.
21. Cheruvu PK, Finn AV, Gardner C, Caplan J, Goldstein J, Stone GW, Virmani R, Muller JE. Frequency and distribution of thin-cap fibroatheroma and ruptured plaques in human coronary arteries: a pathologic study. *J Am Coll Cardiol* 2007;50:940–949.
22. Kolodgie FD, Burke AP, Farb A, Gold HK, Yuan J, Narula J, Finn AV, Virmani R. The thin-cap fibroatheroma: a type of vulnerable plaque: the major precursor lesion to acute coronary syndromes. *Curr Opin Cardiol* 2001;16:285–292.
23. Slager CJ, Wentzel JJ, Gijzen FJ, Schuurbiens JC, van der Wal AC, van der Steen AF, Serruys PW. The role of shear stress in the generation of rupture-prone vulnerable plaques. *Nat Clin Pract Cardiovasc Med* 2005;2:401–407.
24. Stone PH, Coskun AU, Kinlay S, Clark ME, Sonka M, Wahle A, Hegbusi OJ, Yeghiazarians Y, Popma JJ, Orav J, Kuntz RE, Feldman CL. Effect of endothelial shear stress on the progression of coronary artery disease, vascular remodeling, and in-stent restenosis in humans: in vivo 6-month follow-up study. *Circulation* 2003;108:438–444.
25. Cunningham KS, Gotlieb AI. The role of shear stress in the pathogenesis of atherosclerosis. *Lab Invest* 2005;85:9–23.
26. Manfrini O, Mont E, Leone O, Arbustini E, Eusebi V, Virmani R, Bugiardini R. Sources of error and interpretation of plaque morphology by optical coherence tomography. *Am J Cardiol* 2006;98:156–159.
27. Burke AP, Farb A, Malcom GT, Liang YH, Smialek J, Virmani R. Coronary risk factors and plaque morphology in men with coronary disease who died suddenly. *N Engl J Med* 1997;336:1276–1282.
28. Cilingiroglu M, Oh JH, Sugunan B, Kemp NJ, Kim J, Lee S, Zaatari HN, Escobedo D, Thomsen S, Milner TE, Feldman MD. Detection of vulnerable plaque in a murine model of atherosclerosis with optical coherence tomography. *Catheter Cardiovasc Interv* 2006;67:915–923.
29. Boyde ATA. Dimensional changes during specimen preparation for scanning electron microscopy. *Scanning Electron Microsc* 1977;1: 507–518.
30. Fishbein MC, Siegel RJ. How big are coronary atherosclerotic plaques that rupture? *Circulation* 1996;94:2662–2666.
31. Felton CV, Crook D, Davies MJ, Oliver MF. Relation of plaque lipid composition and morphology to the stability of human aortic plaques. *Arterioscler Thromb Vasc Biol* 1997;17:1337–1345.
32. Mann JM, Davies MJ. Vulnerable plaque. Relation of characteristics to degree of stenosis in human coronary arteries. *Circulation* 1996;94: 928–931.
33. Schaar JA, De Korte CL, Mastik F, Srijder C, Pasterkamp G, Boersma E, Serruys PW, Van Der Steen AF. Characterizing vulnerable plaque features with intravascular elastography. *Circulation* 2003;108:2636–2641.



5.4

Witnessed Coronary Plaque Rupture During Cardiac Catheterization

Gonzalo N, Tearney GJ, van Soest G, Serruys PW,
Garcia-Garcia HM, Bouma B, Regar E.

Submitted.

SUMMARY

Acute myocardial infarction is primarily caused by atherosclerotic plaque rupture within coronary arteries accompanied by intraluminal thrombus formation, sudden vessel occlusion, and impaired oxygen supply to the myocardium. However, study of plaque rupture has been previously limited to histologic analysis of autopsy specimens, animal experiments, and *in silico* modeling. Using a high-resolution imaging technique, called intracoronary optical frequency domain imaging (OFDI), we have directly observed the microstructural detail of human coronary plaque rupture *in vivo* at multiple time points. This case of a dynamic observation in a patient provides evidence to support hypotheses about coronary plaque rupture and is illustrative of our current model of the pathogenesis of acute coronary syndromes.

INTRODUCTION

Acute myocardial infarction, characterized by coronary atherosclerotic plaque rupture, thrombus formation, and loss of blood flow and oxygen supply to downstream myocardium, remains a leading cause of death worldwide. Autopsy studies of patients who have died of a heart attack have shown that the majority of plaques found at the culprit site are comprised of a thin ($< 65 \mu\text{m}$) collagen layer termed a cap, overlying a lipid-rich necrotic core¹. These plaques, called thin cap fibroatheromas (TCFA), are commonly inflamed, containing inflammatory cells (macrophages) that produce collagenases that can weaken the cap.

The picture we have from autopsy data is static, however, a two-dimensional snapshot of the artery, often long after rupture has occurred. Information on the time course of human plaque rupture and clot formation and the microstructural changes that take place during these events has been heretofore unattainable. Likewise, the mechanisms and time course of vascular healing after such an event are poorly understood from post mortem observations. In this report, we present a case of coronary plaque rupture that was observed by high-resolution optical imaging at multiple time points during the interventional procedure.

METHODS

The patient underwent standard coronary catheterization using femoral access, 6F sheath and guiding catheters. Periprocedural medication included heparin iv (activated clotting time $> 300\text{s}$), and NTG ic before coronary instrumentation. Intracoronary imaging was performed using optical frequency domain imaging (OFDI),² a high-speed form of optical coherence tomography (OCT), that enables the detailed interrogation of the artery wall at a resolution of $\sim 10 \mu\text{m}$, sufficient to identify many microstructural plaque features *in vivo* such as lipid cores,³ thin caps,⁴ macrophages,⁵ and thrombus.⁶

The OFDI imaging system and catheter, described in a prior publication,⁷ were fabricated at the Massachusetts General Hospital (MGH) and approved for human use by the Thoraxcenter/Erasmus Medical Center's Medical Ethics Committee (MEC). OFDI was performed as part of a test-retest study to demonstrate reproducibility, pre and post intervention. Helical imaging of the coronary artery was performed at 100 frames per second with a 2.0 cm/s pullback rate. Imaging was conducted during displacement of blood via a brief, non-occlusive flush with radiocontrast medium (Iodixanol 370, Visipaque™, GE Health Care, Ireland) through the guide catheter.

Following pullback image acquisition, cross-sectional images for the different imaging time points were registered using side branch landmarks and the known pullback speed. In order to create three-dimensional image representations, images were individually segmented for artery wall, stent, thrombus, lipid, calcium, and macrophages, and volume rendered.⁷

CASE REPORT

On December 9, 2008, a 60 year-old diabetic male presented to the Thoraxcenter-Erasmus Medical Center hospital with chest pain during exertion (stable angina pectoris). A coronary angiogram showed a complex, flow-limiting lesion in the medial left anterior descending coronary artery (LAD) (Fig. 1A), with irregular

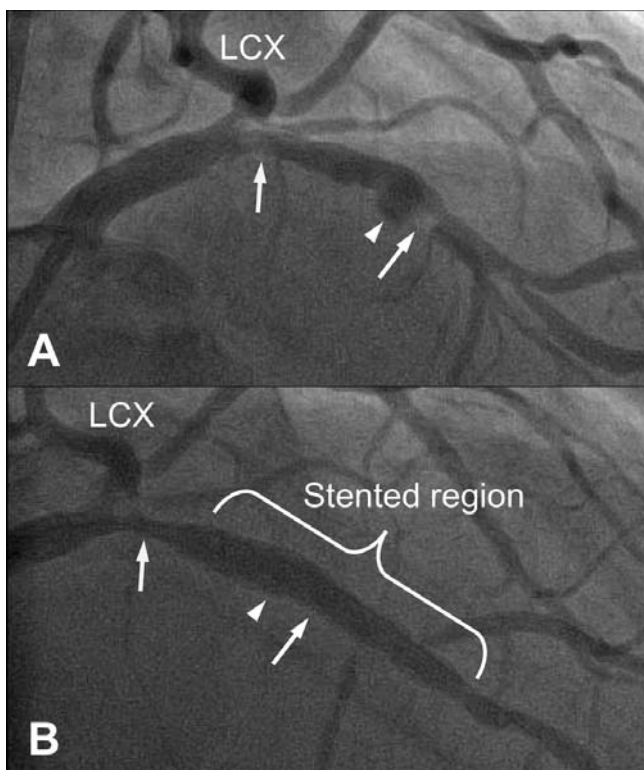


Figure 1: Angiogram obtained at presentation (A) showed a flow limiting, culprit lesion (white arrow) with irregular lumen contour in the mid LAD (white arrowhead) and a remote, moderate lesion proximally (yellow arrow). Angiogram following stent placement (B) shows good result of the PCI at the culprit lesion, while the remote lesion is unchanged. LAD = left anterior descending artery, LCX = left circumflex artery.

lumen contours.. The medial culprit lesion was treated using a stent with good angiographic result (Fig. 1B). Several centimeters proximal to the culprit lesion, a separate, moderate coronary plaque was identified on the angiogram (Fig. 1A and 1B). We imaged this non-flow limiting remote plaque during OFDI⁷ pullback before the stent was placed (baseline), and at roughly 15-minute intervals thereafter. The patient remained asymptomatic after the procedure without elevation of myocardial necrosis markers.

Cross-sectional images of the remote plaque at baseline showed features distinctive of TCFA, including an inflamed thin fibrous cap (min. thickness: 64 ± 5 μm) overlying an eccentric lipid core (Fig. 2A, E). After fifteen minutes and following culprit lesion stent placement, the cap of the remote plaque was disrupted and exposed lipid could be seen in direct communication with the lumen (Fig. 2B, F). Three minutes later, the rupture crater was devoid of lipid and larger (0.06 vs. 0.11 mm^3) (Fig. 2C, G). At forty-two minutes from baseline, a platelet-rich thrombus could be seen, adjoining the two arterial intimal flaps and nearly completely filling the rupture defect (Fig. 2D, H).

Longitudinal reconstruction through the plaque's center at baseline showed that the macrophage-rich thin cap covered the upstream (proximal) side of the lesion (Fig. 3A). The plaque ruptured at its apex, where the distal margin of the thin cap and core abutted a fibrotic portion of the lesion (shoulder) (Fig. 3A). A three-dimensional OFDI image reconstruction of the plaque revealed that while it involved a large portion of the artery wall, the lipid core surfaced focally, covered by a macrophage-laden cap (Fig. 3A). Plaque rupture occurred at the distal portion of the TCFA, forming clumps of retracted intima at the edges of the rupture site (Fig. 3B and 3C).

This witnessed coronary plaque rupture is informative because it links results and hypotheses generated by animal and autopsy studies to the living patient. Inflamed TCFA rupture seen here is consistent with pathologic findings in cadavers¹. The upstream portion of this patient's plaque demonstrated morphologic features of instability (thin cap and high macrophage content), which may be induced by high shear stress⁸. Biomechanical modeling has indicated that peak cap strain, and therefore rupture, should occur at longitudinal shoulders and apices of necrotic core plaques⁹. Because images were obtained serially in the same patient, these results also provide a data point on the sequence and timing of human plaque rupture and resolution, including lipid communication with the lumen, lipid core evacuation, and closure with a platelet plug, all taking place within ~40 minutes of the initial insult.

Other than its morphology, we do not know why this plaque ruptured; there were no abnormalities recorded during the procedure that would bring about such

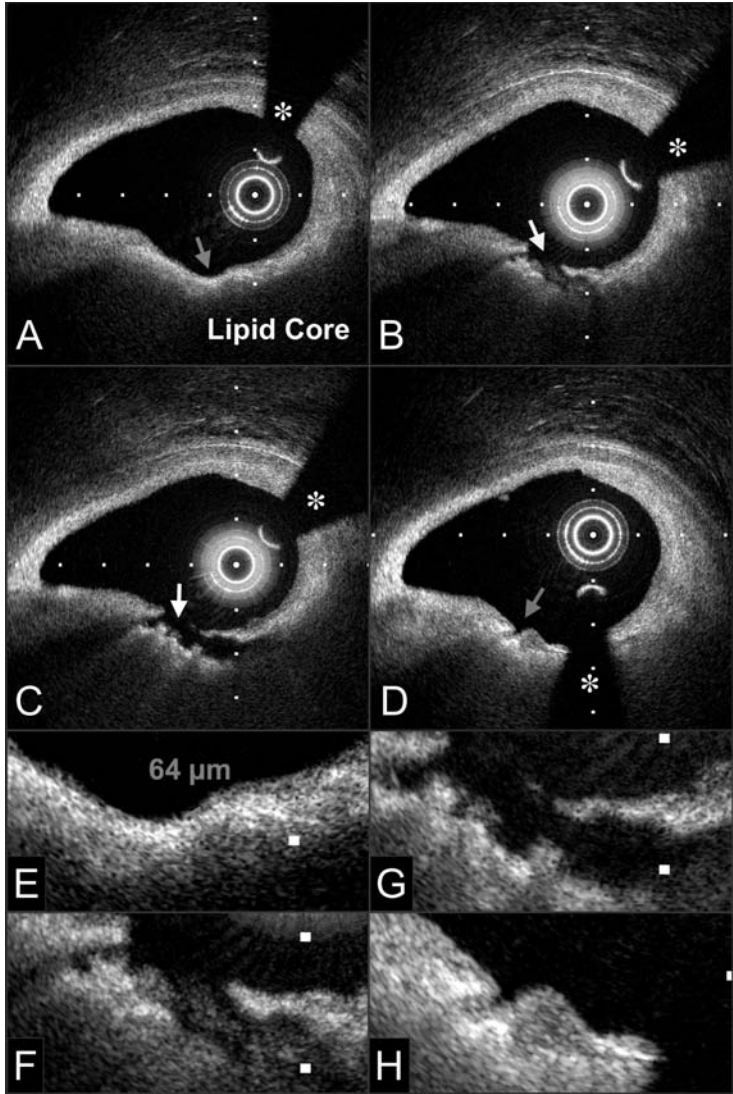


Figure 2: Cross-sectional OFDI images (A-D) and 3x zoomed regions (E-H) of the remote coronary plaque, obtained from this patient at different time points: A, E – baseline, B, F – 15 minutes, C, G – 18 minutes, D, H – 42 minutes. Red arrow in (A) – inflamed, thin fibrous cap; yellow arrow in (B) – lipid core in communication with lumen; white arrow in (C) evacuated rupture site; purple arrow in (D) thrombus, filling rupture defect. Tick marks, 500 μm . * denotes guide wire shadow artifact.

an event. It was probably not caused by the intracoronary devices themselves, as close inspection of two- and three-dimensional reconstructions of the OFDI data did not demonstrate any superficial defects near the rupture site. The rupture did occur after stenting another, more distal lesion in the same artery. A study conducted in rabbit aortas¹⁰ has shown that stenting increases arterial compliance

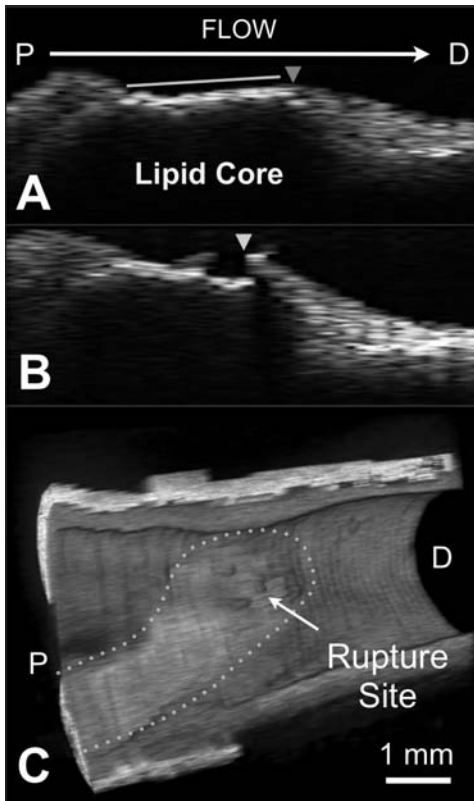


Figure 3: Image reconstructions. A, B. Longitudinal reconstructions of OFDI data acquired before rupture (A) and 18 minutes after baseline (B). C. 3D reconstruction of OFDI image data obtained 18 minutes following baseline. Green line in (A) – leading edge with a thin cap and superficial macrophages; red arrowhead in (A) – apex of lesion; blue arrowhead in (B) rupture site. Dotted region in (C) – thin fibrous cap; P – proximal; D – distal; Color scale for (C): red-artery wall, green-macrophages, white-calcium, yellow-lipid.

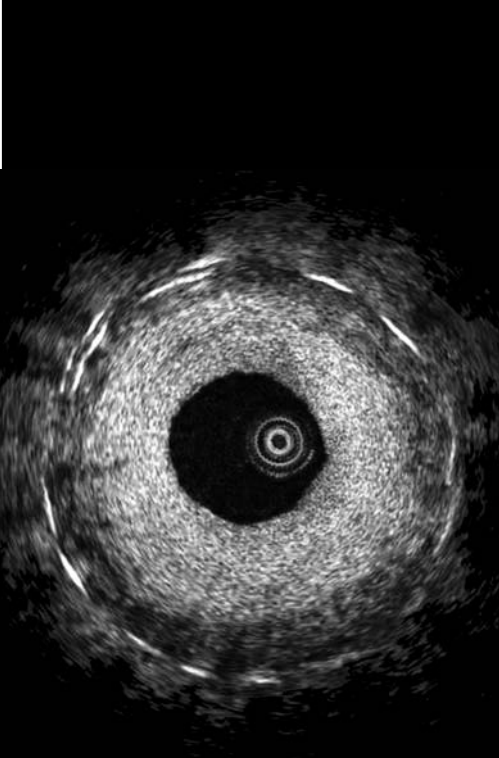
proximally, offering a possible explanation for what was observed here. Images were obtained while the patient was anticoagulated and during radiocontrast flushing to remove blood from the field of view. These results should be interpreted in this pharmacologic and procedural context.

We thank Mireille Rosenberg, Milen Shishkov for their invaluable assistance in this study.

This study was funded in part by the NIH contract 5R01HL076398 and by gifts from Terumo Corporation and Merck Research Laboratories. Terumo Corporation sponsors non-clinical OFDI research in the laboratory of (GT and BB) and has a patent-licensing arrangement with Massachusetts General Hospital.

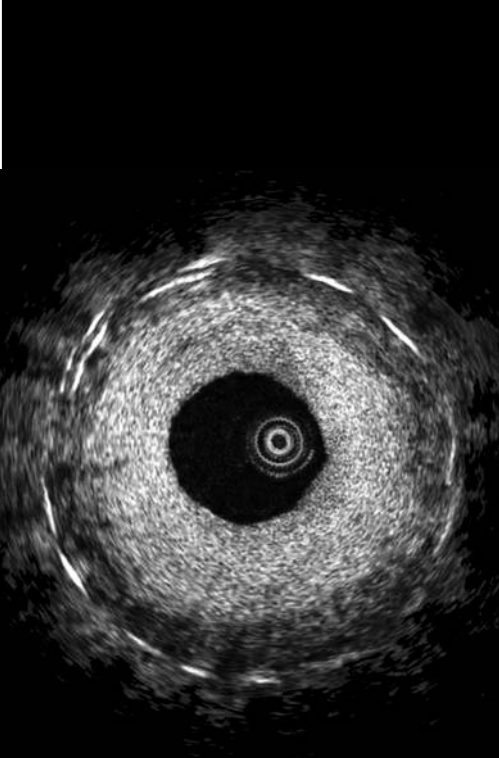
REFERENCES

1. Virmani R, Burke AP, Farb A, Kolodgie FD. Pathology of the vulnerable plaque. *J Am Coll Cardiol* 2006;47:C13-8.
2. Yun SH, Tearney GJ, de Boer JF, Iftima N, Bouma BE. High-speed optical frequency-domain imaging. *Optics Express* 2003;11:2953-63.
3. Yabushita H, Bouma BE, Houser SL, et al. Characterization of human atherosclerosis by optical coherence tomography. *Circulation* 2002;106:1640-5.
4. Kume T, Akasaka T, Kawamoto T, et al. Measurement of the thickness of the fibrous cap by optical coherence tomography. *Am Heart J* 2006;152:755 e1-4.
5. Tearney GJ, Yabushita H, Houser SL, et al. Quantification of macrophage content in atherosclerotic plaques by optical coherence tomography. *Circulation* 2003;107:113-9.
6. Kume T, Akasaka T, Kawamoto T, et al. Assessment of coronary arterial thrombus by optical coherence tomography. *The American journal of cardiology* 2006;97:1713-7.
7. Tearney GJ, Waxman S, Shishkov M, et al. Three-dimensional coronary artery microscopy by intracoronary optical frequency domain imaging. *Jacc* 2008;1:752-61.
8. Slager CJ, Wentzel JJ, Gijzen FJ, et al. The role of shear stress in the destabilization of vulnerable plaques and related therapeutic implications. *Nature clinical practice* 2005;2:456-64.
9. Imoto K, Hiro T, Fujii T, et al. Longitudinal structural determinants of atherosclerotic plaque vulnerability: a computational analysis of stress distribution using vessel models and three-dimensional intravascular ultrasound imaging. *J Am Coll Cardiol* 2005;46:1507-15.
10. Ward MR, Hibi K, Shaw JA, Furukawa E, Resnic FS, Kimura K. Effect of stent implantation on upstream coronary artery compliance--a cause of late plaque rupture? *The American journal of cardiology* 2005;96:673-5.



CHAPTER 6

**In vivo assessment of the effect of
coronary stent implantation with OCT**



6.1

Optical coherence tomography: clinical applications, and the evaluation of drug-eluting stents.

Gonzalo N, Serruys P.W, Regar E.

Minerva Cardiologica. 2008 Oct;56(5):511-25.

Optical coherence tomography: clinical applications and the evaluation of DES

N. GONZALO, P. W. SERRUYS, E. REGAR

Optical coherence tomography (OCT) is a light-based imaging modality that can provide *in vivo* high-resolution images of the coronary artery. In the last years there has been a continuous technical development that has improved the image quality and has simplified the acquisition procedure in order to spread the clinical applicability of this technique. Due to its high resolution OCT, can be a very valuable tool for the evaluation of the coronary vessel wall, the acute and long-term impact of catheter-based intervention on plaque structure and vessel architecture and the assessment of stents. During stenting, OCT offers the possibility to evaluate stent apposition in great detail and can identify the presence of vessel injury due to stent implantation. At follow-up, the tissue coverage of individual struts can be imaged with OCT. This is of increasing interest in drug-eluting stents in which the neointimal proliferation is inhibited to such extent that it might not be visualized with conventional intracoronary imaging techniques such as IVUS. Regarding the analysis of the coronary vessel wall, OCT holds promise for the identification of thin cap fibroatheroma due to its ability to provide information about plaque composition, presence of macrophages and thickness of the fibrous cap.

Key words: Tomography, optical coherence - Drug-eluting stents - Coronary artery disease.

*Thoraxcenter, Erasmus Medical Center
Rotterdam, The Netherlands*

dimensional representation of the lumen without providing information about the vessel wall. This limitation led to the development of new techniques able to image directly the atherosclerotic plaque. The introduction of intravascular ultrasound (IVUS) allowed a much more detailed evaluation of coronary atherosclerosis, but its limited resolution (axial 150-200 μm , radial 200-400 μm) precluded the visualization of certain microstructures (such as the thin fibrous cap).^{1, 2} Optical coherence tomography (OCT) is a light-based imaging modality can be used to study tissues *in vivo* with near-histologic, ultrahigh resolution.³⁻⁵ This has provided new insights into the interaction between the stent and the vessel wall and has allowed a more precise characterization of coronary atherosclerosis.

History

OCT technology was first described in the early 1990s⁶ and its clinical application was initiated in the field of ophthalmology, where it soon became an established method for the assessment of epiretinal and macula pathology.^{7, 8} Later it extended to other fields

Coronary angiography is the standard modality for assessment of atherosclerotic plaques, but it is restricted to a two-

Corresponding author: E. Regar, MD, PhD, Thoraxcenter, Bld 585, Dr.Molewaterplein 40, 3015-GD Rotterdam, The Netherlands. E-mail:e.regar@erasmusmc.nl

demonstrating its potential for the detection of neoplastic changes in different anatomic locations and skin diseases.⁹⁻¹¹ The vascular application of OCT started in the mid 1990s with the imaging of coronary arteries *ex vivo*.^{12, 13} Preclinical studies demonstrated that *in vivo* OCT imaging of normal coronary arteries, intimal dissections, and deployed stents was feasible, and that intracoronary OCT allows high-resolution identification of clinically relevant coronary artery morphology.^{14, 15} These findings were confirmed by *in-vivo* intravascular OCT in patients undergoing cardiac catheterization.¹⁶

Technical principles of OCT

While IVUS uses backscattered ultrasound, OCT uses reflected light to create high-resolution cross sectional images of the vessel. Since the speed of light is much faster than that of sound, an interferometer is required to measure the backscattered light. The interferometer splits the light source into two “arms” – a reference arm and a sample arm, which is directed into the tissue. When the back-reflected optical intensity of the two arms (interference signal) is measured and compared, the optical properties of the tissue can be deduced. The intensity of the back-reflected light can be measured and represented as greyscale values, enabling the creation of a digital image.

Current clinically available OCT systems use time-domain technology (TD-OCT) while newer systems that are currently under development for clinical application, are based on swept source (also called frequency domain or spectral domain) technology. Both, TD-OCT and swept source (SS) OCT, use low-coherent near-infrared light. A wavelength around 1 300 nm is selected because it minimizes the energy absorption in the light beam caused by protein, water, hemoglobin and lipids. In TD-OCT, The reference arm contains a moving mirror. The imaging depth of TD-OCT is approximately 1.5-2.0 mm with an axial and lateral resolution of 15 m and 25 m, respectively. The maximum pullback speed is 3 mm/s. Such system is

commercially available (Lightlab M3CV system).

SS-OCT uses a swept frequency laser as light source. The echo-time delay and amplitude of light reflected from the tissue microstructure at different depths are determined by processing the interference between the tissue sample and a fixed reference mirror to create the OCT images.^{17, 18} These new technology allow a dramatically faster image acquisition (up to 40 mm/s), have a higher axial resolution (up to 7 m) and an increased scan diameter. The SS-OCT systems will be soon available for clinical practice.

Techniques for image acquisition

Red blood cells represent a non-transparent tissue causing multiple light scattering and substantial signal attenuation. Therefore, for an adequate OCT image acquisition blood must be removed from the vessel. With the first available commercial OCT system (Lightlab M2CV system) this was achieved with proximal occlusion of the vessel with a low-pressure balloon (0.5 atm) and simultaneous, distal flush delivery (occlusive technique) during pullback of a dedicated, thin (0.019 inch) OCT imaging probe (ImageWire™ LightLab Imaging Inc., Westford, MA, USA).¹⁹ However, recently the increase in the pullback speed (from 1 mm/s to 3 mm/s) has made possible acquiring an OCT pullback while the blood is removed by continuous flush (X-ray contrast) delivery through the guiding catheter without the need of occluding the vessel (non-occlusive technique).²⁰⁻²²

In the new generation swept-source systems, the optical probe is integrated in a catheter that can be placed in the coronary artery over any conventional 0.014” guidewire in monorail technique. The high pullback speed (up to 40 mm/s) allows imaging of long coronary segments within a few seconds while the blood is temporally removed from the vessel by the injection of x-ray contrast through the guiding catheter, very similar to the acquisition of a coronary angiogram.

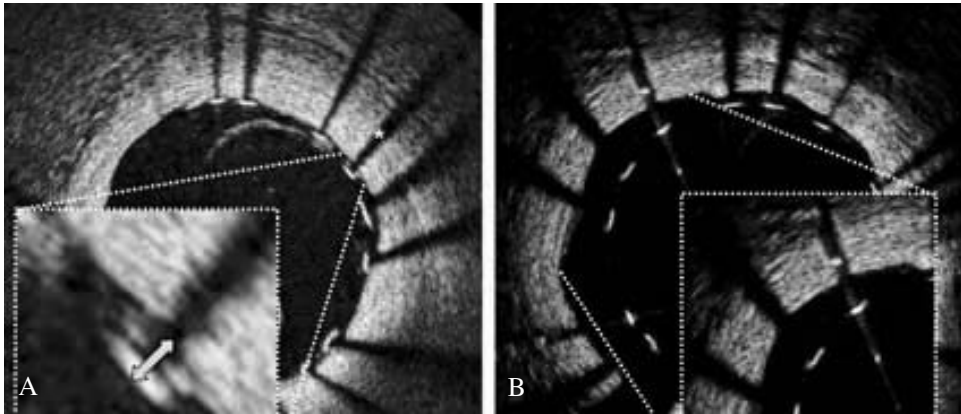


Figure 1.—OCT assessment of stent apposition. A) Stent struts can be identified by OCT as highly reflective surfaces that casts shadows on the underlying vessel wall (*). Since OCT can show only the endoluminal surface of the strut due to limited penetration through the metal, strut and polymer thickness must be considered in assessing apposition for each type of drug eluting stent. Only if the distance from the endo-luminal surface of the strut to the vessel wall is higher than the sum of the metal and polymer thickness (arrow), it can be considered that the strut is incomplete apposed. B. OCT after stent implantation showing incomplete strut apposition.

Safety of intravascular OCT

The applied energies in intravascular OCT are relatively low (output power in the range of 5.0-8.0 mW) and are not considered to cause functional or structural damage to the tissue. Safety issues thus seem mainly dependent on the need of blood displacement for image acquisition. One recently published study evaluated the safety and feasibility of OCT in 76 patients in the clinical setting using the occlusive technique. Vessel occlusion time was 48.3 ± 13.5 seconds. The most frequent complication was the presence of transient events, such as chest discomfort, brady or tachycardia, and ST-T changes on electrocardiogram, all of which resolved immediately after the procedure. There were no major complications, including myocardial infarction, emergency revascularization, or death. The authors reported that acute procedural complications such as acute vessel occlusion, dissection, thrombus formation, embolism, or vasospasm along the procedure-related artery, were not observed.²³ In our experience, the introduction of the non-occlusive technique in clinical practice has led to an important reduction in the procedural time and in the incidence of chest pain and ECG

changes during image acquisition. These side effects are expected to be further reduced by the introduction of SS OCT. In SS OCT, high pullback speeds allow data acquisition of a long coronary segment within in few seconds and thus without introducing relevant ischemia.

Clinical application

Stent evaluation

Due to its high resolution OCT can be a very valuable tool for the evaluation of the acute and long-term impact of catheter-based intervention on plaque structure and vessel architecture.²⁴ This is of increasing interest in drug-eluting and new-generation coronary stents. Drug-eluting stents (DES) have been shown to significantly limit neointimal growth to such extent that the neointima tissue might consist of only a few cell layers that cannot be accurately visualised with IVUS.²⁵ OCT offers the possibility to easily identify coronary stents and individual stent struts as highly reflective surfaces that cast shadows on the underlying vessel wall, to assess stent apposition and the delicate interaction

TABLE I.—*Strut thickness for the most commonly used drug-eluting stents (modified from Tanigawa et al.²⁸).*

Stent	Drug	Metal	Polymer	Total thickness
Cypher Select™ (Cordis)	Sirolimus	140 μm	7 μm	154 μm
Taxus Liberté™ (Boston Scientific)	Paclitaxel	97 μm	15 μm	127 μm
Xience V™ (Abbot)	Everolimus	81 μm	8 μm	89 μm
Endeavor™ (Medtronic)	Zotarolimus	91 μm	8 μm	107 μm

between vessel wall and stent strut as well as neointima growth patterns.²⁶

OCT DURING STENTING

Stent apposition.—Incomplete stent apposition is defined as separation of at least one stent strut from the vessel wall. OCT has demonstrated to be more accurate than IVUS for the detection of incomplete strut apposition to the vessel wall. In a study in porcine coronary arteries *in vivo*, microanatomic relationships between stents and the vessel wall could be clearly identified only by OCT.¹⁴ Bouma *et al.* imaged 42 stents in 39 patients showing that incomplete stent apposition was more often observed with OCT than with IVUS.²⁷ However, to avoid misclassification of struts as malapposed some considerations should be taken into account. Most DES are constituted by a metal body covered by a polymer. Since OCT can show only the endoluminal surface of the strut due to limited penetration through the metal, strut and polymer thickness must be considered in assessing apposition for each type of DES design. Only if the distance from the endoluminal surface of the strut to the vessel wall is higher than the sum of the metal and polymer thickness, it can be considered that the strut is malapposed (Figure 1). The thickness of the metal and polymer differs for each stent type. Therefore the cut-off point to establish malapposition must take into account the type of stent. Table I provides the strut thickness for the most commonly used DES. OCT has demonstrated its value to assess malapposition in the clinical practice.²⁸ Tanigawa *et al.* reported that in overlapping segments in DES 40% of struts were malapposed despite high pressure dilatation with appropriate size balloons.²⁸ The authors hypothesized that this could be related with the reported delayed

endothelization and increased risk of stent thrombosis in those segments. The same group evaluated the usefulness of OCT to assess the struts apposition in heavily calcified lesions showing malapposition even after high pressure balloon dilatation and rotational atherectomy.²⁹

Recently published IVUS observations suggest a possible relation between incomplete DES apposition and subsequent stent thrombosis.³⁰⁻³² The clinical significance of incomplete stent strut apposition as detected by OCT, however is poorly understood. In fact, incomplete apposition of stent struts is a relatively common finding by OCT,³³ while the vast majority of the patients do not experience clinical events in the long-term. The presence of struts not attached to the vessel wall in certain locations such as side branches is derived from the vessel anatomy and its clinical relevance is unknown. In addition, not all patients that experience DES thrombosis show strut malapposition.^{34, 35}

Stent expansion.—OCT could be useful for the *in vivo* assessment of acute stent recoil one of the features identified as a contributor to inadequate stent expansion. Our group reported OCT findings during stepwise post-dilatation of a Cypher stent showing a change in stent diameter from 3.5 at 22 atm to 2.94 at 5 atm.³⁶ This could be clinically relevant as final stent area is known to be an important predictor for restenosis and subsequent clinical events. Stent asymmetry, another of the features related with stent thrombosis in IVUS studies, can also be assessed with OCT.

Identification of vessel injury after stenting.—OCT has a higher sensitivity to detect acute complications after stent implantation such as edge dissection and tissue prolapse as compared to IVUS.²⁷ Edge dissection can

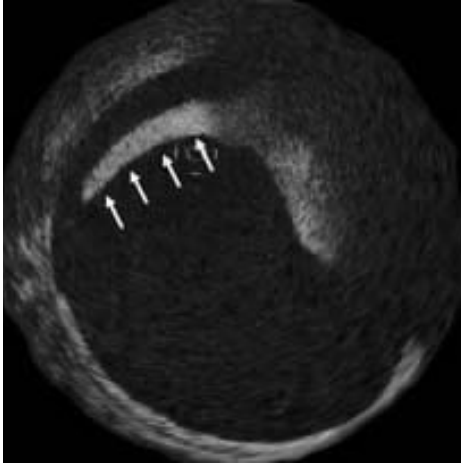


Figure 2—Stent edge dissection. The OCT performed immediately after stent implantation shows a disruption in the vessel continuity with a visible flap (white arrows) in the region of the proximal stent edge.

be easily identified by OCT as a disruption in the vessel continuity with a visible flap (Figure 2). OCT can help to better understand the impact of edge dissections on clinical outcome. While high-pressure stenting techniques have proved to be useful for stent optimization, this stent deployment strategy can often create a certain degree of vessel damage in the stent edges.³⁷ The clinical importance of minor edge dissections is poorly understood. Although animal and post-mortem information correlated vessel injury and in-stent restenosis,^{38, 39} some IVUS studies have shown that non-flow-limiting edge dissections are not necessarily associated with an increase in acute or long-term events or the development of restenosis.^{40, 41} However other data suggested that intracoronary imaging may be helpful to assess which of these residual dissections could be more prone to acute vessel occlusion. Nishida *et al.* reported that the area stenosis by IVUS at the site of the dissection was predictor for the incidence of in-hospital major cardiac adverse events.⁴²

Tissue prolapse can be identified in OCT as protrusion of tissue between the struts⁴³ (Figure 3). The clinical relevance of the detection of this feature after stenting remains con-

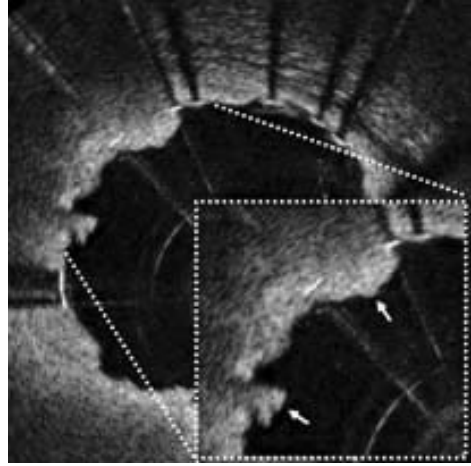


Figure 3.—Tissue prolapse. OCT performed after stent implantation shows protrusion of tissue between the stent struts (white arrows).

troversial. Pathological examinations have associated stent thrombosis with the prolapse of necrotic core between stent struts.⁴⁴ However an IVUS study in diabetic patients undergoing PCI did not show higher incidence of stent thrombosis in patients with plaque prolapse.⁴⁵ This might be related with the resolution of IVUS that is not able to detect small amount of tissue protruding between the stent struts. In this scenario a high resolution technique as OCT could provide valuable information for a better understanding of the clinical implications of this phenomenon.

OCT FOR STENT FOLLOW-UP

Stent apposition.—Stent apposition at follow up can be assessed with OCT using the same criteria previously exposed for evaluation of apposition at baseline. The incomplete stent apposition at follow-up can be persistent or acquired (not present after stent implantation). To distinguish between these two types, imaging of the stent after implantation is required. Several mechanisms have been proposed as cause of late acquired incomplete stent apposition: 1) expansive vessel remodelling; 2) chronic stent recoil;

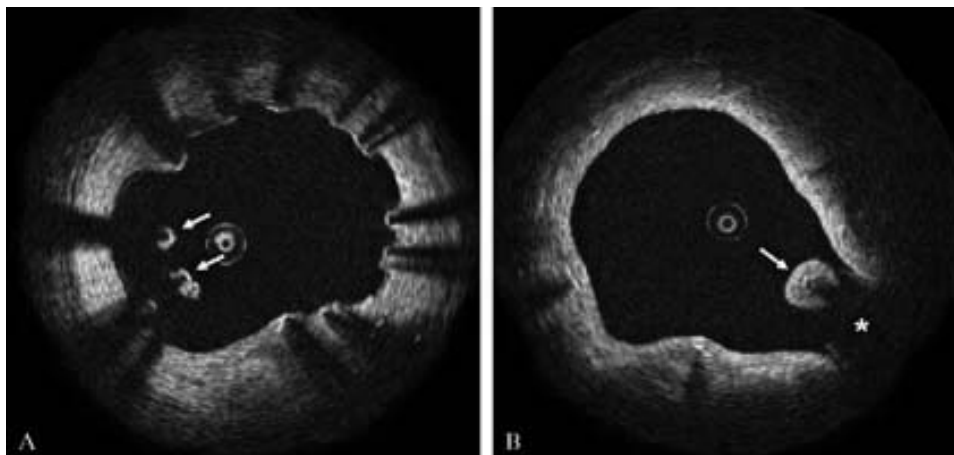


Figure 4.—A) Stent struts not apposed to the vessel wall but covered by tissue (arrows); B) The figure shows a strut covered by tissue but not apposed to the vessel wall due to the presence of a side branch (*).

3) dissolution of thrombus jailed between the stent and the vessel wall in patients undergoing primary PCI for acute myocardial infarction.³¹ The resolution of an intramural hematoma created by vessel dissection during PCI has been also postulated as the origin of late incomplete stent apposition.⁴⁶ OCT can assess stent apposition at follow up with higher accuracy than IVUS (even when the struts are covered with tissue Figure 4) and could be able to provide new insights into its causes. It has been reported that the prevalence of incompletely apposed struts by OCT is higher in sirolimus-eluting stent (SES) than in bare metal stents (BMS).^{33, 47} In another study that evaluated 57 SES at 6 months follow up, 79 out of the 6 840 struts visualized by OCT showed incomplete apposition and were more often located in areas of SES overlap.⁴⁸

Struts coverage following DES implantation.—Endothelial struts coverage has been identified in pathology as the most powerful histological predictor of stent thrombosis.^{49, 50} Finn *et al.* reported that a stent with a ratio of uncovered to total stent struts per section >30% has an odds ratio for thrombus of 9 (95% CI, 3.5 to 22).⁴⁹ Angioscopic studies have shown a correlation between the neo-

intimal coverage and the presence of thrombi.^{51, 52} DES inhibits neointimal proliferation to such extent that it may not be detectable by IVUS.⁵³⁻⁵⁵ The higher resolution of OCT allows the visualization and measurement of tiny layers of tissue covering the stent struts (Figure 5).^{56, 57} A study in carotid rabbit model evaluated the usefulness of OCT to identify struts coverage after stenting. No differences in the mean neointimal thickness measured by histology and OCT were found. Further the intra and interobserver reproducibility of neointimal thickness measurements by OCT was excellent (R2=0.90 and 0.88 respectively).^{58, 59} Recently several OCT studies evaluating the struts coverage in DES in humans at different time intervals have been published. Xie *et al.* compared the neointimal coverage at 3 months follow-up in 16 patients treated with BMS and 24 patients that underwent SES implantation. The neointimal thickness per strut and the percentage of neointimal thickness area per cross section were higher in the BMS group than in the SES group (351±248 vs 31±39 μm; P<0.0001; 45.0±14% vs 10.0±4%; P<0.0001, respectively). The frequency of uncovered struts was higher in the SES group than the BMS group (15% vs 0.1%; P<0.0001 and 15% vs 1.1% P<0.0001 respectively). There was no signi-

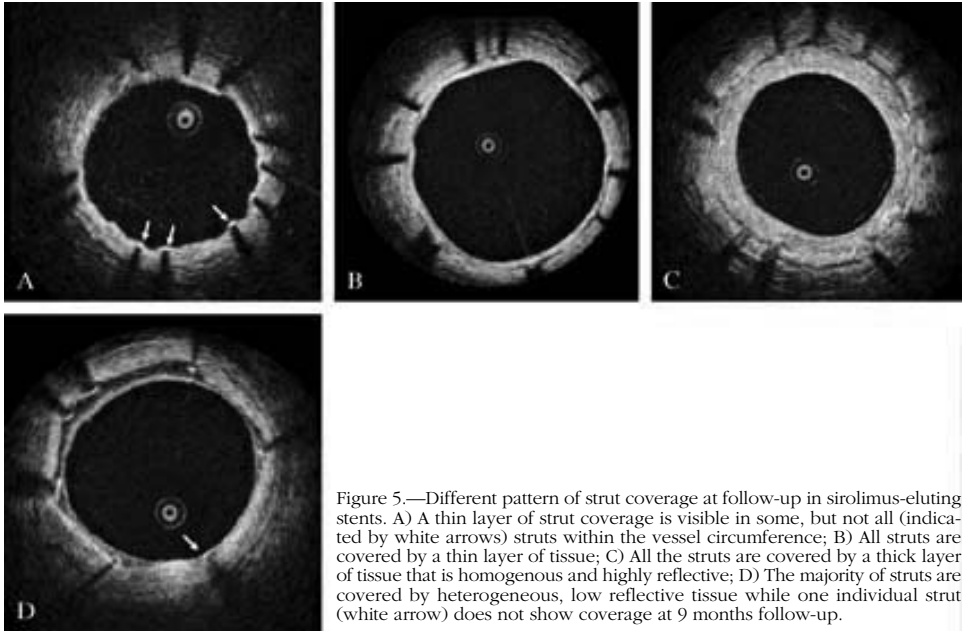


Figure 5.—Different pattern of strut coverage at follow-up in sirolimus-eluting stents. A) A thin layer of strut coverage is visible in some, but not all (indicated by white arrows) struts within the vessel circumference; B) All struts are covered by a thin layer of tissue; C) All the struts are covered by a thick layer of tissue that is homogenous and highly reflective; D) The majority of struts are covered by heterogeneous, low reflective tissue while one individual strut (white arrow) does not show coverage at 9 months follow-up.

ficant difference in the incidence of in-stent thrombus between the 2 groups (14% *vs* 0%; $P=0.23$).³³ These results were confirmed in another study that compared BMS at short and long term follow up with SES. The percentage of uncovered struts in SES was significantly higher than in BMS while the neointimal thickness was lower in SES than in BMS.⁴⁷ Matsumoto *et al.* studied 34 patients (57 SES) with IVUS and OCT at 6 months follow-up. The authors reported that 64% of the struts were covered by thin tissue undetectable by IVUS (median tissue thickness 52.5 μm , 25th and 75th percentiles 28 and 147.6 μm respectively). Overall 89% of the struts were covered by tissue but only in 16% of the stents all the struts were covered.⁴⁸ A recently published study evaluated the struts coverage in SES at 6 and 12 months follow-up. Forty-six SES (6 561 struts) were studied in 36 patients. The authors reported that only 4 SES at 6 months (18.2%) and 10 SES at 12 months (41.7%) were fully covered by tissue. The analysis showed a significant increase in the average thickness of the tissue cover-

ring the struts from 42 ± 28 μm at 6 months to 88 ± 32 μm at 12 months.⁶⁰ Takano *et al.* evaluated the long-term follow up of SES in 21 patients. Overall the frequency of uncovered struts was 5% and 81% of the patients presented uncovered struts at 2 years follow-up. The presence of uncovered struts was more frequent at side branches and at overlapping segments. They observed 3 patients with thrombi by OCT examination but no clinical stent thrombosis was observed.⁶¹

Some data suggest that OCT might be able to provide details on the characteristics of the neointimal tissue such as the presence of neovessels.⁶² Neovascularization adjacent to stent struts is a common finding in experimental animal models but the incidence and significance in human is unknown.

Some considerations must be taken into account when studying struts coverage by OCT. Current OCT can not well distinguish the tissue type covering the struts, e.g. a neointimal layer from fibrin. Furthermore, different types of neointimal tissue can be present and may have different functiona-

lity.^{63, 64} The presence of tissue covering the strut does not automatically imply that normal endothelial function is restored. In the future, higher image resolution or quantitative tissue characterization might help to better characterize tissue coverage clinically.

Assessment of restenosis.—OCT can be useful in the evaluation of the causes that contribute to restenosis after DES implantation such as incomplete lesion coverage or gaps between stents.⁶⁵

Stent fracture (with subsequent defect of local drug delivery) has also been related to restenosis in DES and could be visualized with OCT.⁶⁶ Non-uniform distribution of stent struts could affect the drug delivery and therefore have an influence in restenosis in DES. This has been confirmed in preclinical⁶⁷ and IVUS studies. The maximum interstrut angle has been identified in IVUS as predictor of intimal hyperplasia cross-sectional area.⁶⁸ OCT allows the assessment of strut distribution in vivo with high accuracy. A OCT study in phantoms demonstrated significant differences in the strut distribution of SES and paclitaxel eluting stents (PES) suggesting that SES maintained a more regular strut distribution despite expansion.⁶⁹

Another field of clinical use for OCT might be the assessment of the performance of DES in complex coronary interventions such as bifurcations. Buellesfeld et al reported the 9 month OCT follow-up in a case of crush-stenting with PES. Crush stenting results in three layers of metal in the segment of the main vessel proximal to the stented side branch. There has been concern that this could release a higher dose of drug locally with the potential adverse effect of delayed endothelialization. In this report, OCT imaging showed the overlapping struts layers in the crushed segment completely covered by tissue. Furthermore, OCT allowed clear visualization of the struts located in the ostium demonstrating a non-uniform distribution and different patterns of tissue coverage.⁷⁰ The effect of overlapping stents eluting different drugs in the development of endothelial coverage might also be studied with OCT.

Evaluation of new generation DES.—Fully biodegradable stents have emerged as one of the most promising future stent technologies because they may avoid the potential long-term complications of metallic DES such as late and very late stent thrombosis and the need for prolonged dual anti platelet therapy. The ABSORB trial recently published, showed the feasibility of implantation of the bioabsorbable everolimus-eluting coronary stent (BVS: Abbott Laboratories, IL, USA), composed of a poly-L-lactic acid backbone, coated with a degradable polymer /everolimus matrix. In a subset of 13 patients, OCT was performed after stent implantation and at 6 months follow up. In that scenario OCT allowed not only a very precise characterization of the stent apposition and coverage but also demonstrated structural changes in the bioabsorbable DES along time. At baseline 738 struts were visualized while at follow up only 671 could be identified. Furthermore, the appearance of the struts changed from baseline to follow up reflecting a change in the optical properties probably related with the absorption process.⁷¹ At present OCT appears as the best available tool for the in-vivo visualization of the morphological changes of the stent and within the vessel wall during the absorption process.

Plaque characterization

Acute coronary syndromes caused by the rupture of a coronary plaque are common initial manifestations of coronary atherosclerosis. The detection of the lesions with high risk of rupture (the so called “vulnerable plaques”) would be of main importance for the prevention of future ACS. Over the last years, there has been a growing interest in this field and a lot of different techniques have been developed to evaluate diverse aspects involved in plaque vulnerability.^{72, 73} Among them, OCT has emerged as one of the most promising due to its ability to provide information about the plaque composition, the presence of macrophages and the thickness of the fibrous cap.

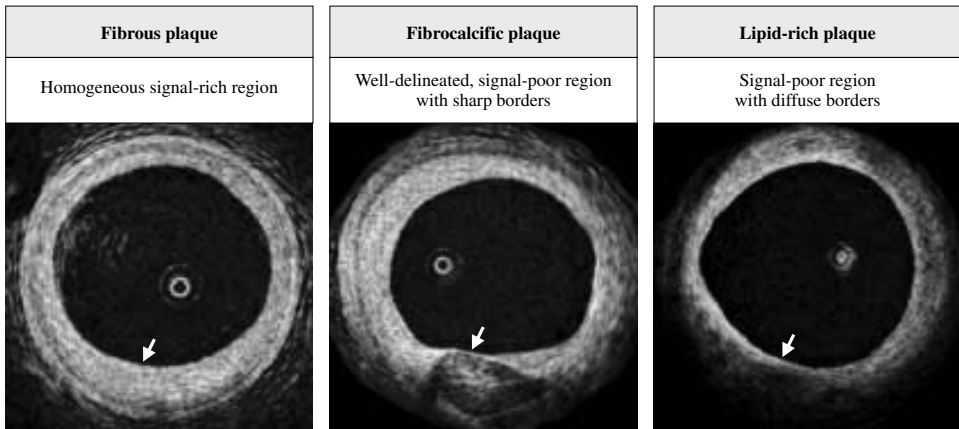


Figure 6.—OCT image criteria for plaque type.

PLAQUE COMPOSITION

The propensity of atherosclerotic lesions to destabilize and rupture is highly dependent on their composition. In comparison with histology OCT has demonstrated to be highly sensitive and specific for characterizing different types of atherosclerotic plaques. Yabushita *et al* analyzed 357 diseased carotid and coronary segments *ex vivo* and classified them as fibrous, fibrocalcific and lipid-rich plaques. The criteria for each plaque type are listed in Figure 6. The comparison with histology showed a sensitivity and specificity ranging from 71-79% and 97-98% for fibrous plaques, 95-96% and 97% for fibrocalcific plaques, and 90-94% and 90-92% for lipid-rich plaques.⁷⁴ *Ex-vivo* validations have also shown that OCT is superior to conventional and integrated backscatter IVUS for the characterization of coronary atherosclerotic plaque composition.⁷⁵⁻⁷⁸ *In vivo*, OCT is able to identify most of the architectural features identified by IVUS and may be superior for the identification of lipid pools and intimal hyperplasia.¹⁶ Several authors have evaluated the OCT appearance of coronary plaques in different groups of patients reporting higher prevalence of lipid-rich plaques in ACS and acute myocardial infarction than in patients with stable angina⁷⁹ and no differences in the culprit plaque imaged by OCT

between diabetics and non-diabetics patients⁸⁰ and men or women with ACS.⁸¹ According to histological and IVUS examinations, the percentage of lipid-rich plaque by OCT has been found to be higher in plaques with expansive remodelling.⁸²

PLAQUE RUPTURE AND INTRACORONARY THROMBUS IDENTIFICATION

Plaque rupture with subsequent thrombosis is the most frequent cause of ACS. OCT can identify plaque rupture and intracoronary thrombus with high accuracy.^{83, 84} Recently, Kubo *et al.* evaluated the ability of OCT for the assessment of the culprit lesion morphology in acute myocardial infarction in comparison with IVUS and angiography. They found an incidence of plaque rupture by OCT of 73%, significantly higher than that detected by both angiography (47%, $P=0.035$) and IVUS (40%, $P=0.009$). Intracoronary thrombus was observed in all cases by OCT and angiography but was identified only in 33% of patients by IVUS.⁸⁵ Furthermore, Kume *et al.* demonstrated that OCT might be able to distinguish between white and red thrombus. Red thrombus appears in OCT as high-backscattering structure with signal-free shadowing (Figure 7) while white thrombus appears as a low-backscattering structure.⁸⁶ OCT could be helpful to identify the culprit

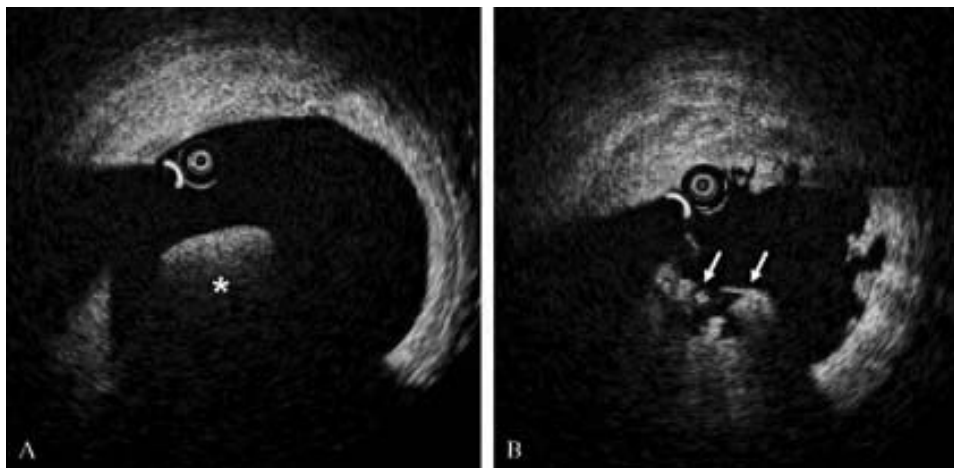


Figure 7.—OCT identification of intracoronary thrombus. A) Red thrombus (*) appears in OCT as a high-backscattering structure with shadowing; B) OCT performed after balloon dilatation in a patient with an acute myocardial infarction. Abundant thrombotic material can be observed in the lumen.

lesion in ACS and might provide additional information about the underlying cause that lead to the plaque rupture.

ASSESSMENT OF THE FIBROUS CAP

Autopsy studies of sudden cardiac death victims have shown that the most frequent cause of the coronary occlusion is rupture of a thin-cap fibroatheroma (TCFA) plaque. Such lesions are characterized by a large necrotic core with a thin fibrous cap usually <65 microns in thickness. While conventional intracoronary imaging techniques such as IVUS do not have enough resolution to evaluate in detail the fibrous cap, OCT has demonstrated in correlation with histological examinations that it is able to provide accurate measurements of the thickness of the fibrous cap.^{87, 88} Therefore it could be useful for the *in vivo* detection of TCFA (Figure 8).⁸⁹ Kubo *et al.* reported in a study with IVUS, OCT and angiography in acute myocardial infarction patients an incidence of TCFA as high as 83%. OCT was the only imaging technology able to estimate the fibrous cap thickness in these patients (mean 49 ± 21 μm). Two studies have reported that the plaque colour by angiography is related to the thickness of the fibrous cap as measured by OCT with yellow plaques often presenting thin

caps.^{90, 91} It has been suggested that the ability of OCT to measure changes in the fibrous cap thickness could be useful to assess the effect of statins in plaque stabilization.^{92, 93} Furthermore, recent data suggest that new OCT technology (such as polarization-sensitive OCT) could be able to assess the collagen content and smooth muscle cell density in the fibrous cap.⁹⁴ This could provide very valuable information about the mechanical stability of the fibrous cap enabling the identification of lesions at high risk of rupture.

MACROPHAGES DETECTION

Intense fibrous cap infiltration by macrophages is another of the features of the vulnerable plaques. An *ex-vivo* study by Tearney *et al.* demonstrated OCT could be able to quantify macrophage within the fibrous cap.⁹⁵ *In vivo*, it has been demonstrated that unstable patients present a significantly higher macrophage density detected by OCT in the culprit lesion than stable patients. Furthermore, in the same population, the sites of plaque rupture demonstrated a greater macrophage density than non-ruptured sites.⁹⁶

Raffel *et al.* reported that macrophage den-

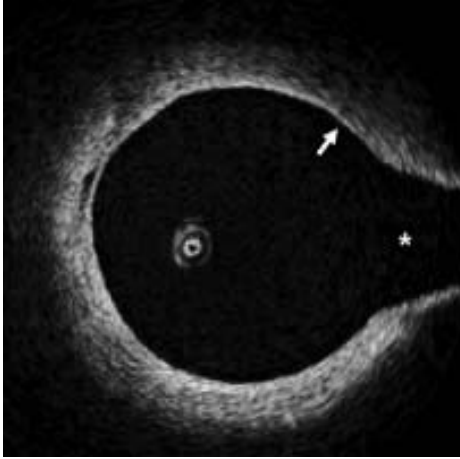


Figure 8.—Assessment of fibrous cap thickness by OCT. The figure shows a lipid-rich plaque (low-signal with diffuse borders) covered by a thin fibrous cap (white arrow). By OCT the fibrous cap measures 60 μm . (*) side branch.

sity in the fibrous cap detected by OCT correlated with the white blood cell count, and both parameters could be useful to predict the presence of TCFA.⁹⁷

COMBINED PLAQUE ASSESSMENT

OCT can provide information for the detection of high-risk plaques *in vivo* especially by visualizing directly the fibrous cap. However due to its limited penetration OCT can not provide a full analysis of large plaques up to the adventitia. Further, histological examinations have demonstrated that OCT readers may have difficulties to distinguish lipid pools from calcium deposits.⁹⁸ On the contrary, other techniques such as IVUS and IVUS radiofrequency data (RFD) analysis can image the complete plaque thickness and can identify the presence of necrotic core but their limited axial resolution does not allow the evaluation of the fibrous cap. Recently, Sawada *et al.* reported how the combined use of IVUS RFD analysis and OCT improved the accuracy for TCFA detection. One hundred and twenty-six plaques in 56 patients with angina were stu-

died. Of the sixty-one plaques diagnosed initially as TCFA by IVUS RFD analysis criteria only 28 had a thin fibrous cap as measured by OCT, so they were definite TCFA. In addition, eight OCT-derived TCFA did not have necrotic core in the IVUS RFD analysis mainly due to the misreading in OCT caused by dense calcium.⁹⁹ This data suggests that the combination of the information provided by different methods could be essential for better identification of high-risk coronary lesions.

Conclusions

The high resolution images provided by OCT open new possibilities into the evaluation of stents and coronary atherosclerosis. During stenting, OCT offers the possibility to assess stent apposition in great detail and can identify the presence of vessel injury due to stent implantation. At follow-up, the tissue coverage of individual struts can be imaged with OCT. Regarding plaque characterization this imaging technique holds promise for the identification of thin cap fibroatheroma due to its ability to provide information about plaque composition, presence of macrophages and thickness of the fibrous cap.

Riassunto

Tomografia a coerenza ottica: applicazioni cliniche e valutazione degli stent a rilascio di farmaci

La tomografia di coerenza ottica (OCT) è una modalità di imaging basata sulla luce in grado di fornire immagini *in vivo* ad alta risoluzione delle arterie coronarie. Negli ultimi anni, vi è stato un continuo sviluppo tecnologico che ha migliorato la qualità dell'immagine ed ha semplificato la procedura di acquisizione, allo scopo di ottenere l'applicazione diffusa di questa tecnica in ambito clinico. Per la sua elevata risoluzione, la OCT può rappresentare uno strumento di elevato valore per la valutazione della parete arteriosa coronarica, l'impatto acuto ed a lungo termine degli interventi percutanei sulla struttura della placca e l'architettura del vaso e la valutazione degli stent. Durante l'applicazione dei stent, la OCT offre la possibilità di valutare il posizionamento dello stent in elevato dettaglio e può identificare la presenza di danni vascolari dovuti all'impianto dello

stent stesso. Al follow-up, la OCT consente di verificare la copertura tissutale delle varie parti del dispositivo. Questo aspetto è di particolare interesse per gli stent a rilascio di farmaci, in cui la proliferazione neointimale è inibita al punto tale che non può essere visualizzata con tecniche di imaging intracoronario convenzionali quali la sonografia intravascolare. In riferimento all'analisi della parete vascolare, la OCT promette la possibilità di identificare la presenza di fibroateromi dotati di capsula sottile, vista la capacità di fornire informazioni sulla composizione della placca, la presenza di macrofagi e lo spessore della capsula fibrosa.

Parole chiave: Tomografia a coerenza ottica - Stent medicati - Malattia coronarica.

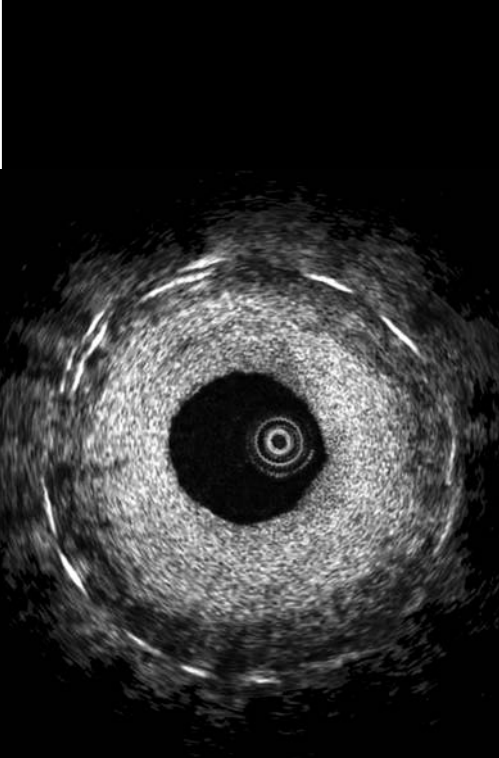
References

- Di Mario C, Gorge G, Peters R, Kearney P, Pinto F, Hausmann D *et al.* Clinical application and image interpretation in intracoronary ultrasound. Study Group on Intracoronary Imaging of the Working Group of Coronary Circulation and of the Subgroup of Intravascular Ultrasound of the Working Group of Echocardiography of the European Society of Cardiology. *Eur Heart J* 1998;19(2):207-29.
- Mintz GS, Nissen S. E, Anderson W. D, Bailey S. R, Erbel R, Fitzgerald P. J, *et al.* American College of Cardiology Clinical Expert Consensus Document on Standards for Acquisition, Measurement and Reporting of Intravascular Ultrasound Studies (IVUS). A report of the American College of Cardiology Task Force on Clinical Expert Consensus Documents. *J Am Coll Cardiol* 2001;37(5):1478-92.
- Boppart SA, Bouma BE, Pitris C, Southern JF, Brezinski ME, Fujimoto JG. In vivo cellular optical coherence tomography imaging. *Nat Med* 1998;4:861-5.
- Regar E, Schaar J, Mont E, Virmani R, Serruys PW. Optical coherence tomography. *Cardiovasc Rad Med* 2003;4:198-204.
- Regar E vLA, Serruys PW, editors. *Optical Coherence Tomography in cardiovascular research*. London: Informa Healthcare; 2007.
- Huang D, Swanson EA, Lin CP, Schuman JS, Stinson WG, Chang W *et al.* Optical coherence tomography. *Science* 1991;254:1178-81.
- Huang D, Wang J, Lin CP, Puliafito CA, Fujimoto JG. Micron-resolution ranging of cornea anterior chamber by optical reflectometry. *Lasers Surg Med* 1991;11:419-25.
- Panozzo G, Gusson E, Parolini B, Mercanti A. Role of OCT in the diagnosis and follow up of diabetic macular edema. *Semin Ophthalmol* 2003;18:74-81.
- Li XD, Boppart SA, Van Dam J, Mashimo H, Mutinga M, Drexler W *et al.* Optical coherence tomography: advanced technology for the endoscopic imaging of Barrett's esophagus. *Endoscopy* 2000;32:921-30.
- Tearney GJ, Brezinski ME, Southern JF, Bouma BE, Boppart SA, Fujimoto JG. Optical biopsy in human urologic tissue using optical coherence tomography. *J Urol* 1997;157:1915-9.
- Welzel J, Lankenau E, Birngruber R, Engelhardt R. Optical coherence tomography of the human skin. *J Am Acad Dermatol* 1997;37:958-63.
- Tearney GJ, Brezinski ME, Boppart SA, Bouma BE, Weissman N, Southern JF *et al.* Images in cardiovascular medicine. Catheter-based optical imaging of a human coronary artery. *Circulation* 1996;94:3013.
- Brezinski ME, Tearney GJ, Bouma BE, Boppart SA, Hee MR, Swanson EA *et al.* Imaging of coronary artery microstructure (in vitro) with optical coherence tomography. *Am J Cardiol* 1996;77:92-3.
- Tearney GJ, Jang IK, Kang DH, Aretz HT, Houser SL, Brady TJ *et al.* Porcine coronary imaging in vivo by optical coherence tomography. *Acta Cardiol* 2000;55:233-7.
- Fujimoto JG, Boppart SA, Tearney GJ, Bouma BE, Pitris C, Brezinski ME. High resolution in vivo intra-arterial imaging with optical coherence tomography. *Heart* 1999;82:128-33.
- Jang IK, Bouma BE, Kang DH, Park SJ, Park SW, Seung KB *et al.* Visualization of coronary atherosclerotic plaques in patients using optical coherence tomography: comparison with intravascular ultrasound. *J Am Coll Cardiol* 2002;39:604-9.
- Yun SH, Tearney GJ, Vakoc BJ, Shishkov M, Oh WY, Desjardins AE *et al.* Comprehensive volumetric optical microscopy in vivo. *Nat Med* 2006;12:1429-33.
- Liu B, Brezinski ME. Theoretical and practical considerations on detection performance of time domain, Fourier domain, and swept source optical coherence tomography. *J Biomed Opt* 2007;12:044007.
- Asawa K, Kataoka T, Kobayashi Y, Hasegawa T, Nishioka H, Yamashita H *et al.* Method analysis for optimal continuous imaging using intravascular optical coherence tomography. *J Cardiol* 2006;47:133-41.
- Prati F CM, Ramazzotti V, Imola F, Giudice R, Albertucci M. Safety and feasibility of a new non-occlusive technique for facilitated intracoronary optical coherence tomography(OCT) acquisition in various clinical and anatomical scenarios. *Eurointervention* 2007;3:365-70.
- Prati F, Cera M, Ramazzotti V, Imola F, Giudice R, Giudice M *et al.* From bench to bedside. *Circ J* 2008;72:839-43.
- Gonzalo N, Regar Evelyn. Tips and tricks for intravascular optical coherence tomography. In: Sabate editor. *Percutaneous Interventions beyond stenting. Tips and tricks for new technology*. Informa Healthcare. In press.
- Yamaguchi T, Terashima M, Akasaka T, Hayashi T, Mizuno K, Muramatsu T *et al.* Safety and feasibility of an intravascular optical coherence tomography image wire system in the clinical setting. *Am J Cardiol* 2008;101:562-7.
- van Beusekom HMM, Regar E, Peters, van der Giessen WJ. Assessment of long-term radiation effects following balloon angioplasty by OCT imaging and histology. In: London: Informa Healthcare; 2007.
- Aoki J, Colombo A, Dudek D, Banning AP, Drzewiecki J, Zmudka K *et al.* Persistent remodeling and neointimal suppression 2 years after polymer-based, paclitaxel-eluting stent implantation: insights from serial intravascular ultrasound analysis in the TAXUS II study. *Circulation* 2005;112:3876-83.
- Grube E, Gerckens U, Buellesfeld L, Fitzgerald PJ. Images in cardiovascular medicine. Intracoronary imaging with optical coherence tomography: a new high-resolution technology providing striking visualization in the coronary artery. *Circulation* 2002;106:2409-10.
- Bouma BE, Tearney GJ, Yabushita H, Shishkov M, Kauffman CR, DeJoseph Gauthier D *et al.* Evaluation of intracoronary stenting by intravascular optical coherence tomography. *Heart* 2003;89:317-20.
- Tanigawa J BP, Dimopoulos K, Di Mario C. Optical coherence tomography to assess malapposition in overlapping drug-eluting stents. *Eurointervention* 2008;3:580-3.
- Tanigawa J, Barlis P, Di Mario C. Heavily calcified coro-

- nary lesions preclude strut apposition despite high pressure balloon dilatation and rotational atherectomy: in-vivo demonstration with optical coherence tomography. *Circ J* 2008;72:157-60.
30. Alfonso F, Suarez A, Perez-Vizcayno MJ, Moreno R, Escaned J, Banuelos C *et al*. Intravascular ultrasound findings during episodes of drug-eluting stent thrombosis. *J Am Coll Cardiol* 2007;50:2095-7.
 31. Cook S, Wenaweser P, Togni M, Billinger M, Morger C, Seiler C *et al*. Incomplete stent apposition and very late stent thrombosis after drug-eluting stent implantation. *Circulation* 2007;115:2426-34.
 32. Feres F, Costa JR, Jr., Abizaid A. Very late thrombosis after drug-eluting stents. *Catheter Cardiovasc Interv* 2006;68:83-8.
 33. Xie Y, Takano M, Murakami D, Yamamoto M, Okamatsu K, Inami S *et al*. Comparison of neointimal coverage by optical coherence tomography of a sirolimus-eluting stent versus a bare-metal stent three months after implantation. *Am J Cardiol* 2008;102:27-31.
 34. Barlis P, Di Mario C, van Beusekom HMM, Gonzalo N, Regar E. Novelities in Cardiac Imaging – Optical Coherence Tomography (OCT). A critical appraisal of the safety concerns tempering the success of drug-eluting stents. *Eurointervention* 2008; In press.
 35. Schinkel AFL vBH, Maugenest AM; van Wunnik S, Serruys PW, Regar E. OCT Findings in very late (4 y years) paclitaxel-eluting stent thrombosis. *J Am Coll Cardiol Interventions* 2008; In press.
 36. Regar E, Schaar J, Serruys PW. Images in cardiology. Acute recoil in sirolimus eluting stent: real time, in vivo assessment with optical coherence tomography. *Heart* 2006;92:123.
 37. Schwarzwacher SP, Metz JA, Yock PG, Fitzgerald PJ. Vessel tearing at the edge of intracoronary stents detected with intravascular ultrasound imaging. *Cathet Cardiovasc Diagn* 1997;40:152-5.
 38. Schwartz RS, Huber KC, Murphy JG, Edwards WD, Camrud AR, Vlietstra RE *et al*. Restenosis and the proportional neointimal response to coronary artery injury: results in a porcine model. *J Am Coll Cardiol* 1992;19:267-74.
 39. Farb A, Sangiorgi G, Carter AJ, Walley VM, Edwards WD, Schwartz RS *et al*. Pathology of acute and chronic coronary stenting in humans. *Circulation* 1999;99:44-52.
 40. Schroeder S, Baumbach A, Mahrholdt H, Haase KK, Oberhoff M, Herdeg C *et al*. The impact of untreated coronary dissections on acute and long-term outcome after intravascular ultrasound guided PTCA. *Eur Heart J* 2000;21:137-45.
 41. Hong MK, Park SW, Lee NH, Nah DY, Lee CW, Kang DH *et al*. Long-term outcomes of minor dissection at the edge of stents detected with intravascular ultrasound. *Am J Cardiol* 2000;86:791-5, A9.
 42. Nishida T, Colombo A, Briguori C, Stankovic G, Albiero R, Corvaja N *et al*. Outcome of nonobstructive residual dissections detected by intravascular ultrasound following percutaneous coronary intervention. *Am J Cardiol* 2002;89:1257-62.
 43. Jang IK, Tearney G, Bouma B. Visualization of tissue prolapse between coronary stent struts by optical coherence tomography: comparison with intravascular ultrasound. *Circulation* 2001;104:2754.
 44. Farb A, Burke AP, Kolodgie FD, Virmani R. Pathological mechanisms of fatal late coronary stent thrombosis in humans. *Circulation* 2003;108:1701-6.
 45. Futamatsu H, Sabate M, Angiolillo DJ, Jimenez-Quevedo P, Corros C, Morikawa-Futamatsu K *et al*. Characterization of plaque prolapse after drug-eluting stent implantation in diabetic patients: a three-dimensional volumetric intravascular ultrasound outcome study. *J Am Coll Cardiol* 2006;48:1139-45.
 46. Sawada T, Shite J, Shinke T, Watanabe S, Otake H, Matsumoto D *et al*. Persistent malapposition after implantation of sirolimus-eluting stent into intramural coronary hematoma: optical coherence tomography observations. *Circ J* 2006;70:x1515-9.
 47. Chen BX, Ma FY, Luo W, Ruan JH, Xie WL, Zhao XZ *et al*. Neointimal coverage of bare-metal and sirolimus-eluting stents evaluated with optical coherence tomography. *Heart* 2008;94:566-70.
 48. Matsumoto D, Shite J, Shinke T, Otake H, Tanino Y, Ogasawara D *et al*. Neointimal coverage of sirolimus-eluting stents at 6-month follow-up: evaluated by optical coherence tomography. *Eur Heart J* 2007;28:961-7.
 49. Finn AV, Joner M, Nakazawa G, Kolodgie F, Newell J, John MC *et al*. Pathological correlates of late drug-eluting stent thrombosis: strut coverage as a marker of endothelialization. *Circulation* 2007;115:2435-41.
 50. Joner M, Finn AV, Farb A, Mont EK, Kolodgie FD, Ladich E *et al*. Pathology of drug-eluting stents in humans: delayed healing and late thrombotic risk. *J Am Coll Cardiol* 2006;48:193-202.
 51. Awata M, Kotani J, Uematsu M, Morozumi T, Watanabe T, Onishi T *et al*. Serial angioscopic evidence of incomplete neointimal coverage after sirolimus-eluting stent implantation: comparison with bare-metal stents. *Circulation* 2007;116:910-6.
 52. Kotani J, Awata M, Nanto S, Uematsu M, Oshima F, Minamiguchi H *et al*. Incomplete neointimal coverage of sirolimus-eluting stents: angioscopic findings. *J Am Coll Cardiol* 2006;47:2108-11.
 53. Serruys PW, Degertekin M, Tanabe K, Abizaid A, Sousa JE, Colombo A *et al*. Intravascular ultrasound findings in the multicenter, randomized, double-blind RAVEL (RAndomized study with the sirolimus-eluting VELOCITY balloon-expandable stent in the treatment of patients with de novo native coronary artery Lesions) trial. *Circulation* 2002;106:798-803.
 54. Stone GW, Ellis SG, Cox DA, Hermiller J, O'Shaughnessy C, Mann JT *et al*. A polymer-based, paclitaxel-eluting stent in patients with coronary artery disease. *N Engl J Med* 2004;350(3):221-31.
 55. Morice MC, Serruys PW, Sousa JE, Fajadet J, Ban Hayashi E, Perin M *et al*. A randomized comparison of a sirolimus-eluting stent with a standard stent for coronary revascularization. *N Engl J Med* 2002;346:1773-80.
 56. Gerckens U, Lim VY, Grube E. Optical coherence tomography imaging in coronary drug-eluting stenting. *Rev Esp Cardiol* 2005;58:1469.
 57. Takano M, Jang IK, Mizuno K. Neointimal proliferation around malapposed struts of a sirolimus-eluting stent: optical coherence tomography findings. *Eur Heart J* 2006;27:1763.
 58. Prati F, Zimmarino M, Stabile E, Pizzicannella G, Fouad T, Rabozzi R *et al*. Does optical coherence tomography identify arterial healing after stenting? An in vivo comparison with histology, in a rabbit carotid model. *Heart* 2008;94:217-21.
 59. Tanimoto S, Rodriguez-Granillo G, Barlis P, de Winter S, Bruining N, Hamers *et al*. A novel approach for quantitative analysis of intracoronary optical coherence tomography. High inter-observer agreement with computer-assisted contour detection. *Catheter Cardiovasc Interv* 2008;6:Epub ahead of print.
 60. Yao ZH, Matsubara T, Inada T, Suzuki Y, Suzuki T. Neointimal coverage of sirolimus-eluting stents 6 months and 12 months after implantation: evaluation by optical coherence tomography. *Chin Med J (Engl)* 2008;121:503-7.

61. Takano M, Yamamoto M, Inami S, Murakami D, Seimiya K, Ohba T *et al*. Long-term follow-up evaluation after sirolimus-eluting stent implantation by optical coherence tomography: do uncovered struts persist? *J Am Coll Cardiol* 2008;51:968-9.
62. Regar E, van Beusekom HMM, van der Giessen WJ, Serruys PW. Optical coherence tomography findings at 5-year follow-up after coronary stent implantation. *Circulation* 2005;112:345-6.
63. Takano M, Xie Y, Murakami D, Inami S, Yamamoto M, Ohba T *et al*. Various optical coherence tomographic findings in restenotic lesions after sirolimus-eluting stent implantation. *Int J Cardiol* 2008. In press.
64. Tanimoto S AJ, Serruys PW, Regar E. Paclitaxel-eluting stent restenosis shows three - layer appearance by optical coherence tomography. *Eurointervention* 2006;1(484).
65. Grube E, Lim V, Buellesfeld L. OCT findings in drug-eluting stents. In: Regar E, van Leeuwen T, Serruys P.W Editors. *Optical coherence tomography in cardiovascular research*. London: Informa Healthcare; 2007.
66. Shite J, Matsumoto D, Yokoyama M. Sirolimus-eluting stent fracture with thrombus, visualization by optical coherence tomography. *Eur Heart J* 2006;27:1389.
67. Schulz C, Herrmann RA, Beilharz C, Pasquantonio J, Alt E. Coronary stent symmetry and vascular injury determine experimental restenosis. *Heart* 2000;83:462-7.
68. Takebayashi H, Mintz GS, Carlier SG, Kobayashi Y, Fujii K, Yasuda T *et al*. Nonuniform strut distribution correlates with more neointimal hyperplasia after sirolimus-eluting stent implantation. *Circulation* 2004;110:3430-4.
69. Suzuki Y, Ikeno F, Yeung AC. Drug-eluting stent strut distribution: a comparison between Cypher and Taxus by optical coherence tomography. *J Invasive Cardiol* 2006;18:111-4.
70. Buellesfeld L, Lim V, Gerckens U, Mueller R, Grube E. Comparative endoluminal visualization of TAXUS crush-stenting at 9 months follow-up by intravascular ultrasound and optical coherence tomography. *Z Kardiol* 2005;94:690-4.
71. Ormiston JA, Serruys PW, Regar E, Dudek D, Thuesen L, Webster MW *et al*. A bioabsorbable everolimus-eluting coronary stent system for patients with single de novo coronary artery lesions (ABSORB): a prospective open-label trial. *Lancet* 2008;371:899-907.
72. Garcia-Garcia HM, Gonzalo N, Regar E, Serruys PW. Diagnosis and treatment of vulnerable plaque. *Expert Rev Cardiovasc Ther* 2008;6:209-22.
73. Serruys PW, Garcia-Garcia HM, Regar E. From post-mortem characterization to the in-vivo detection of thin-capped fibroatheromas: the missing link towards percutaneous treatment. *J Am Coll Cardiol* 2007;50:950-2.
74. Yabushita H, Bouma BE, Houser SL, Aretz HT, Jang IK, Schlerendorf KH *et al*. Characterization of human atherosclerosis by optical coherence tomography. *Circulation* 2002;106:1640-5.
75. Rieber J, Meissner O, Babaryka G, Reim S, Oswald M, Koenig A *et al*. Diagnostic accuracy of optical coherence tomography and intravascular ultrasound for the detection and characterization of atherosclerotic plaque composition in ex-vivo coronary specimens: a comparison with histology. *Coron Artery Dis* 2006;17:425-30.
76. Patwari P, Weissman NJ, Boppart SA, Jesser C, Stamper D, Fujimoto JG *et al*. Assessment of coronary plaque with optical coherence tomography and high-frequency ultrasound. *Am J Cardiol* 2000;85:641-4.
77. Kawasaki M, Bouma BE, Bressner J, Houser SL, Nadkarni SK, MacNeill BD *et al*. Diagnostic accuracy of optical coherence tomography and integrated backscatter intravascular ultrasound images for tissue characterization of human coronary plaques. *J Am Coll Cardiol* 2006;48:81-8.
78. Kume T, Akasaka T, Kawamoto T, Watanabe N, Toyota E, Neishi Y *et al*. Assessment of coronary arterial plaque by optical coherence tomography. *Am J Cardiol* 2006;97:1172-5.
79. Jang IK, Tearney GJ, MacNeill B, Takano M, Moselewski F, Iftima N *et al*. In vivo characterization of coronary atherosclerotic plaque by use of optical coherence tomography. *Circulation* 2005;111:1551-5.
80. Chia S, Raffel OC, Takano M, Tearney GJ, Bouma BE, Jang IK. Comparison of coronary plaque characteristics between diabetic and non-diabetic subjects: An in vivo optical coherence tomography study. *Diabetes Res Clin Pract* 2008. In press.
81. Chia S, Christopher Raffel O, Takano M, Tearney GJ, Bouma BE, Jang IK. In-vivo comparison of coronary plaque characteristics using optical coherence tomography in women vs. men with acute coronary syndrome. *Coron Artery Dis* 2007;18:423-7.
82. Kume T, Okura H, Kawamoto T, Akasaka T, Toyota E, Watanabe N *et al*. Relationship between coronary remodeling and plaque characterization in patients without clinical evidence of coronary artery disease. *Atherosclerosis* 2008;197:799-805.
83. Meng L, Lv B, Zhang S, Yv B. In vivo optical coherence tomography of experimental thrombosis in a rabbit carotid model. *Heart* 2008;94:777-80.
84. Barlis P, Serruys PW, de Vries A, Regar E. Optical coherence tomography assessment of vulnerable plaque rupture: Predilection for the plaque 'shoulder'. *Eur Heart J* 2008 [Epub ahead of print].
85. Kubo T, Imanishi T, Takarada S, Kuroi A, Ueno S, Yamano T *et al*. Assessment of culprit lesion morphology in acute myocardial infarction: ability of optical coherence tomography compared with intravascular ultrasound and coronary angiography. *J Am Coll Cardiol* 2007;50:933-9.
86. Kume T, Akasaka T, Kawamoto T, Ogasawara Y, Watanabe N, Toyota E *et al*. Assessment of coronary arterial thrombus by optical coherence tomography. *Am J Cardiol* 2006;97:1713-7.
87. Kume T, Akasaka T, Kawamoto T, Okura H, Watanabe N, Toyota E *et al*. Measurement of the thickness of the fibrous cap by optical coherence tomography. *Am Heart J* 2006;152:755 e1-4.
88. Cilingiroglu M, Oh JH, Sugunan B, Kemp NJ, Kim J, Lee S *et al*. Detection of vulnerable plaque in a murine model of atherosclerosis with optical coherence tomography. *Catheter Cardiovasc Interv* 2006;67:915-23.
89. Barlis P, Serruys PW, Gonzalo N, Van der Giessen W, Jaeger P, Regar E. Assessment of culprit and remote coronary narrowings using optical coherence tomography with long-term outcomes. *Am J Cardiol* 2008. In press.
90. Kubo TTT, Takarada S, Kuroi A, Ueno S, Yamano T, Tanimoto T *et al*. Implication of plaque color classification for assessing plaque vulnerability. *J Am Coll Cardiol Intv* 2008;1:74-80.
91. Takano M, Jang IK, Inami S, Yamamoto M, Murakami D, Okamatsu K *et al*. In vivo comparison of optical coherence tomography and angiography for the evaluation of coronary plaque characteristics. *Am J Cardiol* 2008;101:471-6.
92. Chia S, Raffel OC, Takano M, Tearney GJ, Bouma BE, Jang IK. Association of statin therapy with reduced coronary plaque rupture: an optical coherence tomography study. *Coron Artery Dis* 2008;19:237-42.

93. Takarada S, Imanishi T, Kubo T, Tanimoto T, Kitabata H, Nakamura N *et al*. Effect of statin therapy on coronary fibrous-cap thickness in patients with acute coronary syndrome: Assessment by optical coherence tomography study. *Atherosclerosis* 2008. In press.
94. Nadkarni SK, Pierce MC, Park BH, de Boer JF, Whittaker P, Bouma BE *et al*. Measurement of collagen and smooth muscle cell content in atherosclerotic plaques using polarization-sensitive optical coherence tomography. *J Am Coll Cardiol* 2007;49:1474-81.
95. Tearney GJ, Yabushita H, Houser SL, Aretz HT, Jang IK, Schlendorf KH *et al*. Quantification of macrophage content in atherosclerotic plaques by optical coherence tomography. *Circulation* 2003;107:113-9.
96. MacNeill BD, Jang IK, Bouma BE, Ifimia N, Takano M, Yabushita H *et al*. Focal and multi-focal plaque macrophage distributions in patients with acute and stable presentations of coronary artery disease. *J Am Coll Cardiol* 2004;44:972-9.
97. Raffel OC, Tearney GJ, Gauthier DD, Halpern EF, Bouma BE, Jang IK. Relationship between a systemic inflammatory marker, plaque inflammation, and plaque characteristics determined by intravascular optical coherence tomography. *Arterioscler Thromb Vasc Biol* 2007;27:1820-7.
98. Manfrini O, Mont E, Leone O, Arbustini E, Eusebi V, Virmani R *et al*. Sources of error and interpretation of plaque morphology by optical coherence tomography. *Am J Cardiol* 2006;98:156-9.
99. Sawada T, Shite J, Garcia-Garcia HM, Shinke T, Watanabe S, Otake H *et al*. Feasibility of combined use of intravascular ultrasound radiofrequency data analysis and optical coherence tomography for detecting thin-cap fibroatheroma. *Eur Heart J* 2008;29:1136-46.



6.2

Incomplete Stent Apposition And Delayed Tissue Coverage Are More Frequent In Drug Eluting Stents Implanted During Primary Percutaneous Coronary Intervention For ST Elevation Myocardial Infarction Than In Drug Eluting Stents Implanted For Stable/Unstable Angina. Insights from Optical Coherence Tomography

Gonzalo N, Barlis P, Serruys PW, Garcia-Garcia HM,
Onuma Y, Ligthart J, Regar E.

JACC Cardiovasc Interv. 2009 May;2(5):445-52.

Incomplete Stent Apposition and Delayed Tissue Coverage Are More Frequent in Drug-Eluting Stents Implanted During Primary Percutaneous Coronary Intervention for ST-Segment Elevation Myocardial Infarction Than in Drug-Eluting Stents Implanted for Stable/Unstable Angina

Insights From Optical Coherence Tomography

Nieves Gonzalo, MD, Peter Barlis, MBBS, MPH, Patrick W. Serruys, MD, PhD, Hector M. Garcia-Garcia, MD, MSc, Yoshinobu Onuma, MD, Jurgen Ligthart, BSc, Evelyn Regar, MD, PhD

Rotterdam, the Netherlands

Objectives The aim of this study was to compare the frequency of incomplete stent apposition (ISA) and struts not covered by tissue at long-term follow-up (as assessed by optical coherence tomography [OCT]) in drug-eluting stents (DES) implanted during primary percutaneous coronary intervention (PCI) for ST-segment elevation myocardial infarction (STEMI) versus DES implanted for unstable and stable angina.

Background Incomplete stent apposition and the absence of strut endothelialization might be linked to stent thrombosis. DES implanted for STEMI might have a higher risk of thrombosis.

Methods Consecutive patients in whom OCT was performed at least 6 months after DES implantation were included in the study. Stent struts were classified on the basis of the presence or absence of ISA and tissue coverage.

Results Forty-seven lesions in 43 patients (1,356 frames, 10,140 struts) were analyzed (49% stable angina, 17% unstable angina, 34% STEMI). Median follow-up time was 9 (range 7 to 72) months. Drug-eluting stents implanted during primary PCI presented ISA more often than DES implanted in stable/unstable angina patients (75% vs. 25.8%, $p = 0.001$). The frequency of uncovered struts was also higher in the STEMI group (93.8% vs. 67.7%, $p = 0.048$). On multivariate analysis, DES implantation in STEMI was the only independent predictor of ISA (odds ratio: 9.8, 95% confidence interval: 2.4 to 40.4, $p = 0.002$) and the presence of uncovered struts at follow-up (odds ratio: 9.5, 95% confidence interval: 1.0 to 90.3, $p = 0.049$).

Conclusions DES implanted for STEMI had a higher frequency of incompletely apposed struts and uncovered struts as assessed by OCT at follow-up. DES implantation during primary PCI in STEMI was an independent predictor of ISA and the presence of uncovered struts at follow-up. (J Am Coll Cardiol Intv 2009;2:445–52) © 2009 by the American College of Cardiology Foundation

From the Thoraxcenter, Erasmus Medical Center, Rotterdam, the Netherlands.

Manuscript received January 15, 2009, accepted January 23, 2009.

Primary percutaneous coronary intervention (PCI) is the recommended treatment for ST-segment elevation myocardial infarction (STEMI) (1). Stent implantation during primary PCI presents some challenges, namely the presence of abundant thrombotic material that can potentially contribute to suboptimal stent deployment. The use of drug-eluting stents (DES) in this setting is under debate due to the concerns about a potentially higher risk of stent thrombosis in this population (2). Recent intravascular ultrasound (IVUS) studies suggest that the presence of incomplete stent apposition (ISA) is potentially linked to late stent thrombosis (3). Gradual absorption of the thrombus that was present during primary PCI has been postulated to contribute to late acquired stent malapposition (4). Endothelial strut coverage has been identified in pathological series as the most powerful histological predictor of stent thrombosis (5). DES inhibit neointimal proliferation to such an extent that it might not be visualized with conventional intracoronary imaging techniques such as IVUS. Optical coherence tomography (OCT) is a high-resolution light-based imaging modality that can provide a very detailed assessment of stent apposition and tissue strut coverage.

Abbreviations and Acronyms

BMS = bare metal stent(s)

DES = drug-eluting stent(s)

ISA = incomplete stent apposition

IVUS = intravascular ultrasound

OCT = optical coherence tomography

PCI = percutaneous coronary intervention

STEMI = ST-segment elevation myocardial infarction

The objective of the present study was to compare the frequency of ISA and uncovered struts (as assessed by OCT) at long-term follow-up in DES implanted during primary PCI for STEMI versus DES implanted for stable or unstable (IB/IIB/IIIB Braunwald classification) angina.

Methods

Patient sample. All consecutive patients between January 2007 and May 2008 in whom OCT was performed for follow-up of a DES implanted at least 6 months prior were included in the study. Exclusion criteria were repeated revascularization in the target vessel, depressed left ventricular function, coronary chronic total occlusions, and impaired renal function. All patients gave written informed consent.

OCT acquisition. The OCT acquisition was performed with a commercially available system for intracoronary imaging (LightLab Imaging, Westford, Massachusetts). The ImageWire (LightLab Imaging) was positioned distal to the region of interest with a double lumen catheter (Twin Pass catheter, Vascular Solutions Inc., Minneapolis, Minnesota) that had been placed in the artery over a conventional guidewire. The automated pullback was performed at 3 mm/s while the blood was removed by the continuous injection of iso-osmolar contrast (Iodixanol 320, Visipaque; GE Health Care, Carrigtohill, County Cork, Ireland) at 37°C through

the guiding catheter. The data were digitally stored for offline analysis.

OCT analysis. Offline analysis was performed with the proprietary LightLab software (LightLab Imaging). The analysts (Cardialysis BV, Rotterdam, the Netherlands) were blinded to clinical and procedural characteristics. The stented region was defined as the region between the first and the last frame with circumferentially visible struts. For this region 1 frame was selected every millimeter, and the lumen and stent area contours were drawn. Stent longitudinal symmetry ratio was defined as minimum stent area/maximum stent area.

INCOMPLETE STENT APPPOSITION DEFINITIONS AND MEASUREMENTS. Incomplete stent apposition was defined as separation of at least 1 stent strut from the vessel wall not related to a side branch (Fig. 1). A strut was considered incompletely apposed if the distance from the endoluminal surface of the strut to the vessel wall was higher than the sum of the metal and polymer thickness. The cutoff points used for each stent type were: paclitaxel-eluting stent (Taxus, Boston Scientific Corp., Natick, Massachusetts) 130 μm , sirolimus-eluting stent (Cypher Select, Cordis, Johnson & Johnson, Miami, Florida) 160 μm , everolimus-eluting stent (Xience V, Abbot Vascular, Santa Clara, California) 90 μm , and biolimus-eluting stent (Biomatrix

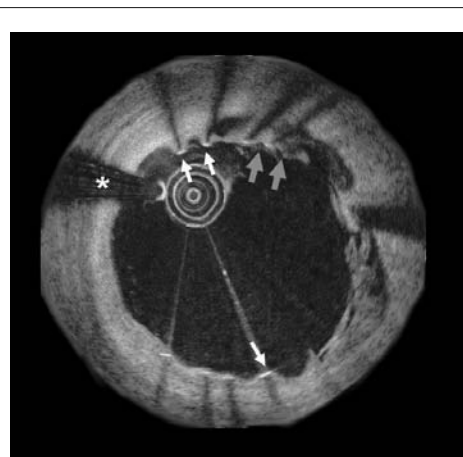


Figure 1. Incomplete Stent Apposition and Uncovered Struts

Optical coherence tomography cross section corresponding to a patient treated with drug-eluting stent implantation during primary percutaneous coronary intervention in the right coronary artery for an inferior ST-segment elevation myocardial infarction 9 months before. The **red arrows** indicate incomplete stent apposition, whereas the **white arrows** show some struts not covered by tissue. From 12 to 5 an irregular material suggestive of organized thrombus can be observed behind the struts. *Guidewire artefact.

III, Biosensors, Morges, Switzerland) 120 μm . The number of malapposed struts, the maximal incomplete stent apposition length (maximum distance from the endoluminal surface of the strut to the vessel wall), and the incomplete stent apposition area were measured. Calcification could not be accurately evaluated due to the shadow caused by stent struts in OCT.

STRUT COVERAGE DEFINITIONS AND MEASUREMENTS. The struts were classified as uncovered when a tissue layer on the endoluminal surface was not visible. In the covered struts, the tissue coverage thickness was measured per strut as the distance from the central aspect of the endoluminal surface of the strut to the lumen. The total tissue coverage area was calculated as: stent area – lumen area. The percentage of tissue coverage area was calculated as: tissue coverage area/stent area \times 100. The tissue coverage volume was calculated as: tissue coverage area \times stent length. The percentage of tissue coverage volume area was calculated as: tissue coverage volume/stent volume \times 100. The tissue coverage symmetry per frame was analyzed with the following ratio: (maximum tissue coverage thickness per frame – minimum tissue coverage thickness per frame)/maximum tissue coverage thickness per frame. This ratio can have values between 0 and 1. The closer the ratio is to 1 the higher is the asymmetry of the tissue coverage (Fig. 2). To evaluate the distribution of the uncovered struts along the

stent we calculated the percentage of frames with at least 1 uncovered strut in the lesions that showed uncovered struts. **Statistical analysis.** Statistical analysis was performed with SPSS 12.0.1 for Windows (SPSS Inc., Chicago, Illinois). Categorical variables are expressed as percentages and continuous variables are expressed as mean \pm SD, median and (range), or median and (interquartile range). The ISA and strut coverage comparisons were performed per lesion. Chi-square was used for the comparisons of categorical variables between groups. For the comparisons of continuous variables, the Student *t* test or nonparametric (Mann-Whitney) test was used according to their distribution. Multiple logistic regression analysis was performed to assess independent predictors of ISA and uncovered struts. Variables considered clinically relevant and with $p < 0.15$ in the univariate analysis were included in the models.

Results

Clinical and procedural characteristics. Fifty patients followed up with OCT after DES implantation were initially enrolled in the study. Seven patients were excluded for image quality not appropriate for analysis. Finally, 43 patients (47 vessels, 47 lesions) were included (16 STEMI, 27 stable/unstable angina).

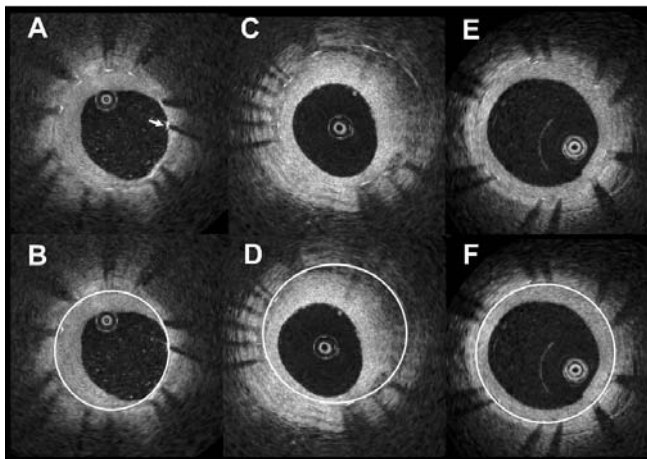


Figure 2. Tissue Coverage Symmetry Patterns

(A and B) Asymmetric tissue coverage with uncovered struts: whereas some struts are covered by a thick layer of tissue, other struts (from 2 to 5) are covered by a very thin layer, and there is even 1 uncovered strut (indicated by the white arrow). **(C and D)** Asymmetric tissue coverage without uncovered struts: all the struts are covered by tissue that shows very different thickness along the vessel circumference. **(E and F)** Symmetric tissue coverage: all the struts are covered by tissue that shows similar thickness along the vessel circumference.

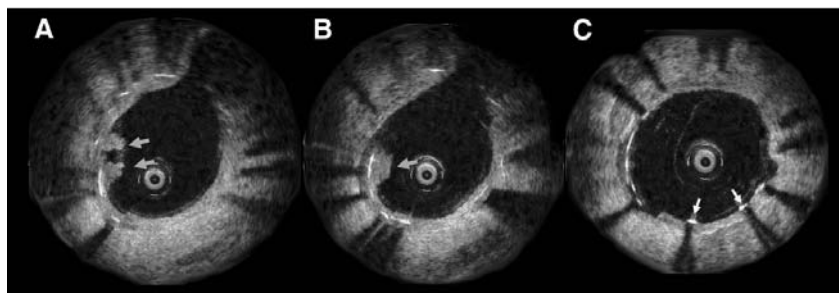


Figure 3. Struts Covered by Organized Thrombus

Optical coherence tomography cross-sections corresponding to a drug-eluting stent implanted in the left anterior descending coronary artery more than 4 years ago due to an anterior ST-segment elevation myocardial infarction. (A and B) The blue arrows indicate the presence of an irregular, highly reflective material (suggestive of organized thrombus) covering some struts. (C) Represents a cross section more proximal where some uncovered struts can be observed (white arrows).

The mean age was 64.5 ± 11.7 years, and 63.8% were men. Regarding cardiac risk factors, 47.8%, 21.3%, and 70.2% had hypertension, diabetes mellitus, and hyperlipidemia, respectively, and 19.1% were smokers. The studied vessel was the left anterior descending in 57%, the circumflex in 19%, and the right coronary artery in 24% of the lesions. The indication for stent implantation was stable angina in 47% (20 of 43), unstable angina in 16% (7 of 43) and STEMI in 37% (16 of 43). The stent implanted was Taxus in 10.6%, Cypher Select in 55.3%, Xience V in 2.1%, and Biomatrix III in 32%. The median time to follow-up angiography and OCT examination was 9 (7 to 72) months. The mean stent diameter, stent number, and stent imaged length were 2.9 ± 0.3 mm, 1.8 ± 0.8 , and 28 ± 15 mm, respectively.

OCT quantitative analysis. A total of 10,140 struts from 1,356 frames were analyzed. The mean lumen area, mean stent area, and mean neointimal area were 6.42 ± 2.11 mm², 7.11 ± 2.06 mm², and 0.67 ± 0.47 mm², respectively. The stent symmetry ratio was 0.63 ± 0.16 .

ISA frequency by OCT. The frequency of incompletely apposed struts was 68 of 10,140 (0.6%). Forty-five of the 68 incompletely apposed struts (66.1%) were not covered by tissue. Forty of 1,356 frames (2.9%) had at least 1 incompletely apposed strut. In 20 of 47 lesions (42.6%), incomplete stent apposition of at least 1 strut was found. In the lesions with ISA, the mean percentage of frames with ISA was $9.3 \pm 7.1\%$.

Strut coverage by OCT. The frequency of uncovered struts in the total sample was 6.1% (624 of 10,140). Twenty-one percent (285 of 1,356) of all the frames analyzed presented at least 1 uncovered strut. In 36 of 47 lesions (76.6%), at least 1 uncovered strut was visualized. The mean neointima symmetry ratio was 0.73 ± 0.13 . Twenty-six struts of the

10,140 (0.2%) were covered by an irregular material suggestive of organized thrombus (Fig. 3).

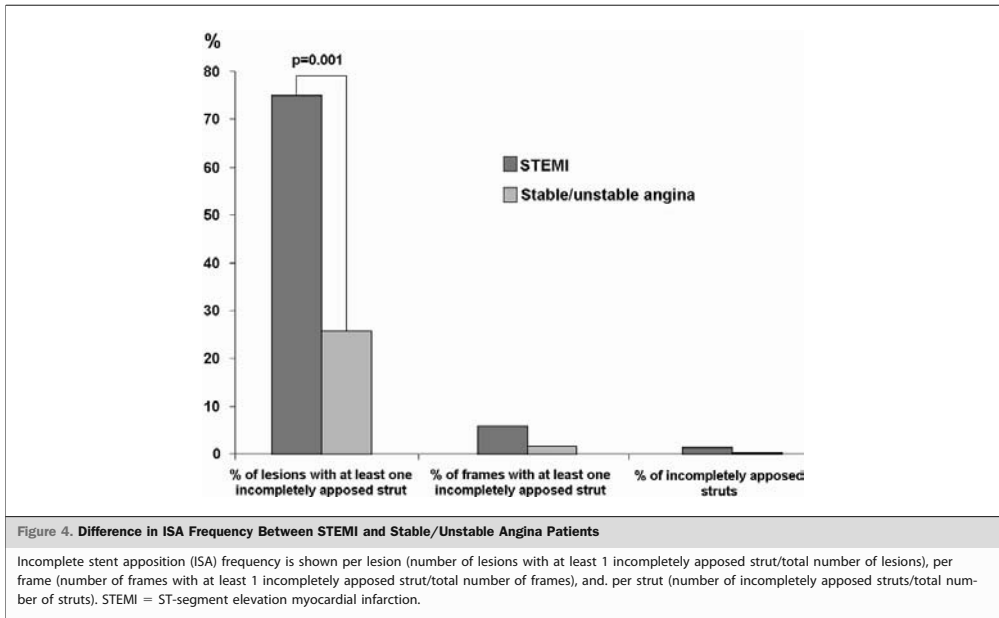
STEMI patients. Sixteen of the 47 lesions studied were treated with DES implantation during primary PCI for STEMI. Table 1 shows the baseline characteristics of the STEMI patients in comparison with the rest of the sample. The time to follow-up was 11.5 months (range 7 to 59

Table 1. Baseline Characteristics in STEMI and Stable/Unstable Angina Patients

	STEMI	Stable/Unstable Angina	p Value
Age (yrs)	64 ± 12	64 ± 11	0.85
Male (%)	50.0	71.0	0.13
Hypertension (%)	50.0	46.7	0.53
DM (%)	31.3	16.1	0.2
Dyslipidemia (%)	75.0	67.7	0.43
Smoker (%)	31.3	12.9	0.13
Family history (%)	62.5	67.7	0.48
Vessel (%)			0.46
LAD	68.8	51.6	
LCX	18.7	19.4	
RCA	12.5	29.0	
Stent type (%)			0.48
Taxus	13.3	9.7	
Cypher	53.3	54.8	
Xience	6.7	0.0	
Biomatrix	26.7	35.5	
Number of stents	1.53 ± 0.52	2.03 ± 0.94	0.08
Stent-imaged length (mm)	24.9 ± 10.5	29.9 ± 17.6	0.3

Age, gender, and cardiovascular risk factors are compared per patient (ST-segment elevation myocardial infarction [STEMI] = 16 stable/unstable angina = 27). The rest of the variables are compared per lesion (STEMI = 16 stable/unstable angina = 31).

DM = diabetes mellitus; LAD = left anterior descending coronary artery; LCX = left circumflex artery; RCA = right coronary artery.



months) for the STEMI group and 9 months (range 9 to 72 months) for the rest of the patients. There were no significant differences in lumen area (6.5 ± 2.0 vs. 6.4 ± 2 for STEMI and stable/unstable angina, respectively, $p = 0.86$), stent area (7.2 ± 2.0 vs. 7.0 ± 2.0 for STEMI and stable/unstable angina, respectively, $p = 0.78$), or stent symmetry ratio (0.58 ± 0.17 vs. 0.65 ± 0.15 for STEMI and stable/unstable angina, respectively, $p = 0.13$).

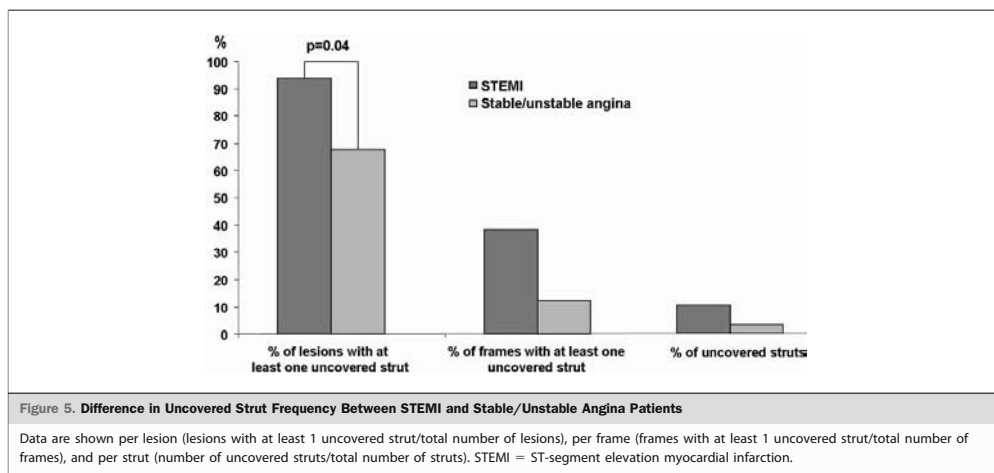
ISA in STEMI patients. Figure 4 represents the frequency of ISA in lesions treated with DES implantation for STEMI and the rest of the lesions. Table 2 shows the differences in the number of incompletely apposed struts (covered and not covered), maximum ISA length, and ISA area in lesions treated for STEMI and lesions treated for stable/unstable angina.

Uncovered struts in STEMI patients. Figure 5 shows the difference in frequency of uncovered struts between lesions treated for STEMI and lesions treated for stable/unstable angina. The number of uncovered struts; the mean tissue coverage thickness, area, and volume; and the tissue coverage symmetry ratio in both groups are indicated in Table 3.

Predictors of ISA. Multiple logistic regression analysis was performed to determine the independent predictors of ISA. The following variables were included in the model: age, follow-up time, stent length, stent symmetry ratio, and stent implantation during primary PCI. The only independent predictor of ISA was DES implantation during primary PCI for STEMI (odds ratio: 9.8, 95% confidence interval: 2.4 to 40.4, $p = 0.002$).

	STEMI (n = 16)	Stable/Unstable Angina (n = 31)	p Value
Number of incompletely apposed struts	2 (0–13)	0 (0–5)	0.001
Number of incompletely apposed uncovered struts	1 (0–13)	0 (0–4)	<0.001
Number of incompletely apposed covered struts	0.5 (0–3)	0 (0–5)	0.02
ISA area (mm ²)	0.28 (0.17–0.67)	0.35 (0.23–0.44)	0.5
Maximum ISA length (μm)	235 (162–297)	250 (230–600)	0.4

Number of struts is expressed as median and range. Incomplete stent apposition (ISA) area and maximum ISA length are expressed as median (interquartile range).
STEMI = ST-segment elevation myocardial infarction.



Predictors of uncovered struts. In the multivariate model for uncovered struts predictors, the following variables were included: age, follow-up time, stent length, stent area, and stent implantation during primary PCI. Drug-eluting stent implantation during primary PCI for STEMI was the only independent predictor of uncovered struts at follow-up (odds ratio: 9.5, 95% confidence interval: 1.0 to 90.3, $p = 0.049$).

Discussion

To our knowledge this is the first such study to use the high-resolution capabilities of intracoronary OCT to examine stent strut apposition and tissue coverage at follow-up in patients with STEMI treated with primary PCI. The main findings are: 1) DES implanted for STEMI had a higher frequency of incompletely apposed

and uncovered struts as assessed by OCT at follow-up, and 2) DES implantation during primary PCI in STEMI is an independent predictor of both ISA and the presence of uncovered struts at follow-up.

Drug-eluting stents have consistently demonstrated a reduction in restenosis rates when compared with bare-metal stents (BMS) in different clinical settings, including primary PCI for the treatment of STEMI (6). However, concerns have been raised about a potentially higher risk of stent thrombosis after DES implantation during primary PCI (7). Furthermore, ISA and lack of complete stent endothelialization have been identified as factors related to stent thrombosis (4,5).

ISA. Overall the frequency of incompletely apposed struts was very low (0.6%). In our study patients with STEMI treated with DES implantation during primary PCI had a higher frequency of ISA. Our results are in concordance with IVUS studies that have identified a higher incidence of late ISA in STEMI patients, especially when treated with DES. Hong et al. (8) reported an incidence of late ISA after primary PCI in STEMI of 11.5% after BMS implantation and 31.8% after DES implantation. In our sample, 75% of the lesions treated with DES during primary PCI showed evidence of ISA. The higher frequency of ISA observed in the present study can be explained by the higher resolution of OCT in comparison with IVUS (9). The results of the present study are also in line with a recent OCT study that identified a higher incidence of ISA in sirolimus-eluting stents implanted in unstable versus stable angina patients (33% vs. 4%) (10).

The dissolution of thrombus jailed after stent implantation during primary PCI has been postulated as 1 of the possible causes of the higher incidence of late ISA in

	STEMI (n = 16)	Stable/Unstable Angina (n = 31)	p Value
Number of uncovered struts	26.8 ± 20.8	6.2 ± 7.5	0.001
Uncovered strut distribution (%)	40.7 ± 25.2	16.4 ± 19.8	0.001
Mean tissue coverage area (mm ²)	0.72 ± 0.63	0.65 ± 0.37	0.68
% tissue coverage area	12.4 ± 9.9	11.0 ± 6.9	0.58
Tissue coverage volume (mm ³)	17.7 ± 21.6	21.9 ± 22.04	0.54
% tissue coverage volume	10.0 ± 9.4	10.3 ± 6.7	0.91
Tissue coverage thickness (μm)	110 ± 48	90 ± 53	0.22
Tissue coverage symmetry ratio	0.79 ± 0.23	0.70 ± 0.13	0.02

STEMI = ST-segment elevation myocardial infarction.

STEMI patients (4). Plaque rupture (characterized by a necrotic core with an overlying thin-ruptured cap infiltrated by macrophages and with paucity of smooth muscle cells) is the most frequent underlying substrate in STEMI. Stent implantation over a ruptured plaque with strut penetration into necrotic core has also been related to ISA in acute coronary syndromes (11). The clinical implications of ISA are controversial. Several studies have reported that the presence of ISA after DES implantation is not associated with adverse events at long-term follow-up (8,12,13). However, recently published IVUS observations suggest a possible relation between incomplete DES apposition and subsequent stent thrombosis (3,4). The clinical significance of ISA as detected by OCT is poorly understood. In fact, incomplete apposition of stent struts is a relatively common finding by OCT, although the vast majority of the patients do not experience clinical events in the long term (14). In addition, not all patients that experience DES thrombosis show strut malapposition (15,16). In the present study none of the patients with ISA as assessed by OCT presented with adverse clinical events.

Strut coverage. DES inhibits neointimal proliferation to such an extent that it might not be detectable by IVUS (17). The high resolution of OCT allows the visualization and measurement of tiny layers of tissue covering the stent struts (18). In the present study, the global frequency of uncovered individual struts was 6.1%, and a high proportion of lesions (36 of 47) presented uncovered struts. This is in agreement with different OCT studies recently published reporting strut coverage in DES at follow-up (14,19). A long-term follow-up with OCT in a group of patients treated with sirolimus-eluting stents revealed that 81% of the patients presented uncovered struts at 2 years' follow-up (20). In the present study 8 of the 9 lesions with more than 2 years' follow-up demonstrated uncovered struts by OCT, and interestingly, in 6 of those 8 lesions the DES were implanted during primary PCI. The frequency of struts with no visible coverage was significantly higher in STEMI patients treated during primary PCI (15 of 16 lesions). Likewise, the distribution of uncovered struts within the stent was more spread in STEMI patients (reflected in a higher proportion of frames with uncovered struts). The mean neointimal thickness did not differ between STEMI and stable/unstable angina patients, but the neointima showed a more asymmetric distribution in STEMI patients. Our findings are in agreement with pathological studies showing delayed endothelialization at the culprit site in acute myocardial infarction patients treated with DES compared with the culprit site in patients receiving DES for stable angina (21). A recent study, reporting a lower incidence of full tissue coverage in unstable angina than in stable angina, is also in line with our observations (10). Pathological data suggest a relation between arterial healing and underlying plaque morphology. In an autopsy study, Nakazawa et al.

(21) found a higher percentage of uncovered struts in patients with stents implanted in plaques with high-risk features (such as plaque rupture and thin cap fibroatheroma) as compared with those with stable plaque morphology. Despite a lack of OCT assessment during the primary PCI procedure in our study, it is accepted that plaque rupture is the most frequent underlying event leading to STEMI (22). The stent contact with an avascular tissue such as necrotic core and the different drug distribution due to the presence of thrombus are some of the factors that could explain the delayed coverage of struts in unstable patients (21,23). The more asymmetric distribution in the cross section of the tissue covering the struts found in STEMI patients might also be related with the eccentricity and composition of the plaque underlying the stent implantation (24). Endothelial struts coverage has been identified in pathological series as the most powerful histological predictor of stent thrombosis (5). Pathological data in humans suggest that neointimal coverage of stent struts might be a surrogate marker of endothelialization (25). However, Kubo et al. (10) reported that the presence of a higher incidence of uncovered struts by OCT in unstable patients was not associated with adverse outcomes at 9 months. In the present study no adverse events occurred at follow-up even when the frequency of uncovered struts was high. The clinical significance of the presence of uncovered struts as assessed by OCT remains unknown and would require specific long-term follow-up studies. Despite the high resolution of the technique, coverage of the strut with an individual cell layer cannot be excluded. Currently, OCT cannot adequately distinguish the tissue type covering the struts (e.g., a neointimal layer from fibrin). Furthermore, different types of neointimal tissue with different optical properties can be observed and might have different functionality (26). The development of quantitative tissue characterization by OCT might be helpful to better understand the clinical implications of strut tissue coverage.

Study limitations. The present study is observational and nonrandomized. No formal sample size calculation was performed. Another limitation is the lack of serial OCT assessments with OCT only performed at long-term follow-up. Therefore, it was not possible to distinguish between persistent and late-acquired ISA. The presence of positive remodeling as a cause of late ISA (as demonstrated previously in IVUS) cannot be excluded. Likewise, no information was available about the underlying plaque in which the stent was implanted. Only DES were included in the study. Therefore we cannot exclude that BMS would not have behaved similarly when implanted in the setting of STEMI.

Conclusions

DES implanted for STEMI had a higher frequency of incompletely apposed struts and uncovered struts as assessed

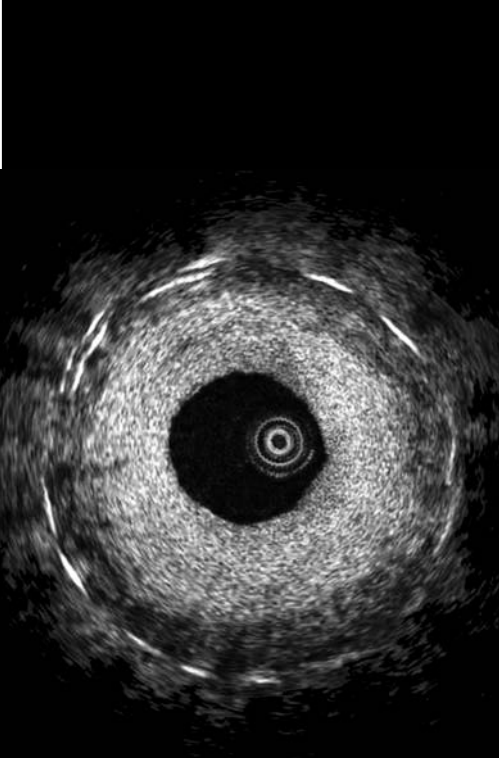
by OCT at follow-up. Drug-eluting stent implantation during primary PCI in STEMI was an independent predictor of ISA and the presence of uncovered struts at follow-up. Whether these findings have a causal link to the heightened rate of stent thrombosis in STEMI patients remains to be confirmed by larger studies.

Reprint requests and correspondence: Dr. Evelyn Regar, Thoraxcenter, Bd 585, Dr. Molewaterplein 40, 3015-GD Rotterdam, the Netherlands. E-mail: e.regar@erasmusmc.nl

REFERENCES

- Boden WE, Eagle K, Granger CB. Reperfusion strategies in acute ST-segment elevation myocardial infarction: a comprehensive review of contemporary management options. *J Am Coll Cardiol* 2007;50:917–29.
- Urban P, Gershlick AH, Guagliumi G, et al. Safety of coronary sirolimus-eluting stents in daily clinical practice: 1-year follow-up of the e-Cypher registry. *Circulation* 2006;113:1434–41.
- Alfonso F, Suarez A, Perez-Vizcayno MJ, et al. Intravascular ultrasound findings during episodes of drug-eluting stent thrombosis. *J Am Coll Cardiol* 2007;50:2095–7.
- Cook S, Wenaweser P, Togni M, et al. Incomplete stent apposition and very late stent thrombosis after drug-eluting stent implantation. *Circulation* 2007;115:2426–34.
- Joner M, Finn AV, Farb A, et al. Pathology of drug-eluting stents in humans: delayed healing and late thrombotic risk. *J Am Coll Cardiol* 2006;48:193–202.
- Spaulding C, Henry P, Teiger E, et al. Sirolimus-eluting versus uncoated stents in acute myocardial infarction. *N Engl J Med* 2006;355:1093–104.
- Daemen J, Tanimoto S, Garcia-Garcia HM, et al. Comparison of three-year clinical outcome of sirolimus- and paclitaxel-eluting stents versus bare metal stents in patients with ST-segment elevation myocardial infarction (from the RESEARCH and T-SEARCH Registries). *Am J Cardiol* 2007;99:1027–32.
- Hong MK, Mintz GS, Lee CW, et al. Late stent malapposition after drug-eluting stent implantation: an intravascular ultrasound analysis with long-term follow-up. *Circulation* 2006;113:414–9.
- Bouma BE, Tearney GJ, Yabushita H, et al. Evaluation of intracoronary stenting by intravascular optical coherence tomography. *Heart* 2003;89:317–20.
- Kubo T, Imanishi T, Kitabata H, et al. Comparison of vascular response after sirolimus eluting stent implantation between patients with unstable and stable angina pectoris. A serial optical coherence tomography study. *J Am Coll Cardiol* 2008;1:475–84.
- Finn AV, Nakazawa G, Ladich E, Kolodgie FD, Virmani R. Does underlying plaque morphology play a role in vessel healing after drug eluting stent implantation? *J Am Coll Cardiol* 2008;1:485–8.
- Degertekin M, Serruys PW, Tanabe K, et al. Long-term follow-up of incomplete stent apposition in patients who received sirolimus-eluting stent for de novo coronary lesions: an intravascular ultrasound analysis. *Circulation* 2003;108:2747–50.
- Tanabe K, Serruys PW, Degertekin M, et al. Incomplete stent apposition after implantation of paclitaxel-eluting stents or bare metal stents: insights from the randomized TAXUS II trial. *Circulation* 2005;111:900–5.
- Xie Y, Takano M, Murakami D, et al. Comparison of neointimal coverage by optical coherence tomography of a sirolimus-eluting stent versus a bare-metal stent three months after implantation. *Am J Cardiol* 2008;102:27–31.
- Schinkel AFL, van Beusekom HMM, Maugeness AM, van Wunnik S, Serruys PW, Regar E. OCT Findings in very late (4 years) paclitaxel-eluting stent thrombosis. *J Am Coll Cardiol* 2008;1:449–51.
- Barlis P, DiMario C, van Beusekom HMM, Gonzalo N, Regar E. Novelty in cardiac imaging—optical coherence tomography (OCT). A critical appraisal of the safety concerns tempering the success of drug-eluting stents Eurointervention 2008;4 Suppl C:C22–6.
- Serruys PW, Degertekin M, Tanabe K, et al. Intravascular ultrasound findings in the multicenter, randomized, double-blind RAVEL (RANdomized study with the sirolimus-eluting VELOCITY balloon-expandable stent in the treatment of patients with de novo native coronary artery Lesions) trial. *Circulation* 2002;106:798–803.
- Prati F, Zimarino M, Stabile E, et al. Does optical coherence tomography identify arterial healing after stenting? An in vivo comparison with histology, in a rabbit carotid model. *Heart* 2008;94:217–21.
- Matsumoto D, Shite J, Shinke T, et al. Neointimal coverage of sirolimus-eluting stents at 6-month follow-up: evaluated by optical coherence tomography. *Eur Heart J* 2007;28:961–7.
- Takano M, Yamamoto M, Inami S, et al. Long-term follow-up evaluation after sirolimus-eluting stent implantation by optical coherence tomography: do uncovered struts persist? *J Am Coll Cardiol* 2008;51:968–9.
- Nakazawa G, Finn AV, Joner M, et al. Delayed arterial healing and increased late stent thrombosis at culprit sites after drug-eluting stent placement for acute myocardial infarction patients: an autopsy study. *Circulation* 2008;118:1138–45.
- Virmani R, Burke AP, Farb A, Kolodgie FD. Pathology of the vulnerable plaque. *J Am Coll Cardiol* 2006;47:C13–8.
- Hwang CW, Levin AD, Jonas M, Li PH, Edelman ER. Thrombosis modulates arterial drug distribution for drug-eluting stents. *Circulation* 2005;111:1619–26.
- Falk E, Shah PK, Fuster V. Coronary plaque disruption. *Circulation* 1995;92:657–71.
- Finn AV, Joner M, Nakazawa G, et al. Pathological correlates of late drug-eluting stent thrombosis: strut coverage as a marker of endothelialization. *Circulation* 2007;115:2435–41.
- Takano M, Xie Y, Murakami D, et al. Various optical coherence tomographic findings in restenotic lesions after sirolimus-eluting stent implantation. *Int J Cardiol* 2008 Apr 8 [Epub ahead of print].

Key Words: drug-eluting stents ■ optical coherence tomography ■ stent apposition ■ stent coverage ■ ST-segment elevation myocardial infarction.



6.3

Optical Coherence Tomography Patterns of Stent Restenosis

Gonzalo N, Serruys P.W, Okamura T, van Beusekom HM, Garcia-Garcia HM, van Soest G, van der Giessen W, Regar E.

Am Heart J. 2009 Aug;158(2):284-93

Optical coherence tomography patterns of stent restenosis

Nieves Gonzalo, MD, Patrick W. Serruys, MD, PhD, Takayuki Okamura, MD, PhD, Heleen M. van Beusekom, MD, PhD, Hector M. Garcia-Garcia, MD, MSc, Gijs van Soest, PhD, Wim van der Giessen, MD, PhD, and Evelyn Regar, MD, PhD
Rotterdam, The Netherlands

Background Stent restenosis is an infrequent but poorly understood clinical problem in the drug-eluting stent era. The aim of the study was to evaluate the morphologic characteristics of stent restenosis by optical coherence tomography (OCT).

Methods Patients (n = 24, 25 vessels) presenting with angiographically documented stent restenosis were included. Quantitative OCT analysis consisted of lumen and stent area measurement and calculation of restenotic tissue area and burden. Qualitative restenotic tissue analysis included assessment of tissue structure, backscattering and symmetry, visible microvessels, lumen shape, and presence of intraluminal material.

Results By angiography, restenosis was classified as diffuse, focal, and at the margins in 9, 11, and 5 vessels, respectively. By OCT, restenotic tissue structure was layered in 52%, homogeneous in 28%, and heterogeneous in 20%. The predominant backscatter was high in 72%. Microvessels were visible in 12%. Lumen shape was irregular in 28% and there was intraluminal material in 20%. The mean restenotic tissue symmetry ratio was 0.58 ± 0.19 . Heterogeneous and low scattering restenotic tissue was more frequent in focal (45.5% and 54.5%, respectively) than in diffuse (0 and 11.1%) and margin restenosis (0 and 0%) ($P = .005$ for heterogeneous, $P = .03$ for low scattering). Restenosis patients with unstable angina symptoms presented more frequently irregular lumen shape (60 vs 6.7%, $P = .007$). Stents implanted ≤ 12 months ago had more frequently restenotic tissue with layered appearance (84.6% vs 16.7%, $P = .003$).

Conclusions We demonstrate the ability of OCT to identify differential patterns of restenotic tissue after stenting. This information could help in understanding the mechanism of stent restenosis. (Am Heart J 2009;158:284-93.)

Restenosis caused by exaggerated neointimal proliferation was the main limitation for the long-term success of bare metal stents (BMSs).¹⁻³ The introduction of drug-eluting stents (DESs) dramatically reduced the incidence of restenosis to levels around 10%.⁴ However, restenosis still exists in the DES era, its pathophysiology is poorly understood, and its treatment remains challenging.⁵ Angiographic restenosis patterns have been shown to carry prognostic value with diffuse restenosis showing a higher incidence of events at 1 year.⁶ Intravascular ultrasound (IVUS) is a useful technique to evaluate the extent and distribution of the neointima tissue within the stented segment but is limited to visualize its complex tissue structure as can be documented by histopathology.⁶⁻⁸ Optical coherence tomography (OCT) is a new intracoronary imaging modality that can produce in vivo

high-resolution images of the coronary artery, providing new insights into the characteristics of the tissue covering the stent struts at follow-up.⁹⁻¹¹ The objective of the present study was to evaluate the morphologic characteristics of stent restenosis by OCT.

Methods

Study population

Between January 2007 and October 2008, all consecutive patients with OCT pullback performed in a vessel with angiographically documented restenosis (defined as diameter stenosis $\geq 50\%$ in the vessel segment within the stent or within 5 mm proximal or distal to the stent) were included in the study.

Quantitative angiography analysis

All angiograms were evaluated after intracoronary administration of nitrates using commercially available software for quantitative coronary angiography (Cardiovascular Angiography Analysis System II [CAAS II], Pie Medical, Maastricht, the Netherlands). The length of the stenotic segment, the minimum luminal diameter, and the percentage of diameter stenosis were measured.

From the Thoraxcenter, Erasmus MC, Rotterdam, The Netherlands.

Submitted March 16, 2009; accepted June 2, 2009.

Reprint requests: Evelyn Regar, MD, PhD, Thoraxcenter, Erasmus MC, Bd 585, 's-Gravendijkwal 230, 3015-CE Rotterdam, The Netherlands.

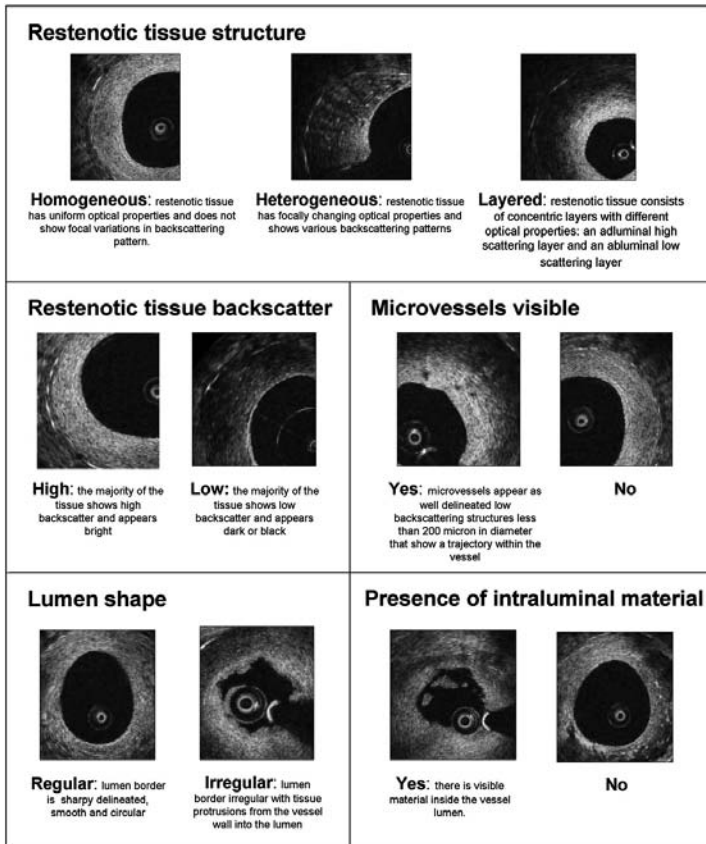
E-mail: e.regar@erasmusmc.nl

0002-8703/\$ - see front matter

© 2009, Mosby, Inc. All rights reserved.

doi:10.1016/j.ahj.2009.06.004

Figure 1



Stent restenosis qualitative OCT assessment.

Qualitative angiography analysis

Restenotic lesion type by angiography was classified as suggested by Mehran et al⁶: (a) diffuse restenosis >10 mm length; (b) focal intrastent restenosis <10 mm length; (c) margin restenosis: focal restenosis located in the proximal, distal margin or both.

Optical coherence tomography acquisition

Optical coherence tomography acquisition was performed using a commercially available system for intracoronary imaging and a 0.019-in ImageWire (LightLab Imaging, Westford, MA). The artery was cleared from blood during imaging, applying continuous flush delivery as described in detail previously.¹²

Flush consisted of iodixanol 370 (Visipaque, GE Health Care, Cork, Ireland) at a flow rate of 3.0 mL/s.

Optical coherence tomography quantitative analysis

Offline analysis was performed with the proprietary LightLab software (LightLab Imaging). The region of interest comprised the stent region and the stent margins defined as the vessel segment 5 mm proximal and distal to the stent. Lumen and stent area were measured at 1 mm longitudinal steps throughout the pullback. The restenotic tissue area was defined as stent area minus lumen area. Restenotic tissue burden was defined as mean restenotic tissue area/mean stent area ×100. The cross section containing the minimum luminal area (MLA) was used to

determine the maximum and the minimum restenotic tissue thickness and to calculate the restenotic tissue symmetry ratio (maximum restenotic tissue thickness – minimum restenotic tissue thickness/maximum restenotic tissue thickness).¹⁰

Optical coherence tomography qualitative analysis

To describe the morphologic appearance of the restenotic tissue, the parameters defined in Figure 1 (restenotic tissue structure, restenotic tissue backscatter, presence of microvessels, lumen shape, and presence of intraluminal material) were analyzed and classified in the region of maximal lumen narrowing by agreement of 2 observers.^{7,15} The 2 observers were blinded for the clinical and procedural characteristics.

To test the interobserver variability of the qualitative OCT assessment, 60 cross sections within the restenotic lesions were selected and analyzed independently by 2 observers not involved in the primary data analysis. One of the observers repeated the analysis 1 week later to assess the intraobserver variability.

Statistical analysis

As this represents an observational, exploratory study, no formal sample size calculation was performed. Continuous variables are expressed as mean \pm SD or median and interquartile range. Categorical variables are expressed as percentages. Comparisons between groups were performed with χ^2 for categorical variables and with Student *t* test or analysis of variance for continuous variables. Because of the performance of multiple univariate comparisons, *P* values presented in this article are exploratory only and should therefore be interpreted with caution. κ test was used to assess the inter- and intraobserver variability for qualitative OCT assessment.

Sources of funding

This study was supported in part by Siemens Healthcare. The authors are solely responsible for the design and conduct of this study, all study analyses, the drafting and editing of the paper and its final contents.

Results

Clinical and procedural characteristics

In the study period, 148 percutaneous coronary interventions were performed in our center in patients with stent restenosis (Table D). Sixteen percent of those cases (24 patients, 25 vessels) were imaged with OCT and included in the study. The inclusion in the study depended mainly in the operator experience with the OCT system and the consent of the patient to participate. Patients with depressed left ventricular function and impaired renal function were excluded. The median time from stent implantation was 12 months (interquartile range, 4-42 months). The stents were implanted originally for stable angina in 11 (44%), unstable angina in 10 (40%), and ST-elevation myocardial infarction in 4 (16%) of the cases. At the time of study inclusion, restenosis was considered the culprit lesion and responsible for clinical symptoms in 20 of 24 patients. The mean

Table I. Baseline characteristics

Demographics	
Age (y)	58.4 \pm 8
Male (%)	18 (75)
HT (%)	9 (37.5)
Dyslipidemia (%)	17 (70.8)
Diabetes mellitus (%)	7 (29.2)
Smoker (%)	4 (16.7)
Family history (%)	11 (45.8)
Cardiac history	
Previous MI (%)	11 (45.8)
CABG (%)	2 (8.3)
Clinical presentation at time of study inclusion	
Asymptomatic (%)	4 (16)
Stable angina (%)	11 (44)
Unstable angina (%)	9 (36)
STEMI (%)	1 (4)
Vessel	
LAD (%)	8 (32)
LCX (%)	5 (20)
RCA (%)	11 (44)
Saphenous vein graft (%)	1 (4)
Stent type	
BMS (%)	4 (16)
Paclitaxel-eluting stent (%)	8 (32)
Sirolimus-eluting stent (%)	2 (8)
Everolimus-eluting stent (%)	3 (12)
Biolimus-eluting stent (%)	2 (8)
Tacrolimus-eluting stent (%)	6 (24)

HT, Hypertension; CABG, coronary artery by-pass surgery; STEMI, ST-elevation myocardial infarction. BMS: bare-metal stent.

acquisition time and volume of contrast used were 8.8 \pm 3 seconds and 20.7 \pm 8 mL, respectively.

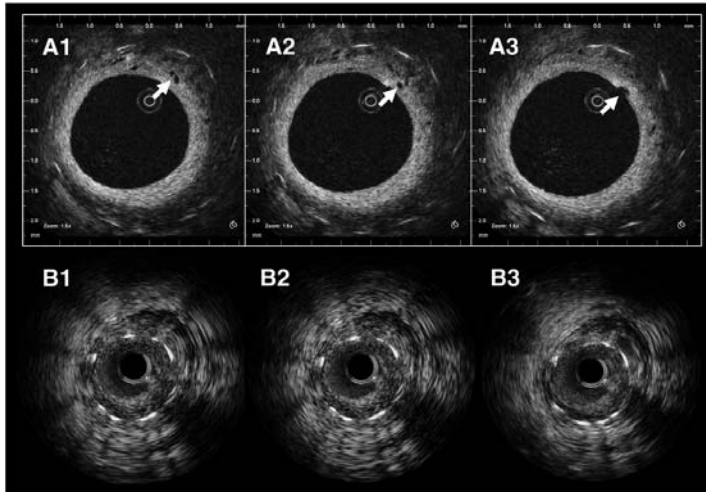
Angiographic analysis

The restenosis type by angiography was diffuse in 9 vessels (36%), focal in 11 vessels (44%), proximal edge in 1 vessel (4%), distal edge in 3 vessels (12%), and proximal and distal edge in 1 vessel (4%). The minimum lumen diameter was 1.0 \pm 0.3, 0.92 \pm 0.4, and 0.96 \pm 0.4 mm in diffuse, focal, and margin restenosis, respectively (*P* = .7). The percentage of diameter stenosis was 54.7% \pm 6.2% for diffuse, 67.8% \pm 10.5% for focal, and 62.8% \pm 9.6% for margin restenosis (*P* = .01)

Optical coherence tomography analysis

The mean imaged stent length was 27.7 \pm 9 mm. The restenotic tissue structure was layered in 13 (52%) cases, homogeneous in 7 (28%), and heterogeneous in 5 (20%). The predominant backscatter was high in 18 cases (72%) and low in 7 cases (28%). Microvessels were visible in 3 cases (12%) (Figure 2). The lumen presented irregular shape in 7 cases (28%), and there was evidence of intraluminal material in 5 cases (20%). The mean restenotic tissue symmetry ratio was 0.58 \pm 0.19. There were no differences in demographics or cardiovascular risk factors between the different patterns of restenosis by OCT.

Figure 2



Microvessels: A1, A2, and A3 represent consecutive OCT cross sections showing a stent restenosis with presence of microvessels. One of them (indicated by the white arrow) shows a trajectory in the vessel (A1 and A2) and ends in the lumen (A3). B1, B2, and B3 show corresponding IVUS cross sections in the same region in which the microvessels are not visible.

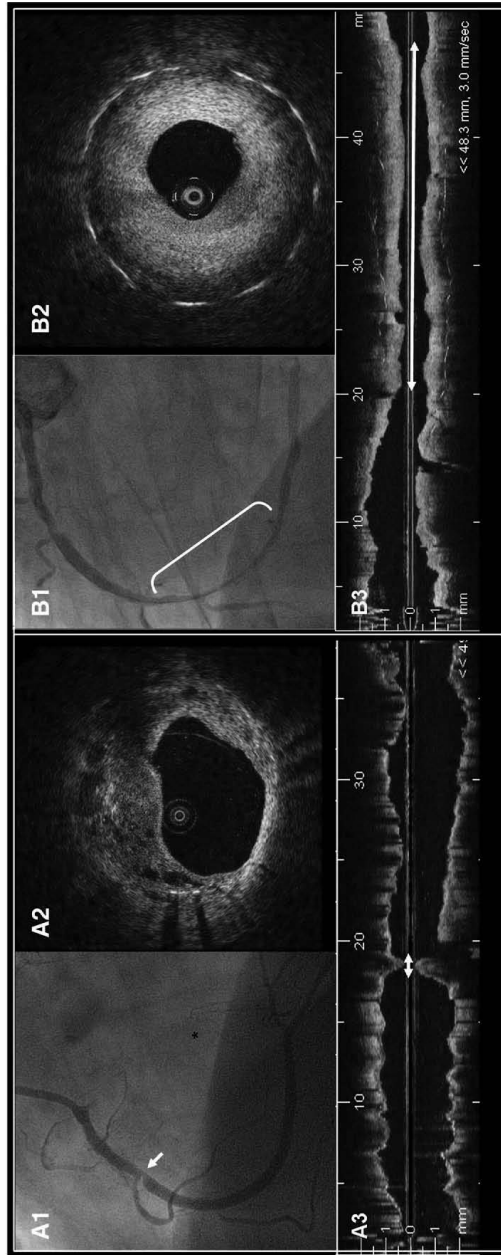
Table II. Relation between restenosis morphology by OCT and angiographic classification

	Angiographic restenosis pattern			P
	Diffuse (n = 9)	Focal (n = 11)	Margin (n = 5)	
OCT qualitative assessment				
Tissue coverage structure				.005
Layered	7 (77.8%)	5 (45.5%)	1 (20%)	
Homogeneous	2 (22.2%)	1 (9.1%)	4 (80%)	
Heterogenous	0	5 (45.5%)	0	
Backscatter				.03
High	8 (88.9%)	5 (45.5%)	5 (100%)	
Low	1 (11.1%)	6 (54.5%)	0	
Neointima symmetry ratio	0.52 ± 0.16	0.63 ± 0.23	0.57 ± 0.10	.4
Irregular lumen shape	1 (11.1%)	5 (45.5%)	1 (20%)	.2
Intraluminal material	1 (11.1%)	3 (27.3%)	1 (20%)	.6
Microvessels	1 (11.1%)	2 (18.2%)	0	.5
OCT quantitative assessment				
Mean lumen area (mm ²)	3.7 ± 1.0	5.2 ± 1.9	4.9 ± 1.4	.1
MLA (mm ²)	1.5 ± 0.5	1.4 ± 0.8	1.79 ± 1.2	.7
Mean stent area (mm ²)	6.5 ± 1.8	7.8 ± 3.2	6.2 ± 1.6	.4
Mean restenotic tissue area (mm ²)	3.4 ± 1.3	2.8 ± 2.1	1.97 ± 2.2	.4
Restenotic tissue burden (%)	50.9 ± 10.8	35.7 ± 15.6	30.4 ± 30.2	.08

Relation between restenosis morphology by OCT and angiographic classification. Optical coherence tomography analysis in the different angiographic restenosis types are shown in Table II (Figure 3).

Relation between restenosis morphology by OCT and clinical presentation. The OCT morphology was compared in patients with stable versus unstable clinical presentation at the time of inclusion in the study

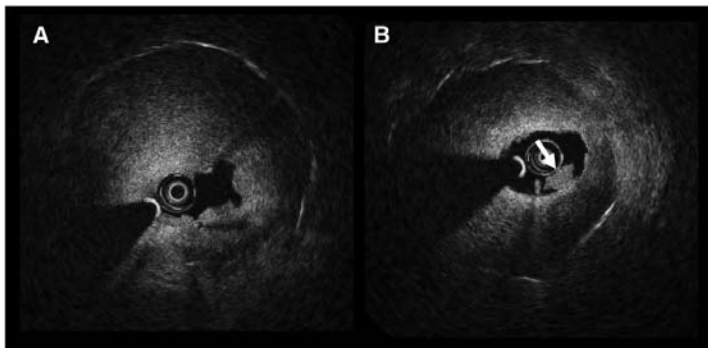
Figure 3



Restenosis morphology by OCT and angiographic classification. **A**, Example of a patient with a focal restenosis by angiography (white arrow in A1). An OCT cross section in the restenosis lesion (A2) shows a heterogeneous tissue with predominant low backscatter. The longitudinal OCT image (A3) shows a very focal restenosis (white arrows). **B**, Example of a patient with a diffuse restenosis by angiography (white bracket in B1). An OCT cross-sectional image in the restenosis region (B2) shows a restenotic tissue with layered structure and predominant high backscatter. The OCT longitudinal reconstruction (B3) also demonstrates a diffuse restenosis (white arrows).

Table III. Relation between restenosis morphology by OCT and clinical presentation at the time of inclusion in the study

	Clinical presentation at time of inclusion in the study		P
	Stable (n = 15)	Unstable (n = 10)	
OCT qualitative assessment			
Tissue coverage appearance			
Layered	10 (66.7%)	3 (30%)	.08
Homogeneous	4 (26.7%)	3 (30%)	
Heterogenous	1 (6.7%)	4 (40%)	
Backscatter			
High	11 (73.3%)	7 (70%)	.6
Low	4 (26.7%)	3 (30%)	
Neointima symmetry ratio	0.51 ± 0.19	0.68 ± 0.16	.04
Irregular lumen shape	1 (6.7%)	6 (60%)	.007
Intraluminal material	1 (6.7%)	4 (40%)	.12
Microvessels	2 (13.3%)	1 (10%)	.6
OCT quantitative assessment			
Stent imaged length (mm)	27.4 ± 11.1	26.6 ± 9.8	.8
Restenosis length (mm)	15.7 ± 11.6	5.8 ± 5.1	.009
Mean lumen area (mm ²)	4.5 ± 1.9	4.70 ± 1.2	.7
MLA (mm ²)	1.7 ± 0.8	1.24 ± 0.7	.1
Mean stent area (mm ²)	7.3 ± 2.5	6.5 ± 2.3	.4
Mean restenotic tissue area (mm ²)	3.2 ± 1.8	2.4 ± 1.9	.3
Restenotic tissue burden (%)	43.2 ± 16.9	35.6 ± 22.1	.3

Figure 4

Lumen shape and intraluminal material: OCT images obtained in a patient referred for coronary angiography for unstable angina. A stent restenosis lesion showing irregular lumen shape (A) and presence of intraluminal material (white arrow in B) was visualized.

(clinical presentation of the restenosis) (Table III) (Figure 4).

Regarding the original indication for stent implantation, there were no significant differences in restenotic tissue structure between stents implanted for unstable angina or acute myocardial infarction and stents implanted for stable angina. The restenosis pattern in stents implanted for unstable syndromes showed more often irregular lumen shape (6/14 [42.9%] vs 1/11 [9.1%]), but the difference did not reach statistical significance ($P = .07$). The restenotic tissue showed also a tendency to be more asymmetric in

stents implanted for unstable angina or acute myocardial infarction (0.63 ± 0.18) than in stents implanted for stable angina (0.50 ± 0.19) ($P = .09$).

Relation between restenosis morphology by OCT and time from stent implantation. Optical coherence tomography findings were compared depending on the time from stent implantation (≤ 12 vs >12 months) (Table IV). A layered structure of the restenotic tissue was more frequent in stents implanted ≤ 12 months before the OCT examination (84.6% vs 16.7%, $P = .003$). There were no differences in any other qualitative parameter.

Table IV. Relation between restenosis morphology by OCT and time from stent implantation

	Time from stent implantation		P
	≤12 m (n = 13)	>12 m (n = 12)	
OCT qualitative assessment			
Tissue coverage appearance			
Layered	11 (84.6%)	2 (16.7%)	.003
Homogeneous	1 (7.7%)	6 (50%)	
Heterogenous	1 (7.7%)	4 (33.3%)	
Backscatter			
High	9 (69.2%)	9 (75%)	.7
Low	4 (30.8%)	3 (25%)	
Neointima symmetry ratio	0.52 ± 0.17	0.64 ± 0.20	.1
Irregular lumen shape	3 (23.1%)	4 (33.3%)	.6
Intraluminal material	3 (23.1%)	2 (16.7%)	.6
Microvessels	2 (15.4%)	1 (8.3%)	.6
OCT quantitative assessment			
Restenosis length (mm)	13.2 ± 9.7	10.16 ± 11.7	.4
Mean lumen area (mm ²)	3.9 ± 1.3	5.3 ± 1.7	.03
MLA (mm ²)	1.33 ± 0.7	1.77 ± 0.8	.1
Mean stent area (mm ²)	6.4 ± 1.8	7.6 ± 3.0	.2
Mean restenotic tissue area (mm ²)	2.9 ± 1.5	2.8 ± 2.2	.9
Restenotic tissue burden (%)	43.9 ± 17.7	35.9 ± 20.4	.3

Regarding the quantitative analysis, the mean lumen area showed a tendency to be smaller in stents with <12 months follow-up (3.9 ± 1.3 vs 5.3 ± 1.7 mm², $P = .03$). No differences were found in the restenosis length, restenotic tissue area, or restenotic tissue burden.

Reproducibility of qualitative OCT assessment.

Interobserver variability for the qualitative OCT assessment was as follows: restenotic tissue structure $\kappa = 0.92$, restenotic tissue backscatter $\kappa = 0.57$, lumen shape $\kappa = 0.85$, intraluminal material presence $\kappa = 0.83$, and microvessels $\kappa = 0.79$. The intraobserver variability showed the following results: restenotic tissue structure $\kappa = 0.94$, restenotic tissue backscatter $\kappa = 0.93$, lumen shape $\kappa = 0.85$, intraluminal material presence $\kappa = 1$, and microvessels $\kappa = 0.92$.

Discussion

Optical coherence tomography for the assessment of stent restenosis

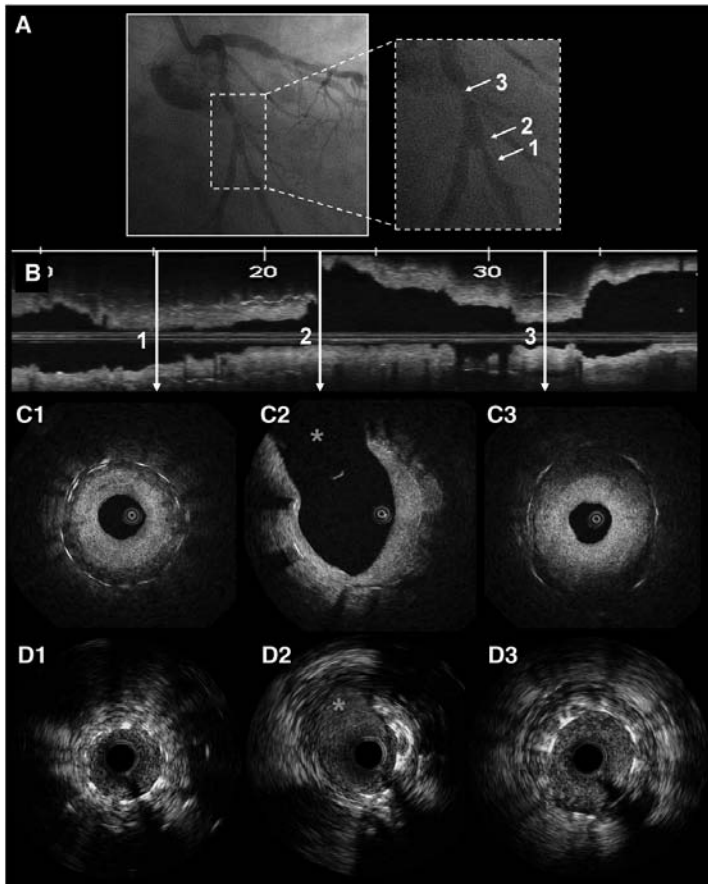
Stent restenosis is an infrequent but poorly understood clinical problem in the drug-eluting stent era and its treatment is challenging. Experimental and clinical studies have identified excessive neointimal hyperplasia as leading cause of stent restenosis.¹⁴⁻¹⁶ Novel means of interrogating the tissue growth causing stent restenosis would be of great interest to improve our understanding about the mechanisms and impact of this important clinical entity. The present study assessed the ability of OCT to provide information about the restenotic tissue.

This high-resolution imaging technique was able to evaluate the hyperplastic tissue in great detail. Interestingly, the tissue showed variation in structure, backscatter, and composition that were widely missed by IVUS in the past.¹⁷ In our study population, OCT was able to visualize details of the lumen shape and content and a wide range of components with different optical properties in the restenotic tissue. Figure 5 illustrates the difference in information gained by IVUS and by OCT in corresponding cross sections in one of our patients.

We applied a systematic approach to describe the OCT findings in stent restenosis. The introduction of relatively simple categories allowed for a consistent reporting of complex findings. The restenotic tissue structure, lumen shape, and the presence of microvessels and intraluminal material were assessed by in vivo OCT with low inter- and intraobserver variability. The evaluation of restenotic tissue backscatter showed a somewhat higher interobserver variability. The qualitative definition of tissue backscatter used in our study has important limitations, and the results regarding this parameter should be taken with caution. First, tissue backscatter is strongly influenced by the position of the OCT catheter relative to the vessel wall.^{18,19} Second, different areas with low and high backscatter are very often observed in the same vessel and sometimes it is difficult to determine the predominant pattern.²⁰ Furthermore, the interobserver reproducibility for tissue backscatter classification was low. Those limitations highlight the need of quantitative methods for tissue backscatter assessment to improve the accuracy and reduce the observer variability.

In our series, an important proportion of stents showed the presence of neointimal materials with different optical properties, suggesting that "restenosis" might be composed of different tissues. Pathologic examinations of human atherectomy specimens have demonstrated that restenosis in DES can consist of heterogeneous components including proteoglycan-rich tissue, organized thrombus, atheroma, inflammation, and fibrinoid.²¹ Although we do not have the direct correlation of histopathology and OCT appearance, it could be hypothesized that those tissue types might show different optical properties resulting in a heterogeneous or layered pattern on OCT. Furthermore, pathologic examinations have demonstrated that the density and orientation of smooth muscle cells vary within restenotic tissue.²² At the inner luminal border, the smooth muscle cells are more compact and show a homogeneous concentric orientation, whereas the density of cells decreases and the orientation becomes more heterogeneous in the tissue located far from the lumen. Around the stent struts, smooth muscle cells are usually oriented in a longitudinal fashion; and atheromatous material, organized thrombus and inflammatory cells can be frequently observed.²² This variation in tissue composition, cell density, and orientation along the

Figure 5



Comparison of OCT and IVUS findings in a restenosis lesion. **A**, Angiographic image showing a paclitaxel-eluting stent restenosis affecting the proximal and distal part of the stent. 1 indicates the distal stent part, 2 indicates the bifurcation left circumflex (LCX)–obtuse marginal (OM), and 3 indicates the proximal stent part. **B**, Longitudinal OCT view showing the restenosis in the distal part of the stent (1), the bifurcation (2), and the proximal part of the stent (3). Corresponding OCT cross sections are shown. C1, Restenosis in the distal part of the stent showing layered appearance with 2 concentric layers (one inner high scattering and one outer low scattering layer). C2, Bifurcation LCX-OM. C3, Restenosis affecting the proximal part of the stent that also shows layered appearance. D shows the corresponding IVUS images of the distal part of the stent (D1), bifurcation (D2), and proximal stent (D3). The clear layered appearance of the restenotic tissue visible by OCT cannot be distinguished by IVUS. Asterisk in C2 and D2 indicates the LCX.

radial axis of the neointima might cause the layered appearance observed by OCT. The presence of organized thrombus in the inner neointimal layer and fibrinoid deposition around the struts might also play a role.^{7,13}

However, currently, there are no OCT criteria validated with histology for the identification of these tissue types. It could be argued that the layered appearance is an artefact, simply reflecting the progressive attenuation of

the light by traveling through the tissue. However, in the present study, the maximum tissue coverage thickness was not different in the cases with and without layered appearance (1.1 ± 0.3 vs 0.9 ± 0.5 mm, respectively, $P = .4$). Furthermore, the presence in some cases of a clearly visible border between the 2 layers suggests that the change in backscatter is related to the presence of a different tissue with different optical properties.

In 3 cases, OCT was able to identify structures suggestive of microvessels in the restenosis. This finding is in line with postmortem histology data where the presence of neovascularization in DES restenosis has been described.^{21,23,24} Until now, we had not had the opportunity to analyze the role of microvessels in restenotic tissue behavior in vivo. Our data illustrate the potential of OCT to clarify this question.

Relation between restenosis morphology by OCT and clinical and angiographic characteristics

As our sample size was small, no formal multivariate analysis was possible. However, exploratory univariate analysis suggests a potential association of OCT characteristics to the angiographic appearance, the clinical presentation, and the time from stent implantation.

Regarding angiographic appearance, there were no differences in the lumen, stent or restenotic tissue area, and restenotic tissue burden between the 3 types of restenosis. This is in agreement with previous IVUS data that showed no significant differences in MLA, stent area, and intimal hyperplasia cross-sectional area between different angiographic types of restenosis.⁶ However, the qualitative assessment revealed a higher incidence of heterogeneous material in focal restenosis than in diffuse and margin restenosis, possibly reflecting a more heterogeneous tissue composition.

In the present study, restenosis presenting with unstable angina symptoms was more frequently associated with irregular lumen shape and intraluminal material, suggestive of the presence of thrombus. The possible contribution of thrombus as assessed by OCT to restenosis has been described in a previous case report.²⁵ Pathologic studies have demonstrated that organized thrombus can be a component of restenosis in both BMS and DES.^{21,24,26} Similarly, the restenotic tissue showed a tendency to be more asymmetric in patients with unstable clinical presentation at the time of inclusion in the study. Intravascular ultrasound studies have demonstrated that plaques causing acute coronary syndromes are more asymmetric than stable plaques.²⁷ However, the observation of an apparent relation between restenotic tissue symmetry and clinical presentation has not been previously reported. Pathologic data have demonstrated that strut tissue coverage is decreased when struts have been implanted over necrotic core-rich areas.²⁸ It could be hypothesized that the eccentricity and composition of the

underlying plaque could influence the amount and symmetry of the tissue covering the stent struts. Recently, we have reported that stents implanted for ST-elevation myocardial infarction show a more asymmetric distribution of the tissue covering the struts at follow-up than stents implanted for stable or unstable angina.¹⁰

Interestingly, the restenosis appearance by OCT varied with the time from stent implantation. The presence of restenotic tissue with layered appearance was more frequent in stents implanted ≤ 12 months before the OCT examination. This might be related to the presence of inflammation and/or fibrinoid tissue around the struts that might hypothetically decrease over time.²³ No signs of stent fracture, a cause of stent restenosis that can be recognized by OCT, were observed.²⁹

Our observational study makes fundamental structural observations, reported for the first time from a reasonable number of patients that might prove useful in restenosis studies in the future.

Limitations

Because of the retrospective character, the limited sample size, and selected nature of the population, and the multiple comparisons performed, the study should be considered primarily hypothesis generating and P values presented should be interpreted cautiously. The main limitation is the lack of histologic data to validate the OCT findings. We acknowledge that the mechanisms leading to restenosis are very different for BMS and DES. However, no comparison between BMS and DES could be performed due to the limited number of patients with BMS. No systematic comparison to IVUS was performed. Intravascular ultrasound was not part of the study protocol but was allowed at the discretion of the operator when considered clinically indicated.

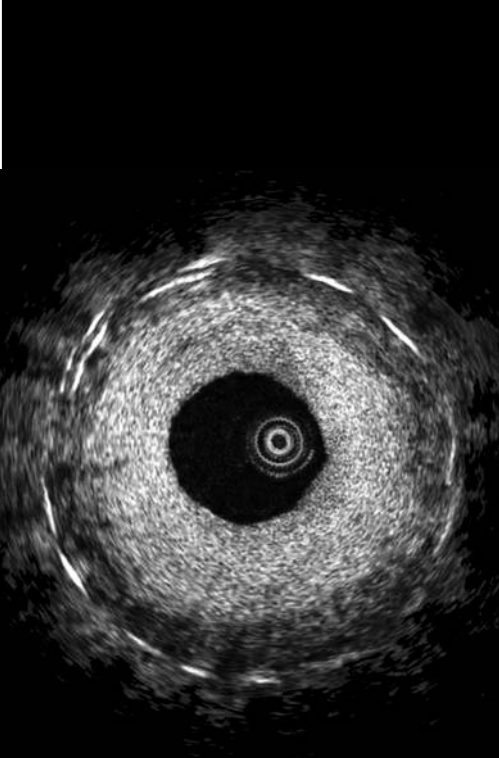
Conclusions

The present study demonstrates the ability of OCT to identify differential patterns of restenotic tissue after stenting. This information could be helpful in understanding the mechanisms of stent restenosis and it might prove useful in restenosis studies in the future. The clinical implications and the possible prognostic value of these findings remain unknown and will require further investigation.

References

1. Serruys PW, de Jaegere P, Kiemeneij F, et al. A comparison of balloon-expandable-stent implantation with balloon angioplasty in patients with coronary artery disease. Benestent Study Group. *N Engl J Med* 1994;331:489-95.
2. Dussaillant GR, Mintz GS, Pichard AD, et al. Small stent size and intimal hyperplasia contribute to restenosis: a volumetric intravascular ultrasound analysis. *J Am Coll Cardiol* 1995;26:720-4.

3. Serruys PW, Kutryk MJ, Ong AT. Coronary-artery stents. *N Engl J Med* 2006;354:483-95.
4. Morice MC, Serruys PW, Sousa JE, et al. A randomized comparison of a sirolimus-eluting stent with a standard stent for coronary revascularization. *N Engl J Med* 2002;346:1773-80.
5. Radke PW, Kaiser A, Frost C, et al. Outcome after treatment of coronary in-stent restenosis; results from a systematic review using meta-analysis techniques. *Eur Heart J* 2003;24:266-73.
6. Mehran R, Dangas G, Abizaid AS, et al. Angiographic patterns of in-stent restenosis: classification and implications for long-term outcome. *Circulation* 1999;100:1872-8.
7. Tanimoto SAJ, Serruys PW, Regar E. Paclitaxel-eluting stent restenosis shows three-layer appearance by optical coherence tomography. *Eurointervention* 2006;1:484.
8. Ohlmann P, Mintz GS, Kim SW, et al. Intravascular ultrasound findings in patients with restenosis of sirolimus- and paclitaxel-eluting stents. *Int J Cardiol* 2008;125:11-5.
9. Gonzalo N, Serruys PW, Regar E. Optical coherence tomography: clinical applications and the evaluation of DES. *Minerva Cardioangiol* 2008;56:511-25.
10. Gonzalo N, Barlis P, Serruys PW, et al. Incomplete stent apposition and delayed tissue coverage are more frequent in drug eluting stents implanted during primary percutaneous coronary intervention for ST elevation myocardial infarction than in drug eluting stents implanted for stable/unstable angina. Insights from optical coherence tomography. *J Am Coll Cardiol Interv* 2009;2:445-52.
11. Meissner OA, Reiber J, Babaryka G, et al. Intravascular optical coherence tomography: differentiation of atherosclerotic plaques and quantification of vessel dimensions in crural arterial specimens. *ROFO* 2006;178:214-20.
12. Gonzalo N, Garcia-Garcia HM, Regar E, et al. In vivo assessment of high-risk coronary plaques at bifurcations with combined intravascular ultrasound virtual histology and optical coherence tomography. *J Am Coll Cardiol Img* 2009;2:473-82.
13. Takano M, Xie Y, Murakami D, et al. Various optical coherence tomographic findings in restenotic lesions after sirolimus-eluting stent implantation. *Int J Cardiol* 2008.
14. Hoffmann R, Mintz GS, Dussaillant GR, et al. Patterns and mechanisms of in-stent restenosis. A serial intravascular ultrasound study. *Circulation* 1996;94:1247-54.
15. Nakatani M, Takeyama Y, Shibata M, et al. Mechanisms of restenosis after coronary intervention: difference between plain old balloon angioplasty and stenting. *Cardiovasc Pathol* 2003;12:40-8.
16. Farb A, Sangiorgi G, Carter AJ, et al. Pathology of acute and chronic coronary stenting in humans. *Circulation* 1999;99:44-52.
17. Saia F, Lemos PA, Sianos G, et al. Effectiveness of sirolimus-eluting stent implantation for recurrent in-stent restenosis after brachytherapy. *Am J Cardiol* 2003;92:200-3.
18. Van Leeuwen TG, Faber DJ, Aalders MC. Measurement of the axial point spread function in scattering media using single-mode fiber-based optical coherence tomography. *IEEE J Sel Top Quantum Electron* 2003;9:227-33.
19. Thrane L, Frosz MH, Jorgensen TM, et al. Extraction of optical scattering parameters and attenuation compensation in optical coherence tomography images of multilayered tissue structures. *Opt Lett* 2004;29:1641-3.
20. Yabushita H, Bouma BE, Houser SL, et al. Characterization of human atherosclerosis by optical coherence tomography. *Circulation* 2002;106:1640-5.
21. van Beusekom HM, Saia F, Zindler JD, et al. Drug-eluting stents show delayed healing: paclitaxel more pronounced than sirolimus. *Eur Heart J* 2007;28:974-9.
22. van Beusekom HM, van der Giessen WJ, van Suylen R, et al. Histology after stenting of human saphenous vein bypass grafts: observations from surgically excised grafts 3 to 320 days after stent implantation. *J Am Coll Cardiol* 1993;21:45-54.
23. Schwartz RS, Chronos NA, Virmani R. Preclinical restenosis models and drug-eluting stents: still important, still much to learn. *J Am Coll Cardiol* 2004;44:1373-85.
24. Komatsu R, Ueda M, Naruko T, et al. Neointimal tissue response at sites of coronary stenting in humans: macroscopic, histological, and immunohistochemical analyses. *Circulation* 1998;98:224-33.
25. Fujii K, Masutani M, Ohyanagi M. Contribution of organized thrombus to in-stent restenosis after sirolimus-eluting stent implantation: optical coherence tomography findings. *Eur Heart J* 2008;29:1385.
26. Glover C, Ma X, Chen YX, et al. Human in-stent restenosis tissue obtained by means of coronary atherectomy consists of an abundant proteoglycan matrix with a paucity of cell proliferation. *Am Heart J* 2002;144:702-9.
27. Sano K, Kawasaki M, Ishihara Y, et al. Assessment of vulnerable plaques causing acute coronary syndrome using integrated backscatter intravascular ultrasound. *J Am Coll Cardiol* 2006;47:734-41.
28. Finn AV, Nakazawa G, Ladich E, et al. Does underlying plaque morphology play a role in vessel healing after drug eluting stent implantation? *J Am Coll Cardiol Img* 2008;1:485-8.
29. Barlis P, Sianos G, Ferrante G, et al. The use of intra-coronary optical coherence tomography for the assessment of sirolimus-eluting stent fracture. *Int J Cardiol* 2008.



6.4

Optical Coherence Tomography Assessment Of The Acute Effects Of Stent Implantation On The Vessel Wall. A Systematic Quantitative Approach.

Gonzalo N, Serruys PW, Okamura T, Shen ZJ, Onuma Y, Garcia-Garcia HM, Sarno G, Schultz C, van Geuns RJ, Ligthart J, Regar E.

Heart. 2009 Dec;95(23):1913-1919. Epub 2009 Aug 10

Optical coherence tomography assessment of the acute effects of stent implantation on the vessel wall: a systematic quantitative approach

N Gonzalo, P W Serruys, T Okamura, Z J Shen, Y Onuma, H M Garcia-Garcia, G Sarno, C Schultz, R J van Geuns, J Ligthart, E Regar

See Editorial, p 1895

Thoraxcenter, Erasmus MC, Erasmus University, Rotterdam, The Netherlands

Correspondence to: Dr E Regar, Thoraxcenter, Erasmus MC, Bd 585, 's-Gravendijkwal 230, 3015-CE Rotterdam, The Netherlands; e.regar@erasmusmc.nl

Accepted 28 July 2009
Published Online First
10 August 2009

ABSTRACT

Objective: To observe and characterise vessel injury after stenting using optical coherence tomography (OCT), to propose a systematic OCT classification for periprocedural vessel trauma, to evaluate its frequency in stable versus unstable patients and to assess its clinical impact during the hospitalisation period.

Setting: Stenting causes vessel injury.

Design and interventions: All consecutive patients in whom OCT was performed after stent implantation were included in the study. Qualitative and quantitative assessment of tissue prolapse, intra-stent dissection and edge dissection were performed.

Results: Seventy-three patients (80 vessels) were analysed. Tissue prolapse within the stented segment was visible in 78/80 vessels (97.5%). Median number of tissue prolapse sites was 8 (IQR 4–19), mean (SD) area 1.04 (0.9) mm². Intra-stent dissection flaps were visible in 69/80 vessels (86.3%) (median number 3 (IQR 1.25–6), maximum flap length 450 (220) µm). Fifty-five out of 80 vessels (68.8%) showed dissection cavities (median number 2 (IQR 0–4.75), maximum depth 340 (170) µm). Edge dissection was visible in 20 vessels (mean (SD) length flap 744 (439) µm). The frequency of tissue prolapse or intra-stent dissection was similar in stable and unstable patients (95.6% vs 100%, $p = 0.5$ for tissue prolapse; 91.1% vs 82.9%, $p = 0.3$ for intra-stent dissection). There were no events during the hospitalisation period.

Conclusions: OCT allows a detailed visualisation of vessel injury after stent implantation and enables a systematic classification and quantification in vivo. In this study, frequency of tissue prolapse or intra-stent dissections after stenting was high, irrespective of the clinical presentation of the patients, and was not associated with clinical events during hospitalisation.

Coronary stent implantation generally creates a certain degree of injury on the vessel wall. Pathological studies have demonstrated plaque compression by the stent and penetration of the struts into the underlying plaque.¹ High-pressure stenting techniques have proved to be useful for an optimal stent implantation in order to reduce the risk of restenosis and subacute thrombosis. However, this stent deployment strategy may also increase the risk of vessel damage in the stented segment or at the edges.²

Optical coherence tomography (OCT) is a high-resolution imaging technique which allows a detailed assessment of the anatomical relation between the stent and the vessel wall.^{3,4} As a

consequence, various degrees of vessel injury after stent implantation are frequently detected with this technique even when they are not visible by cine-angiography or intravascular ultrasound. The different types of acute vessel damage caused by stenting that can be seen by OCT and their frequency in different clinical scenarios have not been described yet. Furthermore, the clinical implications of these OCT findings are not well established.

The objectives of this study were to observe and characterise vessel injury after stenting using OCT, to propose a systematic OCT classification for periprocedural vessel trauma, to evaluate its incidence in stable versus unstable (unstable angina I/II/III/IV Braunwald classification and ST elevation myocardial infarction (MI)) patients and to assess its clinical impact during the hospitalisation period.

PATIENTS AND METHODS

Study population

All consecutive patients in whom OCT was performed after stent implantation between January 2007 and December 2008 were included in the study. All patients gave informed consent.

OCT acquisition

The OCT acquisition was performed using a commercially available system for intracoronary imaging (LightLab Imaging, Westford, Massachusetts, USA). The ImageWire (LightLab Imaging) consists of an optical fibre core (125 µm) covered by a protective sheath with a maximum outer diameter of 0.019". The acquisition technique has been previously described.^{5,6} In seven cases the occlusive technique was used, in which a proximal, low-pressure (0.4 atm) occlusion balloon (Helios, Goodman, Nagoya, Japan) is inflated with simultaneous distal flush delivery (lactated ringer; flow rate 0.8 ml/s) to remove blood from the vessel lumen. Images were acquired during a pullback rate of 1.0 mm/s. In 73 cases OCT was acquired with the non-occlusive technique. In this case, the ImageWire was positioned distal to the region of interest using a double lumen catheter (Twin Pass catheter; Vascular Solutions, Minneapolis, USA) that had been previously placed in the artery over a conventional guide wire. The automated pullback was performed at 3 mm/s while the blood was removed by the continuous injection of iso-osmolar contrast (Iodixanol 370; VisipaqueGE

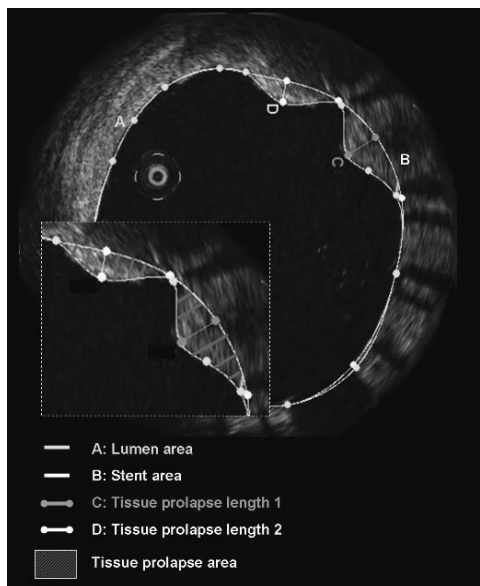


Figure 1 Tissue prolapse: defined as convex shaped, protrusion of tissue between adjacent stent struts towards the lumen without disruption of the continuity of the luminal vessel surface. The figure shows a cross section in which tissue prolapse is visible. The amplified image shows two areas of tissue prolapse. For each tissue prolapse region the maximum length and the area were measured.

Health Care, Ireland) at 37° C through the guiding catheter. The data was stored on CD for offline analysis.

Definitions of acute effects of stent implantation in OCT

Analysis encompassed the intra-stent segment, defined by the first and the last cross section with a visible strut, and the

adjacent vessel segments 5 mm proximal and distal to the stent (edge segments).

- ▶ *Tissue prolapse*: convex-shaped, protrusion of tissue between adjacent stent struts towards the lumen, without disruption of the continuity of the luminal vessel surface' (fig 1). Protrusion of tissue between struts was considered tissue prolapse only if the distance from the arc connecting adjacent stent struts to the greatest extent of protrusion was $>50 \mu\text{m}$.
- ▶ *Intra-stent dissection*: disruption of the luminal vessel surface in the stent segment. It can appear in two forms: (a) dissection: the vessel surface is disrupted and a dissection flap is visible; (b) cavity: the vessel surface is disrupted and an empty cavity can be seen (fig 2).
- ▶ *Edge dissection*: disruption of the luminal vessel surface in the edge segments (within 5 mm proximal and distal to the stent, no struts are visible) (fig 3).
- ▶ *Thrombus*: irregular mass with dorsal shadowing protruding in the lumen (mural thrombus) or a luminal mass with dorsal shadowing that is not connected to the vessel wall (fig 4).

Quantitative OCT analysis of the acute effects of stent implantation

The analysed region comprised the intra-stent and edge segments. The lumen and stent area were measured in 1 mm intervals along the pullbacks. In the proximal and distal edge segments, the lumen area was measured. In cases of tissue prolapse the number of sites with tissue prolapse was counted. Tissue prolapse length was defined as the distance from the arc connecting adjacent stent struts to the greatest extent of protrusion (the maximum and average tissue prolapse length were calculated). The area of tissue protruding between the stent struts was also measured (tissue prolapse area) (fig 1). When there were signs of intra-stent dissection the number of dissection flaps or cavities was counted and the length of the flap (from its tip to the joint point with the vessel wall) or the maximum depth of the cavity (from the lumen to the deepest cavity point inside the vessel wall) was measured (fig 2). When edge dissection was present the length of the dissection flap (in a similar way as described for intra-stent dissection flap) was

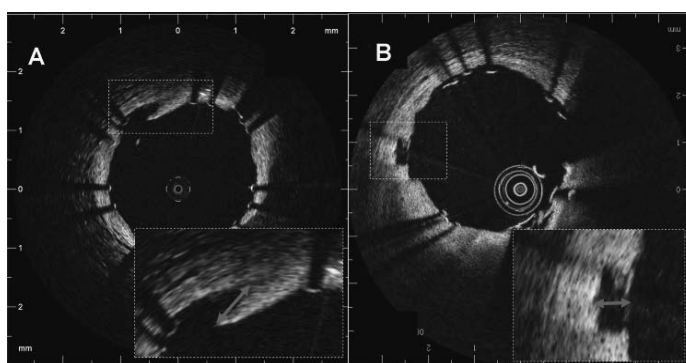


Figure 2 Intra-stent dissection: defined as a disruption of the vessel luminal surface in the stent segment. This entity can appear with two forms: (A) dissection: the vessel surface is disrupted and a dissection flap is visible. The length of the flap (red arrow) was measured as the distance from its tip to the joint point with the vessel wall; (B) cavity: the vessel surface is disrupted and an empty cavity can be seen. The maximum depth of the cavity (red arrow) was measured from the lumen to the deepest cavity point inside the vessel wall.

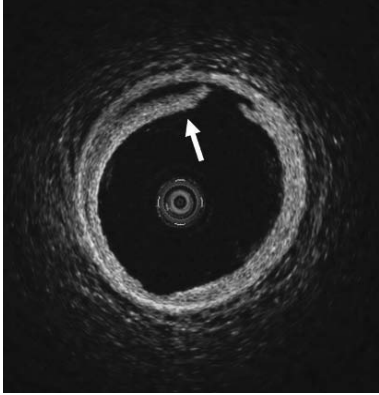


Figure 3 Edge dissection: defined as a disruption of the vessel luminal surface in the edge region (5 mm proximal and distal to the stented region, no struts are visible).

measured. The presence of thrombus was qualitatively assessed and the number of frames with visible thrombus was recorded. When incomplete stent apposition (defined as separation of at least one stent strut from the vessel wall not related with a side branch) was visible, the maximum distance from the endoluminal surface of the strut to the vessel wall was measured (maximum incomplete stent apposition length). To take into account differences in the stent length, the number of tissue prolapse sites, number of dissection flaps and number of cavities were normalised by the stent length and expressed per mm.

The analysts were blinded to the clinical and procedural characteristics.

Clinical follow-up

The presence of events (death, MI, target lesion revascularisation, target vessel revascularisation and stent thrombosis) during the hospitalisation period following stent implantation was registered. MI included reinfarction (defined as recurrence of symptoms together with ST elevation or new left bundle

branch block and an increase in cardiac enzymes following stable or decreasing values) or spontaneous MI (diagnosed by a rise in creatine kinase-MB fraction of three times the upper limit of normal together with symptoms and either new ST elevation or left bundle branch block).

Statistical analysis

Continuous variables are expressed as mean (SD) or median and interquartile range. Categorical variables are expressed as percentages. Comparisons between groups were performed with χ^2 for categorical variables. Continuous variables were compared with the Student t test when they had a normal distribution and with a non-parametric test (Mann-Whitney) when their distribution was not normal.

RESULTS

Clinical and procedural characteristics

Seventy-three patients, 80 vessels were included in the study. Table 1 shows the clinical and procedural characteristics.

Acute effects of stent implantation assessed by OCT

The mean (SD) lumen area measured by OCT was 7.16 (1.7) mm². The minimum lumen area in-stent was 5.65 (1.7) mm². The mean and minimum stent areas were 7.40 (1.9) and 5.70 (1.76) mm², respectively.

Fifty-one out of the 80 vessels (63.8%) showed at least one malapposed strut and the average maximum incomplete stent apposition length was 281 (145) μ m. Findings suggestive of thrombus were visible in 36/80 vessels (45%). The median number of frames with visible thrombus was 0 (IQR 0–1) and the median number of frames with thrombus normalised by the stent length was 0 (IQR 0–0.06).

Tissue prolapse

Table 2 shows the frequency and quantitative assessment of tissue prolapse as assessed by OCT.

Intra-stent dissection

Table 2 presents the frequency and quantitative measurements of intra-stent dissection as assessed by OCT.

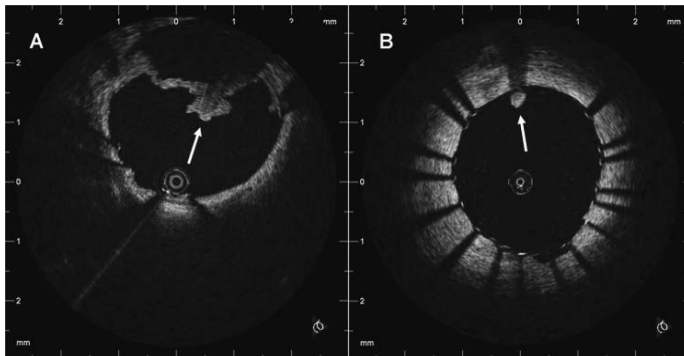


Figure 4 Thrombus: defined as an irregular mass with dorsal shadowing protruding in the lumen (mural thrombus) (white arrow in A) or a luminal mass with dorsal shadowing that is not connected to the vessel wall (white arrow in B).

Table 1 Baseline clinical and procedural characteristics

Clinical characteristics (n = 73 patients)	
<i>Demographics</i>	
Age (years), mean (SD)	62 (10)
Male (%)	57 (78.1)
HT (%)	44 (60.3)
DM (%)	14 (19.2)
Dyslipidaemia (%)	46 (63)
Smoker (%)	22 (30.1)
Family history (%)	25 (34.2)
<i>Cardiac history</i>	
Previous MI (%)	28 (38.4)
Previous CABG (%)	2 (2.7)
Previous PCI (%)	27 (37)
<i>Clinical presentation</i>	
Stable angina (%)	41 (56.2)
Unstable angina (%)	22 (30.1)
STEMI (%)	10 (13.7)
Procedural characteristics (n = 80 vessels)	
<i>Vessel</i>	
LAD (%)	41 (51.3)
LCX (%)	12 (15)
RCA (%)	27 (33.8)
<i>Stent type</i>	
BMS (%)	14 (17.5)
Paclitaxel-eluting stent (%)	5 (6.3)
Sirolimus-eluting stent (%)	4 (5)
Everolimus-eluting stent (%)	44 (55)
Zotarolimus-eluting stent (%)	12 (15)
Tacrolimus-eluting stent (%)	1 (1.3)
<i>Other data</i>	
Number of stents, mean (SD)	1.6 (0.8)
Stent diameter, mean (SD)	3.0 (0.4)
Stent length, mean (SD)	33 (17)
Implantation pressure, mean (SD)	16.8 (3)
Predilatation	39 (48.8)
Postdilatation	34 (42.5)
Rotational atherectomy	1 (1.3)
Thrombectomy	5 (6.3)

Results are shown as number (%) unless stated otherwise.

BMS, bare metal stent; CABG, coronary artery bypass graft surgery; DM, diabetes mellitus; HT, hypertension; LAD, left anterior descending coronary artery; LCX, left circumflex artery; MI, myocardial infarction; PCI, percutaneous coronary intervention; RCA, right coronary artery; STEMI, ST elevation myocardial infarction.

Edge dissection

In four cases edge regions were not visible. Twenty vessels out of 76 showed edge dissection. Four vessels showed both proximal and distal edge dissection. The mean (SD) length of the dissection flap was 744 (439) μ m.

Acute effects of stent implantation as assessed by OCT in relation to the clinical presentation

The effects of stent implantation in the vessel as assessed by OCT were compared in stable versus unstable (unstable angina IB/IIb/IIIb Braunwald classification and ST elevation MI) patients. Table 3 shows the baseline clinical and procedural characteristics of the two groups.

The frequency of incomplete stent apposition was not different between groups (27/45 (60%) for stable vs 24/34 (70.6%) for unstable $p = 0.3$). The maximum incomplete stent apposition length was 280 (74) μ m for stable and 283 (198) μ m for unstable patients ($p = 0.9$). Structures suggestive of thrombus were visible in 20/45 (44.4%) stable patients vs 16/35

Table 2 Tissue prolapse, intra-stent dissection, edge dissection frequency and quantitative optical coherence tomography assessment

Tissue prolapse	
Tissue prolapse visible, n (%)	78 (97.5)
Number of sites of tissue prolapse, median (IQR)	8 (4–19)
Number of sites of tissue prolapse per mm, median (IQR)	0.3 (0.17–0.69)
Tissue prolapse area (mm^2), mean (SD)	1.04 (0.9)
Tissue prolapse area per mm (mm^2), mean (SD)	0.03 (0.03)
Tissue prolapse average length (μ m), mean (SD)	151 (42)
Tissue prolapse maximum length (μ m), mean (SD)	254 (90)
Intra-stent dissection	
Intra-stent dissection visible, n (%)	70 (87.5)
<i>Intra-stent dissection flap</i>	
Intra-stent dissection flap visible, n (%)	69 (86.3)
Number intra-stent dissection flaps, median (IQR)	3 (1.25–6)
Number intra-stent dissection flaps per mm, median (IQR)	0.10 (0.05–0.22)
Intra-stent dissection flap average length (μ m), mean (SD)	300 (130)
Intra-stent dissection flap maximum length (μ m), mean (SD)	450 (220)
<i>Intra-stent dissection cavity</i>	
Intra-stent dissection cavity visible, n (%)	55 (68.8)
Number cavities, median (IQR)	2 (0–4.75)
Number cavities per mm, median (IQR)	0.07 (0–0.16)
Maximum depth cavity (μ m), mean (SD)	340 (170)
Edge dissection	
Edge dissection visible, n (%)	20/76 (26.3)
Length edge dissection flap, mean (SD)	744 (439)

(45.7%) unstable patients ($p = 0.9$). There were also no significant differences in the median number of frames with visible thrombus between stable 0 (IQR 0–1) and unstable 0 (IQR 0–2) patients ($p = 0.9$). The median number of frames with visible thrombus normalised by the stent length was 0 (IQR 0–0.05) for stable and 0 (IQR 0–0.08) for unstable ($p = 0.7$). Table 4 shows the frequency and quantitative assessment of tissue prolapse, intra-stent dissections and edge dissections in patients with stable versus unstable clinical presentation.

In-hospital events

There were no events (death, MI, target lesion revascularisation, target vessel revascularisation or stent thrombosis) during the hospitalisation period.

DISCUSSION

This study proposes a systematic classification and quantification of a variety of acute effects of stent implantation on the vessel wall, as visible by OCT. The main findings are: (a) OCT allows for a detailed visualisation of periprocedural vessel wall trauma in coronary stenting and enables a systematic classification and quantification in vivo; (b) a very high proportion of patients, irrespective of their clinical presentation, showed tissue prolapse or intra-stent dissections visible by OCT after stent implantation, but this finding was not associated with clinical events during hospitalisation.

OCT for the detection of vessel injury after stenting

OCT is a light-based technique which can provide in vivo imaging of the coronary artery with near-histological resolution. This technique has opened new possibilities for the evaluation of stents at follow-up, allowing a very detailed assessment of strut apposition and tissue coverage.^{8–12} This study demonstrates its ability to detect and distinguish different types of

Table 3 Clinical and procedural characteristics of stable versus unstable patients

Characteristics	Stable	Unstable	p Value
<i>Demographics</i>			
Age, mean (SD)	62.3 (9.9)	61.7 (10.4)	0.8
Male (%)	34/41 (82.9)	23/32 (71.9)	0.1
HT (%)	25/41 (61)	19/32 (59.4)	0.8
DM (%)	8/41 (19.5)	6/32 (18.8)	0.9
Dyslipidaemia (%)	30/41 (73.2)	16/32 (50)	0.05
Smoker (%)	10/41 (24.4)	12/32 (37.5)	0.3
Family history (%)	16/41 (39)	9/32 (28.1)	0.2
<i>Cardiac history</i>			
Previous myocardial infarction (%)	18/41 (43.9)	10/32 (31.3)	0.3
Previous CABG (%)	1/41 (2.4)	1/32 (3.1)	1
Previous PCI (%)	16/41 (39)	11/32 (34.4)	0.8
<i>Vessel</i>			
LAD (%)	22/45 (48.9)	19/35 (54.3)	
LCX (%)	8/45 (17.8)	4/35 (11.4)	0.8
RCA (%)	15/45 (33.3)	12/35 (34.3)	
<i>Stent type</i>			
BMS (%)	11/45 (24.4)	3/35 (8.6)	0.08
Pacitaxel-eluting stent (%)	5/45 (11.1)	0	
Sirolimus-eluting stent (%)	1/45 (2.2)	3/35 (8.6)	
Everolimus-eluting stent (%)	19/45 (42.2)	25/35 (71.4)	
Zotarolimus-eluting stent (%)	8/45 (17.8)	4/35 (11.4)	
Tacrolimus-eluting stent (%)	1/45 (2.2)	0	
<i>Other data</i>			
Number of stents, mean (SD)	1.5 (0.8)	1.8 (0.8)	0.2
Stent diameter (mm), mean (SD)	3.0 (0.5)	3 (0.3)	0.7
Stent length (mm), mean (SD)	33 (17)	35 (17)	0.5
Implantation pressure (atm), mean (SD)	17 (4)	17 (3)	0.7
Predilatation (%)	25/45 (55.6)	14/35 (40)	0.2
Postdilatation (%)	21/45 (46.7)	13/35 (37.1)	0.4
Rotational atherectomy (%)	1/45 (2.2)	0	1

Results are shown as number (%) unless stated otherwise.

BMS, bare metal stent; CABG, coronary artery bypass graft surgery; DM, diabetes mellitus; HT, hypertension; LAD, left anterior descending coronary artery; LCX, left circumflex artery; PCI, percutaneous coronary intervention; RCA, right coronary artery.

vessel injury during stent implantation. Furthermore, OCT allows not only qualitative but also quantitative evaluation of the acute effects of stenting *in vivo*. Previous reports have shown that OCT can also visualise vascular effects of other coronary devices such as balloon-induced dissections and cuts made by the blades of a cutting balloon.¹⁵ Furthermore, OCT has proved to be useful for the evaluation of strut symmetry or the presence of intracoronary thrombus after stenting.¹⁴⁻¹⁶

Tissue prolapse after stenting

In a postmortem study, compression of the coronary plaque after stent implantation with protrusion of tissue between the struts was seen in 94% of the patients.¹ This is in agreement with our study in which tissue prolapse between the struts was visible in the vast majority of patients. It is in contrast to intravascular ultrasound (IVUS) studies, which have reported a relatively low plaque prolapse incidence ranging from 18% to 35%.¹⁷ The higher sensitivity of OCT in comparison with IVUS for the detection of this phenomenon has been previously published.^{7, 18} The clinical impact of the presence of tissue prolapse after stenting, however, is not well established. An IVUS study demonstrated a correlation between creatine kinase-MB elevation post-procedure and the extent of plaque prolapse.¹⁷ However, IVUS has failed to show differences in the

rate of stent thrombosis or stent restenosis between patients with and without plaque prolapse.^{19, 20} In our study, even when almost all patients had visible tissue prolapse by OCT, no clinical events during hospitalisation occurred. Therefore, non-flow-limiting tissue prolapse as visualised by OCT in our study appears to be a benign phenomenon in the short term that might not require further treatment.

Intra-stent and edge dissections

OCT allows the visualisation of the disruption of the endoluminal vessel wall continuity in the intra-stent segment and it can distinguish between the presence of a flap or a region with loss of material (cavity). IVUS (with an axial resolution of around 150 µm) is hampered in distinguishing intra-stent dissections from plaque prolapse. However, by OCT those two entities can be clearly differentiated and might have different clinical implications. In our series, despite a high frequency of visible intra-stent dissections by OCT, no in-hospital events were registered. However, the long-term impact of the presence of vessel wall disruption in the stent segment in the incidence of restenosis or stent thrombosis is not known. The endothelial integrity is important to prevent thrombus deposition, and pathological examinations have associated stent thrombosis with the disruption of the vessel continuity and prolapse of the necrotic core between stent struts.²¹ Several animal and pathological studies have associated vessel injury with stent restenosis.^{1, 22} On the other hand, non-flow-limiting edge dissections detected by IVUS have not been associated with an increase in acute or long-term events such as restenosis but the impact of intra-stent dissections is not established.²³⁻²⁵ Furthermore, the location of a stent strut floating over an empty cavity without direct wall contact might also influence its coverage by tissue at follow-up.²⁶

Acute effects of stent implantation in stable versus unstable patients

In our series, the frequency of tissue prolapse did not differ between stable and unstable patients but the tissue prolapse area was higher in the stable group. This result seems to be in contradiction with the concept of the underlying plaque type in stable and unstable patients. In theory, the plaque type in stable patients might be mainly fibrous while in unstable patients more lipid-rich and/or thrombosed plaques would be expected and those might be more prone to prolapse. However, to the best of our knowledge there are no reported data about differences in tissue prolapse between stable and unstable patients. Furthermore, pre-stent OCT examination was not performed in our sample and therefore no information is available about the underlying plaque type. No differences in the frequency of intra-stent or edge dissections were found between stable and unstable patients.

This study demonstrates the feasibility of a systematic classification and quantification of periprocedural vessel injury *in vivo*. This might allow the development of an injury score, analogous to the vascular injury score in histopathology, and may help to study vascular healing and to optimise stent design and implantation technique in the future. To date the reasons for stent failure (thrombosis and restenosis) are poorly understood and vessel trauma after stenting might be a missing link to help us improve our understanding of this important clinical problem.^{27, 28}

However, correlation with clinical events, both early and late, is required to determine whether these OCT observations have clinical significance, and this should be the aim of future studies.

Table 4 Acute effects of stent implantation in the vessel wall in stable versus unstable patients

Acute effects	Stable (n = 45)	Unstable (n = 35)	p
Tissue prolapse			
Tissue prolapse visible, n (%)	43/45 (95.6)	35/35 (100)	0.5
Number of sites of tissue prolapse, median (IQR)	11 (5–22)	7 (3–16)	0.06
Number of sites of tissue prolapse per mm, median (IQR)	0.42 (0.22–0.80)	0.26 (0.14–0.44)	0.047
Tissue prolapse area (mm ²), mean (SD)	1.21 (1.0)	0.80 (0.6)	0.028
Tissue prolapse area per mm (mm ²), mean (SD)	0.04 (0.03)	0.03 (0.02)	0.03
Tissue prolapse average length (µm), mean (SD)	147 (43)	157 (40)	0.2
Tissue prolapse maximum length (µm), mean (SD)	260 (95)	247 (85)	0.5
Intra-stent dissection			
Intra-stent dissection visible, n (%)	41/45 (91.1)	29/35 (82.9)	0.3
<i>Intra-stent dissection flap</i>			
Intra-stent dissection flap visible, n (%)	39/45 (86.7)	30/35 (85.7)	0.9
Number of intra-stent dissection flaps, median (IQR)	3 (2–7)	3 (1–4)	0.3
Number of intra-stent dissection flaps per mm, median (IQR)	0.12 (0.05–0.25)	0.12 (0.04–0.18)	0.3
Intra-stent dissection flap average length (µm), mean (SD)	297 (134)	289 (120)	0.8
Intra-stent dissection flap maximum length (µm), mean (SD)	488 (238)	419 (197)	0.1
<i>Intra-stent dissection cavity</i>			
Intra-stent dissection cavity visible, n (%)	32/45 (71.1)	23/35 (65.7)	0.6
Number cavities, median (IQR)	2 (0–4.5)	1 (0–5)	0.6
Number cavities per mm, median (IQR)	0.07 (0–0.15)	0.04 (0–0.17)	0.8
Maximum depth cavity (µm), mean (SD)	336 (183)	357 (150)	0.6
Edge dissection			
Edge dissection visible, n (%)	9/42 (21.4)	11/34 (32.3)	0.3
Edge dissection length (µm), mean (SD)	860 (579)	650 (277)	0.3

Limitations

The lack of clinical events during the study period does not allow a proper correlation of OCT-assessed vessel trauma with clinical outcome and it is the main limitation of the study. Intra-stent dissection and tissue prolapse were almost universal. Therefore identification of their presence alone has no significance. In order to find a more discriminatory OCT measure of vessel trauma we described different quantitative parameters for each type of post-stenting vessel injury. However, the lack of clinical events did not allow us to evaluate which parameter may be clinically significant. We assessed the acute effects of stent implantation visible by OCT and their clinical impact at short-term follow-up. Long-term follow-up studies including OCT imaging are needed in order to better define the clinical implications of these findings. The clinical presentation classification used has limitations as it included syndromes with different pathophysiology (unstable angina/NSSTMI and STEMI) in the same group. However, owing to the limited sample size, it was not possible to divide the population into multiple subgroups. We acknowledge that the stent type might influence the vessel trauma observed by OCT. However, owing to the heterogeneity of the population, with different drug-eluting stents and a limited number of bare metal stents, no comparison between stent types was performed.

CONCLUSIONS

OCT allows for a detailed visualisation of periprocedural vessel wall trauma in coronary stenting and enables a systematic classification and quantification in vivo. In our study, the incidence of tissue prolapse or intra-stent dissections after stent implantation was high, irrespective of the clinical presentation

of the patients, and was not associated with clinical events during the hospitalisation period.

Competing interests: None.

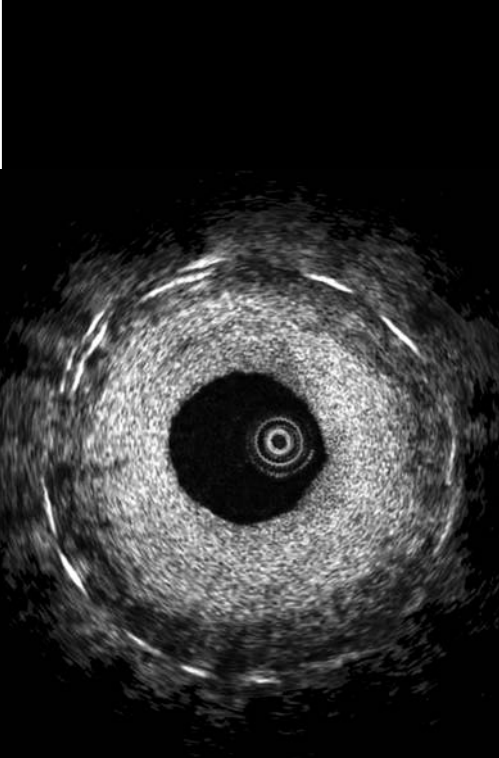
Patient consent: Obtained.

Provenance and peer review: Not commissioned; externally peer reviewed.

REFERENCES

1. Farb A, Sangiorgi G, Carter AJ, et al. Pathology of acute and chronic coronary stenting in humans. *Circulation* 1999;**99**:44–52.
2. Schwarzscher SP, Metz JA, Yock PG, et al. Vessel tearing at the edge of intracoronary stents detected with intravascular ultrasound imaging. *Cathet Cardiovasc Diagn* 1997;**40**:152–5.
3. Gonzalo N, Serruys PW, Regar E. Optical coherence tomography: clinical applications and the evaluation of DES. *Minerva Cardioangiologica* 2008;**56**:511–25.
4. Barlis P, Gonzalo N, Di Mario C, et al. A multi-centre evaluation of the safety of intracoronary optical coherence tomography. *Eurointervention* 2009;**5**:90–5.
5. Gonzalo N, Garcia-Garcia HM, Regar E, et al. In vivo assessment of high-risk coronary plaques at bifurcations with combined intravascular ultrasound virtual histology and optical coherence tomography. *JACC Cardiovasc Imaging* 2009;**2**:473–82.
6. Gonzalo N, Ligthart J, Regar E. Tips and tricks for intravascular optical coherence tomography. In: Sabate, ed. Percutaneous interventions beyond stenting. Tips and tricks for new technology. *Infarma Healthcare* (in press).
7. Bouma BE, Tearney GJ, Yabushita H, et al. Evaluation of intracoronary stenting by intravascular optical coherence tomography. *Heart* 2003;**89**:317–20.
8. Gonzalo N, Barlis P, Serruys PW, et al. Incomplete stent apposition and delayed tissue coverage are more frequent in drug eluting stents implanted during primary percutaneous coronary intervention for ST elevation myocardial infarction than in drug eluting stents implanted for stable/unstable angina. Insights from optical coherence tomography. *JACC Cardiovasc Interv* 2009;**2**:445–52.
9. Takano M, Yamamoto M, Inami S, et al. Long-term follow-up evaluation after sirolimus-eluting stent implantation by optical coherence tomography: do uncovered struts persist? *J Am Coll Cardiol* 2008;**51**:968–9.
10. Chen BX, Ma FY, Luo W, et al. Neointimal coverage of bare-metal and sirolimus-eluting stents evaluated with optical coherence tomography. *Heart* 2008;**94**:566–70.
11. Regar E, van Beusekom HMM, van der Giessen WJ, et al. Optical coherence tomography findings at 5-year follow-up after coronary stent implantation. *Circulation* 2005;**112**:345–6.

12. **Serruys PW**, Ormiston JA, Onuma Y, *et al*. A bioabsorbable everolimus-eluting coronary stent system (ABSORB): 2-year outcomes and results from multiple imaging methods. *Lancet* 2009;**373**:897–910.
13. **Diaz-Sandoval LJ**, Bouma BE, Tearney GJ, *et al*. Optical coherence tomography as a tool for percutaneous coronary interventions. *Catheter Cardiovasc Interv* 2005;**65**:492–6.
14. **Suzuki Y**, Ikeno F, Yeung AC. Drug-eluting stent strut distribution: a comparison between Cypher and Taxus by optical coherence tomography. *J Invasive Cardiol* 2006;**18**:111–4.
15. **Kume T**, Akasaka T, Kawamoto T, *et al*. Assessment of coronary arterial thrombus by optical coherence tomography. *Am J Cardiol* 2006;**97**:1713–7.
16. **Takano M**, Yamamoto M, Murakami D, *et al*. Optical coherence tomography after new scoring balloon angioplasty for in-stent restenosis and de novo coronary lesions. *Int J Cardiol* 2009 Jan 5. [Epub ahead of print].
17. **Kim SW**, Mintz GS, Ohlmann P, *et al*. Frequency and severity of plaque prolapse within Cypher and Taxus stents as determined by sequential intravascular ultrasound analysis. *Am J Cardiol* 2006;**98**:1206–11.
18. **Jang IK**, Tearney G, Bouma B. Visualization of tissue prolapse between coronary stent struts by optical coherence tomography: comparison with intravascular ultrasound. *Circulation* 2001;**104**:2754.
19. **Hong MK**, Park SW, Lee CW, *et al*. Long-term outcomes of minor plaque prolapsed within stents documented with intravascular ultrasound. *Catheter Cardiovasc Interv* 2000;**51**:22–6.
20. **Futamatsu H**, Sabate M, Angiolillo DJ, *et al*. Characterization of plaque prolapse after drug-eluting stent implantation in diabetic patients: a three-dimensional volumetric intravascular ultrasound outcome study. *J Am Coll Cardiol* 2006;**48**:1139–45.
21. **Farb A**, Burke AP, Kolodgie FD, *et al*. Pathological mechanisms of fatal late coronary stent thrombosis in humans. *Circulation* 2003;**108**:1701–6.
22. **Schwartz RS**, Huber KC, Murphy JG, *et al*. Restenosis and the proportional neointimal response to coronary artery injury: results in a porcine model. *J Am Coll Cardiol* 1992;**19**:267–74.
23. **Schroeder S**, Baumbach A, Mahrholdt H, *et al*. The impact of untreated coronary dissections on acute and long-term outcome after intravascular ultrasound guided PTCA. *Eur Heart J* 2000;**21**:137–45.
24. **Hong MK**, Park SW, Lee NH, *et al*. Long-term outcomes of minor dissection at the edge of stents detected with intravascular ultrasound. *Am J Cardiol* 2000;**86**:791–5, A799.
25. **Sheris SJ**, Canos MR, Weissman NJ. Natural history of intravascular ultrasound-detected edge dissections from coronary stent deployment. *Am Heart J* 2000;**139**:59–63.
26. **Finn AV**, Joner M, Nakazawa G, *et al*. Pathological correlates of late drug-eluting stent thrombosis: strut coverage as a marker of endothelialization. *Circulation* 2007;**115**:2435–41.
27. **Barlis P**, DiMario C, van Beusekom HMM, *et al*. Novelities in cardiac imaging – optical coherence tomography (OCT). A critical appraisal of the safety concerns tempering the success of drug-eluting stents. *Eurointervention* 2008;**4**(Suppl C):C22–6.
28. **Schinkel AFL**, van Beusekom HM, Maugenest AM, *et al*. OCT findings in very late (4 years) paclitaxel-eluting stent thrombosis. *JACC Cardiovasc Interv* 2008;**1**:449–51.



6.5

Relation between plaque type and dissections at the edges after stent implantation: an optical coherence tomography study

Gonzalo N, Serruys PW, Okamura T, Shen ZJ, Garcia-Garcia HM, Onuma Y, van Geuns RJ, Ligthart J, Regar E

Submitted

ABSTRACT

Background: Stent implantation can create vessel damage such as edge dissections. The objectives were i) to evaluate the frequency of edge dissections after stenting visible by intracoronary optical coherence tomography (OCT) in comparison with angiography. ii) to assess with OCT the plaque type left at the stent edges after implantation. iii) to study whether there is an association between plaque type and dissections at stent edges.

Methods: Seventy-three consecutive patients (80 vessels) with OCT post-stent implantation were included in the study. By OCT, plaque type at stent edges and presence of edge dissection was assessed. Angiograms were analyzed by two independent observers to assess the presence of edge dissections.

Results: Distal and proximal edge were visible by OCT in 72/80 and 45/80 vessels respectively. OCT and angiography agreed in the detection of 7 dissections at distal edge ($\kappa=0.32$) and 1 dissection at proximal edge ($\kappa=0.22$). Plaque type at distal edge was: fibrotic 55.6%, fibrocalcific 22.2%, fibroatheroma 15.3% and thin-cap fibroatheroma (TCFA) 6.9%. At proximal edge plaque type was: fibrotic 31.1%, fibrocalcific 33.3%, fibroatheroma 28.9% and TCFA 6.7%. In the distal edge, presence of edge dissection was significantly more frequent when the plaque type at the edge was fibrocalcific (43.8%) or lipid-rich (37.5%) than when the plaque was fibrous (10%) $p=0.009$.

Conclusions: OCT showed higher sensitivity compared to angiography for the identification of edge dissections. A high proportion of patients showed lipid-rich plaques at stent edges. Plaque type at the stent edges has impact on the presence of edge dissections.

Key words: edge dissections, optical coherence tomography, intracoronary imaging, plaque composition.

INTRODUCTION

Stenting is the standard technique for the percutaneous treatment of severe coronary artery stenosis(1). Stent implantation can create vessel damage such as dissections at the stent edges(2). Angiography, due to its limited resolution, has low sensitivity for the detection of edge dissection in comparison with intracoronary imaging techniques such as intravascular ultrasound(3).

An adequate coverage of the lesion is crucial for the success of stent implantation. Usually, stents are implanted from angiographic normal to normal segments. However, significant plaque burden can be present at the stent edges even when those are apparently normal by angiography(4). Furthermore, angiography has a very limited ability to differentiate the plaque tissue types with the exception of large calcium deposits.

Optical coherence tomography (OCT) is an intracoronary imaging modality able to provide high-resolution (10 μm) images of the coronary artery(5-8). Moreover, the technique has demonstrated its ability to distinguish atherosclerotic plaques with different composition(9-11).

We hypothesized that the presence of edge dissection after stenting can be related to the composition of the plaque located at the stent edge.

The objectives of the present study were: i) to evaluate the frequency of edge dissections after stenting visible by OCT in comparison with angiography ii) to assess with OCT the plaque type left at the stent edges after implantation. iii) to study whether there is an association between plaque type and dissections at the stent edges.

METHODS

Study population

All consecutive patients in whom OCT was performed after stent implantation in our institution between January 2007 and December 2008 were included in the study (n=73 patients, 80 vessels). The indication for the OCT study was the assessment of stent apposition after implantation.

OCT acquisition

The OCT acquisition was performed using a commercially available system for intracoronary imaging and the. ImageWire (LightLab Imaging Inc, Westford,

Massachusetts, US). In 7 vessels the occlusive technique was used in which a proximal, low-pressure (0.4 atm) occlusion balloon (Helios, Goodman Inc, Nagoya, Japan) is inflated with simultaneous distal flush delivery (lactated ringer; flow rate 0.8ml/sec) to remove blood from the vessel lumen. Images were acquired during a pullback rate of 1.0 mm/sec. In 73 vessels OCT was acquired with the non-occlusive technique. In those cases the automated pullback was performed at 3 mm/s while the blood was removed by the continuous injection of iso-osmolar contrast (Iodixanol 370, Visipaque™, GE Health Care, Ireland) at 37° Celsius through the guiding catheter.

Angiographic analysis

All the angiograms were analyzed by two independent observers not involved in the OCT analysis in order to assess the presence and type of edge dissections visible by angiography (12).

OCT assessment of edge dissections

Edge dissection by OCT was defined as a disruption of the vessel luminal surface in the stent edges (5 mm proximal and distal) with visible flap (Figure 1). To quantify the dimensions of the edge dissection, the longitudinal extension of the dissection along the vessel and the length of the dissection flap (from its tip to the joint point with the vessel wall) were measured

OCT plaque type classification

The plaque type at the stent edges (5mm proximal and distal) was classified by agreement of two observers as: fibrous (homogeneous signal rich), fibrocalcific (signal poor with defined borders) or lipid-rich (signal poor with diffuse borders) (9). In all the lipid-rich plaques, the thickness of the fibrous cap was measured at the thinnest point in order to classify them as fibroatheromas when the fibrous cap thickness was $>65\mu\text{m}$ or thin cap fibroatheromas (TCFA) when the fibrous cap thickness was $\leq 65\mu\text{m}$ (13,14) (Figure 2)

Statistical analysis

Continuous variables are expressed as mean \pm standard deviation. Categorical variables are expressed as percentages. Comparisons between groups were performed with χ^2 for categorical variables and with ANOVA for continuous variables. The

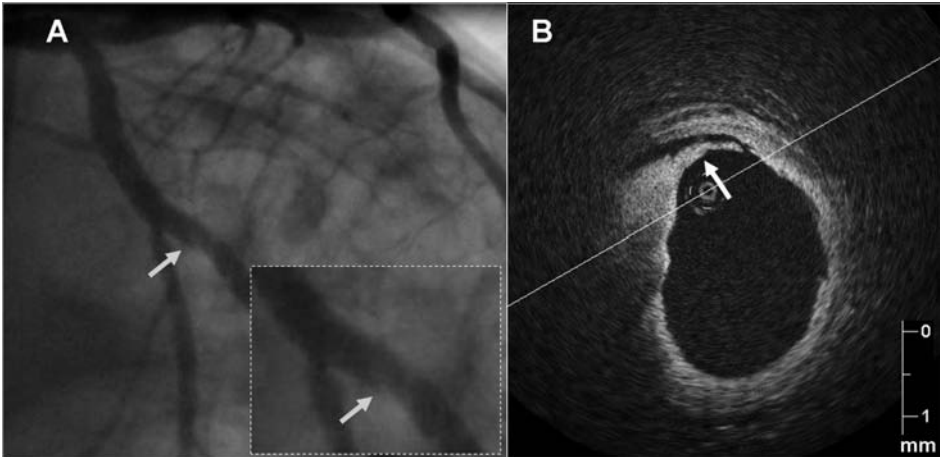


Figure 1. Edge dissection detection by angiography and optical coherence tomography (OCT). A: angiographic image showing a distal edge dissection (yellow arrow). The dissection can be observed with more detail in the amplified image. B: OCT shows a disruption of the vessel luminal surface in the distal stent border with a visible flap (white arrow).

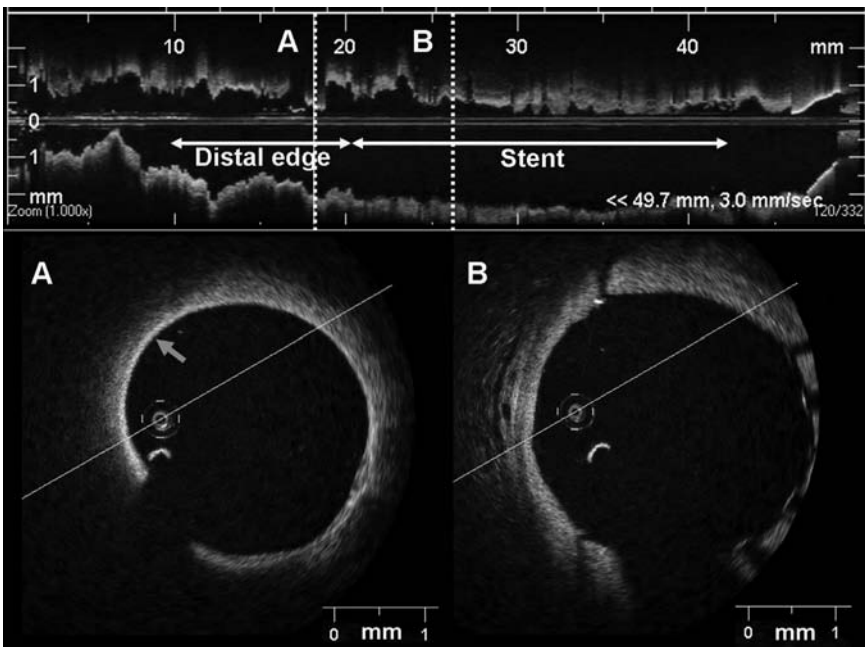


Figure 2. Plaque type at stent edges. Example of a patient treated with primary percutaneous coronary intervention and stent implantation for inferior ST elevation myocardial infarction. The upper panel shows the longitudinal optical coherence tomography (OCT) image. The yellow arrow indicates the distal edge and the white arrow indicates the stented region. The lower panels show two cross sections. A: distal edge. A low backscattering plaque with diffuse borders covered by a thin fibrous cap (red arrow, thin cap fibroatheroma) can be observed. B: stented region.

kappa coefficient (K) was used to test agreement between OCT and angiography for edge dissection detection.

RESULTS

Clinical and procedural characteristics

Eighty vessels (73 patients) were included in the study. The mean age was 62 ± 10 years. Fifty-seven out of 73 (78%) were males, 44/73 (60.3%) had hypertension, 14/73 (19.2%) were diabetics and 46/73 (63%) had dyslipidemia. Twenty-two out of 73 (30.1%) were smokers. Regarding previous cardiac history 28/73 (38.4%) had a previous myocardial infarction, 2/73 (2.7%) had coronary artery by-pass surgery and 27/73 (37%) had previous percutaneous coronary interventions. The majority of patients (41/73, 56.2%) were treated for stable angina, 22/73 (30.1%) for unstable angina and 10/73 (13.7%) for ST elevation myocardial infarction. The analyzed vessel was: LAD 41/80 (51.3%), LCX 12/80 (15%) and RCA 27/80 (33.7%). The implanted stent was a bare-metal stent in 14/80 (17.5%) and a drug-eluting stent in 66/89 (82.5%). The mean number of stents was 1.6 ± 0.8 with a mean stent diameter and length of 3.0 ± 0.4 mm and 26.7 ± 10 mm respectively.

Edge dissections by OCT

The distal and proximal edge were visible by OCT in 72/80 and 45/80 vessels respectively. Overall, 20 vessels showed distal or proximal edge dissection. The frequency of edge dissection were 17/72 (23.6%) and 7/45 (15.5%) for distal and proximal edge respectively. Four vessels showed both proximal and distal edge dissection. The mean length of the dissection flap was 702 ± 460 μ m and 687 ± 289 μ m for distal and proximal edge dissections respectively. The longitudinal extension of the dissection along the vessel was was: 1.20 ± 0.65 mm for distal edge and 1.6 ± 1.0 mm for proximal edge.

Edge dissection by angiography

By angiography a total of 14 edge dissections were identified (13 in the distal edge and 1 in the proximal edge). The type was A in 12/14 (85.7), B in 1/14 (7.1) and C in 1 vessel (7.1).

Agreement OCT and angiography for edge dissection

OCT and angiography agreed in the detection of 7 dissections in the distal edge and 1 dissection in the proximal edge ($K=0.32$ for distal edge dissection and 0.22 for proximal edge dissection).

Plaque type at stent edges

Table 1 shows the frequency of each plaque type at the stent edges.

Table 1. Plaque type at stent edges.

	Fibrous	Fibrocalcific	Fibroatheroma	TCFA	Total
Proximal edge	14 (31.1%)	15 (33.3%)	13 (28.9%)	3 (6.7%)	45
Distal edge	40 (55.6%)	16 (22.2%)	11 (15.3%)	5 (6.9%)	72
Total	54	31	24	8	117

TCFA: thin cap fibroatheroma

Relation between plaque type and edge dissection by OCT

There were no significant differences in the procedural characteristics between the vessels with different plaque types left at the stent edges (Table 2). In the distal edge, the frequency of edge dissection was significantly higher in fibrocalcific (7/16, 43.8%) or lipid-rich plaque (6/16, 37.5%) as compared to fibrous plaque (4/40, 10%) $p=0.009$. In the proximal edge a similar tendency was observed (edge dissection 4/15 26.7% for fibrocalcific, 2/16 12.5% for lipid-rich and 1/14, 7.1% for fibrous) but the differences did not reach statistical significance ($p=0.3$). (Figure 3). The longitudinal length of the dissection and the length of the dissection flap for the different plaque types at the edges are shown in Table 3.

Table 2. Procedural characteristics in relation to the plaque type left at the stent edge

Distal edge	Fibrous	Lipid-rich	Fibrocalcific	p
Stent Length (mm)	27.7±11.2	21.6±8.5	27.8±9.1	0.1
Stent diameter (mm)	3.0±0.3	3.1±0.4	3.2±0.5	0.2
Predilatation (%)	55.3	40	56.3	0.5
Implantation pressure (atm)	16±3	16±4	17±3	0.9
Post dilatation (%)	44.7	40	33.3	0.7
Proximal Edge	Fibrous	Lipid-rich	Fibrocalcific	
Stent Length (mm)	23.2±8	24.1±10	28.7±9	0.2
Stent diameter (mm)	3.0±0.4	2.9±0.4	3.2±0.4	0.2
Predilatation (%)	46.2	66.7	50	0.5
Implantation pressure (atm)	14±2	14±4	17±3	0.2
Post dilatation (%)	30.8	20	61.5	0.06

Table 3. Longitudinal length of the edge dissection and length of the dissection flap for the different plaque types.

Distal edge	Fibrous	Lipid-rich	Fibrocalcific	p
Longitudinal length (mm)	1.14 ± 0.60	1.03 ± 0.68	1.37 ± 0.71	0.6
Flap length (µm)	485 ± 164	748 ± 521	855 ± 531	0.4
Proximal Edge	Fibrous	Lipid-rich	Fibrocalcific	
Longitudinal length (mm)	0.85*	1.04 ± 0.33	2.06 ± 1.23	0.4
Flap length (µm)	1090*	390 ± 226	735 ± 187	0.09

* There was only one case of proximal edge dissection in relation with a fibrous plaque.

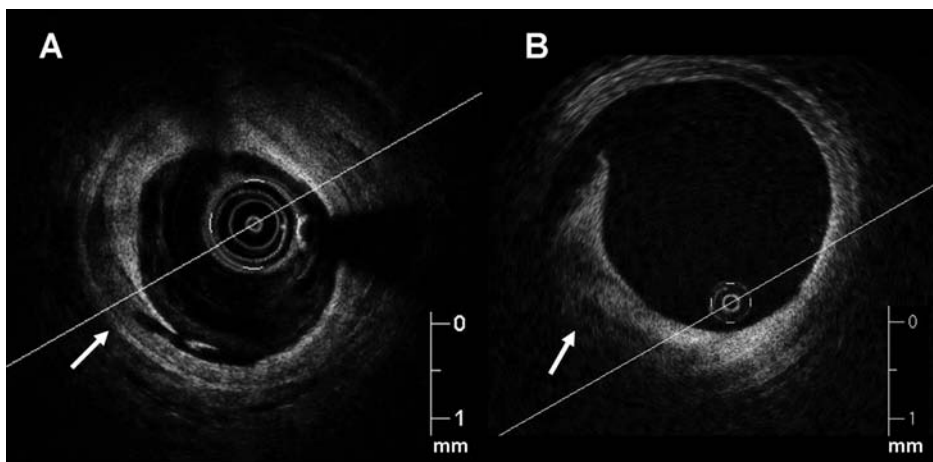


Figure 3. Relation between plaque type at the stent edge and presence of dissection. A: distal edge dissection in relation with a low backscattering plaque with defined borders (white arrow, fibrocalcific plaque) B: distal edge dissection in relation with a low backscattering plaque with diffuse, not well defined borders (white arrow, lipid-rich plaque)

DISCUSSION

The main findings of the present study are: i) OCT showed higher sensitivity compared to angiography for the identification of edge dissections after stenting. ii) A high proportion of patients showed lipid-rich plaques at the stent edges. iii) The plaque type at the stent edges has impact on the presence of edge dissections.

OCT in comparison with angiography for edge dissection detection

In the present study edge dissection was detected more often with OCT than with angiography. In the proximal edge only one dissection was detected by angiography while OCT detected 7. In the distal edge angiography and OCT agreed in the detection of 7 dissections. However, there were 10 edge dissections detected by OCT that were not visible by angiography. Interestingly, there were 6 cases in

which the observers saw edge dissections in angiography that were not present in OCT (false positives in angiography). OCT has also demonstrated its superior ability for the detection of edge dissection in comparison with IVUS(15). The clinical importance of minor edge dissections visible only with OCT is unknown. Although experimental and clinical information have correlated vessel trauma and extent of neointima formation (16,17), IVUS studies have shown that non-flow-limiting edge dissections are not necessarily associated with an increase in acute or long-term events or the development of restenosis(18-20). However some data suggested that intracoronary imaging may be helpful to assess the risk of vessel occlusion of residual dissections after stenting (21,22).

Plaque type left at the borders after stenting

OCT has demonstrated its ability to characterize coronary atherosclerosis with good sensitivity and specificity and high reproducibility (9). Furthermore, its high resolution allows the measurement of the thickness of the fibrous cap, one of the parameters associated with the risk of rupture of coronary plaques(14,23). Several studies have evaluated the effect of stent implantation in the plaque located at the borders at follow up(24,25). However, there is lack of data about the plaque type left at the borders after stenting. In the present study using OCT the plaque type more frequently found at the stent borders after implantation was fibrous. However, more than 20% of the patients had lipid rich plaques at the distal edge and more than one third showed plaques with high lipid content in the proximal edge. Interestingly, in around 7% of the cases, the plaques left at the border after stenting were TCFA's (considered the plaque type at higher risk of rupture) (13,26). Those results are in agreement with a previous study with IVUS-virtual histology after implantation of paclitaxel eluting stents showing that the main component of the plaque at the borders after stenting was fibrous tissue followed by necrotic core(4).

Those findings might have clinical implications. IVUS studies have related disease in the reference segments with edge restenosis and stent thrombosis but no data about the predominant plaque type left after stent implantation in the reference segment has been published(27,28). It could be hypothesized that different plaque types left at the stent edges might be associated with different risk of clinical events. Indeed, the disruption of lipid-rich plaques by the stent struts have been proposed as a possible mechanism of stent thrombosis in pathological studies(29). However, the clinical implications of the presence of high-risk plaques at the stent edges after implantation remain unknown and will require further investigation.

Relation between plaque type at the stent borders and edge dissection

Our results showed that edge dissection was more frequent when the plaque at the border was fibrocalcific or lipid rich than when the plaque was fibrous. Previous IVUS studies have reported that the underlying plaque morphology in edge dissections is more frequently echolucent (30). Soft (echolucent) plaques in IVUS have been related to high lipid content(31). There was a tendency towards longer edge dissections in fibrocalcific plaques but no significant differences could be demonstrated.

The development of stent technology with the introduction of drug-eluting stents has reduced dramatically the restenosis rate. However, some patients still develop severe neointimal growth, in some cases at the stent edges. Furthermore, there is an important concern about the risk of late stent thrombosis(7,32). The use of OCT to evaluate the plaque type and the presence of dissections at the stent edges may provide a new piece of information to better understand the causes of stent failure.

LIMITATIONS

The present study was observational and no formal sample size calculation was performed. The limited length of the OCT pullbacks did not allow the visualization of the proximal and distal edge in all the cases.

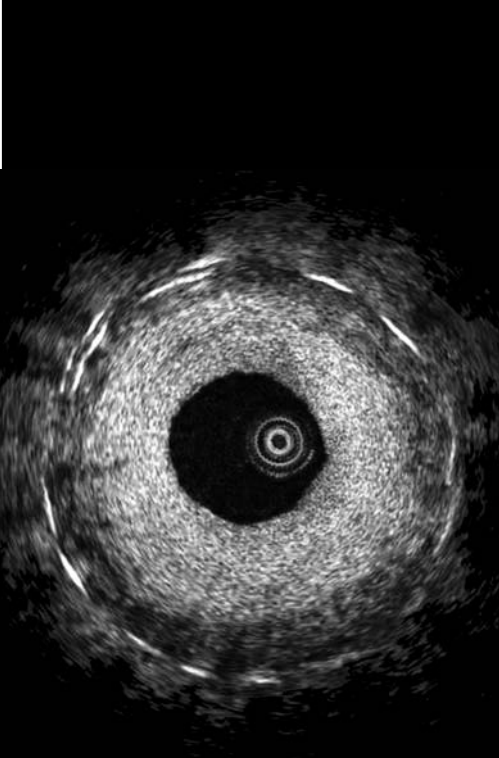
CONCLUSIONS

OCT showed higher sensitivity compared to angiography for the identification of edge dissections after stenting. A high proportion of patients showed lipid rich plaques at the stent edges. The plaque type at the stent edges has impact on the presence of edge dissections.

REFERENCES

1. Serruys PW, Kutryk MJ, Ong AT. Coronary-artery stents. *N Engl J Med* 2006;354:483-95.
2. Carter AJ, Lee DP, Suzuki T, et al. Experimental evaluation of a short transitional edge protection balloon for intracoronary stent deployment. *Catheter Cardiovasc Interv* 2000;51:112-9.
3. Schwarzacher SP, Metz JA, Yock PG, Fitzgerald PJ. Vessel tearing at the edge of intracoronary stents detected with intravascular ultrasound imaging. *Cathet Cardiovasc Diagn* 1997;40:152-5.
4. Garcia-Garcia HM, Gonzalo N, Tanimoto S, Meliga E, de Jaegere P, Serruys PW. Characterization of edge effects with paclitaxel-eluting stents using serial intravascular ultrasound radiofrequency data analysis: the BETAX (BEside TAXus) Study. *Rev Esp Cardiol* 2008;61:1013-9.
5. Gonzalo N, Serruys PW, Regar E. Optical coherence tomography: clinical applications and the evaluation of DES. *Minerva Cardioangiologica* 2008;56:511-25.
6. Gonzalo N, Barlis P, Serruys PW, Garcia-Garcia HM, Onuma Y, Ligthart J, Regar E. Incomplete Stent Apposition And Delayed Tissue Coverage Are More Frequent In Drug Eluting Stents Implanted During Primary Percutaneous Coronary Intervention For ST Elevation Myocardial Infarction *J Am Coll Cardiol Interv* 2009;2:445-52.
7. Barlis P, Di Mario C, van Beusekom HMM, Gonzalo N, Regar E. Novelty in Cardiac Imaging – Optical Coherence Tomography (OCT). A critical appraisal of the safety concerns tempering the success of drug-eluting stents *Eurointervention* 2008;4:Suppl C:C22-6.
8. Barlis P, Gonzalo N, Di Mario C, Prati F, Buellesfeld L, Rieber J, Dalby MC, Ferrante G, Cera M, Grube E, Serruys PW, Regar E. A Multi-Centre Evaluation of the Safety of Intra-Coronary Optical Coherence Tomography. *Eurointervention* 2009;5:90-95
9. Yabushita H, Bouma BE, Houser SL, et al. Characterization of human atherosclerosis by optical coherence tomography. *Circulation* 2002;106:1640-5.
10. Gonzalo N, Serruys PW, Barlis P, Ligthart J, Garcia Gacria H, Regar E. Multi-Modality Intra-Coronary Plaque Characterization: A Pilot Study. *Int J Cardiol* 2008.
11. Barlis P, Serruys PW, Gonzalo N, Van der Giessen W, Jaegere P.J, Regar E. Assessment of Culprit and Remote Coronary Narrowings Using Optical Coherence Tomography with Long-Term Outcomes. *Am J Cardiol* 2008.
12. Huber MS, Mooney JF, Madison J, Mooney MR. Use of a morphologic classification to predict clinical outcome after dissection from coronary angioplasty. *Am J Cardiol* 1991;68:467-71.
13. Virmani R, Burke AP, Kolodgie FD, Farb A. Vulnerable plaque: the pathology of unstable coronary lesions. *J Interv Cardiol* 2002;15:439-46.
14. Gonzalo N, Garcia-Garcia HM, Regar E, Barlis P, Wentzel J, Onuma Y, Ligthart J, Serruys PW. In Vivo Assessment of High-risk Coronary Plaques at Bifurcations with Combined Intravascular Ultrasound Virtual Histology and Optical Coherence Tomography. *J Am Coll Cardiol Img* 2009;2:473-82.
15. Bouma BE, Tearney GJ, Yabushita H, et al. Evaluation of intracoronary stenting by intravascular optical coherence tomography. *Heart* 2003;89:317-20.

16. Schwartz RS, Huber KC, Murphy JG, et al. Restenosis and the proportional neointimal response to coronary artery injury: results in a porcine model. *J Am Coll Cardiol* 1992;19:267-74.
17. Farb A, Sangiorgi G, Carter AJ, et al. Pathology of acute and chronic coronary stenting in humans. *Circulation* 1999;99:44-52.
18. Schroeder S, Baumbach A, Mahrholdt H, et al. The impact of untreated coronary dissections on acute and long-term outcome after intravascular ultrasound guided PTCA. *Eur Heart J* 2000;21:137-45.
19. Hong MK, Park SW, Lee NH, et al. Long-term outcomes of minor dissection at the edge of stents detected with intravascular ultrasound. *Am J Cardiol* 2000;86:791-5, A9.
20. Sheris SJ, Canos MR, Weissman NJ. Natural history of intravascular ultrasound-detected edge dissections from coronary stent deployment. *Am Heart J* 2000;139:59-63.
21. Nishida T, Colombo A, Briguori C, et al. Outcome of nonobstructive residual dissections detected by intravascular ultrasound following percutaneous coronary intervention. *Am J Cardiol* 2002;89:1257-62.
22. Kobayashi Y, Amaro M, Fitzgerald PJ. Acute coronary closure after stenting: a lesson from intravascular ultrasound. *Int J Cardiovasc Intervent* 1999;2:51-54.
23. Kume T, Akasaka T, Kawamoto T, et al. Measurement of the thickness of the fibrous cap by optical coherence tomography. *Am Heart J* 2006;152:755 e1-4.
24. Serruys PW, Degertekin M, Tanabe K, et al. Vascular responses at proximal and distal edges of paclitaxel-eluting stents: serial intravascular ultrasound analysis from the TAXUS II trial. *Circulation* 2004;109:627-33.
25. Sakurai R, Hongo Y, Yamasaki M, et al. Detailed intravascular ultrasound analysis of Zotarolimus-eluting phosphorylcholine-coated cobalt-chromium alloy stent in de novo coronary lesions (results from the ENDEAVOR II trial). *Am J Cardiol* 2007;100:818-23.
26. Garcia-Garcia HM, Gonzalo N, Granada JF, Regar E, Serruys PW. Diagnosis and treatment of coronary vulnerable plaques. *Expert Rev Cardiovasc Ther* 2008;6:209-22.
27. Liu J, Maehara A, Mintz GS, et al. An integrated TAXUS IV, V, and VI intravascular ultrasound analysis of the predictors of edge restenosis after bare metal or paclitaxel-eluting stents. *Am J Cardiol* 2009;103:501-6.
28. Okabe T, Mintz GS, Buch AN, et al. Intravascular ultrasound parameters associated with stent thrombosis after drug-eluting stent deployment. *Am J Cardiol* 2007;100:615-20.
29. Farb A, Burke AP, Kolodgie FD, Virmani R. Pathological mechanisms of fatal late coronary stent thrombosis in humans. *Circulation* 2003;108:1701-6.
30. Ziada KM, Tuzcu EM, De Franco AC, et al. Intravascular ultrasound assessment of the prevalence and causes of angiographic "haziness" following high-pressure coronary stenting. *Am J Cardiol* 1997;80:116-21.
31. DeMaria AN, Narula J, Mahmud E, Tsimikas S. Imaging vulnerable plaque by ultrasound. *J Am Coll Cardiol* 2006;47:C32-9.
32. McFadden EP, Stabile E, Regar E, et al. Late thrombosis in drug-eluting coronary stents after discontinuation of antiplatelet therapy. *Lancet* 2004;364:1519-21.



6.6

A critical appraisal of the safety concerns tempering the success of drug eluting stents.

**Novelties in cardiac imaging:
Optical Coherence Tomography**

Barlis P, di Mario C, van Beusekom H, Gonzalo N, Regar E.



Eurointervention 2008; 4 Suppl C33-38.

Novelties in cardiac imaging – Optical Coherence Tomography (OCT)

Peter Barlis¹, MBBS, MPH, FRACP; Carlo Di Mario², MD PhD, FESC, FSCAI, FACC FRCP; Heleen van Beusekom³, PHD; Nieves Gonzalo³, MD; Evelyn Regar^{3*}, MD, PhD

1. Department of Cardiology, The Northern Hospital, Victoria Australia; 2. Department of Invasive Cardiology, Royal Brompton Hospital, London, United Kingdom; 3. Department of Cardiology, Erasmus MC, Rotterdam, The Netherlands

The authors have no conflict of interest to declare.

Introduction

In order to improve our understanding of late stent thrombosis and to assess the individual risk of a patient or lesion, there is clinical need to assess vascular healing after stenting *in vivo*. We will discuss the potential and limitations of optical coherence tomography (OCT) for imaging of drug eluting stents (DES).

OCT, a light based imaging modality¹, has recently become available for intracoronary application²⁻⁴. Because of the shorter wavelength of infrared light compared to ultrasound, OCT has a ten-fold higher image resolution than conventional intravascular ultrasound (IVUS), 150 micron for IVUS as compared to 15 micron for OCT. This advantage renders OCT particularly useful for the assessment of coronary stents.

OCT observations in drug-eluting stents immediately after implantation

For the past two decades, IVUS has been used to assess the acute result following stenting, giving valuable information on stent expansion, strut apposition and signs of vessel trauma including dissections and tissue prolapse^{5,6}. IVUS studies^{7,8} suggested that stent strut malapposition is a relatively uncommon finding, observed in approx 7% of cases, and that strut malapposition does not increase the risk of subsequent major adverse cardiac events. In contrast, OCT can visualise the complex coronary arterial wall structure after stenting in much greater detail⁹. As a result, OCT studies in the acute post stent setting¹⁰ have demonstrated

a relatively high proportion of stent struts, not completely apposed to the vessel wall, even after high pressure post-dilatation. Furthermore, this phenomenon is particularly evident at regions of stent overlap¹¹. Tanigawa et al¹² examined a total of 6,402 struts from 23 patients (25 lesions) and found 9.1±7.4% of all struts in each lesion treated were malapposed. Univariate predictors of malapposition where: implantation of a sirolimus-eluting stent (SES), presence of overlapping stents, longer stent length and type C lesions. Likely mechanical explanations for malapposition of stent struts include increased strut thickness, closed cell design or acute stent recoil. The latter has been demonstrated in SES to be in the range of 15%, despite the use of high pressure balloon dilatation¹³.

While these findings are impressive and helpful for the improvement of future stent designs, today the clinical relevance and potentially long-term sequelae of malapposed struts as detected by OCT are currently unknown.

OCT observations in drug eluting stents at long-term follow-up

Unlike conventional stents, which develop circumferential coverage with an average thickness of 500 micron or more, well visualised with IVUS and angiography, drug-eluting stents delay and prevent the hyperplastic response so that the average late lumen loss for drug-eluting stents can be lower than 100 micron⁴ which means this thin layer of intimal thickening can be below the resolution of IVUS. Coronary angiography is able to visualise strut tissue coverage

* Corresponding author: Department of Cardiology, Thoraxcenter, Thoraxcenter, Ba583a Erasmus MC, 's-Gravendijkwal 230, 3015 CE Rotterdam, The Netherlands

E-mail: e.regar@erasmusmc.nl

© Europa Edition 2008. All rights reserved.

to a certain extent, but this highly specialised technique lacks the ability for quantification and the ability to assess thin amounts of neointima. Hence, OCT is an attractive alternative, able to circumvent many of these limitations and, with its high-resolution, can precisely assess the *in vivo* tissue responses following stent implantation¹⁴. Specific applications of OCT relevant for late stent thrombosis are discussed below.

a) Visualisation and quantification of stent strut tissue coverage

OCT can reliably detect early and very thin layers of tissue coverage on stent struts (Figure 1-4). Several small studies have recently been published highlighting the application of OCT in the detection of stent

tissue coverage at follow-up. Importantly, OCT permits the quantification of tissue coverage with high reliability¹⁵. Matsumoto et al¹⁶ studied 34 patients following sirolimus eluting stent (SES) implantation. The mean neointima thickness was 52.5 microns, and the prevalence of struts covered by thin neointima undetectable by IVUS was 64%. The average rate of neointima-covered struts in an individual SES was 89%. Nine SES (16%) showed full coverage by neointima, whereas the remaining stents had partially uncovered struts. Similarly, Takano et al¹⁷ studied 21 patients (4,516 struts), three months following SES implantation. Rates of exposed struts and exposed struts with malapposition were 15% and 6%, respectively. These were more frequent in patients with acute coronary syndrome

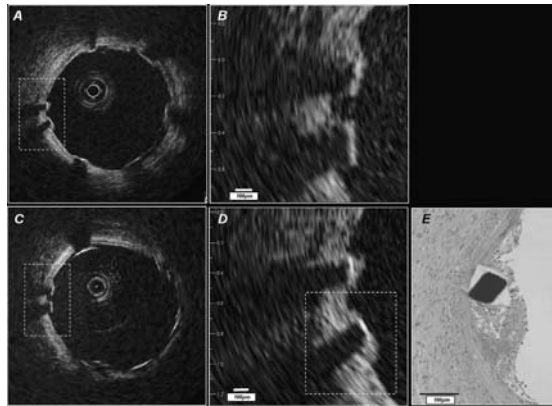


Figure 1. *In vivo* OCT (LightLabImaging™, Boston, MA, USA) in a porcine coronary artery. A) Baseline OCT immediately after stent implantation shows adequate stent expansion and apposition of the struts against the normal coronary wall. B) Magnification demonstrating the stent strut vessel wall interface. C) Follow-up investigation at five days. The stent struts are clearly visible and show thin, bright reflective tissue coverage in the magnification D) Histology E) confirms the presence of a thin neointimal layer.

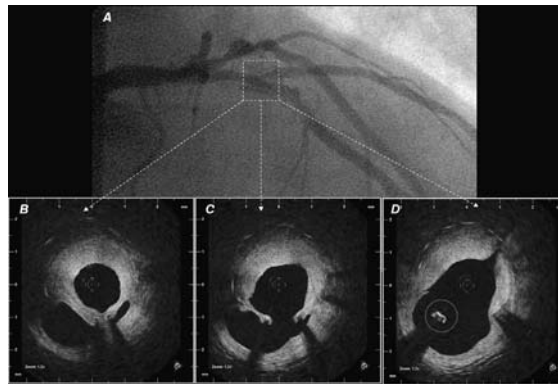


Figure 2. *In vivo* OCT (LightLabImaging™, Boston, MA, USA) in the LAD in a patient presenting with in-stent restenosis. A) The coronary angiogram shows a lumen narrowing within the stent that is covering the second diagonal branch. OCT visualises the complex coronary anatomy in great detail. The stent is covered by a thick neointima that shows a layered appearance with a bright, highly reflective luminal layer, an intermediate layer and a dark, signal poor layer surrounding the struts (B). The diagonal take off can be clearly seen (C) as well as a stent strut that is "floating" in the carina (D).

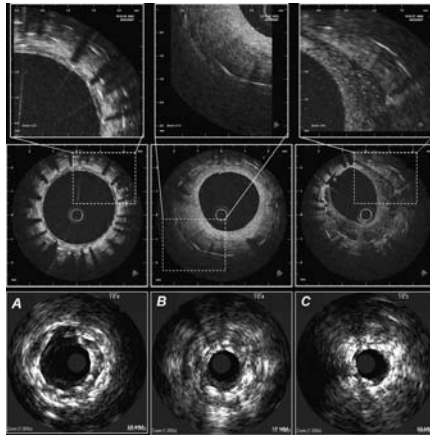


Figure 3. Demonstrates the information that can be gathered from IVUS (20Mhz, lower panels) and from OCT imaging (mid and upper panels, LightLabImaging™, Boston, MA, USA) in patients at follow-up after stent implantation. These are corresponding cross sections within a stent, imaged by both, OCT in the upper panels and by IVUS in the lower panels. The images represent the same spots within a coronary artery (A, B, C), and illustrates the different quality of information that can be obtained by OCT as compared to conventional grey scale IVUS. A) Three layers of stents can be seen. OCT is able to clearly visualise the individual stent struts, the neointimal layers separating the different stents and the very thin coverage of the most inner, luminal stent struts. B) a bright, eccentric and relatively thick neointimal layer can be seen C) an eccentric thick neointimal layer is visible, however, the structure of this neointima differs considerably from the example B) with a low-reflective and speckled appearance.

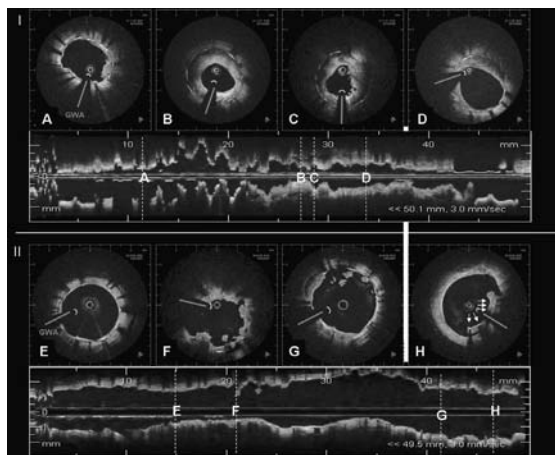


Figure 4. OCT (LightLabImaging™, Boston, MA, USA) findings in two patients presenting with late drug-eluting stent (DES) thrombosis. OCT was performed in both cases immediately after thrombus aspiration and reveals completely different morphologic findings, possible suggesting two different mechanisms for late stent thrombosis, focal restenosis and incomplete strut coverage. I) Patient with late stent thrombosis three months after DES implantation in the left circumflex artery. OCT reveals an adequately expanded stent, all struts are well apposed against the vessel wall. All struts show tissue coverage, which is more pronounced in the proximal portion of the stent (D) as compared to the distal stent portion (A). There is focal in-stent restenosis (B, C) with severe lumen narrowing (MLA 1.63 mm²). The neointima shows a layered appearance with a luminal bright, highly reflective layer, an intermediate layer and a dark, signal poor layer surrounding the struts. Remnants of the thrombus are focally seen as irregular mural structures, protruding into the lumen (A, C). II) Patient with very late stent thrombosis four years after DES implantation in the left anterior descending artery. OCT reveals an adequately expanded stent, however, there is incomplete stent strut apposition at the proximal stent edge with incomplete tissue coverage in 21% of struts. (E) The distal stent portion, shows a well expanded and apposed stent with thin tissue coverage by OCT. (F) irregular lumen borders with intraluminal remnants of the thrombus. (G) proximal stent portion showing a strut without visible tissue coverage in 12 o'clock position and thrombus fragments in the lumen. (H) proximal stent edge with incomplete apposition of five stent struts (arrows) against the vessel wall. The distance to the vessel wall is 200 micron. OCT shows tissue around the stent struts (DD thrombus, neointima). GWA: guidewire artefact.

(ACS) than in those with non-ACS (18% vs 13%, $p < 0.001$; 8% vs 5%, $p < 0.005$, respectively). The same group recently reported two year follow-up OCT findings¹⁸ with the thickness of neointimal tissue at 2-years being greater than that at 3-months (71 ± 93 micron vs. 29 ± 41 micron, respectively; $p < 0.001$). Frequency of uncovered struts was found to be lower in the 2-year group compared to the 3-month group (5% vs. 15%, respectively; $p < 0.001$). Conversely, prevalence of patients with uncovered struts did not differ between the 3-month and the 2-year follow-up study (95% vs. 81%, respectively) highlighting that uncovered struts continued to persist at long-term follow-up. Chen et al¹⁹ recently used OCT to image SES and bare metal stents (BMS) at different time points following implantation. Of the 10 SES and 13 BMS imaged, the authors identified a significantly higher number of incompletely apposed and uncovered stent struts in patients receiving SES compared to BMS.

The results of these small observational studies are compatible with evidence from animal and human post-mortem series showing that DES cause impairment in arterial healing, some with suggested incomplete re-endothelialisation and persistence of fibrin(oid)^{20,21} possible triggering late stent thrombosis²².

However, OCT observations need to be interpreted with caution. OCT is limited by its resolution of 15 micron which is greater than the thickness of an individual layer of endothelial cells. Therefore, coverage that is not visible by OCT does not exclude the presence of an endothelial layer. Second, the presence of tissue coverage does not necessarily imply the presence of a functionally intact endothelium. Early experimental stent data showed that endothelial function can vary considerably and show evidence of damage when subjected to the Evan's blue dye exclusion test²³, even in the presence of a well structured neointimal layer. In consequence, morphology should not be confused with function.

b) Assessment of structural details of tissue coverage

OCT also permits the characterisation of neointimal tissue in a qualitative way. This is a great advantage as such information has not been available *in vivo* until now. The limited resolution together with artefacts induced by metallic stent struts do not allow the characterisation of such details by IVUS. With OCT, neointimal tissue can show a variety of morphologies ranging from homogeneous, bright, uniform tissue to optically heterogeneous tissue or eccentric tissue of various thickness. Furthermore, structural details within the tissue can be observed such as intimal neovascularisation²⁴ or a layered appearance, typically observed in restenotic regions²⁵. Variations in the appearance of strut coverage can be seen within an individual patient, within an individual stent or within stents of different design.

OCT findings, such as dark, signal-poor halos around stent struts may reflect fibrin deposition and incomplete healing, as described in pathologic and animal experimental series^{20,21}. However, there is paucity of data demonstrating directly the OCT appearance of different components in neointimal tissue as defined by histology. Post-mortem imaging of DES in human coronaries is difficult and might be limited by the fact that the optical tissue properties show variations with temperature and fixation²⁶. Long-term animal OCT observations in DES are scarce.

c) Assessment of stent strut vessel wall interaction and strut apposition

The interest in the long-term stent strut vessel wall interaction is manifold and includes the assessment of the stability of the acute result, the visualisation of complex anatomy that is not accessible by angiography or IVUS and the clearer understanding of reasons for stent failures, when they do occur. The unique optical properties of OCT can also be applied to the study and evaluation of new stent designs including bioabsorbable stents. Morphologic changes of the absorbable, polylactic acid stent struts and the vessel wall during follow-up have been recently described and show the unique capabilities of this *in vivo* imaging modality²⁷.

Stent strut malapposition remains an important consideration. Postulated causes for stent strut malapposition are various and include incomplete stent expansion, stent recoil or fracture, late outward vessel remodelling or the dissolution of thrombus that was compressed during PCI between the stent strut and the vessel wall. Regardless of the pathophysiologic mechanism, the major concern in stent malapposition remains in the assumption that areas of strut malapposition cause non-laminar and turbulent blood flow characteristics, which in turn can trigger platelet activation and thrombosis. Here, prospective, serial OCT observations immediately and at longer term follow-up after stenting may improve our understanding of these complex mechanisms and shed light on the likely clinical significance of this phenomenon.

Reasons for DES failure are poorly understood. With the reduction of in-stent hyperplasia, other mechanisms of restenosis due to mechanical stent failure have become apparent. Of the two established first generation DES, the sirolimus-eluting stent (Cordis, Johnson&Johnson, Miami, FL, USA) has been particularly linked to cases of stent fracture, likely as a result of its closed cell design compared with other DES employing an open cell system²⁸. The higher imaging resolution of OCT compared to IVUS permits a detailed assessment in such cases, as demonstrated recently by Shite et al²⁹.

Conclusion & future developments

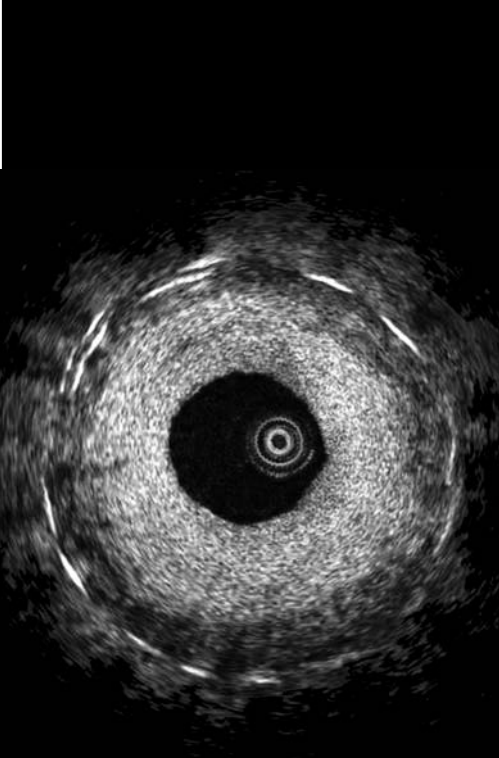
OCT is a light-based diagnostic tool that allows *in vivo* imaging of the coronary artery wall in unparalleled detail³⁰. OCT can reliably visualise very thin stent strut tissue coverage as early as five days after implantation, and permits for its qualitative and precise quantitative assessment. These unique capabilities favour OCT as the new golden standard for the evaluation of coronary stents.

Recent improvements in OCT technology, with frequency-domain OCT, will allow for a simple imaging procedure and offer the potential for large scale, prospective studies, indispensable to address vexing clinical questions such as the relationship of drug-eluting stent deployment, vascular healing, the true time course of endothelial stent coverage and late stent thrombosis. This may also better guide the optimal duration of dual anti-platelet therapy that currently remains unclear and rather empiric.

References

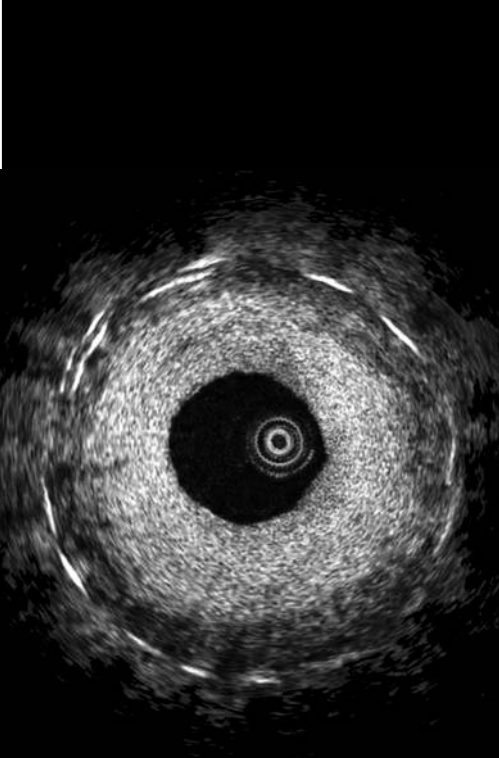
1. Huang D, Swanson EA, Lin CP, Schuman JS, Stinson WG, Chang W, Hee MR, Flotte T, Gregory K, Puliafito CA, et al. Optical coherence tomography. *Science*, 1991;254:1178-81.

2. Brezinski ME, Tearney GJ, Bouma BE, Boppart SA, Hee MR, Swanson EA, Southern JF, Fujimoto JG. Imaging of coronary artery microstructure (in vitro) with optical coherence tomography. *Am J Cardiol*, 1996;77:92-3.
3. Fujimoto JG, Boppart SA, Tearney GJ, Bouma BE, Pitris C, Brezinski ME. High resolution in vivo intra-arterial imaging with optical coherence tomography. *Heart*, 1999;82:128-33.
4. Regar E, Schaar J, van der Giessen W, van der Steen A, Serruys P. Real-time, in-vivo optical coherence tomography of human coronary arteries using a dedicated imaging wire. *Am J Cardiol* 2002;90(suppl 6A): 129H.
5. Colombo A, Hall P, Nakamura S, Almagor Y, Maiello L, Martini G, Gaglione A, Goldberg SL, Tobis JM. Intracoronary stenting without anticoagulation accomplished with intravascular ultrasound guidance [see comments]. *Circulation*, 1995;91:1676-88.
6. de Jaegere P, Mudra H, Figulla H, Almagor Y, Doucet S, Penn I, Colombo A, Hamm C, Bartorelli A, Rothman M, Nobuyoshi M, Yamaguchi T, Voudris V, DiMario C, Makovski S, Hausmann D, Rowe S, Rabinovich S, Sunamura M, van Es GA. Intravascular ultrasound-guided optimized stent deployment. Immediate and 6 months clinical and angiographic results from the Multicenter Ultrasound Stenting in Coronaries Study (MUSIC Study). *Eur Heart J*, 1998;19:1214-23.
7. Meerkin D, Lee SH, Tio FO, Grube E, Wong SC, Hong MK. Effects of focused force angioplasty: pre-clinical experience and clinical confirmation. *J Invasive Cardiol*, 2005;17:203-6.
8. Tanabe K, Serruys PW, Degertekin M, Grube E, Guagliumi G, Urbaszek W, Bonnier J, Lablanche JM, Siminiak T, Nordrehaug J, Figulla H, Drzewiecki J, Banning A, Hauptmann K, Dudek D, Bruining N, Hamers R, Hoye A, Ligthart JM, Disco C, Koglin J, Russell ME, Colombo A; TAXUS II Study Group. Incomplete stent apposition after implantation of paclitaxel-eluting stents or bare metal stents: insights from the randomized TAXUS II trial. *Circulation*, 2005;111:900-5.
9. Tearney GJ, Jang IK, Kang DH, Aretz HT, Houser SL, Brady TJ, Schlenkorf K, Shishkov M, Bouma BE. Porcine coronary imaging in vivo by optical coherence tomography. *Acta Cardiol*, 2000;55:233-7.
10. Hauger C, Worz M, Hellmuth T. Interferometer for optical coherence tomography. *Appl Opt*, 2003;42:3896-902.
11. Tanigawa J, Barlis P, Dimopoulos K, Di Mario C. Optical coherence tomography to assess malapposition in overlapping drug-eluting stents. *EuroInterv*, 2008;3:580-583.
12. Tanigawa J, Barlis P, Kaplan S, Goktekin O, Di Mario C. Stent strut apposition in complex lesions using optical coherence tomography. *Am J Cardiol*, 2006;98:Suppl 1: 97M.
13. Regar E, Schaar J, Serruys P. Acute recoil in sirolimus eluting stent: real time, in vivo assessment with optical coherence tomography. *Heart*, 2006;92:123.
14. Regar E, Ong A, McFadden EP, de Jaegere PPT, van Beusekom HMM, van der Giessen WJ, de Feyter P, Serruys PW. Long-term follow-up of drug-eluting stents (DES) - optical coherence tomography (OCT) findings. *Eur Heart J*, 2005;P4047 (abstract).
15. Tanimoto S, Rodriguez-Granillo G, Barlis P, de Winter S, Bruining N, Hamers R, Knappen M, Verheye S, Serruys PW, Regar E. A Novel Approach for Quantitative Analysis of Intracoronary Optical Coherence Tomography. High inter-observer agreement with computer-assisted contour detection. *Catheter Cardiovasc Interv*, 2008;Mar 6; [Epub ahead of print].
16. Matsumoto D, Shite J, Shinke T, Otake H, Tanino Y, Ogasawara D, Sawada T, Paredes OL, Hirata K, Yokoyama M. Neointimal coverage of sirolimus-eluting stents at 6-month follow-up: evaluated by optical coherence tomography. *Eur Heart J*, 2007;28:961-7.
17. Takano M, Inami S, Jang IK, Yamamoto M, Murakami D, Seimiya K, Ohba T, Mizuno K. Evaluation by optical coherence tomography of neointimal coverage of sirolimus-eluting stent three months after implantation. *Am J Cardiol*, 2007;99:1033-8.
18. Takano M, Yamamoto M, Inami S, Murakami D, Seimiya K, Ohba T, Seino Y, Mizuno K. Long-term follow-up evaluation after sirolimus-eluting stent implantation by optical coherence tomography: do uncovered struts persist? *J Am Coll Cardiol*, 2008;51:968-9.
19. Chen BX, Ma FY, Luo W, Ruan JH, Xie WL, Zhao XZ, Sun SH, Guo XM, Wang F, Tian T, Chu XW. Neointimal Coverage of Bare Metal and Sirolimus-Eluting Stents Evaluated with optical coherence tomography. *Heart*. 2008 May;94(5):566-70.
20. Finn AV, Joner M, Nakazawa G, Kolodgie F, Newell J, John MC, Gold HK, Virmani R. Pathological correlates of late drug-eluting stent thrombosis: strut coverage as a marker of endothelialization. *Circulation*, 2007;115:2435-41.
21. Finn AV, Nakazawa G, Joner M, Kolodgie FD, Mont EK, Gold HK, Virmani R. Vascular responses to drug eluting stents: importance of delayed healing. *Arterioscler Thromb Vasc Biol* 2007;27:1500-10.
22. Joner M, Finn AV, Farb A, Mont EK, Kolodgie FD, Ladich E, Kutys R, Skorija K, Gold HK, Virmani R. Pathology of drug-eluting stents in humans: delayed healing and late thrombotic risk. *J Am Coll Cardiol*, 2006;48:193-202.
23. van Beusekom HM, Whelan DM, Hofma SH, Krabbandam SC, van Hinsbergh VW, Verdouw PD, van der Giessen WJ. Long-term endothelial dysfunction is more pronounced after stenting than after balloon angioplasty in porcine coronary arteries. *J Am Coll Cardiol*, 1998;32:1109-17.
24. Regar E, van Beusekom HM, van der Giessen WJ, Serruys PW. Images in cardiovascular medicine. Optical coherence tomography findings at 5-year follow-up after coronary stent implantation. *Circulation*, 2005;112:e345-6.
25. Tanimoto S, Aoki J, Serruys PW, Regar E. Paclitaxel-eluting stent restenosis shows three - layer appearance by optical coherence tomography. *EuroInterv*, 2006 2006;1:484.
26. Meer FJvd, Faber DJ, Cilesiz I, Gemert MJCv, Leeuwen TGv. Temperature-dependent optical properties of individual vascular wall components measured by optical coherence tomography. *Journal of Biomedical Optics*, 2006;11:041120.
27. Ormiston JA, Serruys PW, Regar E, Dudek D, Thuesen L, Webster MW, Onuma Y, Garcia-Garcia HM, McGreevy R, Veldhof S. First-In-Man Evaluation of a Bioabsorbable-Everolimus Eluting Coronary Stent System (BVS) in the Treatment of Patients with Single de-novo Native Coronary Artery Lesions: The ABSORB Trial. *The Lancet*, 2 2008;371:899-907.
28. Lee SH, Park JS, Shin DG, Kim YJ, Hong GR, Kim W, Shim BS. Frequency of stent fracture as a cause of coronary restenosis after sirolimus-eluting stent implantation. *Am J Cardiol*, 2007;100:627-30.
29. Shite J, Matsumoto D, Yokoyama M. Sirolimus-eluting stent fracture with thrombus, visualization by optical coherence tomography. *Eur Heart J*, 2006;27:1389.
30. Regar E, van Leeuwen AMGJ, Serruys PW (Eds): Optical coherence tomography in cardiovascular research. London: Informa Healthcare. 2007. ISBN 1841846112.



CHAPTER 7

OCT for the evaluation of new generation stents. Assessment of biodegradable stents



7.1

A bioabsorbable everolimus-eluting coronary stent system (ABSORB): 2-year outcomes and results from multiple imaging methods.

Serruys PW, Ormiston JA, Onuma Y, Regar E, Gonzalo N, Garcia-Garcia HM, Nieman K, Bruining N, Dorange C, Miquel-Hébert K, Veldhof S, Webster M, Thuesen L, Dudek D.

Lancet. 2009 Mar 14;373(9667):897-910

A bioabsorbable everolimus-eluting coronary stent system (ABSORB): 2-year outcomes and results from multiple imaging methods



Patrick W Serruys, John A Ormiston, Yoshinobu Onuma, Evelyn Regar, Nieves Gonzalo, Hector M Garcia-Garcia, Koen Nieman, Nico Bruining, Cécile Dorange, Karine Miquel-Hébert, Susan Veldhof, Mark Webster, Leif Thuesen, Dariusz Dudek

Summary

Background Drug-eluting metallic coronary stents predispose to late stent thrombosis, prevent late lumen vessel enlargement, hinder surgical revascularisation, and impair imaging with multislice CT. We assessed the safety of the bioabsorbable everolimus-eluting stent (BVS).

Methods 30 patients with a single de-novo coronary artery lesion were followed up for 2 years clinically and with multiple imaging methods: multislice CT, angiography, intravascular ultrasound, derived morphology parameters (virtual histology, palpography, and echogenicity), and optical coherence tomography (OCT).

Findings Clinical data were obtained from 29 of 30 patients. At 2 years, the device was safe with no cardiac deaths, ischaemia-driven target lesion revascularisations, or stent thromboses recorded, and only one myocardial infarction (non-Q wave). 18-month multislice CT (assessed in 25 patients) showed a mean diameter stenosis of 19% (SD 9). At 2-year angiography, the in-stent late loss of 0.48 mm (SD 0.28) and the diameter stenosis of 27% (11) did not differ from the findings at 6 months. The luminal area enlargement on OCT and intravascular ultrasound between 6 months and 2 years was due to a decrease in plaque size without change in vessel size. At 2 years, 34.5% of strut locations presented no discernible features by OCT, confirming decreases in echogenicity and in radiofrequency backscattering; the remaining apparent struts were fully apposed. Additionally, vasomotion occurred at the stented site and adjacent coronary artery in response to vasoactive agents.

Interpretation At 2 years after implantation the stent was bioabsorbed, had vasomotion restored and restenosis prevented, and was clinically safe, suggesting freedom from late thrombosis. Late luminal enlargement due to plaque reduction without vessel remodelling needs confirmation.

Funding Abbott Vascular (USA).

Introduction

A bioabsorbable stent might have less potential for late stent thrombosis than might a drug-eluting metallic stent because there will eventually be no foreign material exposed to blood if endothelialisation is delayed or incomplete.^{1,2} Furthermore, permanent metallic stenting could preclude surgical revascularisation and jail-side branches, prevent expansive remodelling, eliminate reactive vasomotion, and impair the non-invasive imaging of coronary arteries with multislice CT and MRI. A study of a bioabsorbable but non-drug-eluting poly-L-lactic acid (PLLA) stent³ showed long-term results similar to those after bare-metal stent implantation, lending support to the feasibility and safety of a bioabsorbable PLLA polymer stent.⁴ The restenosis rate after implantation of a magnesium stent was high because rapid biocorrosion resulted in only brief opposition to vessel recoil forces and because there was no antiproliferative drug to prevent neointimal hyperplasia.⁵

As an alternative approach to the metallic drug-eluting stent, bioabsorbable polymer drug-eluting stents could provide short-term vessel scaffolding combined with

drug delivery capability but avoid the long-term restrictions of metallic stents. We reported the 6-month angiographic and intravascular ultrasound outcomes and 12-month clinical outcomes of the ABSORB trial,⁶ which used the bioabsorbable everolimus-eluting stent (BVS) system (Abbott Vascular, Santa Clara, CA, USA). The BVS stent has a bioabsorbable polylactic acid backbone with a bioabsorbable polylactic acid coating that contains the antiproliferative drug, everolimus (Novartis, Basel, Switzerland). In a series of 30 patients, the BVS stent at 6-month follow-up showed an angiographic in-stent loss of 0.44 mm (SD 0.35) mainly due to a mild shrinkage of the stent area (−11.8%) that, along with a small neointimal response (5.5%), resulted in an overall 16.8% reduction of the luminal area.⁶ Furthermore, the only major adverse cardiac event was a non-Q-wave myocardial infarction. No ischaemic target lesion revascularisations were noted and no stent thromboses occurred in the first 12 months. From immediately after the procedure to 6 months after, morphological change of the stent struts was documented by optical coherence tomography (OCT), and by echogenicity and radiofrequency backscattering.

Lancet 2009; 373: 897–910

See Comment page 869

See Perspectives page 887

Thorax Center

(Prof P W Serruys MD, Y Onuma MD, E Regar MD, N Gonzalo MD, K Nieman MD, N Bruining PhD) and Department of Radiology (K Nieman MD), Erasmus Medical Center, Rotterdam, Netherlands; Auckland City Hospital, Auckland, New Zealand (Prof J A Ormiston MB, M Webster MB); Cardialysis BV, Rotterdam, Netherlands (H M Garcia-Garcia MD); Abbott Vascular, Diegem, Belgium (C Dorange MSc, K Miquel-Hébert PhD, S Veldhof RN); Skejby Sygehus, Aarhus University Hospital, Skejby, Denmark (L Thuesen MD); and Jagiellonian University, Krakow, Poland (D Dudek MD)

Correspondence to:

Prof P W Serruys,
¹s Gravenhijkwal 230,
 3015 CE Rotterdam, Netherlands
 p.w.j.c.serruys@erasmusmc.nl

However, the medium-term outcomes of biodegradation of the BVS stent in human coronary arteries remain to be investigated.

We now report the 18-month multislice CT scanning results, the 2-year clinical follow-up, and longitudinal assessments of the stent and vessel wall at 6 months and 2 years, by several invasive imaging methods.

Methods

Study design and population

The design of the present study has been published.⁶ Briefly, in this single-group, prospective, open-label study, with safety and imaging endpoints, 30 patients were enrolled at four participating sites between March 7, and July 18, 2006. Patients were older than 18 years, and had a diagnosis of stable or unstable angina, or silent ischaemia. All treated lesions were single, de-novo in a native coronary artery of 3.0 mm, shorter than 8 mm for the 12 mm stent, or shorter than 14 mm for the 18 mm stent (only two patients received an 18 mm stent), with a percentage diameter stenosis greater than 50% and less than 100%, and with a thrombolysis in myocardial infarction (TIMI) flow grade of more than 1. Major exclusion criteria were patients presenting with an acute myocardial infarction or unstable arrhythmias, or those who had left ventricular ejection fraction less than 30%, restenotic lesions, lesions located in the left main

coronary artery, lesions involving a side branch more than 2 mm in diameter, and the presence of thrombus or another clinically significant stenosis in the target vessel. A risk analysis of several imaging methods based on previously published reports was provided to the local ethics committee.^{7,8}

The protocol was approved by the ethics committee at the four participating institutions, and enrolled patients (intention-to-treat population) gave written informed consent before inclusion. Clinical endpoints were assessed at 6 months, 1 year, and 2 years, and follow-up will continue to 5 years. Angiography, intravascular ultrasound, and derived morphology parameters (virtual histology, palpography, and echogenicity) were assessed at 6 months (within 14 days) and were repeated at 2 years (within 28 days). An OCT substudy was done in one of the centres (Thorax Center, Rotterdam, Netherlands). Non-invasive coronary angiography with multislice CT was done at 18 months. All major adverse cardiac events were adjudicated by an independent clinical events committee, and a data safety monitoring board monitored patient safety. All core laboratory analyses (QCA, vasomotion test, intravascular ultrasound gray-scale, virtual histology, palpography, echogenicity, multislice CT, and OCT) were analysed by an independent central research organisation (Cardialysis BV, Rotterdam, Netherlands).

Study device

The study device, the description of the polymers, and in-vitro and preclinical data have been described in detail.⁶ The stent is balloon expandable and consists of a backbone of PLLA coated with poly-D,L-lactide (PDLLA) that contains and controls the release of the antiproliferative drug, everolimus. Both PLLA and PDLLA are fully bioabsorbable. During bioabsorption, the long chains of PLLA and PDLLA are progressively shortened as ester bonds between lactide repeat units are hydrolysed, and small particles less than 2 µm in diameter are phagocytosed by macrophages. Ultimately, PLLA and PDLLA degrade to lactic acid, which is metabolised via the Krebs cycle.

Procedures

The BVS stent was implanted after mandatory predilatation. Four patients who received a non-BVS stent in addition to a study stent were excluded from the per-treatment-evaluable population but were included for the clinical endpoints. When additional stenting was necessary, the Cypher sirolimus-eluting stent (Cordis, Miami, FL, USA) was used since no animal or preclinical data for overlapping BVS stents were available at the time of patient enrolment. All patients were required to receive aspirin (>75 mg) daily for the study duration (5 years) and clopidogrel 75 mg daily for a minimum of 6 months.

The composite clinical endpoint was cardiac death, myocardial infarction, and ischaemia-driven target lesion

	PTE (n=26)	ITT (n=30)
Age (years)	62 (9)	62 (9)
Men	15 (58%)	18 (60%)
Present smokers	6 (23%)	6 (20%)
Diabetes	1 (4%)	1 (3%)
Hypertension requiring medication	16 (62%)	18 (60%)
Hyperlipidaemia requiring medication	16 (62%)	19 (63%)
Previous target vessel intervention	2 (8%)	3 (10%)
Previous myocardial infarction	1 (4%)	1 (3%)
Stable angina	18 (69%)	21 (70%)
Unstable angina	7 (27%)	8 (27%)
Silent ischaemia	1 (4%)	1 (3%)
Target vessel		
Left anterior descending	13 (50%)	15 (47%)
Left circumflex	6 (23%)	9 (30%)
Right coronary artery	7 (27%)	7 (23%)
AHA/ACC lesion classification (%)		
B1	65%	60%
B2	35%	40%
Mean reference vessel diameter (mm)	2.78 (0.47)	2.72 (0.47)
Minimum luminal diameter (mm)	1.10 (0.26)	1.06 (0.26)
Diameter stenosis (%)	59% (12)	60% (11)
Lesion length (mm)	8.66 (3.97)	9.15 (3.99)

Data are mean (SD) or number (%), unless otherwise indicated.
AHA/ACC=American Heart Association/American College of Cardiology.

Table 1 Baseline characteristics in the per-treatment-evaluable (PTE) population and intention-to-treat (ITT) population

revascularisation, according to the definitions from the Academic Research Consortium.⁹ For a diagnosis of non-Q-wave myocardial infarction, a rise of creatine kinase concentrations more than twice the upper limit of normal with raised creatine kinase isoenzyme MB was required.

In every patient, we analysed the stented segment and the peri-stent segments (defined by a length of 5 mm proximal and distal to the stent edge), as well as their combination (in-segment analysis), by quantitative coronary angiography (QCA) with the coronary angiographic analysis II system (Pie Medical Imaging, Maastricht, Netherlands).¹⁰ Small radiomarkers (37 µm) at the ends of the stents helped with the localisation of the non-radio-opaque stent for QCA. We computed the following QCA parameters: minimal luminal diameter, reference vessel diameter obtained by an interpolated method, and binary restenosis defined in every segment—stent and peri-stent segment—as diameter stenosis greater than 50% at follow-up. Late loss was defined as the difference between the minimal luminal diameter after the procedure and at follow-up.

To study vasomotion at 2 years, either the endothelium independent vasoconstrictor methylethylergometrine maleate (methergin, Novartis, Basel, Switzerland), or the endothelium dependent vasoactive agent acetylcholine (Ovisot, Daiichi-Sankyo, Tokyo, Japan) was given, dependent on local practice. We measured mean lumen diameters by QCA after baseline saline infusion and subsequent intracoronary administration of acetylcholine infused through a microcatheter at increasing dose up to 10⁻⁶ M.^{11,12} For methergine test, QCA was measured 5 min after intravenous bolus injection of methergin (0.4 mg).¹³ Both tests were terminated by intracoronary administration of 200 µg of nitroglycerin (nitronal, Pohl-Boskamp GmbH, Hohenlockstedt, Germany).

Stented vessel segments from after the procedure and from follow-up were examined with phased array intravascular ultrasound catheters (EagleEye; Volcano Corporation, Rancho Cordova, CA, USA) with automated pullback at 0.5 mm per s. We examined a region of interest beginning 5 mm distal to and extending 5 mm proximal to the stented segment. The vessel area, the stent area and lumen area, the intrastent neointimal area, and the lumen area stenosis were measured with a computer-based contour detection programme.^{14,15} The mean luminal diameter (mm) derived from intravascular ultrasound—so-called projected mean luminal diameter—was computed according to algorithms described previously.^{16,17} The percentage obstruction of the stent area was calculated as: (intrastent neointimal area/stent area)×100%. The percentage of lumen area stenosis was also calculated as [(mean lumen cross-sectional area [CSA] within stent–minimal lumen area within stent)/mean lumen CSA]×100%. Incomplete apposition was defined as one or more stent struts

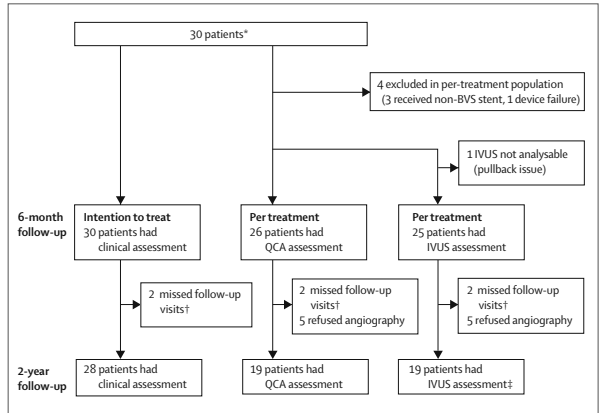


Figure 1: Flow-chart of patient follow-up

IVUS=intravascular ultrasound. QCA=quantitative coronary angiography. *Intention-to-treat population. †One patient withdrew consent and missed the visits at 9, 12, and 18 months, and at 2 years. One patient died from a non-cardiac cause 706 days after the procedure. ‡One patient with no 6-month IVUS data had a 2-year IVUS follow-up.

	6 months (n=30)	12 months (n=29)*	18 months (n=29)*	2 years (n=28)†
Cardiac death	0%	0%	0%	0%
MI	3.3% (1)‡	3.4% (1)‡	3.4% (1)‡	3.6% (1)‡
Q-wave MI	0%	0%	0%	0%
Non-Q-wave MI	3.3% (1)‡	3.4% (1)‡	3.4% (1)‡	3.6% (1)‡
Ischaemia-driven TLR	0%	0%	0%	0%
By PCI	0%	0%	0%	0%
By CABG	0%	0%	0%	0%
Ischaemia-driven MACE (cardiac death, MI, or ischaemia-driven TLR)	3.3% (1)‡	3.4% (1)‡	3.4% (1)‡	3.6% (1)‡
Stent thrombosis	0%	0%	0%	0%

Data are % (number of patients). MI=myocardial infarction. TLR=target lesion revascularisation. PCI=percutaneous intervention. CABG=coronary artery bypass graft. MACE=major adverse cardiac event. *One patient officially withdrew from the study, but his vital status and clinical follow-up are made available through his referring physician. †One patient died from a non-cardiac cause. ‡Same patient. This patient also underwent a target lesion revascularisation, not qualified as ischaemia-driven target lesion revascularisation (diameter stenosis=42%).

Table 2: Clinical outcomes at 2 years

separated from the vessel wall, whereas acquired late incomplete apposition was defined as incomplete apposition of one or more stent struts at follow-up that was not present after the procedure.⁵

For plaque characterisation, and to assess echogenicity of polymeric struts after stenting, we used a computer-aided grey-scale value analysis programme.^{18–20} On the basis of the mean grey level (brightness) of the adventitia, plaque was classified as more (hyperechogenic) or less bright (hypoechoic) in relation to the adventitia. Upper tissue was defined as tissue that had a mean grey value higher than the mean adventitial intensity plus twice its standard deviation.^{18,19} Calcified

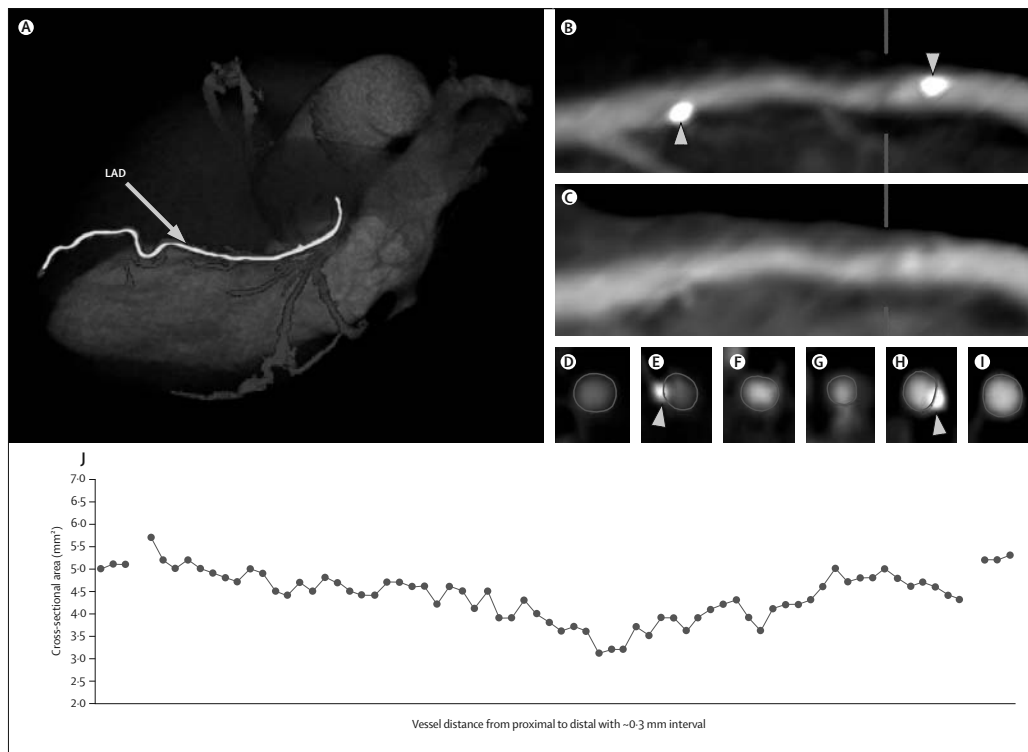


Figure 2: Results from multislice CT

After the coronary arteries are automatically segmented (blue), a centre-lumen line (yellow) can be constructed (A) in the left anterior descending coronary artery (LAD), in which a BVS stent (arrow) has been implanted. The thin-slab maximum intensity projection image (B) of the LAD in longitudinal cross-section shows the platinum indicators (arrowheads) at the proximal and distal ends of the stent, which are not in plane of the corresponding multiplanar reconstruction (C). The vessel lumen area is measured semi-automatically on the cross-sectional images, with examples proximal to the stent (D), at the level of the proximal indicator (E), within the stented segment (F, G), the distal indicator (H), and the distal reference (I). A graph (J) shows the area measurements, with interruptions to indicate the stent borders.

plaque and stent struts were in this upper tissue range, and for the purpose of the present analysis were combined with hyperechogenic tissue. We calculated the percentage of hypoechogenic plaque for the entire region of interest, excluding upper tissue.

Backscattering of radiofrequency signals provides information about tissue composition of the vessel wall (intravascular ultrasound–virtual histology; Volcano Corporation, Rancho Cordova, CA, USA).^{21–24} Typically, necrotic core, dense calcium, fibro-fatty tissue, and fibrous tissue are represented as red, white, yellow-green, and green areas, respectively, on ultrasonic cross-sections and are expressed as percentages (with each area totalling 100%). On each cross-section, polymeric stent struts were detected as areas of apparent dense calcium surrounded by necrotic

core due to the strong backscattering properties of the polymer. We used the change in quantitative analyses of these areas between implantation and follow-up as a surrogate assessment of the polymer bioabsorption process.

Palpography based on intravascular ultrasound assesses deformability of the vessel wall. The underlying principle is that softer tissue is more readily deformed than is harder or scaffolded tissue when force (eg, pulsatile arterial pressure) is applied.^{25–28} The rationale of this analysis for the study was to detect some subtle changes in strain resulting from scaffolding and late bioabsorption of the stent. The deformability of vessel wall was quantified with the analysis of back-scattering radiofrequency signals at different diastolic pressure levels. This method allowed the construction of a

ABSORB 2-year outcomes and results from imaging methods

colour-coded strain image in which harder (low strain in blue) and softer (high strain in yellow) regions of the coronary arteries could be identified, with radial strain

values ranging between 0% and 2%.²⁶

Multislice CT imaging was done 18 months after the index procedure. Single or dual-source, 64-slice spiral CT

	After procedure	6 months	2 years	Difference after procedure vs 6 months (95% CI)	Difference 6 months vs 2 years (95% CI)	Difference after procedure vs 2 years (95% CI)	p value after procedure vs 6 months	p value 6 months vs 2 years	p value after procedure vs 2 years
QCA (unpaired)									
n	26	26	19
In-stent RVD (mm)	2.79 (0.41)	2.64 (0.44)	2.43 (0.33)	-0.15 (-0.25 to -0.05)	-0.12 (-0.21 to -0.03)	-0.29 (-0.40 to -0.19)	0.0094	0.0058	<0.0001
In-stent MLD (mm)	2.32 (0.31)	1.89 (0.31)	1.76 (0.35)	-0.43 (-0.58 to -0.28)	-0.08 (-0.19 to 0.04)	-0.48 (-0.61 to -0.35)	<0.0001	0.23	<0.0001
In-stent DS (%)	16% (6)	27% (14)	27% (11)	10.51% (5.11 to 15.92)	0.58% (-3.57 to 4.72)	10.10% (4.58 to 15.62)	0.0002	0.81	0.0021
In-stent late loss (mm)	..	0.43 (0.37)	0.48 (0.28)	..	0.08 (-0.04 to 0.19)	0.233	..
Proximal late loss (mm)	..	0.23 (0.31)	0.34 (0.33)	..	0.11 (-0.01 to 0.23)	0.0553	..
Distal late loss (mm)	..	0.23 (0.27)	0.36 (0.37)	..	0.16 (0.04 to 0.29)	0.0091	..
In-stent absolute minimal luminal area ED (mm ²)	4.81 (1.75)	3.22 (1.93)	2.68 (1.21)	-1.59 (-2.67 to -0.52)	-0.02 (-0.45 to 0.41)	-1.89 (-2.65 to -1.12)	0.0002	0.93	<0.0001
In-stent minimal luminal cross sectional area VD (mm ²)	5.53 (2.11)	3.86 (2.26)	3.18 (1.55)	-1.67 (-2.92 to -0.42)	-0.15 (-0.79 to 0.49)	-2.04 (-2.96 to -1.11)	<0.0001	0.73	<0.0001
In-segment late loss (mm)	..	0.35 (0.32)	0.37 (0.27)	..	0.07 (-0.06 to 0.20)	0.42	..
In-stent binary restenosis (%)	..	7.7% (2/26)	0 (0/19)	..	-5.3% (-25.2 to 13.8)	1	..
In-segment binary restenosis (%)	..	7.7% (2/26)	0 (0/19)	..	-5.3% (-25.2 to 13.8)	1	..
MSCT*									
n	24
Mean luminal area (mm ²)	5.2 (1.3)
Minimal luminal area (mm ²)	3.6 (0.9)
Reference area (mm ²)	5.5 (1.0)
Mean area stenosis (%)	34% (15)
Minimal diameter (mm)	2.12 (0.26)
Mean diameter stenosis (%)	19% (9)
Grey-scale IVUS (unpaired)									
n	25	25	19
Vessel (EEM) area (mm ²)	13.49 (3.74)†	13.79 (3.84)	12.75 (3.43)	-0.06 (-0.49 to 0.37)	-0.19 (-0.98 to 0.59)	-0.21 (-1.21 to 0.78)	0.98	0.24	0.68
Vessel volume (mm ³)	173.17(52.04)†	187.65 (72.75)	178.21 (64.63)†	12.29 (-4.11 to 28.69)	1.01 (-27.27 to 29.30)	4.36 (-22.03 to 30.76)	0.21	0.86	0.71
Average lumen area (mm ²)	6.04 (1.12)	5.19 (1.33)	5.47 (2.11)	-1.01 (-1.30 to -0.71)	0.68 (0.04 to 1.32)	-0.40 (-1.18 to 0.38)	<0.0001	0.0174	0.12
Lumen volume (mm ³)	78.23 (22.98)	70.66 (26.88)	77.60(35.98)†	-9.20 (-16.84 to -1.56)	12.42 (-1.19 to 26.03)	-1.33 (-16.29 to 13.62)	0.0032	0.0443	0.97
Plaque area (mm ²)	7.44 (2.83)†	8.60 (2.85)	7.10 (2.02)	0.93 (0.45 to 1.40)	-1.06 (-1.48 to -0.64)	0.01 (-0.71 to 0.72)	<0.0001	0.0001	0.80
Plaque volume (mm ³)	94.56(35.43)†	116.99 (48.96)	98.75 (36.47)†	21.11 (9.51 to 32.72)	-13.38 (-30.22 to 3.47)	4.09 (-11.81 to 20.00)	<0.0001	0.0063	0.71
Minimal lumen area (mm ²)	5.09 (1.02)	3.92 (0.98)	4.34 (1.74)	-1.26 (-1.55 to -0.96)	0.76 (0.22 to 1.31)	-0.59 (-1.26 to 0.08)	<0.0001	0.0026	0.0323
Lumen area stenosis (%)	15.83%(7.64)	23.62%(10.25)	20.38%(6.92)	7.28% (3.54 to 11.02)	-4.12% (-8.30 to 0.07)	4.07% (-1.30 to 9.44)	0.0009	0.0569	0.0799
Projected MLD (mm)	2.28 (0.26)	2.04 (0.26)	2.17 (0.43)	-0.26 (-0.35 to -0.18)	0.19 (0.06 to 0.33)	-0.07 (-0.26 to 0.11)	<0.0001	0.0052	0.23

(Continues on next page)

	After procedure	6 months	2 years	Difference after procedure vs 6 months (95% CI)	Difference 6 months vs 2 years (95% CI)	Difference after procedure vs 2 years (95% CI)	p value after procedure vs 6 months	p value 6 months vs 2 years	p value after procedure vs 2 years
(Continued from previous page)									
IVUS virtual histology (unpaired)§									
n	25	25	18
Dense calcium (%)	29.82% (15.57)	20.65% (11.50)	26.42% (15.76)	-8.93% (-13.64 to -4.22)	2.81% (-4.08 to 9.70)	-5.87% (-13.84 to 2.11)	0.0003	0.64	0.21
Dense calcium area (mm ²)	1.02 (0.58)	0.94 (0.64)	0.81 (0.67)	-0.11 (-0.36 to 0.15)	-0.11 (-0.40 to 0.17)	-0.16 (-0.45 to 0.13)	0.5046	0.31	0.21
Fibro-fatty tissue (%)	4.31% (3.35)	7.19% (6.17)	5.47% (5.22)	2.94% (0.40 to 5.48)	-0.41% (-3.50 to 2.67)	1.72% (-0.09 to 3.53)	0.0142	0.85	0.21
Fibro-fatty area (mm ²)	0.21 (0.22)	0.40 (0.43)	0.19 (0.24)	0.19 (0.02 to 0.35)	-0.12 (-0.27 to 0.04)	0.01 (-0.05 to 0.07)	0.0096	0.0267	0.80
Fibrous (%)	38.83% (13.41)	50.54% (12.69)	43.66% (14.69)	11.79% (6.84 to 16.74)	-3.38% (-10.59 to 3.82)	6.75% (-0.68 to 14.17)	<0.0001	0.35	0.20
Fibrous area (mm ²)	1.72 (1.22)	2.62 (1.44)	1.35 (0.92)	0.80 (0.51 to 1.10)	-0.92 (-1.25 to -0.58)	-0.25 (-0.61 to 0.10)	<0.0001	<0.0001	0.25
Necrotic core (%)	27.04% (7.00)	21.62% (8.70)	24.45% (6.84)	-5.79% (-9.45 to -2.13)	0.99% (-2.48 to 4.46)	-2.60% (-5.83 to 0.63)	0.0028	0.64	0.30
Necrotic core area (mm ²)	1.17 (0.82)	1.13 (0.87)	0.79 (0.51)	-0.13 (-0.38 to 0.11)	-0.26 (-0.53 to -0.00)	-0.28 (-0.50 to -0.05)	0.342	0.1089	0.0268
Palpography (unpaired)									
n	24	23	17
Strain values	0.16 (0.10)	0.28 (0.12)	0.31 (0.17)	0.12 (0.06 to 0.17)	0.02 (-0.05 to 0.08)	0.13 (0.06 to 0.21)	0.0002	0.81	0.0052
Echogenicity (ITT)									
n	27	26	21
Hyperechogenicity (%)	18.5% (9.1)	10.3% (7.6)	7.7% (6.5)	-8.15% (-11.00 to -5.31)	-3.75% (-6.20 to -1.29)	-12.81% (-16.19 to -9.44)	<0.0001	0.001	<0.0001
Optical CT (serial)									
n	7	7	7
Discernible struts	403	368	264
Mean lumen area (mm ²)	6.53 (0.91)	4.72 (1.13)	5.80 (2.93)	-1.81 (-3.39 to -0.23)	1.08 (-0.93 to 3.08)	-0.74 (-3.42 to 1.94)	0.0313	0.22	0.38
Minimal lumen area (mm ²)	4.50 (1.03)	2.65 (1.49)	3.80 (2.42)	-1.84 (-3.48 to -0.21)	1.15 (-0.14 to 2.43)	-0.7 (-2.62 to 1.22)	0.0156	0.0781	0.47
Mean lumen diameter (mm)	2.87 (0.21)	2.41 (0.31)	2.63 (0.61)	-0.46 (-0.87 to -0.05)	0.23 (-0.17 to 0.62)	-0.23 (-0.79 to 0.33)	0.0313	0.22	0.30

Data are mean (SD) or % (n/N), unless otherwise indicated. QCA=quantitative coronary angiography, RVD=reference vessel diameter, MLD=minimal lumen diameter, DS=diameter stenosis, ED=edge detection, VD=videodensitometry, MSCT=multislice CT, IVUS=intravascular ultrasound, EEM=external elastic membrane, ITT=intention to treat. *MSCT data were acquired at 18 months after the procedure. †24 measurements for that parameter. ‡The length of the pullback could not be assessed. §In a series of patients in whom virtual histology and palpography were done before and after stenting, the percentage of dense calcium was 9.83% (SD 9.64) before stenting and 25.42% (11.27) after stenting (n=13, p=0.0002), whereas the strain values were 0.5 (0.27) before and 0.20 (0.10) after stenting (n=12, p=0.0034).

Table 3: Results from imaging methods immediately after the procedure, at 6 months, and at 2 years

with intravenous contrast enhancement and electrocardiograph-gated image reconstruction was done (Siemens Definition, Forchheim, Germany [n=18]; GE Lightspeed, Milwaukee, USA [n=5]; Philips Brilliance, Best, Netherlands [n=2]).²⁹ After transfer of the MSCT data to the core laboratory, we measured the amount of in-stent stenosis using a semi-automated software programme for vessel segmentation and lumen area quantification (Circulation, Siemens, Forchheim, Germany). The BVS stent is radiolucent and therefore undetected by multislice CT, apart from the platinum markers at each end of the stent. Along the automatically constructed centre-lumen line, the cross-sectional lumen

area was measured at 0.3 mm longitudinal intervals within the stented segment. We calculated the lumen diameter from the measured area, assuming a circular shape of the lumen area. Severity of in-stent diameter stenosis or area stenosis was calculated as a ratio of the smallest in-stent lumen diameter or area and the reference vessel diameter or area, which was calculated by interpolation of the proximal and distal lumen reference. Additionally, we measured the length of vessel between the platinum stent markers.

OCT was done in the subset of patients who enrolled at the Thorax Center, Rotterdam, Netherlands, with the commercially available OCT system (ImageWire, LightLab

Imaging, Westford, MA, USA). This technique, using an infrared light source, has a resolution of 15 microns (ten-times higher than intravascular ultrasound) that facilitates imaging of intracoronary structures in great detail.³⁰ The imaging method and its quantitative and qualitative analysis has been described.⁶ Stent struts apposition was classified as apposed (embedded), aligned (protruding), or incompletely apposed (incomplete stent apposition).³¹ We assessed persistent, late acquired, and resolved incomplete stent apposition at follow-up. Changes in strut appearance at follow-up were categorised as previously published:⁶ preserved box, open box, dissolved bright box, and dissolved black box. OCT appearance was assessed by side-by-side comparison of OCT cross-sectional images that were acquired after the procedure, at 6 months, and at 2 years.

Statistical analysis

This study was a feasibility trial that was designed to provide preliminary observations and generate hypotheses for future studies. The sample size was not defined on the basis of an endpoint hypothesis, but rather to provide some information about device feasibility and safety. The sample size requirement was established by assessment of the minimum number of patients needed to provide reliable and non-trivial results. For binary variables, we calculated percentages. For continuous variables, mean and standard deviation are presented. Paired comparisons between the different timepoints were done by a Wilcoxon’s signed rank test for continuous variables and by exact McNemar test for binary restenosis. Differences and confidence intervals are also based on paired data. Since no formal hypothesis testing was planned, no statistical adjustment was applied. Three sets of comparisons were available: unpaired comparison of all available observations; paired comparison of truly serial observations; and last observation carried forward (when 6-month result was not available, we imputed the value from after the procedure; when 2-year result was not available, we imputed 6-month result, if available, or value from after the procedure, if 6-month data not available). Since no inconsistencies between these three types of observations could be ascertained, we selected the most complete set of actual observations without imputations. Taking into account the large number of parameters with multiple comparisons, p values presented in this paper are exploratory only and should therefore be interpreted with caution. Unless otherwise noted, the analysis was based on the per-treatment population for the imaging parameters and on the intention-to-treat population for the clinical endpoints.

This study is registered with ClinicalTrials.gov, number NCT00300131.

Role of funding source

The sponsor was involved in the design and conduct of the study; the collection, management, initial analysis,

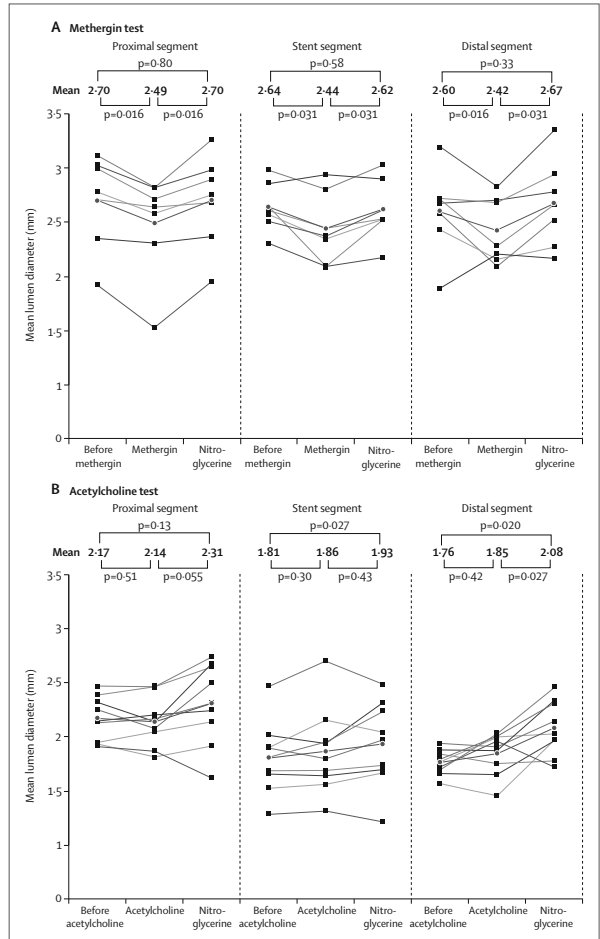


Figure 3: Results of methergin (A) and acetylcholine (B) testing in proximal, stented, and distal segments. Red circular dots represent means of measurements at each phase.

and interpretation of the data; and had the right to a non-binding review of the report. Full monitoring ensured accuracy of data collection. The two senior authors (PWS and JAO) had full access to all the data and had final responsibility for the decision to submit for publication.

Results

Table 1 shows the patient demographics, and figure 1 the trial profile. Clinical follow-up data were obtained from 29 of 30 enrolled patients. Although one patient

withdrew from the study, his vital and clinical status remained available from his referring physicians. One patient died from non-cardiac cause at 706 days after the procedure. On day 699, the patient was admitted to hospital because of a haemoglobin drop due to bleeding of the upper gastrointestinal tract. On day 703, the patient had a duodenal perforation, leading to non-cardiac death on day 706. This patient had stopped clopidogrel 364 days after the procedure and was not taking aspirin. The mean duration of follow-up was 740.9 days (range 707–800).

Table 2 shows clinical outcomes at 2 years. Up to 2 years, there was only one non-Q-wave myocardial infarction (peak troponin 2.21 µg/L) related to the treatment of a non-flow-limiting stenosis (QCA diameter stenosis 42%) of a BVS implanted 46 days earlier, in a patient who had one episode of angina at rest without electrographic evidence of ischaemia. For a perceived

safety reason, the polymeric stent was covered by a drug-eluting metallic stent. We recorded no new major adverse cardiac events between 6 months and 2 years. No instances of stent thrombosis arose according to the protocol or definitions from the Academic Research Consortium.⁹ The protocol mandated a minimum of 6 months duration of combined antiplatelet therapy, but the actual duration was left to the discretion of the investigator who generally followed the new guidelines of the European Society of Cardiology, American College of Cardiology, and the American Heart Association.^{22,23} 15 patients were receiving dual antiplatelet therapy at 1 year, and only one patient was at 2 years.

After exclusion of five patients (three refusals, one contrast allergy, one revascularisation), multislice CT scanning was done at 18 months in 25 patients from the intention-to-treat population. One multislice CT angiogram was not interpretable because of severe

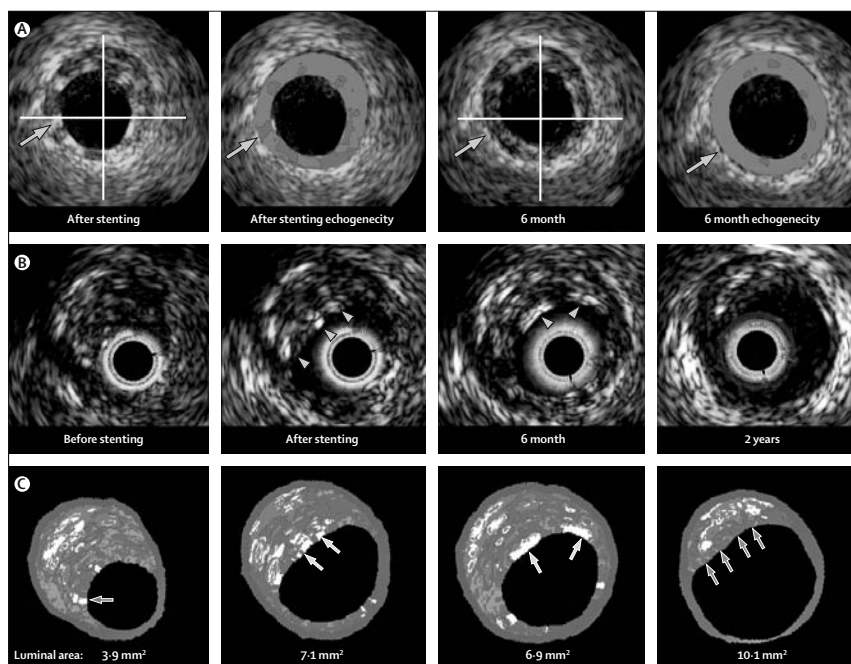


Figure 4: Results from echogenicity, grey-scale intravascular ultrasound, and intravascular ultrasound virtual histology
 (A) Grey-scale appearance after stenting and at 6 months with echogenicity analysis (red: hypoechoogenic tissue, green: hyperechoogenic tissue). The arrows show a strut of the implanted stent. (B) Examples of grey-scale intravascular ultrasound before stenting, after stenting, at 6 months, and at 2 years. The arrowheads show struts that remain visible at each follow-up time. (C) Serial assessment by intravascular ultrasound radiofrequency backscattering. Before stenting, there is a large plaque with a necrotic core. The red arrow indicates the necrotic core in contact with the lumen. After stenting, the lumen has enlarged to 7.1 mm² and two struts (yellow arrows) are depicted as (pseudo) dense calcium. At 6 months, the two struts remained visible (yellow arrows) with partial reduction of the luminal area. At 2 years, the endoluminal pseudo-dense calcium depicting struts has disappeared, which is consistent with strut absorption. There is now a fibrous cap covering the necrotic core (green arrows), and late enlargement of the lumen (10.1 mm²) and shrinkage of the plaque.

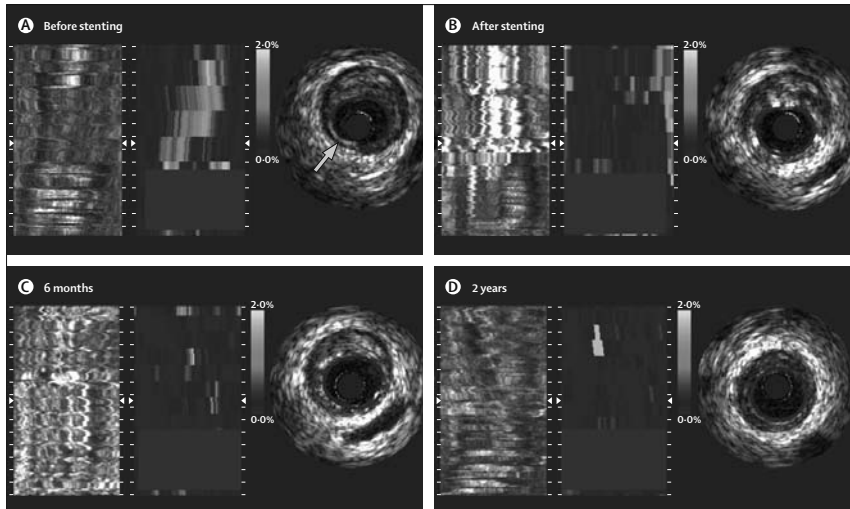


Figure 5: Sequential changes in strain assessed by intravascular ultrasound palpography

(A) Before stenting, a long area of high strain (colour-coded for strain ranging from 1% to 2%) is seen; on a single cross-section, the high strain region is located at the shoulder (arrow) of the plaque. (B) Abolition of this high strain spot after stenting. (C) and (D) show continued absence of high strain at 6 months and 2 years after stenting.

motion artifacts. All stents were qualitatively patent. Mean luminal area was 5.2 mm² (SD 1.3), minimal lumen area was 3.6 mm² (0.9), and mean area stenosis was 34% (15) (figure 2). The calculated mean diameter stenosis was 19% (SD 9, range 1–33).

Tables 1 and 3 show QCA results from baseline, after the procedure, 6 months, and 2 years. In-stent angiographic late loss was 0.48 mm (SD 0.28) at 2 years. We noted binary restenosis at 6 months in three patients. Repeat revascularisation was not done at 6 months because of lack of symptoms and objective signs of ischaemia. At 2 years, two of the three lesions had regressed to less than 50% stenosis. The third patient refused angiography. The reference diameter decreased significantly from after the procedure to 6-month and 2-year follow-up, with an average loss of about 0.3 mm (table 3). Between 6 months and 2 years, we recorded no significant differences in in-stent minimal lumen diameter, percentage of diameter stenosis, and in-stent late loss (table 3). Therefore, the significant decrease in minimal lumen diameter, reference vessel diameter, and luminal area already recorded at 6 months, remained significant at 2 years. Distal segment late loss increased significantly at 6 months and 2 years (table 3).

In the methergin group (n=7), we noted significant vasoconstriction in proximal and stented segments (figure 3). After nitroglycerin, the three segments (proximal, stented, and distal) dilated significantly with

their diameters returning to their baseline values (figure 3). In the acetylcholine group (n=9), five patients had vasodilation of at least 3% in mean luminal diameter. Nitrates induced a significant vasodilatation in the stented and distal segments (figure 3). These results show the restoration of vasomotor function in the stented segment.

Grey-scale intravascular ultrasound showed the significant increase in minimal luminal area and average luminal area and volume, together with a significant decrease in plaque area and volume between 6 months and 2 years (table 3, figure 4). With the exception of the minimal luminal area, findings for vessel area, average luminal area, plaque area, and lumen area stenosis at 2 years did not differ significantly from the measurement taken immediately after the procedure (table 3). The vessel area and volume remained constant between the follow-ups, showing the absence of significant remodelling.

We detected a significant reduction in percentage of hyperechogenic tissue between after the procedure and at 6 months, and between 6 months and 2 years, in the intention-to-treat population (table 3, figure 4). The residual level of hyperechogenicity at 2 years was similar to the natural hyperechogenicity of plaques (7.7% [SD 6.5] vs 5.6% [4.8], n=12) that was measured in one investigating centre (Thorax Center, Rotterdam, Netherlands). Importantly, persistent and late acquired incomplete apposition detected at 6 months and previously

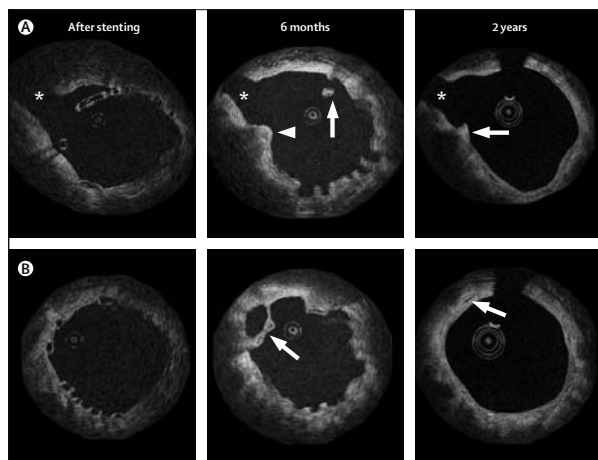


Figure 6: Serial assessment of stent struts by optical coherence tomography
 (A) After stenting, incomplete apposition of struts (preserved box) in front of a side-branch ostium. At 6 months, persistent incomplete stent apposition (arrow) and resolved incomplete stent apposition (arrowhead), with open box appearance. At 2 years, there is now smooth appearance of the endoluminal lining without strut malapposition since struts have been absorbed. There is guidewire shadowing (at the top of the image), and a strut is still just discernible as a bright spot (arrow). (B) Complete apposition of strut (box appearance) after the procedure. At 6 months, there is late acquired incomplete stent apposition of the struts (preserved box appearance) with tissue bridging connecting the struts (arrow). The endoluminal lining is corrugated. At 2 years, smooth endothelial lining with almost circular cross section. Generally, the struts are no longer discernible, although there is a bright reflection that could indicate a strut (arrow). Asterisk indicates a side branch.

reported,⁶ were no longer detectable at 2-year follow-up.

The intravascular ultrasound–virtual histology assessments showed that the percentage of each plaque component did not differ significantly between 6 months and 2 years (table 3, figure 4). The absolute fibro-fatty area and fibrous-plaque area decreased significantly between 6 months and 2 years (table 3). When compared with measurements taken immediately after the procedure, none of the 2-year parameters differed significantly, apart from necrotic core area (table 3).

In palpography assessments, the cumulative strain value increased significantly from after the procedure to 6-month follow-up, with no subsequent changes between 6 months and 2 years (table 3, figure 5).

Seven patients had serial data for OCT immediately after the procedure, at 6 months, and at 2 years (intention-to-treat population). The number of apparent struts decreased from 403 at baseline to 368 at 6-month follow-up and to 264 at 2 years (34.5% reduction over 2 years; figure 6). For preserved box, appearance of stent strut changed from $n=0$ at 6 months to $n=9$ at 2 years, for open box from $n=143$ to $n=68$, for dissolved bright box from $n=225$ to $n=185$, and for dissolved black box from $n=56$ to $n=25$. All apparent struts were well covered and apposed to the vessel wall. All incomplete appositions (incomplete, persistent, and late acquired incomplete

stent apposition) were resolved. The lumen shape was regular with smooth, well delineated borders in all cases, and we recorded no intraluminal tissue. The coronary vessel wall showed a homogenous, bright backscattering appearance, with no signs of tissue optical heterogeneity. Importantly, minimal and mean luminal area decreased significantly between immediately after the procedure and 6 months, but enlarged between 6 months and 2 years (table 3).

Discussion

In this prospective, single-group, open-label study, the BVS stent showed excellent clinical safety with only one major adverse cardiac event (a non-Q-wave myocardial infarction) by 2 years. The multi-imaging approach has shown several important findings. Echogenicity, virtual histology, and OCT indicate that by 2 years, this biodegradable stent was incorporated into the vessel wall and bioabsorbed. Reduction in molecular weight and mass had occurred to such an extent that struts were no longer recognisable by intravascular ultrasound, leaving behind few visible features; thus a third of stents were no longer discernible by OCT. Importantly, OCT showed an optically homogeneous vessel wall structure that, taken together with the documented restoration of vasomotion, suggests healing of the artery.

We used multislice CT to assess the midterm results at 18 months. Patency and absence of binary restenosis was established non-invasively, and subsequently confirmed by conventional angiography. In a subset of patients previously reported and investigated after the procedure, the quantitative results of two-dimensional and three-dimensional QCA conventional angiography, three-dimensional intravascular ultrasound, and multislice CT angiography were positively correlated from immediately after the procedure to 6 months, although the two-dimensional QCA tended to be smaller than the three-dimensional-based quantitative methods.³⁴ The feasibility and accuracy of the use of multislice CT in analysis of radiolucent biodegradable stents in a multicentre study could indicate a new era for non-invasive assessment of patients treated with radiolucent stents.^{35,36}

Despite the discontinuation of thienopyridine drugs, no stent thrombosis occurred, and no additional clinical restenosis was evident by 2 years. Two lesions initially categorised as binary restenosis at 6 months regressed below the threshold of 50% diameter stenosis. On average, the diameter stenosis of 27% measured at 6 months remained unchanged at 2 years. However, QCA showed that the vessel size significantly decreased between 6 months and 2 years, and the minimal lumen diameter tended to decrease so that the intrastent late loss tended to rise. The late loss in the 5 mm distal to the stent increased significantly. When truly serial observations were used ($n=19$), we recorded similar results.

These angiographic results are consistent with the

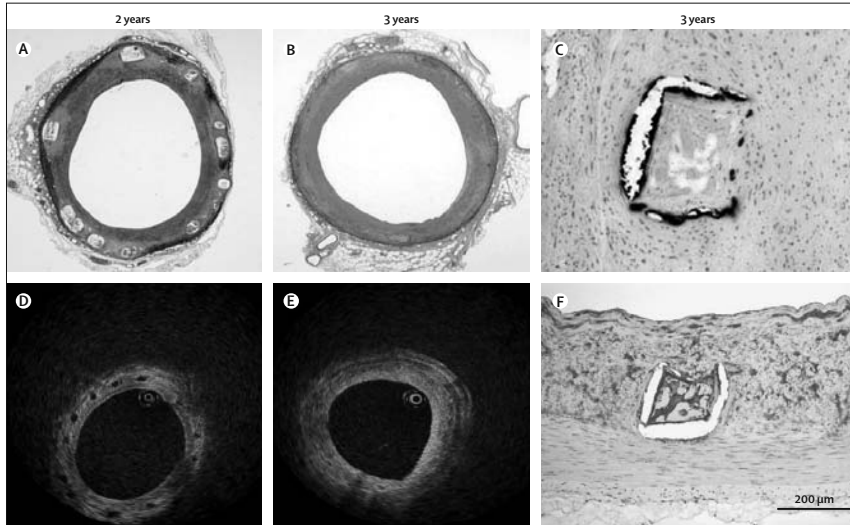


Figure 7: Preclinical porcine studies at 2 years and 3 years after stent implantation

(A) and (B) represent 2 year and 3 year porcine histology with haematoxylin-eosin staining, showing disappearance of the void previously occupied by a polymeric strut. The box-like spaces were visible on OCT (D) and are still visible at 2 years but almost indiscernible at 3 years (E). Detailed histology (C and F) shows the apparent voids previously occupied by the polymeric struts have been preserved, but filled in by proteoglycan material. In the Von Kossa stain (C), mineralisation is seen around the previous site of a strut. In the Alcian blue stain (F), proteoglycan has replaced the BVS stent strut.

findings of intracoronary imaging from after the procedure to 6 months, but differ from observations from the three-dimensional-based methods at later follow-up. The average luminal area and minimal luminal area measured by intravascular ultrasound and OCT increased significantly between 6 months and 2 years, which contrasts with the non-significant decrease in angiographic luminal dimensions during that period. Several explanations for the discordant late luminal changes between angiography and intracoronary imaging have been considered. First, at the 2-year follow-up, QCA follows immediately after the vasomotion test is terminated by an intracoronary injection of nitrate. Kurnik and colleagues³⁷ have described the prolonged vasoconstrictor effect of ergonovine maleate. Furthermore, the two intracoronary imaging assessments with intravascular ultrasound and OCT were both preceded by additional injections of nitroglycerin, which could have resulted in improved vasodilation and could explain discrepancy between measurements. The TAXUS II study also showed a discrepancy between results from angiography and intravascular ultrasound at 2 years. In this study, serial changes measured in the TAXUS group showed late lumen enlargement on angiography between 6 months and 2 years but lumen loss on intravascular ultrasound.³⁶ This discrepancy was mainly attributed to the difference between the focal measurement (minimal

lumen diameter and loss) of angiography and the continuous measurement of three-dimensional intravascular ultrasound.

Another possible explanation for the angiographic and intracoronary imaging discrepancy is a possible long-term change in lumen occurring between 6 months and 2 years, especially in view of the finding from OCT that the corrugated endoluminal lining at 6 months evolved into an almost circular appearance at 2 years. Differences in systematic measurement between angiography and intravascular ultrasound might also explain the discordant changes in late lumen. Dimensions measured by QCA are repeatedly smaller than measurements from intravascular ultrasound or OCT,^{33,34} and substantial overestimation of lumen area by intravascular ultrasound has been reported,³⁸ especially in vessels of small diameter. When projected minimal lumen diameter³⁹ derived from intravascular ultrasound assessment is compared with that from QCA, we note that the intravascular ultrasound measurement underestimates the larger lumen and overestimates the smaller lumen. Accordingly, this method can underestimate late loss when compared with QCA or conversely, QCA can overestimate late loss compared with intravascular ultrasound.³⁹ Finally, the discrepancy between two-dimensional QCA and three-dimensional intravascular ultrasound or OCT could also be the result of the small

patient population.

The reappearance of vasomotion of the stented and persistent segments in response to methergin or acetylcholine suggests that vessel vasoreactivity has been restored and that a physiological response to vasoactive stimulus might occur anew. Unlike previous studies reporting endothelial dysfunction in the distal segment, our primary intention was to report vasomotor tone in the stented segment, once the scaffolding properties of the stent had disappeared as a result of its bioabsorption. Importantly, five of nine patients tested with acetylcholine showed vasodilatation (at least 3% of the mean diameter⁴¹) during the highest dose infused, suggesting direct vasodilator or flow-mediated response to acetylcholine and thus the presence of functionally active endothelium at the site of the stent implantation. However, this finding is a seminal observation that clearly needs to be confirmed.

As previously reported in a subset of 12 patients studied in one investigating centre, mean cumulative strain value measured before and after stenting decreased significantly, indicating a reduction in vessel wall deformability due to the scaffolding properties of the stent.²⁸ The vessel wall deformability reappears to some extent in the initial 6 months and remained stable.

The significant decrease in plaque area recorded between 6 months and 2 years without concomitant change in vessel area also needs to be confirmed. The plaque shrinkage documented by intracoronary techniques could be real, since implantation of metallic everolimus-eluting stents in an atherosclerotic rabbit model resulted in a reduction of macrophage in a process involving autophagy.⁴² However, the absorption of the polymeric material and the resulting mass loss could partly contribute to the plaque reduction. Preclinical porcine studies 3 years after stent implantation show that although struts disappear by 2 years, the spaces they occupied become filled with proteoglycan material (figure 7). The changes in tissue composition occurring during the first 6 months, with a decrease in percentage of dense calcium and percentage of necrotic core⁹ and an increase in fibro-fatty and fibrous tissue in relative percentages and absolute values, was previously interpreted as a reduction of radiofrequency backscattering from the polymeric struts. The modest decrease in the necrotic core between 6 months and 2 years has to be interpreted with caution. In a cohort of 12 patients enrolled at one site (Thorax Center), we compared the necrotic core before stenting, after stenting, at 6 months, and at 24 months. From before to after stenting, we noted an increase in the necrotic core due to the implantation of the polymeric struts detected and misclassified by radiofrequency analysis as dense-calcium surrounded with necrotic core (figure 4).²⁸ In that cohort, we noted that the amount of necrotic core at 2 years was similar to the amount before stenting, suggesting that the appearance

and disappearance of polymeric struts is mainly responsible for the pseudo-regression of the necrotic core between 6 months and 24 months (data not reported).

In the future, the potential advantages of drug-eluting bioabsorbable stents will be assessed with a second iteration of the device. The first-generation device, for which stent shrinkage was seen at 6 months, might not have retained its mechanical integrity and radial strength long enough to resist fully the negative vessel wall remodelling forces generated by percutaneous coronary intervention.⁴¹ The polymer used in the next generation device is processed differently so that its integrity and radial strength are retained for a longer time. The design of the next generation device is zigzag hoops linked by straight bridges, which is similar to the design of the original MultiLink stent (Abbott Vascular, Santa Clara, CA, USA). This design will provide added uniform vessel support and drug application. These features are expected to reduce the stent shrinkage that at 6 months contributed to late loss and restenosis. These potential improvements will be tested when the stent is implanted in challenging lesion subsets.

Our study had some limitations. It included small numbers of patients (n=30) with very few truly serial observations. In view of the large number of parameters with several comparisons, some of the findings are merely hypothesis generating and should therefore be interpreted cautiously. Additionally, the investigation uses novel imaging methods that have not been specifically validated for the assessment of polymeric struts *in vitro* and *ex vivo*. Animal studies (figure 7E) suggest that features visible by OCT will completely disappear once the homogeneity of the vessel wall is achieved and cells repopulate strut sites. At 2 years, animal studies show that the polymer has been absorbed and replaced by proteoglycan of roughly the same dimensions, with a discernible translucent appearance by OCT. Occasional mineralisation at absorbed strut edges is also present, and could paradoxically be discernible by this technique. That some apparent strut signals persist on OCT at 2 years in our patients suggest that tissue homogeneity is not completely restored.

In conclusion, many of the salient observations made in the present study are therapeutically clinically relevant and highly favourable. We detected transient but long-term effective scaffolding of the vessel, device bioabsorption, complete strut apposition, potential late lumen enlargement associated with decrease of plaque burden, and restoration of vasomotion. Non-invasive sequential monitoring of the stent patency with multislice CT is feasible. The absence of a foreign body and the restoration of vasomotion raise the hope of a normal healed vessel that could be without the risk of late stent thrombosis. All these findings need to be confirmed in larger studies, but this or similar devices

could become of paramount importance for the restoration of vascular integrity in the treatment of flow-limiting plaque.

Contributors

PWS, JAO, and SV contributed to the conception and design of the study. ER, KN, NG, HMG-G, YO, CD, KMH, PWS, and JAO analysed and interpreted the data. PWS, JAO, and SV drafted the report, which was critically revised for important intellectual content by PWS, JAO, YO, KN, ER, NG, DD, IT, HMG-G, MWIW, and SV. PWS and JAO approved the report and obtained funding. SV provided administrative, technical, or logistical support. Data were acquired by PWS and ER (n=16 patients), DD (n=6), JAO and MWIW (n=5), and IT (n=3). *Clinical events committee*—C Hanet, Brussels, Belgium; D McClean, Christchurch, New Zealand; and V Umans, Alkmaar, Netherlands. *Data safety monitoring board*—J Tijssen, Amsterdam, Netherlands; T Lefevre, Massy, France; and P Urban, Geneva, Switzerland.

Conflict of interest statement

JAO and DD are members of the Abbott Vascular advisory board. SV, CD, and KM-H are employees of Abbott Vascular. All other authors declare that they have no conflict of interest.

Acknowledgments

This study was sponsored by Abbott Vascular (Santa Clara, CA, USA). We thank Wai-Fung Cheong, Krishnankutty Sudhir, and Robert McGreevy for their intellectual input in writing the report.

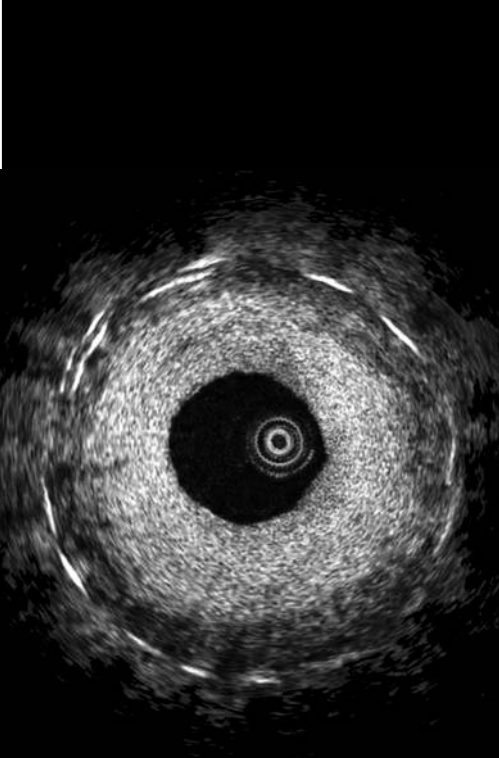
References

- 1 Kotani J, Awata M, Nanto S, et al. Incomplete neointimal coverage of sirolimus-eluting stents: angioscopic findings. *J Am Coll Cardiol* 2006; **47**: 2108–11.
- 2 Finn AV, Joner M, Nakazawa G, et al. Pathological correlates of late drug-eluting stent thrombosis: strut coverage as a marker of endothelialization. *Circulation* 2007; **115**: 2435–41.
- 3 Tamai H, Igaki K, Kyo E, et al. Initial and 6-month results of biodegradable poly-l-lactic acid coronary stents in humans. *Circulation* 2000; **102**: 399–404.
- 4 Tamai H. Biodegradable stents four year follow-up. Washington: Transcatheter Cardiovascular Therapeutics, 2004.
- 5 Erbel R, Di Mario C, Bartunek J, et al. Temporary scaffolding of coronary arteries with bioabsorbable magnesium stents: a prospective, non-randomised multicentre trial. *Lancet* 2007; **369**: 1869–75.
- 6 Ormiston JA, Serruys PW, Regar E, et al. A bioabsorbable everolimus-eluting coronary stent system for patients with single de-novo coronary artery lesions (ABSORB): a prospective open-label trial. *Lancet* 2008; **371**: 899–907.
- 7 Jang IK, Bouma BE, Kang DH, et al. Visualization of coronary atherosclerotic plaques in patients using optical coherence tomography: comparison with intravascular ultrasound. *J Am Coll Cardiol* 2002; **39**: 604–09.
- 8 Nissen SE, Gurley JC, Grines CL, et al. Intravascular ultrasound assessment of lumen size and wall morphology in normal subjects and patients with coronary artery disease. *Circulation* 1991; **84**: 1087–99.
- 9 Cutlip DE, Windecker S, Mehran R, et al. Clinical end points in coronary stent trials: a case for standardized definitions. *Circulation* 2007; **115**: 2344–51.
- 10 Foley DP, Escaned J, Strauss BH, et al. Quantitative coronary angiography (QCA) in interventional cardiology: clinical application of QCA measurements. *Prog Cardiovasc Dis* 1994; **36**: 363–84.
- 11 Hofma SH, van der Giessen WJ, van Dalen BM, et al. Indication of long-term endothelial dysfunction after sirolimus-eluting stent implantation. *Eur Heart J* 2006; **27**: 166–70.
- 12 Sabate M, Kay IP, van Der Giessen WJ, et al. Preserved endothelium-dependent vasodilation in coronary segments previously treated with balloon angioplasty and intracoronary irradiation. *Circulation* 1999; **100**: 1623–29.
- 13 Serruys PW, Lablanche JM, Reiber JH, Bertrand ME, Hugenholz PG. Contribution of dynamic vascular wall thickening to luminal narrowing during coronary arterial vasomotion. *Z Kardiol* 1983; **72** (suppl 3): 116–23.
- 14 Bruining N, von Birgelen C, de Feyter PJ, et al. ECG-gated versus nongated three-dimensional intracoronary ultrasound analysis:

implications for volumetric measurements. *Cathet Cardiovasc Diagn* 1998; **43**: 254–60.

- 15 von Birgelen C, de Vrey EA, Mintz GS, et al. ECG-gated three-dimensional intravascular ultrasound: feasibility and reproducibility of the automated analysis of coronary lumen and atherosclerotic plaque dimensions in humans. *Circulation* 1997; **96**: 2944–52.
- 16 Tsuchida K, Serruys PW, Bruining N, et al. Two-year serial coronary angiographic and intravascular ultrasound analysis of in-stent angiographic late lumen loss and ultrasonic neointimal volume from the TAXUS II trial. *Am J Cardiol* 2007; **99**: 607–15.
- 17 von Birgelen C, Kutryk MJ, Gil R, et al. Quantification of the minimal luminal cross-sectional area after coronary stenting by two- and three-dimensional intravascular ultrasound versus edge detection and videodensitometry. *Am J Cardiol* 1996; **78**: 520–25.
- 18 Aoki J, Abizaid AC, Serruys PW, et al. Evaluation of four-year coronary artery response after sirolimus-eluting stent implantation using serial quantitative intravascular ultrasound and computer-assisted grayscale value analysis for plaque composition in event-free patients. *J Am Coll Cardiol* 2005; **46**: 1670–76.
- 19 De Winter S, Heller I, Hamers R, et al. Computer assisted three-dimensional plaque characterization in intracoronary ultrasound studies. *Comp Cardiol* 2003; **30**: 73–76.
- 20 Bruining N, Verheye S, Knaapen M, et al. Three-dimensional and quantitative analysis of atherosclerotic plaque composition by automated differential echogenicity. *Catheter Cardiovasc Interv* 2007; **70**: 968–78.
- 21 Nair A, Kuban BD, Tuzcu EM, Schoenhagen P, Nissen SE, Vince DG. Coronary plaque classification with intravascular ultrasound radiofrequency data analysis. *Circulation* 2002; **106**: 2200–26.
- 22 Nair A, Kuban BD, Obuchowski N, Vince DG. Assessing spectral algorithms to predict atherosclerotic plaque composition with normalized and raw intravascular ultrasound data. *Ultrasound Med Biol* 2001; **27**: 1319–31.
- 23 Nair A, Pauliina Margolis M, Kuban BD, Vince DG. Automated coronary plaque characterisation with intravascular ultrasound backscatter: ex vivo validation. *EuroIntervention* 2007; **3**: 113–20.
- 24 Van Mieghem CA, McFadden EP, de Feyter PJ, et al. Noninvasive detection of subclinical coronary atherosclerosis coupled with assessment of changes in plaque characteristics using novel invasive imaging modalities: the Integrated Biomarker and Imaging Study (IBIS). *J Am Coll Cardiol* 2006; **47**: 1134–42.
- 25 Serruys PW, Garcia-Garcia HM, Buszman P, et al. Effects of the direct lipoprotein-associated phospholipase A2 inhibitor darapladib on human coronary atherosclerotic plaque. *Circulation* 2008; **118**: 1172–82.
- 26 Schaar JA, De Korte CL, Mastik F, et al. Characterizing vulnerable plaque features with intravascular elastography. *Circulation* 2003; **108**: 2636–41.
- 27 Schaar JA, Regar E, Mastik F, et al. Incidence of high-strain patterns in human coronary arteries: assessment with three-dimensional intravascular palpography and correlation with clinical presentation. *Circulation* 2004; **109**: 2716–19.
- 28 Garcia-Garcia HM, Gonzalo N, Pawar R, et al. Assessment of the absorption process following bioabsorbable everolimus-eluting stent implantation: temporal changes in strain values and tissue composition using intravascular ultrasound radiofrequency data analysis. A substudy of the ABSORB clinical trial. *EuroIntervention* 2008; **4**: 443–48.
- 29 Meijboom WB, Meijis MF, Schuijff JD, et al. Diagnostic accuracy of 64-slice computed tomography coronary angiography: a prospective, multicenter, multivendor study. *J Am Coll Cardiol* 2008; **52**: 2135–44.
- 30 Regar E, Van Leeuwen A, Serruys PW. Optical coherence tomography in cardiovascular research, 1st edn. London: Informa Healthcare, 2007.
- 31 Tanigawa J, Barlis P, Mario CD. Intravascular optical coherence tomography: optimisation of image acquisition and quantitative assessment of stent strut apposition. *EuroIntervention* 2007; **3**: 128–36.
- 32 Silber S, Albertsson P, Aviles FF, et al. Guidelines for percutaneous coronary interventions. The Task Force for Percutaneous Coronary

- Interventions of the European Society of Cardiology. *Eur Heart J* 2005; **26**: 804–47.
- 33 Smith SC Jr, Feldman TE, Hirshfeld JW Jr, et al. ACC/AHA/SCAI 2005 guideline update for percutaneous coronary intervention: a report of the American College of Cardiology/American Heart Association Task Force on Practice Guidelines (ACC/AHA/SCAI Writing Committee to Update the 2001 Guidelines for Percutaneous Coronary Intervention). *J Am Coll Cardiol* 2006; **47**: e1–121.
 - 34 Bruining N, Tanimoto S, Otsuka M, et al. Quantitative multi-modality imaging analysis of a bioabsorbable poly-l-lactic acid stent design in the acute phase: a comparison between 2- and 3D-QCA, QCU and QMSCT-CA. *EuroIntervention* 2008; **4**: 1–7.
 - 35 Eggebrecht H, Rodermann J, Hunold P, et al. Images in cardiovascular medicine. Novel magnetic resonance-compatible coronary stent: the absorbable magnesium-alloy stent. *Circulation* 2005; **112**: e303–04.
 - 36 Lind AY, Eggebrecht H, Erbel R. Images in cardiology: the invisible stent: imaging of an absorbable metal stent with multislice spiral computed tomography. *Heart* 2005; **91**: 1604.
 - 37 Kurnik PB, Spadaro JJ Jr, Nordlicht SM, Tiefenbrunn AJ, Ludbrook PA. Prolonged coronary vasoconstrictor effect of ergonovine maleate. *Cathet Cardiovasc Diagn* 1984; **10**: 353–61.
 - 38 Haase J, Ozaki Y, Di Mario C, et al. Can intracoronary ultrasound correctly assess the luminal dimensions of coronary artery lesions? A comparison with quantitative angiography. *Eur Heart J* 1995; **16**: 112–19.
 - 39 Bruining N, Sabate M, de Feyter PJ, et al. Quantitative measurements of in-stent restenosis: a comparison between quantitative coronary ultrasound and quantitative coronary angiography. *Catheter Cardiovasc Interv* 1999; **48**: 133–42.
 - 40 Verheye S, Martinet W, Kockx mm, et al. Selective clearance of macrophages in atherosclerotic plaques by autophagy. *J Am Coll Cardiol* 2007; **49**: 706–15.
 - 41 Mintz GS, Popma JJ, Pichard AD, et al. Arterial remodeling after coronary angioplasty: a serial intravascular ultrasound study. *Circulation* 1996; **94**: 35–43.



7.2

Intracoronary optical coherence tomography (OCT) and histology 2, 3 and 4 years after implantation of bioresorbable everolimus-eluting stents in porcine coronary model: An attempt to decipher the human OCT images in the Absorb trial

Onuma Y , Okamura K, Gonzalo N, Regar E, van der Giessen W, Perkins L, Powers J, van Beusekom H, Rapoza, R, Renu Virmani R, Serruys PW

Submitted

ABSTRACT

Background: Using optical coherence tomography (OCT), alterations of the bioresorbable everolimus-eluting stent (BVS) struts have been reported in humans. In the absence of histology, the interpretation of the appearances of the struts by OCT remains speculative. We therefore report OCT findings with corresponding histology in the porcine coronary artery model immediately and at 2, 3 and 4 years after BVS implantation.

Methods: The BVS (3.0 x 12.0 mm) were implanted in 18 pigs that underwent OCT and were euthanized either immediately (n=2), at 2 years (n=3), at 3 years (n=5) or at 4 years (n=8) after implantation. For histological examination, sections were taken from the proximal, mid, and distal implanted arterial segment. Corresponding OCT and histology images were selected using the distal and proximal markers as landmarks. The appearance of struts by OCT were categorized into four subgroups and aligned with the histological counterpart.

Results: At 2 years, by OCT, 57.3 ± 16.6 struts were discernible per BVS with 80% strut sites as a box-shaped appearance. Despite their defined appearance by OCT, by histology, these structures were composed of proteoglycan without any polymeric material detectable by chromatography. At 3 years, by OCT, recognizable struts decreased to 27.6 ± 8.5 struts per BVS: 43.9% showed dissolved black box, 34.8% dissolved bright box, 16.3% open box, and 5% preserved box appearance. Histology shows that connective tissue cells within a proteoglycan-rich matrix replaced the areas previously occupied by the polymeric struts and coalesced into the arterial wall. At 4 years, by OCT, 10.1 ± 6.3 struts were recognizable as either dissolved black or dissolved bright box. In histology, these struts are minimally discernible by a focal lower density of smooth muscle cells.

Conclusions: Still discernible struts by OCT at 2 years are compatible with completely bioresorbed struts by histological analysis. At three and four years, both OCT and histology confirm complete integration of the struts into the arterial wall.

INTRODUCTION

Bioabsorbable polymer drug-eluting stents (DES) are a novel approach to the interventional treatment of coronary artery disease, providing short-term vessel scaffolding combined with drug delivery capability while avoiding the long-term limitations of metallic drug-eluting stent (DES). Such limitations of metallic DES include retardation of the growth of healthy endothelium over stent struts (1, 2) or endothelial dysfunction resulting in abnormal endothelial responses to acetylcholine (3, 4). Permanent metallic stenting may also preclude surgical revascularization, jail side branches, prevent late luminal enlargement, and impair non-invasive imaging of coronary arteries with multislice computed tomography and magnetic resonance. Recently, the fully bioabsorbable BVS coronary system (Abbott Vascular, Santa Clara, USA) was tested in the first-in-man ABSORB study with a series of 30 patients. In this trial, BVS demonstrated excellent long-term clinical results up to 2 years with a low major adverse cardiac event rate of 3.4% (5). The device consists of a backbone of poly-L-lactide (PLLA) coated with poly-D, L-lactide (PDLLA) that contains and controls the release of the anti-proliferative drug, everolimus (Novartis, Basel, Switzerland).

So far, it is unknown which diagnostic modality is most suitable to confirm the complete bioresorption. In the ABSORB trial, where multiple modalities of invasive imaging, for instance, intra-vascular ultrasound grey-scale (IVUS) with additional analysis of echogenicity and radiofrequency backscattering, were used, optical coherence tomography (OCT) was able to demonstrate serial changes in the optical properties of the struts over time, probably reflecting the bioresorption process (5,6,7,8). At 2 years, OCT analysis demonstrated that 34.5% of the struts were no longer discernible. Alterations of the struts in their optical appearance at follow-up was categorized into four subgroups: preserved box, open box, dissolved bright box and dissolved black box (6). According to these subgroups, strut appearance in serial comparative analyses (7 struts) changed from 6 months to 2 years, respectively: preserved box n=0 and n=9, open box n=143 and n=68, dissolved bright box n=225 and n=185 and dissolved black box n=56 and n=25 (5). Although the absence of visible struts in OCT was considered as a sign of complete bioresorption, there is no histological correlate to confirm this. Furthermore, the correlation of differential appearances by OCT and histology have not yet been investigated.

Herein, we report the results of this investigation correlating the appearance of BVS and the related arterial response by OCT with corresponding histology in porcine coronary arteries model acute, at 28 days and at 2, 3 and 4 years after

implantation. This is a study initiated in 2005, as a preamble to the completed and currently ongoing clinical studies.

METHODS

Experimental studies received protocol approval from the Institutional Animal Care and Use Committee and were conducted in accordance with American Heart Association (AHA) guidelines for preclinical research and the Guide for the Care and Use of Laboratory Animals (NIH, 1996). Two Yorkshire landrace swine (Thorax Center, Rotterdam, NL) and fourteen Yucatan mini-swine (Synecor, NC, USA) were implanted via femoral access according to standard procedures, with each pig receiving a single 3.0 x 12.0 mm BVS implant in one, two or three of the three main coronary arteries. The prototype of BVS systems used in the porcine study were of similar construct as those used in the ABSORB clinical trial. Fifteen pigs implanted with 31 BVS were examined by OCT and were subsequently examined by histology immediately post procedure, at 2, at 3 or at 4 years after implantation (Figure 1). Five BVS implanted in two pigs at 2 years were analyzed for polymer content via gel permeation chromatography, which demonstrated the polymer to be below detectable limits (data not presented). Immediately, at 3 and 4 years after implantation, all BVS implanted arteries in the pigs were processed for histology following OCT (immediately after implant: n=4, 3 year: n=8, 4 year: n=12).

18 pigs implanted with BVS fully bioabsorbable stents

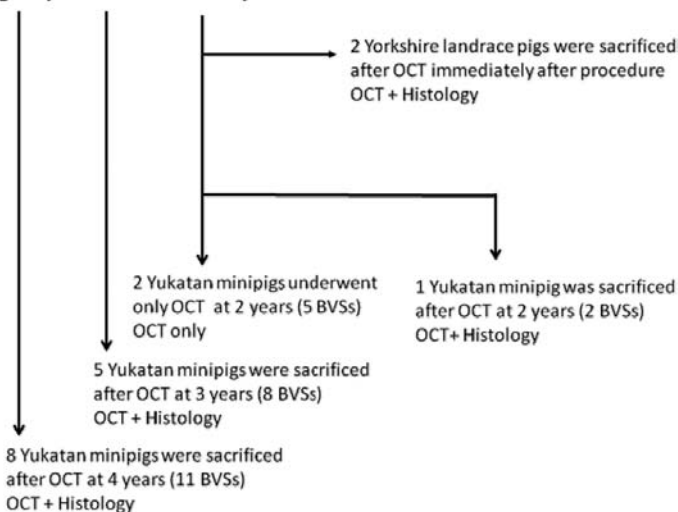


Figure 1. Flowchart of the pigs implanted with BVS in the main coronary arteries and evaluated by OCT and/or histology.

Evaluation by OCT was performed immediately after implant ($n = 2$), at 2 ($n = 3$), at 3 years ($n = 5$), or at 4 years ($n=8$) post-implant using a commercially available OCT system (M2 system, LightLab Imaging, Westford, MA, USA). An OCT catheter (Helios™ proximal occlusion catheter) was initially advanced distal to the area of interest over a conventional coronary guidewire, which was then replaced with the OCT imaging wire (ImageWire™). The OCT catheter was withdrawn manually proximal to the implanted segment, the balloon was inflated at low pressure, crystalloids were used to clear the blood and the wire containing the imaging core was withdrawn at 1 mm/sec. During image acquisition, coronary blood flow was replaced by continuous flushing of Ringer's lactate at 0.5-1.0 ml/sec using a power injector (Mark V ProVis, Medrad, Inc. Indianola, PA, US). The highly compliant occlusion balloon remained inflated proximal to the lesion at 0.5 or 0.7 atm. Cross-sectional images were acquired at 15.6 frames/sec. Immediately following OCT, all pigs were humanely euthanized.

Hearts were explanted from the thoracic cavity and flushed using pressure perfusion with saline followed by 10% buffered formalin in preparation for histology. Implanted arteries were carefully dissected from the heart, routinely processed, embedded in methyl methacrylate, and sectioned in duplicate at 5 μm . Three sections were taken from an implanted segment: i) the proximal section at 2mm distal to the proximal metallic marker, ii) the middle section at approximately 6 mm distal to the proximal marker, and iii) the distal section at 2 mm proximal to the distal marker. Sections were stained with hematoxylin and eosin (HE) and elastic Van Gieson (EVG). Duplicate sections from selected arteries at 2 and 3 years also were stained with Alcian Blue and Von Kossa histochemical stains for the detection of acid mucopolysaccharides (proteoglycans) and calcification, respectively.

For qualitative and quantitative analysis of the OCT, images were selected at 1 mm intervals in the implanted segment, which was defined as the region between the metallic markers. The struts sites were categorized according to the four morphological subcategories that have been applied in the clinical study (Figure 2) (5,6). The first subset (preserved box) can be described as a box appearance with sharply defined borders with bright reflection, while the strut body shows low reflection. The second subset is characterized as an open box i.e. luminal and abluminal "long-axis" borders thickened with bright reflection while the short-axis borders are no longer visible at follow-up. The third subset is categorized as a dissolved bright box i.e. partially visible bright spot with contours poorly defined and no box shaped appearance. The fourth subset is a dissolved black box i.e. black spot with contours poorly defined, often confluent but with no box shaped appearance. The other OCT endpoints were the interaction of the struts and

Stent Strut Appearance at Follow-up

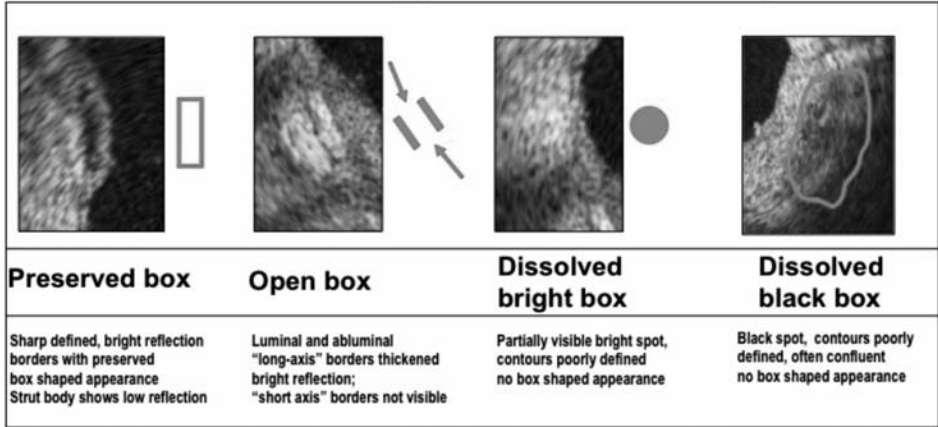


Figure 2. Representative photographs of the four subcategories of reflectance characteristics by OCT in BVS struts at follow-up as observed in the first-in-man ABSORB trial. Description of each subcategory is included in the illustration. (modified from Ormiston, *et al.* ⁶)

vessel wall (e.g. apposition and coverage) (5,6). Incomplete strut apposition was defined as clear separation of one strut from the vessel wall, with evidence of flush between the strut and vessel wall. Coverage of the strut by tissue was categorized as complete, incomplete or not visible (5,6). Qualitative analysis of BVS and the vascular response involved the selection and comparison of corresponding OCT and histology images using the distal and proximal markers as landmarks.

RESULTS

OCT findings

Immediately after implantation, all struts had a preserved box appearance (Figure 3) and were well apposed to the vessel wall. In one of the two pigs with OCT and sacrifice immediately after stent implantation, the BVS was placed after heparinization but without antiplatelet therapy. In this animal, a strut of one BVS was covered with highly reflective structures without shadowing, suggesting the presence of the white thrombus.

The OCT findings at 2, 3 and 4 years are summarized in Table 1. At 2 years, on average, 56.0 ± 17.5 struts were discernible per BVS device. Endoluminal lining of the implanted segment was smooth and circular (Figure 4). Four fifth of struts showed preserved box appearance and 17% showed dissolved black box,

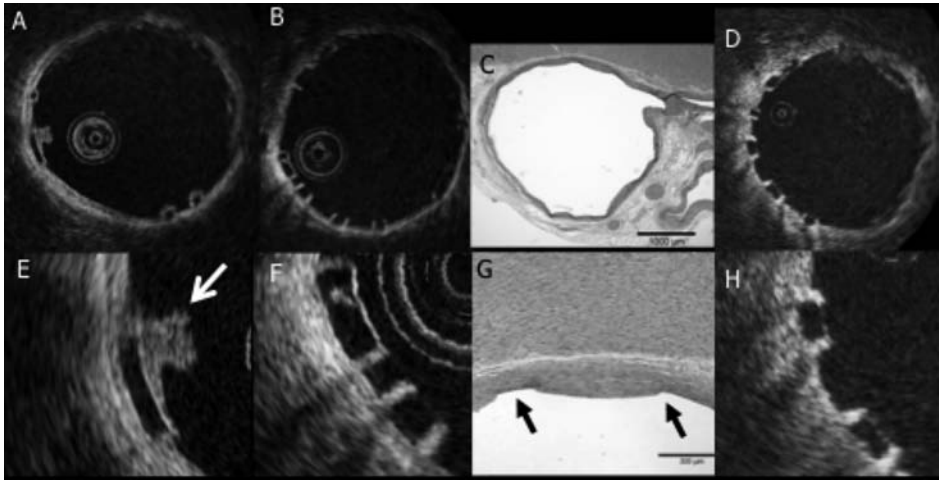


Figure 3. OCT images immediately after BVS implantation. In a pig to whom a BVS was implanted with heparin (A, E), at 9 o'clock, the strut with preserved box appearance was covered with high intensity irregular material without shadowing, suggesting presence of a white thrombus (E shows a magnified image). In a pig implanted with clopidogrel, aspirin and heparin (B, F), all struts showed preserved box appearance without any tissue coverage. Histology after the removal of polymeric struts showing the footprints of the struts on the intima of the vessel wall (C, G). Note the absence of fracture of the internal elastic membrane. Similarly, in humans, all struts demonstrate preserved box appearance without tissue coverage immediately after stent implantation (D, H).

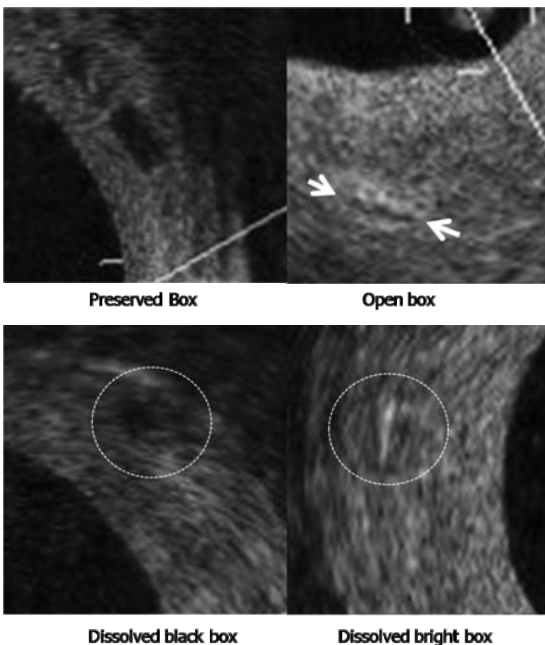


Figure 4. Examples of strut appearances assessed with OCT in porcine coronary arteries.

Table 1. Results of OCT evaluation in the current porcine model and ABSORB trial

<i>OCT Findings</i>	<i>ABSORB study immediately after implantation</i>	<i>ABSORB study 2 years*</i>	<i>Porcine model 2 years</i>	<i>Porcine model 3 years</i>	<i>Porcine model 4 years</i>
Number of BVS evaluated	7	7	7	8	12
Mean discernible struts per BVS	58±19	38±30	57±17	28±9	10±6
<i>Strut appearance</i>					
Preserved box, %	100	3.0	84.9	5.0	0
Open box, %	0	21.7	2.6	16.3	0
Dissolved bright box, %	0	62.0	0.0	34.8	51.2
Dissolved black box, %	0	13.3	17.6	43.9	48.8
<i>Strut/ Vessel wall interaction</i>					
Strut apposition, %	90.1	99.2	100	99.5	100
Strut alignment, %	4.1	0	0	0	0
Incomplete strut apposition, %	5.8	0.8	0	0.5	0
<i>Strut coverage</i>					
Complete, %	0	100	100	100	100
Incomplete, %	0	0	0	0	0
Not visible, %	100	0	0	0	0

* Data at 2-year follow-up in the matched seven patients who underwent serial OCT assessment at baseline, 6 month and 2 years^{5, 6}. The percentage was recalculated as follows: number of strut in each category / total number of discernible struts at that time point

while only few struts (2.6%) demonstrated open box appearance. All struts were completely embedded in the vessel wall and were covered by tissue.

At 3 years, the number of recognizable struts decreased to 27.6±8.5 struts per BVS device: 43.9% of discernible struts showed dissolved black box, while 34.8% showed dissolved bright box, 16.3% showed open box, and 5% remained as preserved boxes. One strut showed malapposition at the ostium of sidebranch, while all others were fully apposed. At 4 years, only 10.1±6.3 struts per BVS were recognized by OCT: 51.2% of struts were classified as dissolved bright while 48.8% as dissolved black appearance.

Comparison between OCT and histology

The corresponding OCT and histology images are summarized in the Table 2. At two years, most locations of pre-existing struts were detectable by OCT, showing the “preserved box” appearance. By histology, these “preserved box” structures likewise had discrete borders and were composed of hyaline material that stained

Table 2. Summary of correlation between OCT findings and histology

Subcategory	Histology
2 Year Preserved box appearance	Struts were replaced by acid mucopolysaccharides. By gel permeation chromatography, the BVS polymer was no longer detectable at 2 years (data not shown), confirming that there was complete polymer degradation, and these structures visible by OCT and histology represented locations of bioresorbed BVS struts.
3 Year Preserved box	Strut has been also replaced by proteoglycan and tends to be coalesced with the surrounding neointimal tissue. Minimal calcification is occasionally present, then outlining locations of pre-existing struts.
Dissolved black box appearance	Pre-existing strut has been replaced by proteoglycan with variable connective tissue cellular infiltrates and coalesced with the surrounding neointimal tissue, indicating complete, benign bioresorption.
Indiscernible	Regions having been occupied by struts were barely recognizable, being now entirely composed of connective tissue by histology.
4 Year Indiscernible	Struts are minimally discernible, only illustrated by focal regions of low smooth muscle cell density. Scant remnant calcification is the solitary evidence remaining of prior struts.

OCT = Optical coherent tomography

positively with Alcian Blue, indicating that they were composed of acid mucopolysaccharides (proteoglycans) (Figure 5). By gel permeation chromatography, the BVS polymer was no longer detectable at two years (data not shown), con-

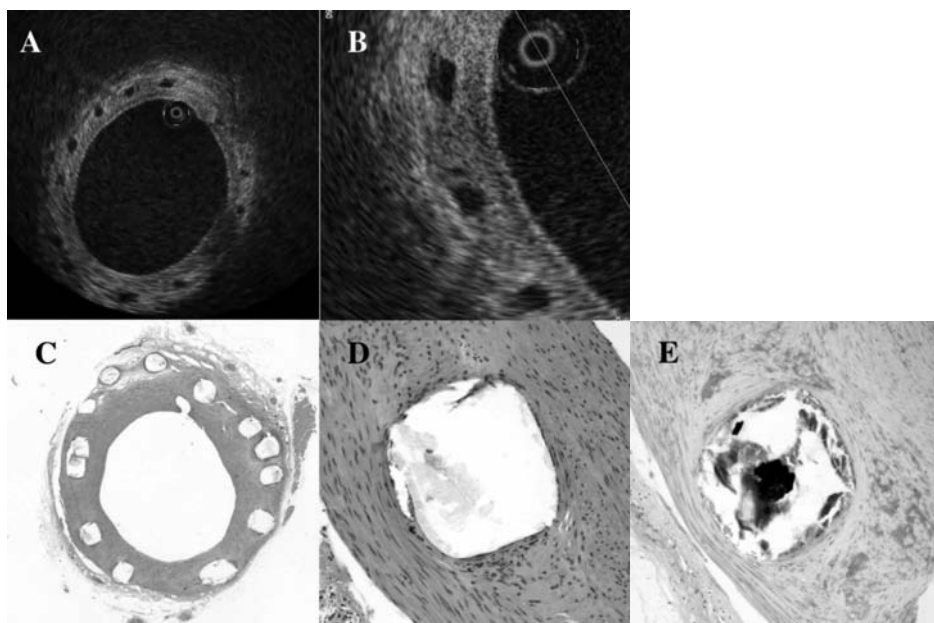


Figure 5. OCT images and corresponding histology at 2 years after stent implantation: Strut conforming to the “preserved box” subcategory as visible by OCT (A, B) and corresponding histological photomicrographs (C, D and E). Location of bioresorbed struts are readily visible in histological sections stained with standard hematoxylin and eosin, but material staining positively for Alcian blue filled in the regions previously occupied by the struts. (proteoglycan, E)

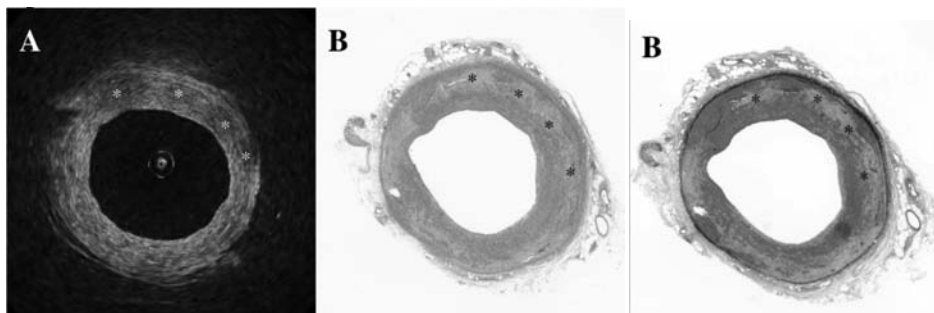


Figure 6. OCT image and histology at 3 years after stent implantation: Struts are suspected to be present as dissolved black box (A) and are hardly discernible by histology (B: Hematoxylin and eosin, C: elastic Van Gieson staining). Poorly defined regions of low signal intensity visible by OCT correspond with regions of low cell-density connective tissue visible by histology (asterisks in B and C). These regions may indicate prior locations of bioresorbed BVS struts.

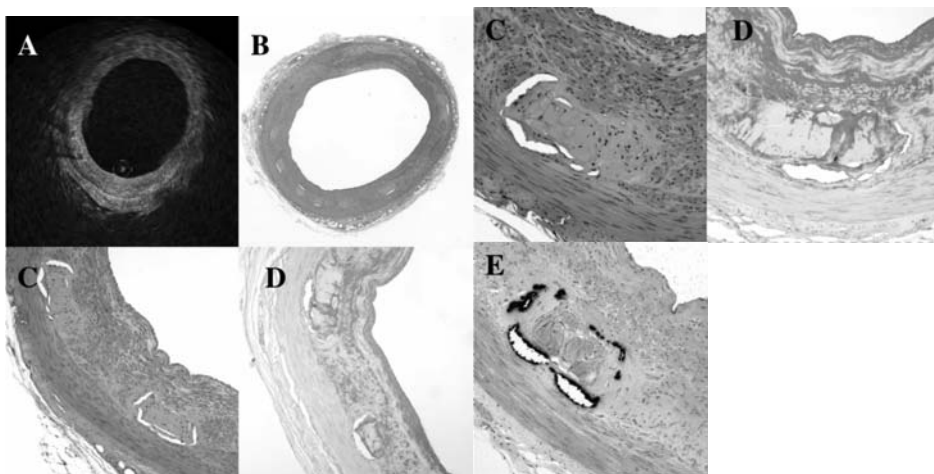


Figure 7. OCT image and histology at 3 years after stent implantation: Struts clearly conforming to “preserved box” subcategory are visible on OCT only at 8 and 9 o’clock. These preserved boxes were accompanied with shadowing effect. (A) Corresponding histological photomicrographs (B, C, D, E). As compared to 2 years, strut footprints now coalesced with the surrounding tissue. With Alcian Blue staining, struts have been replaced by connective tissue cells admixed in a proteoglycan matrix (D). Staining with Van Kossa demonstrates minimal calcification outlining the sites previously occupied by the polymeric struts. (E).

firming that there was complete polymer degradation. Therefore, these structures visible by OCT and histology represented locations of bioresorbed BVS struts. Due to the high water content of the matrix replacing the polymer, there was likely processing-induced swelling that made these footprints appear falsely larger by histology as compared to OCT.

Overall at three years, translucent regions suggestive of remnant struts were hardly discernible by OCT, although one single animal showed clearly a persistence of preserved box appearance of the struts. In the other cases, the struts were either indiscernible or suspected to be present as dissolved black box (Figure 6). In both cases (preserved box and dissolved black box), histology at 3 years shows that the sites previously occupied by the polymeric struts were still detectable on histology but coalesced with the surrounding neointimal tissue. As compared to two years, locations of pre-existing struts were largely composed of connective tissue cells within a proteoglycan-rich matrix (Figure 6). In other words, strut footprints classified as “dissolved black box” generally shared the same histological morphology as those categorized as “preserved box”, though there were regions of low cellular density connective tissue visible by histology that indicated complete, benign involution of the struts into the arterial wall (Figure 6 and 7). At both

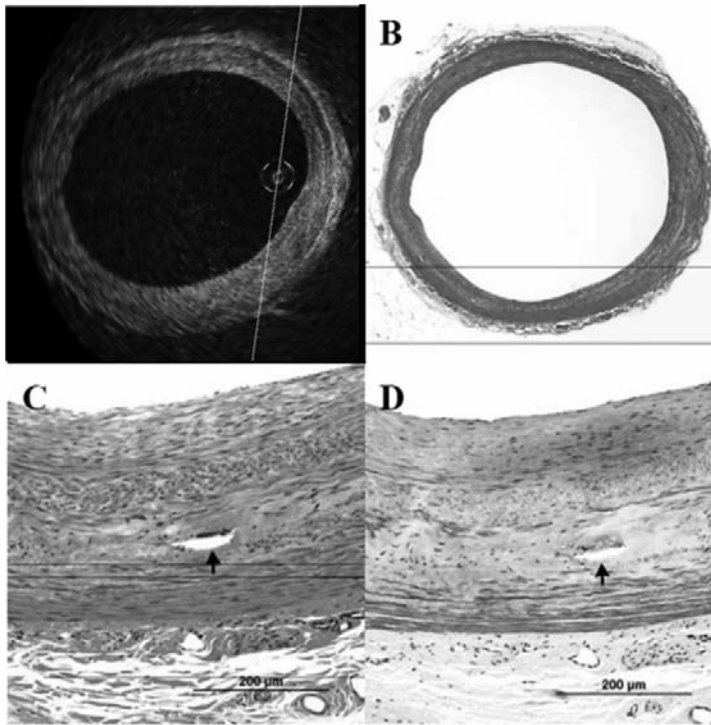


Figure 8. OCT image and histology at 4 years after implantation: Struts are no longer discernible by either OCT (A) or by histology using HE (B, C). Locations in the arterial wall suggestive of prior strut location are minimally discernible with Movat's Pentachrome staining (D), which are illustrated by focal regions of low smooth muscle cell density. Scant remnant calcification (arrow), now less notable as compared with that observed at 2 and 3 years, is the solitary evidence remaining of prior strut.

two and three years, sporadic, thin demarcation line of calcification delineating pre-existing strut locations were inconsistently observed histologically (Figure 7). When the struts were not detectable in OCT, these regions of strut site were poorly discernible in histology (Figure 6). At four years, struts are minimally discernible in histology. The only suggestive findings to previous presence of struts are a localized lower density of smooth muscle cells and remnant calcification. (Figure 8)

DISCUSSION:

In the current study, we describe the preclinical experience using BVS in a porcine coronary model. Two years after BVS implantation, OCT images demonstrated that 81% of the struts still had a preserved box appearance. Nonetheless, the corresponding histological images showed that the polymeric struts were already resorbed and replaced by proteoglycan matrix. Three years after BVS implantation, OCT images demonstrated that only 5% of the struts retained a preserved box appearance while 44% had evolved to a dissolved black box appearance. In addition, at 3-year follow-up we observed on OCT dissolved black boxes that, on histology, reflected infiltration of the sites of pre-existing struts by connective tissue cells. At 3 years, absolute count of discernible struts was approximately reduced by 50% and the no longer discernible strut footprints on OCT seem to correspond in histology to complete integration into the surrounding arterial wall. Furthermore, at 4 years, only one fifth of the struts were discernible in OCT with dissolved black or dissolved bright appearance, which were minimally discernible in histology.

Histological response after BVS implantation

The current study suggests the following histological responses after implantation of the BVS PLLA/PDLA device: first, the polymeric struts are resorbed and replaced by proteoglycan matrix; second, the strut areas are infiltrated by connective tissue cells and become assimilated to the surrounding tissues; and third, the strut areas become difficult to be discerned on histology due to their coalescence with the arterial wall. Strictly speaking, the process of “bioresorption” finishes at the first phase. Subsequent phases represent an “integration” process of the struts within the arterial wall; ultimately locations of pre-existing strut voids become completely indiscernible on histology.

Assessment of the “bioresorption” process by OCT

In the first-in-man trial using the BVS, the OCT classification of the four strut appearances was developed to characterize the process of bioresorption (5,6). Immediately post implantation, the polymeric struts appear on OCT as clear-cut boxes lying on the vessel wall rather than being embedded (Figure 3). The disappearance of this box appearance is considered to be the initial stages of the bioresorption process since it was no longer seen at 6-months (5,6). The first optical change of this box appearance in the ABSORB trial was the “opening” of the extremities of the box in its short axis which was considered as a first sign of biochemical or histological alteration (Figure 4), observed in 34% of struts at 6 months, and still in 14% at 2 years. The dissolved black box and dissolved bright box appearance were considered to reflect further stages of bioresorption and vessel wall integration. The indiscernibility of the strut footprints on OCT was interpreted as a sign of complete bioresorption. At 2-years, 36.3% of the struts were indiscernible by OCT in human. So far, no attempt has been made to interpret these human OCT observations by correlating OCT and histological observation in animal model.

In contrast to what was initially thought after the first-in-man BVS trial and according to the current animal study, the “preserved box” appearance does not exclude the resorption of polymeric struts. By gel permeation chromatography, the BVS polymer was no longer detectable at two years (data not shown), confirming that there was complete resorption of the polymer, and these structures visible by OCT and histology represented voids of former BVS struts. In other words, the preserved box appearance with optical translucency is compatible with complete polymer dissolution.

Assessment of “integration” process by OCT

Although OCT might not be sensitive enough to evaluate the degradation process of the polymer, it may, on the other hand, provide more detailed information on the “integration” process. In the current study, the transition from the preserved box appearance (at 2 years) to the full disappearance of the strut footprints on OCT or the presence of dissolved black box (at 3 years) appears to be related to the replacement of the pre-existing strut by proteoglycan matrix and connective tissue cells. While the demarcation of the pre-existing struts become undetectable on OCT image, by histology these ultimately coalesce with the arterial wall. This suggests that changes in strut appearances on OCT mirror the “integration” process of the matrix replacing the struts. In a few cases, a demarcating line of

mineralization seems to be the sole histological remnant of the pre-existing strut, and it is still unclear whether this thin line of mineralization would be seemingly detectable on OCT (Figure 7).

Inflammatory Reaction

Recently, Jiang, *et al.* demonstrated in *in vitro* and *in vivo* studies that a strong correlation exists between the rate of material degradation and the degree of inflammatory response to implanted material (9). In Swiss Webster mice implanted with polymeric disks into the peritoneum, the PLLA disk – which has longer degradation time compared to the mixed polymer of PLLA and PEG - showed least inflammatory response. However, in a rat study by Polimeni, *et al* (10), when the PLA devices was implanted subcutaneously in contact with bones, the polymer triggered a foreign body reaction including multinucleated giant cells, macrophages and lymphocytes. Expert of biodegradable polymer have repeatedly emphasized the importance of the locus of the implant on its rate of degradation and also in the inverse relationship between rates of biodegradation and the presence of inflammatory process (9). In the current histological study, the BVS did not show significant inflammatory response at 2 year and 3 years, although a likely short-term inflammatory response during the resorption phase of the stents was not evaluated as part of this study.

Differences between human and porcine coronary artery

At 2-year follow-up, the distribution of OCT strut appearances observed in the porcine animal model differed from the results of the human FIM trial (table 3). More specifically, the open box and dissolved bright box appearance observed in 13.8% and 39.5% of struts in the ABSORB trial were scarcely observed at 2 years in the current animal study (open box 2.4%, dissolved bright box 0%). Furthermore, in the ABSORB trial, the number of discernible struts per device was 38 at 2 years, while in the current animal model, 57 struts voids per device were still discernible at 2 years. This suggests a slower integration process of the struts voids filled with proteoglycans in porcine arteries than in human arteries.

One possible explanation is the absence of underlying atherosclerotic plaque with or without inflammatory component in the implanted lesion of the animal model. The vascular response of aged, human atherosclerotic arteries has distinction from that of juvenile, healthy animal arteries. In some human cases, the deployed polymeric struts are possibly apposed against highly inflammatory atherosclerotic plaque with activated macrophage and metalloproteinase. In a single

cross section of OCT heterogeneity of strut appearance (four categories) is not uncommon.

It has been reported in the ABSORB trial that the lesion morphology of implanted segments affected the degree of “late recoil” seen at 6 months with the BVS (11). Calcified plaques resulted in significantly less late recoil (0.20 +/- 1.54 mm² and 1.97 +/- 22.2%) than fibronectin plaques (1.03 +/- 2.12 mm² and 12.4 +/- 28.0%, p = 0.001 and p = 0.001, respectively) or fibrocellular plaque (0.74 +/- 1.48 mm² and 8.90 +/- 19.8%, p = 0.001 and p = 0.001, respectively). This suggests that the underlying fibronectin or fibrocellular plaque might have a determinant role in early alteration of polymeric struts in the first 6 months, which seems to evolve into a more favorable integration process at 2 years as reflected by the striking difference between the OCT appearance in human at 6 months and 2 years. .

Another possible explanation for the slower integration in the current porcine study than in the ABSORB is presumably the longer degradation time of the polymeric strut constructions in this study compared to the BVS in the ABSORB trial. It is known that polylactic polymer with greater monomer content has faster degradation rate. Polylactic acid degrades by hydrolysis, and this process is catalyzed at early stages of degradation by the presence of carboxyl moieties. This autocatalytic process is initiated either from the ends of each chain or from the presence of free residual monomer in the polymer matrix. The polymeric BVS coronary system used in the FIM trial has greater monomer content in its polymer than the device used in the current animal study. These facts may explain the faster integration process observed in the human FIM trial than in the current animal study.

The limitations

The limitations of this study are the following. The number of specimens examined was small. Since there are no serial OCT images acquired after implantation, the changes from baseline to follow-up were not evaluated. In addition, as discussed above, differences between the healthy porcine coronary artery and diseased human coronary artery could limit the generalizability of the hypothetical concepts put forward in this report.

CONCLUSION

In conclusion, the current porcine animal study potentially elucidates the histological responses after implantation of the BVS - bioresorption and integration.

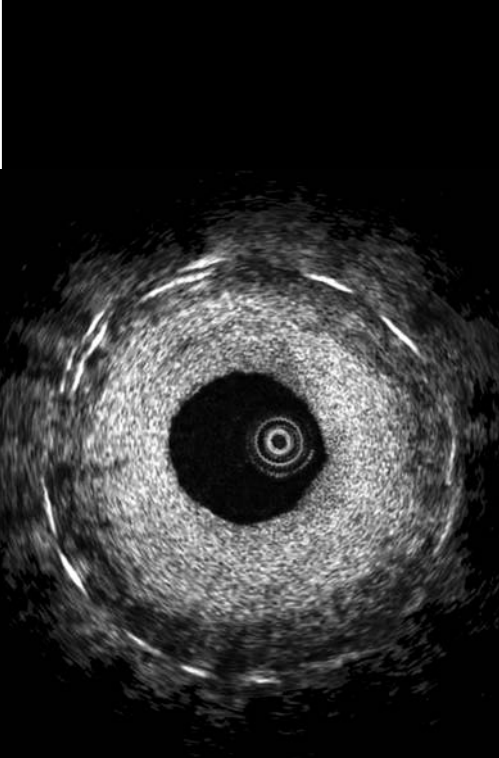
OCT might be more sensitive to assess the integration process rather than the polymer alteration. Ultimately absence of the BVS device footprint on OCT suggests complete integration of the struts into the arterial wall.

ACKNOWLEDGEMENT

We thank Dr. Garcia-Garcia for his careful and critical review of the manuscript.

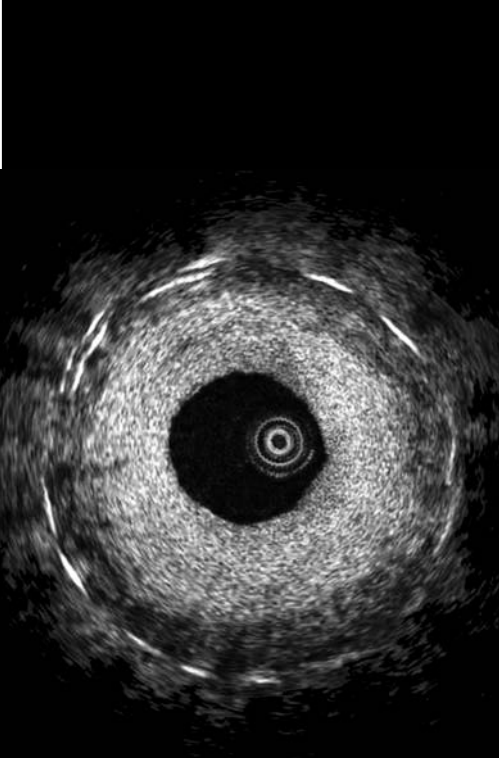
REFERENCES

1. Finn AV, Joner M, Nakazawa G, Kolodgie F, Newell J, John MC, Gold HK, Virmani R. Pathological correlates of late drug-eluting stent thrombosis: strut coverage as a marker of endothelialization. *Circulation*. 2007;115(18):2435-2441.
2. Joner M, Finn AV, Farb A, Mont EK, Kolodgie FD, Ladich E, Kutys R, Skorija K, Gold HK, Virmani R. Pathology of drug-eluting stents in humans: delayed healing and late thrombotic risk. *J Am Coll Cardiol*. 2006;48(1):193-202.
3. Hoffma SH, van der Giessen WJ, van Dalen BM, Lemos PA, McFadden EP, Sianos G, Ligthart JM, van Essen D, de Feyter PJ, Serruys PW. Indication of long-term endothelial dysfunction after sirolimus-eluting stent implantation. *Eur Hear J*. 2006;27:166-71.
4. Togni M, Windecker S, Cocchia R, Wenaweser P, Cook S, Billinger M, Meier B, Hess OM. Sirolimus-eluting stents associated with paradoxical coronary vasoconstriction. *J Am Coll Cardiol*. 2005;46(2):231-236.
5. Serruys PW, Ormiston JA, Onuma Y, Regar E, Gonzalo N, Garcia-Garcia HM, Nieman K, Bruining N, Dorange C, Miquel-Hebert K, Veldhof S, Webster M, Thuesen L, Dudek D. A bioabsorbable everolimus-eluting coronary stent system (ABSORB): 2-year outcomes and results from multiple imaging methods. *Lancet*. 2009;373(9667):897-910.
6. Ormiston JA, Serruys PW, Regar E, Dudek D, Thuesen L, Webster MW, Onuma Y, Garcia-Garcia HM, McGreevy R, Veldhof S. A bioabsorbable everolimus-eluting coronary stent system for patients with single de-novo coronary artery lesions (ABSORB): a prospective open-label trial. *Lancet*. 2008;371(9616):899-907.
7. Bruining N, Tanimoto S, Otsuka M, Weustink A, Ligthart J, de Winter S, van Mieghem C, Nieman K, de Feyter PJ, van Domburg RT, Serruys PW. Quantitative multi-modality imaging analysis of a bioabsorbable poly-L-lactic acid stent design in the acute phase: a comparison between 2- and 3D-QCA, QCU and QMSCT-CA. *EuroIntervention*. 2008;4(2):285-291.
8. Garcia-Garcia HM, Gonzalo N, Pawar R, Kukreja N, Dudek D, Thuesen L, Ormiston JA, Regar E, Serruys PW. Assessment of the absorption process following bioabsorbable everolimus-eluting stent implantation: temporal changes in strain values and tissue composition using intravascular ultrasound radiofrequency data analysis. A substudy of the ABSORB clinical trial. *EuroIntervention*. 2009;4(4):443-448.
9. Jiang WW, Su SH, Eberhart RC, Tang L. Phagocyte responses to degradable polymers. *J Biomed Mater Res A*. 2007;82(2):492-497.
10. Polimeni G, Koo KT, Pringle GA, Agelan A, Safadi FF, Wikesjo UM. Histopathological observations of a polylactic acid-based device intended for guided bone/tissue regeneration. *Clin Implant Dent Relat Res*. 2008;10(2):99-105.
11. Tanimoto S, Bruining N, van Domburg RT, Rotger D, Radeva P, Ligthart JM, Serruys PW. Late stent recoil of the bioabsorbable everolimus-eluting coronary stent and its relationship with plaque morphology. *J Am Coll Cardiol*. 2008;52(20):1616-1620.



CHAPTER 8

OCT in secondary revascularisation



8.1

Optical coherence tomography in secondary revascularisation. Stents and grafts assessment

Gonzalo N, Serruys PW, Piazza N, Regar E.

EuroIntervention. 2009 May;5 Suppl D:D93-D100

Optical coherence tomography (OCT) in secondary revascularisation: stent and graft assessment

Nieves Gonzalo, MD; Patrick W. Serruys, MD, PhD, FESC, FACC; Nicolo Piazza, MD; Evelyn Regar*, MD, PhD

Thoraxcenter, Erasmus Medical Center, Rotterdam, The Netherlands

The authors have no conflict of interest to declare.

KEYWORDS

Secondary coronary revascularisation, optical coherence tomography, stent, coronary graft

Abstract

Optical coherence tomography is a recently introduced intracoronary imaging modality with higher spatial resolution than intravascular ultrasound. For this reason, it is increasingly applied to investigate the characteristics of vulnerable atheromatous plaques and the result of stent implantation, struts coverage and restenosis, as well as in procedural decision-making. OCT is also useful in the field of secondary revascularisation, particularly in assessing implanted stents, evaluating relevant technologies like biodegradable stents, and in studying surgical grafts. In this article we perform a review of current developments and evidence in this area.

* Corresponding author: Thoraxcenter, Erasmus MC, Bd 585, 's-Gravendijkwal 230, 3015 CE Rotterdam, The Netherlands
E-mail: e.regar@erasmusmc.nl

Introduction

Optical Coherence Tomography (OCT) is a light-based intracoronary imaging modality. Its ability to provide high resolution (in the range of 15 micron) images has revealed new aspects of the acute and long-term effects of coronary interventions not previously recognised. The technical development leading to the simplification of the acquisition procedure has extended its use and OCT systems are now available at many catheterisation laboratories worldwide. The present article aims to illustrate the clinical potential of OCT for the evaluation of patients with previous coronary interventions.

OCT for the assessment of implanted stents

OCT can be a valuable tool for the evaluation of the long-term impact of stent implantation on the coronary artery. This technique has unique capabilities for the detailed assessment of strut apposition and tissue coverage¹. OCT can increase our understanding of the mechanisms implicated in the pathogenesis of in-stent restenosis. Furthermore, it can provide unique information for the evaluation of new generation bioabsorbable stents.

Stent apposition (Figure 1)

Incomplete stent apposition (ISA), also referred to as “malapposition”, is defined as a separation of a stent strut from the vessel wall. The separation distance is measured from the endoluminal side of the stent strut to the leading edge of the vessel wall. As drug-eluting stents (DES) are typically composed of a metal frame that is visible by OCT as a highly reflective structure and covered by a polymer containing the drug that is not visible, the separation distance must be larger than the strut thickness (metal plus polymer) for each specific stent type.

The clinical significance and long-term influence of ISA is poorly understood. In principal, ISA can (i) persist in this configuration (persistent ISA); or (ii) gain complete vessel wall contact over time (resolved ISA). Furthermore, ISA can be (iii) acquired over time whereas struts showed complete attachment to the vessel wall immediately after stent implantation, however become clearly separated from the vessel wall over time (late acquired ISA). The clinical impact and mechanism of late acquired ISA is poorly understood as well. Because OCT has a much higher accuracy than

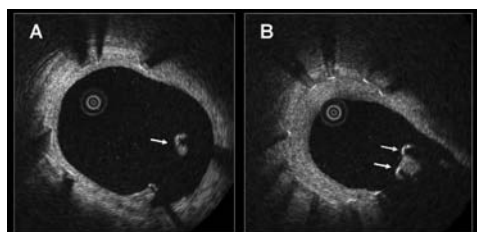


Figure 1. Incomplete stent apposition in optical coherence tomography. A: example of a malapposed strut covered by tissue (white arrow). B: example of malapposed struts in relation with a side-branch. One of the struts is covered by a thin layer of tissue (white arrow) while in the other no tissue coverage is visible (yellow arrow).

IVUS to assess strut apposition (even when the struts are covered with tissue)², it may provide new insights into its pathogenesis. Chronic stent recoil or dissolution of a thrombus jailed between the stent and vessel wall in patients undergoing primary percutaneous coronary intervention for acute myocardial infarction, have been proposed as possible causes of late ISA. Recently, we have demonstrated that patients who underwent DES implantation for ST elevation myocardial infarction (STEMI) showed a higher incidence of incomplete strut apposition than patients with stable or unstable angina³. Different follow-up studies have characterised the degree of stent apposition for different stent types. Several authors have reported on a higher frequency of malapposed struts by OCT in sirolimus-eluting stent (SES) than in bare metal stents (BMS)^{4,5}. Another study evaluating SES at six months follow-up showed that malapposed struts were more often located in areas of overlapping stents⁶. More specifically, up to 40% of struts in overlapping segments of DES are malapposed despite high pressure dilatation⁷. The authors hypothesised that the presence of incomplete stent apposition could be associated with delayed endothelialisation and increased risk of stent thrombosis in overlapping regions⁷. OCT has also demonstrated malapposition in severely calcified lesions, even after high pressure balloon dilatation and rotational atherectomy⁸. Strut thickness and cell design can have an impact on incomplete stent apposition. An OCT study observed incomplete stent apposition more frequently in stents with closed design cells and thicker struts⁹. IVUS data have suggested a possible relation between incomplete DES apposition and subsequent stent thrombosis¹⁰. However, the clinical impact of incomplete stent strut apposition as detected by OCT is not well established. In fact, OCT is able to visualise incomplete strut apposition with a much higher sensitivity and specificity than IVUS, but this observation has not been associated with an increase in clinical adverse events^{5,9}. As a corollary, not all patients that experience DES thrombosis show strut malapposition^{11,12}.

Struts coverage following DES implantation (Figure 2)

Endothelial strut coverage has been identified as the most powerful histological predictor of stent thrombosis¹³. It is unclear, however, to what extent these post mortem findings in a very select population can be translated into the clinical arena given that it is difficult to assess strut endothelialisation *in vivo*. DES typically inhibit neointimal proliferation to such an extent that it may not be detectable by IVUS. On the other hand, OCT can visualise and quantify with high sensitivity and reproducibility very thin layers of tissue covering stents^{14,15}. Clinical OCT studies are currently shedding light on the complex vascular healing process after stenting.

STRUT COVERAGE IN BMS AND DES

Recently, several *in vivo* OCT studies evaluating strut coverage in DES and BMS at different time intervals have been published. Xie et al compared tissue coverage at three months follow-up in 16 and 24 patients who underwent implantation with BMS and SES, respectively. The neointimal thickness per strut was higher in the BMS than in the DES group and the frequency of struts with no visible coverage by OCT was higher in the SES group. However, no

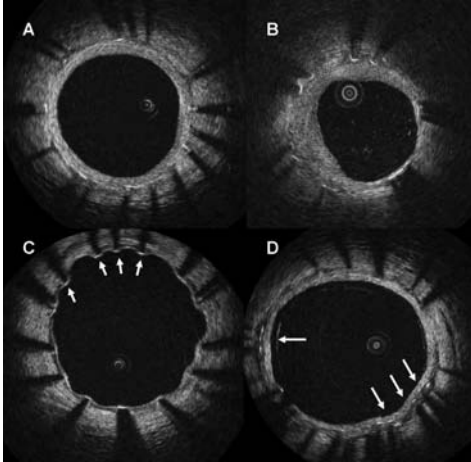


Figure 2. Tissue coverage at follow up in drug eluting stents. **A:** Symmetric tissue coverage: all the struts are covered by a layer of tissue of similar thickness. **B:** asymmetric tissue coverage: some struts are covered by a thick layer of tissue while in others (white arrows) only a small layer of tissue coverage is visible. **C:** the majority of struts are covered by a thin layer of tissue while some (white arrows) do not show visible tissue coverage. **D:** overlap region. All the struts are covered but some of them (white arrows) are surrounded by a heterogeneous low backscattering material.

significant difference in the incidence of in-stent thrombus was observed in this small cohort⁵. Another study comparing BMS at short- and long-term follow-up with SES showed similar results⁴.

CHANGES IN DES STRUT COVERAGE OVER TIME

Matsumoto et al compared 6-month IVUS and OCT findings in 34 patients implanted with a total of 57 SES. In this study, tissue coverage was appreciated in 36% of the struts on IVUS (median tissue thickness 52.5 μm , 25th and 75th percentiles 28 and 147.6 μm respectively). In contrast, OCT identified 89% of the struts with tissue coverage, but only 16% of the stents had complete stent coverage⁶. In another OCT study, only 18% (8/42) of SES implants showed complete tissue coverage by six months. Furthermore, tissue coverage thickness increased from 6 to 12 months (from 42 \pm 28 μm to 88 \pm 32 μm) but only 41% of the stents had complete tissue coverage by 12 months¹⁶. Other investigators using OCT have demonstrated that 81% of patients have struts with incomplete tissue coverage two years after implantation with SES. The presence of struts without visible tissue coverage was more frequent at side branches and at overlapping segments. Findings suggestive of thrombus were observed in three patients but there were no cases of clinical stent thrombosis¹⁷.

RELATION BETWEEN DES COVERAGE AND CLINICAL PRESENTATION

Clinical presentation has been associated to the presence of struts without visible tissue coverage by OCT. Kubo et al reported that

patients with unstable angina presented more frequently with incomplete stent apposition and “uncovered” struts than patients with stable angina¹⁸. Our group has shown that struts without visible tissue coverage by OCT are more frequent in patients receiving DES during primary PCI for STEMI than in patients treated with DES for stable or unstable angina³. A possible explanation for this observation could lie in the differences in the underlying plaque. Pathological studies have demonstrated a higher frequency of uncovered struts in stents implanted over lipid-rich high-risk plaques as compared with stents implanted over plaques with stable morphology¹⁹. Investigations such as the recently presented HORIZONS-OCT substudy comparing paclitaxel-eluting stents vs BMS implanted for STEMI will provide more information about the coverage of different stent types in specific clinical scenarios²⁰.

COMPARISON OF TISSUE COVERAGE IN DIFFERENT DES

Initial results of several studies comparing tissue coverage in different DES have been reported in the last months. The OCT substudy of the LEADERS compared the differences in tissue coverage at nine months between a durable polymer sirolimus-eluting stent (Cypher Select, Cordis, Johnson&Johnson, Miami, FL, USA) and an erodible polymer biolimus A9-eluting stent (Biomatrix III, Biosensors, Morges, Switzerland). When applying a threshold of 95% of struts covered by OCT, the bioabsorbable polymer stent achieved a higher rate of coverage.²¹ The ODESSA (OCT for DES Safety) study compared tissue coverage at overlapping sites in BMS and different DES types (SES, paclitaxel-eluting and zotarolimus-eluting stents). The authors reported a trend towards a higher frequency of uncovered and malapposed struts at overlapping sites and differences in the number of uncovered struts and the amount of tissue coverage between different DES types²².

The effect of implanting several stent strut layers (e.g., techniques used for bifurcation treatment) or overlapping stents with different eluting drugs on strut coverage may also be studied with OCT²³. Interpretation of strut coverage by OCT should be done with caution. While OCT has been proven to reliably visualise very thin tissue layers covering stent struts, its resolution is limited to 15 micron and thus, a single cell layer can not be visualised with OCT. Second, the presence of tissue coverage should not be considered synonymous with recovery of normal endothelial function. Furthermore, it is important to realise that several OCT studies have reported the presence of uncovered struts at follow-up, but these findings were not associated with clinical adverse events^{17,18}. Specially designed studies, including long-term follow-up, are warranted to better understand the clinical significance of incomplete strut coverage observed by OCT.

Assessment of restenosis

OCT can be a very valuable tool for the assessment of restenosis through its ability to image the neointima and identify possible causes contributing to restenosis. Animal and human data suggest that restenosis is a response to vessel injury during stent implantation. High-pressure stenting techniques have demonstrated their usefulness for stent optimisation but they can increase periprocedural vessel damage. OCT is a highly sensitive imaging

modality that can detect acute complications after stent implantation (e.g. edge dissection, intrastent dissections and tissue prolapse between the stent struts)². The clinical relevance of these findings on OCT, and their relation to restenosis, are not well established. Serial OCT studies could help to understand a possible link between periprocedural vessel trauma and future restenosis in DES.

Potential mechanisms implicated in the pathogenesis of restenosis can be readily identified with OCT; these may include gaps between stents, incomplete lesion coverage or stent under-expansion²⁴. Stent fracture with subsequent defects in local drug delivery has been associated with restenosis after DES implantation, especially with SES. Stent fractures are identified on OCT by the lack of circumferential struts as well as distortion of stent and lumen geometry²⁵.

Preclinical and IVUS studies have confirmed that the non-uniform distribution of stent struts can affect drug delivery and thus have an influence on restenosis. Strut distribution can be studied *in vivo* with OCT, where preliminary experiences in phantom models demonstrated significant differences between different DES types²⁶. The effect of different devices used to treat restenosis (such as cutting balloon or scoring balloon) can also be assessed with OCT^{27,28}.

Furthermore, OCT can provide further insight into the association between restenosis and other entities such as stent thrombosis¹¹. Due to its high resolution, OCT is able to provide detailed characteristics of restenotic lesions that were not previously appreciated by IVUS. It has been previously noted that the presence of a high reflective endoluminal layer and a low reflective abluminal layer around the struts may represent a layered structure of the neointima indicating the presence of different tissue components in the restenotic tissue^{29,30} (Figure 3).

OCT can also quantify the symmetry of tissue coverage. This has been shown to be related to clinical presentation³. Furthermore, some data suggest that OCT might be able to detect the presence of

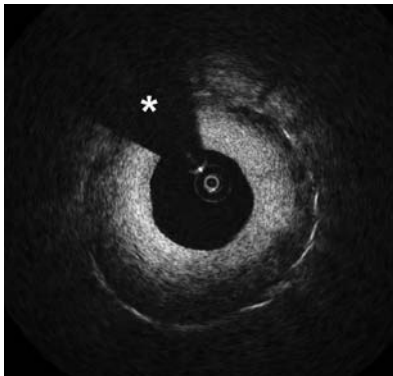


Figure 3. Stent restenosis. Stent restenosis 4 months after implantation of a drug eluting stent. Note the layered appearance of the restenotic tissue with a inner high backscattering layer and an external low backscattering layer. * guidewire artifact.

neovasculature in the neointimal tissue³¹. The clinical implications of these OCT findings in restenotic lesions remains unknown and will require further evaluation.

Evaluation of new generation DES

Among the new stent technologies, biodegradable stents have emerged as one of the most promising. Metallic stents remain forever in the vessel as foreign material with the potential risk of stent thrombosis. In case of the need for secondary revascularisation, metallic stenting can preclude surgical treatment. Furthermore, they do not allow proper assessment by noninvasive imaging modalities such as multislice computed tomography or magnetic resonance imaging. A fully biodegradable stent that could provide scaffolding and drug delivery until the vessel has healed and then disappear completely might potentially avoid the previously mentioned drawbacks of permanent metallic stenting. OCT has demonstrated its value for the evaluation of bioabsorbable stents through its ability to image *in vivo* the morphological changes of the stent and the vessel wall during the absorption process. The ABSORB trial showed the feasibility of implantation of the bioabsorbable everolimus-eluting coronary stent (BVS; Abbott Laboratories, IL, USA), composed of a poly-L-lactic acid backbone, coated with a degradable polymer /everolimus matrix. OCT was performed in a subset of patients after stent implantation, at six months and at two years follow-up. In this group of patients, OCT was able to demonstrate temporal structural changes in the bioabsorbable stent with a reduction in the number of visible struts and modifications in the appearance of the struts^{32,33}. OCT has also been able to characterise the degradation process of the bioabsorbable magnesium-based AMS stent (Biotronik; Erlangen, Germany) in a porcine coronary model³⁴.

OCT for the assessment of surgical coronary grafts

In the past, OCT imaging of coronary grafts has been limited by challenging vessel anatomy, the vessel size and the need of vessel occlusion. Some of those limitations, however, have been supplanted by advances in OCT technology. For instance, OCT can now be performed without the need of vessel occlusion. In the new generation systems (also called ODFI, swept source, Fourier domain) the optical probe is integrated in a short monorail catheter with better navigability properties than the current commercial systems (ImageWire™). This may facilitate imaging of vessels with complex anatomy such as coronary grafts. The increase in the scan diameter may also allow visualisation of bigger vessels. Preliminary experience, in select cases in our centre, has demonstrated that *in vivo* imaging of venous and arterial coronary grafts with OCT is feasible and can provide valuable information (Figure 4). IVUS studies have suggested that saphenous vein grafts (SVG) undergo an “arterialisation” process with intimal fibrous thickening, medial hypertrophy and lipid deposition that creates an echolucent zone around the vessel that mimics the arterial external elastic membrane (EEM)³⁵. In early stage SVG, OCT shows wall thickening with a monolayered appearance and without a visible EEM (Figure 5). In later stages, the extent and distribution of the atherosclerotic disease along the graft can be visualised with great detail. After stenting OCT can assess strut apposition and vessel injury (Figure 5). SVGs are

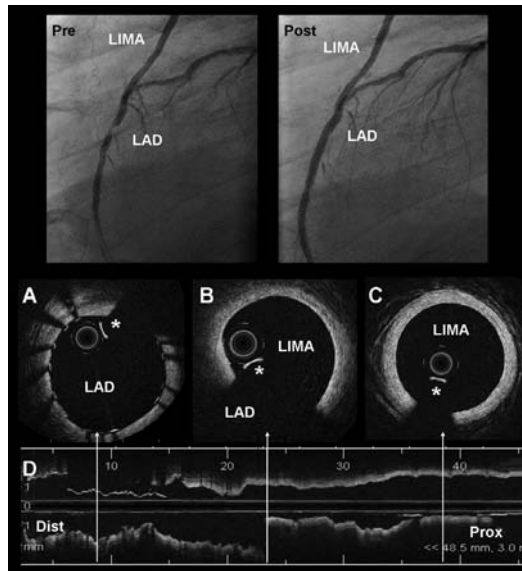


Figure 4. Optical coherence tomography (OCT) visualisation of left internal mammary artery (LIMA). The superior panel shows the angiogram of a patient with a graft of LIMA to the LAD. The left panel (Pre) shows a significant lesion on the LAD distal to the anastomosis of the LIMA. The right panel (Post) shows the result after implantation of a stent in the LAD. A: OCT cross section of the LAD with the implanted stent. B: OCT cross section on the region of the anastomosis of the LIMA to the LAD. C: OCT image of the LIMA that shows only intimal thickening without signs of significant atherosclerosis disease. D: longitudinal OCT view. The arrows indicate the location of the cross sections A, B and C. * Guidewire artifact

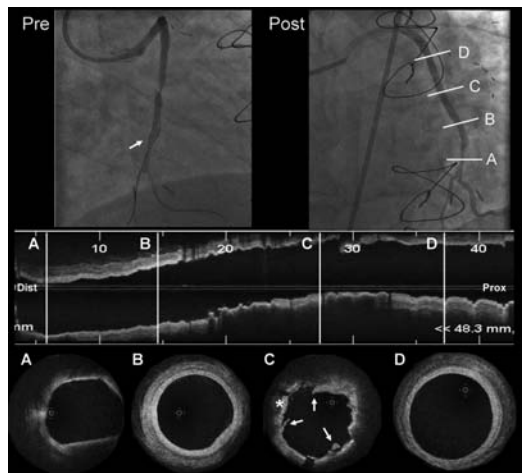


Figure 5. Optical coherence tomography (OCT) visualisation of saphenous vein graft (SVG) after stenting. Pre: angiogram showing a significant focal stenosis in a SVG to the obtuse marginal (white arrow indicates the distal protection device, FilterWire™). Post: angiographic result after treatment of the lesion with stent implantation. A to D show OCT longitudinal and cross sections images of the SVG after treatment. A: distal segment of the SVG showing low backscattering plaque with diffuse borders (suggestive of lipid content) but without significant lumen stenosis. B: SVG showing wall thickening (more pronounced at 5 o'clock). C: SVG in the stented region. The stent struts are well apposed and it can be observed the presence of tissue prolapse (*) and intrastent dissections (white arrows). D: OCT cross section of the proximal SVG segment. The vessel shows mono-layered appearance with minimal wall thickening and without signs of significant atherosclerotic disease. Dist: distal Prox: proximal.

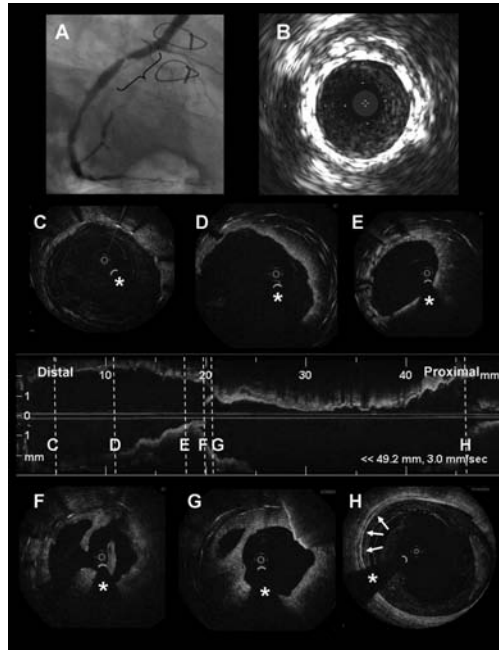


Figure 6. Saphenous vein graft restenosis imaged with optical coherence tomography. The figure shows the case of a patient treated with coronary artery bypass surgery in 1994. Saphenous vein grafts (SVG) were implanted in the LAD, diagonal, obtuse marginal and RCA. In 2003 and 2005 the patient underwent stent implantation in the SVG to the RCA for acute coronary syndrome. In 2008 the patient was referred to the catheterisation laboratory for stable angina. A: coronary angiogram showing a stent restenosis in the SVG to the RCA. B: IVUS image in the region of the restenosis showing different stent layers and severe neointimal growth. C to H show OCT longitudinal and cross sectional images of the SVG to the RCA. C: distal part of one of the stents previously implanted in the SVG. D: shows the different layers of stents previously implanted in the SVG. E: restenosis area. Multiple stent layers and severe neointimal growth are visible. F and G: restenosis area showing severe neointimal growth and irregular material protruding in the lumen. H: proximal venous graft showing a calcified plaque (white arrows) but without lumen stenosis. * Guidewire artefact.

known to have a high risk of non-reflow phenomenon after stenting. This has been related to the presence of distal embolisation during stent implantation. The presence of mobile elements inside SVG (potentially at risk of embolisation) has been described by IVUS and can be visualised with higher accuracy by OCT (Figure 6). At follow-up, OCT can provide unique information about the characteristics of stent restenosis in grafts (Figure 6).

Recent reports suggest that OCT could be useful as an intraoperative tool to select conduits for coronary artery bypass graft surgery (CABG). The outcome of CABG is related to pre-existent pathology on the harvested vessel and with vessel injury during the harvesting. Brown et al evaluated the characteristics of radial arteries and saphenous veins with OCT obtained from 35 patients scheduled for CABG. They demonstrated that OCT was able to visualise atherosclerotic lesions in the radial arteries and vessel injury related to the harvesting process (intimal trauma, thrombus)³⁶. The same group showed that OCT is also able to evaluate and quantify the degree of spasm and vessel injury in radial arteries harvested with different methods (harmonic scalpel

vs electrocautery; open vs endoscopic harvest)^{37,38}. This ability to assess the quality of the conduits during harvesting opens new possibilities for the application of OCT in the surgical field.

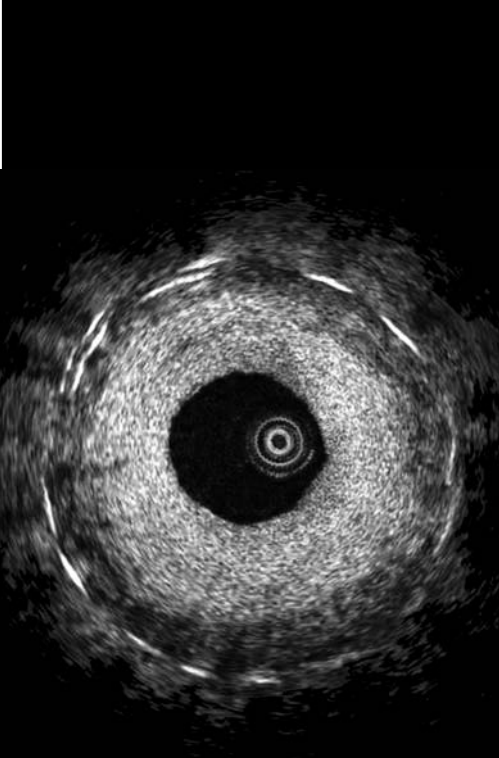
References

1. Tearney GJ, Jang IK, Kang DH, Aretz HT, Houser SL, Brady TJ, Schlendorf K, Shishkov M, Bouma BE. Porcine coronary imaging in vivo by optical coherence tomography. *Acta Cardiol* 2000;55:233-7.
2. Bouma BE, Tearney GJ, Yabushita H, Shishkov M, Kauffman CR, DeJoseph Gauthier D, MacNeill BD, Houser SL, Aretz HT, Halpern EF, Jang IK. Evaluation of intracoronary stenting by intravascular optical coherence tomography. *Heart* 2003;89:317-20.
3. Gonzalo N, Barlis P, Serruys PW, Garcia-Garcia HM, Onuma Y, Ligthart J, Regar E. Incomplete Stent Apposition And Delayed Tissue Coverage Are More Frequent In Drug Eluting Stents Implanted During Primary Percutaneous Coronary Intervention For ST Elevation Myocardial Infarction Than In Drug Eluting Stents Implanted For Stable/Unstable Angina. Insights from Optical Coherence Tomography. *J Am Coll Cardiol Intv* 2009; In press.

4. Chen BX, Ma FY, Luo W, Ruan JH, Xie WL, Zhao XZ, Sun SH, Guo XM, Wang F, Tian T, Chu XW. Neointimal coverage of bare-metal and sirolimus-eluting stents evaluated with optical coherence tomography. *Heart* 2008;94:566-70.
5. Xie Y, Takano M, Murakami D, Yamamoto M, Okamatsu K, Inami S, Seimiya K, Ohba T, Seino Y, Mizuno K. Comparison of neointimal coverage by optical coherence tomography of a sirolimus-eluting stent versus a bare-metal stent three months after implantation. *Am J Cardiol* 2008;102:27-31.
6. Matsumoto D, Shite J, Shinke T, Otake H, Tanino Y, Ogasawara D, Sawada T, Paredes OL, Hirata K, Yokoyama M. Neointimal coverage of sirolimus-eluting stents at 6-month follow-up: evaluated by optical coherence tomography. *Eur Heart J* 2007;28:961-7.
7. Tanigawa J, Barlis P, Dimopoulos K, Di Mario C. Optical coherence tomography to assess malapposition in overlapping drug-eluting stents. *EuroInterv* 2008;3:580-583.
8. Tanigawa J, Barlis P, Di Mario C. Heavily calcified coronary lesions preclude strut apposition despite high pressure balloon dilatation and rotational atherectomy: in-vivo demonstration with optical coherence tomography. *Circ J* 2008;72:157-60.
9. Tanigawa J, Barlis P, Dimopoulos K, Dalby M, Moore P, Di Mario C. The influence of strut thickness and cell design on immediate apposition of drug-eluting stents assessed by optical coherence tomography. *Int J Cardiol* 2008.
10. Cook S, Wenaweser P, Togni M, Billinger M, Morger C, Seiler C, Vogel R, Hess O, Meier B, Windecker S. Incomplete stent apposition and very late stent thrombosis after drug-eluting stent implantation. *Circulation* 2007;115:2426-34.
11. Barlis P, Di Mario C, van Beusekom HMM, Maugeness AM, Gonzalo N, Regar E. Novelities in Cardiac Imaging – Optical Coherence Tomography (OCT). A critical appraisal of the safety concerns tempering the success of drug-eluting stents. *EuroIntervention* 2008 Vol. 4 (Supplement C) C22-C26.
12. Schinkel AFL, Barlis P, van Beusekom HMM, Serruys PW, Regar E. OCT Findings in Very Late (4 Years) Paclitaxel-Eluting Stent Thrombosis. *J Am Coll Cardiol Interv* August 2008; 1: 449-451.
13. Finn AV, Joner M, Nakazawa G, Kolodgie F, Newell J, John MC, Gold HK, Virmani R. Pathological correlates of late drug-eluting stent thrombosis: strut coverage as a marker of endothelialization. *Circulation* 2007;115:2435-41.
14. Gonzalo N, Garcia-Garcia HM, Serruys PW, Commissaris K, Bezerra H, Gobbens P, Costa MA, Regar E. Reproducibility of quantitative optical coherence tomography for stent analysis. *EuroInterv*. 2009; In press.
15. Prati F, Zimarino M, Stabile E, Pizzicannella G, Fouad T, Rabozzi R, Filippini A, Pizzicannella J, Cera M, De Caterina R. Does optical coherence tomography identify arterial healing after stenting? An in vivo comparison with histology, in a rabbit carotid model. *Heart* 2008;94:217-21.
16. Yao ZH, Matsubara T, Inada T, Suzuki Y, Suzuki T. Neointimal coverage of sirolimus-eluting stents 6 months and 12 months after implantation: evaluation by optical coherence tomography. *Chin Med J (Engl)* 2008;121:503-7.
17. Takano M, Yamamoto M, Inami S, Murakami D, Seimiya K, Ohba T, Seino Y, Mizuno K. Long-term follow-up evaluation after sirolimus-eluting stent implantation by optical coherence tomography: do uncovered struts persist? *J Am Coll Cardiol* 2008;51:968-9.
18. Kubo T, IT, Kitabata H, Kuroi A, Ueno S, Yamano T, Tanimoto T, Matsuo Y, Masho T, Takarada S, Tanaka A, Nakamura N, Mizukoshi M, Tomobuchi Y, Akasaka T. Comparison of vascular response after sirolimus eluting stent implantation between patients with unstable and stable angina pectoris. A serial optical coherence tomography study. *J Am Coll Cardiol Img* 2008;1.
19. Nakazawa G, Finn AV, Joner M, Ladich E, Kutys R, Mont EK, Gold HK, Burke AP, Kolodgie FD, Virmani R. Delayed arterial healing and increased late stent thrombosis at culprit sites after drug-eluting stent placement for acute myocardial infarction patients: an autopsy study. *Circulation* 2008;118:1138-45.
20. Guagliumi G, Sirvu V, Costa MA, Musumeci G, Trivisonno A, Matiashvili A, Lortkipanidze N, Mihalcsik L, Valsecchi O, Suzuki N, Coletta J, Mintz GS, Maehara A, Parise H, Lansky AJ, Cristea E, Mehran R, Stone GW. Long-Term Strut Coverage of Paclitaxel Eluting Stents Compared with Bare-Metal Stents Implanted During Primary PCI in Acute Myocardial Infarction: A Prospective, Randomized, Controlled Study Performed with Optical Coherence Tomography. HORIZONS-OCT. *Circulation* 2008;118:2309-2317.
21. Barlis P, Regar E, Dimopoulos K, van der Giessen W, van Geuns RJ, van der Ent M, Sianos G, Gonzalo N, de Vries A, Ligthart J, de Feyter P, Ferrante G, Davies SW, Foran J, Collinson J, Leatham J, Clague J, Serruys PW, Di Mario C. A Randomized Optical Coherence Tomography Study of an Erodible versus Durable Polymer-Coated Limus-Eluting Stent. *Am J Cardiol* 2008;Suppl 102:151.
22. Guagliumi G, Musumeci G, Sirbu V, Suzuki N, Biondi Zoccai, Mihalcsik L, Matiashvili A, Trivisonno A, Lortkipanidze N, Fiocca L, Coletta J, Bezerra H, Valsecchi O, Costa MA. A prospective, Randomized, Controlled Study Using Optical Coherence Tomography to Evaluate Strut Coverage of Sirolimus-, Paclitaxel- and Zotarolimus-Eluting Coronary Stents in Long Lesions Requiring Overlapping. TCT Abstract 2008.
23. Buellesfeld L, Lim V, Gerckens U, Mueller R, Grube E. Comparative endoluminal visualization of TAXUS crush-stenting at 9 months follow-up by intravascular ultrasound and optical coherence tomography. *Z Kardiol* 2005;94:690-4.
24. Grube E, Lim V, Buellesfeld L. OCT findings in drug-eluting stents. *London Informa Healthcare*, 2007:161-170.
25. Barlis P, Sianos G, Ferrante G, Del Furia F, D'Souza S, Di Mario C. The use of intra-coronary optical coherence tomography for the assessment of sirolimus-eluting stent fracture. *Int J Cardiol* 2008.
26. Suzuki Y, Ikeno F, Yeung AC. Drug-eluting stent strut distribution: a comparison between Cypher and Taxus by optical coherence tomography. *J Invasive Cardiol* 2006;18:111-4.
27. Kume T, Akasaka T, Yoshida K. Optical coherence tomography after cutting balloon angioplasty. *Heart* 2007;93:546.
28. Takano M, Yamamoto M, Murakami D, Takano H, Asai K, Yasutake M, Seino Y, Mizuno K. Optical coherence tomography after new scoring balloon angioplasty for in-stent restenosis and de novo coronary lesions. *Int J Cardiol* 2009.
29. Tanimoto S AJ, Serruys PW, Regar E. Paclitaxel-eluting stent restenosis shows three - layer appearance by optical coherence tomography. *EuroInterv* 2006;1:484.
30. Takano M, Xie Y, Murakami D, Inami S, Yamamoto M, Ohba T, Seino Y, Mizuno K. Various optical coherence tomographic findings in restenotic lesions after sirolimus-eluting stent implantation. *Int J Cardiol* 2008.
31. Regar E, van Beusekom HM, van der Giessen WJ, Serruys PW. Optical coherence tomography findings at 5-year follow-up after coronary stent implantation. *Circulation* 2005;112:345-346.

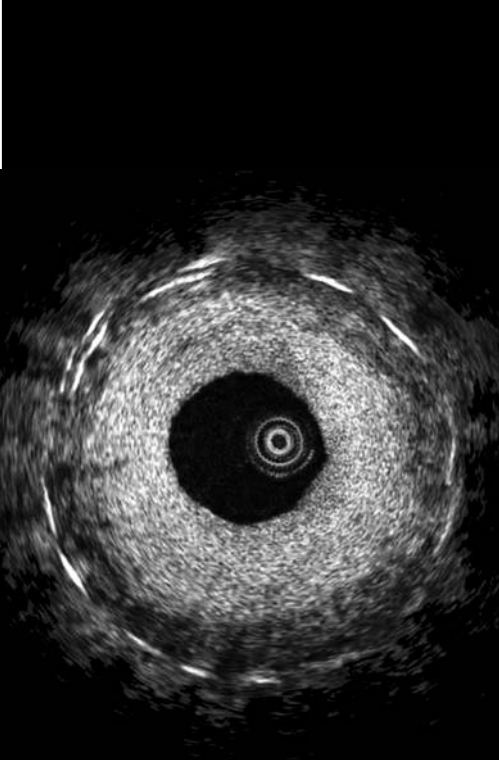
Chapter 8.1

32. Ormiston JA, Serruys PW, Regar E, Dudek D, Thuesen L, Webster MW, Onuma Y, Garcia-Garcia HM, McGreevy R, Veldhof S. A bioabsorbable everolimus-eluting coronary stent system for patients with single de-novo coronary artery lesions (ABSORB): a prospective open-label trial. *Lancet* 2008;371:899-907.
33. Gonzalo N, Serruys PW, Freire R, Ligthart J, van der Giessen W, Bruining N, Regar E. Abstract 5999: Optical Coherence Tomography Findings At Two Years Follow Up In Fully Biodegradable Everolimus Eluting Stents. *Circulation* 2008;118:S_1043-.
34. Slottow TL, Pakala R, Okabe T, Hellinga D, Lovec RJ, Tio FO, Bui AB, Waksman R. Optical coherence tomography and intravascular ultrasound imaging of bioabsorbable magnesium stent degradation in porcine coronary arteries. *Cardiovasc Revasc Med* 2008;9:248-54.
35. Mintz GS, Nissen SE, Anderson WD, Bailey SR, Erbel R, Fitzgerald PJ, Pinto FJ, Rosenfield K, Siegel RJ, Tuzcu EM, Yock PG. American College of Cardiology Clinical Expert Consensus Document on Standards for Acquisition, Measurement and Reporting of Intravascular Ultrasound Studies (IVUS). A report of the American College of Cardiology Task Force on Clinical Expert Consensus Documents. *J Am Coll Cardiol* 2001;37:1478-92.
36. Brown EN, Burris NS, Gu J, Kon ZN, Laird P, Kallam S, Tang CM, Schmitt JM, Poston RS. Thinking inside the graft: applications of optical coherence tomography in coronary artery bypass grafting. *J Biomed Opt* 2007;12:051704.
37. Burris NS, Brown EN, Grant M, Kon ZN, Gibber M, Gu J, Schwartz K, Kallam S, Joshi A, Vitali R, Poston RS. Optical coherence tomography imaging as a quality assurance tool for evaluating endoscopic harvest of the radial artery. *Ann Thorac Surg* 2008;85:1271-7.
38. Brazio PS, Laird PC, Xu C, Gu J, Burris NS, Brown EN, Kon ZN, Poston RS. Harmonic scalpel versus electrocautery for harvest of radial artery conduits: reduced risk of spasm and intimal injury on optical coherence tomography. *J Thorac Cardiovasc Surg* 2008;136:1302-8.



CHAPTER 9

New Generation OCT in Clinical Practice



9.1

Second Generation Optical Coherence Tomography in Clinical Practice. - High speed data acquisition shows excellent reproducibility in patients undergoing percutaneous coronary interventions

Gonzalo N, Tearney GJ, Serruys P.W, van Soest G, Okamura T, Garcia-Garcia HM, van Geuns RJ, van der Ent M, Ligthart J, Bouma BE, Regar E.

Submitted

ABSTRACT

Background: a second generation of optical coherence tomography (OCT) systems (Fourier Domain, FD-OCT) able to perform high speed pullbacks without the need to transiently occlude the coronary artery during imaging has been developed.

Objectives: to assess the reproducibility of FD-OCT systems for plaque characterization and stent implantation assessment in patients undergoing coronary percutaneous interventions.

Methods: Forty-five patients scheduled for percutaneous coronary intervention were enrolled between May and December 2008. FD-OCT acquisition was performed in a non occlusive technique with pullback speeds ranging from 5 to 20 mm/s. The interstudy, interobserver and intraobserver reproducibility for plaque characterization and stent analysis were assessed.

Results: Fourier domain imaging was successfully performed in all patients (n=45). The average flush rate was 3 ± 0.4 ml/s and the contrast volume per pullback was 16.1 ± 3.5 ml. The mean pullback duration and length were 3.2 ± 1.2 sec and 53.3 ± 12.4 mm. The interstudy reproducibility for the visualization of edge dissection, tissue prolapse, intrastent dissection and malapposition was excellent ($\kappa=1$). The kappa values for inter-study, interobserver and intraobserver agreement for plaque characterization were 0.92, 0.82 and 0.95 respectively.

Conclusions: The second generation OCT technology (FD-OCT) with high speed data acquisition shows good inter-study, interobserver and intraobserver reproducibility for plaque characterization and stent implantation assessment in patients undergoing coronary percutaneous interventions.

INTRODUCTION

Optical Coherence Tomography (OCT) has emerged over the last years as one of the most promising intracoronary diagnostic tools(1,2). This light based imaging technique is able to generate images of the coronary artery with a level of resolution (10 μm) never reached before in vivo. This has offered new insights into atherosclerotic plaque pathology as well as into acute and long-term vessel wall response to stent implantation(3-7).

Up to now, the main challenge for a widespread clinical application of intracoronary OCT was a rather complex imaging procedure. Blood causes multiple light scattering and substantial signal attenuation, and needs to be temporally cleared from the vessel during OCT image acquisition. The first generation commercially available time domain (TD) OCT systems employed proximal occlusion of the vessel with a low-pressure balloon (0.5atm), similar to angiography, and simultaneous, distal flush delivery during pullback of the OCT imaging probe (8). This protocol limited the coronary segment that could be imaged, and intrinsically created myocardial ischemia during imaging, restricting OCT to selected patient cohorts(9,10).

The new generation OCT systems [other monikers for the same technology are Fourier domain (FD) OCT, optical frequency domain imaging (OFDI), spectral domain imaging or swept source OCT] were developed to overcome this limitation. Most distinctively, these second generation OCT systems do not require transient balloon occlusion. Unprecedented capacity for data acquisition and pullback speeds (20 mm/sec) allow for the visualization of long coronary segments within few seconds while blood is temporally displaced by the injection of flush through the guiding catheter (11).

While this concept is attractive, there has been no systematic research investigating the impact of such high pullback speeds on the reproducibility of data obtained in the clinical setting. On theoretical grounds, the rapid acquisition reduces the motion artefacts during heart cycle, and thus, potentially sources of error, whereas an increased pitch between consecutive, cross sectional images could add sources of error. The FD-OCT frame rate is typically 100 frames per second, which at a pullback speed 20mm per second, results in 5 frames per mm or a frame pitch of 200 micron. A typical TD-OCT frame rate is 20 frames per second, with a pullback speed of 3 mm per second, resulting in 7 frames per mm or a pitch of 142 micron.

The objective of the present study was to assess the reproducibility of the new generation, intracoronary FD-OCT systems for plaque and stent assessment in vivo. We investigated therefore the reproducibility of morphologic features that

have been described in the past to be of potential clinical relevance in patients undergoing percutaneous coronary intervention (PCI).

METHODS

Study population

Patients scheduled for elective PCI were enrolled between May and December 2008. The study protocol was approved by the Ethics Committee of Erasmus Medical Center. All the patients gave written informed consent.

Technical principles of new generation OCT

OCT uses reflected light to create high-resolution cross sectional images of the vessel. An interferometer splits the light source into two “arms” – a reference arm and a sample arm, which is directed into the tissue. The images are created based on the comparison of the back-reflected optical intensity from the two arms (interference signal).

The first clinically available OCT systems used TD technology while new generation systems are based on FD technology.

Both TD-OCT and FD-OCT use low-coherent near-infrared light. A wavelength around 1300 nm is selected because it minimizes the energy absorption in the light beam caused by protein, water, haemoglobin and lipids. TD-OCT uses a broadband light source and the reference arm contains a moving mirror that allows scanning of each depth position in the image pixel by pixel. This mechanical scanning process limits the rate at which images can be acquired. FD-OCT uses a wavelength-swept laser as a light source and the reference mirror is fixed. This change in technology results in a better signal-to-noise ratio (12) and faster sweeps, allowing a dramatically higher A-line rate, and hence a faster image acquisition and pullback speed than TD-OCT (13,14).

FD-OCT Systems

Two different FD-OCT prototypes were used (LightLab Imaging, Inc, Westford, MA and Wellman Center for Photomedicine, MGH, Boston, MA). All systems use a wavelength-swept laser as a light source. Table 1 resumes the specifications of the second generation systems compared to TD-OCT (LightLab Imaging, Inc, Westford, MA). All FD-OCT imaging catheters had a short monorail design with

Table 1. Comparison of time domain optical coherence tomography (TD-OCT) and the new generation, Fourier domain (FD) OCT systems.

	TD-OCT	FD-OCT
Pullback speed	3 mm/s	Up to 20 mm/s
Frame rate	20 fps	Up to 100 fps
Lines per frame	240	450-500
Axial Resolution	10-20 μ m	10-20 μ m
Lateral Resolution	25-30 μ m	25-30 μ m
Penetration depth	1.5-2 mm	1.5-2 mm
Scan diameter	7 mm	8.3-10 mm
Catheter	ImageWire 0.019"	Rx catheter 2.9-3.2F

Rx: rapid exchange

catheter profiles ranging from 2.4Fr to 3.2Fr, but all of them were compatible with 6F guiding catheters. FD-OCT imaging catheters contained a fibre-optic imaging core covered by and withdrawn within a translucent sheath. The optical imaging core rotated at approximately 100 revolutions per second and the pullback speed ranged from 5 to 20 mm/s using a dedicated pullback device. Data were processed in real-time and digitally stored.

Optical coherence tomography data acquisition

We used standard femoral approach in all patients. Weight adapted, unfractionated heparin was given to maintain an activated clotting time > 300s. After placement of the guiding catheter (6F) into the coronary ostium, a standard PCI guide wire was advanced into the coronary artery in conventional manner. FD-OCT imaging was performed before stenting (cohort A) and after stent implantation (Cohort B). After administration of nitrates (0.2mg NTG ic), the FD-OCT imaging catheter was advanced into the coronary artery in rapid exchange technique,

Radiopaque markers at the distal catheter tip and at the imaging core allowed positioning of the optical probe distal to the region of interest. (Figure 1).After FD-OCT catheter placement, blood was cleared by injection of iso-osmolar contrast (Iodixanol 370, Visipaque™, GE Health Care, Ireland) at 37° Celsius with an injection pump (Mark-V ProVis, Medrad, Inc. Indianola, PA, US; flow rate 3ml/sec) through the guiding catheter. The FD-OCT pullback was started as soon as the artery was cleared from blood and stopped when the imaging core reached the guiding-catheter.

Assessment of interstudy and interobserver reproducibility

Pullbacks in native coronaries as well as after stent implantation were analysed as follows: To evaluate the interstudy reproducibility, a FD-OCT pullback through

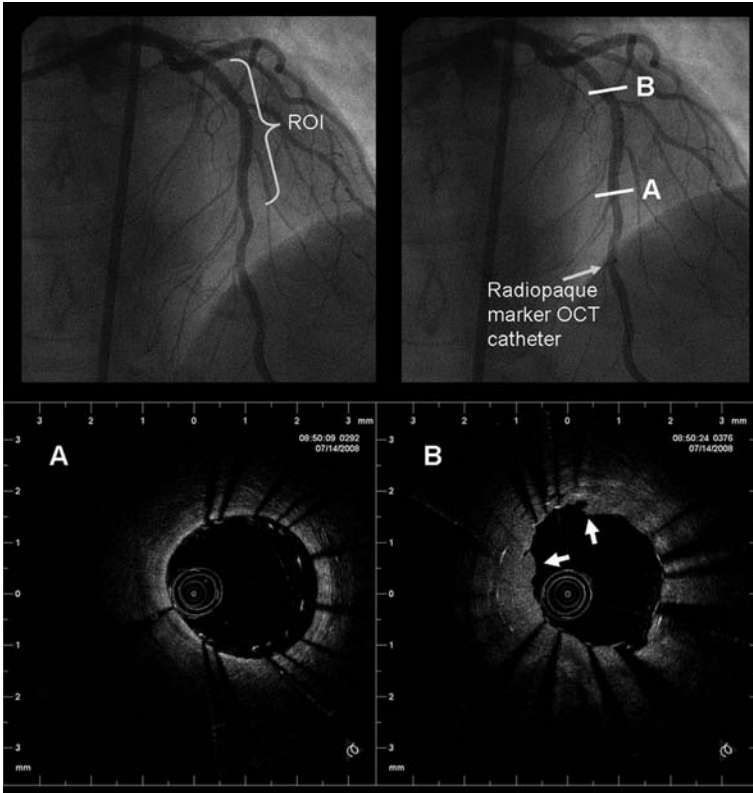


Figure 1. Fourier Domain-OCT image acquisition procedure. The angiogram on the left shows a LAD treated by repeat stenting for stent restenosis. The region of interest (ROI) for the OCT examination was the stented area. The image on the right shows the radiopaque marker of the OCT catheter positioned distal to the ROI. The two lower panels show two FD-OCT images obtained in the stented area (Lightlab Imaging Inc system). A: distal part of the newly implanted stent in which strut malapposition is visible. B: cross section obtained in the region of the restenosis after the new stent implantation. Two layers of struts are visible and the neointimal tissue appears disrupted and protrudes into the lumen (white arrows).

the region of interest was repeated using the same catheter twice under identical conditions in terms of pullback speed, frame rate and flush rate. The catheter was not removed from the artery between the two acquisitions. These two pullbacks were then analyzed independently. To evaluate the interobserver variability, two experienced OCT analysts reviewed the first FD-OCT pullbacks independently. To evaluate intraobserver variability, one observer repeated the analysis of the same pullback one week later.

Stent assessment

After stent implantation, study and observer agreement for the following parameters was evaluated according to the following definitions(15): i) Edge dissection: disruption of the endoluminal vessel surface at the stent edges (5 mm prox and distal) ii) Tissue prolapse: protrusion of tissue between the stent struts without disruption of the continuity of the endoluminal vessel surface iii) Intra-stent dissection: disruption of the vessel endoluminal vessel surface in the stent segment iv) Malapposition: presence of at least one strut separated from the vessel wall (Figure 2). Incidence of these phenomena was assessed on a per vessel basis.

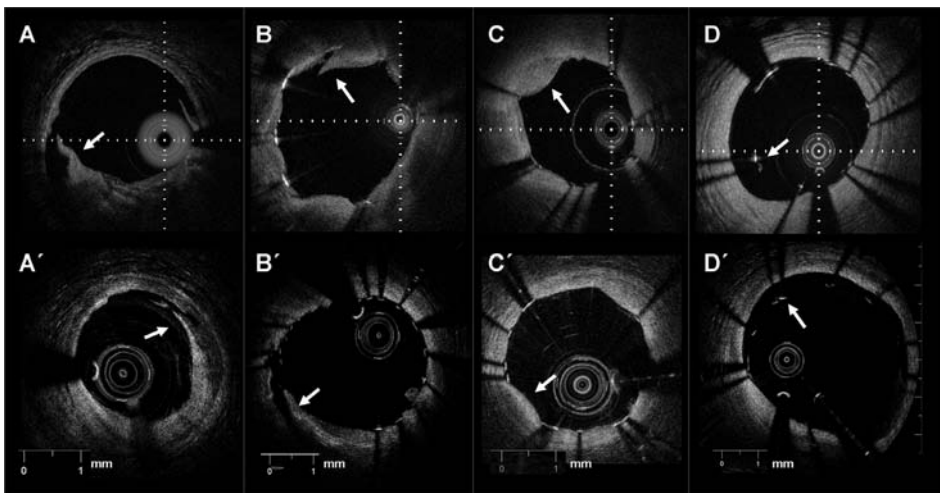


Figure 2. Stent implantation assessment. Clinical examples of edge dissection (A, A'), intrastent dissection (B, B'), tissue prolapse (C,C') and malapposition (D, D') obtained with different Fourier Domain-OCT systems in different patients (upper panel Wellman Center for Photomedicine, MGH; lower panel Lightlab Imaging Inc)

Plaque type assessment

Native coronary segments were evaluated as follows: Sixty corresponding atherosclerotic plaques were selected in both pullbacks using landmarks such as side branches or stent edges. The two observers assessed these pre-selected plaques according to the following definitions: i) Fibrous plaque: homogeneous, highly backscattering regions. ii) Fibrocalcific plaque: low scattering regions with sharply delineated borders. iii) Lipid-rich plaque: diffusely bordered low scattering regions (5). (Figure 3)

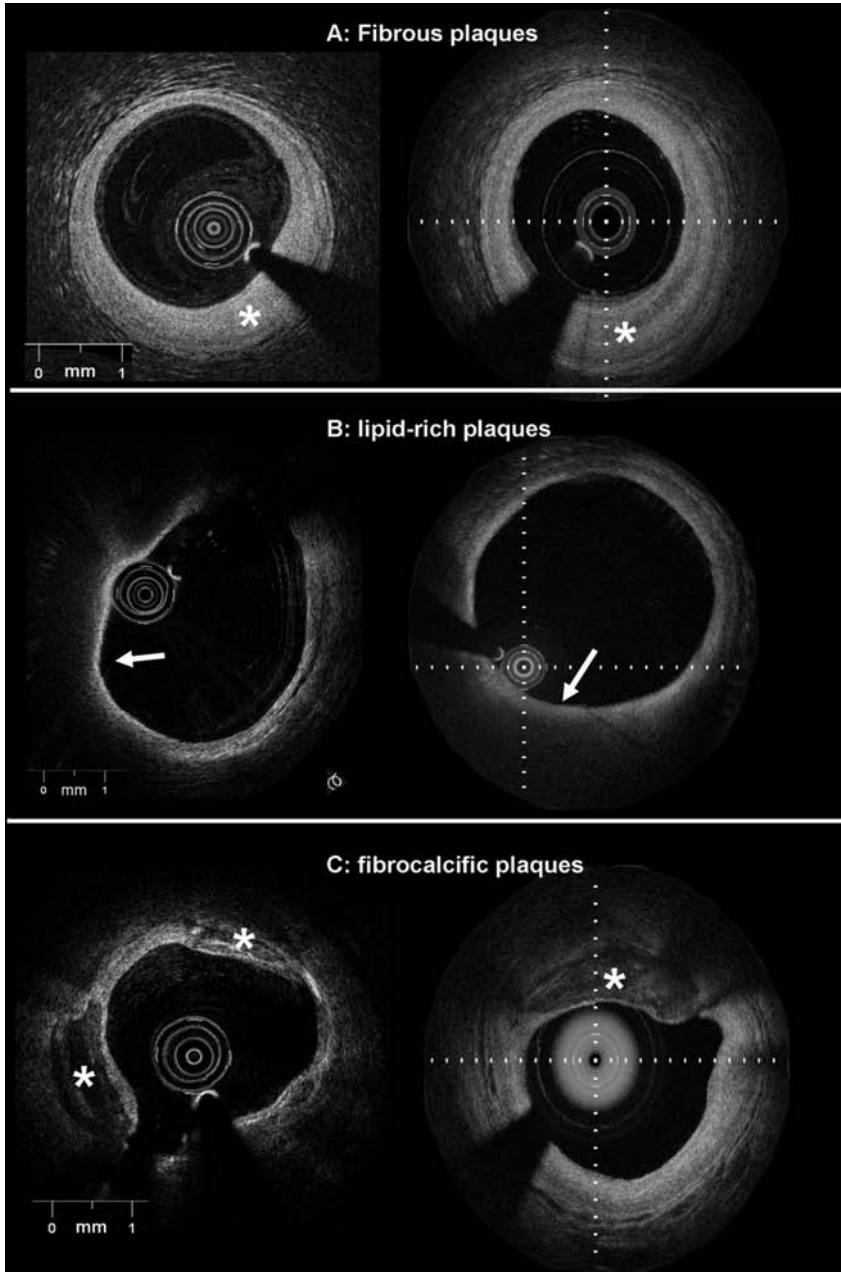


Figure 3. Examples of different plaque types obtained with two Fourier Domain-OCT systems in different patients. A. fibrous plaques (*) are visualized as homogeneous, high scattering regions. B. lipid rich plaques appear as low backscattering regions without sharp borders and usually covered by a fibrous cap (white arrow). C. fibrocalcific plaques (*) appear as low backscattering regions with sharp well delineated borders.

(left panel Lightlab Imaging Inc; right panel Wellman Center for Photomedicine, MGH)

Statistical analysis

Continuous variables are expressed as mean \pm standard deviation and categorical variables are expressed as percentages. The kappa coefficient (K) was used to test the inter-study, interobserver and intraobserver agreement for plaque characterization and stent assessment.

RESULTS

Patient characteristics and FD-OCT imaging success

Forty-five patients (49 vessels) were enrolled in the study. The average age was 63 ± 10 years and 80% were males. The incidence of cardiovascular risk factors was as follows: 23/45 (51.1%) hypertension, 12/45 (26.7%) diabetics, 29/45 (64.4%) dyslipidemia and 13/45 (28.9%) current smoking. Nineteen patients (42.2%) had suffered a previous myocardial infarction, 7/45 (15.6%) had coronary artery bypass surgery and 22/45 (48.9%) had previous PCI. The indication for the elective PCI was stable angina in 31/45 (68.8%), unstable angina in 10/45 (22.2%) and acute myocardial infarction in 4/45 (8.9%).

The imaging probe could be positioned successfully in the coronary artery in all patients. In, $n = 10$ patients, FD-OCT was performed before and after stent implantation at the discretion of the operator. Ninety-seven pullbacks showed excellent image quality. Artefacts that did not allow a proper image assessment were observed in 12 pullbacks and 2 pullbacks were not evaluable due to incomplete blood clearance. The procedural characteristics are summarized in Table 2.

Table 2. Fourier Domain-OCT imaging characteristics.

Vessel	
LAD	21/49 (42.8%)
LCX	14/49 (28.6%)
RCA	13/49 (26.6%)
LIMA	1/49 (2.0%)
Pullback Speed	
20 mm/s	32/49 (65.3%)
10 mm/s	10/49 (20.4%)
15 mm/s	1/49 (2.0%)
5 mm/s	6/49 (12.3%)
Flush rate (ml/s)	3 ± 0.4
Pullback duration (sec)	3.2 ± 1.2
Pullback length (mm)	53.3 ± 12.4
Contrast volume per pullback (ml)	16.1 ± 3.5

During FD-OCT imaging, transient chest pain and ECG changes were observed in 8% and 10% of the patients respectively. The ECG changes consisted of ST depression or T wave changes. ST elevation was not observed in any case. No coronary dissection, perforation spasm, embolisation, arrhythmia or other adverse event occurred.

Stent assessment reproducibility

OCT analysis after stent implantation was performed in 27 patients (28 vessels). Edge dissection was observed in 14 vessels (50%). Twenty-five (89%) showed evidence of tissue prolapse and 26 (93%) showed intrastent dissection. Malapposition of at least one strut was visible in 23 vessels (82%). The interstudy reproducibility (n=17 vessels) for the visualization of edge dissection, tissue prolapse, intrastent dissection and malapposition was excellent ($\kappa=1$ $p<0.001$). The kappa values for inter and intraobserver reproducibility are shown in Table 3.

Table 3. Inter and intraobserver reproducibility for stent assessment.

	Interobserver	Intraobserver
Malapposition	0.83	0.83
Edge dissection	0.77	1
Tissue prolapse	0.78	1
Intrastent dissection	1	1

The values in the table indicate the kappa coefficients for each parameter.

Plaque characterization reproducibility

A total of 60 plaques were identified in both pullbacks. Table 4 summarizes the classification results. There was agreement between the 2 pullbacks for plaque classification in 57 out of the 60 plaques ($\kappa =0.92$, $p<0.001$) (Figure 4). Interobserver variability showed agreement for 2 observers in the classification of 53 out of 60 plaques ($\kappa =0.82$, $p<0.001$). The intraobserver variability showed agreement in the classification of 58 out of 60 plaques ($\kappa =0.95$, $p<0.001$).

DISCUSSION

The main findings of the present study are: The new generation, FD-OCT technology with high speed pullback i) has excellent inter-study reproducibility in vivo ii) allows for reproducible plaque classification iii) allows assessment of

Table 4. Interstudy, interobserver and intraobserver reproducibility for plaque characterization.

Plaque type pb1					
	Fibrous	Lipid-rich	Fibrocalcific	Total	
Plaque type pb2	Fibrous	19	1	0	20
	Lipid-rich	2	18	0	20
	Fibrocalcific	0	0	20	20
	Total	21	19	20	60
Plaque type observer1					
	Fibrous	Lipid-rich	Fibrocalcific	Total	
Plaque type observer2	Fibrous	18	1	1	20
	Lipid-rich	3	16	1	20
	Fibrocalcific	1	0	19	20
	Total	22	17	21	60
Plaque type observation1					
	Fibrous	Lipid-rich	Fibrocalcific	Total	
Plaque type observation2	Fibrous	19	1	0	20
	Lipid-rich	1	19	0	20
	Fibrocalcific	0	0	20	20
	Total	20	20	20	60

Pb= pullback

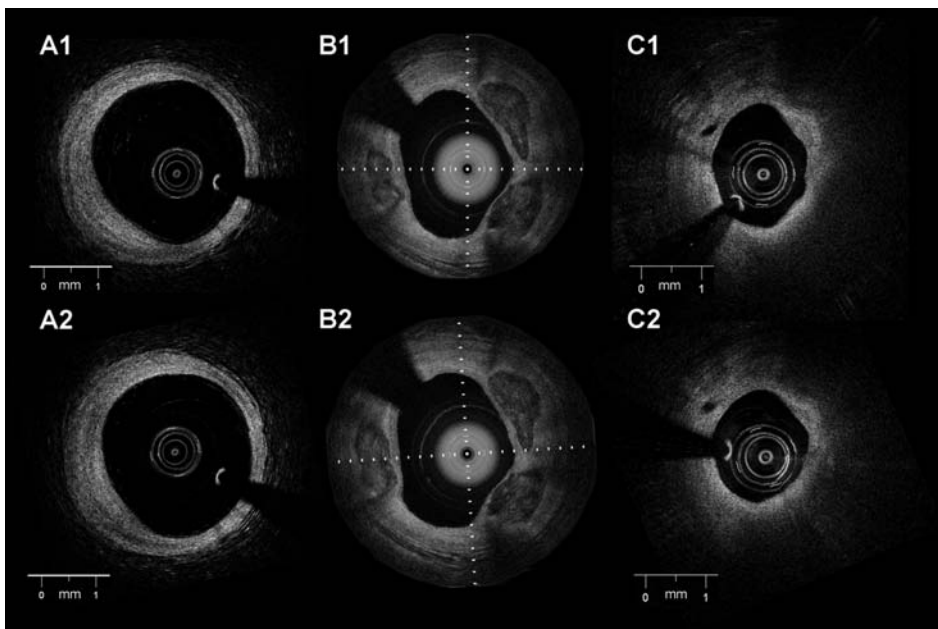


Figure 4. Inter-study reproducibility for plaque characterization: The figure shows corresponding images of the same plaques obtained in two different pullbacks in the artery. A1 and A2: fibrous plaque. B1 and B2: fibrocalcific plaque C1 and C2: lipid-rich plaque (A and C Lightlab Imaging Inc; B Wellman Center for Photomedicine, MGH).

periprocedural vessel trauma associated with coronary stent implantation with low interobserver, intraobserver and interstudy variability.

The present study also confirms that the new OCT systems allow to visualize longer coronary segments (average 54.4 ± 12.5 mm) in less time (average 3.5 ± 1.4 sec) and with less flush volume as compared to previously reported data for time domain OCT(9)

OCT has rapidly evolved to an attractive intracoronary imaging tool for the interventional cardiologists as it offers the potential to address clinically relevant issues to improve routine stent implantation and in consequence, potentially long term outcome. Its high in-vivo resolution allows for an accurate assessment of the mechanical stent vessel wall interaction, including strut apposition and periprocedural dissections(3,15). In the drug-eluting stent era, reasons for failure, including restenosis and late stent thrombosis are poorly understood. In this particular clinical scenario, detailed assessment of the vascular microstructure might be helpful to prevent potentially life threatening events, such as stent thrombosis, as it has been linked to incomplete healing, mechanical stent failure and incomplete coverage of lipid rich or necrotic core lesions(3,4,16-19). The relatively complex imaging procedure hampered the use of the first generation, time domain OCT in patients undergoing PCI. In the present study, we evaluated the new FD-OCT systems that simplify the acquisition procedure and can contribute to spread the clinical application of this imaging technology.

Stent assessment reproducibility

OCT has proven useful for the evaluation of the acute effects of stent implantation on the vessel wall(3,15,20). In the present study, a high proportion of the patients showed evidence of tissue prolapse between the stent struts or intra-stent dissections, likewise edge dissections were visible in half of the cases. Even more pronounced, malapposition of at least one individual strut was observed in the majority of the cases. The inter-study reproducibility for the identification of edge dissection, tissue prolapse, intrastent dissection and malapposition was excellent. The inter and intraobserver reproducibility showed a certain degree of variability, especially for malapposition assessment. In the present study, malapposition was evaluated by visual assessment. This qualitative analysis can be affected by the artefact of the shadow produced by the struts. Furthermore, in drug-eluting stents, the presence of polymer must be taken into account when evaluating malapposition and a correction for the strut thickness of each individual stent type should be applied. The use of a quantitative method to define malapposition could help improving the inter and intraobserver reproducibility(21).

The assessment of stent malapposition is of clinical relevance as there is IVUS data suggesting a possible relation between this phenomenon and stent thrombosis(22). Previous studies have suggested increased malapposition at overlap areas and in closed cell designs(21). This could represent a potential link to stent fracture and restenosis. Second-generation OCT has made this information much more accessible due to a simplified acquisition procedure. This greatly facilitates studies to understand the clinical relevance of these findings in large patient populations, especially with quantitative assessment methods for malapposition.

Plaque characterization reproducibility

The present study demonstrates also an excellent interstudy reproducibility for plaque characterization. Fifty-seven out of the 60 plaques were classified congruently in both pullbacks. There were only 3 cases of misclassification between fibrous and lipid-rich plaques. This could be explained by the presence of artefacts derived from the catheter position(23). The observed inter and intraobserver variability for plaque characterization is in line with reported with time domain OCT in-vitro data ($k=0.88$ and 0.91 for inter and intraobserver respectively)(5). In contrast to earlier reported data, that have highlighted the risk of misclassification between lipid-pools and calcium deposits(24), in our series the most frequent disagreement between observers was for the classification of fibrous and lipid-rich plaques. Quantitative plaque characterization methods under development could help to overcome the limitations of observer-dependent, visual evaluation (25). Three-dimensional reconstructions of human coronary stented arteries with plaque characterization and macrophages detection derived from optical frequency domain imaging have been reported(11). This opens new possibilities for the in vivo evaluation of coronary atherosclerosis and the effect of coronary stenting.

The assessment of plaque characteristics in the catheterization laboratory can be helpful to guide PCI (e.g. to recognize the lower distensibility of heavily calcified lesions) and has potential value for the detection of plaques with high risk of rupture. When compared to histology, OCT has proven to have high sensitivity and specificity to detect some of the features associated with rupture-prone lesions such as necrotic core, presence of macrophages and thin fibrous cap(5,6,26-30).

LIMITATIONS

The present study is observational and with a limited sample size.

CONCLUSIONS

The second generation OCT technology (FD-OCT) with high speed data acquisition shows good inter-study, interobserver and intraobserver reproducibility for plaque characterization and stent implantation assessment in patients undergoing PCI.

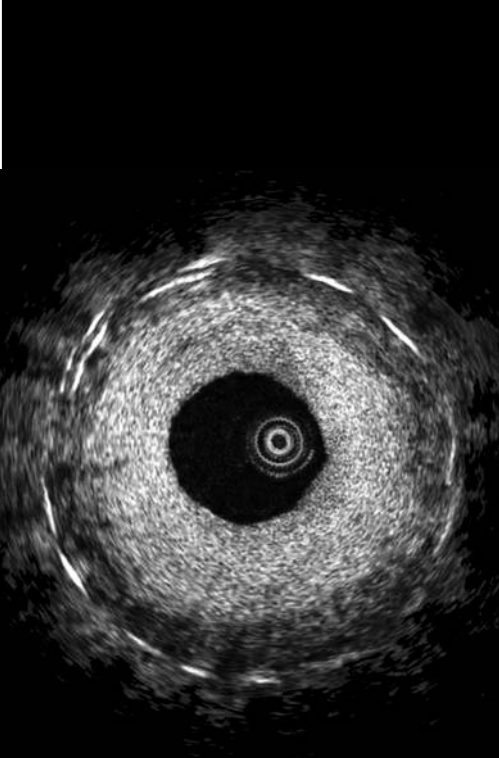
ACKNOWLEDGMENTS

This study was supported in part by Ligthlab Imaging Inc and the Wellman Center of Photomedicine. We would like to thank Robert Beurskens for invaluable technical assistance with the imaging systems.

REFERENCES

1. Regar E, van Leeuwen A, Serruys PW ed. Optical coherence tomography in cardiovascular research. . London: Informa Healthcare, 2007.
2. Gonzalo N, Serruys PW, Regar E. Optical coherence tomography: clinical applications and the evaluation of DES. *Minerva Cardioangiol* 2008;56:511-25.
3. Bouma BE, Tearney GJ, Yabushita H, et al. Evaluation of intracoronary stenting by intravascular optical coherence tomography. *Heart* 2003;89:317-20.
4. Prati F, Zimarino M, Stabile E, et al. Does optical coherence tomography identify arterial healing after stenting? An in vivo comparison with histology, in a rabbit carotid model. *Heart* 2008;94:217-21.
5. Yabushita H, Bouma BE, Houser SL, et al. Characterization of human atherosclerosis by optical coherence tomography. *Circulation* 2002;106:1640-5.
6. Tearney GJ, Yabushita H, Houser SL, et al. Quantification of macrophage content in atherosclerotic plaques by optical coherence tomography. *Circulation* 2003;107:113-9.
7. Gonzalo N, Serruys PW, Okamura T, et al. Optical coherence tomography patterns of stent restenosis. *Am Heart J* 2009;158:284-93.
8. Asawa K, Kataoka T, Kobayashi Y, et al. Method analysis for optimal continuous imaging using intravascular optical coherence tomography. *J Cardiol* 2006;47:133-41.
9. Barlis P, Gonzalo N, Di Mario C, et al. A Multi-Centre Evaluation of the Safety of Intra-Coronary Optical Coherence Tomography. *Eurointervention* 2009;5.
10. Yamaguchi T, Terashima M, Akasaka T, et al. Safety and feasibility of an intravascular optical coherence tomography image wire system in the clinical setting. *Am J Cardiol* 2008;101:562-7.
11. Tearney G, Waxman S, Shishkov M, et al. Three-Dimensional Coronary Artery Microscopy by Intracoronary Optical Frequency Domain Imaging. *J Am Coll Cardiol Img* 2008;1:752-761.
12. Choma M, Sarunic M, Yang C, et al. Sensitivity advantage of swept source and Fourier domain optical coherence tomography. *Opt. Express* 2003;11:2183-2189.
13. Yun SH, Tearney GJ, Vakoc BJ, et al. Comprehensive volumetric optical microscopy in vivo. *Nat Med* 2006;12:1429-33.
14. Liu B, Brezinski ME. Theoretical and practical considerations on detection performance of time domain, Fourier domain, and swept source optical coherence tomography. *J Biomed Opt* 2007;12:044007.
15. Gonzalo N, Serruys PW, Okamura T, et al. Optical Coherence Tomography Assessment Of The Acute Effects Of Stent Implantation On The Vessel Wall. A Systematic Quantitative Approach. *Heart* 2009.
16. Matsumoto D, Shite J, Shinke T, et al. Neointimal coverage of sirolimus-eluting stents at 6-month follow-up: evaluated by optical coherence tomography. *Eur Heart J* 2007;28:961-7.
17. Barlis P, DiMario C, van Beusekom HMM, et al. Novelities in Cardiac Imaging – Optical Coherence Tomography (OCT). A critical appraisal of the safety concerns tempering the success of drug-eluting stents *Eurointervention* 2008;4 Suppl C:C22-6

18. Gonzalo N, Barlis P, Serruys PW, et al. Incomplete stent apposition and delayed tissue coverage are more frequent in drug-eluting stents implanted during primary percutaneous coronary intervention for ST-segment elevation myocardial infarction than in drug-eluting stents implanted for stable/unstable angina: insights from optical coherence tomography. *JACC Cardiovasc Interv* 2009;2:445-52.
19. Finn AV, Joner M, Nakazawa G, et al. Pathological correlates of late drug-eluting stent thrombosis: strut coverage as a marker of endothelialization. *Circulation* 2007;115:2435-41.
20. Jang IK, Tearney G, Bouma B. Visualization of tissue prolapse between coronary stent struts by optical coherence tomography: comparison with intravascular ultrasound. *Circulation* 2001;104:2754.
21. Tanigawa J, Barlis P, Dimopoulos K, Di Mario C. Optical coherence tomography to assess malapposition in overlapping drug-eluting stents. *Eurointervention* 2008;3:580-583.
22. Cook S, Wenaweser P, Togni M, et al. Incomplete stent apposition and very late stent thrombosis after drug-eluting stent implantation. *Circulation* 2007;115:2426-34.
23. Van Leeuwen TG, Faber DJ, Aalders MC Measurement of the axial point spread function in scattering media using single-mode fiber-based optical coherence tomography." *IEEE Journal Of Selected Topics In Quantum Electronics* 2003;9:227-233.
24. Manfrini O, Mont E, Leone O, et al. Sources of error and interpretation of plaque morphology by optical coherence tomography. *Am J Cardiol* 2006;98:156-9.
25. Van Soest G, Goderie TPM, Regar E, et al. Atherosclerotic tissue characterization in vivo by optical coherence tomography attenuation imaging. *Journal of Biomedical Optics* 2009;in press.
26. Gonzalo N, Garcia-Garcia HM, Regar E, et al. In vivo assessment of high-risk coronary plaques at bifurcations with combined intravascular ultrasound and optical coherence tomography. *JACC Cardiovasc Imaging* 2009;2:473-82.
27. Barlis P, Serruys PW, Gonzalo N, et al. Assessment of Culprit and Remote Coronary Narrowings Using Optical Coherence Tomography with Long-Term Outcomes. *Am J Cardiol* 2008.
28. Gonzalo N, Serruys PW, Barlis P, et al. Multi-modality intra-coronary plaque characterization: A pilot study. *Int J Cardiol* 2008.
29. Kubo T, Imanishi T, Takarada S, et al. Assessment of culprit lesion morphology in acute myocardial infarction: ability of optical coherence tomography compared with intravascular ultrasound and coronary angiography. *J Am Coll Cardiol* 2007;50:933-9.
30. Kume T, Akasaka T, Kawamoto T, et al. Measurement of the thickness of the fibrous cap by optical coherence tomography. *Am Heart J* 2006;152:755 e1-4.



SUMMARY AND CONCLUSIONS

SUMMARY AND CONCLUSIONS

The high resolution images obtained with OCT have provided new insights into coronary atherosclerosis and stent-vessel wall interaction. The technology refinement achieved in the last years has made this imaging modality less procedurally demanding opening its possibilities for clinical use. The present thesis provides important data regarding the safety of image acquisition in the clinical setting, the validation of quantitative OCT analysis and the potential clinical applications of OCT for atherosclerosis assessment and stents evaluation. Furthermore, it attempts to standardize and to systematically appraise OCT findings in several clinical scenarios.

Safety of OCT

We evaluated the safety of OCT in a multicentre registry that included cases acquired with and without balloon occlusion. The majority of events recorded were transitory chest pain or ECG changes. Major complications were uncommon (ventricular fibrillation 1.1%, air embolism 0.6%, vessel dissection 0.2%) and they were mainly related with deep guide catheter intubation or balloon occlusion.

Quantitative analysis with OCT

Our validation study for lumen measurements demonstrated that both OCT and IVUS overestimated the lumen area in comparison with histomorphometry in fixed human coronary arteries. The *in vivo* study demonstrated that lumen dimensions measured by IVUS are larger than those measured with OCT and showed the impact of the OCT acquisition technique (occlusive or non-occlusive) in the lumen measurements.

We developed a systematic methodology for stent analysis at follow up with OCT and demonstrated an excellent reproducibility of the technique for struts number count, incomplete stent apposition and struts tissue coverage measurements. This supports the incorporation of OCT into large multi-centre randomised stent trials to complement the angiographic and clinical endpoints. The present thesis includes also the validation of a new full-automated quantitative analysis software for OCT. This type of automatic analysis will help core laboratories to provide accurate and reproducible assessment of OCT findings.

Atherosclerosis assessment with OCT

We evaluated the ability of OCT for coronary atherosclerosis plaque assessment in comparison with histology. OCT showed good correlation with histology in the majority of the cases. However, the study identified some OCT artifacts (scattering caused by dense macrophage infiltration, catheter eccentricity) that can induce misclassification of intimal thickenings as fibroatheromas or thin-cap fibroatheromas. The development of of automatic quantitative methods for plaque characterization based on OCT could improve the diagnostic accuracy of the technique eliminating the observer variability. The comparison with other intracoronary imaging techniques showed in general a good agreement for plaque characterization with some variations inherent to the different imaging resolution and the different classifications used for each technique.

Regarding high-risk plaque detection, OCT can provide very valuable information due to its ability to measure the thickness of the fibrous cap. However its limited penetration precludes the analysis of large plaques. On the contrary, IVUS-VH can image the complete plaque thickness and can identify the presence of necrotic core, but its limited axial resolution does not allow the evaluation of the fibrous cap. The present thesis explored the performance of the combination of OCT and IVUS-VH to identify high-risk plaques. The results using histology as the benchmark, demonstrate an improvement in the diagnostic accuracy when combining the properties of the two techniques. We applied this combined methodology in bifurcations, a complex lesion subset with a higher rate of procedural complications and stent failure. Our study demonstrated a differential distribution of the high-risk plaques along the bifurcation with a preferential localization of the TCFA at the proximal rim of the ostium of the side branch. The thesis includes also a case where OCT allowed the visualization of a human coronary plaque rupture *in vivo* providing new links between the data generated from *ex vivo* studies and the living patient.

In vivo assessment of the effect of coronary stent implantation with optical coherence tomography

Due to its imaging capabilities OCT is a unique tool to assess the relation of the stent with the vessel wall and to evaluate the acute and long-term effects of coronary stent implantation on the vessel structure. These effects might depend on the stent type but also on the underlying plaque. We evaluated the apposition and tissue coverage of struts at follow up in stents implanted during primary PCI for STEMI and stents implanted for stable/unstable angina showing a higher rate

of incomplete stent apposition and uncovered struts in STEMI patients. Those results may be related with the procedural characteristics (abundant thrombus in primary PCI) but also with the characteristics of the plaque leading to the event and being treated with the stent.

Regarding the acute effects of stent implantation, the high-resolution images obtained with OCT have allowed a detailed identification of the vessel damage induced by stent implantation (such as edge dissection, intra-stent dissection and tissue prolapse). In the present thesis we proposed a systematic method for the classification and quantification of these phenomena. Furthermore, our data suggest that the vessel injury caused by the stent (especially at the edges) can be influenced by the composition of the atherosclerotic plaque located in these regions.

OCT can provide very useful information to understand the mechanisms of stent failure at follow up (such as late stent thrombosis or stent restenosis). Even when its frequency has been reduced dramatically with the introduction of drug-eluting stents, restenosis is still an important clinical problem. We demonstrated the value of OCT to evaluate the restenotic tissue with a level of detail never reached before in vivo and its ability to identify differential patterns.

OCT for the evaluation of bioabsorbable stents

Absorbable stents have emerged as a very attractive alternative in order to avoid some complications associated with permanent metallic stenting (i.e. stent thrombosis). The ABSORB trial, evaluated a fully-absorbable everolimus-eluting stent. The vessel treated was imaged with multiple imaging modalities at 2 years follow-up. Among them, OCT showed the ability to detect changes in the optical properties of the stent struts during time, probably reflecting the absorption and integration processes.

New generation OCT

The clinical application of the first commercially available generation of OCT was limited by a cumbersome acquisition procedure. The development of the second generation Fourier domain (FD) OCT has simplified the acquisition procedure by increasing the pullback speed (20 mm/s). This allows the visualization of long coronary segments in few seconds without the need of vessel occlusion. The present thesis shows a good reproducibility of the new systems for plaque characterization and stent implantation assessment.

Conclusions

OCT has emerged in the last years as the most promising intracoronary imaging technique. The simplification of the acquisition procedure achieved with the new generation systems will contribute to spread the use of OCT in many catheterization laboratories worldwide. The present thesis shows the value of OCT for the characterization of coronary atherosclerosis in vivo alone or in combination with other intracoronary modalities. The unique imaging capabilities of OCT allow a detailed evaluation of the effects of stent implantation on the vessel wall at different time points. The technique may also provide new insights into the mechanisms of stent failure and appears as a useful tool for the evaluation of new generation stents (i.e. reabsorbable) developed to overcome the limitations of metallic stenting. Further studies with long term follow up are required to clarify the clinical implications of the important amount of new information provided by OCT.

SAMENVATTING EN CONCLUSIES

De beelden met hoge resolutie die met OCT worden verkregen, hebben nieuwe inzichten opgeleverd in coronaire arteriosclerose en de interactie tussen stents en de vaatwand. De verfijning van de technologie die de laatste jaren is bereikt, heeft deze imaging techniek minder belastend gemaakt voor de patiënt. Hierdoor openen zich de mogelijkheden voor toepassingen bij de behandeling van coronair vaatlijden. Dit proefschrift levert belangrijke data over de veiligheid van de opname van OCT beelden in een klinische omgeving, de validatie van kwantitatieve OCT analyses en de potentiële klinische toepassingen van OCT voor de vaststelling van arteriosclerose en de beoordeling van stents. Bovendien wordt er getracht om de OCT bevindingen in verschillende klinische situaties te standaardiseren en de resultaten op een systematische manier te evalueren.

De veiligheid van OCT

Wij hebben de veiligheid van OCT geëvalueerd in een register waar meerdere centra aan deelnamen. Dit register bevat cases waarbij de OCT met ballon occlusie was opgenomen, alsmede cases waarbij de opname zonder ballon occlusie is uitgevoerd. Het merendeel van de waargenomen events waren korte perioden van pijn op de borst of ECG veranderingen. Serieuze complicaties kwamen zelden voor (ventrikel fibrillatie 1.1%, lucht embolie 0.6%, dissectie van het vat 0.2%) en waren voornamelijk gerelateerd met het diep inbrengen van de katheter of ballon occlusie.

Kwantitatieve OCT analyse

De validatie studie voor lumen metingen die door ons is uitgevoerd heeft laten zien dat zowel OCT als IVUS de lumen afmetingen overschatten in vergelijking met histomorphometry in geprepareerde menselijke coronairen. De in-vivo studie toonde aan dat lumen afmetingen gemeten met IVUS groter zijn dan die gemeten met OCT. Daarnaast toonde deze studie de impact die de OCT opname techniek (mét of zonder occlusie ballon) heeft op de lumen afmetingen.

Er is een systematische methodologie door ons ontwikkeld voor de analyse van stents bij een follow-up OCT opname. Met deze methodologie wordt een uitstekende reproduceerbaarheid bereikt voor het meten van het aantal struts, incomplete appositie van de stent en metingen van de dikte metingen van de laag weefsel die de struts bedekt. Deze methodologie ondersteunt het gebruik van OCT in grote multi-centra gerandomiseerde stent studies als ondersteuning

van de angiografische en klinische studie eindpunten. Dit proefschrift bevat ook de validatie van nieuwe, volledig geautomatiseerde kwantitatieve analyse software voor OCT. Deze vorm van automatische analyse zal core labs in staat stellen om nauwkeurig en reproduceerbaar OCT gegevens te produceren.

De identificatie van arteriosclerose met OCT

De mogelijkheden van OCT om de coronaire plaque te beoordelen zijn door ons onderzocht en vergeleken met histologische gegevens. Er bestond een goede correlatie tussen OCT en histologie in de meerderheid van de gevallen. Toch vertoont OCT verschillende beeld artefacten (strooiing veroorzaakt door infiltratie van macrofagen, excentrische positie van de katheter) die een verkeerde classificatie tot gevolg kunnen hebben van intimale verdikking als “fibroatheroma” of “thin-cap fibroatheroma”. De ontwikkeling van kwantitatieve methoden voor plaque karakterisatie gebaseerd op OCT kan de nauwkeurigheid van de diagnose gebaseerd op OCT verbeteren door de variabiliteit van de waarnemer te elimineren. De vergelijking met andere intra-coronaire technieken vertoonde in het algemeen een goede overeenkomst in de plaque karakterisatie met enkele variaties die inherent zijn aan de resolutie en de verschillende classificaties van de diverse technieken.

Voor de detectie van plaques met een hoog risico kan OCT waardevolle informatie leveren vanwege de mogelijkheid om de dikte te meten van de fibreuze laag op de coronaire plaque. Aan de andere kant belemmert de beperkte penetratie diepte van het OCT beeld de evaluatie van grote plaques. In tegenstelling tot OCT kan IVUS-RF de volledige plaque dikte in beeld brengen en kan de aanwezigheid van een necrotische kern identificeren. Aan de andere kant kan de fibreuze laag van de plaque niet worden beoordeeld vanwege de beperkte axiale resolutie van IVUS.

In dit proefschrift worden de prestaties van de combinatie van OCT en IVUS-RF voor de identificatie van plaques met een hoog risico verkend. Met histologie als maatstaf is de toegevoegde waarde voor de diagnostische nauwkeurigheid van het combineren van de informatie van de twee technieken aangetoond.

Deze gecombineerde methodologie is toegepast in bifurcatie lesions, een gecompliceerde subset met een hogere incidentie van complicaties tijdens de interventie procedure en van stent falen. De gepresenteerde studie rapporteert een heterogene verdeling van de plaques met een hoog risico langs de bifurcatie. Dergelijke plaques met een dunne fibreuze laag bevinden zich voornamelijk op de proximale rand van het ostium van de zijtak. In dit proefschrift is ook een klinische case opgenomen waar door middel van OCT het scheuren van een coronaire plaque

zichtbaar kon worden gemaakt. Dit voorbeeld legt een verband tussen de data van studies op basis van ex-vivo materiaal en de gebeurtenissen in een levende patiënt.

In-vivo identificatie van de effecten van coronaire stent implantatie met OCT

OCT is een uniek gereedschap vanwege de mogelijkheden van deze imaging techniek om de relatie tussen de stent en de vaatwand in beeld te brengen en om de lange termijn effecten van coronaire stent implantatie op de vaat structuur te beoordelen. Deze effecten zijn mogelijk afhankelijk van het type stent maar ook van het type plaque in het onderliggende weefsel. Er is een evaluatie uitgevoerd van de appositie en weefsel bedekking van de struts bij een follow-up OCT van stents die waren geïmplanteed tijdens een primaire PCI bij STEMI en van stents in gevallen van onstabiele angina pectoris. STEMI patiënten vertoonden meer incomplete appositie en een hoger aantal onbedekte struts. Deze resultaten kunnen in verband worden gebracht met procedurele factoren (abundante trombose tijdens primaire PCI) maar ook met de eigenschappen van de plaque die het event heeft veroorzaakt en tot een stent behandeling heeft geleid.

Ook voor de acute effecten van stent implantatie kan OCT van grote waarde zijn. De OCT beelden hebben het met hun hoge resolutie mogelijk gemaakt om in detail vast te stellen wat voor schade de stent implantatie aan de vaatwand heeft veroorzaakt (zoals rand dissecties, in-stent dissecties en weefsel protrusie). In dit proefschrift wordt een methode voorgesteld voor de classificatie en kwantificatie van deze fenomenen. Bovendien wekt de gepresenteerde data de suggestie dat schade aan het vat veroorzaakt door de stent (vooral aan de randen) mede afhankelijk is van de compositie van de atherosclerotische plaque in die regio's. OCT levert nuttige informatie voor het begrip van de mechanismen achter stent falen tijdens follow-up (zoals late stent trombose of stent re-stenose). Desondanks dat de frequentie van voorkomen drastisch is afgenomen sinds de introductie van drugafgevendende stents, is re-stenose nog steeds een relevant klinisch probleem. De waarde van OCT om het stenotische weefsel in-vivo in ongekend detail weer te geven, alsmede de mogelijkheid om hierin verschillende patronen te herkennen worden hier gepresenteerd.

OCT voor the evaluatie van bio-absorbeerbare stents

Absorbeerbare stents zijn recent opgekomen als een aantrekkelijk alternatief ter voorkoming van verscheidene complicaties van de behandeling met metallische stents (bijvoorbeeld stent trombose). De ABSORB studie, onderzocht een volledig absorbeerbare everolimus-afgevendende stent. Het behandelde vat werd 2 jaar na

de behandeling met meerdere medische beeldtechnieken onderzocht. OCT was (naast andere technieken) in staat om de veranderende optische eigenschappen van de stent struts waar te nemen die waarschijnlijk werden veroorzaakt door het proces van bioabsorptie.

Nieuwe generatie OCT

De klinische toepassing van de eerste commerciële OCT systemen was beperkt door de moeizame methode van beeldopname. De ontwikkeling van een tweede generatie Fourier domein (FD) OCT heeft de beeld acquisitie procedure drastisch vereenvoudigd door de terugtrek snelheid te verhogen (naar 20 mm/s). Hierdoor werd het mogelijk om een lang coronair segment in beeld te brengen zonder dat daarvoor een occlusie van het vat noodzakelijk was. Dit proefschrift toont de goede reproduceerbaarheid van deze nieuwe generatie systemen voor plaque karakterisatie en de beoordeling van stent implantatie.

Conclusies

OCT is de laatste jaren naar voren gekomen als de meest veelbelovende intra-coronaire imaging techniek. De vereenvoudiging van de beeld acquisitie methode die is bereikt met de nieuwe generatie systemen zal bijdragen aan de verspreiding van het gebruik van OCT in vele katheterisatie laboratoria over de hele wereld. Dit proefschrift toont de waarde van OCT voor de karakterisatie van in-vivo coronaire arteriosclerose op zichzelf of in combinatie met andere intra-coronaire modaliteiten. De unieke imaging mogelijkheden van OCT brengen een gedetailleerde evaluatie van de effecten van stent implantatie op de vaatwand op verschillende tijdstippen binnen bereik. De techniek brengt mogelijk ook nieuwe inzichten in de mechanismen voor stent-falen en komt naar voren als een nuttig gereedschap voor de evaluatie van nieuwe generaties stents (zoals bio-absorbeerbare) die worden ontwikkeld om de limitaties van de huidige metallische stents te overwinnen. Verder onderzoek met een lange termijn follow-up zijn nodig om inzicht te geven in de klinische implicaties van de grote hoeveelheid informatie die nu met OCT binnen bereik is gekomen.

ACKNOWLEDGEMENTS

This thesis would not have been possible without the support of many people. I would like to thank everyone that contributed in one way or the other and I hope I will not forget anybody.

In the fourth year of my cardiology training I started considering the possibility of becoming an interventional cardiologist and the idea of a post-graduate experience abroad started to take shape on my mind. At that time, Manel Sabate was my tutor at the Hospital Clínico San Carlos in Madrid, and he encouraged me to follow his steps and go to Rotterdam for a fellowship. This plan was reinforced by Javier Escaned, who had also been a fellow at the Thoraxcenter. They introduced me to Professor Serruys in the World Congress in Barcelona 2006 and helped me to write a project for my grant. I would like to express my gratitude to both of them for all their support, advice and friendship. I owe them a big part of this great experience.

Dear Professor Serruys, it has been a real privilege to work with you. I really admire your incredible energy and intelligence and the capacity you have to make people show the best of themselves. You have been a great inspiration for a lot of generations of interventional cardiologists and I feel very proud to have been “one of your fellows”. Thank you for your patience and for the hours you have shared with us in your attic teaching us how to think in a scientific way, how to design a project and how to write a paper. This type of knowledge is not measurable but it is the most precious gift that you have given us. Thank you also for your understanding in some difficult moments that I had to live through during my stay in Rotterdam. I would also like to express my gratitude to your wife Danielle for always being so nice to me.

Dear Evelyn, this thesis is mainly the result of our excellent collaboration. We started with the most difficult paper as you usually say but in the end working together has been a great and enjoyable experience for me. Thank you for your trust and for letting me share your enthusiasm for OCT. You know that this thesis is also your thesis because it would have never been possible without all your help and support.

Héctor, for me you have been more than a colleague in Rotterdam, you have been a friend that I hope I can keep for life. I have always felt that I could count on you for everything and you know that you can always count on me. I am sorry that I have not improved much my cooking skills yet but I promise I will try it as

soon as I have some more free time. Thank you also to your wife Lulú and your son Andres for their friendship. You have a really wonderful family.

My dear Italian colleague Lele. It was a real pleasure to share some of my time at Rotterdam with you. I know that sometimes it was “too much” but we had a lot of fun in our office at the Z building. I hope you will always keep that “amazing” sense of humour.

Dear Yoshi-san, you are such an incredible colleague and friend. We started working together on the IBIS-2 (a lot of evenings drawing circles) and after that we have shared a lot of good moments. Thank you for being always ready to offer your help and support. I am sure that all your hard work will be rewarded. I am happy that you are enjoying so much your European experience. You are welcome here in the south whenever you want.

Dear Nick, I was very lucky to have a colleague like you at the Thoraxcenter. We share a lot of ideas about what it means to be a doctor and this has made us good friends. Thank you for listening in some difficult moments. I really enjoyed the time we spend together with you and Lisa (we should repeat the sailing some other time). I wish you the best for the new period you are going to start. You still have to come to visit Madrid, I will try to get some good tickets so you can visit the most beautiful soccer stadium in the world (Santiago Bernabeu). Maybe you could come with Paul Cummins, another person that I would like to acknowledge for his help.

Special thanks to Peter Barlis and Takayuki Okamura, the two fellows that collaborated with me in OCT. It was a pleasure to work with you both. Thank you also to all the other fellows who shared their experience at the Thoraxcenter with me.

I would like to express my special gratitude to all the interventional cardiologists at the Thoraxcenter that helped me in any way to develop and carry out my projects and to the committee members of my thesis.

One of the great advantages of the Thoraxcenter is the possibility to work with people involved in different fields of research. It was a great pleasure to collaborate in some OCT papers with Gijs van Soest from the biomedical engineering department. I also want to thank Jolanda Wentzel, Frank Gijzen and Hans Schuurbijs from the biomechanics lab and Heleen van Beusekom for helping me with their expertise. Nico Bruining gave me the opportunity to take part in interesting projects regarding OCT analysis.

I would also like to acknowledge the work and support of all the technicians and nurses at the cathlab. Special mention should be made to my dear friend Jurgen. Your passion for work is only comparable with the size of your heart. Thank you for providing a warm welcome and for helping me to integrate into the

“Thoraxcenter life”. You are not only an incredible intracoronary imaging expert but also a great person. Thank you also to Sander, Elco, John, Gio and Patrick for offering always their help with a smile. Javier Orellana, the Spanish anaesthesiologist from the cathlab was so nice inviting me for lunch with his family the first weekend I spent in Rotterdam. From the personnel department I would like to thank Will Barthelemy and specially Sara Franksen for being always so nice to me.

During my fellowship I had the opportunity to spend a lot of time at Cardialysis and this has been a great experience for the knowledge I gained and for the people I met there. Gerrit-Anne van Es was always supportive in my objective of obtaining the PhD. A big thank you to Marie-Angele Morel, we were usually the ones “closing” Cardialysis in the evenings. Thank you also to Ali, Ravindra and Jamal from the core-lab and Dick Goedhart from the statistics department.

I would also like to express my gratitude to my colleagues from Hospital Clinico San Carlos in Madrid. Carlos Macaya, the chief of Cardiology encouraged the idea of working abroad for some time and offered me the possibility to work in the cath lab when I returned to Madrid. Big thank to my colleagues from Interventional Cardiology (Rosana Hernández, Camino Bañuelos, Pilar Jiménez, Javier Escaned and Fernando Alfonso) for all the things they have taught me and for their friendship. I feel very privileged for having the opportunity to work with you everyday.

All my friends have contributed to this thesis giving me all their support whenever I needed it. Cecilia, I know you are always there, distance does not matter. Dear Vera, thank you for helping me to move and for making the start much easier. I really enjoyed our time together in Rotterdam.

I could have not achieved my objectives without the commitment and support of those close to me. My parents have worked tirelessly to giving me the opportunities in life that they never had. What I am now is the result of their enormous effort. Unfortunately, my father will not have the chance be there the day I defend my thesis. In any case, I know he would have been as proud of me as I am of him being my father. Thank you also to my dear brother Daniel.

Finally, I would like to thank Koen. The beginning in Rotterdam was not easy for me but everything changed after I met you. You have been my biggest support, the person that has given me the energy to make this dream come true. I could never express in words all my gratitude and love.

Living in Rotterdam has been one of the most enriching experiences of my life. During that time, I had to face some very difficult personal moments but I have also lived some of the happiest times that I can remember. Being a fellow at the Thoraxcenter has been a great opportunity for me to grow not only as a doctor but also as a person and I will always be grateful for that.

CURRICULUM VITAE

Family name: Gonzalo López
First name: Nieves
Date of birth: May 16th 1976
Place of birth: Madrid, Spain
E-mail: nieves_gonzalo@yahoo.es
Professional qualifications: Medicine degree
Awarded by: Universidad Autónoma de Madrid, Spain.
Date: 2000
Specialization School: Cardiology
Awarded by: Cardiology Department, Hospital Clínico San Carlos,
Universidad Complutense, Madrid, Spain
From 2001 to 2006
Grants: Research Grant Spanish Society of Cardiology
2007

LIST OF PUBLICATIONS

Gonzalo N, Garcia-Garcia HM, Regar E, Barlis P, Wentzel J, Onuma Y, Ligthart J, Serruys P.W. *In Vivo Assessment of High-risk Plaques at Bifurcations with Combined Intravascular Ultrasound Virtual Histology and Optical Coherence Tomography*. J Am Coll Cardiol Img 2009 2: 473-482.

Gonzalo N, Serruys P.W, Barlis P, Garcia-Garcia HM, Regar E. *Incomplete Stent Apposition And Delayed Tissue Coverage Are More Frequent In Drug Eluting Stents Implanted During Primary Percutaneous Coronary Intervention For ST Elevation Myocardial Infarction Than In Drug Eluting Stents Implanted For Stable/Unstable Angina. Insights from Optical Coherence Tomography*. JACC Interventions 2009 May;2(5):445-52

Gonzalo N, Serruys PW, Okamura T, van Beusekom H, Garcia-Garcia HM, van Soest G, van der Giessen W, Regar E. *Optical coherence tomography patterns of stent restenosis*. Am Heart J. 2009 Aug;158(2):284-93

Gonzalo N, Serruys PW, Okamura T, Shen ZJ, Onuma Y, Garcia-Garcia HM, Sarno G, Schultz C, van Geuns RJ, Ligthart J, Regar E. *Optical Coherence Tomography Assessment Of The Acute Effects Of Stent Implantation On The Vessel Wall. A Systematic Quantitative Approach*. Heart. 2009 Dec;95(23):1913-1919. Epub 2009 Aug 10

Gonzalo N, Serruys PW, García-García HM, van Soest G, Okamura T, Ligthart J, Knaapen M, Verheye S, Bruining N, Regar E. *Quantitative ex vivo and in vivo comparison of lumen dimensions measured by optical coherence tomography and intravascular ultrasound in human coronary arteries*. Rev Esp Cardiol. 2009 Jun; 62(6):615-24.

Serruys PW, Ormiston J, Onuma Y, Regar E, Gonzalo N, Garcia-Garcia HM, Nieman K, Bruining N, Dorange C, Miquel-Hebert K, Veldhof S, Webster M, Thuesen L, Dudek D. *A bioabsorbable everolimus-eluting coronary stent system (ABSORB): 2-year outcomes and results from multiple imaging methods*. Lancet. 2009 Mar 14;373(9667):897-910.

van Soest G, Goderie TP, Gonzalo N, Koljenović S, van Leenders GL, Regar E, Serruys PW, van der Steen AF. *Imaging atherosclerotic plaque composition with intracoronary optical coherence tomography*. Neth Heart J. 2009 Nov;17(11):448-50

Garcia-Garcia HM, Gonzalo N, Regar E, Serruys PW. *Virtual histology and optical coherence tomography: from research to a broad clinical application*. Heart. 2009 Aug;95(16):1362-74

Gonzalo N, Serruys PW, Piazza N, Regar E. *Optical coherence tomography in secondary revascularization. Stent and grafts assessment*. EuroIntervention Supplement (2009) Vol. 5 (Supplement D) D93-D100.

Gonzalo N, Garcia-Garcia HM, Serruys PW, Bezerra H, Commissaris K, Gobbens P, Costa MA, Regar E. *Reproducibility of quantitative optical coherence tomography for stent analysis*. EuroIntervention. 2009 Jun;5(2):224-32.

Barlis P, Gonzalo N, di Mario C, Prati F, Buellesfeld L, Rieber J, Dalby MC, Ferrante G, Cera M, Grube E, Serruys P. W, Regar E. *A Multi-Center Evaluation of the Safety of Intra-Coronary Optical Coherence Tomography*. EuroIntervention 2009;5:90-95.

Ramcharitar S, Gonzalo N, van Geuns RJ, Garcia-Garcia HM, Wykrzykowska JJ, Ligthart JM, Regar E, Serruys PW. *First case of stenting of a vulnerable plaque in the SECURITT I trial-the dawn of a new era?* Nat Rev Cardiol. 2009 May;6(5):374-8.

Sihan K, Botha C, Post F, de Winter S, Gonzalo N, Regar E, Serruys PJ, Hamers R, Bruining N. *Fully automatic three-dimensional quantitative analysis of intracoronary optical coherence tomography: method and Validation*. Catheter Cardiovasc Interv. 2009 May 7. [Epub ahead of print]

Garcia-Garcia HM, Gonzalo N, Pawar R, Kukreja N, Dudek Dariusz, Thuesen Leif, Ormiston JA, Regar E, Serruys PW. *Assessment of the Absorption Process Following Bioabsorbable Everolimus-Eluting Stent Implantation: Temporal Changes in Strain Values and Tissue Composition Using Intravascular Ultrasound Radiofrequency Data Analysis. A substudy of the ABSORB clinical trial*. Eurointervention 2009 4:443-448.

Garcia-Garcia HM, van Mieghem C, Gonzalo N, Meijboom B, Weusting AC, Onuma Y, Mollet NR, Schultz CJ, Meliga E, van der Ent M, Sianos G, Goedhart D, den Boer A, de Feyter P, Serruys PW. *Computed Tomography in Total Coronary*

Occlusions (CTTO Registry): radiation exposure and predictors of successful percutaneous intervention. EuroIntervention. 2009 Mar;4(5):607-16.

Schuurbiers JCH, Gonzalo N, Ligthart J, Gijsen FJH, Dijkstra J, Serruys P. W, Wentzel J. *Validation of CAAS QCA-3D system for coronary 3D reconstruction using fusion of angiography and intravascular ultrasound (ANGUS).* Catheterization and Cardiovascular Interventions 2009. In press.

Onuma Y, Kukreja N, Daemen J, Garcia-Garcia HM, Gonzalo N, Cheng JM, van Twisk PH, van Domburg R, Serruys PW; *Interventional Cardiologists of Thoraxcenter. Impact of sex on 3-year outcome after percutaneous coronary intervention using bare-metal and drug-eluting stents in previously untreated coronary artery disease: insights from the RESEARCH (Rapamycin-Eluting Stent Evaluated at Rotterdam Cardiology Hospital) and T-SEARCH (Taxus-Stent Evaluated at Rotterdam Cardiology Hospital) Registries.* JACC Cardiovasc Interv. 2009 Jul;2(7):603-10

Gonzalo N, García-García HM, Ligthart J, Rodríguez-Granillo G, Meliga E, Onuma Y, Schuurbiers JC, Bruining N, Serruys PW. *Coronary plaque composition as assessed by greyscale intravascular ultrasound and radiofrequency spectral data analysis.* Int J Cardiovasc Imaging. 2008 Dec;24(8):811-8.

Gonzalo N, Serruys PW, Barlis P, Ligthart J, Garcia-Garcia HM, Regar E. *Multi-Modality Intra-Coronary Plaque Characterization: A Pilot Study.* Int J Cardiol. 2008 Sep 5. [Epub ahead of print]

Gonzalo N, Serruys PW, Regar E. *Optical coherence tomography: clinical applications, and the evaluation of DES.* Minerva Cardioangiol. 2008 Oct;56(5):511-25.

Garcia-Garcia HM, Gonzalo N, Granada JF, Regar E, Serruys P.W. *Diagnosis and treatment of Coronary Vulnerable Plaques.* Expert Rev Cardiovasc Ther. Feb 2008; 6(2):209-222.

Barlis P, di Mario, van Beusekom H, Gonzalo N, Regar E. *Novelties in cardiac Imaging: OCT. A critical appraisal of the safety concerns tempering the success of drug eluting.* EuroIntervention Supplement (2008) Vol. 4 (Supplement C) C22-C26

Barlis P, Serruys P.W, Gonzalo N, Van der Giessen W, Jaegere P.J, Regar E *Assessment of Culprit and Remote Coronary Narrowings Using Optical Coherence Tomography with Long-Term Outcomes.* Am J Cardiol. 2008 Aug 15;102(4):391-5

Garcia-Garcia HM, Gonzalo N, Tanimoto S, Meliga E, Jaegere P, Serruys P. W. *Tissue Characterization of the Edge Effects of Paclitaxel-Eluting Stents as Assessed by Serial Intravascular Ultrasound Radiofrequency Data Analysis: BETAX (BEside TAXus) study*. Rev Esp Cardiol. 2008 Oct;61(10):1013-9.

Garcia-Garcia HM, Gonzalo N, Alfonso F. *Greyscale Intravascular Ultrasound and IVUS-Radiofrequency Tissue Characterization to Improve Understanding of the Mechanisms of Stent Thrombosis in Drug-eluting Stents*. EuroIntervention Supplement (2008) Vol. 4 (Supplement C) C33-C38.

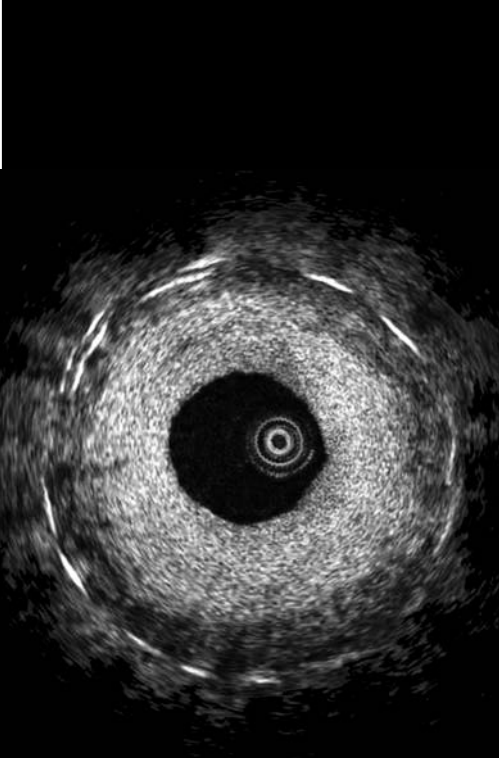
Meliga E, Garcia-Garcia HM, Valgimigli M, Chieffo A, Biondi-Zoccai G, Maree AO, Gonzalo N, Cook S, Marra S, Moretti C, De Servi S, Palacios IF, Windecker S, van Domburg R, Colombo A, Sheiban I, Serruys PW. *Impact of drug-eluting stent selection on long-term clinical outcomes in patients treated for unprotected left main coronary artery disease: The sirolimus vs paclitaxel drug-eluting stent for left main registry (SP-DELFT)*. Int J Cardiol. 2008 Aug 5. [Epub ahead of print]

Meliga E, Garcia-Garcia HM, Valgimigli M, Chieffo A, Biondi-Zoccai G, Maree AO, Gonzalo N, Cook S, Cruz-González I, Marra S, De Servi S, Palacios IF, Windecker S, van Domburg R, Colombo A, Sheiban I, Serruys PW. *Diabetic patients treated for unprotected left main coronary artery disease with drug eluting stents: a 3-year clinical outcome study. The Diabetes and Drug Eluting stents for leFT main registry (D-DELFT)*. EuroInterv.2008;4:77-83

Garcia-Garcia N, Kukreja N, Daemen J, Tanimoto S, van Mieghem C, Gonzalo N, van der Ent M, Sianos G, de Feyter P, Serruys P. W. *Contemporary treatment of patients with chronic total occlusion: critical appraisal of different state-of-the-art techniques and devices*. EuroIntervention.2007;3:188-196

Escaned J, Conde C, Ferrer MC, Gonzalo N. *Intravascular techniques for the physiologic evaluation of coronary circulation*. Cardiovascular Risk Factors 2005; 14: 81-103

Rojo EC, Rodrigo JL, Pérez de Isla L, Almería C, Gonzalo N, Aubele A, Cinza R, Zamorano J, Macaya C. *Disagreement between tissue Doppler imaging and conventional pulsed wave Doppler in the measurement of myocardial performance index*. Eur J Echocardiogr. 2006 Oct;7(5):356-64



COLOUR SECTION

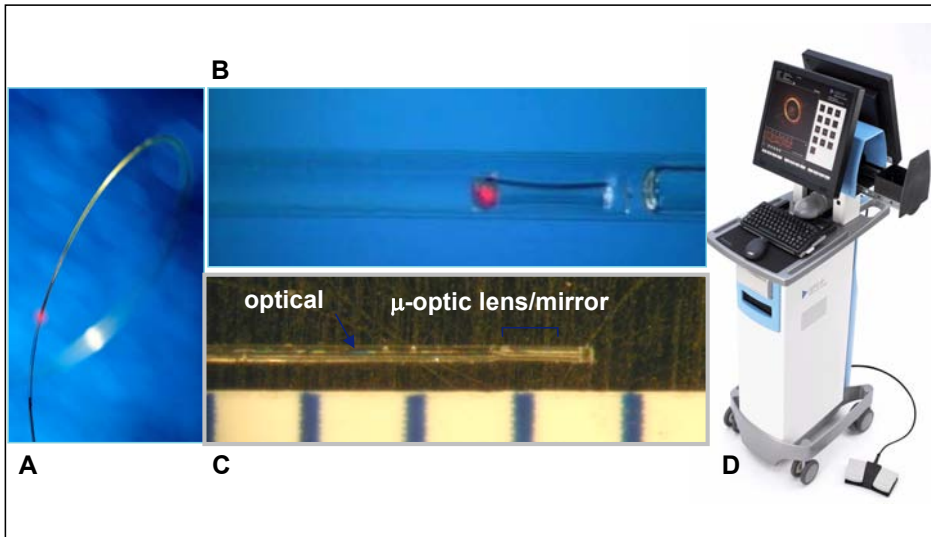
CHAPTER 1.1

Figure 1 The currently commercially available TD-OCT system (Lightlab Imaging, Westford, MA, USA). A) The OCT imaging wire with an outer diameter of 0.019 inch B) Magnification of the distal catheter tip C) Magnification of the 0.006 inch rotating single-mode fibre-optic core, located within the distal sleeve of the imaging wire D) Imaging console with pullback device allowing for real-time image display and data storage.

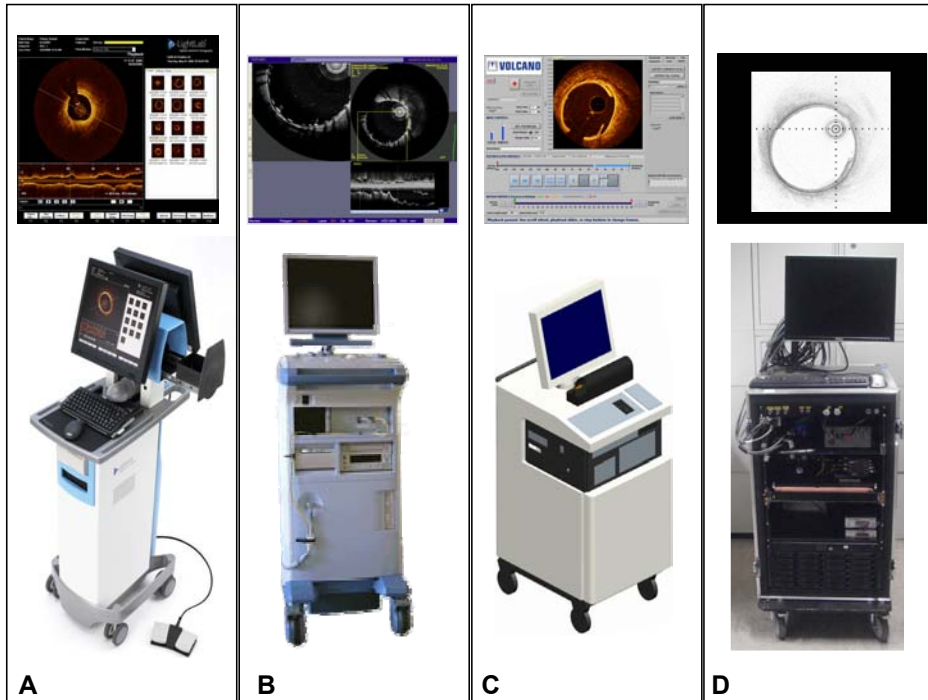


Figure 2 Different FD-OCT prototypes as used at the Thoraxcenter in 2008 A) M4 system, Lightlab Imaging, Westford, MA, USA , B) Terumo OCT C) Volcano OCT D) MGH OFDI system (G. Tearney and B. Bouma, Wellman Center for Photomedicine, MGH, Boston, MA, USA)

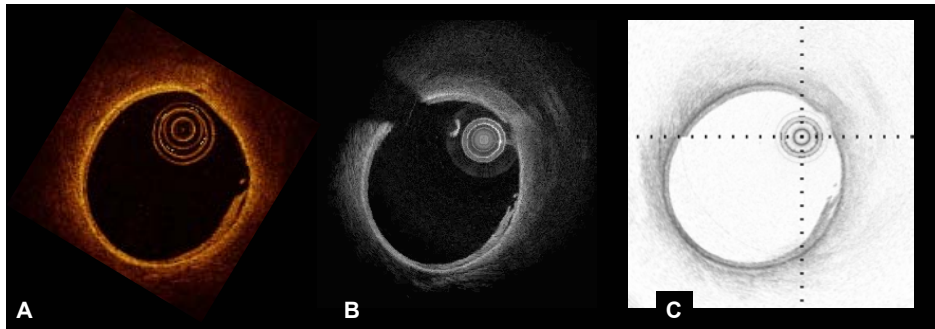


Figure 3 FD-OCT images as obtained in in-vivo in normal porcine coronary artery. The coronary vessel wall shows a three layer appearance and an intimal dissection is visible in 4 o'clock position. A) M4 prototype, Lightlab Imaging, Westford, MA, USA , B) Terumo OCT C) MGH OFDI system (G. Tearney and B. Bouma, Wellman Center for Photomedicine, MGH, Boston, MA, USA)

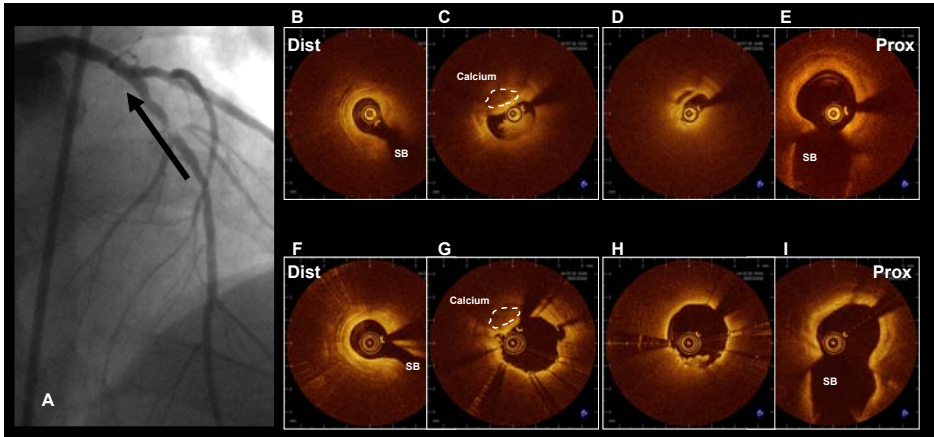


Figure 4 OCT findings before and immediately after stent implantation in a patient presenting with acute myocardial infarction (M4 prototype FD OCT system, Lightlab Imaging, Westford, MA, USA). A) Coronary angiography revealed a subtotal occlusion of the left anterior descending artery. The black arrow indicates the vessel segment imaged by OCT B-E) pre-interventional OCT showing the distal reference (B), the lesion with mural thrombus (C), the minimal lumen area (D) and the proximal reference (E): F-I) postinterventional OCT: corresponding images can be easily identified using anatomical landmark such as side branches (SB) or calcium nodules. Metallic stent struts appear as bright structures with dorsal shadowing. The distal reference (F) and the lesion site that can be easily identified using the small calcium nodule as a landmark (G) the site of the original minimal lumen area shows tissue protrusion in 6 o'clock position (H) , the proximal reference (I).

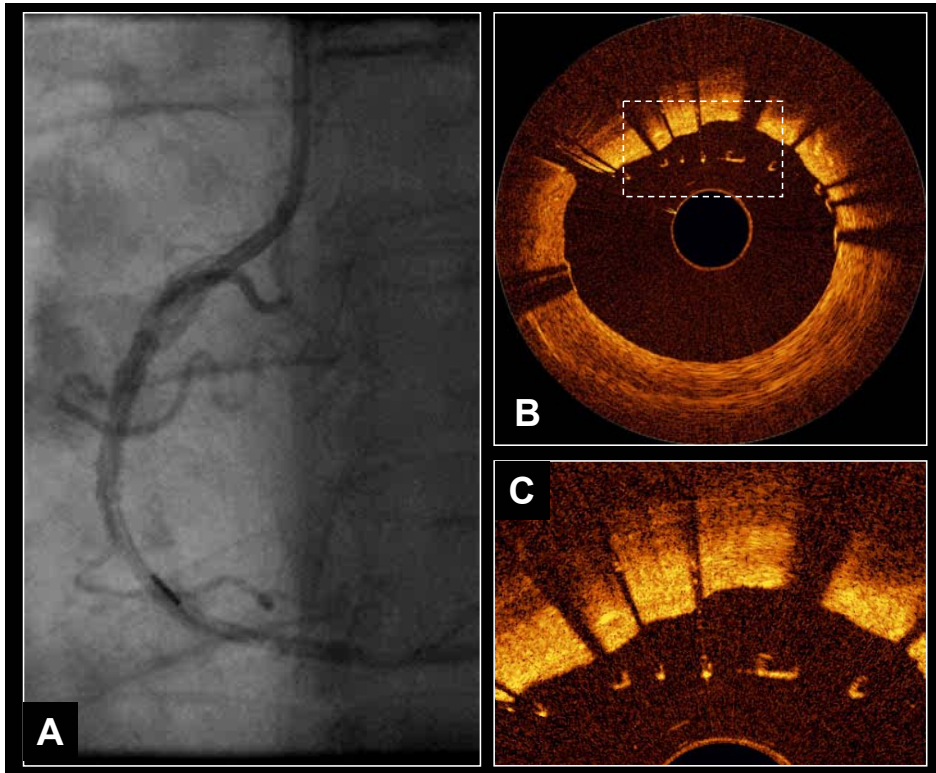


Figure 5 Incomplete stent strut apposition immediately after stenting (Volcano OCT prototype). A) Coronary angiogram of the right coronary artery after stent implantation. B) OCT image of the proximal stent edge showing malapposition of stent struts C) Magnification clearly illustrating that individual stent struts do not have contact to the vessel wall.

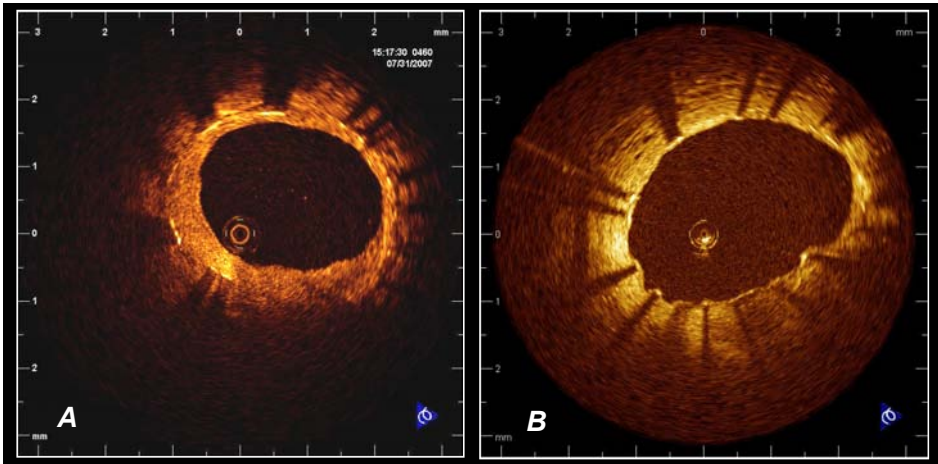


Figure 6 In vivo OCT of human coronaries at 6 months follow up. This figure illustrates the different degree of neointima coverage typically seen in bare metal stents as compared to drug eluting stents. A) bare metal stent B) drug eluting stent (TD OCT system, Lightlab Imaging, Westford, MA, USA).

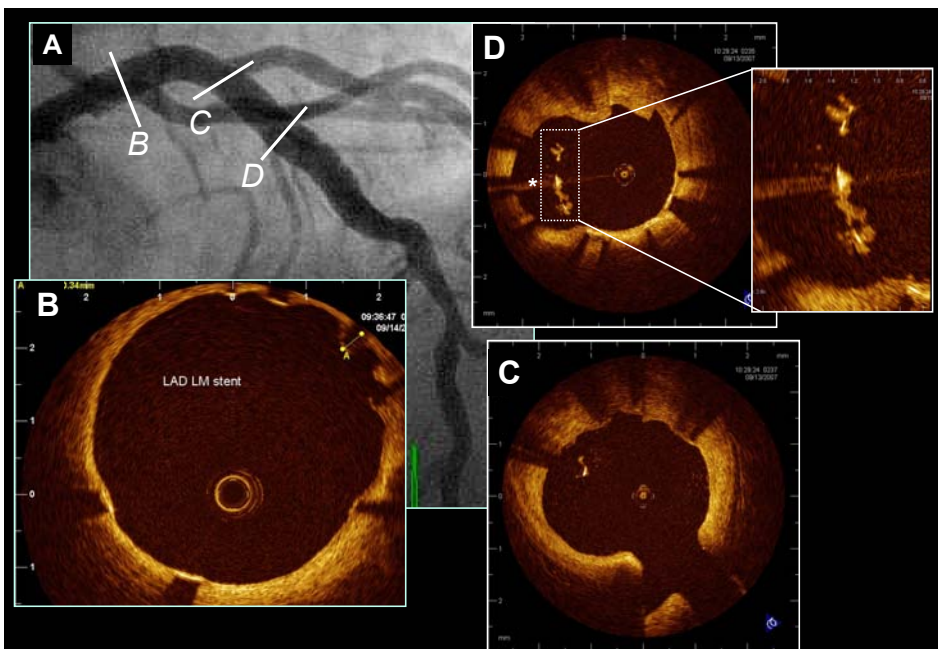


Figure 7 OCT findings at longterm follow up after DES implantation in the LEADERS OCT substudy. A) Coronary angiogram of the left coronary artery. Overlapping stents were implanted in the proximal left anterior descending artery and in the left main stem B) The application of the non-occlusive imaging acquisition technique allowed to image the stent in the left main stem as well as the proximal left anterior descending artery C,D. C) eccentric stent struts with very thin

coverage visible, an individual strut in 11 o'clock position is malapposed D) stent struts showing malapposition and tissue coverage with irregular borders, possible indicating thrombus formation. (TD OCT system, Lightlab Imaging, Westford, MA, USA).

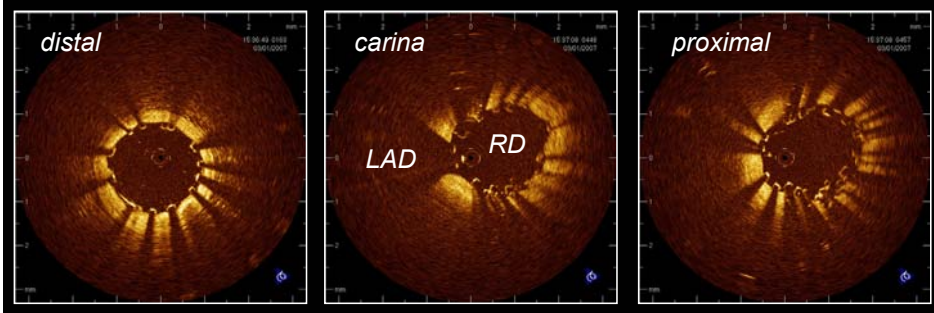


Figure 8 Clinical OCT after bifurcation stenting of the ramus descendens anterior and the ramus diagonalis in crush technique. A) OCT pullback is started distally in the diagonal branch. The stent is well expanded and all struts are apposed against the vessel wall B) OCT at the carina shows the lumen of the ramus descendens anterior in 9 o'clock position wide open. Note the double layer of stent struts separating the ostium of the diagonal branch from the ramus descendens anterior. C) proximal stent portion in the ramus descendens anterior. In 12 to 6 o'clock position, three layer of struts originating from the proximal, crushed diagonal branch stent and from the stent in the ramus descendens anterior can be observed. (TD OCT system, Lightlab Imaging, Westford, MA, USA).

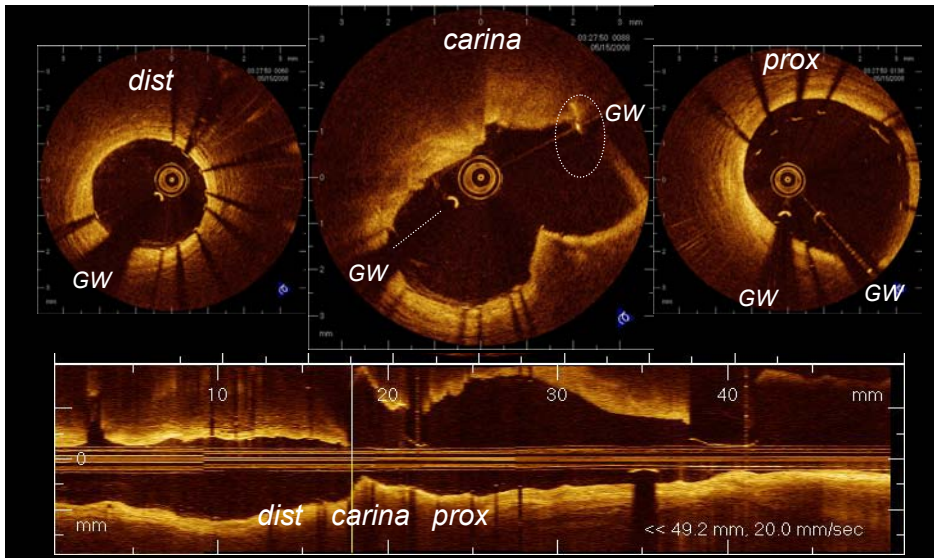


Figure 9 Clinical OCT after bifurcation stenting of the ramus descendens anterior and the ramus diagonalis with a dedicated bifurcation stent (Nile croco stent) A) OCT pullback is started distally in the ramus descendens anterior. The stent is well expanded and all struts are apposed against the vessel wall B) OCT at the carina shows the lumen of the carina wide open, no struts are obstructing the access to the diagonal branch C) proximal stent portion in the ramus descendens anterior. Despite

a rather good stent expansion is some strut malapposition visible in 11 to 1 o'clock position. GW= guide wire. (M4 prototype FD OCT prototype, Lightlab Imaging, Westford, MA, USA).

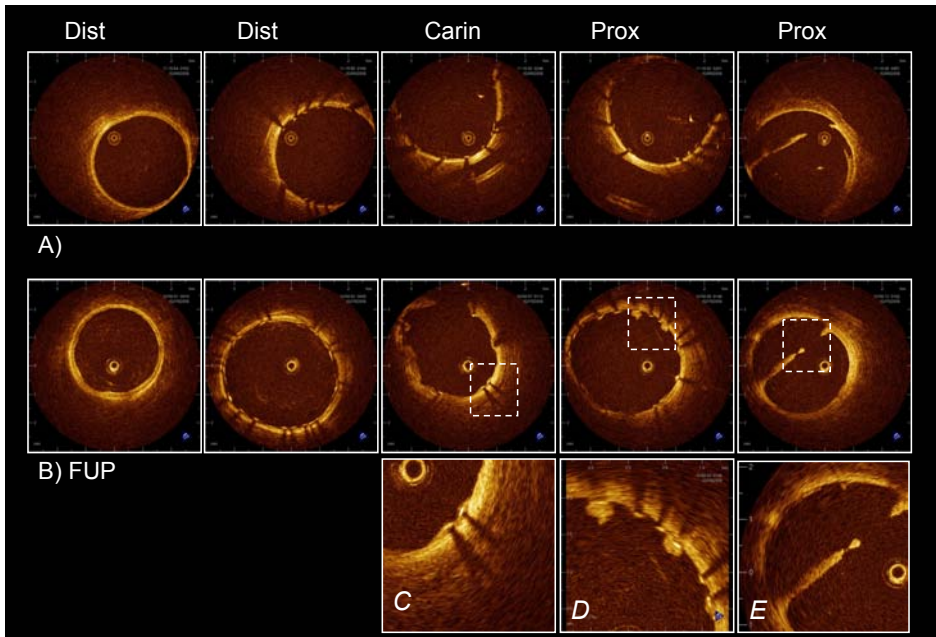
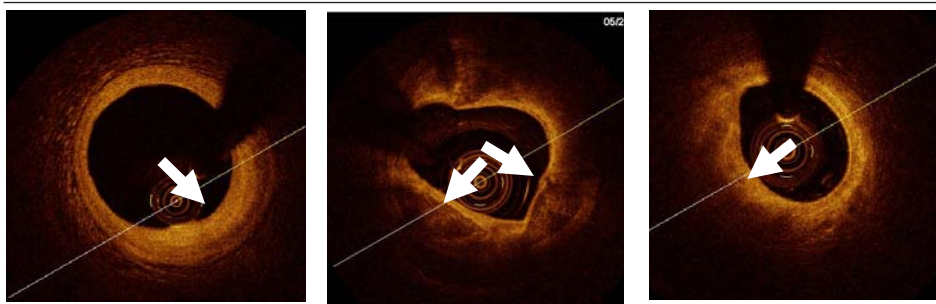


Figure 10 Bifurcation stent implantation in normal pigs. Serial, in vivo OCT A) immediately after stenting and B) at 7 day follow up. Tissue coverage is visible in various degrees from C) very thin coverage to more pronounced, irregular coverage in D) Furthermore, a persistent dissection flap can be observed at the proximal reference segment E) (TD OCT system, Lightlab Imaging, Westford, MA, USA).

Table 3. OCT image criteria for plaque type.

Fibrous plaque	Fibrocalcific plaque	Lipid-rich plaque
Homogeneous signal-rich region	Well-delineated, signal-poor region with sharp borders	Signal-poor region with diffuse borders



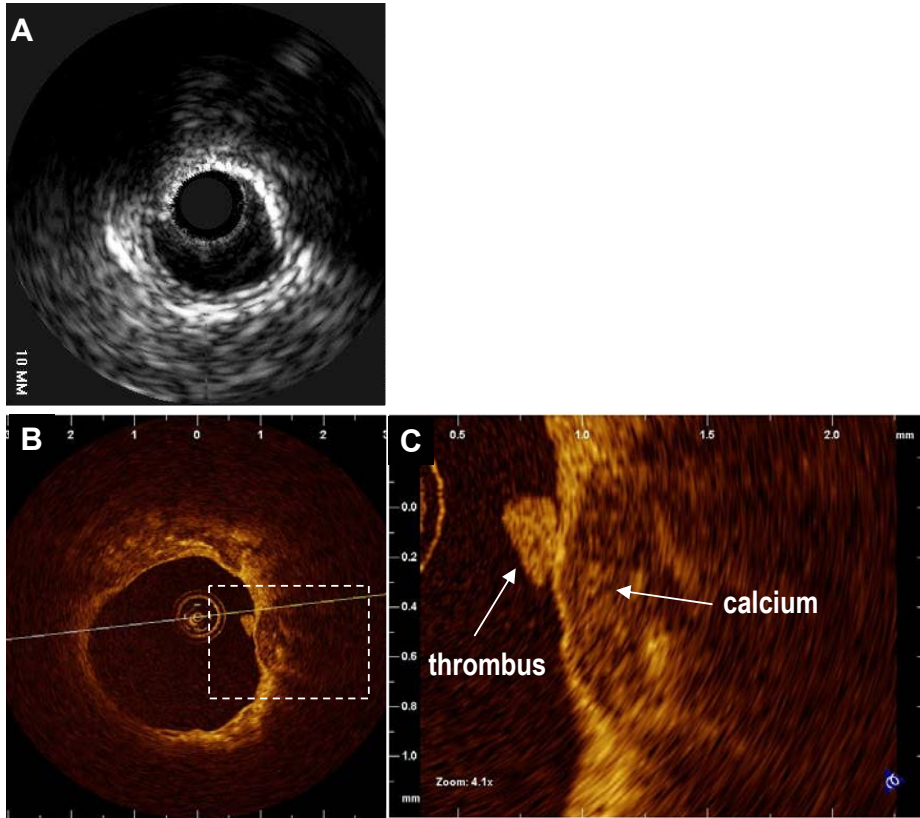


Figure 11 In vivo intravascular imaging of a calcified coronary plaque. A) Intravascular ultrasound shows an eccentric, calcified plaque as echodense structure with typical dorsal shadowing, while 180 degree of vessel wall show normal, three layer appearance B) Intravascular OCT of the same plaque. By OCT, calcium appears signal poor (dark) with sharp, well delineated borders. C) The magnification reveals a small mural thrombus. Note, that the calcium nodule is covered towards the lumen by a thin layer and is not in direct contact to the lumen as seen by IVUS.

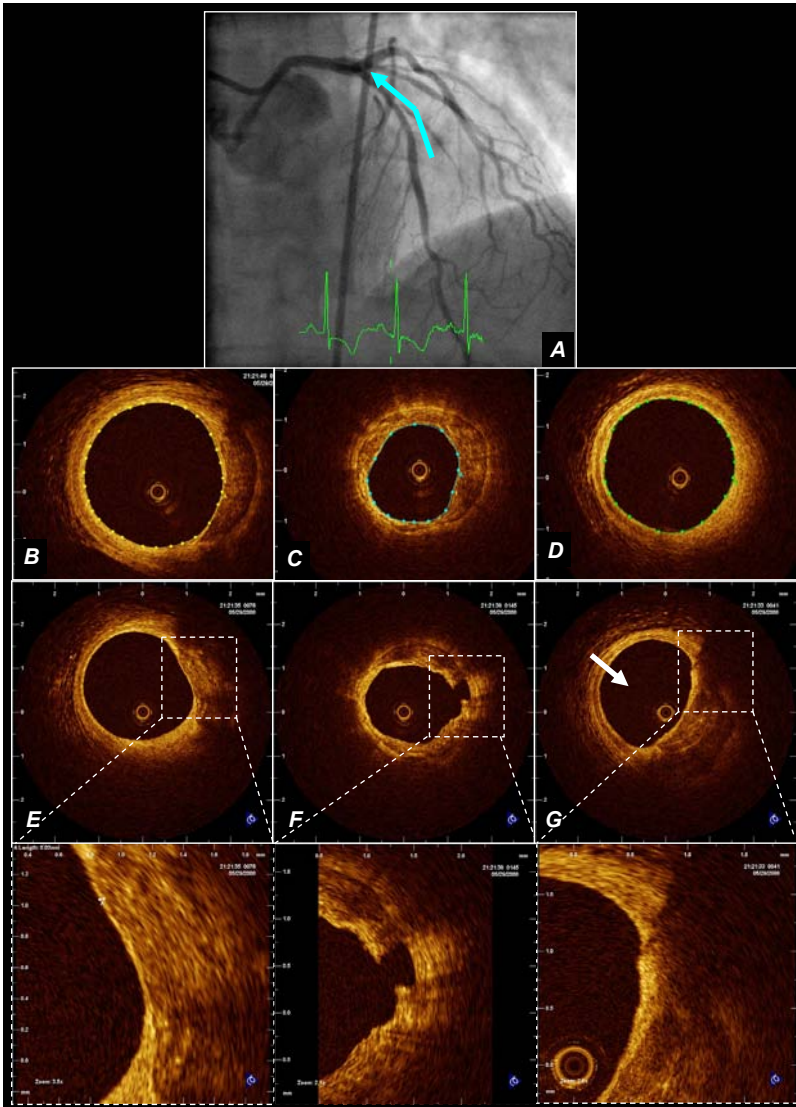


Figure 12 OCT findings in a 74 year old female patient presenting with acute coronary syndrome, Braunwald class IIIIC with positive Trop T ($0.57\mu\text{g/l}$) and CK (181 U/l) at the time of admission to the cathlab. A) Coronary angiography showed a moderate narrowing of the mid left descending anterior artery with TIMI III antegrade flow, the other epicardial arteries were normal. Intracoronary OCT confirmed a moderate lesion with approx 50% area stenosis B) proximal reference lumen area 6.82mm^2 C) minimal lumen area 2.81mm^2 D) distal lumen area 4.49mm^2 . Detailed inspection of the OCT images revealed E) an eccentric plaque that showed a very thin endothelial lining ($<30\mu\text{m}$) F) a site with plaque rupture/ulceration and G) a fine fissure on the surface of the plaque. Plaque erosion, rupture/ulceration and fissure have been associated with coronary thrombosis in pathology series and could be the possible pathophysiologic substrate for the clinical syndrome observed in our patient, (TD OCT system, Lightlab Imaging, Westford, MA, USA).

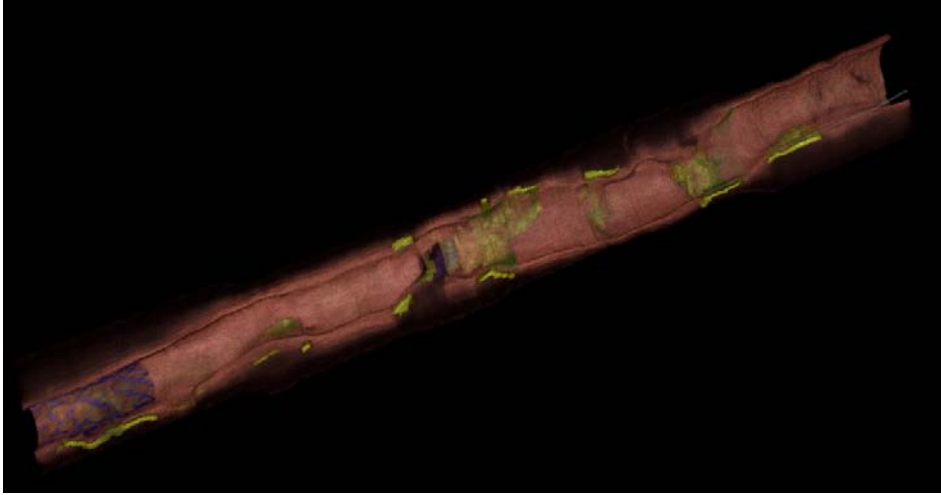


Figure 13 Longitudinal cut view of an in vivo FD OCT pullback through a coronary artery. At the distal end, a coronary stent is visible. Different components of the vessel wall are represented in a color coded way. MGH OFDI system (G. Tearney and B. Bouma, Wellman Center for Photomedicine, MGH, Boston, MA, USA)



Figure 14 Occlusive image acquisition technique (TD OCT imaging Lightlab Imaging, Westford, MA, USA). The imaging catheter directs the infrared light into the tissue and returns the reflected light back to the optical engine. During imaging, blood flow is limited by a dedicated, over the wire,

low pressure (0.4 atm) occlusion balloon catheter (Helios, Goodman, Japan), that is positioned proximally in the artery. The central lumen of the balloon occlusion catheter allows for distal flush deliver during imaging of the target segment with automated pullback. The proximal end of the catheter has a chamber that captures the imaging core and allows it to move along the catheter axis to perform an “automated pullback”. The outside of the imaging catheter is stationary with respect to the vessel wall. The imaging core is rotated and translated inside of the external catheter sheath.

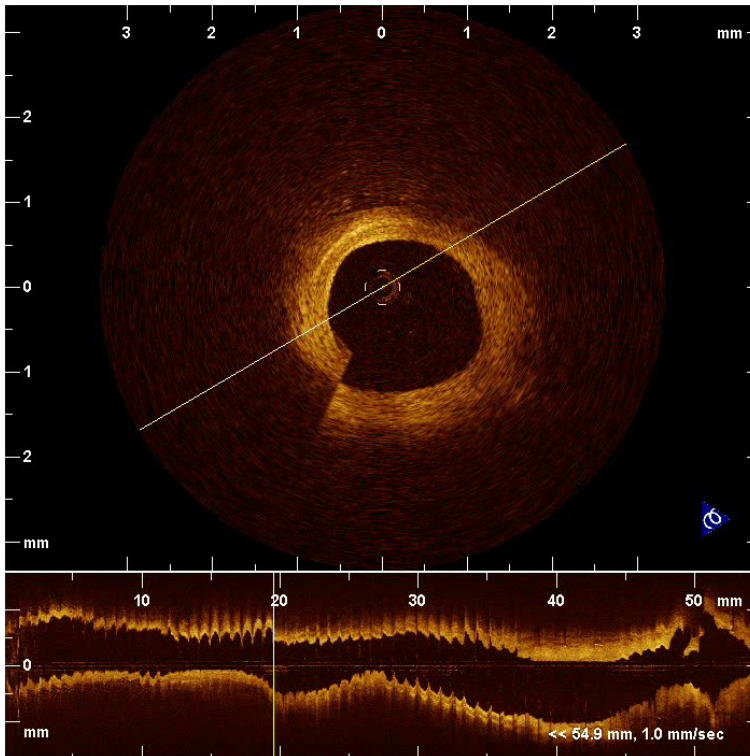


Figure 17 In-vivo intracoronary OCT. A) Illustrates the motion artefact during heart cycle in the cross sectional view, causing a “seamline” B) illustrates the motion artefact caused in the longitudinal view. Note the irregular lumen contour caused by three-dimensional motion of the artery relative to the OCT imaging catheter.

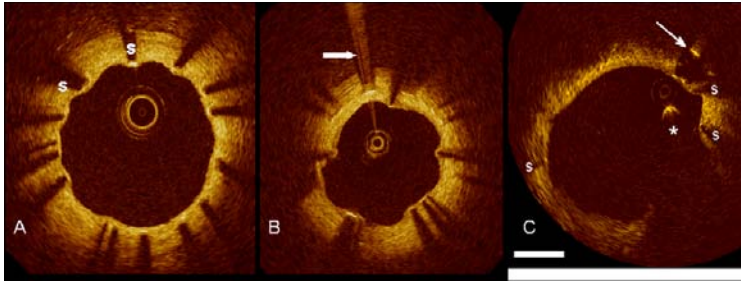


Figure 18 OCT artefacts in stent imaging. A) Circumferential stent struts are shown covered by a thin layer of tissue. Dorsal shadowing is evident behind the stent struts (S) with only the luminal surface of the strut visible with OCT. B) demonstrates circumferential stent struts with shadowing and bright reflections caused by saturation of the detector registering the interferogram (arrow) C) Arrow indicates a double reflection between stent and catheter. This can occur if a stent strut is imaged face-on, and reflects the OCT beam specularly. Shadows of other stent struts are marked by s; stent struts that do not show up as the typical bright dot, but do cast a shadow, are imaged under an oblique angle. * is a guide wire artefact. White bar is 1 mm.

CHAPTER 3.1

Figure 1. Matching of IVUS, OCT, and histology ex vivo. The distal side of the bifurcation of the LAD to the LCX (*) was used as the starting point for the first histology section. From this point to the distal and proximal side, histology sections were taken at 5-mm intervals to the end of the specimen (A). The histology sections (B) were used to identify the corresponding location in the OCT image data set (C) based on the similar visual appearance of the lumen morphology. Following this identification, the visualization software synchronized the OCT and IVUS image data sets and identified the corresponding IVUS image (D).

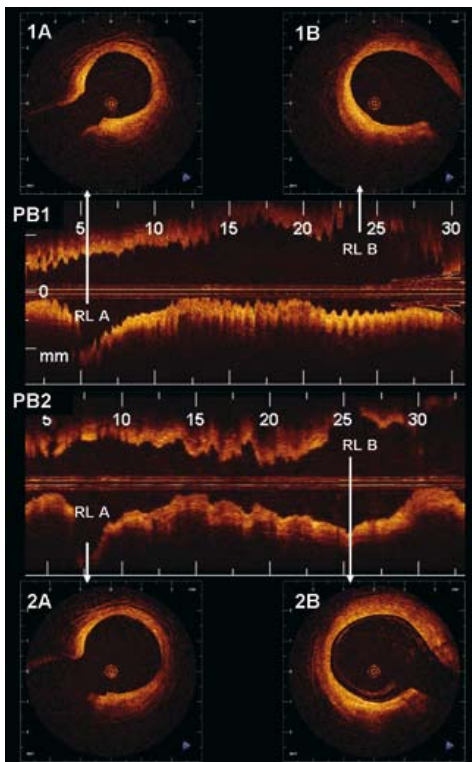
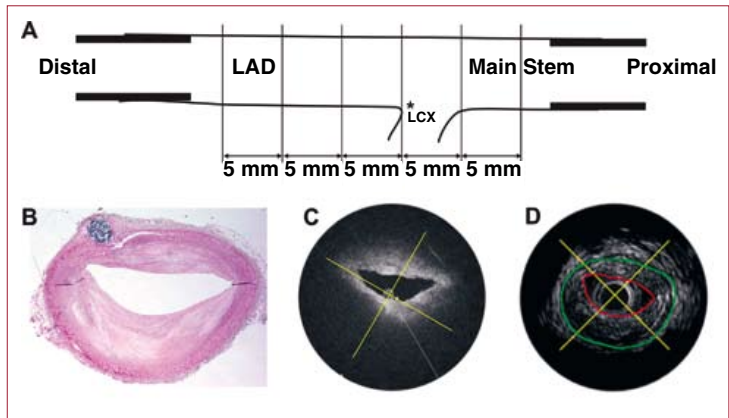


Figure 2. Selection of the region of interest in OCT pullbacks acquired with and without occlusion. PB1 and PB2 show the longitudinal view of the pullbacks acquired with and without occlusion, respectively. The white arrows indicate the side branches (SBA and SBB) used for matching of the region of interest. 1A and 2A show corresponding cross-sections of SBA with and without occlusion. 1B and 2B show corresponding cross-sections of the SBB with and without occlusion.

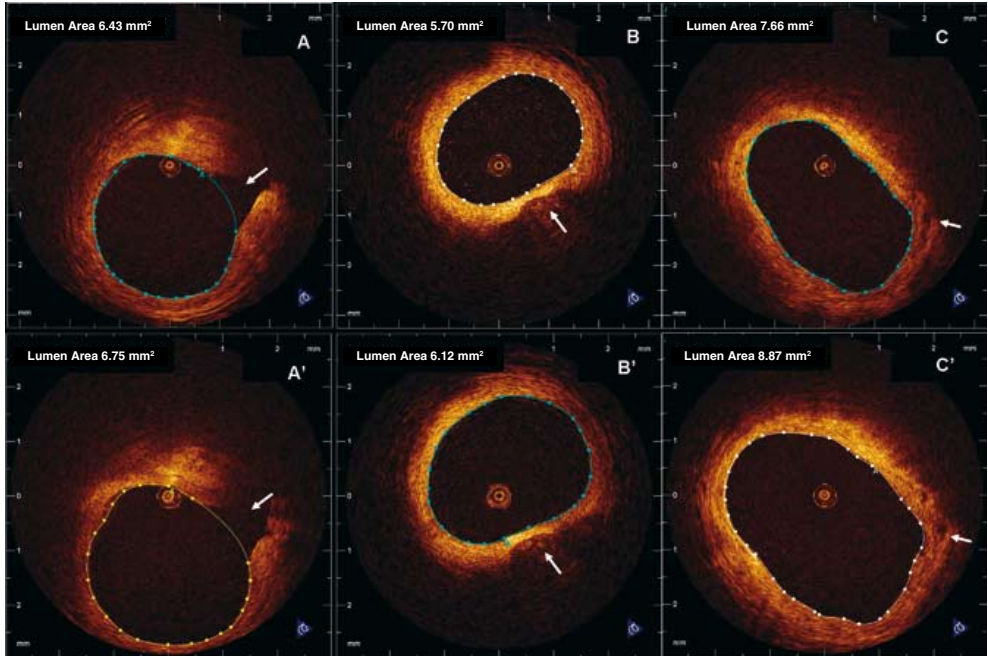


Figure 4. Example of differences in lumen measurements between OCT with and without occlusion. The figure shows corresponding images acquired with occlusion (A, B, and C) and without occlusion (A', B', and C'). The white arrows indicate the landmarks used for matching of the pullbacks (side branches in A and C and calcium spot in B). In all the examples, the lumen dimensions are smaller in the pullback acquired with occlusion.

CHAPTER 3.2

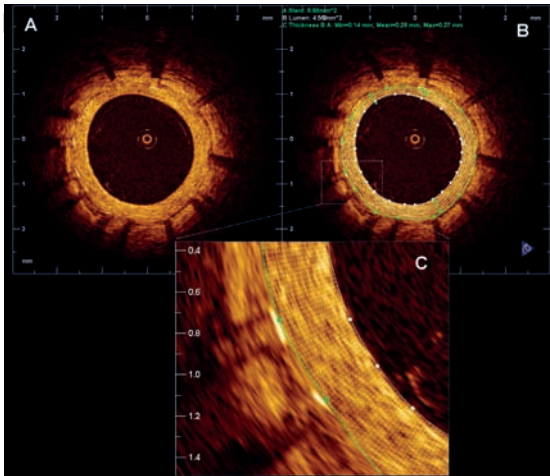


Figure 1. Tissue coverage measurement. A. Sirolimus eluting stent 9 months after stent implantation. B. The figure shows the lumen contour (white) and the stent contour (green). The tissue coverage area was calculated as stent area minus lumen area. The tissue coverage thickness was measured in 360 points (represented by the white chords). C. Magnification of 2 struts showing all the measurements (white chords) of the tissue coverage in front of every strut. For every strut the minimum, maximum and mean strut coverage was calculated.

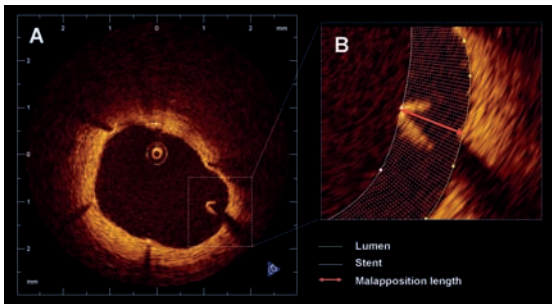


Figure 2. Malapposition. A. Example of a malapposed strut in a sirolimus eluting stent at 9 months follow up. B. Magnification of the malapposed strut. The yellow line represents the lumen contour and the white line corresponds to the stent contour. The distance from the endoluminal surface of the strut to the vessel wall (red arrow) was $440\ \mu\text{m}$ (higher than the sum of the metal and polymer thickness for this type of stent).

CHAPTER 4.1

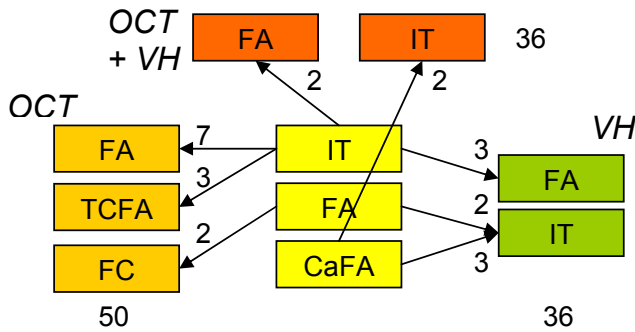


Figure 1. Chart of misclassifications. Only misclassifications occurring ≥ 2 are included in the figure. Misclassifications are derived from 36 cross-sections in VH-IVUS and OCT and VH-IVUS combined, misclassifications in OCT are derived from 50 cross-sections. Yellow = histology, green = VH-IVUS, orange = OCT, OCT/VH-IVUS = red. IT = intimal thickening, FC = fibrocalcific, FA = fibro-atheroma, CaFA = calcified fibroatheroma, TCFA = thin-cap fibro-atheroma. For example: of the lesions that were identified as IT in histology, 7 were classified as FA in OCT, 3 as FA in VH-IVUS, and 2 as FA in OCT and VH-IVUS combined.

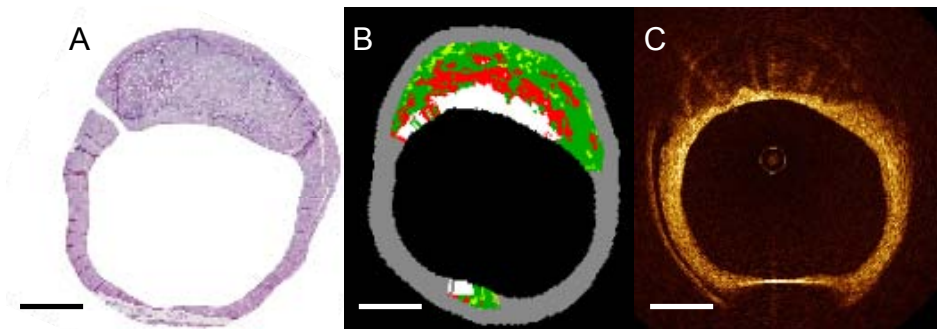


Figure 2. (A) Histology of a calcified fibroatheroma. (B) Corresponding VH-IVUS classified as calcified fibroatheroma. (C) Corresponding OCT classified as calcified fibroatheroma. The needle used to mark the site can be seen in the bright feature at 6 o'clock in OCT, as well as in the appearance of dense calcium in that location in VH-IVUS.

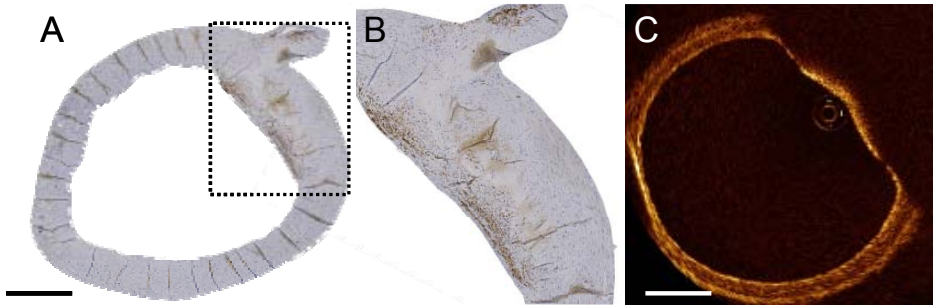


Figure 3 (A) CD68 stained cross-section. The intima consisting of a collagen/glycoprotein matrix is densely infiltrated by macrophages. (B) Magnification of selected region in A. (C) Corresponding OCT image. The region infiltrated by macrophages appears as a thin-cap fibro-atheroma. The bar indicates 1 mm.

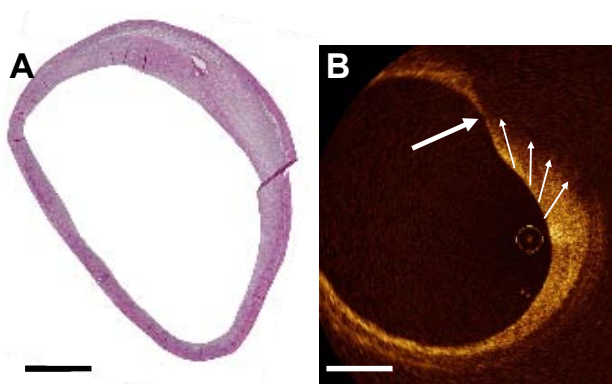


Figure 4. (A) Hematoxylin-eosin stained cross-section. (B) Intimal thickening is misinterpreted as thin-cap fibro-atheroma (TCFA) in optical coherence tomography (OCT). The large arrow points at the spot interpreted as a thin-cap. The four small arrows indicate the OCT beams and are all of the same length. The loss of signal due to tissue penetration is similar for each arrow. Because of eccentric catheter position this cross-section, classified as intimal thickening in histology, appears as a thin-cap fibro-atheroma (TCFA) in OCT. The bar indicates 1 mm.

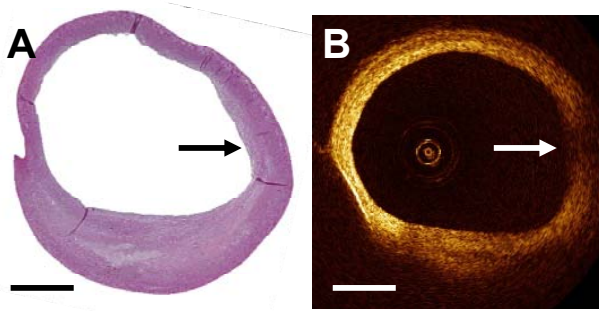


Figure 5. (A) H&E stained cross-section with (B) the corresponding optical coherence tomography (OCT). The arrow indicates a collagenous region in histology mistaken for a lipid region in OCT. Reduced optical efficiency of the catheter in this image section creates a dark sector, making mild intimal thickening appear as a fibro-atheroma. The bar indicates 1 mm.

CHAPTER 4.2

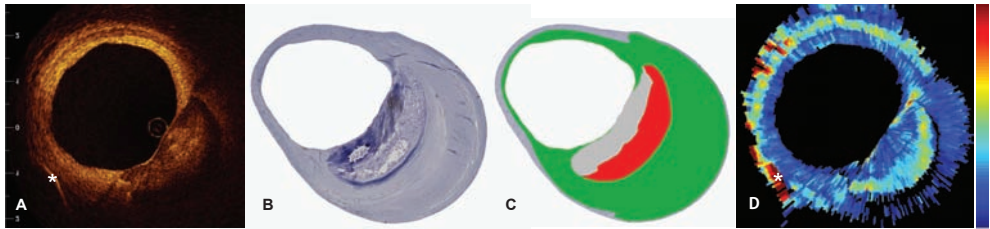


FIG. 2: A: OCT image of a coronary atherosclerotic lesion *ex vivo*. * indicates the needle used for marking the imaged site. B: Corresponding histology, H&E stain. C: Cartoon histology, overlaid on the original histology slide. It indicates an advanced necrotic core (red) behind a calcification (gray), and a slight fibrotic (green) circumferential intimal thickening. D: OCT-derived attenuation coefficient μ_t , plotted on a continuous color scale from 0 mm^{-1} to 15 mm^{-1} . The area corresponding to the necrotic core exhibits a higher attenuation coefficient (8–10 mm^{-1}) than the calcification next to it or the surrounding fibrous tissue (2–3 mm^{-1}).

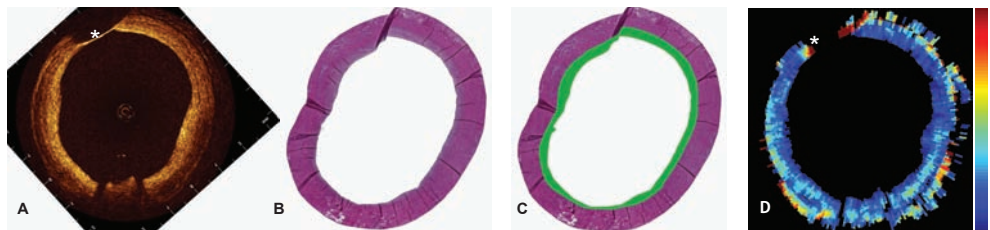


FIG. 3: A: OCT image of a circumferential homogeneous intimal thickening case. B: Corresponding histology, EvG stain. C: Cartoon histology, confirming a fibrous thickened intima. D: The attenuation coefficient μ_t is uniform and low, 2–4 mm^{-1} , in the area corresponding to the fibrous lesion. The color scale runs from 0–15 mm^{-1} .

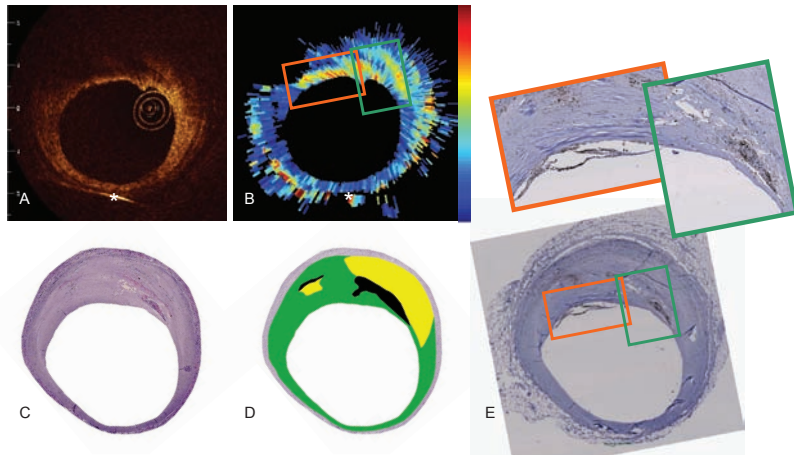


FIG. 4: A complex lesion containing necrotic core, haemorrhage, and macrophages. A: OCT image. B: Attenuation coefficient; scale from $0\text{--}15\text{ mm}^{-1}$. C: Histology, H&E stain. D: Cartoon, indicating an early stage necrotic lesion, with a thin fibrous cap, and intraplaque haemorrhage. E: CD68 stain, showing macrophage infiltration. The green and orange boxes are magnified above, and correspond to the indicated areas in B. Both areas show high attenuation coefficient ($10\text{--}12\text{ mm}^{-1}$), coinciding with the presence of necrotic core (green box) and macrophages (green and orange boxes).

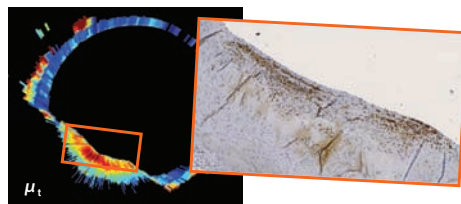


FIG. 5: An intimal xanthoma case. High attenuation (color scale $0\text{--}15\text{ mm}^{-1}$ as before) in a fibrous lesion occurs due to macrophage infiltration, as evidenced by the CD68 stain in the inset.

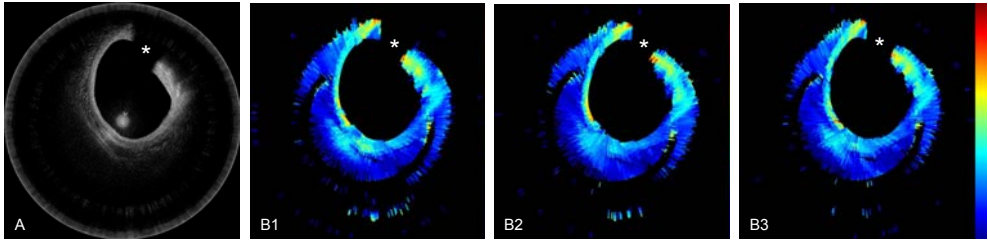


FIG. 6: Optical attenuation imaging *in vivo*. A: OFDI image of a coronary fibroatheroma (12–3 o'clock); marks the guidewire shadow. B1–3: Optical attenuation coefficient of three consecutive heart cycles, B1 corresponding to the data shown in A. The color scale runs from 0–12 mm^{-1} .

TABLE I: Color coding used for tissue type in the cartoon histology.

	Fibrous and smooth muscle cells
	Early necrotic core
	Advanced necrotic core
	Calcification
	Haemorrhage

CHAPTER 4.3

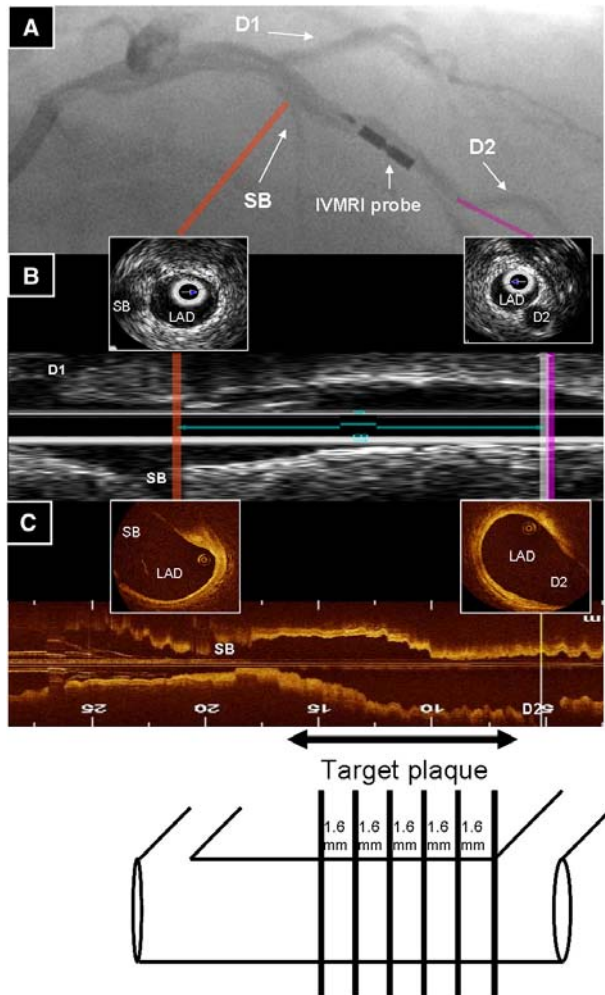
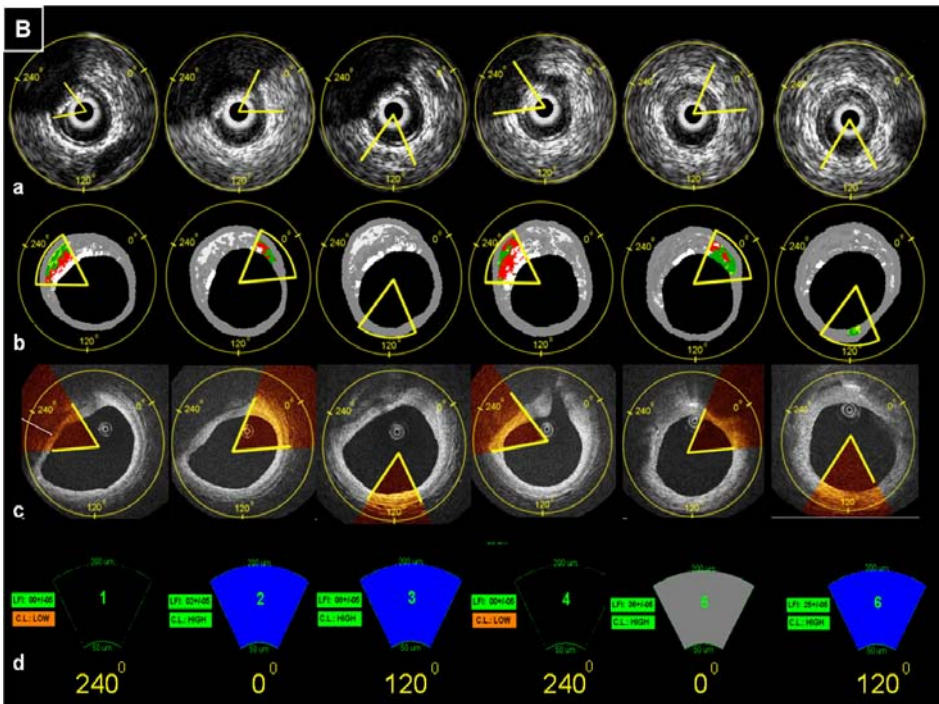
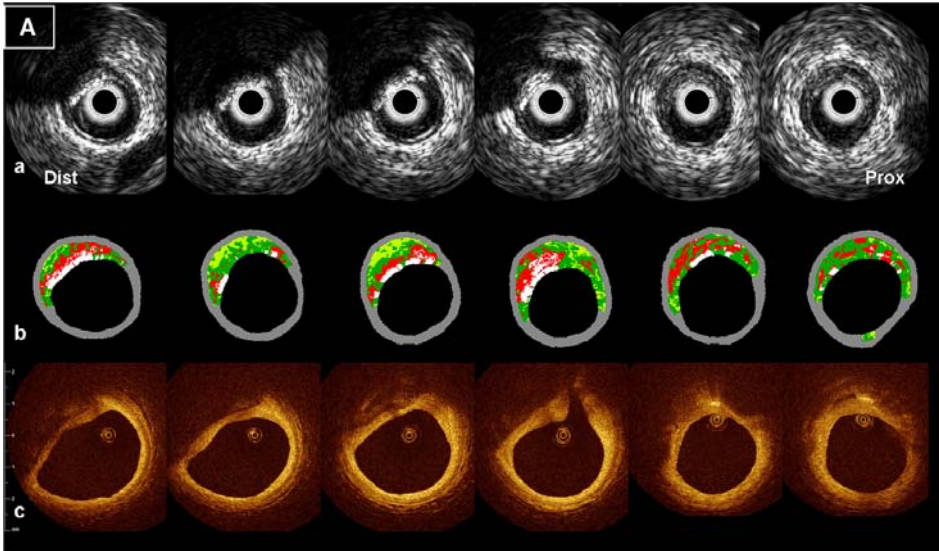


Fig. 1. Matching of the OCT and IVUS pullbacks. The position of the IVUS, optical coherence tomography (OCT) and intravascular magnetic resonance spectroscopy (IVMR) probe along the vessel was filmed before and after each acquisition (A). The "matching" of the region of interest in the IVUS (B) and OCT (C) pullback was based on the presence of anatomical landmarks (e.g. side branches visible in the longitudinal and cross-sectional views). To determine the longitudinal position of the IVMR probe in the vessel, a side branch was used as a marker. From the landmark to the proximal part of the vessel one frame every 1.6 mm was selected. D1: first diagonal, D2: second diagonal, SB: septal branch, LAD: left anterior descending coronary artery. CS: cross section.



CHAPTER 5.1

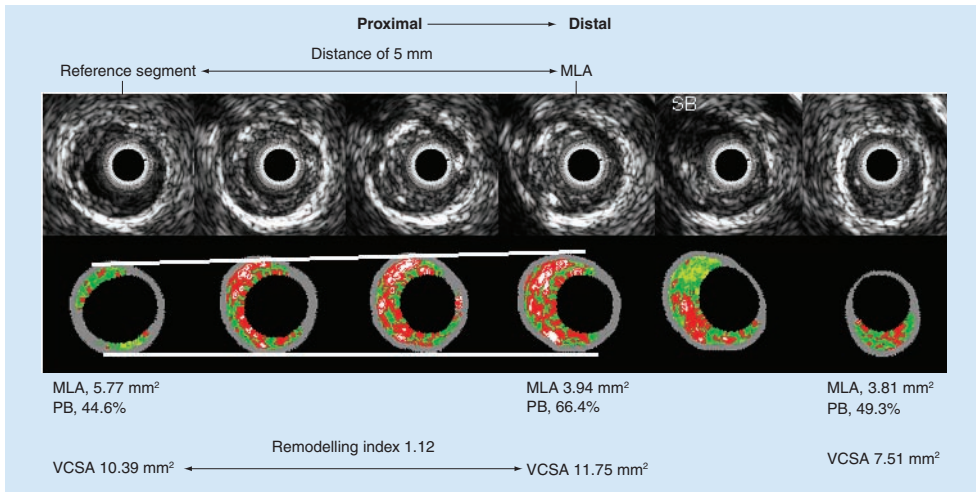


Figure 3. Intravascular ultrasound (IVUS) gray-scale frames and their corresponding virtual histology frames of an IVUS-derived thin-cap fibroatheroma (four central frames) and the proximal and distal reference segment in which the remodeling index was calculated.

MLA: Minimum luminal area; PB: Plaque burden; VCSA: Vessel cross-sectional area.

Virtual histology color code: green is fibrous, greenish is fibrofatty, red is necrotic core and white is dense calcium.

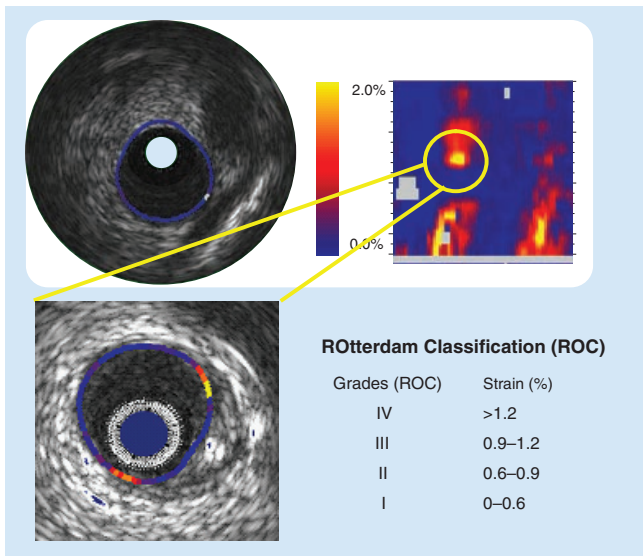


Figure 4. IVUS palpography. The local strain is calculated from the gated radiofrequency traces using cross-correlation analysis and displayed, color-coded, from blue (for 0% strain) to red to yellow (for 2% strain).

Plaque strain values are assigned a Rotterdam Classification (ROC) score ranging from 1 to 4 (ROC I= 0 to <0.6%; ROC II= 0.6 to <0.9%; ROC III= 0.9 to <1.2%; ROC IV >1.2%).

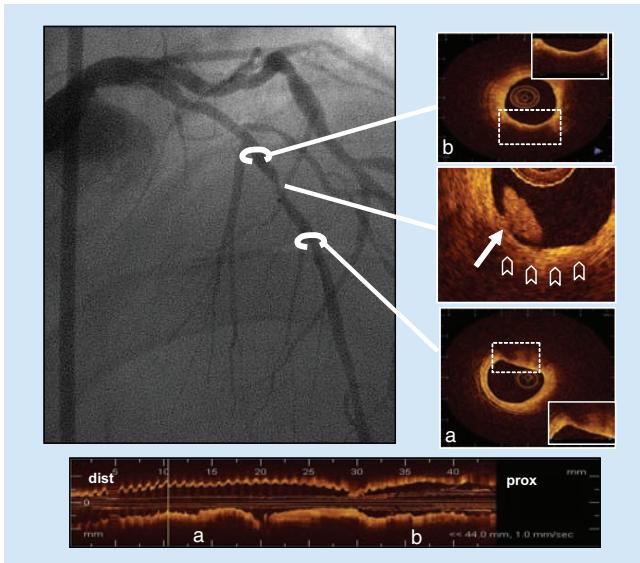


Figure 5. OCT and standard coronary angiography correlation. Angiography shows a complex lesion in the mid left anterior descending. The optical coherence tomography image shows a ruptured plaque with thrombus at that site (white arrow). Proximally and distally to the culprit lesion, thin-capped fibroatheroma lesions are present (**B**) and (**A**) respectively.

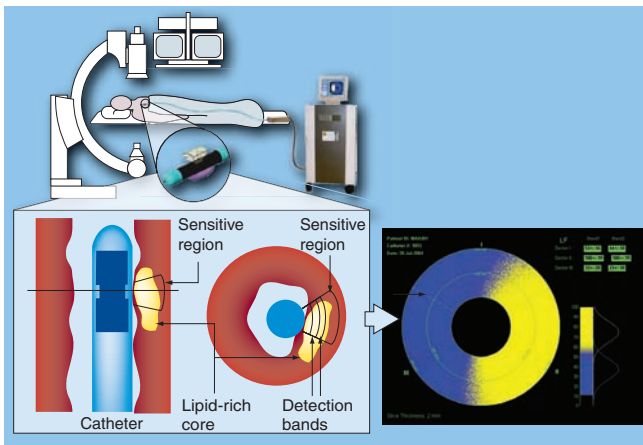


Figure 6. Intravascular magnetic resonance. The magnetic fields generated by the probe located at the tip of the catheter, create a FOV with a sector shape, looking sideways into the artery wall. The FOV has a lateral resolution of 60° , a longitudinal length of 2 mm and a depth of $200 \mu\text{m}$. It makes the analysis for the area comprised between 50 and $200 \mu\text{m}$ from the lumen. Acquired data is displayed as color-code sectors based of the lipid fraction index for each zone of the FOV. Blue indicates no lipid, gray correspond to intermediate lipid content and yellow indicates high lipid content. FOV: Field of view.

Colour Section

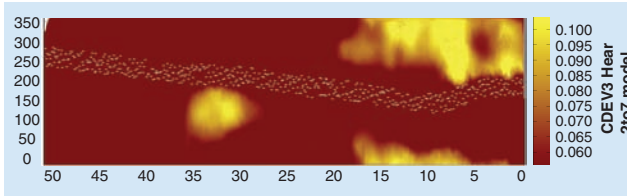


Figure 7. Near infra-red spectroscopy. Demonstration of spectral findings in the left anterior descending coronary artery of an autopsy specimen (unpublished data, on file InfraReDx, Inc., Burlington, Massachusetts). The panel shows the results of the scan, with distance along the lumen on the x-axis and arc of rotation on the y-axis. As indicated by the yellow signal, the scan successfully detected lipid necrotic core rich areas. Image courtesy of James E Muller.

CHAPTER 5.2

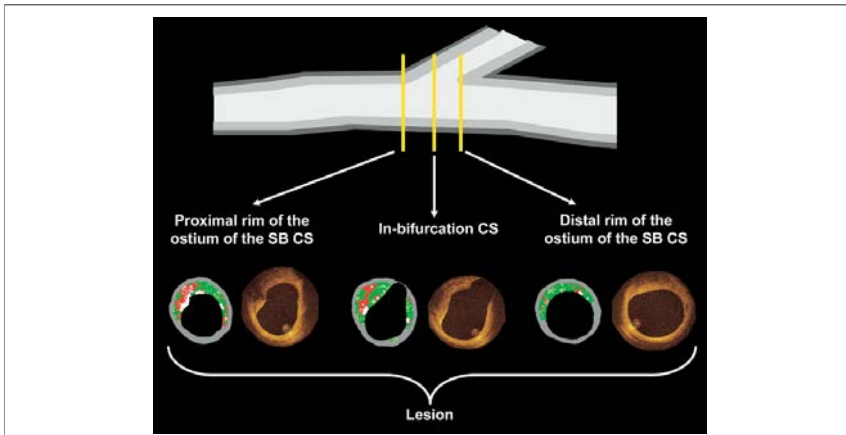


Figure 1. Bifurcation Selection and Analysis

Bifurcations that could be identified in both intravascular ultrasound-virtual histology (IVUS-VH) and optical coherence tomography (OCT) pullbacks were included. A strict selection of the analyzed cross-sections (CS) was followed to ensure correct matching between the 2 techniques. Plaques were analyzed only in the main branch. The lesion analysis included: 1) proximal rim of the ostium of the side branch (SB) CS (first frame proximal to the take-off of the SB); 2) in-bifurcation CS (frame with the larger ostial diameter of the SB); and 3) distal rim of the ostium of the SB CS (first frame distal to the take off of the SB).

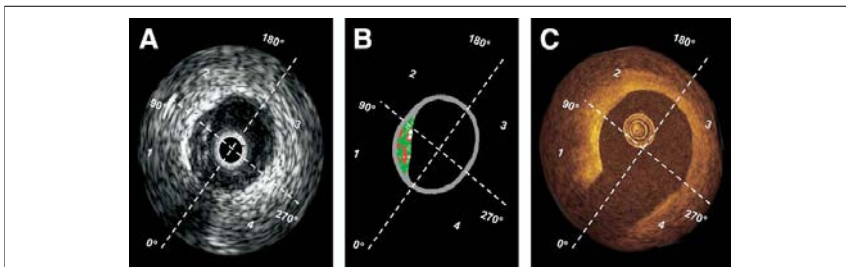


Figure 2. Location of the Plaque in Relation to the Flow Divider

To describe the plaque location in relation to the flow divider, the vessel cross-section was divided in 4 quadrants according to the position of the side branch. Quadrants 1 and 4 correspond to the ostium of the side branch, whereas quadrants 2 and 3 correspond to the part of the vessel wall located in front of the ostium of the side branch. (A) Grayscale IVUS. (B) Virtual histology. (C) OCT. Abbreviations as in Figure 1.

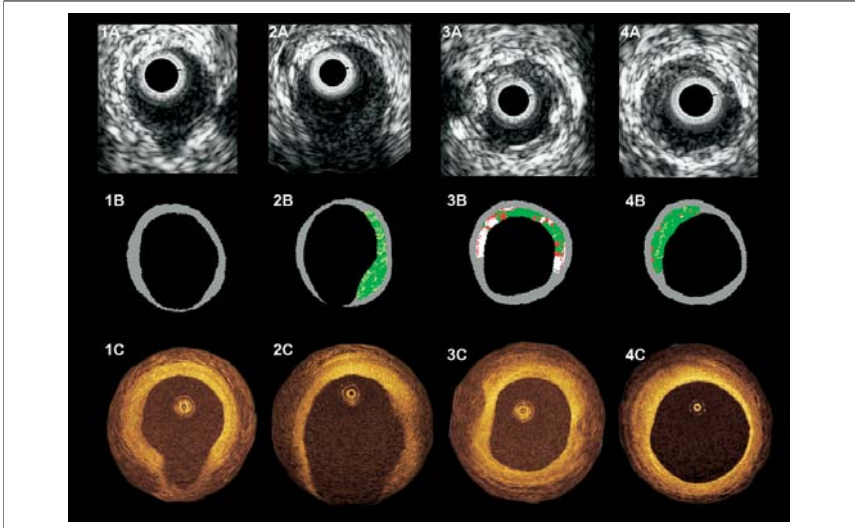


Figure 4. Low-Risk Plaques

Matched images of grayscale IVUS (A), virtual histology (B), and OCT (C) for the 4 types of plaques considered at low risk: 1: adaptive intimal thickening, 2: pathological intimal thickening, 3: fibrocalcific plaque, 4: fibrotic plaque. Abbreviations as in Figure 1.

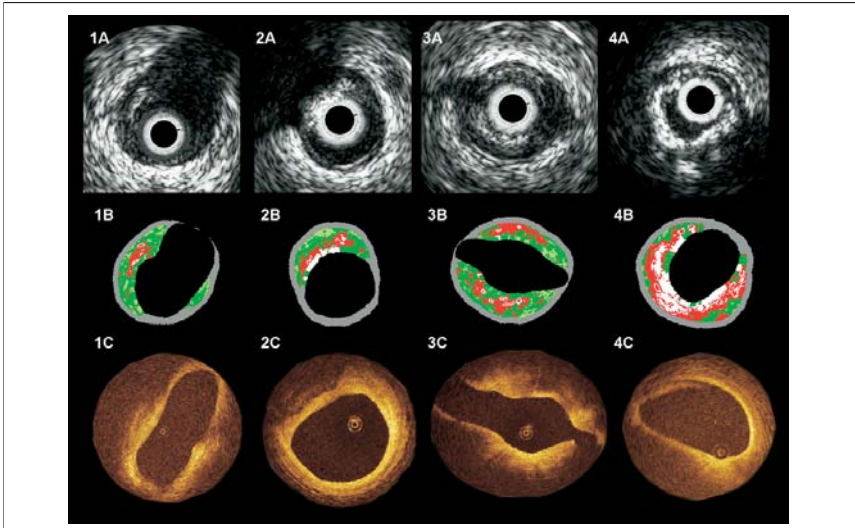


Figure 5. High-Risk Plaques

Matched images of grayscale IVUS (A), virtual histology (B), and OCT (C) for the 4 types of plaques considered at high risk of rupture. 1: fibroatheroma, 2: calcified fibroatheroma, 3: thin-cap fibroatheroma, 4: calcified thin-cap fibroatheroma. Abbreviations as in Figure 1.

CHAPTER 5.3

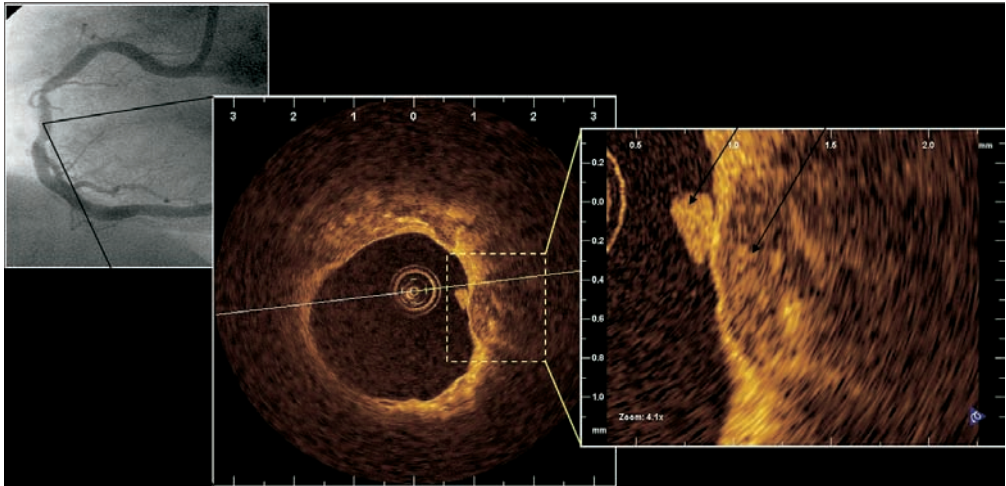


Figure 1. Angiography shows a calcific midvessel lesion. An additional calcific plaque with sharp and well-delineated margins was also observed using OCT remote and distal to the culprit lesion with attached mural thrombus.

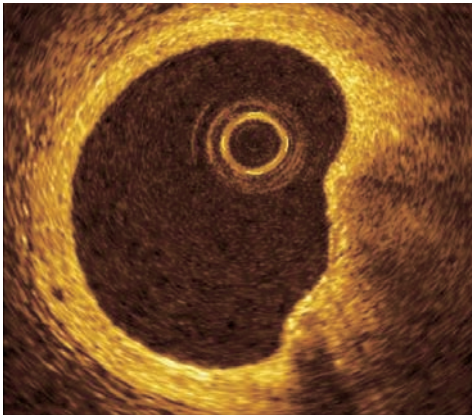


Figure 2. TCFA assessed using OCT overlying a large lipid-rich plaque (2 to 5 o'clock position). The bright highly reflective fibrous cap measured 30 to 80 μm .

CHAPTER 5.4

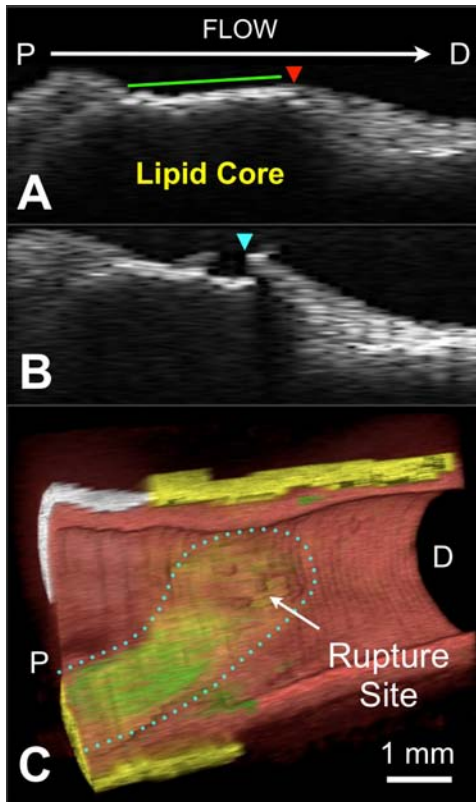


Figure 3: Image reconstructions. A, B. Longitudinal reconstructions of OFDI data acquired before rupture (A) and 18 minutes after baseline (B). C. 3D reconstruction of OFDI image data obtained 18 minutes following baseline. Green line in (A) – leading edge with a thin cap and superficial macrophages; red arrowhead in (A) – apex of lesion; blue arrowhead in (B) rupture site. Dotted region in (C) – thin fibrous cap; P – proximal; D – distal; Color scale for (C): red-artery wall, green-macrophages, white-calcium, yellow-lipid.

CHAPTER 6.2

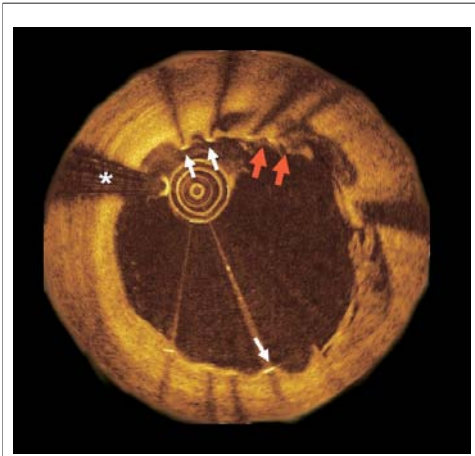


Figure 1. Incomplete Stent Apposition and Uncovered Struts

Optical coherence tomography cross section corresponding to a patient treated with drug-eluting stent implantation during primary percutaneous coronary intervention in the right coronary artery for an inferior ST-segment elevation myocardial infarction 9 months before. The **red arrows** indicate incomplete stent apposition, whereas the **white arrows** show some struts not covered by tissue. From 12 to 5 an irregular material suggestive of organized thrombus can be observed behind the struts. *Guidewire artefact.

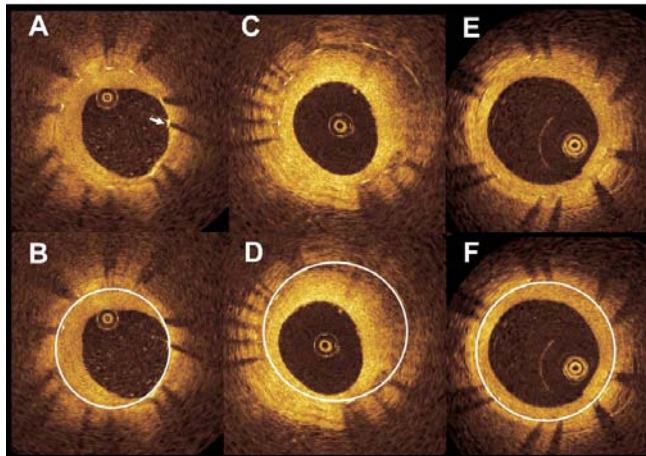


Figure 2. Tissue Coverage Symmetry Patterns

(A and B) Asymmetric tissue coverage with uncovered struts; whereas some struts are covered by a thick layer of tissue, other struts (from 2 to 5) are covered by a very thin layer, and there is even 1 uncovered strut (indicated by the **white arrow**). **(C and D)** Asymmetric tissue coverage without uncovered struts: all the struts are covered by tissue that shows very different thickness along the vessel circumference. **(E and F)** Symmetric tissue coverage: all the struts are covered by tissue that shows similar thickness along the vessel circumference.

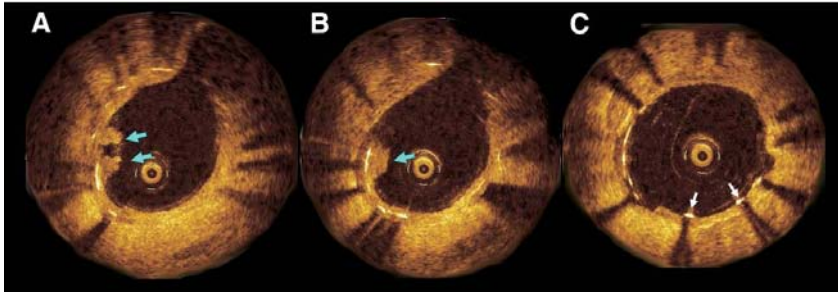
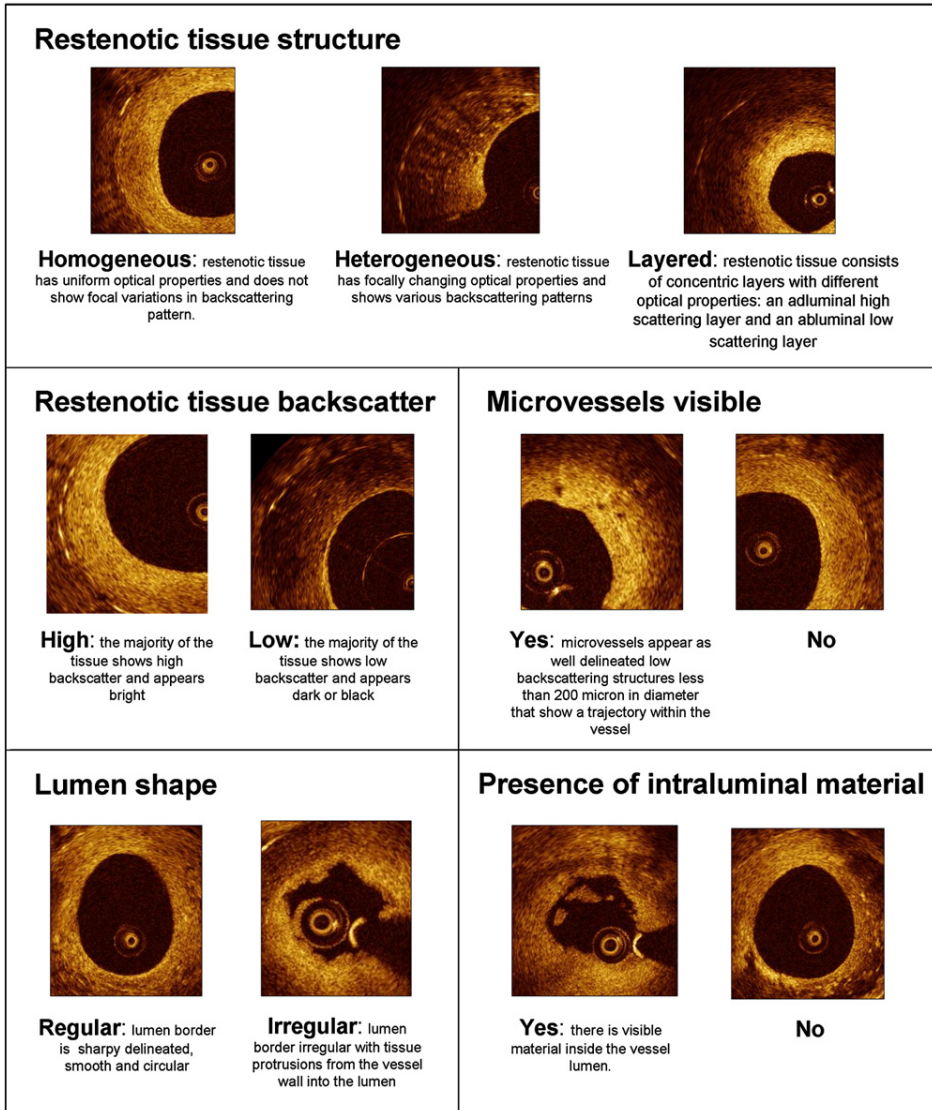


Figure 3. Struts Covered by Organized Thrombus

Optical coherence tomography cross-sections corresponding to a drug-eluting stent implanted in the left anterior descending coronary artery more than 4 years ago due to an anterior ST-segment elevation myocardial infarction. **(A and B)** The **blue arrows** indicate the presence of an irregular, highly reflective material (suggestive of organized thrombus) covering some struts. **(C)** Represents a cross section more proximal where some uncovered struts can be observed (**white arrows**).

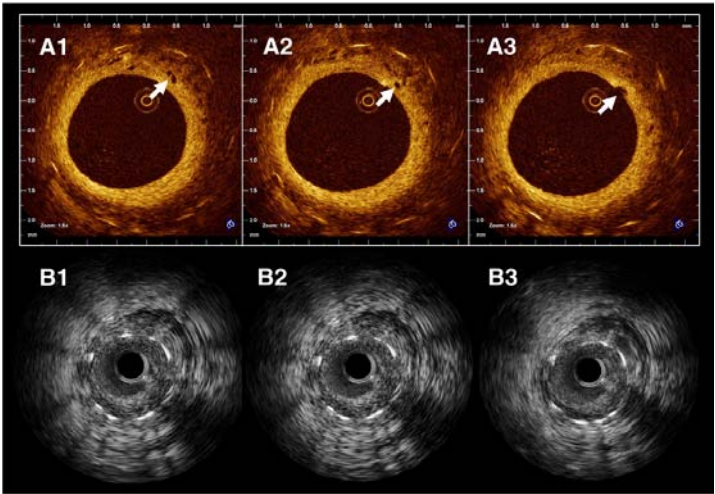
CHAPTER 6.3

Figure 1



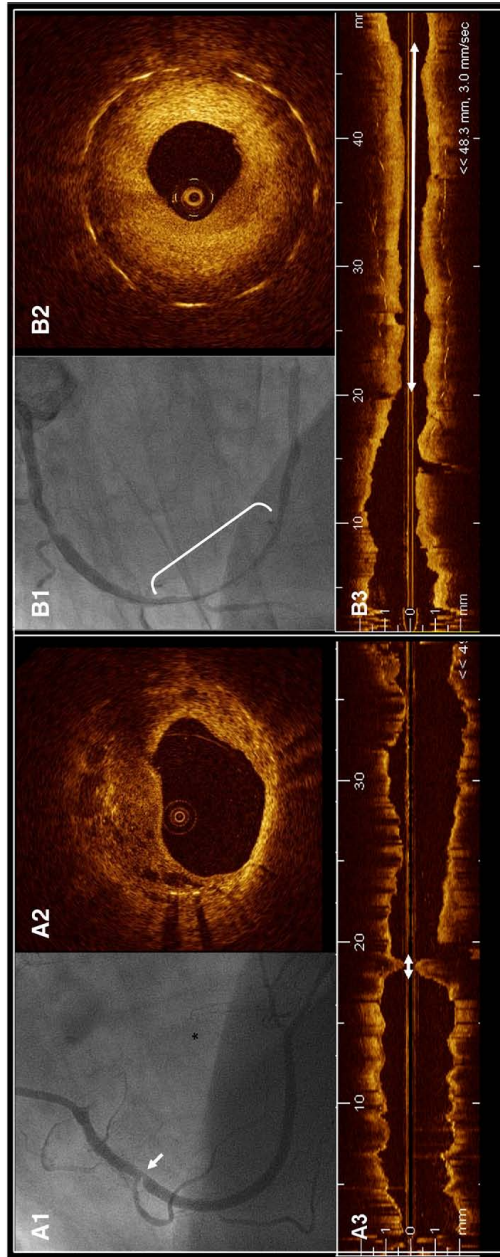
Stent restenosis qualitative OCT assessment.

Figure 2



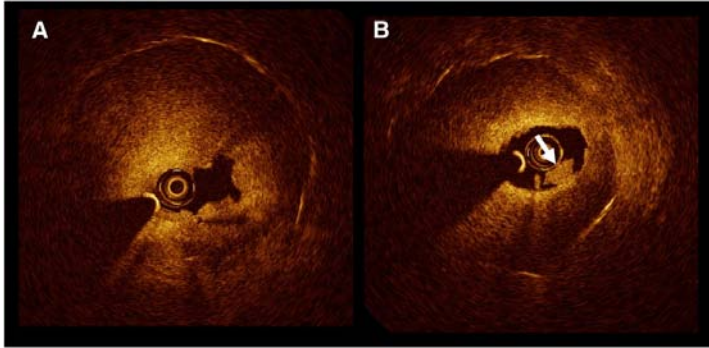
Microvessels: A1, A2, and A3 represent consecutive OCT cross sections showing a stent restenosis with presence of microvessels. One of them (indicated by the white arrow) shows a trajectory in the vessel (A1 and A2) and ends in the lumen (A3). B1, B2, and B3 show corresponding IVUS cross sections in the same region in which the microvessels are not visible.

Figure 3



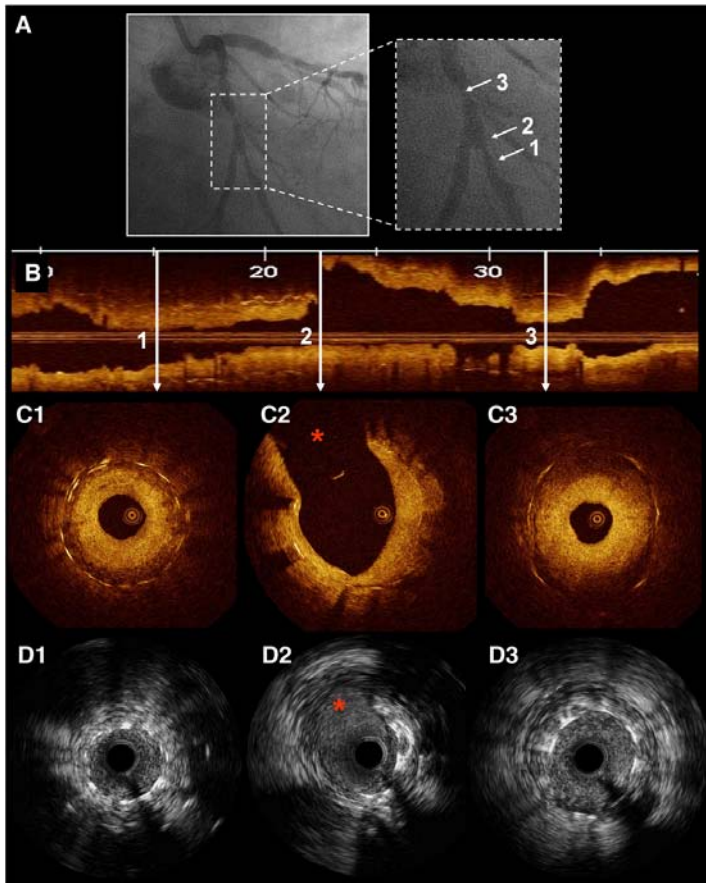
Restenosis morphology by OCT and angiographic classification. **A**, Example of a patient with a focal restenosis by angiography (white arrow in A1). An OCT cross section in the restenosis lesion (A2) shows a heterogeneous tissue with predominant low backscatter. The longitudinal OCT image (A3) shows a very focal restenosis (white arrows). **B**, Example of a patient with a diffuse restenosis by angiography (white bracket in B1). An OCT cross-sectional image in the restenosis region (B2) shows a restenotic tissue with layered structure and predominant high backscatter. The OCT longitudinal reconstruction (B3) also demonstrates a diffuse restenosis (white arrows).

Figure 4



Lumen shape and intraluminal material: OCT images obtained in a patient referred for coronary angiography for unstable angina. A stent restenosis lesion showing irregular lumen shape (**A**) and presence of intraluminal material (white arrow in **B**) was visualized.

Figure 5



Comparison of OCT and IVUS findings in a restenosis lesion. **A**, Angiographic image showing a paclitaxel-eluting stent restenosis affecting the proximal and distal part of the stent. 1 indicates the distal stent part, 2 indicates the bifurcation left circumflex (LCX)—obtuse marginal (OM), and 3 indicates the proximal stent part. **B**, Longitudinal OCT view showing the restenosis in the distal part of the stent (1), the bifurcation (2), and the proximal part of the stent (3). Corresponding OCT cross sections are shown. C1, Restenosis in the distal part of the stent showing layered appearance with 2 concentric layers (one inner high scattering and one outer low scattering layer). C2, Bifurcation LCX-OM. C3, Restenosis affecting the proximal part of the stent that also shows layered appearance. D shows the corresponding IVUS images of the distal part of the stent (D1), bifurcation (D2), and proximal stent (D3). The clear layered appearance of the restenotic tissue visible by OCT cannot be distinguished by IVUS. Asterisk in C2 and D2 indicates the LCX.

CHAPTER 6.4

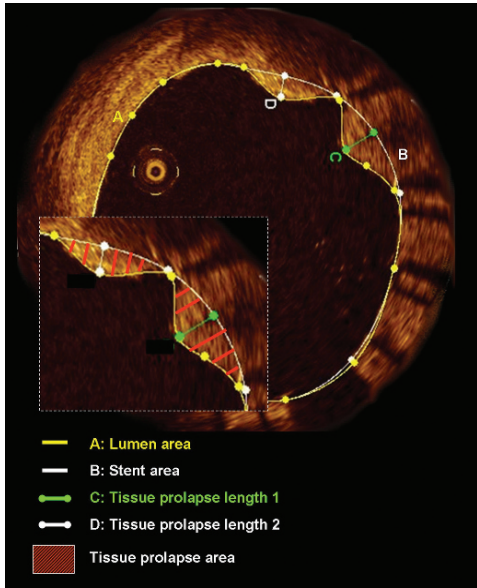


Figure 1 Tissue prolapse: defined as convex shaped, protrusion of tissue between adjacent stent struts towards the lumen without disruption of the continuity of the luminal vessel surface. The figure shows a cross section in which tissue prolapse is visible. The amplified image shows two areas of tissue prolapse. For each tissue prolapse region the maximum length and the area were measured.

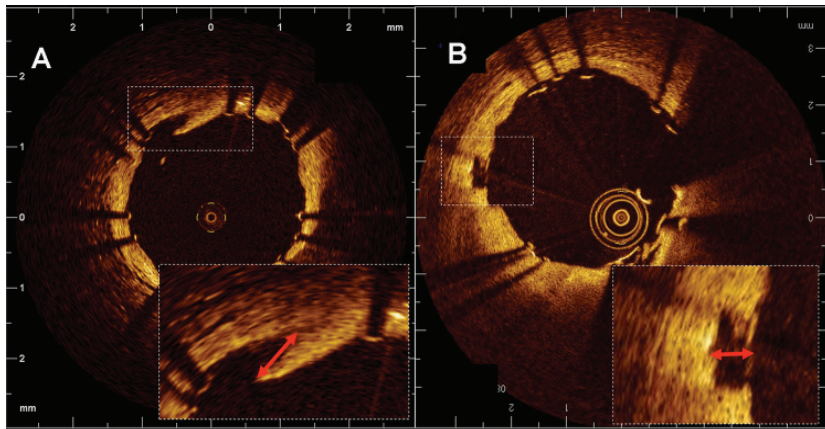


Figure 2 Intra-stent dissection: defined as a disruption of the vessel luminal surface in the stent segment. This entity can appear with two forms: (A) dissection: the vessel surface is disrupted and a dissection flap is visible. The length of the flap (red arrow) was measured as the distance from its tip to the joint point with the vessel wall; (B) cavity: the vessel surface is disrupted and an empty cavity can be seen. The maximum depth of the cavity (red arrow) was measured from the lumen to the deepest cavity point inside the vessel wall.

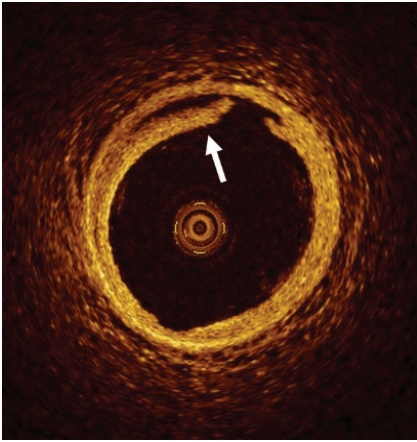


Figure 3 Edge dissection: defined as a disruption of the vessel luminal surface in the edge region (5 mm proximal and distal to the stented region, no struts are visible).

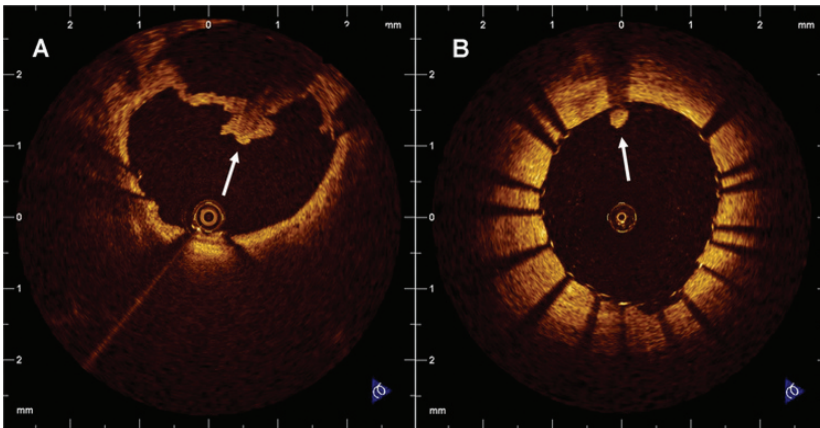


Figure 4 Thrombus: defined as an irregular mass with dorsal shadowing protruding in the lumen (mural thrombus) (white arrow in A) or a luminal mass with dorsal shadowing that is not connected to the vessel wall (white arrow in B).

CHAPTER 6.5

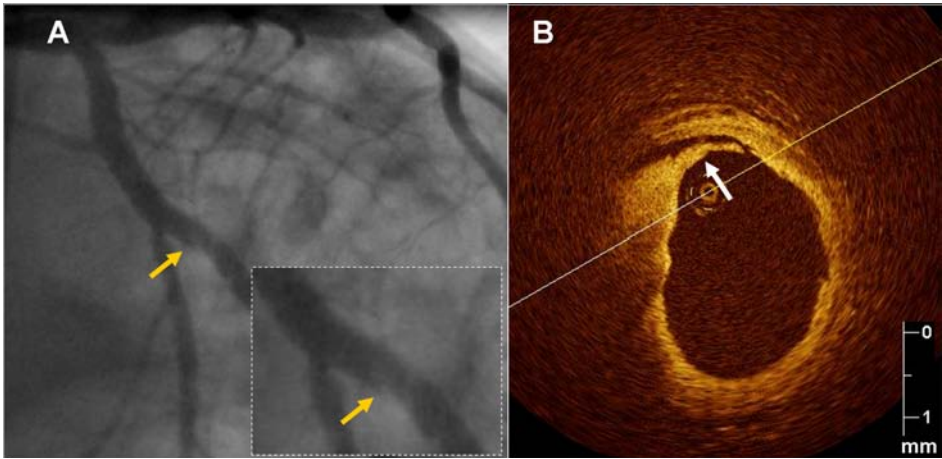


Figure 1. Edge dissection detection by angiography and optical coherence tomography (OCT). A: angiographic image showing a distal edge dissection (yellow arrow). The dissection can be observed with more detail in the amplified image. B: OCT shows a disruption of the vessel luminal surface in the distal stent border with a visible flap (white arrow).

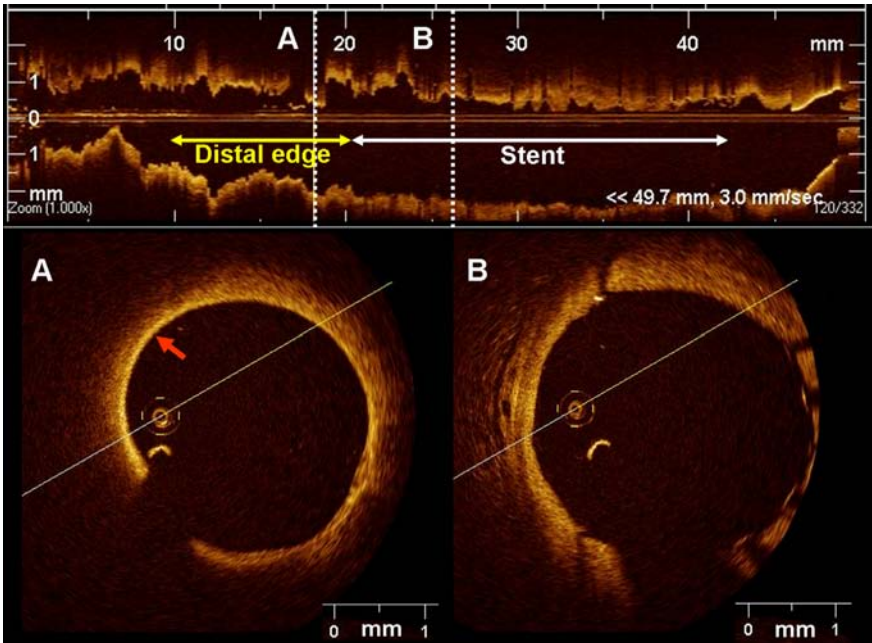


Figure 2. Plaque type at stent edges. Example of a patient treated with primary percutaneous coronary intervention and stent implantation for inferior ST elevation myocardial infarction. The upper panel shows the longitudinal optical coherence tomography (OCT) image. The yellow arrow

indicates the distal edge and the white arrow indicates the stented region. The lower panels show two cross sections. A: distal edge. A low backscattering plaque with diffuse borders covered by a thin fibrous cap (red arrow, thin cap fibroatheroma) can be observed. B: stented region.

CHAPTER 6.6

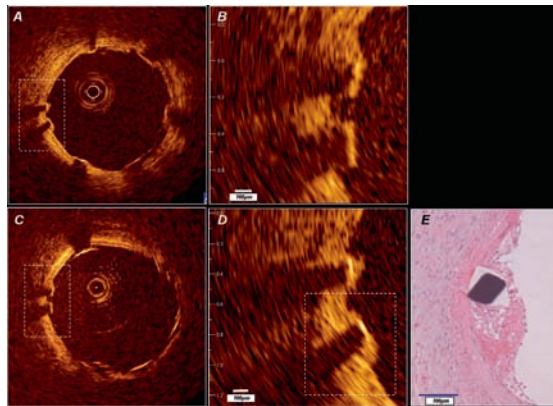


Figure 1. In vivo OCT (LightLabImaging™, Boston, MA, USA) in a porcine coronary artery. A) Baseline OCT immediately after stent implantation shows adequate stent expansion and apposition of the struts against the normal coronary wall. B) Magnification demonstrating the stent strut vessel wall interface. C) Follow-up investigation at five days. The stent struts are clearly visible and show thin, bright reflective tissue coverage in the magnification D) Histology E) confirms the presence of a thin neointimal layer.

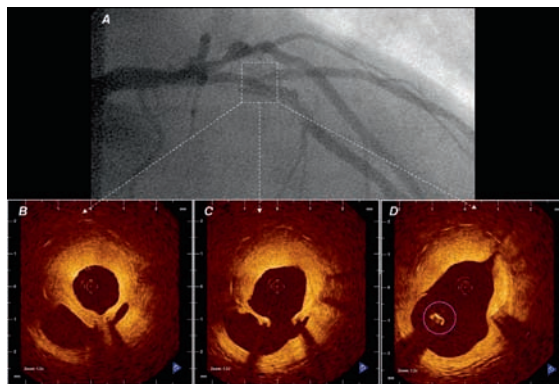


Figure 2. In vivo OCT (LightLabImaging™, Boston, MA, USA) in the LAD in a patient presenting with in-stent restenosis. A) The coronary angiogram shows a lumen narrowing within the stent that is covering the second diagonal branch. OCT visualises the complex coronary anatomy in great detail. The stent is covered by a thick neointima that shows a layered appearance with a bright, highly reflective luminal layer, an intermediate layer and a dark, signal poor layer surrounding the struts (B). The diagonal take off can be clearly seen (C) as well as a stent strut that is "floating" in the carina (D).

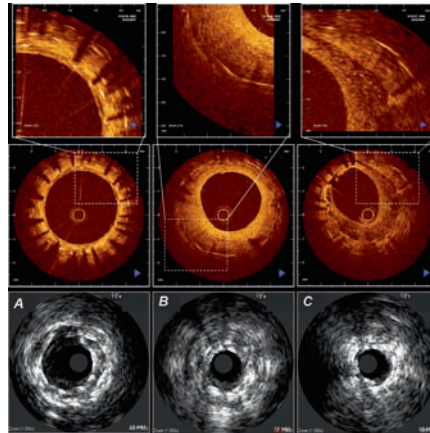


Figure 3. Demonstrates the information that can be gathered from IVUS (20Mhz, lower panels) and from OCT imaging (mid and upper panels, LightLabImaging™, Boston, MA, USA) in patients at follow-up after stent implantation. These are corresponding cross sections within a stent, imaged by both, OCT in the upper panels and by IVUS in the lower panels. The images represent the same spots within a coronary artery (A, B, C), and illustrates the different quality of information that can be obtained by OCT as compared to conventional grey scale IVUS. A) Three layers of stents can be seen. OCT is able to clearly visualise the individual stent struts, the neointimal layers separating the different stents and the very thin coverage of the most inner, luminal stent struts. B) a bright, eccentric and relatively thick neointimal layer can be seen C) an eccentric thick neointimal layer is visible, however, the structure of this neointima differs considerably from the example B) with a low-reflective and speckled appearance.

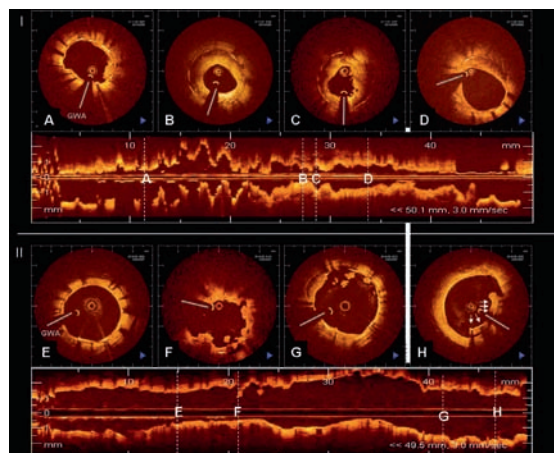


Figure 4. OCT (LightLabImaging™, Boston, MA, USA) findings in two patients presenting with late drug-eluting stent (DES) thrombosis. OCT was performed in both cases immediately after thrombus aspiration and reveals completely different morphologic findings, possible suggesting two different mechanisms for late stent thrombosis, focal restenosis and incomplete strut coverage. I) Patient with late stent thrombosis three months after DES implantation in the left circumflex artery. OCT reveals an adequately expanded stent, all struts are well apposed against the vessel wall. All struts show tissue coverage, which is more pronounced in the proximal portion of the stent (D) as compared to the distal stent portion (A). There is focal in-stent restenosis (B, C) with severe lumen narrowing (MLA 1.63 mm²). The neointima shows a layered appearance with a luminal bright, highly reflective layer, an intermediate layer and a dark, signal poor layer surrounding the struts. Remnants of the thrombus are focally seen focally as irregular mural structures, protruding into the lumen (A, C). II) Patient with very late stent thrombosis four years after DES implantation in the left anterior descending artery. OCT reveals an adequately expanded stent, however, there is incomplete stent strut apposition at the proximal stent edge with incomplete tissue coverage in 21% of struts. (E) The distal stent portion, shows a well expanded and apposed stent with thin tissue coverage by OCT. (F) irregular lumen borders with intraluminal remnants of the thrombus. (G) proximal stent portion showing a strut without visible tissue coverage in 12 o'clock position and thrombus fragments in the lumen. (H) proximal stent edge with incomplete apposition of five stent struts (arrows) against the vessel wall. The distance to the vessel wall is 200 micron. OCT shows tissue around the stent struts (DD thrombus, neointima). GWA: guidewire artefact.

CHAPTER 7.1

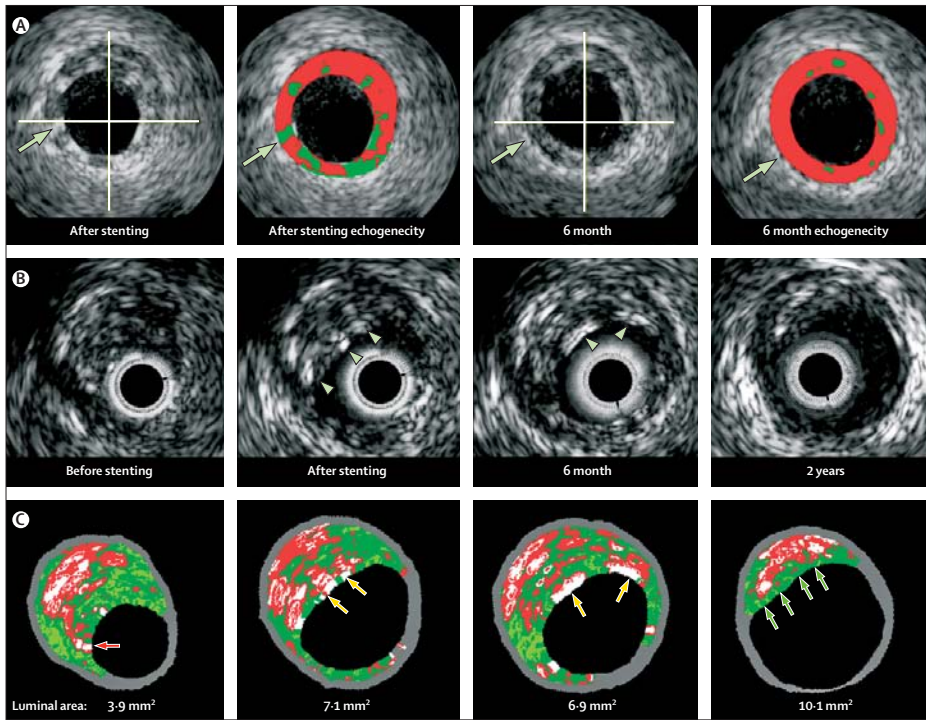


Figure 4: Results from echogenicity, grey-scale intravascular ultrasound, and intravascular ultrasound virtual histology

(A) Grey-scale appearance after stenting and at 6 months with echogenicity analysis (red: hypoechoic tissue, green: hyperechoic tissue). The arrows show a strut of the implanted stent. (B) Examples of grey-scale intravascular ultrasound before stenting, after stenting, at 6 months, and at 2 years. The arrowheads show struts that remain visible at each follow-up time. (C) Serial assessment by intravascular ultrasound radiofrequency backscattering. Before stenting, there is a large plaque with a necrotic core. The red arrow indicates the necrotic core in contact with the lumen. After stenting, the lumen has enlarged to 7.1 mm² and two struts (yellow arrows) are depicted as (pseudo) dense calcium. At 6 months, the two struts remained visible (yellow arrows) with partial reduction of the luminal area. At 2 years, the endoluminal pseudo-dense calcium depicting struts has disappeared, which is consistent with strut absorption. There is now a fibrous cap covering the necrotic core (green arrows), and late enlargement of the lumen (10.1 mm²) and shrinkage of the plaque.

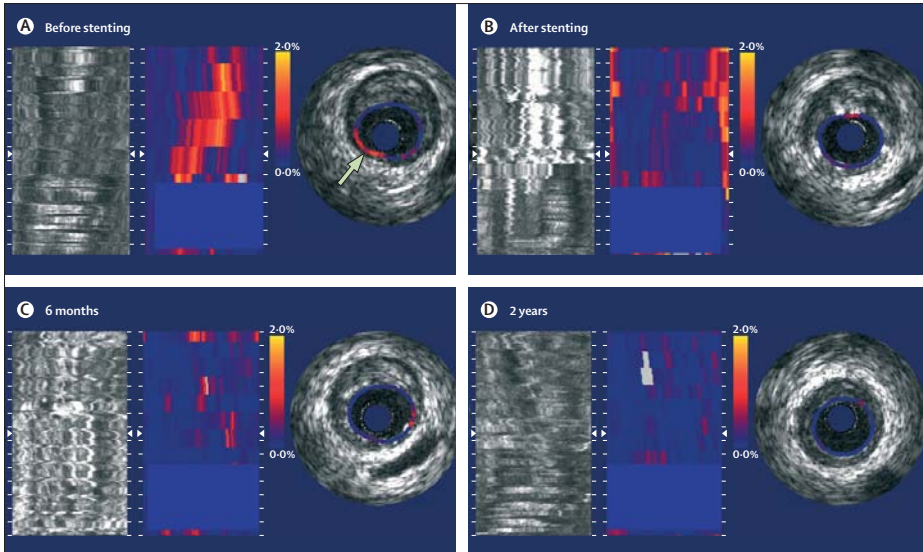


Figure 5: Sequential changes in strain assessed by intravascular ultrasound palpography

(A) Before stenting, a long area of high strain (colour-coded for strain ranging from 1% to 2%) is seen; on a single cross-section, the high strain region is located at the shoulder (arrow) of the plaque. (B) Abolition of this high strain spot after stenting. (C) and (D) show continued absence of high strain at 6 months and 2 years after stenting.

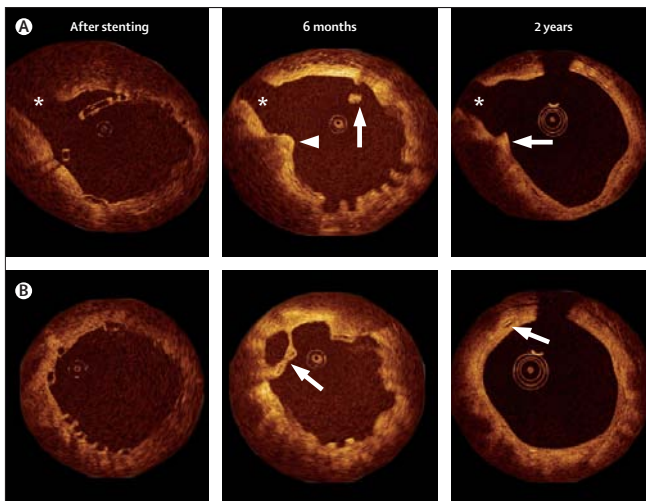


Figure 6: Serial assessment of stent struts by optical coherence tomography

(A) After stenting, incomplete apposition of struts (preserved box) in front of a side-branch ostium. At 6 months, persistent incomplete stent apposition (arrow) and resolved incomplete stent apposition (arrowhead), with open box appearance. At 2 years, there is now smooth appearance of the endoluminal lining without strut malapposition since struts have been absorbed. There is guidewire shadowing (at the top of the image), and a strut is still just discernible as a bright spot (arrow). (B) Complete apposition of strut (box appearance) after the procedure. At 6 months, there is late acquired incomplete stent apposition of the struts (preserved box appearance) with tissue bridging connecting the struts (arrow). The endoluminal lining is corrugated. At 2 years, smooth endothelial lining with almost circular cross section. Generally, the struts are no longer discernible, although there is a bright reflection that could indicate a strut (arrow). Asterisk indicates a side branch.

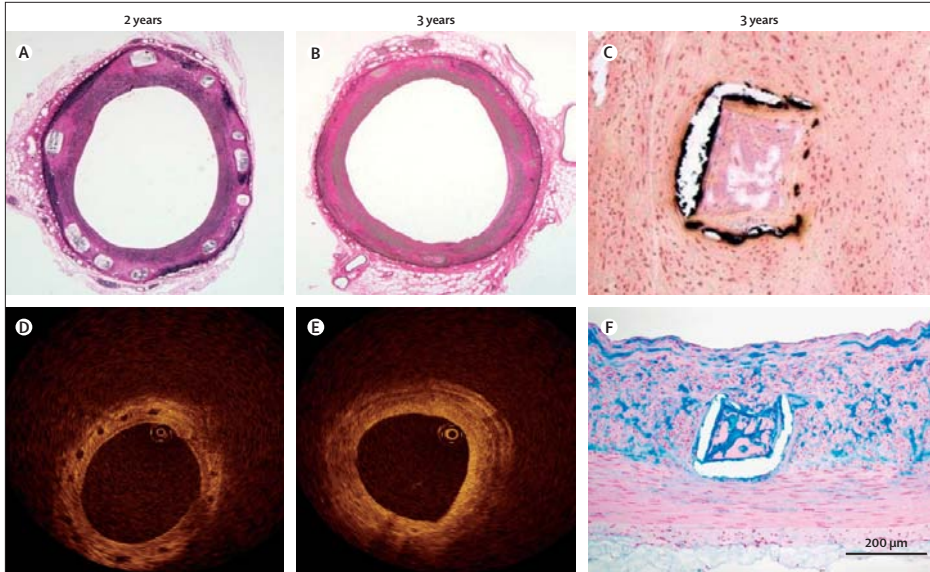


Figure 7: Preclinical porcine studies at 2 years and 3 years after stent implantation

(A) and (B) represent 2 year and 3 year porcine histology with haematoxylin-eosin staining, showing disappearance of the void previously occupied by a polymeric strut. The box-like spaces were visible on OCT (D) and are still visible at 2 years but almost indiscernible at 3 years (E). Detailed histology (C and F) shows the apparent voids previously occupied by the polymeric struts have been preserved, but filled in by proteoglycan material. In the Von Kossa stain (C), mineralisation is seen around the previous site of a strut. In the Alcian blue stain (F), proteoglycan has replaced the BVS stent strut.

CHAPTER 7.2

Stent Strut Appearance at Follow-up

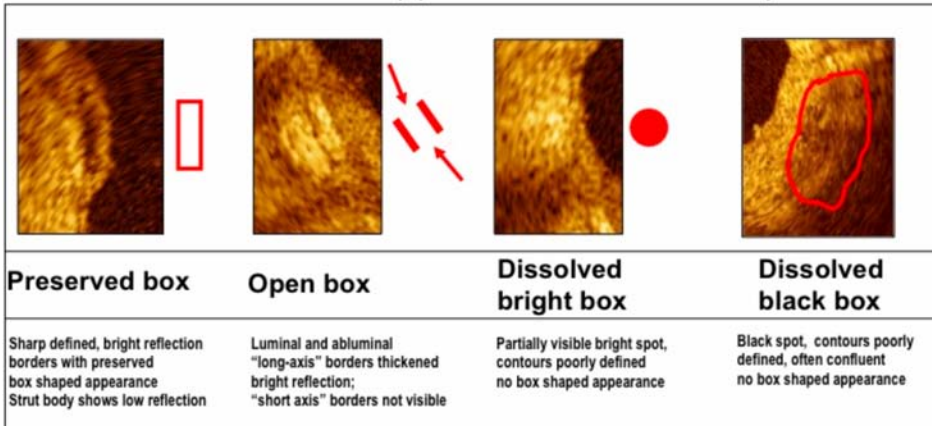


Figure 2. Representative photographs of the four subcategories of reflectance characteristics by OCT in BVS struts at follow-up as observed in the first-in-man ABSORB trial. Description of each subcategory is included in the illustration. (modified from Ormiston, *et al.* ⁶)

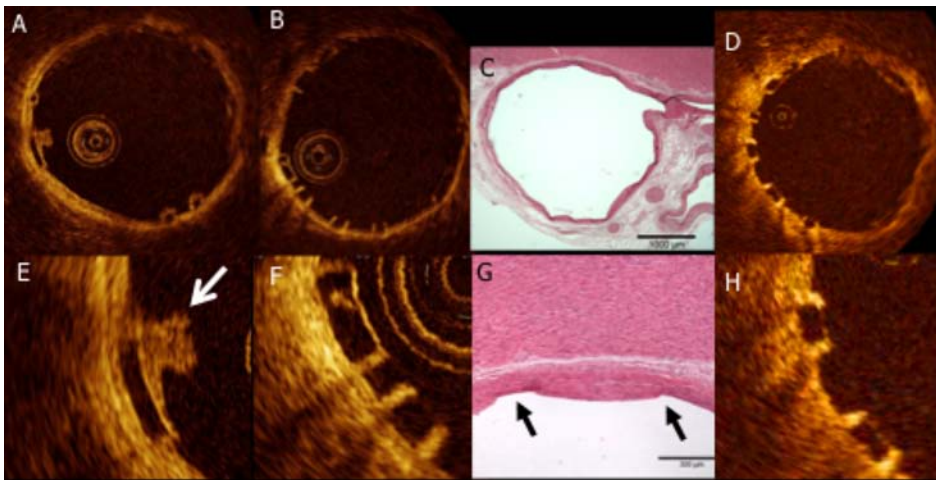


Figure 3. OCT images immediately after BVS implantation. In a pig to whom a BVS was implanted with heparin (A, E), at 9 o'clock, the strut with preserved box appearance was covered with high intensity irregular material without shadowing, suggesting presence of a white thrombus (E shows a magnified image). In a pig implanted with clopidogrel, aspirin and heparin (B, F), all struts showed preserved box appearance without any tissue coverage. Histology after the removal of polymeric struts showing the footprints of the struts on the intima of the vessel wall (C, G). Note the absence of fracture of the internal elastic membrane. Similarly, in humans, all struts demonstrate preserved box appearance without tissue coverage immediately after stent implantation (D, H).

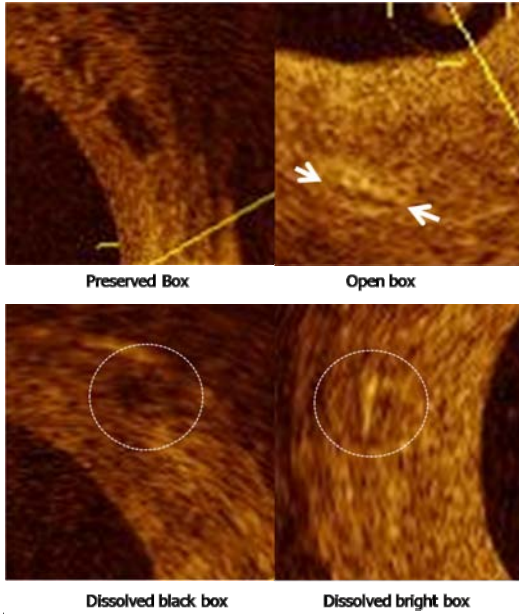


Figure 4. Examples of strut appearances assessed with OCT in porcine coronary arteries.

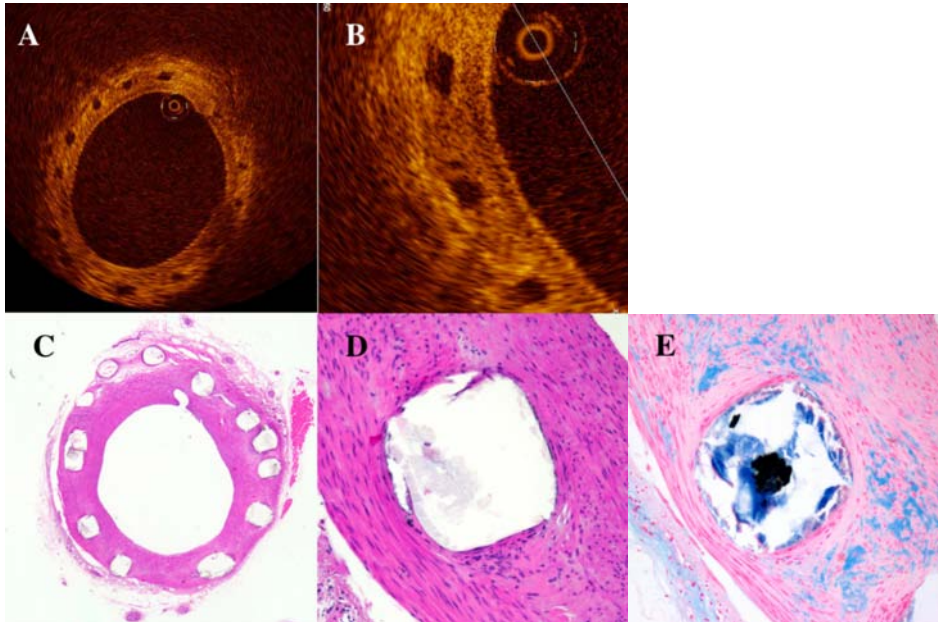


Figure 5. OCT images and corresponding histology at 2 years after stent implantation: Strut conforming to the “preserved box” subcategory as visible by OCT (A, B) and corresponding histological photomicrographs (C, D and E). Location of bioresorbed struts are readily visible in histological sections stained with standard hematoxylin and eosin, but material staining positively for Alcian blue filled in the regions previously occupied by the struts. (proteoglycan, E)

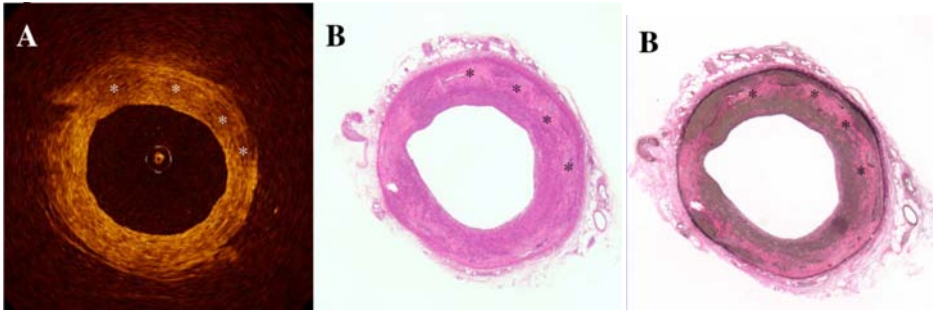


Figure 6. OCT image and histology at 3 years after stent implantation: Struts are suspected to be present as dissolved black box (A) and are hardly discernible by histology (B: Hematoxylin and eosin, C: elastic Van Gieson staining). Poorly defined regions of low signal intensity visible by OCT correspond with regions of low cell-density connective tissue visible by histology (asterisks in B and C). These regions may indicate prior locations of bioreabsorbed BVS struts.

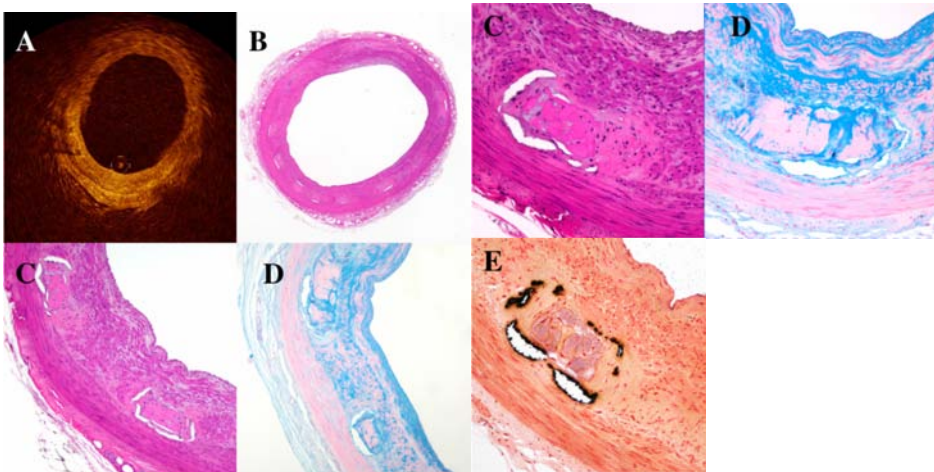


Figure 7. OCT image and histology at 3 years after stent implantation: Struts clearly conforming to “preserved box” subcategory are visible on OCT only at 8 and 9 o’clock. These preserved boxes were accompanied with shadowing effect. (A) Corresponding histological photomicrographs (B, C, D, E). As compared to 2 years, strut footprints now coalesced with the surrounding tissue. With Alcian Blue staining, struts have been replaced by connective tissue cells admixed in a proteoglycan matrix (D). Staining with Van Kossa demonstrates minimal calcification outlining the sites previously occupied by the polymeric struts. (E).

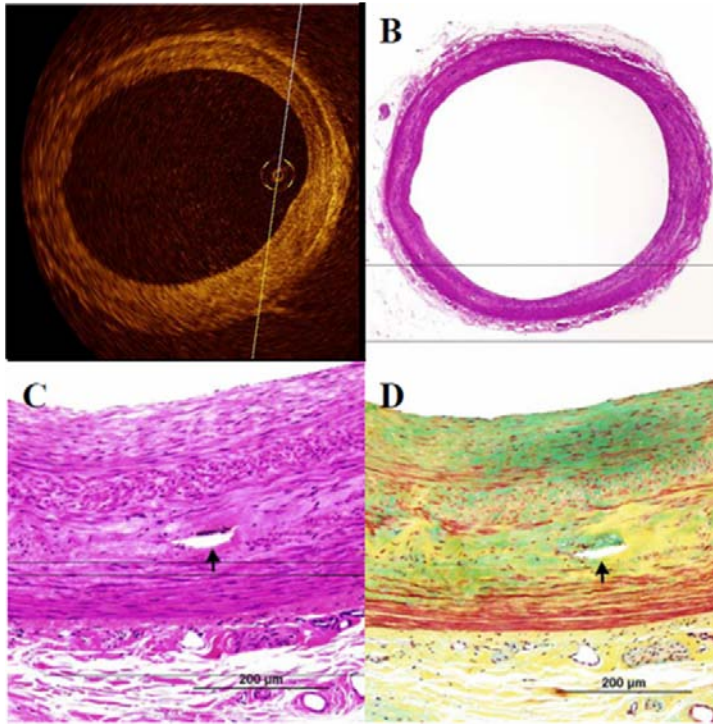


Figure 8. OCT image and histology at 4 years after implantation: Struts are no longer discernible by either OCT (A) or by histology using HE (B, C). Locations in the arterial wall suggestive of prior strut location are minimally discernible with Movat's Pentachrome staining (D), which are illustrated by focal regions of low smooth muscle cell density. Scant remnant calcification (arrow), now less notable as compared with that observed at 2 and 3 years, is the solitary evidence remaining of prior strut.

CHAPTER 8.1

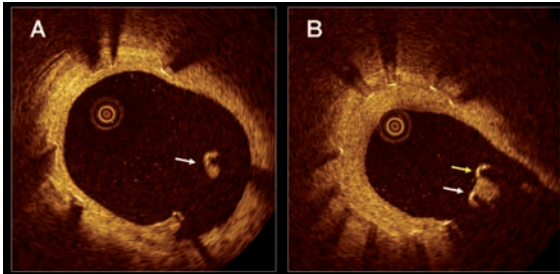


Figure 1. Incomplete stent apposition in optical coherence tomography. A: example of a malapposed strut covered by tissue (white arrow). B: example of malapposed struts in relation with a side-branch. One of the struts is covered by a thin layer of tissue (white arrow) while in the other no tissue coverage is visible (yellow arrow).

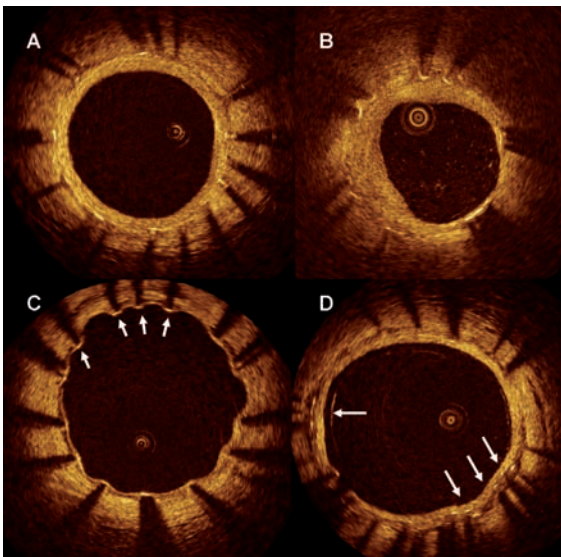


Figure 2. Tissue coverage at follow up in drug eluting stents. A: Symmetric tissue coverage: all the struts are covered by a layer of tissue of similar thickness. B: asymmetric tissue coverage: some struts are covered by a thick layer of tissue while in others (white arrows) only a small layer of tissue coverage is visible. C: the majority of struts are covered by a thin layer of tissue while some (white arrows) do not show visible tissue coverage. D: overlap region. All the struts are covered but some of them (white arrows) are surrounded by a heterogeneous low backscattering material.

Colour Section

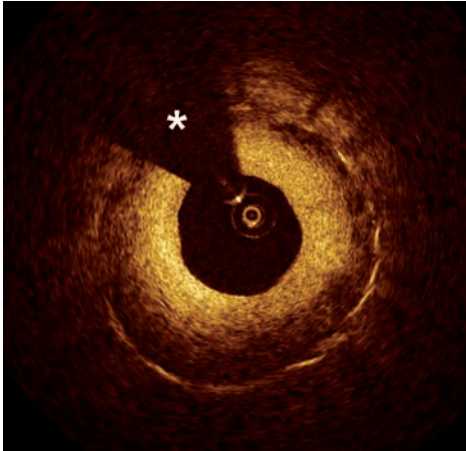


Figure 3. Stent restenosis. Stent restenosis 4 months after implantation of a drug eluting stent. Note the layered appearance of the restenotic tissue with a inner high backscattering layer and an external low backscattering layer. * guidewire artifact.

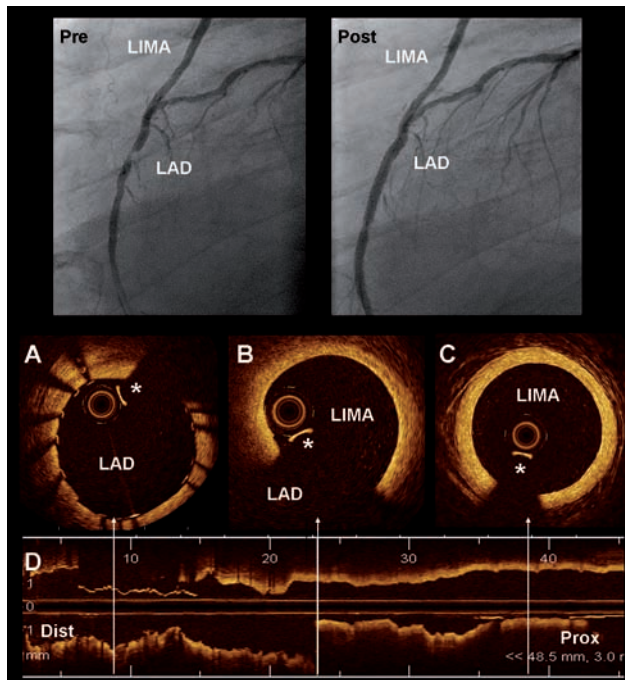


Figure 4. Optical coherence tomography (OCT) visualisation of left internal mammary artery (LIMA). The superior panel shows the angiogram of a patient with a graft of LIMA to the LAD. The left panel (Pre) shows a significant lesion on the LAD distal to the anastomosis of the LIMA. The right panel (Post) shows the result after implantation of a stent in the LAD. A: OCT cross section of the LAD with the implanted stent. B: OCT cross section on the region of the anastomosis of the LIMA to the LAD. C: OCT image of the LIMA that shows only intimal thickening without signs of significant atherosclerosis disease. D: longitudinal OCT view. The arrows indicate the location of the cross sections A, B and C. * Guidewire artifact

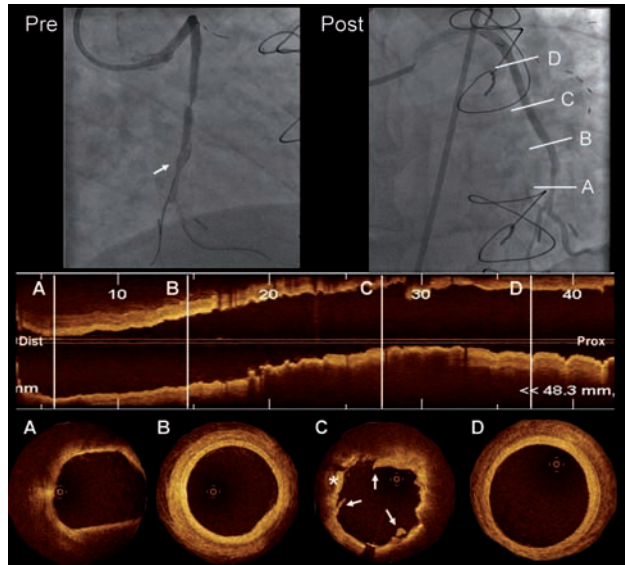


Figure 5. Optical coherence tomography (OCT) visualisation of saphenous vein graft (SVG) after stenting. Pre: angiogram showing a significant focal stenosis in a SVG to the obtuse marginal (white arrow indicates the distal protection device, FilterWire™). Post: angiographic result after treatment of the lesion with stent implantation. A to D show OCT longitudinal and cross sections images of the SVG after treatment. A: distal segment of the SVG showing low backscattering plaque with diffuse borders (suggestive of lipid content) but without significant lumen stenosis. B: SVG showing wall thickening (more pronounced at 5 o'clock). C: SVG in the stented region. The stent struts are well apposed and it can be observed the presence of tissue prolapse (*) and intrastent dissections (white arrows). D: OCT cross section of the proximal SVG segment. The vessel shows mono-layered appearance with minimal wall thickening and without signs of significant atherosclerotic disease. Dist: distal Prox: proximal.

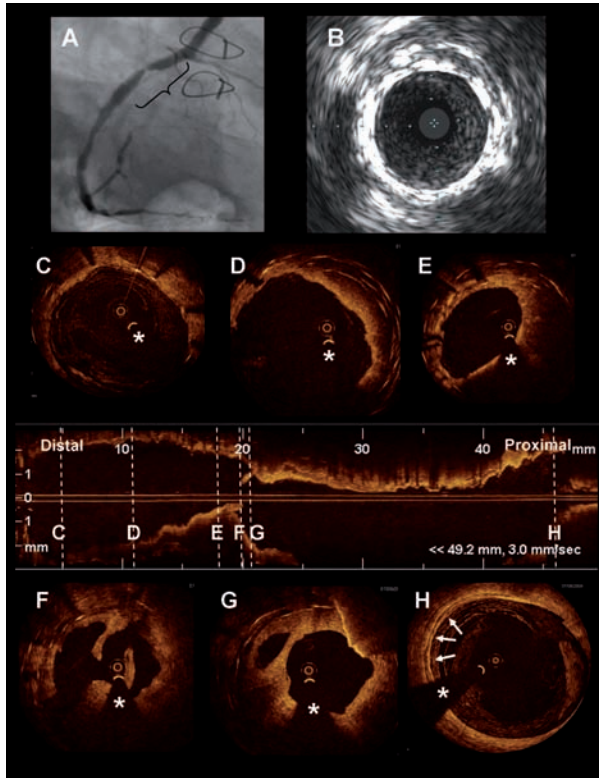


Figure 6. Saphenous vein graft restenosis imaged with optical coherence tomography. The figure shows the case of a patient treated with coronary artery bypass surgery in 1994. Saphenous vein grafts (SVG) were implanted in the LAD, diagonal, obtuse marginal and RCA. In 2003 and 2005 the patient underwent stent implantation in the SVG to the RCA for acute coronary syndrome. In 2008 the patient was referred to the catheterisation laboratory for stable angina. A: coronary angiogram showing a stent restenosis in the SVG to the RCA. B: IVUS image in the region of the restenosis showing different stent layers and severe neointimal growth. C to H show OCT longitudinal and cross sectional images of the SVG to the RCA. C: distal part of one of the stents previously implanted in the SVG. D: shows the different layers of stents previously implanted in the SVG. E: restenosis area. Multiple stent layers and severe neointimal growth are visible. F and G: restenosis area showing severe neointimal growth and irregular material protruding in the lumen. H: proximal venous graft showing a calcified plaque (white arrows) but without lumen stenosis. * Guidewire artefact.

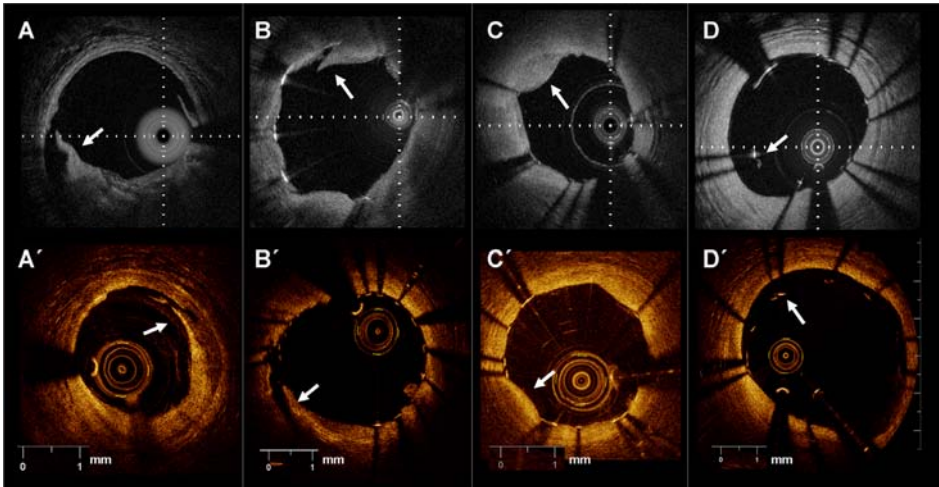
CHAPTER 9.1

Figure 2. Stent implantation assessment. Clinical examples of edge dissection (A, A'), intrastent dissection (B, B'), tissue prolapse (C,C') and malapposition (D, D') obtained with different Fourier Domain-OCT systems in different patients (upper panel Wellman Center for Photomedicine, MGH; lower panel Lightlab Imaging Inc)

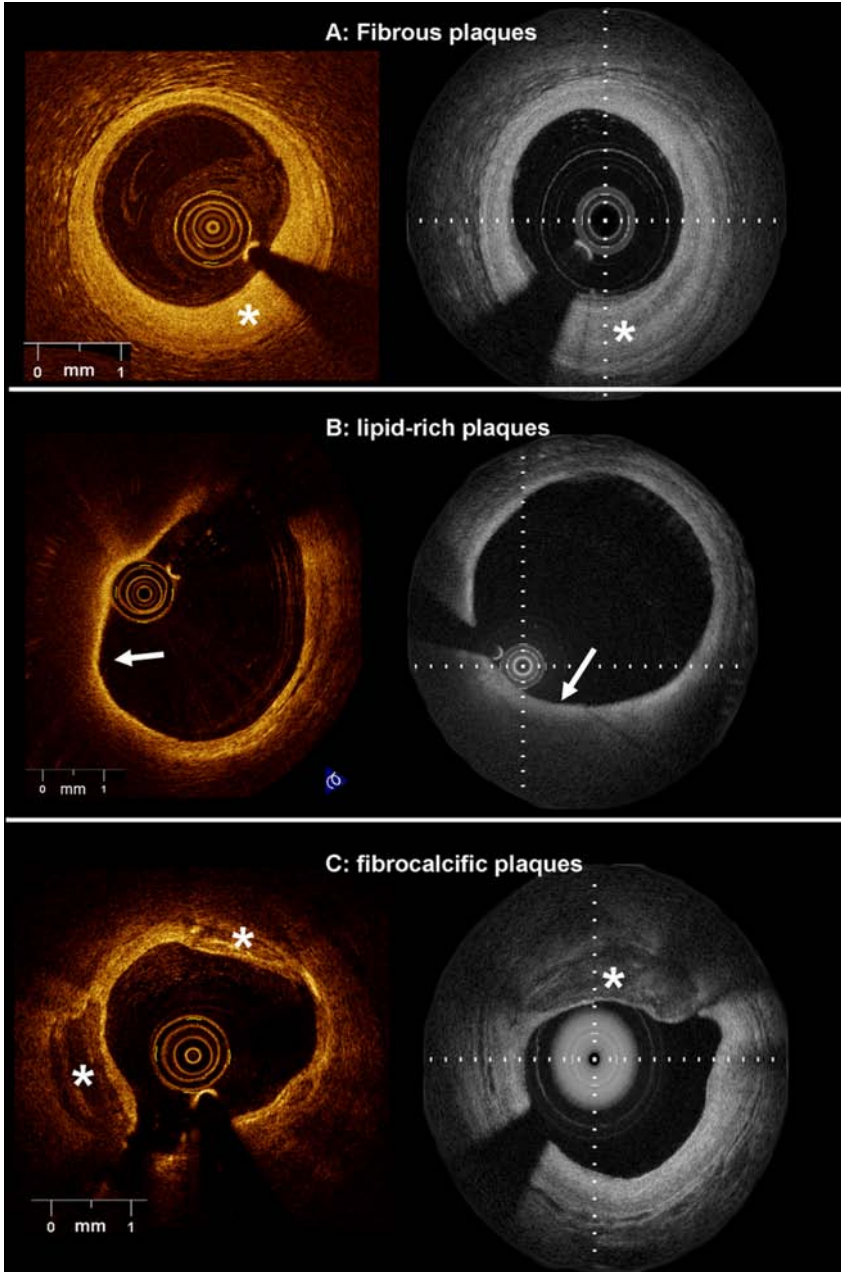


Figure 3. Examples of different plaque types obtained with two Fourier Domain-OCT systems in different patients. A. fibrous plaques (*) are visualized as homogeneous, high scattering regions. B. lipid rich plaques appear as low backscattering regions without sharp borders and usually covered by a fibrous cap (white arrow). C. fibrocalcific plaques (*) appear as low backscattering regions with sharp well delineated borders.

(left panel Lightlab Imaging Inc; right panel Wellman Center for Photomedicine, MGH)

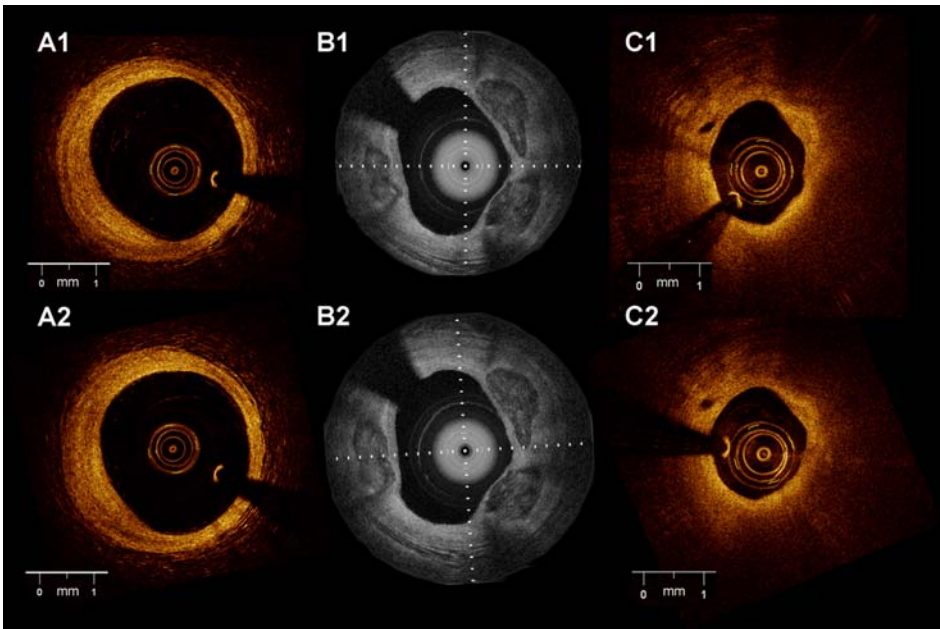


Figure 4. Inter-study reproducibility for plaque characterization: The figure shows corresponding images of the same plaques obtained in two different pullbacks in the artery. A1 and A2: fibrous plaque. B1 and B2: fibrocalcific plaque C1 and C2: lipid-rich plaque (A and C Lightlab Imaging Inc; B Wellman Center for Photomedicine, MGH).